NASA/CP-1999-209101/PT1

First International Symposium on Strain Gauge Balances

Edited by
John S. Tripp and Ping Tcheng
Langley Research Center, Hampton, Virginia

Proceedings of a symposium sponsored by the
National Aeronautics and Space
Administration, Washington, D.C.,
and held at Langley Research Center,
Hampton, Virginia
October 22–25, 1996

National Aeronautics and
Space Administration

Langley Research Center
Hampton, Virginia 23681-2199

March 1999

Acknowledgments

The following individuals assisted in preparation and execution of the symposium program: Thomas C. Moore, Alice T. Ferris, Risé W. Ramsey, Tammy L. Seward, Jennifer D. McCardell, Cristina L. Rector, Warren C. Higgs, Pamela J. Verniel, Mark W. Frye, Ray D. Rhew, Paul W. Roberts, Jerome T. Kegelman, and Robert A. Kilgore.

The undersigned editors wish to dedicate these proceedings to their colleague, Frank L. Wright, Boeing Commercial Airplane Group, who passed away in October 1998.

Ping Tcheng, General Chairman

John S. Tripp, Technical Chairman

Available from:

NASA Center for AeroSpace Information (CASI)
7121 Standard Drive
Hanover, MD 21076-1320
(301) 621-0390

National Technical Information Service (NTIS)
5285 Port Royal Road
Springfield, VA 22161-2171
(703) 605-6000

Executive Summary

The concept of an international strain gauge balance symposium was advocated in a technology assessment entitled "A White Paper on Internal Strain Gauge Balances." An internal document published by NASA Langley Research Center (LaRC) staff members in March 1995, this white paper was based on an international survey of internal strain gauge balances conducted under contract in 1994-1995 (ref. 1). The conclusions of the white paper were presented to a peer review panel on wind tunnel testing technology, composed of selected leaders from major commercial and government aeronautical facilities, held in July 1995 at LaRC. The panel strongly endorsed the proposed international strain gauge balance symposium, which was the first of its kind.

Based on the 1995 peer review endorsement, the first International Symposium on Strain Gauge Balances was sponsored under the auspices of the LaRC during October 22-25, 1996. Held at the LaRC Reid Conference Center, Hampton, Virginia, the Symposium provided an open international forum for presentation, discussion, and exchange of technical information among wind tunnel test technique specialists and strain gauge balance designers. The Symposium also served to initiate organized professional activities among the participating and relevant international technical communities. The program included a panel discussion (summarized in the Appendix), technical paper sessions, tours of local facilities, and vendor exhibits.

Over 130 delegates from 15 countries were in attendance, including Australia, Canada, China, Finland, France, Germany, India, Indonesia, Israel, the Netherlands, Russia, South Africa, Sweden, United Kingdom, and the United States. The program opened with a panel discussion, followed by technical paper sessions, and guided tours of the National Transonic Facility (NTF) wind tunnel, a local commercial balance fabrication facility, and the LaRC balance calibration laboratory. Vendor exhibits were also available.

The opening panel discussion addressed "Future Trends in Balance Development and Applications." The nine panel members included eminent balance users and designers representing eight organizations and five countries. Formal presentation of papers in technical sessions followed the panel discussion. Forty-six technical papers were presented in 11 technical sessions covering the following areas: calibration, automatic calibration, data reduction, facility reports, design, accuracy and uncertainty analysis, strain gauges, instrumentation, balance design, thermal effects, finite element analysis, applications, and special balances. A general overview of the past several years' activities of the AIAA/GTTC (Ground Testing Techniques Committee) Internal Balance Technology Working Group was presented. At the conclusion of the Symposium, a steering committee representing most of the nations and several US organizations attending the Symposium was established to initiate planning for a second international balance symposium, to be held in 1999 in the UK.

A Summary Report of the First International Symposium on Strain Gauge Balances, by John S. and Ping Tcheng, NASA LaRC, was presented at the 81st Fluid Dynamics Panel Symposium on Advanced Measurement Technology held in Seattle, Washington, USA, 22-25 September 1997. This paper is attached as an appendix to these symposium proceedings.

Also attached are a group photograph taken during the symposium, an index of authors, and a roster of names and addresses of the registered delegates to the symposium.

Page intentionally left blank

Contents

Session 3 SPECIAL BALANCES
Chair: Eberhard Graewe, Daimler-Benz Aerospace, Germany

Session 4 ACCURACY AND UNCERTAINTY ANALYSIS
Chair: David Cahill, Sverdrup/AEDC, USA

Session 5 AUTOMATIC CALIBRATION
Chair: Frank L. Wright, Boeing Commercial Airplane Group, USA

Session 6 APPLICATIONS
Chair: Robin D. Galway, National Research Council of Canada, CANADA

PART 2*

Session 7 SPECIAL BALANCES II
Chair: Pieter Fuijkschot, National Aerospace Laboratory, The Netherlands

Session 8 BALANCE DESIGN
Chair: Maurice Bazin, ONERA, France

Session 9 INSTRUMENTATION, STRAIN GAUGES, AND THERMAL EFFECTS
Chair: Paul W. Roberts, NASA Langley Research Center, USA

*Part 2 is presented under separate cover.

Author Index

List of Attendees

Page intentionally left blank

International Symposium on Strain Gauge Balances

NASA Langley Research Center, October 22-25, 1996

Registered US Delegates

Name	Affiliation	Street Address	City	FAX, email
Adcock, Jerry B.	NASA LaRC	MS 267	Hampton, VA 23681	PH:757-864-5135
Arnold, Vern		624 Island View	Fillmore CA 93015	FAX:805-524-1407 PH:805-524-1407
Bader, Jon	NASA Ames	MS 227-1	Moffett Field, CA 94035	jbader@mail.arc.nasa.gov
Baker, Wink	Lockheed Martin Tactical Aircraft Systems	PO Box 748	Ft. Worth, TX 76101	wmbaker@lmtas.lmco.com PH:817-763-1987
Belew, H. W. (Bud)	Dynamic Engineering, Inc., Huntsville Div.	9172 Hwy 36	Lacey's Spring, AL 35754	FAX:205-883-8660 PH:205-883-9277
Booth, Dennis	Microcraft Technol	3050 Pacific Hwy	San Diego, CA 92101	dbooth@microcraft.com
Brewster, Rick	Sverdrop Tech.	MS 213-5, NASA Ames	Moffett Field, CA 94035	brewster@crusher.arc.nasa.gov PH:415-604-1581
Broeren, Andy	University of Illinois	Dept. of Aero/Astro Engineering, 306 Talbot Lab, 104 S. Wright St.	Urbana, IL 61801	broeren@uiuc.edu FAX:217-244-0720 PH:217-244-3128
Burner, Alpheus W.	NASA LaRC	MS 236	Hampton, VA 23681	a.w.burner@larc.nasa.gov FAX:757-864-7607 PH:757-864-4635
Cahill, David M.	Sverdrup Technology Inc./AEDC Group	740 Fourth St.	Arnold AFB, TN 37389-6001	cahill@hap.arnold.af.mil FAX:615-454-7640 PH:615-454-6725
Clark, Edward L.	Sandia National Labs	3900 Pitt St., NE	Albuquerque, NM 87111	edlclark@aol.com PH:505-296-4541
Creekmore, Murrel	Lockheed Martin Aeronautical Systems	1055 Richardson Rd.	Smyrna, GA 30080	FAX:770-494-4790 PH:770-494-5619
Crooks, Richard S.	Microcraft San Diego	3050 Pacific Hwy	San Diego, CA 92101	RCrooks@microcraft.com FAX:619-683-8910 PH:619-683-8900 Ext 101
Davis, Tim	Modern Machine & Tool Co., Inc.	11844 Jefferson Avenue	Newport News, VA 23606	mmtool@aol.com
DeLoach, Richard	NASA LaRC	MS 236	Hampton, VA 23681	FAX:757-864-7607 PH:757-864-4657
Delcarpio, Danny	The Boeing Co.	P.O. Box 3707	Seattle, WA 98124-2207	danny.delcarpio@boeing.com FAX:206-655-1042 PH:206-655-2765
Ferris, Alice T.	NASA LaRC	MS 238	Hampton, VA 23681	a.t.ferris@larc.nasa.gov FAX:757-864-7607 PH:757-864-4702
Frisoli, Michele	National Technical Systems	Rye Canion Research, Dev., and Test Center, Building 202, 25100 Rye Canion Road, Bldg 202	Valencia, CA 91355	wndtnnl@aol.com FAX:805-257-3539 PH:805-259-8184
Garrell, Andrew F.	Calspan SRL Corporation	P. O. Box 400, 4455 Genesee Street	Buffalo, NY 14225	garrell@calspan.com FAX:716-631-4175 PH:716-631-6724
Gray, David L.	NASA LaRC	MS 236	Hampton, VA 23681	d.l.gray@alrc.nasa.gov FAX 757-864-7607
Hatten, Steven	Boeing Commercial Airplane Group	MS 1W-02, P.O. Box 3707	Seattle, WA 14225	steven.a.hatten@boeing.com FAX:206-655-0523 PH:206-655-0011
Heaman, John P.	NASA Marshall Space Flight Center	Experimental Facilities Branch, ED 34,	Huntsville, AL 35812	john.heaman@msfc.nasa.gov FAX:205-544-9358
Hemsch, Dr. Michael J.	Lockheed Martin	MS 267 NASA Langley	Hampton, VA 23681-0001	m.j.hemsch@larc.nasa.gov

Name	Affiliation	Street Address	City	FAX, email
Hertzler, Jim	Modern Machine & Tool Co., Inc.	11844 Jefferson Avenue	Newport News, VA 23606	j.a.hertzler@larc.nasa.gov FAX:757-873-8239 PH:757-873-8228
Higgs, Warren C.	NASA LaRC	MS 238	Hampton, VA 23681	w.c.higgs@larc.nasa.gov FAX:757-864-7607 PH:757-864-4706
Holmes, Harlan K.	Holmes Enterprises, Inc.	106 Normandy Lane	Newport News, VA 23606	FAX:757-930-2400 PH:757-930-2400
Hudgins, Mark	The Boeing Company	Mail Stop 1W-82, P.O. Box 3707	Seattle, WA 98124-2207	m.s.hudgins@boeing.com
Hultberg, Randy	Bihrle Applied Research	18 Research Drive	Hampton, VA 23666	FAX:757-766-9227 PH:757-766-2416
Jordan, Thomas L.	NASA LaRC	MS 237	Hampton, VA 23681	t.l.jordan@larc.nasa.gov FAX:757-864-7607
Kahng, Seun K.	NASA LaRC	MS 235	Hampton, VA 23681	s.k.kahng@larc.nasa.gov FAX:757-864-7607
Kammeyer, Mark E.	McDonnell Douglas	MC 5102-2272 P.O. Box 516	St Louis, MO 63166	
Kassaee, Ahmad	University of Maryland	Glenn L. Martin Wind Tunnel Bldg 081	College Park, MD 20742	kassaee@windvane.umd.edu FAX:301-314-9628 PH:301-405-6861
Kegelman, Dr. Jerome T.	NASA LaRC	MS 238	Hampton, VA 23681	j.t.kegelman@larc.nasa.gov FAX:757-864-7607
Kelly, Joel	Modern Machine & Tool Co., Inc.	11844 Jefferson Avenue	Newport News, VA 23606	mmtool@aol.com FAX:757-873-8239 PH:757-873-1212
Kilgore, Dr. Robert A.	CES - Hampton	P. O. Box 4006	Hampton, VA 23664-0006	RAKilgore@aol.com FAX:757-851-5212
Kilgore, W. Allen	Calspan Langley Operations	MS 267 NASA Langley	Hampton, VA 23681	w.a.kilgore@larc.nasa.gov
Kutney, John T., Sr	KCS - COS - Inc.	110 Wentworth Avenue	Cincinnati, OH 45215	FAX:513-821-3789 PH:513-821-3789
Lafferty, John F.	Naval Surface Warfare Center	10901 New Hamphire Ave.	Silver Spring, MD 20903	jlaffer@nswc.navy.mil PH:301-394-1750
Lindell, Michael C.	NASA LaRC	MS 431	Hampton, VA 23681	m.c.lindell@larc.nasa.gov
Lockwood, Chris	Calspan SRL Corporation	MS 207-2 NASA Ames	Moffett Field, CA 94035	clockwood@mail.arc.nasa.gov
Meadors, Brent G.	Modern Machine & Tool Co., Inc.	11844 Jefferson Avenue	Newport News, VA 23606	mmtool@aol.com FAX:757-873-8239 PH:757-873-1212
Mitchell, Dr. James	Microcraft, Inc.	207 Big Springs Ave, P.O. Box 370	Tullahoma, TN 37388	jmitchell@microcraft.com FAX:615-455-7060 PH:615-455-2617 Ext 213
Moore, Thomas C.	NASA Langley	MS 238	Hampton, VA 23681	t.c.moore@larc.nasa.gov FAX:757-864-7607 PH:757-864-4703
Muhlstein, Lado, Jr	NASA Ames	Mail Stop 227-4	Moffett Field, CA 94035-1000	lmuhlstein@mail.arc.nasa.gov
Ogden, Tony	NASA Ames			togden@mail.arc.nasa.gov
Paeschliman, Dan	Sandia			d.paesch@sandia.gov FAX:505-844-4523
Parker, Peter	Modern Machine & Tool Company Incorporated	11844 Jefferson Avenue	Newport News, VA 23606	peter.a.parker@larc.nasa.gov
Patel, Naresh R.	Modern Machine & Tool Company Incorporated	11844 Jefferson Avenue	Newport News, VA 23606	mmtool@aol.com FAX:757-873-8239 PH:757-873-1212
Paulk, Bob	Sverdrup Technology, Inc	760 Fourth Street	Arnold AFB, TN 37389-6001	FAX:615-454-7640 PH:615-454-3863
Pochel, Cathy	NASA Ames	Mail Stop 227-5	Moffett Field, CA 94035-1000	cpochel@mail.arc.nasa.gov
Price, Barry L.	NASA LaRC	MS 238	Hampton, VA 23681	b.l.price@larc.nasa.gov FAX:757-864-7607

Name	Affiliation	Street Address	City	FAX, email
Putnam, Lawrence E.	NASA LaRC		Hampton, VA 23681	PH:757-864-5116
Rhew, Ray D.	NASA LaRC	MS 238	Hampton, VA 23681	r.d.rhew@larc.nasa.gov FAX:757-864-7607 PH:757-864-4705
Richardson, Stan	Sverdrop/AEDC	760 Fourth Street	Arnold AFB, TN 37389-6200	RichardsonSG@hap.arnold.af.mil FAX:615-454-5432 PH:615-454-7283
Rivera, Jose A. Jr.	NASA LaRC	MS 340	Hampton, VA 23681	PH:757-864-1270
Roberts, Paul W.	NASA LaRC	MS 238	Hampton, VA 23681	p.w.roberts@larc.nasa.gov FAX:757-864-7607 PH:757-864-4704
Rock, Thomas, Lt.	NAIC/TANW USAF	2180 Watson Way	WPAFB, OH 45433	PH:513-257-8799
Rumble, Carl V.	Application Technology, Inc.	P.O. Box 9303	Hampton, VA 23670	FAX:757-722-3510 PH:757-722-6857
Sewall, J. W.	NASA LaRC	MS 373	Hampton, VA 23681	PH:757-864-4735
Shelton, P. Duane	Boeing Defense & Space Group	P.O.Box 3999 MS 86-11	Seattle, WA 98124-2499	shedp900@ccamil.ca.boeing.com
Singh, Dr. Jag J.	NASA LaRC	MS 235	Hampton, VA 23681	j.j.singh@larc.nasa.gov FAX:757-864-7607
Smith, Brooke C.	Eidetics Corporation	3425 Lomita Blvd	Torrance, CA 90505-5010	brooke@eideticscorp.com FAX:310-326-9358 PH:310-326-8228
Springfield, Robert D.	Northrop Grumman Corp.	8900 E. Washington Blvd., 9A21/GS	Pico Rivera, CA 90660-3737	FAX:310-948-8146 PH:310-942-5612
Steinle, Frank	AEDC			FRANK.STEINLE@ccmail.arnold.af.mil FAX:615-454-6317
Stewart, James R. (Rod)	Sverdrop Technology	1103 Ave B	Arnold AFB, TN 37389-1300	FAX:615-454-7741 PH:615-454-7221
Stokes, Thomas R.	Modern Machine & Tool Co., Inc.	11844 Jefferson Avenue	Newport News, VA 23606	mmtool@aol.com
Stryker, Doug	Calspan SRL Corp.	Transonic Wind Tunnel, 4455 Genesee Street	Buffalo, NY 14225	stryker@calspan.com FAX:716-631-4175 PH:716-631-6882
Suarez, C. J. ABSENT. Presented by Brooke Smith	Eidetics Corporation	3415 Lomita Blvd.	Torrance, CA 90505	eidetics@cerf.net FAX:310-326-9358
Tcheng, Dr. Ping	NASA LaRC	MS 238	Hampton, VA 23681	p.tcheng@larc.nasa.gov FAX:757-864-7607 PH:757-864-4717
Tinapple, Jon A.	U S A F , WL/FIMO	Bldg. 24C, 2145 Fifth Street, Suite 1	WPAFB, OH 45433-7005	tinappja@wl.wpafb.af.mil FAX:513-476-7652 PH:513-255-6032
Tinsley, Charles R. (Rick)	Sverdrop Technology	1103 Ave B	Arnold AFB, TN 37389-1300	FAX:615-454-7741 PH:615-454-6743
Tripp, Dr. John S.	NASA LaRC	MS 238	Hampton, VA 23681	j.s.tripp@larc.nasa.gov FAX:757-864-7607 PH:757-864-4711
Ulman, Richard J.	The Boeing Company	Mail Stop 1W-02, P.O. Box 3707	Seattle, WA 98124-2207	RICHARD.J.ULMAN@boeing.com FAX:206-655-1042 PH:206-655-4219
Van Aken, Johannes M.	Sterling Software	M/S T12-B, NASA Ames Research Center	Moffett Field, CA 94035	jvanaken@mail.arc.nasa.gov FAX:415-604-1089 PH:415-604-6668

Name	Affiliation	Street Address	City	FAX, email
Voss, Douglas J.	The Boeing Company	Mail Stop 1W-78, P.O. Box 3707	Seattle, WA 98124-2207	DOUGLAS.J.VOSS@boeing.com FAX:206-655-1042 PH:206-655-6270
Walker, Jimmy	Lockheed-Martin Aeronautical Systems	1055 Richardson Road	Smyrna, GA 30080	FAX:770-494-4790 PH:770-494-4218
Wilcox, Floyd J., Jr	NASA LaRC	MS 413	Hampton, VA 23681	PH:757-864-5593
Wilcox, Randall	Calspan Ames Operations	M/S 207-2, NASA Ames Research Center	Moffett Field, CA 94035-1000	rwilcox@mail.arc.nasa.gov FAX:415-968-8035 PH:415-604-6335
Wright, Frank L.	Boeing Commercial Airplane Group	P.O.Box 3707 MS 1W-82	Seattle, WA 98124-2207	FAX:206-655-1042 PH:206-655-4213
Yu, Dr. James C.	NASA LaRC	MS 235	Hampton, VA 23681	j.c.yu@larc.nasa.gov FAX:757-864-7607 PH:757-864-4755

International Symposium on Strain Gauge Balances
NASA Langley Research Center, October 22-25, 1996
Registered Foreign Delegates

Name	Affiliation	Street Address	City	Country	FAX/Phone
Alons, Henk-Jan	National Aerospace Laboratory NLR	Voorsterweg 31 8316 PR Marknene	1006 BM Amsterdam	THE NETHERLANDS	alonshj@nlr.nl FAX:31-527-248210 PH:31-527-248611
Baumann, Peter, H.	DLR	SM-SK, DLR Bunsenstr. 10,	D-37075 Goettinggen	GERMANY	Peter.Baumann@dlr.de FAX:49-551-709-2830 PH:49-551-709-2474/73
Bazin, Maurice	ONERA	B.P. 72,29 Avenue Division Leclere	F-92320 Chatillon	FRANCE	FAX:33-1-46-734144
Bock, Dr. Karl-Wilhelm	DLR	Abteilung Windkanaele Bunsenstr 10	D-37073 Goettingen	GERMANY	bock@gemini.wk.go.dlr.de
Bogdanov, Vasily V.	The Central AeroHydrodynamics Institute (TsAGI)	1 Zhukovsky Str.	Zhukovsky 140 160, Moscow Region	RUSSIA	buran@mx.iki.rssi.ru FAX:7-095-556-4335
Burkush, Shaya	Israel Aircraft Industries	Engineering Division	Ben Gurion Int'l Airport, Lod 70100, Dpt. 4455	ISRAEL	sburkush@engdiv.iai.co.il FAX:9723-935-4456 PH:9723-935-8570
Cheng, Yinghui	China Society for Aerodynamics, CARDC	P. O. Box 211	Mianyang, Sichuan Province	CHINA	FAX:0816-236-2490
Coulech, Vladimir	The Central AeroHydrodynamics Institute (TsAGI)	1 Zhukovsky Str.	Zhukovsky 140 160, Moscow Region	RUSSIA	Same as S. Fonov
Coulton, David G.	Aircraft Research Association, Ltd.	Manton Lane	Bedford MK41 7PF	U.K.	dgcoulton@ie.org.uk FAX:44-1234-328584 PH:44-1234-350681
Drouin, Gedeon	Defence Research Establishment Valcartier	2459 Pie-XI Blvd.	North Val-Belair QC G3J 1X5	CANADA	Gedeon.Drouin@drev.dnd.ca FAX:418-844-4502 PH:418-844-4425
Ewald, Prof. Bernd	Technical University of Darmstadt	Petersenstraße 30	D-64287 Darmstadt	GERMANY	ewald@HRZ2.HRZ.TH-Darmstadt.DE FAX:49-6151-16-2201 PH:49-6151-16-2490
Fagerstrom, Bo R.	Helsinki Univ. of Technology	Laboratory of Aerodynamics	Sahkomiehentie 4, FIN-02150 Espoo	FINLAND	Bo.Fagerstrom@hut.fi FAX:358-9-451-3418
Fariduzzaman	PUSIPIPTEK	Aero-Gas Dynamics and Vibration Laboratory (UPT-LAGG-BPPT), Serpong	Tangerang-15310	INDONESIA	itst@idola.net.id FAX:062-021-7560901 PH:062-021-7560902
Fonov, Serguei D.	The Central AeroHydrodynamics Institute (TsAGI)	1 Zhukovsky Str.	Zhukovsky 140 160, Moscow Region	RUSSIA	fonov@astris.msk.ru FAX:7-095-911-0019
Fuykschot, Pieter Herman	National Aerospace Laboratory NLR	P.O. Box 90502	1006 BM Amsterdam	THE NETHERLANDS	mahe@nlr.nl FAX:31-20-511-3210
Galway, Robert D. (Robin)	National Research Council of Canada	Institute for Aerospace Research, Aerodynamics Laboratory (Uplands)	Ottawa, Ontario K1A 0R6	CANADA	robin.galway@nrc.ca FAX:613-998-1281 PH:613-998-3410
Geldman, Chaim	Balance Technologies LTD.	MADID-DA, 46 Ben-Eliezer Street	Ramat-Gan 52290	ISRAEL	FAX:972-3-6772146
Gorbushin, Anton R.	Central AeroHydrodynamics Institute (TsAGI)	1 Zhukovsky Str.	Zhukovsky 140160, Moscow Region	RUSSIA	FAX:7-095-556-4329
Graewe, Eberhard	Daimler-Benz Aerospace	Airbus GmbH, Dep EFG	28283 Bremen	GERMANY	FAX:421-538-4999 PH:49-421-538-2215

Name	Affiliation	Street Address	City	Country	FAX/Phone
Gross, Uwe	Daimler Benz Aerospace	British Aerospace (Military Aircraft) Ltd., P.B. 801160	81663 München	GERMANY	
Gu, Xingruo	China Society for Aerodynamics, CARDC	P. O. Box 211	Mianyang, Sichuan Province	CHINA	FAX:0816-236-2490
Guo, Kaike	Beijing Institute of Aerodynamics	P. O. Box 7215	Beijing	CHINA	FAX:086-010-68374758
He, Dexin	China Society for Aerodynamics, CARDC	P. O. Box 211	Mianyang, Sichuan Province	CHINA	FAX:0816-236-2490
Hechler, Burkhard	Technical University of Darmstadt	Flughafenstrasse 19	D-64347 Griesheim	GERMANY	FAX:49- 6151-166-246 PH:49- 6151-166-210
Hufnagel, Klaus	Technical University of Darmstadt	Flughafenstrasse 19	D-64347 Griesheim	GERMANY	FAX:49-6151-16-2201 PH:49-6151-16-6200
Jermey, Chris	Aeronautical and Maritime Research Laboratory	DSTO, Air Operations Division, P.O. Box 1500	Salisbury, S. A. 5108	SOUTH AFRICA	
Johnson, Gustav Ingmar	FFA, The Aeronautical Research Institute of Sweden	Experimental Aerodynamics, P.O. Box 11021	S-161 11 Bromma	SWEDEN	FAX:46-8-253480
Joosen, Cor J. J.	Duits-Nederlandse Windtunnel (DNW)	Department of Instrumentation, P.O. Box 175	8300 AD Emmeloord	THE NETHERLANDS	cjoosen@nlr.nl FAX:31-527-24-8582
Kapoor, Kul Bhushan	National Research Council of Canada	Institute for Aerospace Research, M-10, Montreal Road	Ottawa, Ontario K1A 0R6	CANADA	FAX:613-592-7677 PH:613-990-7209
Kemppainen, Pasi	Helsinki Univ. of Technology	Laboratory of Aerodynamics	Sahkomiehentie 4, FIN-02150 Espoo	FINLAND	pasi.kemppainen@hut.fi PH:358-9-451-3429 FAX:358-9-451-3418
Kharitonov, Anatolii M.	ITAM, Russian Academy of Sciences	4/1 Instituteskaya Str.	Novosibirsk 630090	RUSSIA	khar@itam.nsc.ru
Kuzin, Alexander	Moscow Aviation Technological Institute	Petrovka 27	103737 Moscow	RUSSIA	kouzine@glas.apc.org
Lagutin, Vyacheslav I.	TSNIIMASH	Pionerskaia st. 4	Kaliningrad city, Moscow Region 141 070	RUSSIA	res@tsexp.msk.su FAX:7-095-513-4359
Lapygin, Vladimir I.	TSNIIMASH	Pionerskaia st. 4	Kaliningrad city, Moscow Region 141 070	RUSSIA	res@tsexp.msk.su
Law, Ron D.	Defence Research Agency - Bedford	High Speed & Weapon Aero. Dept., Bldg 17, Tunnel Site, DRA-Bedford	Bedford, MK41 6 AE	ENGLAND	FAX:44-1234-225-848 PH:44-1234-22-5950
Leslie G. Green	British Aerospace (Military Aircraft) Ltd.	5.5m L.S.W.T. (W175), Warton Aerodrome	Preston, Lancashire PR4 1AX	ENGLAND	FAX:44-1772-855501 PH:44-1772-852802
Levin, Dr. Daniel	Technion Israel Institute of Technology	Department of Aerospace Engineering, Technion City	Haifa 32 000	ISRAEL	aerdldl@aerodyne.technion.ac.il
Levkovitch, Michael	Israel Aircraft Industries	Engineering Division, Dept. 4451	Ben Gurion Int'l Airport, Lod 70100, Dpt. 4451	ISRAEL	mlevko@engdiv.iai.co.il FAX:972-2-9354456
Liao, Li Xin	Beijing Institute of Aerodynamics	P. O. Box 7215-14	Beijing	CHINA	FAX:086-010-68374758
Liu, Yufu	China Society for Aerodynamics, CARDC	P. O. Box 211	Mianyang, Sichuan Province	CHINA	FAX:0816-236-2490
Matheson, Neil	Aeronautical & Maritime Research Laboratory	Air Operations Divsion, GPO BOX 4331	Melbourne, Victoria 3001	AUSTRALIA	neil.matheson@dsto.defence.gov.au

Name	Affiliation	Street Address	City	Country	FAX/Phone
Murthy, H. Sundara	National Aerospace Laboratories	Experimental Aerodynamics Division, P.B. No. 1779	Bangalore 560 017	INDIA	FAX:91-80-527-3942 PH:91-80-526-4024
Panchenko, Ivan N.	The Central AeroHydrodynamics Institute (TsAGI)	1 Zhukovsky Str.	Zhukovsky 140 160, Moscow Region	RUSSIA	buran@mx.iki.rssi.ru FAX:7:095:556:4337
Pretorius, Ockert	CSIR Aerotek	PO Box 395	Pretoria, 0001	SOUTH AFRICA	opretori@csir.co.za FAX:27-12-349-1156 PH:27-12-841-4895
Quade, Matthias	Technical University of Darmstadt	Flughafenstrasse 19	D-64347 Griesheim	GERMANY	matthias@hrz2.hrz.th-darmstadt.de FAX:49-6151-16-6246 PH:49-6151-16-6208
Rajendra, G. CANCELLED	National Aerospace Laboratories	NTAF, Experimental Aerodynamics Division, P.B. No. 1779	Bangalore 560 017	INDIA	FAX:91-80-527-3942
Ramaswamy, Mathagondapally Aswathaiengar	Indian Institute of Science	Department of Aerospace Engineering	Bangalore 560 012	INDIA	maram@aero.iisc.ernet.in
Rao, Dr. Satheesh D.	Aerobalance Associate	96, 3rd Main, KEB Layout	Bangalore - 560 076	INDIA	FAX:91-80-6684937
Rebstock, Ruediger	DLR	Wind Tunnel Division, Kryo-Kanal Koln, Linder Hoehe	D-51147 Koeln	GERMANY	FAX:2203-695-961
Rosen, John T. N.	AKTIEBOLAGET ROLLAB	Box 7073	Järvstigen 5, S-171 07 Solna	SWEDEN	FAX:46-885-3632 PH:46-885-0315
Stock, J. R.	DRA Farnborough	5m Wind Tunnel, Building X80	Farnborough, Hampshire GU14 6TD	ENGLAND	FAX:01252-395275 PH:01252-395369
Vasudevan, Balasubramanian	Indian Institute of Science	Department of Aerospace	Bangalore 560 012	INDIA	vasu@aero.iisc.ernet.in
Wang, Chao-an	CAE SARI	P.O.Box 701	Shenyang 110034	CHINA	FAX:024-6520827
Yin, Liming	Changsha Institute of Techology	Automatic Control Department of CIT, Deya Road	Changsha, 410073, Hunan	CHINA	FAX:086-0731-451-8307
Zhai, Junnai	Technical University of Darmstadt	Petersenstraße 30	D-664287 Darmstadt	GERMANY	FAX:49-61-51-16-2201
Zhang, Yingpei	China Society for Aerodynamics, CARDC	P. O. Box 211	Mianyang, Sichuan Province	CHINA	FAX:0816-2362490

CALIBRATION OF MULTICOMPONENT STRAIN GAUGE BALANCES USING METHOD OF OPTIMUM EXPERIMENT PLANNING

Vladimir S.Krivoruchenko, Ivan N.Panchenko
Central Aerohydrodynamic Institute (TsAGI)
Zhukosky, Moscow region, Russia

Let's consider under the term «calibration of aerodynamic balances» the experiment aimed to search of a functional relation between loads applied to balances and readings of a measuring equipment. The goal of this experiment is an attainment of operational calibration formulas of balances having a nominated precision at a maximum reduction of a total time for calibration, i.e. reduction of a total number of loading combinations. The totality of all loading combinations, applied within one calibration, we'll name the plan of an experiment.

The traditional methodology of multicomponent aerodynamic balances calibration conduction comprises doubled conduction of single calibrations for each component. Readings are taken during direct and inverse loading processes in differently located points. Using results of single calibrations main coefficients and terms describing influence of separate components are determined. For the determination of corrections from twin interactions additional calibrations with additional loadings are conducted.

As its disadvantage may be considered long duration and difficulty of calibrations since as a result the main part of experimental data doesn't include considerable information for getting coefficients in operation formulas. Besides that, during calibration using traditional methodology there is not envisaged calculation of coefficients reflecting interactions of more higher orders.

There are existing methodologies of calibrations conduction based on application of arbitrary combinations of loads with consequent results procession using least square method. Let's name X - vector of independent variables (loads) matrix, Y - vector of observations, B - vectors with elements being coefficients of regression equation. In a matrix form solution of a system of equations has the following form:

$$(X`X)*B=X`*Y$$
$$(X`X)^*(X`X)*B=(X`X)^*(X`Y)$$
$$B=(X`X)^*(X`*Y)$$

where (X`X) is a matrix reverse to a matrix (X`X).

But, as it's known, despite a good least square approximation of a function as a whole, greatly correlated evaluations of coefficients in a regression equation don't reflect real process of separate variables variation. Consequently variation of a polynomial order or omitting in it even a part of terms leads to variation of numerical values of all regression coefficients. Such uncertainty in regression coefficients evaluation makes difficult their physical interpretation. This uncertainty can be avoided if to use methods of optimum planning of experiments. These methods

particularly include a plan of an overall factorial experiment which for K - component balances represents $N=2^K$ different loading combinations and loads' values are equal to limit values within a variation interval.

For all that (X`X) matrix becomes a diagonal one and all its elements are equal to 1/N and coefficients B=(1/N).(X`.Y) are determined independently. Therefore such kind of planning is also called an orthogonal one.

Since each regression coefficient for all components is evaluated by results of all N readings, the dispersion in coefficients evaluation is N times less than the dispersion for a single measurement error. Using a traditional methodology the factors were varied independently and, naturally, in evaluation of each regression coefficients only a part of readings participates.

It can be said that this planning is optimum in the following sense:

1.All calculations are extremely simple

2.All regression coefficients are determined independently with the same minimum dispersion

3.operation formulas for different components are calculated with the same dispersion.

Let's illustrate all said above by a sample of a plan for three factors (components) X_1, X_2, X_3 and corresponding vectors of observations (results) Y. Loading ranges divided by components let's norm to the interval (-1/+1) using formulas

$$x=(X-X_0)/((X_{max}-X_{min})/2), \text{where } X_0=(X_{max}+X_{min})/2$$

Then the planning matrix X will be written in a form (here and below for shortening under an expression $X_1X_2X_3$ their multiplication is understood)

$$X=\begin{array}{cccccccc} x_0 & x_1 & x_2 & x_3 & x_1x_2 & x_1x_3 & x_2x_3 & x_1x_2x_3 \\ +1 & -1 & -1 & -1 & +1 & +1 & +1 & -1 \\ +1 & -1 & -1 & +1 & +1 & -1 & -1 & +1 \\ +1 & -1 & +1 & -1 & -1 & +1 & -1 & +1 \\ +1 & -1 & +1 & +1 & -1 & -1 & +1 & -1 \\ +1 & +1 & -1 & -1 & -1 & -1 & +1 & +1 \\ +1 & +1 & -1 & +1 & -1 & +1 & -1 & -1 \\ +1 & +1 & +1 & -1 & +1 & -1 & -1 & -1 \\ +1 & +1 & +1 & +1 & +1 & -1 & -1 & -1 \end{array}$$

transposed

$$X`=\begin{array}{cccccccc} -1 & -1 & -1 & -1 & +1 & +1 & +1 & +1 \\ -1 & -1 & +1 & +1 & -1 & -1 & +1 & +1 \\ -1 & +1 & -1 & +1 & -1 & +1 & -1 & +1 \\ +1 & +1 & -1 & -1 & -1 & -1 & +1 & +1 \\ +1 & -1 & +1 & -1 & -1 & +1 & -1 & +1 \\ +1 & -1 & -1 & +1 & +1 & -1 & -1 & +1 \\ -1 & +1 & +1 & -1 & +1 & -1 & -1 & +1 \end{array} \qquad Y=\begin{array}{c} y_2 \\ y_3 \\ y_4 \\ y_5 \\ y_6 \\ y_7 \\ y_8 \end{array}$$

(diag {8} is a diagonal matrix 8*8 with elements equal to 8)

Coefficients of a regression equation B are calculated according to formulas:

$$
B = \begin{array}{ll}
b_0 & (+Y_1+Y_2+Y_3+Y_4+Y_5+Y_6+Y_7+Y_8)/8 \\
b_1 & (-Y_1-Y_2-Y_3-Y_4+Y_5+Y_6+Y_7+Y_8)/8 \\
b_2 & (-Y_1-Y_2+Y_3+Y_4-Y_5-Y_6+Y_7+Y_8)/8 \\
b_3 & (-Y_1+Y_2-Y_3+Y_4-Y_5+Y_6-Y_7+Y_8)/8 \\
b_{12} & (+Y_1+Y_2-Y_3-Y_4-Y_5-Y_6+Y_7+Y_8)/8 \\
b_{13} & (+Y_1-Y_2+Y_3-Y_4-Y_5+Y_6-Y_7+Y_8)/8 \\
b_{23} & (+Y_1-Y_2-Y_3+Y_4+Y_5-Y_6-Y_7+Y_8)/8 \\
b_{123} & (-Y_1+Y_2+Y_3-Y_4+Y_5-Y_6-Y_7+Y_8)/8
\end{array}
$$

The regression equation will be the following:

$$Y= b_0 + b_1 * x_1 + b_2 * x_2 + b_3 * x_3 + b_{12}*x_1x_2 + b_{13} * x_1x_3 + b_{23} * x_2x_3 + b_{123} * x_1x_2x_3$$

By analogous way there may be constructed plans and made calculations for an every number of independent variables with a total number of loading combinations equal to $N=2^K$.

It can be easily seen that if in a plan matrix X to extract columns, corresponding to variables X_1, X_2, X_3 (i.e. the loading plan) and change values +1 to -1 and -1 to 0, then in lines we'll obtain a sequence (up-down) of binary numbers 0, 1, 2, 3.

x_1	x_2	x_3	N		x_1	x_2	x_3
0	0	0	0		x_{1min}	x_{2min}	x_{3min}
0	0	1	1		x_{1min}	x_{2min}	x_{3max}
0	1	0	2		x_{1min}	x_{2max}	x_{3min}
0	1	1	3	oder	x_{1min}	x_{2max}	x_{3max}
1	0	0	4		x_{1max}	x_{2min}	x_{3min}
1	0	1	5		x_{1max}	x_{2min}	x_{3max}
1	1	0	6		x_{1max}	x_{2max}	x_{3min}
1	1	1	7		x_{1max}	x_{2max}	x_{3max}

The complexity of calibrations is directly related to a total number of loadings (P), i.e. transitions from 0 to 1 and back. If one arranges the lines in a plan matrix not in order of binary numbers but in order of numbers sequence in Gray code, the complexity may be reduced almost two times. Each consequent number in Gray code differs from a previous one only in one digit.

Binary code

x_1	x_2	x_3	N	P	
0	0	0	0	0	
0	0	1	1	1	
0	1	0	2	2	
0	1	1	3	1	
1	0	0	4	3	
1	0	1	5	1	
1	1	0	6	2	
1	1	1	7	1	
0	0	0		3	bask to 0
Tottaly				14	

Gray code

x_1	x_2	x_3	N	P
0	0	0	0	0
0	0	1	1	1
0	1	1	2	1
0	1	0	3	1
1	1	0	4	1
1	1	1	5	1
1	0	1	6	1
1	0	0	7	1
0	0	0		1
Totally				8

When deriving calibration formulas for multicomponent aerodynamic balances the influences (or effects) of three or more components in the same time are usually neglected, i.e. there are neglected terms of the third order and the following regression model is used:

$$Y = b_0 + SUM\ (i=1,k)\ (b_i * x_j) + SUM\ (i, j=1,k \quad i<>J)\ (b_{ij} * x_i * x_j)$$

With an increase of factors the number of loadings in a total factorial experiment increases in an exponential way $N=2^K$. At the same time the number of coefficients in a regression model presented above increases by a paraboloidal law. Therefore there appears an excess of a number of loadings particularly if one remembers that not all twin influences are significant.

The number of loadings may be reduced using plans of fractional-factorial experiment. The main idea of this method is construction of orthogonal plans in which effects of higher order with a low probability of appearance are mixed with new independent variables (loads). So, in an example presented above, it's possible to restrict oneself only by terms of the first and second orders for components X_1, X_2, X_3 and introduce a fourths loading component X_4 in a plan matrix X instead of a product $X_1X_2X_3$ assuming also twin interactions of a X_4 component with other insignificant ones. Then the plan matrix X will have the following form:

	x_0	x_1	x_2	x_3	x_4	x_1x_2	x_1x_3	x_2x_3
	+1	-1	-1	-1	-1	+1	+1	+1
	+1	-1	-1	+1	+1	+1	-1	-1
	+1	-1	+1	-1	+1	-1	+1	-1
X=	+1	-1	+1	-1	-1	-1	-1	+1
	+1	+1	-1	-1	+1	-1	-1	+1
	+1	+1	-1	-1	-1	-1	+1	-1
	+1	+1	+1	-1	-1	+1	-1	-1
	+1	+1	+1	+1	+1	+1	+1	+1

Conducting calibrations and calculations using a methodology presented we'll obtain coefficients for four component balances with 8 loading combinations instead 16. But we suppose that influences $X_1X_2X_3X_4$, $X_1X_2X_3$, $X_1X_2X_4$, $X_2X_3X_4$, $X_1X_3X_4$,

X_2X_4 and X_3X_4 are insignificant, since during calculations they will be introduced correspondingly into coefficients B_0, B_4, B_3, B_1, B_2, B_{23}, B_{13}, B_{12} of a regression equation

$$Y= b_0 + b_1 * x_1 + b_2 * x_2 + b_3 * x_3 + b_4 + b_{12} * x_1 x_2 + b_{13} * x_1 x_3 + b_{23} * x_2 x_3$$

That means that compared with full equation

$$Y= b_0 + b_1 * x_1 + b_2 * x_2 + b_3 * x_3 + b_4 + b_{12} * x_1 x_2 + b_{13} * x_1 x_3 + b_{23} * x_2 x_3 +$$
$$+ b_{14} * x_1 x_4 + b_{24} * x_2 x_4 + b_{34} * x_3 x_4 + b_{123} * x_1 x_2 x_3 + b_{124} * x_1 x_2 x_4 + b_{234} * x_2 x_3 x_4 +$$
$$+ b_{134} * x_1 x_3 x_4 + b_{1234} * x_1 x_2 x_3 x_4$$

(which we could obtain after 16 loadings), we are neglecting last 8 terms and besides that we increase by $\sqrt{2}$ times an arbitrary error, but we reduce two times a calibration program.

For standard six component aerodynamic balances that means 32 (or even less) loading combinations instead 64 according to plan of a full factorial experiment.

The methodology of calibration tests conduction includes a sequential conduction of several calibrations. First calibration is conducted at maximum loads in a variation range according to a plan of a full factorial experiment. As a result the main coefficients, essential single and twin influences of other components are evaluated.

Selection of experiments' plans (total or fractional) and loads variation ranges for further calibrations is conducted on a basis of a necessity of a check of main coefficients linearity, specification of twin influences values and provision of required balances formulas errors.

As a rule the second calibration is conducted at variation ranges reduced two times. At the same time the comparison with obtained earlier values of regression coefficients is conducted in order to reveal second order non-linearities. If coefficients variations are insignificant, the calibration procedure is finished. If they are significant, the correction of equation coefficients is conducted. In order to reveal non-linearities sometimes it's needed to conduct up to six calibrations. Nevertheless even in these cases the total number of loading points is of the order of magnitude smaller compared to traditional methodology.

After calibrations conduction there is conducted an inversion of a system of equation with respect to readings of a measurement equipment and receiving of balances operation formulas in a standard form. An inversion procedure is presented in a report of Ivan N.Panchenko at this conference.

It appeared to be reasonable to use plans of a factorial experiment also for investigations of a calibration stand itself and also for another calibration equipment and for technology of their application.

Page intentionally left blank

THE DEVELOPMENT OF A MODERN MANUAL CALIBRATION AND MEASURING SYSTEM FOR INTERNAL BALANCES

Dipl.-Ing. Matthias Quade
Dr.-Ing. Klaus Hufnagel

Darmstadt University of Technology, Germany
Department of Aerodynamics and Measuring Techniques
Faculty for Mechanical Engineering

Abstract

Calibration of internal wind tunnel balances is a time consuming task. Therefore several approaches have been made to automate the process. Nevertheless there are facilities with few balances that do not need (or cannot afford) an automatic calibration machine. Those facilities do still have a need for manual calibration procedures. Many have purchased calibration software from the balance manufacturer, others have written their own procedures and some will work forever with the matrices that came along with the balance and never recalibrate the instrument.

This paper presents a manual calibration and measuring software that was developed with the following goals in mind:

- All routines necessary for a calibration should be in one program
- User friendly interface (GUI).
- Extensive on-line help
- Extensive error checking and mistake avoiding
- Quick look for calibration results
- Exchangeable data format
- Interface to an existing matrix calculation program
- Reuse data acquisition software for wind tunnel measurements
- Software should run on a widespread hardware and software platform

1 Introduction

Although the accuracy of force measurements is one of the most important issues in a wind tunnel, calibration of internal force balances after the initial calibration by the manufacturer is not very popular with the tunnel staff due to several reasons:

- the task is time consuming and, in case of larger balances, strenuous
- due to the long intervals between calibrations staff members have to get used to the calibration software and put together the pieces they need for the job

Several approaches have been made to shorten the time and manpower needed for a calibration by developing automatic calibration machines. Although these machines work successful they are expensive and there are facilities with few balances that do not need an automatic machine. If those facilities want a balance to be calibrated they can give it away. If they choose to make the calibration on their own they need (besides a calibration rig and dead-weights) a piece of software not necessarily provided by the manufacturer.

The department of Aerodynamics and Measuring Techniques of the Technical University of Darmstadt develops and manufactures internal wind tunnel balances since several years. Load ranges allowing, these balances are calibrated by the department. Calibration software was developed by different members of the department on different platforms. Older platforms like the HP86 or a 286-PC were very limited in computing power and memory sizes and forced the programmer to split the task in several parts and to restrict visualisation of data to the inevitable. The human interface consisted at best of some screen menus but mostly it was the simple question and answer scheme, documentation was rather rudimentary. Supported by an external contract we decided to gather our experience and build a program from scratch that combined all the elements needed for a calibration.

2 Basic Hardware and Software

Computer platforms and operating systems are rather short-lived compared to wind tunnel balances. Therefore enhancing existing software is not always possible and you have to consider the possible lifetime of a platform before you start the project. The Intel-486 or Pentium-based PC with its various Windows operating systems is a widespread affordable platform with a well-known user interface that probably will not vanish in the nearer future. For easier programming especially of the graphical user interface (GUI) and the data acquisition task we used a package by National Instruments called LabWindows/CVI. It consists mainly of an ANSI compatible C-compiler generating 32-bit code, an graphical editor for the user interface and several libraries for data acquisition and analysis in an integrated development environment. The finished program comes with a runtime module.

3 Contents of the program

The program can be used for calibration of a balance as well as for data acquisition in the wind tunnel.

In any case the user interface is consistent on every level, i.e. wherever possible the same types of controls (buttons, displays etc.) have been used for similar tasks to make orientation easier. Controls can be operated by mouse or keyboard.

The program supports the user by offering default values for inputs and by disabling controls that are unreasonable in that circumstance while maintaining configuration freedom at a certain degree.

Having in mind that working with a calibration program is an intermittent process one cannot expect that the user remembers the meaning of a control after a year or so. Therefore extensive on-line help is available for every step of calibration or data acquisition. Apart from a 'Help'-button in every panel (window) there is a popup help for every control in the panel.

Parameters entered for a calibration can be saved and automatically reloaded upon the next program start.

4 Structure of the program

4.1 Calibration process

The calibration process is divided into the following main segments:

- Preparation of a calibration
- Running through a calibration
- Analysis of a calibration

4.1.1 Preparing a calibration

This is the part of the program where the major part of the input has to be done. Most of the parameters do not change during a complete balance calibration (e.g. the balance parameters), some won't change forever (e.g. the g-constant of the calibration place and the masses of the dead-weights) while others have to be set for every series of loads. Therefore the parameters are divided in groups that can be changed individually. Groups used by the program are

- balance parameters
- load combination
- load point on the sleeve
- load steps to be applied
- measuring instrument settings
- stability settings for automatic acquisition

This is also the preferred order to enter the parameters which can be followed when entering parameters for a new balance. However the user is not bound to this order. On the other hand not all parameter groups are independent of each other, e.g. changing the load point on the sleeve with a given stack of dead-weights will alter the moment. With every change in a group of parameters the program cross-checks with relevant groups. Parameter groups that prevent the program from starting the calibration or that might damage the balance are marked in the main window. The program will not allow to start a calibration with insufficient parameters.

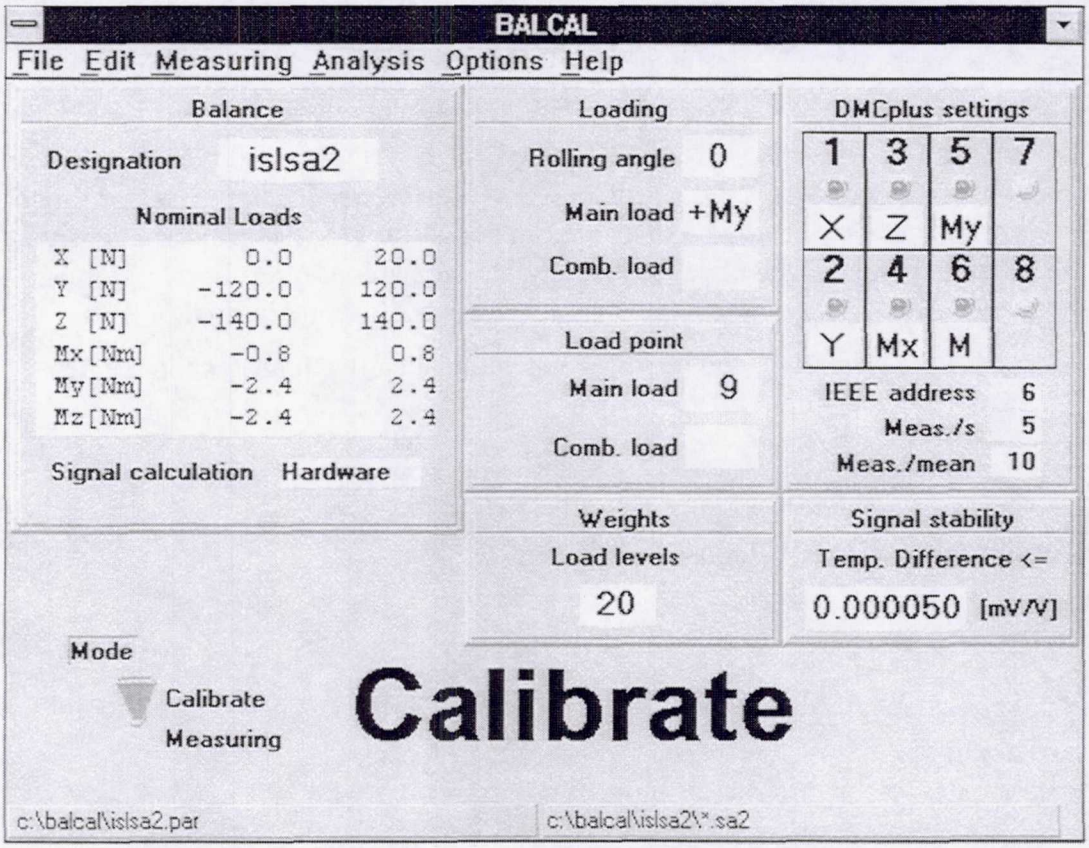

Fig. 1 Main window

Balance parameters include mechanical and electrical parameters.

- Mechanical parameters describe the load envelope of the balance.
  Although the program cannot prevent a user from inadvertently damage the balance by applying intolerable loads, it can warn on several occasions during the parameter input if the calculated loads extend the balance's boundaries. Different models for defining the envelope are offered (rectangle, rhombus, THD/DASA set of equations based on maximum allowed stress).
- Electrical parameters describe the wiring of the balance's bridges.
  This is necessary because there are balances that provide more signals than load components. The calculation of the load signal has to be done in the computer. These factors define how to combine balance signals to load signals. This information is necessary for the calculation of the matrix and for calculating forces and moments in the measuring mode.

Selection of the load combination, i.e. of the main and combined load, depends on the chosen rolling angle. This program version supposes that all loads with exception of the X-load (drag) are applied without pulleys in the Z-direction. Therefore only loads that can be generated under a given rolling angle are selectable.

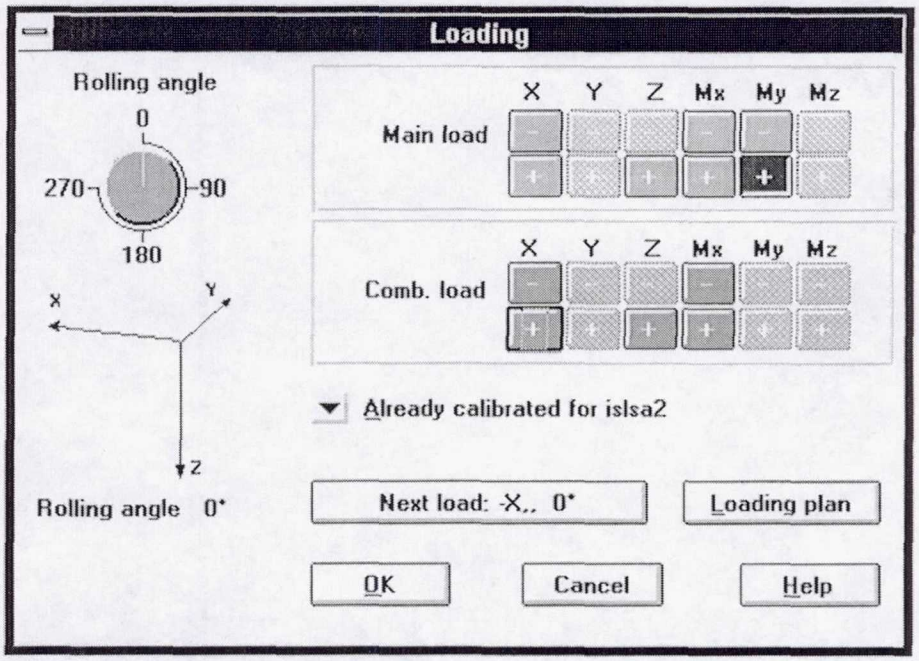

Fig. 2 Selection of load combination

The program then offers those (earlier defined) points on the sleeve that are able to generate the desired load, if there is more than one applicable point.

Defining and putting on dead-weights is based on the following principle: instead of entering a mass value or a dead-weight number during the calibration one defines the set of available dead-weights once. Every dead-weight in this set has a unique number. The user selects his stack of dead-weights for a load series from this set. During the calibration the user will be requested to put on a certain weight. While the dead-weights are selected the program calculates the generated forces generated and displays them with respect to the balance's boundaries. If boundaries are exceeded there are several warnings. However it is possible to calibrate the balance with this load.

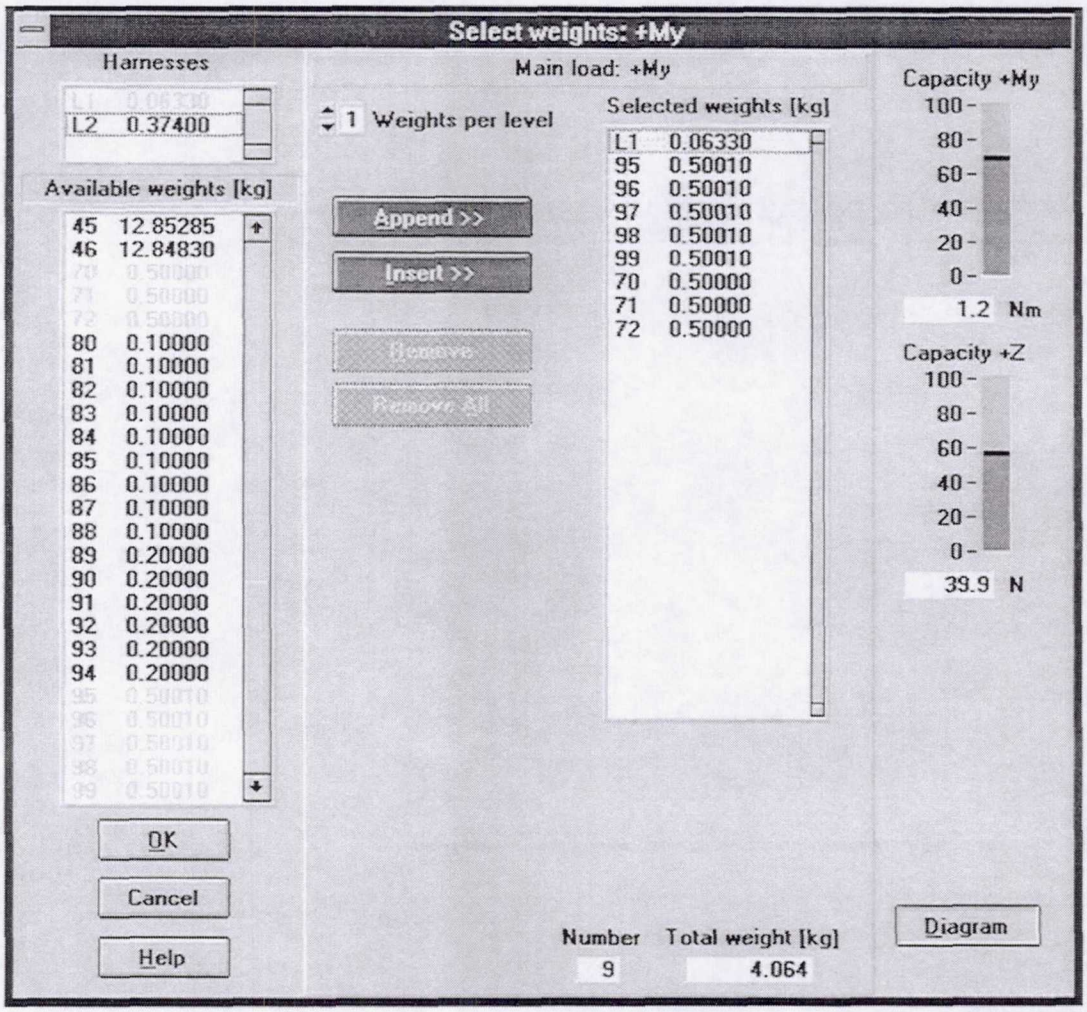

Fig. 3 Selection of load levels

Preparing the measuring instrument depends on the instrument used. In the current version the program supports a HBM DMCplus connected via an IEEE-488 bus. The DMCplus is a high resolution multichannel A/D system working with carrier frequency amplifiers. Apart from the instrument specific settings balance signals are assigned to instrument channels in this panel. This gives the opportunity to reconfigure the measuring system, should one channel become defective. Also sample frequency and samples per mean value are selectable. All settings are transmitted to the instrument prior to every calibration run. The operator has a chance to test his settings without starting an actual calibration run. A 'Signal Test' panel with a similar appearance to that of the calibration can be started to test connections and proper function of the measuring chain.

One of the unpleasant effects of dead-weight calibration is the pendulum oscillation of the weight stack induced by every weight applied or put off. The program offers during the calibration run several means to observe the incoming data. The user can try to dampen the oscillation according to this data displays. Above that he can set two signal derived limits that govern the automatic triggering of data logging. These are the differences between two

consecutive mean values of a signal (long-term stability) and the standard deviations of the latest mean values.

4.1.2 Calibration run

Supposed the program finds complete and valid parameters for a calibration, a run can be started. During a calibration run the user interacts basically with two panels. One that displays incoming data under different aspects and lets the user save a reading, the other requesting him to do some action like applying or putting off weights or load harnesses. The operator is guided through the process by these panels and the underlying code. He can observe the effect of applying weights on several graphic displays.

- Each averaged signal is displayed in an analogue meter and as a number.
- The standard deviation of every averaged signal is displayed as a number.
- Signal stability is displayed by bar graphs showing the difference of consecutive mean values or the standard deviation of the latest reading. The user defined stability limits are shown with the bar graphs and can be changed during the process.
- A strip chart display (optional) shows the incoming readings and their averaged values.
- A x-y graph (optional) depicts the current signals over force compared to the previous saved readings.

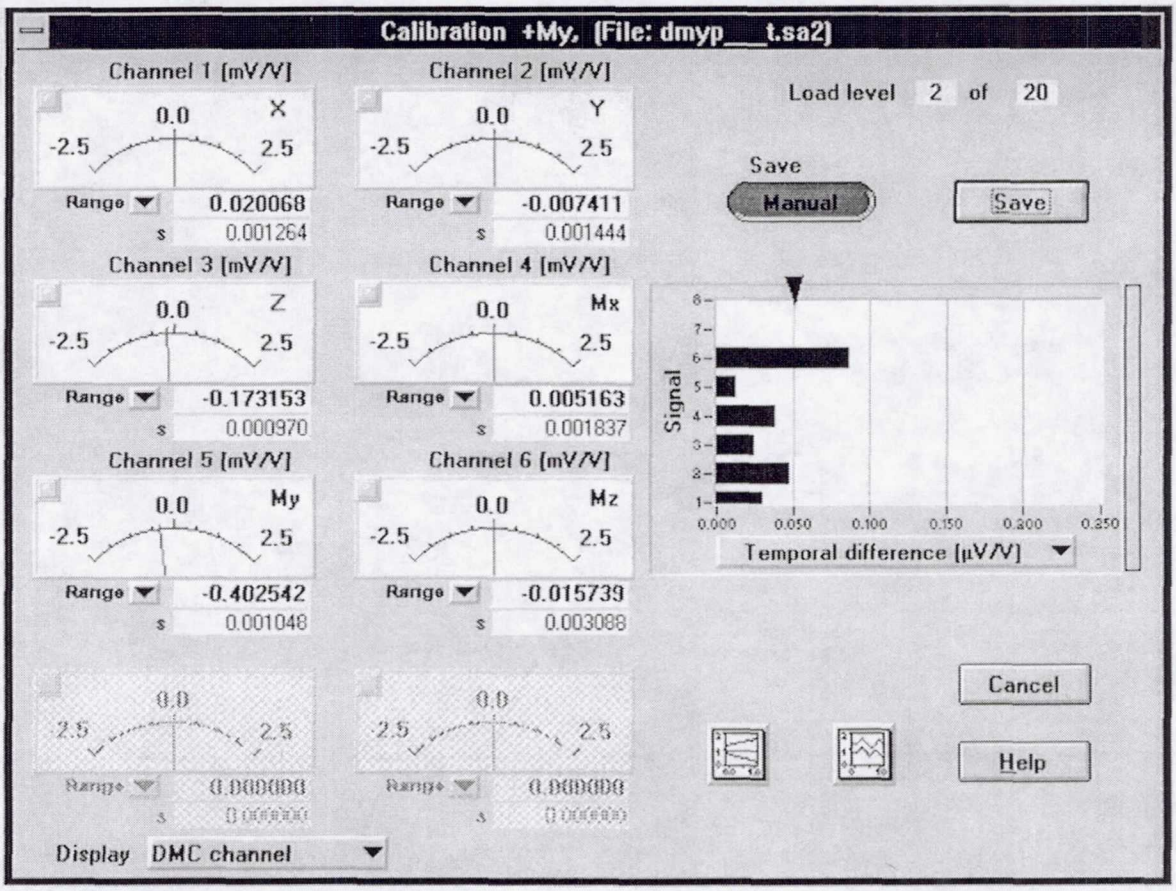

Fig. 4 Display of incoming signals

The operator can change the order of the meters to channel sequence, signal sequence and component sequence where the rules for combining balance signals to component signals (see above) are taken into account. Readings are always saved in signal sequence.

All the displays above help the operator to view the data from every possible angle during calibration in order to detect faulty data as early as possible.

Over years we observed that one major source of error is the operator himself. The calibration process can sometimes be boring and one distraction that leads to omitting a weight or an adjustment makes the calibration run worthless. So the panel that requests the operator to move a weight not only tells him the number of the weight and the action to carry out. It also shows an illustration how the weight stack should appear after the operation. Since signal reading is continued during the request panel the operator has also access to the meters and graphic displays. If he confirms the weight stack change the program calculates with a linear extrapolation the probable signal based on the previous load stages and warns the user if there is a too big difference to the real signal (wrong or no weight applied). Should the user detect an error only after registration of a reading (e.g. balance not adjusted) he can go one step back in the calibration run. All these methods help to avoid calibration run repeats.

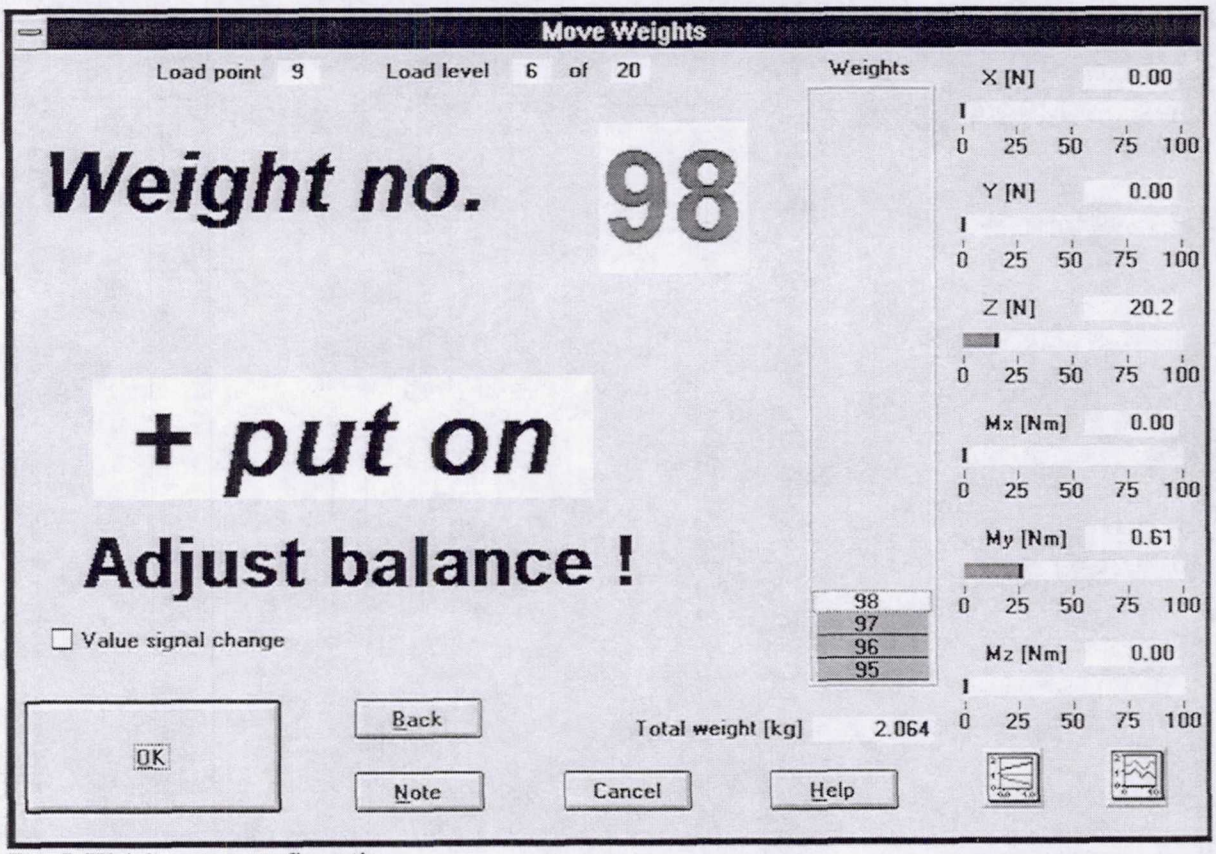

Fig. 5 Weight move confirmation

The data file generated by the calibration run is an ASCII-file designed so that it can be read easily by most spreadsheet programs (e.g. MS-Excel) should the user wish to evaluate the data in any way.

4.1.3 Analysis

The first analysis however can take place in the program itself. Measured signals are graphically displayed over applied forces. Polynomial approximations of first, second and third degree are calculated and the differences between measured values and approximations are depicted. For all approximations one can examine their coefficients.

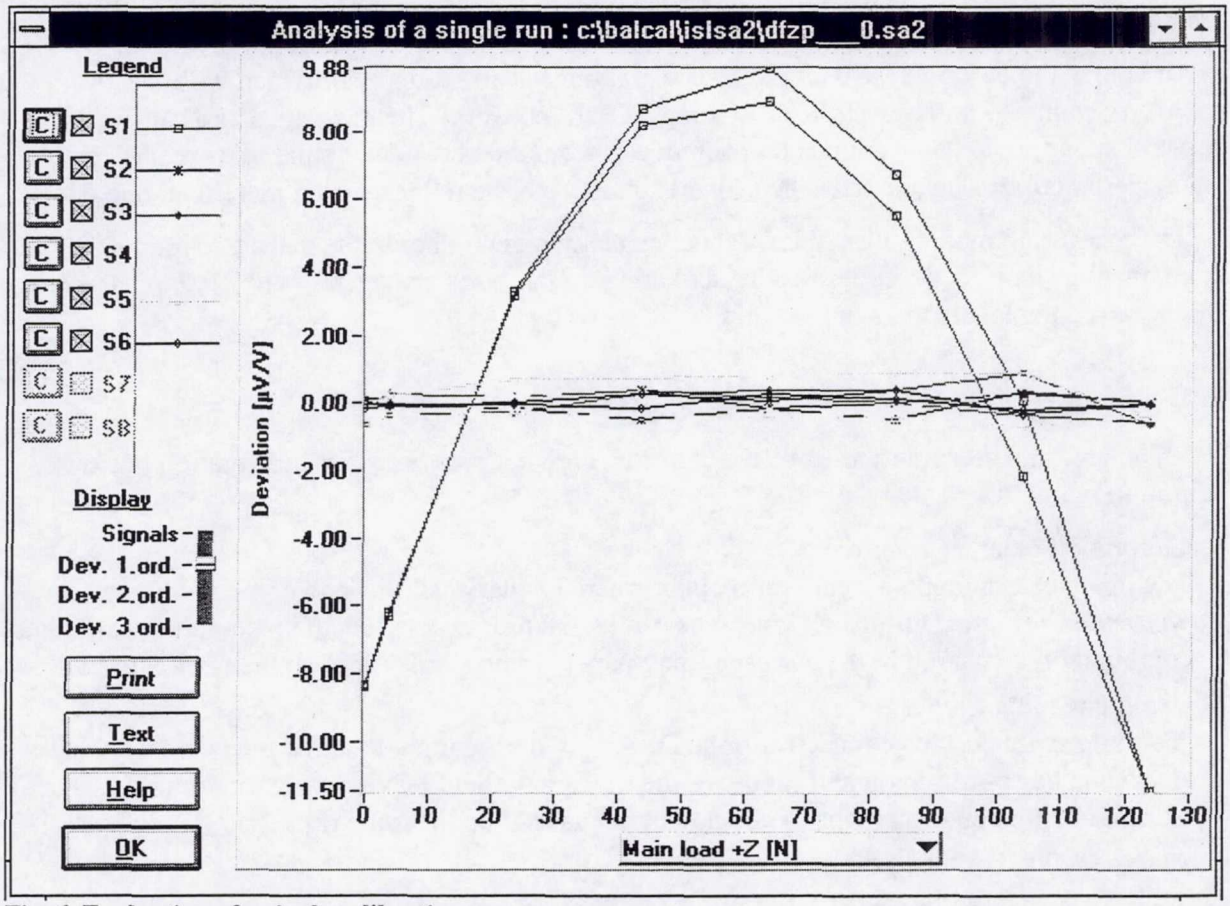

Fig. 6 Evaluation of a single calibration run

The overall analysis, i.e. the calculation of the matrix, is done with another program. The reason for not integrating this essential part of a calibration in the current program was the existence of well tested and optimised FORTRAN code. Considering limited time and the risk of introducing bugs in the converted program code lead to the decision to use the existing program and create an interface between it and the calibration program.

The analysis program is able to calculate matrices of first, second or third order and to verify the matrices against the calibration data. The underlying mathematical method is mentioned in another paper of this meeting [1].

4.2 Measuring process

It is obvious that using the same equipment for calibration and wind tunnel data acquisition offers advantages in terms of accuracy. While this is true for the measuring cascade from the balance to the A/D converter in this project we went a step farther. Instead of programming data acquisition routines for the connection between the host system of the customer an the measuring instrument, there is a built-in section in this program that is able to take readings, calculate forces with the appropriate matrix and display them. By integrating this measurement section the program can use the same data acquisition routines and instrument settings like that of the calibration. The parameter files describing the properties of the balance and the measuring instrument are reused.

Of course the customer's existing data acquisition system has to be provided with the calculated values. For that we use an existing TCP/IP network. The program acts as an TCP/IP server responding to connection and data requests from the network. A small data request and answer protocol was developed. The server can reply to data requests from more than one client.

The measuring mode is also able to generate alarm signals should the permitted load on a component be exceeded. It does this by activating digital ports provided by the DMCplus, which can be wired to signal lamps or switches.

5 Other features

The program contains some other features that are not necessary for a calibration but are helpful in many ways.

- Calibration plan
  The operator can prepare a calibration plan where he marks all the load combinations he wishes to calibrate. During calibration he can let the program follow the plan. Every calibrated combination is marked in the corresponding panel giving a quick look at the work still to do.
- Remote reading trigger
  A simple switch can be connected to the DMCplus' digital input to allow the operator weight stack change confirmation and saving of the reading without leaving the calibration rig. This is helpful in situations where the PC could not be placed very near the rig.
- Automatic load of the latest parameter file
- Entering comments in data files
- Multilingual support
  The language for menus, panel labelling and the help systems can be set to the users preference (currently supported languages are German, English and French).

6 Summary

A software system for the manual calibration of internal balances has been developed with a state-of-the-art human interface. Efforts were made to suite the software to the needs of the inexperienced calibrator without neglecting the flexibility required by the experienced. All tools including a hypertext help system have been combined in one easy to use package with consistent interfaces for every task. Extensive error checking is done for input as well as for data acquisition.

References

1. Ewald, Bernd; and Hufnagel, Klaus: *The Development of Advanced Internal Balances for Cryogenic and Conventional Tunnels*, NASA International Symposium on Strain-Gage Balances, 1996

Page intentionally left blank

TRANSFORMATION OF AERODYNAMIC BALANCES FORMULAS TO THE RESOLVED RESPECTING TO LOADING FORM

Ivan N.Panchenko
Central Aerohydrodynamic Institute (TsAGI)
Zhukovsky, Moscow Region, Russia

Formulas of strain-gauge balances introduce by themselves dependencies between loads $X, Y, \ldots M_z$ applied to balances and signals of measuring channels $N_x, N_y, \ldots N_{M_z}$. Introducing loads of n-component strain gauge balances with n-dimensioned vector $\overline{X}$, and signals of measuring channels , correspondingly, with vector $\overline{N}$, dependencies between loads and signals can be introduced in the common form:

$$f = (\overline{X}, \overline{N}) = 0 \tag{1}$$

Introducing system (1) in the real form relatively to $\overline{N}$ or $\overline{X}$, we'll have:

$$\overline{N} = f_1(\overline{X}) \tag{2}$$

$$\overline{X} = f_2(\overline{N}) \tag{3}$$

Functions (2) and (3) are usually introduced with power line, and are restricted in most cases with second polynomial's power. For some strain gauge balances it is necessary to input members of the third power.

If restricting dependencies (2) and (3) with polynomials of the second power, they get the form:

$$N_i = \sum_{i=1}^{n} A_{i,j} X_j + \sum_{r=1}^{n} \sum_{s=r}^{n} A_{i,rs} X_r X_s \tag{4}$$

$$X_j = \sum B_{j,i} N_i + \sum_{p=1}^{n} \sum_{q=p}^{n} B_{j,pq} N_p N_q \tag{5}$$

where n is a number of balance's components.

In traditional calibration of strain gauge balances there are obtained formulas in the form of system (4), because in this case as arguments there are considered loads of components and active test can be carried out, i.e. it is possible to pose loads with determined, earlier chosen way.

Each one equation of systems (4) and (5) consists of $\frac{(n+3)n}{2}$ terms. Number of terms in formulas of six-component strain gauge balances is 27. Traditional calibration of strain gauge balances on determination of formulas coefficients consists of two steps.

On the first step there are posed loads on one component for example, X_a. In this case nonzero will be only two terms of each equation of system (4):

$$N_i = A_{i,a} X_a + A_{i,aa} X_a^2$$

where: $i = 1,2,...n$.

Results of calibration of component X_a are processed with respect to method of least squares and coefficients $A_{i,a}$ and $A_{i,aa}$ are determined.

By fulfilling consequently calibrations of each one component there are determined all coefficients in single loads and their squares.

On the second step there are determined coefficients in multiplying of loads. For this purpose there are posed loads of two corresponding components, for example, for determination of coefficients in multiplying of loads X_aX_b, there is carried out simultaneous loading of these components. In this case each equation of system (4) will have the form:

$$N_i = A_{i,a} X_a + A_{i,aa} X_a^2 + A_{i,b} X_b + A_{i,bb} X_b^2 + A_{i,ab} X_a X_b \tag{6}$$

and will connect 5 terms. Coefficients of the first 4 terms are determined on the first step of calibration. Unknown remains one coefficient $A_{i,ab}$ in each equation, which is determined with respect to materials of calibrations, using also the method of least squares.

Carrying out calibrations of each one pair combination of components there are determined all coefficients in loads' multiplyings. Number of terms with multiplyings of loads for n-component strain gauge balances is $\dfrac{n(n-1)}{2}$.

Equations of the system (4) are origin equations, obtained as the result of traditional calibration of strain gauge balances. These equations are called non-inverted formulas of strain gauge balances. They can be used for determination of signals of measuring channels with respect to known loads of the components.

Determination of loads with formulas (4) is possible using process of consequent approximations (iteration method).

Let's introduce the algorithm of one of methods of iterations, because we use it for obtaining of inverted formulas of strain gauge balances. Lets introduced system of equations (4) in total form:

$$\left.\begin{array}{l}
N_1 = A_{1,1}X_1+\ldots+A_{1,j}X_j+\ldots+A_{1,n}X_n + A_{1,11}X_1^2 + A_{1,12}X_1X_2+\ldots+A_{1,rs}X_rX_s+\ldots \\
\text{---} \\
N_i = A_{i,1}X_1+\ldots+A_{i,j}X_j+\ldots+A_{i,n}X_n + A_{i,11}X_1^2 + A_{i,12}X_1X_2+\ldots+A_{i,rs}X_rX_s+\ldots \\
\text{---} \\
N_n = A_{n,1}X_1+\ldots+A_{n,j}X_j+\ldots+A_{n,m}X_n + A_{n,11}X_1^2 + A_{n,12}X_1X_2+\ldots+A_{n,rs}X_rX_s+\ldots
\end{array}\right\} \tag{7}$$

Dividing each equation of the system (7) for coefficients in diagonal terms (i = 1) and carrying out regroup of terms, we'll obtain:

$$\left.\begin{array}{l} X_1 = \dfrac{N_1}{A_{1,1}} - \left[\dfrac{A_{1,2}}{A_{1,1}} X_2 + \ldots + \dfrac{A_{1,n}}{A_{1,1}} X_n + \dfrac{A_{1,11}}{A_{1,1}} X_1^2 + \ldots + \dfrac{A_{1,rs}}{A_{1,1}} X_r X_s\right] \\ \text{---} \\ X_j = \dfrac{N_i}{A_{j,j}} - \left[\dfrac{A_{j,1}}{A_{j,j}} X_1 + \ldots + \dfrac{A_{j,n}}{A_{j,j}} X_n + \dfrac{A_{j,11}}{A_{j,j}} X_1^2 + \ldots + \dfrac{A_{j,r.s}}{A_{j,j}} X_r X_s\right] \\ \text{---} \\ X_n = \dfrac{N_n}{A_{n,n}} - \left[\dfrac{A_{n,1}}{A_{n,n}} X_1 + \ldots + \dfrac{A_{n,n-1}}{A_{n,n}} X_{n-1} + \dfrac{A_{n,11}}{A_{n,n}} X_1^2 + \ldots + \dfrac{A_{n,rs}}{A_{n,n}} X_r X_s + \ldots\right] \end{array}\right\} \quad (8)$$

or

$$\left.\begin{array}{l} X_1 = S_1 N_1 - \left[K_{1,2} X_2 + \ldots + K_{1,n} X_n + K_{1,11} X_1^2 + \ldots + K_{1,rs} X_r X_s + \cdots\right] \\ \text{---} \\ X_j = S_j N_j - \left[K_{j,1} X_1 + \cdots + K_{j,n} X_n + K_{j,11} X_1^2 + \ldots + K_{j,rs} X_r X_s + \ldots\right] \\ \text{---} \\ X_n = S_n N_n - \left[K_{n,1} X_1 + \ldots + K_{n,n-1} X_{n-1} + K_{n,11} X_1^2 + \ldots + K_{n,rs} X_r X_s + \ldots\right] \end{array}\right\} \quad (9)$$

The equations of the form (9) are called balances semiinverted formulas. Transforming the system (9) into the form convenient for its' listing in the matrix form. For this purpose load and their combinations from the right part of the equation $X_1, X_2, ... X_n, X^2, X_1X_2, ... X_2X_s, ... X_n^2$ are substituted for $F_1, F_2, ... F_i ... F_d$ and coefficients' indexes are posing into correspondence with them. As result we'll have:

$$\left.\begin{array}{l} X_1 = S_1 N_1 - \left[0 + K_{1,2} F_2 + K_{1,3} F_3 + \ldots + K_{1,n} F_n + \ldots + K_{1,d} F_d\right] \\ \text{---} \\ X_2 = S_2 N_2 - \left[K_{2,1} F_1 + 0 + K_{2,3} F_3 + \ldots + K_{2,n} F_n + \ldots K_{2,d} F_d\right] \\ \text{---} \\ X_n = S_n N_n - \left[K_{n,1} F_1 + K_{n,2} F_2 + \ldots + K_{n,n-1} F_{n-1} + 0 + \ldots + K_{n,d} F_d\right] \end{array}\right\} \quad (10)$$

Here $d = n/2(n+3)$

Introducing matrix designations:

$\{X\} = \begin{Bmatrix} X_1 \\ X_2 \\ \vdots \\ X_n \end{Bmatrix}$ - vector of loads;

$$\{N\} = \begin{Bmatrix} N_1 \\ N_2 \\ \vdots \\ N_n \end{Bmatrix}$$ - vector of output signals;

$$[S] = \begin{bmatrix} S_1 & 0 \dots 0 \\ 0 & S_2 \dots 0 \\ - - - - - - \\ 0 & 0 \quad S_n \end{bmatrix}$$ - array of diagonal elements;

$[S]^{-1}$ array of sensitivity

$$\{F\} = \begin{Bmatrix} F_1 \\ F_2 \\ \vdots \\ F_d \end{Bmatrix}$$ - array of forces and moments of influences;

$$[K] = \begin{bmatrix} 0 & K_{1,2} \dots K_{1,n} \dots K_{1,d} \\ K_{2,1} & 0 \quad K_{2,n} \cdots K_{2,d} \\ - - - - - - - - - - - - - - \\ K_{n,1} \dots K_{n,n-1} & 0 \quad \dots K_{n,d} \end{bmatrix}$$ - array of coefficients of influences

The system of equations (10) can be introduced in the form of the matrix equation, taking into account above-mentioned notations:

$$\{X\} = [S]\{N\} - [K]\{F\} \tag{11}$$

Arrays $[S]$ and $[K]$ are known from strain gauge balances calibration, the array of output signals $\{N\}$ is known from measuring equipment observations in wind-tunnel testing.

Calculation of loads with respect to method of successive approximations fulfilled in the following way: at first the approximate values of loads by the first term of array equation (11) are determined:

$$\{X\}_0 = [S]\{N\}$$

after this loads are made more precise with respect to iterations method. The first iteration: elements of the array of forces and moments of influences are determined:

$$(F_i)_1 = (X_1)_0, \dots (X_i)_0 \dots (X_n)_0, \left(X_1\right)_0^2, (X_1)_0 (X_2)_0, \dots (X_i)_0 (X_j)_0, \dots \left(X_n\right)_0^2$$

where

$$\{X\}_1 = \{X\}_0 - [K]\{F\}_1$$

The second iteration:

$$(F_i)_2 = (X_1)_1, \dots (X_i)_1, \dots (X_n)_1, (X_1)_1^2, (X_1)_1 (X_2)_1, \dots (X_i)_1 (X_j)_1, \dots$$

$$\{X\}_2 = \{X\}_0 - [K]\{F\}_2$$

K-th iteration:

$$(F_i)_k = (X_1)_{k-1}, \ldots (X_i)_{k-1}, \ldots (X_n)_{k-1}, \left(X_1\right)^2_{k-1} \ldots (X_i)_{k-1}(X_j)_{k-1},$$

$$\{X\}_k = \{X\}_0 - [K]\{F\}_k$$

The iteration process usually breaks out if the following terms have place:

$$|[K]\{F\}_k - [K]\{F\}_{k-1}| < \{\varphi\}, \tag{12}$$

where coefficients φ_i of the array $\{\varphi\}$ are numerically equal to the corresponding diagonal coefficients S_i of the array $[S]$. In this case the absolute value of remainder $[K]\{F\}_k - [K]\{F\}_{k-1}$ becomes less than minimum resolvable values of loads.

For common six-component strain gauge balances in the case of substitution in the system (10) of different combinations of observations of the measuring equipment N_i the term (12) fulfills after 3/5 iterations. In non good conditions for fulfilling of this term (12) there can be required considerably high number of iterations, and in some cases the process can not be fulfilled at all. This a considerable loss in determination of loads in aerodynamic test, because the calculations must be carried out in the real time. The process can be broken after some number of iterations, but in this case there is a real opportunity to get high errors in determination of loads.

For determination of loads in the time of aerodynamic test it is best of all to have the formulas of strain gauge balances in the form of system (5). The formulas in the form of system (5) can be obtained from the formulas of system (4). The process of obtaining of formulas of system (5) from formulas of system (4) we'll call invention of formulas of strain gauge balances, and formulas by themselves - inverted.

There exist different variants of obtaining of inverted formulas of strain gauge balances from noninverted, which are mainly reduced to approximate solution of systems of nonlinear equations. They require invention of arrays of the line, equal to maximum number of terms in equations (for equations of the second power - 27 terms). For lattice strain gauge balances with nonconsiderable weight of nonlinear terms these methods permit to distinguish the required precision of inventions.

In the case of existing in formulas of high nonlinear terms of the terms of the third power, known methods do not provide required precision of invention. Practice of invention of formulas of strain gauge balances has shown that for providing of equation of the inverted formulas to the origin ones it is necessary to input into inverted formulas term of the third power, though such terms don't exist in non-inverted formulas. But a priori we don't know which terms of the third power can exist in inverted formulas, so they are to be reserved. In this case the line of arrays for six-component strain gauge balances is equal to 83.

Offered method of invention permits to obtain formulas, resolved relatively to loads (inverted), which contain term up to the third power. Non depending from the number of terms in formulas of strain gauge balances, algorithms of calculations contain invention of arrays of the size not higher than 3·3. The inventions method does not have limits on the number of terms in equations, on power of invented equations and weight of terms and influences, including nonlinear.

The main specialty of offered method is modeling of the process of calibration of strain gauge balances, as arguments in which there are used signal of measuring channels, i.e. there is modeling an active test in relation to signals of measuring channels.

In modeling of calibrations there are posed necessary combinations of signals of measuring channels, for which with respect to semiinverted formulas, using method of iterations, there are determined loads of the components.

Posing necessary combinations of signals (active test) and obtaining for them values of loads it is possible to determine coefficients of inverted formulas.

Let's consider algorithm of determination of coefficients of inverted formulas, which contain terms up to the third power. For this purpose we'll add the system (5) with terms of the third power:

$$X_j = \sum_{i=1}^{n} B_{j,i} N_i + \sum_{p=1}^{n} \sum_{q=p}^{n} B_{j,pq} N_p N_q + \sum_{k=1}^{n} \sum_{l=k}^{n} \sum_{m=l}^{n} B_{j,klm} N_k N_l N_m \tag{13}$$

Transforming system (5.9) in the way that first sum contains terms with observations of one channel, second sum - of two, third sum - of three channels:

$$\left.\begin{aligned} X_i = &\sum_{i=1}^{n}\left(B_{j,i}\ N_i + B_{j,i^2}\ N_i + B_{j,i^3}\ N_i^3\right) + \\ &+\sum_{p=1}^{n-1}\ \sum_{q=p+1}^{n}\left(B_{j,pq}\ N_p\ N_q + B_{j,pq^2}\ N_p\ N_q^2 + B_{j_1,p^2q}\ N_p^2\ N_q\right) + \\ &+\sum_{k=1}^{n-2}\ \sum_{l=k+1}^{n-1}\ \sum_{m=l+1}^{n} B_{j,klm}\ N_k\ N_l\ N_m \\ j = &1,2,3\ldots n \end{aligned}\right\} \tag{14}$$

Process of determination of coefficients is divided into three steps, at each one terms of one sum will be determined.

Introducing the first sum of the system (14) with respect to representation of nonzero observation of i-th channel of system (14) we'll have the form:

$$\begin{aligned} X &= B_{j,i}\ N_i + B_{j,i^2}\ N_i^2 + B_{j,i^3} N_i^3 \\ i &= 1,2,3\ldots n \end{aligned} \tag{15}$$

Each one n of equations of this system contains three terms and has three undetermined coefficients. For determination of these coefficients it is necessary to represent three values of observations N_i and with respect to one of described above methods of iterations to determine loads X_j of all n components.

Every time, when it is necessary to represent three levels of observations, we'll multiply maximum observations of channels at coefficients, ρ_1, ρ_2 and ρ_3, if it is necessary, to represent two levels - for ρ_1 and ρ_2. Maximum observations of channels we'll introduce as M_i. Then system of equations for determination of coefficients of observations of i - th channel will have the form:

$$\begin{aligned} \left(X_j\right)_1 &= B_{j,i}\left(\rho_1 M_i\right) + B_{j,i^2}\left(\rho_1 M_i\right)^2 + B_{j,i^3}\left(\rho_1 M_i\right)^3 \\ \left(X_j\right)_2 &= B_{j,i}\left(\rho_2 M_i\right) + B_{j,i^2}\left(\rho_2 M_i\right)^2 + B_{j,i^3}\left(\rho_2 M_i\right)^3 \\ \left(X_j\right)_3 &= B_{j,i}\left(\rho_3 M_i\right) + B_{j,i^2}\left(\rho_3 M_i\right)^2 + B_{j,i^3}\left(\rho_3 M_i\right)^3 \end{aligned} \tag{16}$$

Introducing system (16) in the matrix form:

$$[X]_i = [N]_i [B]_i \tag{17}$$

where $i = 1,2,...n$ - number of channel, for which coefficients are determined

$$[X]_i = \begin{bmatrix} (X_1)_1 & (X_2)_1 \ldots\ldots (X_6)_1 \\ (X_1)_2 & (X_2)_2 \ldots\ldots (X_6)_2 \\ (X_1)_3 & (X_2)_3 \ldots\ldots (X_6)_3 \end{bmatrix} \tag{18}$$

$$[B]_i = \begin{bmatrix} B_{i,1} & B_{i,2} \ldots\ldots B_{i,n} \\ B_{i^2,1} & B_{i^2,2} \ldots\ldots B_{i^2,n} \\ B_{i^3,1} & B_{i^3,2} \ldots\ldots B_{i^3,n} \end{bmatrix} \tag{19}$$

$$[N]_i = \begin{bmatrix} (\rho_1 M_i) & (\rho_1 M_i)^2 & (\rho_1 M_i)^3 \\ (\rho_2 M_i) & (\rho_2 M_i)^2 & (\rho_2 M_i)^3 \\ (\rho_3 M_i) & (\rho_3 M_i)^2 & (\rho_3 M_i)^3 \end{bmatrix} \tag{20}$$

Array $[N]_i$ can be introduced as boundle of two arrays:

$$[N]_i = \begin{bmatrix} \rho_1 & \rho_1^2 & \rho_1^3 \\ \rho_2 & \rho_2^2 & \rho_2^3 \\ \rho_3 & \rho_3^2 & \rho_3^3 \end{bmatrix} \times \begin{bmatrix} M_i & 0 & 0 \\ 0 & M_i{}^2 & 0 \\ 0 & 0 & M_i{}^3 \end{bmatrix} \tag{21}$$

or

$$[N]_i = [T]\,[M]_i \tag{22}$$

Coefficients B are determined from (17):

$$[B]_i = [X]_i\,[N]_i^{-1}$$

or taking into account (22)

$$[B]_i = [X]_i\,[M]_i^{-1}\,[T]^{-1} \tag{23}$$

Described processes is fulfilled n times and all coefficients of the first sum of system (14) are determined.

Array $[T]^{-1}$ is generic for all channels, that's why in determination of coefficients of the first sum of system (14) they are calculated for one time.

In representation of observations of two channels, for example p and q (in determination of coefficients of the second sum), system (14) will have the form:

$$\begin{aligned} X_j = {} & B_{j,p} N_p + B_{j,p^2} N_p^2 + B_{j,p^3} N_p^3 + \\ & + B_{j,q} N_q + B_{j,q^2} N_q^2 + B_{j,q^3} N_q^3 + \\ & + B_{j,pq} N_p N_q + B_{j,pq^2} N_p N_q^2 + B_{j,p^2q} N_p^2 N_q \end{aligned} \tag{24}$$

Each equation of system (24) has 9 terms, but coefficients of first six terms have been determined already on the first step, so only three last coefficients are undetermined. For their determination, as in the first case, we'll form three equations with different combinations of observations N_p and N_q:
1) - $\rho_1 M_p$, $\rho_1 M_q$; 2) - $\rho_1 M_p$, $\rho_2 M_q$; 3) - $\rho_2 M_p$, $\rho_1 M_q$, where M_p and M_q, as before, are maximum observations of channels p and q. By use of semiinverted formulas we'll determine loads X for represented observations. Lets also calculate load, determined with respect to sum of terms with determinate coefficients. For that purpose we'll enter designation:

$$X_j'' = B_{j,p} N_p + B_{j,p^2} N_p^2 + B_{j,p^3} N_p^3 + B_{j,q} N_q + B_{jq^2} N_q^2 + B_{jq^3} N_q^3 \tag{25}$$

Let's introduce this system for pointed above combinations of signals in the matrix form:

$$[X]_{pq}'' = [N]_{pq}''\,[B]_{pq} \tag{26}$$

where:

$$[X]_{pq} = \begin{bmatrix} (X_1)_1 & (X_2)_1 \dots (X_n)_1 \\ (X_1)_2 & (X_2)_2 \dots (X_n)_2 \\ (X_1)_3 & (X_2)_3 \dots (X_n)_3 \end{bmatrix}$$

$$[N]_{pq}'' = \begin{bmatrix} \rho_1 M_p & \rho_1^2 M_p^2 & \rho_1^3 M_p^3 & \rho_1 M_q & \rho_1^2 M_q^2 & \rho_1^3 M_q^3 \\ \rho_1 M_p & \rho_1^2 M_p^3 & \rho_1^3 M_p & \rho_2 M_q & \rho_2^2 M_q^2 & \rho_2^3 M_q^3 \\ \rho r_2 M_p & \rho_2^2 M_p^2 & \rho_2^3 M_p^3 & \rho_1 M_q & \rho_1^2 M_q^2 & \rho_1^3 M_q^3 \end{bmatrix}$$

$$[B]_{pq} = \begin{bmatrix} B_{p,1} & B_{p,2} \dots B_{p,j} \dots B_{p,n} \\ B_{p^2,1} & B_{p^2,2} \dots B_{p^2,j} \dots B_{p^2,n} \\ B_{p^3,1} & B_{p^3,2} \dots B_{p^3,j} \dots B_{p^3,n} \\ B_{q,1} & B_{q,2} \dots B_{q,j} \dots B_{q,n} \\ B_{q^2,1} & B_{q^2,2} \dots B_{q^2,j} \dots B_{q^2,n} \\ B_{q^3,1} & B_{q^3,2} \dots B_{q^3,j} \dots B_{q^3,n} \end{bmatrix}$$

By use of system (25) loads X_i'' are determined.

Entering designation

$$Y_j = B_{j,pq} N_p N_q + B_{j,pq}{}^2 N_p N_q{}^2 + B_{j,p}{}^2{}_q N_q{}^2 N_q \tag{27}$$

from expression (24) we'll have:

$$Y_j = X_j - X_j'' \tag{28}$$

From this expression we determine loads Y_j.

System (27) is used for determination of coefficients. Introducing it in the matrix form:

$$[Y]_{pq} = [N]_{pq} [B]_{pq} \tag{29}$$

Here:

$$[Y]_{pq} = \begin{bmatrix} (Y_1)_1 & (Y_2)_1 \dots (Y_j)_1 \dots (Y_n)_1 \\ (Y_1)_2 & (Y_2)_2 \dots (Y_j)_2 \dots (Y_n)_2 \\ (Y_1)_3 & (Y_2)_3 \dots (Y_j)_3 \dots (Y_n)_3 \end{bmatrix}$$

$$
\left.
\begin{aligned}
[N]_{pq} &= \begin{vmatrix} \rho_1^2 M_p M_q & \rho_1^3 M_p M_q^2 & \rho_1^3 M_p^2 M_q \\ \rho_1 \rho_2 M_p M_q & \rho_1 \rho_2^2 M_p M_q^2 & \rho_1^2 \rho_2 M_p^2 M_q \\ \rho_1 \rho_2 M_p M_q & \rho_1^2 \rho_2 M_p M_q^2 & \rho_1 \rho_2^2 M_p^2 M_q \end{vmatrix} = \\
&= \begin{vmatrix} \rho_1^2 & \rho_1^3 & \rho_1^3 \\ \rho_1 \rho_2 & \rho_1 \rho_2^2 & \rho_1^2 \rho_2 \\ \rho_1 \rho_2 & \rho_1^2 \rho_2 & \rho_1 \rho_2^2 \end{vmatrix} \begin{vmatrix} M_p M_q & 0 & 0 \\ 0 & M_p M_q^2 & 0 \\ 0 & 0 & M_p^2 M_q \end{vmatrix} \\
&= [Z] \times [M]_{pq}
\end{aligned}
\right\} \qquad (30)
$$

$$
[B]_{pq} = \begin{bmatrix} B_{pq,1} \cdots & B_{pq,j} \cdots & B_{pq,n} \\ B_{pq^2,1} \cdots & B_{pq^2,j} \cdots & B_{pq^2,n} \\ B_{p^2q,1} \cdots & B_{p^2q,j} \cdots & B_{p^2q,n} \end{bmatrix}
$$

System (29) with taking into account (30) will have a form:

$$[Y]_{pq} = [Z]\,[M]_{pq}\,[B]_{pq}$$

From this we have the following:

$$[B]_{pq} = [M]^{-1}_{pq}\,[Z]^{-1}\,[Y]_{pq} \qquad (31)$$

With respect to this expression coefficients B of the second sum of system (14) with observations of channels p and q are determined. For determination of all coefficients of the second sum described process must be doubled for all $n/2(n\text{-}1)$ pair combinations of channels.

For determination of coefficients of the third sum of system (14) it is necessary to represent observations of three channels, for example k, l, m, then system will have the form:

$$
\begin{aligned}
X_j = {} & B_{j,k} N + B_{j,k^2} N_k^2 + B_{j,k^3} N_k^3 + B_{j,l} N_l + B_{j,l^2} N_l^2 + B_{j,l^3} N_l^3 + \\
& + B_{j,m} N_m + B_{j,m^2} N_m^2 + B_{j,kl} N_k N_l + B_{j,kl^2} N_k N_l^2 + B_{j,k^2l} N_k N_l + \\
& + B_{j,km} N_k N_m + B_{j,km^2} N_k N_m^2 + B_{j,k^2m} N_k^2 N_m + B_{j,lm} N_l N_m + \\
& + B_{j,lm^2} N_l N_m^2 + B_{j,l^2m} N_l^2 N_m + B_{j,klm} N_k N_l N_m
\end{aligned} \qquad (32)
$$

The equations of system (32) have 19 coefficients, but all of them, besides the last one, have been determined before, so for determination of coefficients of the third sum it is necessary to represent one combination of observations, for example ρM_k, ρM_l, ρM_m.

If designate loads, determined by sum of all terms with determined coefficients, through $[X]''_{klm}$, and the last term through $[Y]_{klm}$, then system (32) in the matrix form will be:

$$[X]_{klm} = [X]''_{klm} + [Y]_{klm},$$

From here

$$[N]_{klm}\,[B]_{klm}$$

$$[Y]_{klm}\,[X]_{klm} - [X]''_{klm}\,[X]_{klm} = [N]_{klm}\,[B]_{klm}$$

Here:

$$[Y]_{klm} = [(Y_1)_{klm}\,(Y_2)_{klm} \ldots (Y_j)_{klm} \ldots (Y_n)_{klm}]$$

$$[B]_{klm} = [B_{klm,1}\ B_{klm,2}\ldots B_{klm,j}\ldots B_{klm,n}] \qquad \text{and}$$

$$[N]_{klm} = [N_k N_l N_m] = N_k N_l N_m \qquad \text{then}$$

$$[B]_{klm} = (N_k N_l N_m)^{-1}[Y]_{klm}$$

Above process is repeated C_n^3 times.

All determined with respect to this way coefficients form a generic array.

Described above method of invention of formulas of multi-component strain gauge balances permits to obtain formulas of strain gauge balances with invention error, which does not exceed $(1\ldots3)\cdot10^{-2}$% from the ranges of components. For balances, which have mean square errors (0.1...0.3)%, invention error practically does not influence summary error of strain gauge balances' formulas.

As result of calculation errors all the coefficients of inverted formulas have zero values. It is necessary to work out the process of excluding of non considerable terms , because they lead to increase of mean square errors in determination of loads. For this purpose into diagonal components of non-inverted formulas there are introduced corresponding loads and signals are determined. Lets call them maximum signals of components. These signals are introduced into inverted formulas and relative weight of each term in percents to the range of component C is determined. There is chosen criteria K. If for term there is true the term then this term is getting zero value. How to chose coefficient K? For this purpose there were carried out special tests. There were determined sums of relative loads of all extra terms of each one component. They for six-component strain gauge balances were approximately (2...3) K. From another side there was determined error of inverted formulas in dependence from the coefficient. For this purpose there were posed different combinations of loads $\overline{X}_3$ and with respect to non-inverted formulas there were determined signals $\overline{N}$. After that these signals were introduced into inverted formulas and loads $\overline{X}_p$ were calculated. Difference of these loads, related to the range of component gave relative calculation error with respect to inverted formulas, which was also equal approximately to (2...3)K. In such way if we pose criteria K = 0.1%, then formulas of balances will give the error in loads determination because of invention errors (0.2...0.3)% from the components' ranges.

LITERATURE

1. K.Lantsosh. Practical methods of an applied analysis. Moscow, 1961 (in Russian).
2. F.R.Gantmacher. Matrix theory. Nauka, Moscow, 1967 (in Russian).
3. B.P.Demidovich, I.A.Maron. Basics of a computational mathematics. Nauka, Moscow, 1966.

Limitations of Internal Balance Calibration Math Models for Simulating Multicomponent Interactions

Richard S. Crooks
Micro Craft Technology
San Diego

Dr. Allen Zwan
Micro Craft Technology
San Diego

SUMMARY

Multi-component internal force and moment balances have been utilized in wind tunnels for over 50 years as the primary measurement instrument for defining aerodynamic performance. Designs for these instruments have evolved to meet the increasing accuracy requirements. However, much less has been done to improve the processes used to calibrate these important instruments.

Conventional wind tunnel test applications require that the balance perform in a 6 degree of freedom environment; yet standard calibration processes characterize the balance using primarily single, two or in very limited cases, three combined loads. Additionally, the common practice is to use matrix based math models representing only two combined load terms.

Data acquired from a number of different balances and from both manual and automatic calibration processes will be presented. The data suggests that second order combined load characterizations described by standard error of the curve fit statistics are not indicative when used to predict performance under combined load conditions outside the calibration envelope. There is substantial opportunity to reduce uncertainty (improve the quality and robustness of the calibration) by tailoring the loading combinations and including higher order combined load terms in the math model when interactions and non-linearity's are present.

The Conventional Wind Tunnel Balance Calibration Process

The internal force/moment balance remains one of the fundamental instruments used in wind tunnel testing yet the calibration of these important instruments in most facilities is infrequent. A number of wind tunnel balance designs have evolved over the years (ie: single piece moment balances, Task/Able force balances, two-shell force balances). All designs depend upon a calibration process to develop repeatable relationships between the six strain gage outputs and applied loads/moments.

The calibration process relates the recorded output of the strain gages to a specified and defined force vector (magnitude, and direction) applied at a known position relative to the Balance Moment Center (BMC). The six degrees of freedom are referred to as normal force (NF), side force (SF), axial force (AF), pitching moment (PM), yawing moment (YM) and rolling moment (RM). A math model is used to develop the correlation between output of the gages and applied load (and moment). A math model of matrix form is generally used to develop a series of constants which provide resultant applied loads determined from raw balance outputs. The typical form of this math model is the equation shown below, a 2nd order polynomial expansion in six variables. This form of equation is the typical 6x27 matrix (27 constants required to solve for each of the 6 components).

$$F_i = \sum_{j=1}^{6} c_{ij} X_j + \sum_{j=1}^{6} d_{ij} F_j^{\,2} + \sum_{j=1}^{5} \sum_{k=j+1}^{6} c_{jk} F_j F_k$$

F_i, F_j, F_k = *Computed Load*
X_j = *Balance Channel Readout*
c_{ij} = *Linear Coefficient*
d_{ij} = *Squared term Coefficient*
c_{jk} = *Cross-Product Coefficient*

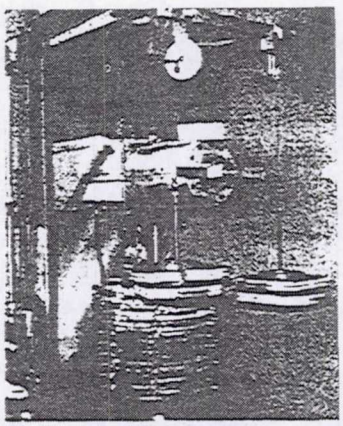

Figure 1 - The conventional method of balance calibration uses dead weight, cables and and pulley's.

To obtain the highest quality data during test, great care is exercised in both the design of the balance and the calibration methods. Presently, the most commonly used method of calibration consists of the manual application of dead weight. Calibrated increments of dead weight are applied to the balance at precise locations relative to the balance moment center. Prior to taking each data point, the balance is typically loaded and re-leveled to establish the load vector direction. This process is used for both positive and negative loadings at various stations along the balance centerline (thus applying moments).

If the balance has interaction sensitivity between components, combined load effects must also be developed. To determine these effects, two (or more) components are loaded simultaneously using a cable and pulley or bell crank system. Great care must be exercised to align and re-level during combined loadings; misalignments cause the resultant applied load vectors to deviate from target input values resulting in errors in developing the constant matrix set. These errors are undetectable without performing an additional

calibration using a different process, or repeating the same calibration after fully disassembling the calibration fixture. Figure 1 shows a typical set-up for manual calibration of a wind tunnel balance. In this calibration, a combined load including normal force, pitching moment and rolling moment are applied using a cable-pulley system. Prior to acquiring each data point, the balance must be re-aligned to ensure that the loads are perpendicular to the balance reference axis.

The manual process of dead weight loading is tedious and labor intensive typically consisting of between 250 and 800 individual load points. It usually requires two or more experienced calibration technicians 2 to 4 weeks to complete. The excessive resources required for manual calibration inherently prohibits studies on calibration repeatablity. These practical calibration limitations have hampered the ability of the balance design engineer to fully explore the sensitivities of the balance system to combined load terms, limiting the development of the math model to combined order terms of two with limited 3rd order terms.

Use of Automated Calibration Machines

The use of automated calibration systems provide the ability to quickly and easily apply a wide variety of loadings. Both single component and combined loads (of any combination) are applied with the same ease and process resulting in a constant uncertainty for the calibration process.

The automatic calibration system used to acquire data for part of this study was the Automatic Balance Calibration System (ABCS) developed by Israel Aircraft Industries. The ABCS is a fully self-contained and integrated 6 degree of freedom calibration system capable of performing all tasks required for the balance calibration process (see Figure 2). The machine applies a force to the balance using hydraulic actuators. Precision load cells and high resolution optical sensors are used to determine applied load vector magnitude and direction. Load position is determined from mechanical measurements.

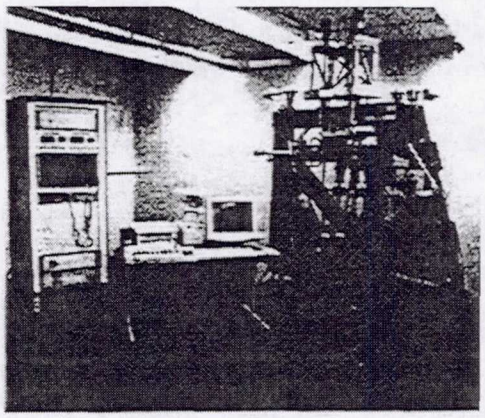

Figure 2 - The Automated Balance Calibration System used to develop the calibration data.

The ABCS is based on a non-repositioning principle. The applied force actuators are allowed to move as a result of balance deflection. The position of the deflected balance is measured relative to the fixed end of the balance axis using six (6) 0.5 micron incremental optical linear displacement gages. By measuring this deflection, the applied force vectors may be established mathematically. The calibration machine is further described in reference (1).

Contribution of Error Sources to the Calibration Process

It is important to understand the contribution of the uncertainties of the calibration process to the total uncertainty of the force measurement system in use. These error sources are identified and shown in Figure 3. Typically, the calibration process errors are grouped together and are difficult to differentiate. In most cases, the end user may not be concerned with the relative contribution of each of the error sources; the combination of sources result in bias errors which are propagated to the wind tunnel data. However, the relative contributions are important to the balance designer or calibration laboratory.

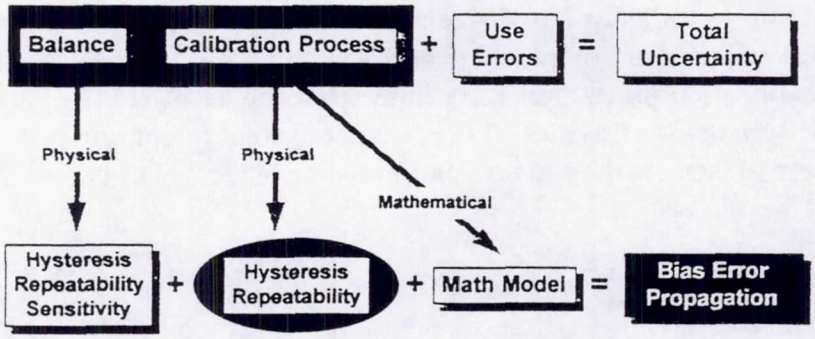

Figure 3 - Uncertainty sources for the wind tunnel balances include physical as well as non-physical errors.

The *Calibration Process* errors may be categorized as either *physical* or *mathematical* errors. The *physical* error sources include uncertainties resulting from precision and bias errors in the application of calibration load vectors (magnitude, direction and location). Other sources of physical error include hysteresis, drift and repeatability (resulting from temperature changes, dynamics, calibration technique or other physical phenomena of the balance).

The *mathematical* error sources result largely from the experimental math model used to characterize the performance of the balance. The selection of the input load sequences used to develop the calibration math model, the checkloads used to evaluate the performance of the math model (robustness), the form or order of the matrix, and the regression technique all contribute to the creation of 'standard errors'. These 'standard errors' (the standard deviation of the difference between applied load and calculated load) are routinely propagated to the wind tunnel test experiment as bias errors and are used as 'goodness' measures of the calibration and balance.

The Matrix Form and Math Model commonly used for Wind Tunnel Balances

While there is currently no standard practice for calibration and implementation of a math model to characterize a balance, most facilities use some form of multi-variable matrix model. The form described previously (a 6x27 matrix) is the most common; however, a number of adaptations have been developed such as, adding cubic terms (a 6x33 matrix) or absolute value terms (a 6x96 matrix).

Global least squares regression processes are used to define optimum constants necessary to fit the balance output to the applied loads. Once these constants are established, the calibration 'goodness' is generally checked by back-calculating the loads from the original calibration dataset and comparing those with the actual applied loads. The difference between applied loads and calculated loads (average error) and the standard deviation of these errors over the total data set are then used to measure how well the math model fits the calibration data set.

It is important to recognize that the math modeling process can only provide an optimum solution to fit *data in the calibration set.* How well that math model fits data which is not contained in the calibration set is dependent upon the selection of applied loads and the form of the math model. The robustness of a calibration can only be determined by developing a set of check-loads which are not contained in the original data set.

The 6x27 form commonly used is an expansion of two variable combinations of a possible 6 components and requires a minimum of 27 independent data points (6 components per data point) to solve for the necessary constants (300-800 points are common). When performing the matrix algebra, it is important that the data points are independent. If an iterative technique is utilized, a singularity will exist during matrix inversion. Whereas, if a non-iterative technique is used, an improper solotion will be generated.

If only 27 data points were provided to develop the matrix, the back-calculations would show a standard error of 0% since the model would fit all the calibration data. As additional data points are added (over defining the problem), the standard errors will rise as the model adjusts (linear regression) to compensate for the additional information. It seems that selecting a minimum number of calibration points appears to give favorable back-calculated results. However, it is important to recognize that a calibration completed with this few data points will provide misleading calculated loads when load conditions deviate even a small amount from the original calibration loadings. Selection of the calibration load points (number of points, distribution of points and combinations) is critical to developing a characterization that accurately models the performance of the balance over a wide operating range.

The Selection of Calibration Loads

The selection of calibration loads is one of the most important elements in the balance calibration process. Ideally, the balance would be calibrated over only those loads expected during a specific test program. However in general, calibrations are performed for universal usage and frequently are used for years, perhaps with only limited check loads applied for verification during the interim.

The minimum number of calibration points required to characterize the balance is related to the selection of the math model. A 6x27 matrix requires 27 independent data points. Higher order models, 6x33 for instance, require 33 data points. Equally important, the calibration data points must include sufficient loads to characterize all the terms used in

the math model. If the math model includes a NF-AF combination term, non trivial data must be provided which combines NF and AF.

If insufficient combination term calibration loading data is provided, and the regression process manages to provide a solution (very possible if there exists interactions about the zero point), the combined load term constant will be highly erroneous. Yet, by examining the back-calculated results, the standard errors and bias may be quite acceptable. The erroneous constant may only be detected by applying check loads not included in the original calibration load set.

The distribution of the calibration data points is also important. Should the distribution of points be imbalanced (skewed toward a certain load level), the resulting slope will also be skewed, since the global least squares process equally weights each point. For example, assume the axial force is calibrated from 0 to full scale and back to 0 in 20% increments, representing 11 data points. Combination loads (perhaps 100 data points) performed on other components while holding axial at full scale will skew the development of the axial primary slope and force the interaction scatter errors into the primary slope of axial force.

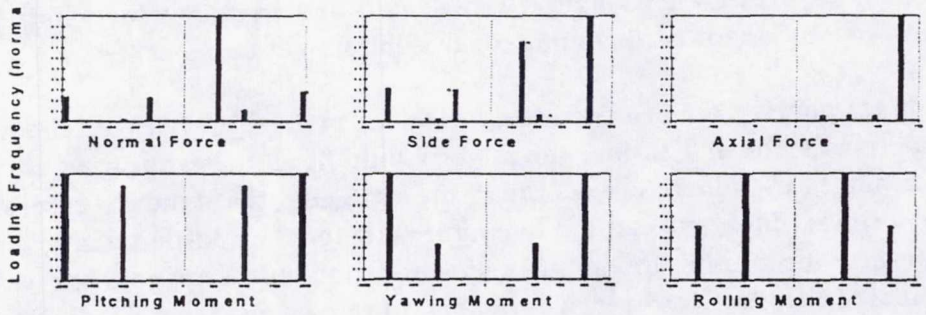

Figure 4 - Typical 285 point calibration histogram of axial force showing the frequency of occurrence of each loading condition. Note that the y-axis is normalized by the count of the maximum occurence.

Figure 4 illustrates the distribution of data points for an actual calibration sequence of 285 data points. Notice how the load sequences are distributed. Full scale axial force occurs 10 times more often than the incremental loadings of axial; in addition, axial is loaded in only one direction. The resulting scatter in axial data at full scale (caused by interactions), will shift the slope of the primary constant and force the incremental data to accommodate higher errors in the curve fit. Some calibration labs reduce this effect by using a subset of the loads to determine the linear coefficients. Figure 5 illustrates the same histogram (distribution of data point frequency) for a 1322 point calibration sequence. Note that the distribution of data points is more balanced.
Larger numbers of well distributed calibration points will produce a better characterization of the balance. It should be noted that these larger calibration sequences will lead to higher standard errors when comparing back-calculations. However, the true standard

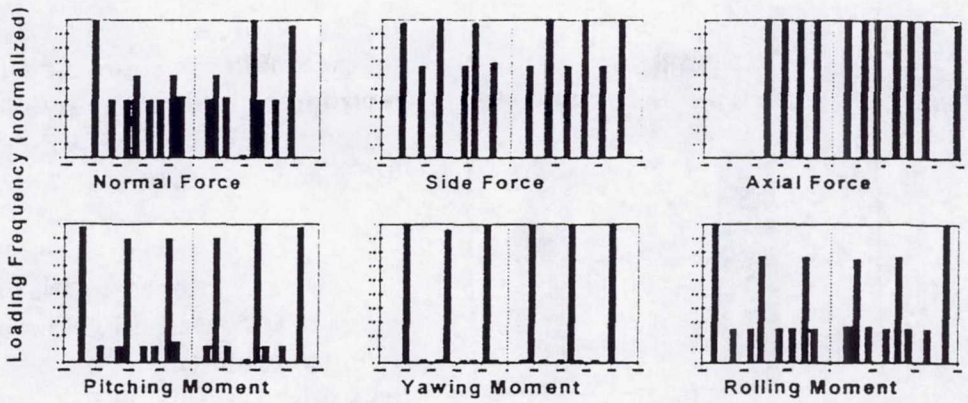

Figure 5 - A 1322 point calibration has a balanced distribution of data point occurences thus providing a more balanced constant solution.

errors resulting from wind tunnel test data will be much smaller due to the increased robustness of the math model.

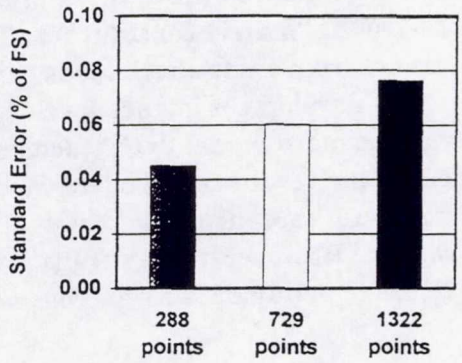

Figure 6 - Illustrates how both a 288 point calibration and a 729 point calibration compare with a 1322 point calibration (back-calculated RMS results).

Comparisons between calibrations with differing applied loads (285 points, 729 points and 1322 points).

To illustrate the differences between calibration sizes, we compared the standard error results for differing calibration load schedules. The standard error back-calculated results of a 288 point calibration and a 729 point calibration were compared with those of a 1322 point calibration (see Figure 6). As expected the smaller calibration files generally produced smaller standard errors, resulting from back calculated data. The more data used to develop the matrix sensitivities, the more degrees of freedom are characterized. The 1322 point calibration significantly over-defines the problem thus leading to higher *back calculated* standard errors.

The largest calibration (1322 points) represents an even distribution of data points over the full scale range of the balance. The smaller calibration sets, while replicating many of the exact points in the 1322 point file, also contain an imbalanced distribution of data points.

While higher order calibration schedules will increase the standard errors of the back-calculated results, the calibration will be more *robust* to higher order terms and thus, will more accurately reflect performance of the balance during wind tunnel testing. To illustrate this, a solution of the calibration data from the large calibration set (1322 points) using the matrix for each of the smaller sets (288 and 729 point calibration) was performed. Because the 1322 point set contains a large number of load conditions not included in either

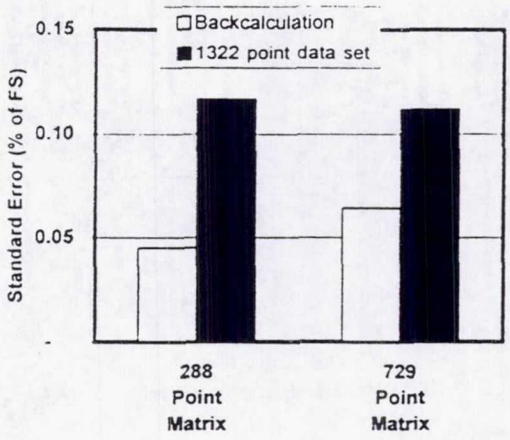

Figure 8 - Cross comparing the standard errors by running the large data set (1322 points) through each of the smaller data sets (288 and 729 point) illustrates how the smaller sets are less robust to data not included in the original calibration matrix. Note that the 1322 point data set contains only 2 component combined loads.

of the smaller sets, the model is required to extrapolate. Thus, the standard errors resulting from the cross-comparison are higher than back calculations (shown in Figure 8).

Effects of Combined Loads and use of check loads to validate calibration quality (robustness test)

The intent of the calibration process is to provide a math model which accurately and reliably predicts the applied loads from balance outputs (ie: develop a robust calibration). One way to test for calibration robustness is to acquire multi-component check load data which was not included in the data set used to develop the original matrix constant set. The standard errors from these check loads can then be used to develop confidence levels in the ability of the math model to characterize the balance. If the results of the check loads are consistent with those from the back-calculations, then the calibration could be considered robust. However, these results are highly dependent on the check loads selected. It is desirable to acquire 3,4,5 or 6 component combined loads for check loads.

Results from combination loadings from both manual and automatic calibrations are shown in Figure 7. While the back-calculated data from the applied data set containing only single and two component loadings shows nominal standard errors around 0.05%, these errors are higher for three component check loads and significantly higher for six component check loads.

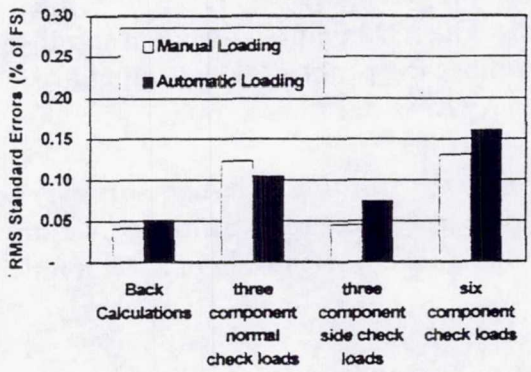

Figure 7 - RMS Check load errors resulting from combined loadings illustrates the limitations of the math model to account for higher order relationships between components.

These check load errors are indicative that the characterization process (the applied calibration loads *combined with the* math model) are not robust to multi-component combined loads. These results illustrate that while initial calibration shows the balance to perform near 0.05% (for back calculated data), errors 3 to 5

times these values are likely during combined load conditions. This is disturbing since typical wind tunnel test programs always include 6 component combined load terms, even during the simplest of test programs.

Limitations of the math model

The typical math model used to characterize the balance considers terms with a maximum combination of two components. Additionally, the form of the equation is generally limited to second order. If a balance contains higher order or multiple combined order terms (relationships which could be characterized by combinations of three, four or even six components), these relationships can not be represented by the math model and show up as precision (scatter) errors.

The problem is illustrated in Figure 9. These higher order combinations may be dealt with in two ways; the math model can be left unchanged or the influences of the higher order and multiple combined load terms can be incorporated. If the form of the math model is not modified and should combined loads exist during testing which were not part of the original calibration matrix, conventionally accepted uncertainty bands placed on the original calibration can not represent the accuracy of the balance with any degree of mathematical certainty (refer to the Test Process portion of Figure 9).

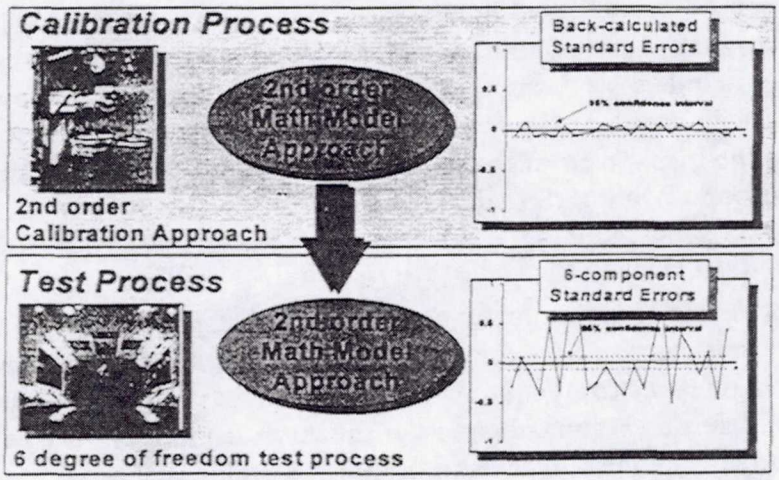

Figure 9 - A calibration load set limited to combined load cases with two components will not accurately model an applied load population containing 6 component combined load terms. Therefore, confidence intervals developed using commonly accepted practices are not valid

However, the additional combined load terms can be added to the data set used to develop the original constants; this will incorporate the influences of these higher order relationships and the resulting standard errors (which will be substantially higher than those developed using 2 component combined load calibration approaches) can be accepted. This process provides a more accurately defined balance.

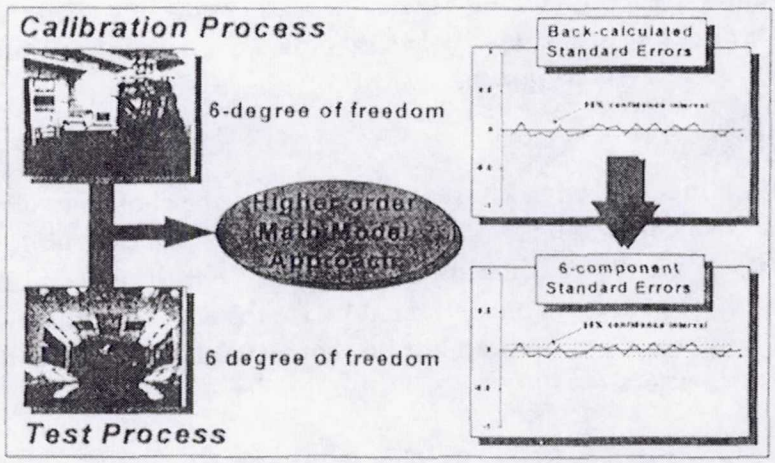

Figure 10 - By increasing the order of the input calibration, we can either expand our math model to accommodate the increased order, or use the lower order simulation and accept a higher, more representative error.

The calibration quality can be improved by modifing the math model to include the influences of high order and multiple combined load terms as required (shown pictorially in Figure 10). In this way, the model provides for combinations more accurately reflecting those loading conditions achieved in test. Relationships not previously modeled are now accounted for as higher order combined load terms. However, substantial calibration efforts are required to include a large number of combined load terms. Performing these calibrations are only feasible with automated processes. This approach provides the best method for eliminating the bias effects of the math model, and reduces the problem to predominantly the precision errors of the calibration process.

Adding Additional Terms to the Calibration Model

To verify the presence of higher order combined loads terms, a 729 point data set, with check load data sets containing 3 component and 6 component combined loads, was used as a baseline. A single three component combined term was selectively added to the original calibration, the resulting standard errors of the modified model were compared to those of the original model. The form of the equation was as follows:

$$F_i = \sum_{j=1}^{6} c_{ij} X_j + \sum_{j=1}^{6} d_{ij} F_j^{\,2} + \sum_{j=1}^{5} \sum_{k=j+1}^{6} c_{jk} F_j F_k + c_{lmn} F_l F_m F_n$$

Where:

c_{lmn} is the additional combined load term selected from the 56 possible combinations.

This modified form become a 6x28 matrix and the additional combined load term (using 3 components) was developed from existing data. There were 56 combinations of three components to be evaluated. A new matrix was developed for each; the six component combined load check calibration data was then passed through the revised matrix. The stan-

dard errors for each component were compared with the check loads from the original 6x27 matrix (without the additional combined load term). After computing all combinations (56 possible), the combination load set which provided the most dramatic improvement in standard errors was plotted. Substantial improvements could be made in most components by adding a single term (combining 3 components). Figure 11 shows this data plotted against the 6x27 baseline solution and the original back-calculated data without the check loads. The added term is identified as a PYA (Pitch, Yaw, Axial) combination. Notice that by adding the PYA term, the standard errors from the 6 component check loads were reduced significantly.

It is noted that there was no improvement in the standard errors when the combined load term was a cubic form of a single variable (ie: NF^3). This was also true of second order combinations with two variables (ie: NF^2*AF). This would seem to indicate that the relationships do not require higher order curve fits and that the improvements may be made by including first order combined load terms.

Adding 4 combined load terms and six combined load terms was also explored. The results were inconclusive since there was insufficient data for these additional terms to be generated. Additional calibration loads were required to evaluate the potential for improvement when adding these terms.

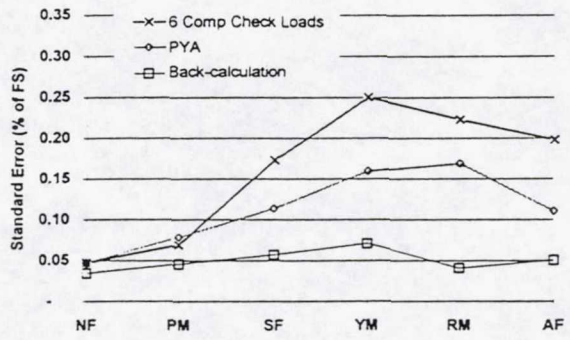

Figure 11 - By adding a single combination term, in this case a PYA term to the matrix model, standard errors for each component could be reduced. (The matrix was developed using the 729 point calibration file and standard errors are plotted using six component check loads).

Conclusions

The calibration processes the industry has used for over 50 years must be re-evaluated. The use of standard error methods, prediction levels, and uncertainty practices on the presently accepted calibration loading files and second order math model do not represent the combined loading environment to the degree that is indicated. Futhermore, the selection of applied calibration loads has a strong influence on the performance of the calibration model.

This evaluation shows that the calibration process must include multi-component load sequences tailored specifically to the loads expected in test. While the quality of calibration is dependent on the calibration process (manual or automatic), the selection of the math model and input calibration loads has an equally large effect on the quality of the resulting calibration.

Additional investigation is required. Experiments must be developed to define a 'best-practice' math model for use in the calibration problem. Additionally, calibration load sequences must be defined to ensure the highest quality data in the range of interest during testing.

References

1. "The Automatic Balance Calibration System", Israel Aircraft Industries, Ltd. publication,
Michael Levkovitch, August 1996.

DESIGN AND CONSTRUCTION OF INTERNAL BALANCES FOR THE GERMAN/NETHERLANDS WIND TUNNEL (DNW)

Dipl.Ing. Eberhard Graewe, Daimler Benz Aerospace, Germany
Prof. Dipl.Ing. Bernd Ewald, Technical University of Darmstadt, Germany
Dr.-Ing. Eckert, DNW, Netherlands

Abstract

The „German-Netherlands Wind Tunnel" (**DNW**) is a modern large atmospheric Low Speed Wind Tunnel. The tunnel is equipped with a six component external balance and with a tail sting mounting. During the construction period of this tunnel in 1978 a request for proposal for an Internal Balance was published and in 1984 and 1989 two additional balances were purchased. For all three balances VFW in Bremen (now Daimler Benz Aerospace, Deutsche Airbus GmbH) got the contract.

These balances were a large step forward with respect to size, ranges and required requested accuracy. For design and fabrication of the balances the technology of the electron beam welded balance, which was invented at VFW, was used.

The first balance (designated „W 605") had conventional cone joints for sting and model attachment. The two other balances (designated „W 608" and „W 616") were designed with flange joints.

The large size of these balances allowed the application of rather large strain gages, which resulted in excellent stability of the measurement. Combined with the excellent stability and accuracy of the signal acquisition electronics of the DNW thermal effects were observed. Especially the influence of spatial thermal gradients reduced the accuracy. So as a combined effort of VFW and DNW some research on correction of thermal effects was performed. The result finally was a force measuring technology in the DNW with outstanding accuracy and reliability.

1. INTRODUCTION

The „Deutsch-Niederländischer Windkanal" (DNW) was designed and constructed between 1976 and 1980. The DNW is a large subsonic atmospheric wind tunnel with four exchangeable test sections :

			Max. Speed
-	Open test section	6 x 8 m^2	90 m/s
-	Closed (or slotted) test section	6 x 8 m^2	110 m/s
-	Closed test section	6 x 6 m^2	145 m/s
-	Closed (or slotted) test section	9,5 x 9,5 m^2	62 m/s

For force testing the tunnel is equipped with a six component external balance and with a tail sting mounting for Internal Balances. For more details see [1].

In 1978 the DNW sent out a Request for Proposal for an Internal Balance. This competition was won by VFW with the proposal „Internal Balance W 605".

2. BALANCE W 605

The specified Load Ranges (for simultaneously acting loads) for this balance were :

Axial Force	X	=	12.500	N
Side Force	Y	=	12.500	N
Normal Force	Z	=	30.000	N
Rolling Moment	Mx	=	9.000	Nm
Pitching Moment	My	=	11.500	Nm
Yawing Moment	Mz	=	9.000	Nm
Maximum Diameter	D	=	200	mm
Maximum Length	L	=	1.250	mm

An extraordingly high accuracy was requested for this DNW balance.

Fabrication of a balance of this size was absolutely new territory at VFW. Some time before the technology of the electron beam welded balance was developed at VFW. With this concept the balance is fabricated from several parts, which are assembled by electron beam welding. With a correct selection of the material and with a sophisticated heat treatment the strength and other properties of the material are perfectly restored in the welding seam, so this fabrication method gives complete freedom in the design of the structure and the resulting balance behaves exactly like a one piece balance. One of the first balances fabricated with this method was the roll and spin balance W 64. Details of the fabrication steps are shown in the Figures 1 to 3.

Figure 1 shows the parts of the balance before welding. The two main parts are already clamped together by two screws in their position to each other. The two other parts are the „spring plates". Figure 2 shows the balance right after the welding process. The balance is assembled by four straight welding seams between the outrigger beams and the spring plates.

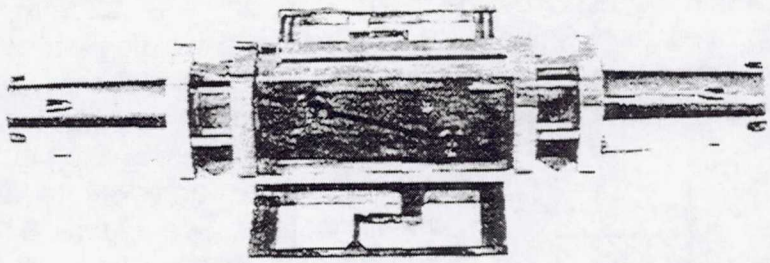

Figure 1 : Parts of balance W 64 before welding

Figure 3 shows the appearance of the finished electron beam welded balance. Only some remains of the welding seam at the inner edge between outrigger beam and springplate shows the fabrication procedure of this balance. The result is a de facto one-piece balance. We decided to fabricate the first DNW balance W 605 according to this principle regardless of its much larger size. Nevertheless we ran into problems, since at that time the performance of the available electron beam welding machine was limited.

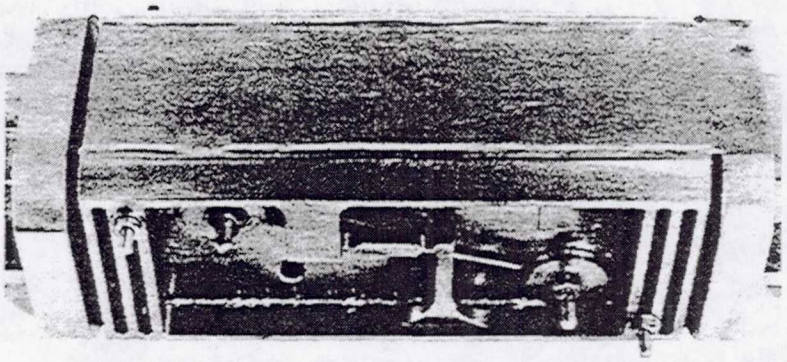

Figure 2 : Balance W 64 after welding with mounting screws still attached

The new DNW balance W 605 was designed as a conventional double bending beam. The bending positions were designed as cages for maximum stiffness. Maraging 300 was used for this balance. Figure 4 demonstrates the principle design.

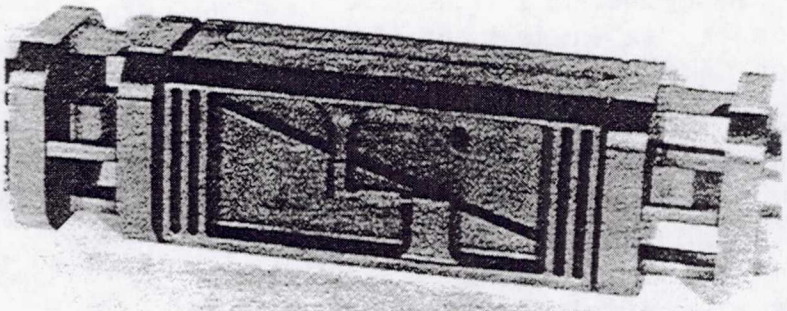

Figure 3 : Finished Central Part of Balance W 64

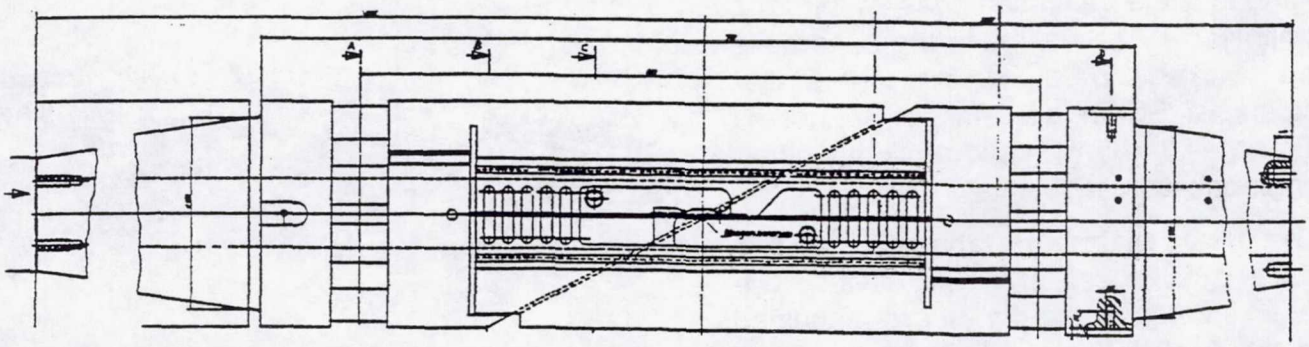

Figure 4 : Design of Balance W 605

Figure 5 shows a cross section of this balance. The total required depth of the welding seam was 22 mm. It proved to be impossible to achieve a welding with the electron beam welding machine available at the company at that time. So we used a special welding seam design. The necessary depth of the seam was achieved in two welding steps, see Figure 6. A first welding was applied, which covered only the inner part of the parallelogram spring plate. Then a strip of the same alloy was inserted and the welding was completed with two additional welding seams at the outer part of the spring plate.

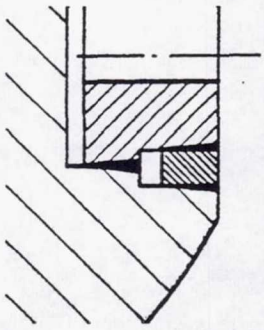

Figure 6 : Welding seam design of W 605

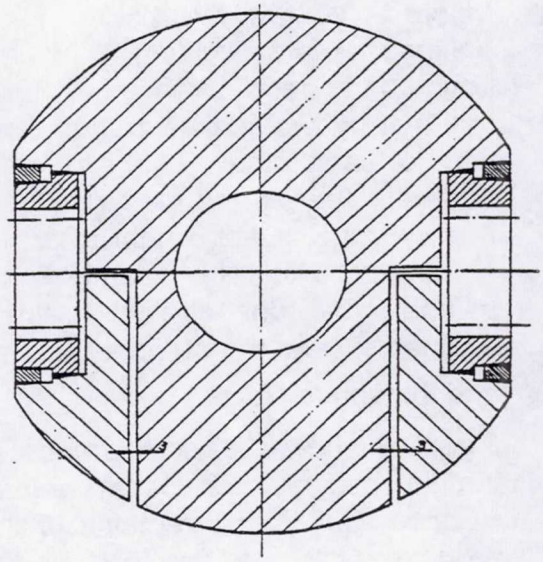

Figure 5 : Cross Section of W 605

Certainly we ran a considerable risk with this welding design. Nevertheless it worked quite well. The very low hysteresis of this balance observed during the calibration showed, that the welding design was totally successful.

Figure 7 shows the parts of this balance including the strips for the double welding seam. Please note, that the spring plates are finally machined including all the springs and the axial force element.

Figure 8 shows the balance after welding, heat treatment and final finishing of all outer surfaces. One disadvantage of this fabrication process is not visible in this photograph. The spring plates were slightly distorted by the welding process.

Although the distortion was within the limits and barely visible to the naked eye we wanted to avoid this in further balances. So for all balances fabricated after the W 605 we used a slightly different fabrication sequence.

The spring plates are fabricated prior to welding as closed and solid plates. The inner surface of the plates are machined to the final depth of all elements visible

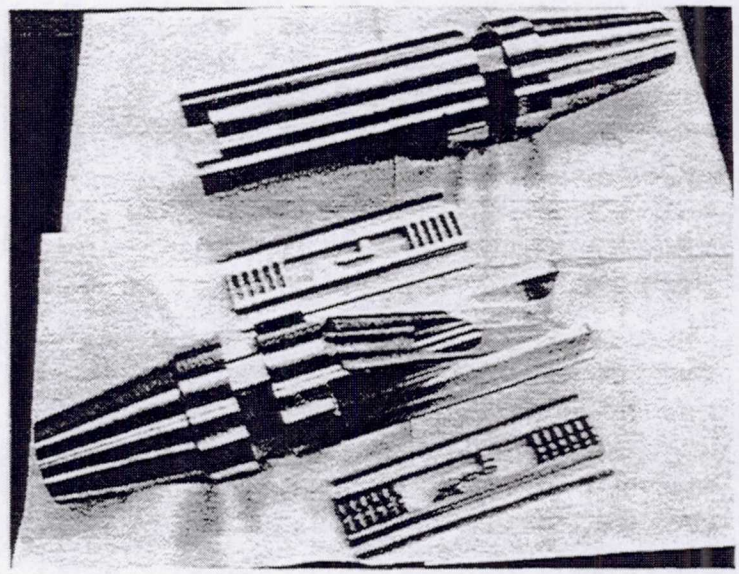

Figure 7 : Parts of Balance W 605

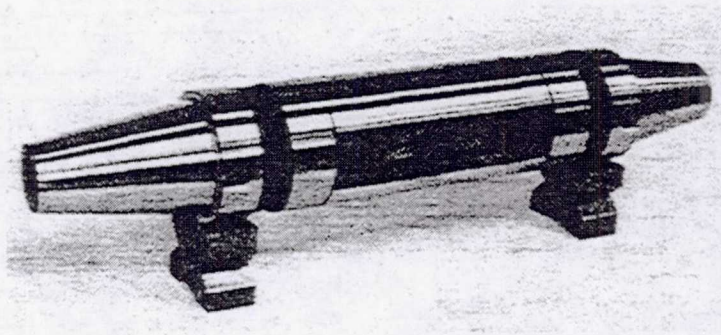

Figure 8 .: Balance W 605 ready for gaging

later in the parallelogram. Nevertheless the springs and the axial force sensor arrangement are still parts of a solid plate. After welding and heat treatment all external surfaces of the balance are machined. During these fabrication steps the spring plates are still solid plates, so the balance is a very rigid body and machining forces are no problem. Springs and axial force sensors are fabricated as the last step of machining milling and/or EDM from the outside. With this procedure the distortions due to welding are much reduced.

3. BALANCE W 608

In 1984 the DNW sent out another request for proposal for a strain gage balance, which in size was very similar to the W 605. VFW won this competition with the proposal „Balance W 608". The specifications for this balance were :

Load Ranges (for simultaneously acting loads) :

	Load Ranges „A"				Load Ranges „B"			
Axial Force	X	=	12.500	N	X	=	20.000	N
Side Force	Y	=	12.500	N	Y	=	6.250	N
Normal Force	Z	=	30.000	N	Z	=	50.000	N
Rolling Moment	M_X	=	9.000	Nm	M_X	=	4.500	Nm
Pitching Moment	M_Y	=	11.500	Nm	M_Y	=	15.000	Nm
Yawing Moment	M_Z	=	9.000	Nm	M_Z	=	4.500	Nm

The load range combination „A" was identical to the load ranges of balance W 605. The load range combination „B" was defined for testing cases with very high longitudinal loads and restricted lateral loads. A design study demonstrated, that for a balance design according to load ranges „A" the load ranges „B" are included in the safe overload ranges. So both load range combination could be fulfilled easily with one balance design and separate calibrations for both cases.

The balance was designed from the very beginning for the use in combination with a force free air-bridge to transmit drive air to the engine simulators (TPS) of the model. To provide enough space in the model for the drive air ducts, the balance length was limited. So for the model and sting joints of this balance flange joints were used. Apart from the shorter length the mounting procedure with flanges is simpler than with a cone joint.

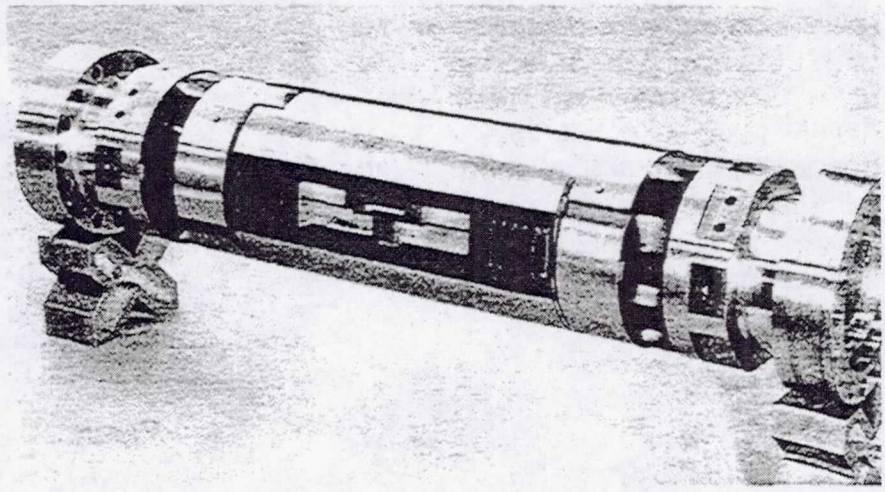

Figure 9 : DNW-Balance W 608

The structural design of this balance is very similar to the balance W 608. One important difference is, that in the meantime a more powerful electron beam welding machine became available. So in this balance the welding was done with a single welding seam only with a depth of 20 mm. The other difference is the fully symmetrical coupling of the axial force bending beam.

The body diameter of the balance W 608 is 200 mm and the maximum flange diameter is 218 mm. Total length is 1.000 mm.

4. BALANCE W 616

The third balance was acquired by DNW in 1990 and again the company, now called DASA Deutsche Airbus GmbH, won the contract. The load ranges were chosen for sensitive measurements with slightly smaller models. The specification was :

Axial Force	X	=	6.500	N
Side Force	Y	=	10.000	N
Normal Force	Z	=	20.000	N
Rolling Moment	Mx	=	4.500	Nm
Pitching Moment	My	=	7.500	Nm
Yawing Moment	Mz	=	3.000	Nm

Maximum Diameter	D	=	150	mm
Maximum Length	L	=	700	mm

Also this balance was a conventional design with cage bending positions. For optimum accuracy of axial force measurement the spring parallelogram was designed with a large number (9) of springs. The axial force bending beam was designed as a trapezoidal beam for near constant bending stress. Also this balance was fabricated as a welded balance; the single welding seams had a depth of 14 mm.

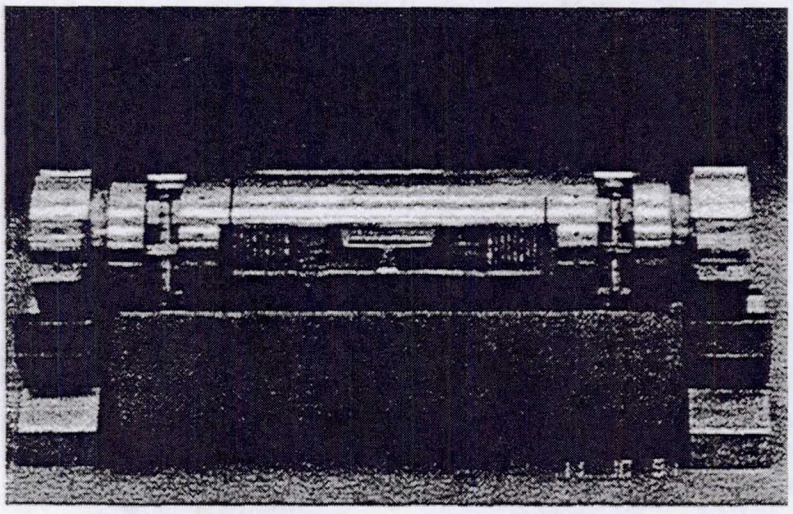

Figure 10 : DNW-Balance W 616

5. ACCURACY OF DNW BALANCES

For the accuracy of the DNW-balances very high standards were required. For a precise specification of the accuracy the following formula was specified between the DNW and VFW already for the first balance W 605 :

$$\delta_i \leq 0{,}001 \cdot |F_i| \cdot \left[a_i + \sum_{n=1}^{6} \left| \frac{F_n}{F_{n,max}} \right| \right]$$

with

δ_i	tolerated error in component „i" related to F_i
F_i	specified load of component „i"
a_i	accuracy coefficient of component „I"
F_n	actually acting load in component „n"
$F_{n,max}$	specified load of component „n"

This formula takes into account, that balance accuracy is reduced by simultaneous acting components but is valid for a single acting component as well. The accuracy coefficients are :

Accuracy Coefficients	W 605 , W 608	W 616
a_X	**1,5**	**1,2**
a_Y	**1,7**	**1,1**
a_Z	**1,3**	**1,0**
a_{Mx}	**1,5**	**1,4**
a_{My}	**1,0**	**1,2**
a_{Mz}	**1,0**	**1,4**

The repeatability was specified to be better than 1/3 of the specified accuracy. All DNW-Balances fulfilled this accuracy specification.

6. CALIBRATION PROCEDURES

When the first of the DNW-Balances was designed and fabricated, calibration equipment for balances of this size was not available at VFW. So a calibration rig for loads up to 5 metric tons was designed and constructed in a very short time. Since the preparation of a calibrated dead-weight set up to 5 tons seemed to expensive, the calibration loads were generated by rough

dead-weights and the loads were measured by high precision load cells between the balance loading sleeve and the dead-weight.

For the balance 605 the calibration loads were generated by a very comfortable procedure. Fuel oil tanks with a total capacity of more than 3000 litre's were mounted on a lightweight platform. The platform with the empty tanks was carefully weighted and attached to the loading sleeve as the first loading step via a high precision load cell. The dead-weight was increased and decreased by pumping water into the tanks or by draining the tanks.

When the balance W 608 asked for a calibration load up to 5 tons, the available space in the calibration rig was not sufficient for the water tanks, so the dead weight was made from iron blocks, which were loaded by a simple mechanic device.

Figure 11 shows the balance enclosed by the loading sleeve in the Deutsche Airbus calibration rig. Unfortunately this calibration rig is erected so tightly in a building, that it is nearly impossible to get a good total photographic view of this calibration rig !

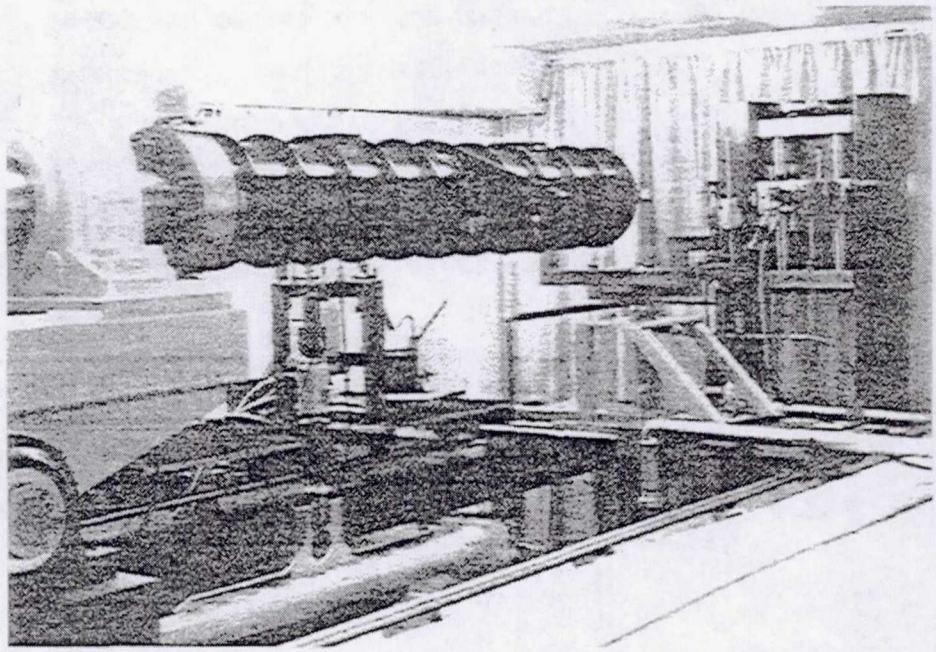

Figure 11 : Balance W 608 with Loading Sleeve in the Calibration Rig

Balance Calibration in this manual rig is very time consuming. The procedure results in excellent calibration accuracy if the calibration is done with utmost care and patience. So a lot of man power is consumed for a complete calibration.

The balance W 605 was recalibrated in the same rig after nearly 10 years of use in the DNW. The result of this recalibration was remarkable for two aspects. The calibration matrix was very close to the original matrix, so the stability of the balance and especially the long term stability of the strain gage application was excellent.

The second remarkable result was that the total scatter of the calibration results in terms of standard deviation was clearly improved in the case of the second calibration. We assume there are two reasons behind this effect. The first effect may be the improved experience of the calibration crew. Nevertheless the results indicate, that the hysteresis of the balance was lower in the second calibration. Obviously the internal hysteresis of the balance material is reduced by years of balance utilisation. The balance, at least the balance body, becomes better by the years like a good wine. Unfortunately is was not possible to separate the two mentioned effects.

7. THERMAL EFFECTS

During a typical measurement of the high-lift performance of a transport aircraft in the atmospheric test section of the DNW the wind-on runs of about half an hour are succeeded by wind-off activities for the change of slat and flap elements or other model parts. These model modifications last typically also half an hour. As a consequence of this wind-on/wind-off sequence an up and down drift of the wind tunnel air temperature during a test is unavoidable although a heat exchanger is used to stabilise the temperature.

The temperature variations of the order of magnitude of three centigrade per hour are experienced by the internal balance in the following manner: by the metallic surface of the model heat will be picked-up from the test section air and conducted via the model structure to the balance. Through the balance the heat is conducted to the sting support which is connected to structures which normally have a temperature level lower than the test section air. This heat transport through the balance has been addressed as being the cause of a significant drift of the balance axial sensor readings which was observed during wind-off periods when the tunnel was stopped after a measurement. The reason for this must be a small deformation of the axial load measuring element as a consequence of the heat flux through the extremely non-homogeneous mass distribution of the balance body. This deformation is sensed by the strain gages as mechanical stress although caused by thermal gradients inside the balance.

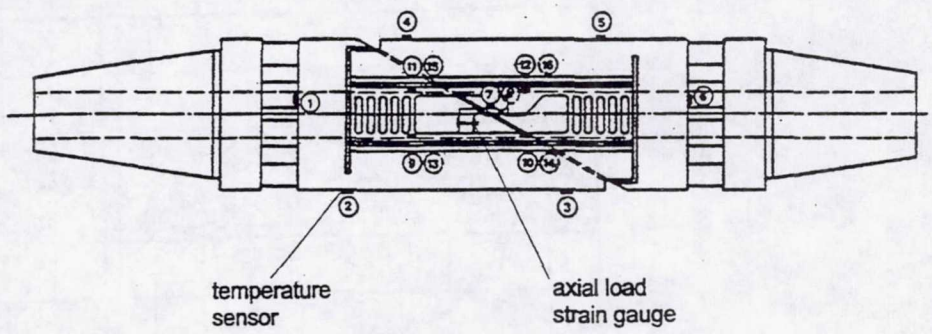

Figure 12 : Temperature Sensor Distribution, Balance W 605

In order to provide the possibility to separate the thermal effects from the mechanical stresses caused by the aerodynamic loads which should be measured a distribution of 16 temperature sensors has been installed at the balance W605. 6 of these sensors are located on the centre line, 5 each at the axial load parallelograms at both sides of the balance body, see Fig. 12. The output of these sensors was calibrated against the R1 drift during representative heating/cooling tests with the balance. The Figs. 13 and 14 show the non-linear and non-symmetric behaviour of the local temperatures together with the drifting R1 signal during a

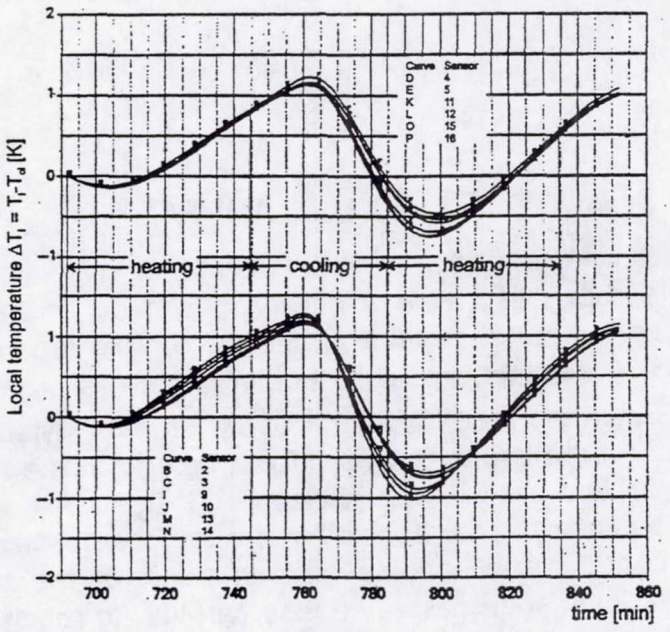

Figure 13 : Temperature Drift Calibration

calibration cycle. From this calibrations it became obvious that there exists no simple correlation between the temperatures and R1 which could be used for correcting the R1 drift by using a first and a second zero measurement and assuming a linear drift between them during the wind-on measurements. In order to cope with the observed non-linear behaviour a relatively simple deformation hypothesis of the balance body was created to correlate the distributed temperatures with local lengthening or bending of the four main parts of the balance body, see Fig. 12. A formulae containing a set of 11 linear combinations of subsets of the 16 temperatures with calibrated constants [3] was found to be an optimum representation of the actual deformation of the balance due to the drift of the local temperatures relative to the zero measurement. For the evaluation of the constants a comprehensive calibration data base was analysed with the aid of a least square method.

In Fig. 14 the correction of the R1 reading using this formulae is shown in comparison with a +/- .03% error bandwidth for R1. A resolution of .02 centigrade is necessary for the measurement of the PT 100 sensors to come out in this error band.

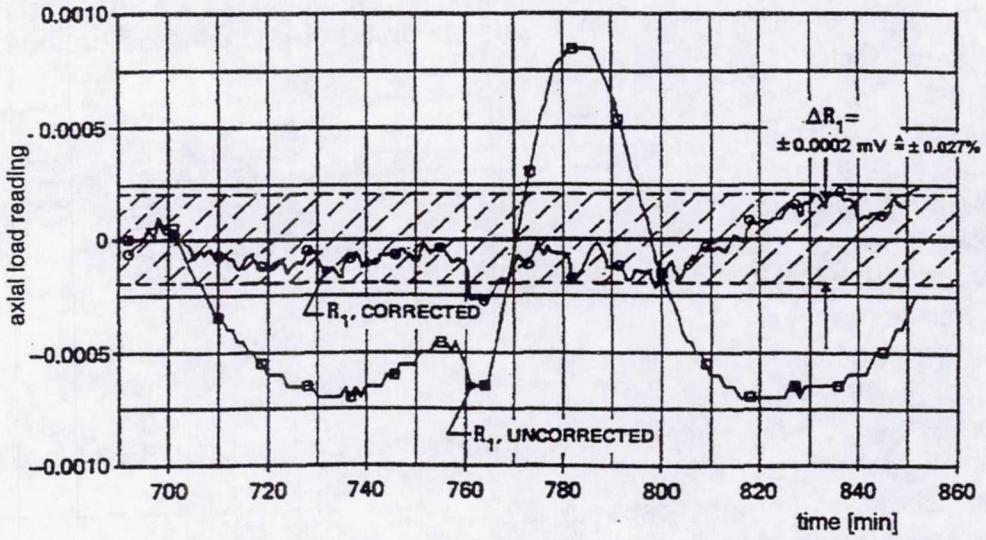

Figure 14 : Correction of Axial Force Signal Drift

8. OPERATIONAL ASPECTS

Since the model weight is distributed over all components of the internal balance load during aerodynamic tests with varying attitude of the model the balance measurements have to be corrected for this weight influence. This means for example that the axial load of the balance which is the main contribution to the drag has to be corrected by a term $W \cdot \sin(angle\ of\ attack)$. Since the weight W is relatively large for typical models at DNW the high accuracy desired for the drag evaluation asks for a very accurate angle of attack determination. For this reason at DNW a set of inclinometers is located on a stiff platform mounted to the model flange of the balance. At the beginning of a test the misalignment of this platform against the balance reference plane and the misalignments of the balance plane against the model reference coordinates are calibrated very carefully to reach the desired angle of attack accuracy of +/- .015 degrees.

During measurements with turbine driven engine simulators (TPS) mounted to an aircraft model compressed drive air has to be conducted over the balance from the non-weighted to the weighted part of the model structure. This is done at DNW with so-called airline bridges, see Fig. 15, which are combined from low reaction flexures. The small residual reactions of the balance on the bridges have to be calibrated dependent on the pressure and the temperature of the drive flow through the air lines. From this and the calibration of the stiffening effects of the bridge system corrections of the balance measurements are available during a test. To guarantee for the accuracy of this calibrations for more than one model assemblage the balance and the bridge structure as separated units are combined mechanically via interface planes at the balance body which allow for an accurate reproducing mounting, see Fig. 15.

In order to avoid an increase of the aforementioned thermal problems the balance body has been isolated from the air lines by a cylindrical shell which shields the balance against heat conduction and radiation.

All these measures have been necessary to take full benefit of the excellent accuracy and repeatability characteristics of the large balances during more than ten years of operation at DNW.

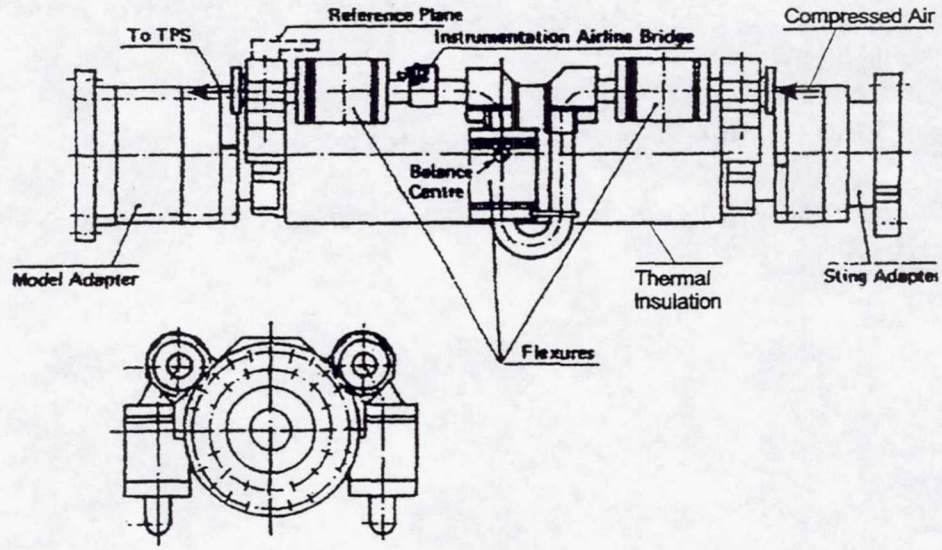

Figure 15 : Balance W 608 with Low Reaction Air Bridge

9. SUMMARY

The large size of the Internal Balances for the DNW was a special challenge for the balance technology. Regardless of the large dimensions the electron beam welded balances concept was successful also for these balances.

The large dimensions allowed the application of relatively large strain gages with excellent stability, so the very high accuracy requirements were met. Nevertheless due to the large dimensions of the balances thermal effects developed, which reduced the accuracy. So a sophisticated temperature gradient correction was developed.

For tests with TPS engine simulation force free air-bridges were developed for use together with these balances.

REFERENCES

[1] M. Seidel (Editor), *Construction 1976-1980, Design, Manufacturing, Calibration of the German-Dutch Wind Tunnel DNW.*
DNW-Publication

[2] B. Ewald, VFW Bremen, *Internal Strain Gage Balance*, In [1]

[3] D.Eckert, *Verbesserung der Temperaturkorrektur der internen Waage W605;*
DNW -TR- 86.04, 1986.

RECENT ADVANCES OF WIND TUNNEL BALANCE TECHNIQUES IN CARDC

HE Dexin GU Xingruo
China Aerodynamics Research and Development Center
Mianyang, Sichuan, P.R. of China

ABSTRACT

This paper gives a brief introduction to different kinds of wind tunnel balances, calibration machines and their applications in CARDC.

INTRODUCTION

Founded in 1968, China Aerodynamic Research and Development Center (CARDC) is a national establishment for aerodynamics research. Extensively research on the fields such as aeronautics, astronautics and wind engineering by three major means of wind tunnel tests, numerical calculations and model free flight tests.

At present, CARDC is equipped with over 30 aerodynamic and aerothermodynamic test facilities with the speed range covering low speed through high speed to hypervelocity among which are: 8m×6m/12m×16m, 4m×3m, Φ3.2m low speed wind tunnel, 1.2m×1.2m and 0.6m×0.6m trisonic wind tunnels, Φ0.5m hypersonic wind tunnel; Φ2m and Φ 0.6m shock tunnels, Φ0.6m hypersonic propulsion wind tunnel, Φ0.3m low density wind tunnel, arc heaters and arc-heated wind tunnel, 200m free-flight ballistic range and under building 2.4m×2.4m transonic wind tunnel being under construction ect., Table 1. The simulation abilities are: Mach number M=0.015 ~ 24, Reynolds number Re/m=2×10^4 ~ 10^9, altitude H=0 ~114 km, total pressure p_0 =1.0×10^5 Pa ~ 65 MPa, total temperature T_0 =823 ~ 700 K, enthalpy E=4 ~ 25 MJ/Kg.

In various kinds of wind tunnels and test facilities, mechanical balances, strain gauge balances, piezoelectric balances, special balances and the correspondent calibration machines are set up.

MECHANICAL BALANCE

In 1.4m×1.4m, 4m×3m and Φ3.2m low speed wind tunnels, each is equipped with six

components platform or pyramidal balances. The twin-ring pull-press strain elements are used in both kinds of balances, this avoids the nonlinear problem due to large loads when only single-ring strain elem ent is used.

CONVENTIONAL STRAIN GAGE BALANCE

Up to now, there are over 100 conventional strain gage balances used in wind tunnels and test facilities in CARDC. These balances have been classified into series according to sizes and designed loads.

Box Balance

Box balances used in low speed wind tunnels are mainly internal balances. Their dimensions range from 200mm (length) ×70mm(width)×50mm(height) to 550mm×160mm×130mm. The designed loads of normal force components range from 3~25KN. Several typical balances of these kind used in CARDC 8m×6m wind tunnel are shown in Fig 1. The balance is composed of a fixed frame and a float frame. There are seven cantilever type sensitive elements in the fixed frame on which strain gages are mounted. Seven elastic linkers, four in the direction Y, two in direction Z and one in direction X, each with elastic hinge on both ends, are used to connect the fixed frame and floating frame, and the floating frame is connected with the linkers of models. For the sake of two free degrees, the linkers can only transform press/ pull forces in direction of axles to perform force resolutions. In CARDC, eighteen internal box type balances have been developed since the first application in 1980 (table 2). The application shows that this kind of balances are high rigidity, low interference, and better mechanical property. The precision and accuracy are within 0.3% and 0.5%, respectively. So we think them to be a kind of balances with good future in low speed wind tunnel.

In addition to the internal box type balances, CARDC has developed an external balance in 1995 (Fig 2), which is applied to measure forces on real automobiles in 8m×6m wind tunnel. The contour size of this balance is 200mm(length)×1000mm(width)×500mm(height), and the designed normal load 50 KN. There are four load cells between the fixed and floating frames. Each of the cells can measure the perpendicular forces Fxi, Fyi and Fzi (i=1~4), and by means of following matrix the aerodynamic forces and moments acting on models can be found

$$\begin{bmatrix} Y \\ X \\ M_z \\ Z \\ M_y \\ M_x \end{bmatrix} = \begin{bmatrix} 1 & 1 & 1 & 1 & 0 & 0 & 0 & 0 & 0 & 0 & 0 & 0 \\ 0 & 0 & 0 & 0 & 1 & 1 & 1 & 1 & 0 & 0 & 0 & 0 \\ \frac{L_{M_z}}{2} & \frac{L_{M_z}}{2} & \frac{-L_{M_z}}{2} & \frac{-L_{M_z}}{2} & 0 & 0 & 0 & 0 & 0 & 0 & 0 & 0 \\ 0 & 0 & 0 & 0 & 0 & 0 & 0 & 0 & 1 & 1 & 1 & 1 \\ 0 & 0 & 0 & 0 & \frac{L_{M_X}}{2} & \frac{L_{M_X}}{2} & \frac{-L_{M_z}}{2} & \frac{-L_{M_z}}{2} & \frac{-L_{M_z}}{2} & \frac{L_{M_z}}{2} & \frac{-L_{M_z}}{2} & \frac{L_{M_z}}{2} \\ \frac{-L_{M_z}}{2} & \frac{-L_{M_z}}{2} & \frac{L_{M_X}}{2} & \frac{L_{M_X}}{2} & 0 & 0 & 0 & 0 & 0 & 0 & 0 & 0 \end{bmatrix} \cdot \begin{bmatrix} Y_1 \\ \vdots \\ Y_4 \\ X_1 \\ \vdots \\ X_4 \\ Z_1 \\ \vdots \\ Z_4 \end{bmatrix} \quad (1)$$

The accuracy of each component of the balance is better than 0.03% within the designed load range.

Sting Balance

This kind of balances are mostly used in transonic and supersonic wind tunnel tests. More and more usage in low speed wind tunnel is also found. The diameters of this kind of balances range from 3.5mm to 120mm in CARDC, designed normal forces 30N~ 40kN (tables 3 and 4). For the axle force, I-shaped beams are usually used as measurement elements of normal forces. Sometimes flexible plates are used directly. For the other forces components the measuring elements usually are single or triple beams that are arranged symmetrically. A sting balance used in 1.2m×1.2m trisonic wind tunnel for full scale model tests is shown in Fig 3.

Fig 4 shows another kind of sting balance, which can be used in force tests of store models. During a wind tunnel test, for example, eight balances were used and 40 aerodynamic components of store and store frame were measured at the same time.

SPECIAL STRAIN GAGE BALANCE

Hinge Moment Balances

A variety kinds of hinge moment balances are used in CARDC in which half-model and full-model balances are the mostly used two types. The full-model hinge moment balances include lateral type(the axle of balance are perpendicular to the model's) and longitudinal type (the axles of balance and model are parallel), and elastic plate type.

A full scale tail hinge moment balance used in 8m× 6m low speed wind tunnel is shown in Fig 5.

Fig 6 shows a lateral balance and a longitudinal balance used in 1.2m ×1.2m trisonic wind tunnel

for the hinge moment measurements of rudder models. The advantages of the lateral balance are high stiffness and easy design of the drag force element. The advantages of longitudinal type are the efficient usage of space, the matched left and right measuring values. The disadvantages are smaller space. more difficult to design, mount and conduct the measuring line.

Fig 7 shows various kinds of elastic plate type hinge moment balances used in 1.2m ×1.2m trisonic wind tunnel for hinge moment measurement of half-model and full-model rudders. By combining balance and model together, the elastic plate hinge balance ascertains the overlap of hinge axle with balance calibration center. The normal force has less effects on the hinge moment and always is perpendicular to balance. These simplify the data processing. However, every angle of rudder requires a balance, and this is its main disadvantage.

Dynamic Derivative Balances

This kind of balances have been equipped in low speed, transonic, supersonic and hypersonic wind tunnels in CARDC. There are two types, forced vibration and free vibration type. Fig 8 shows a forced vibration derivative balance and its test equipment used in CARDC 4m × 3m low speed wind tunnel. The model can vibrate in three uncoupled freedoms, vertical, pitching and rolling , in a certain frequency. Digital data processing method is used to acquire dynamic derivatives of high angle of attack. Fig 9 shows a forced vibration derivative balance with its test equipment used in 1.2m × 1.2m trisonic wind tunnel in CARDC. This balance is used to measure the damping derivative of pitch. According to the mounting method, it can be divided into two types: one is single sting type, which is mainly used for derivative measurement of long -thin models, and another is double sting type composed of inner and outer shelves mainly used for the derivation measurement of aircraft models.

Jet-Flow Balances

The jet-flow balance systems used in CARDC 0.6m × 0.6m trisonic wind tunnel is given in Fig 10. As a six-component ring balance, the center hole of the balance element is used to install high pressure jet-flow pipe and hollow balance sting. As shown in the figures, the inner side of spring beam at B-B section is used for axial force measurement and eight rectangular members at the A-A cross section are used to measure the other five load components.

High-Frequency Base Balance

This kind of balances are used for measuring dynamic loads on civil structures. High sensitivity and rigidity are required. A five-component high-frequency base balance used in 1.4m × 1.4m low

speed wind tunnel of CARDC is given in Fig 11. A base tray cross member and shear force rod constitute the structure of the balance. The shear force rod elements is connected with drag and side force and the cross beam elements is connected with wind tunnel turntable measure three moments. The balance body's natural frequency is higher than 250Hz. A six-component high frequency base balance used in CARDC 4m ×3m wind tunnel is shown in Fig 12. This balance is composed of cross-shaped frame, elastic linkers, strain elements and turntable. Multi-edged frame is used as the base of the balance and six elastic levers are used to connect the frame and the strain elements to form a floating frame with six degree of freedoms. The model is fixed by the frame in test so that the aerodynamic force acting on the model can be resulted according to the foreseeable coordinate system and pass through the strain elements.

For this balance, the static calibrating accuracy of each element is 0.1%~0.5%,the precision is 0.3%~0.8%. The minimal scale is 0.1g~0.5g. The natural frequency is higher than 260Hz for lift and side force elements and 480Hz for other elements.

Wire Suspension Balance

To decrease the interference and increase the stiffness of support, a wire type-support system for high angle of attack test in CARDC Φ3.2m subsonic wind tunnel has been developed. The test setup of the system consists of internal strain gage balance, struts, strut support, right and left columns, upper beam, base and transmission mechanism (see Fig 13). The model is mounted by attaching to both ends of the balance which is supported in wind tunnel by 8-struts with one end connected to the inner rod of the balance and other connected with to the support via load cell. The two strut supports are placed coaxially and driven by a servo motor via transmission mechanism housed in the right and left columns and the base of the setup to fulfill unlimited angle of attack variation. The setup is mounted the turntable of the tunnel to fulfill variation of model side slip.

To evaluate the performance of the system a delta wing-body combination model has been tested. Some typical results are given in Fig 14. No vibration of the model-balance-support was observed during the test.

Rotor Balance

The CARDC 8m×6m low speed wind tunnel is also equipped with a rotor/fuselage combination test device (Fig 15) in which a rotor balance, a fuselage balance and a torque meter is included. The rotor balance is a box type strain gage balance which is composed of a upper plate, seven flexible links, seven load cells and a base plate, Fig 16. The load cell consists of two force transducers for static loads and a piezoelectric transducer for dynamic loads. In the load cell two force transducers are arranged oppositely and preloading is applied to the force transducer unit to get symmetric output

characteristics. Four vertical load cells placed symmetrically to the rotor shaft are used to measure the thrust, pitching moment and rolling moment . Two horizontal load cells placed symmetrically to the rotor shaft are used to measure the side force and the moment produced by the bearing supporting the rotor shaft. The load cell measuring the drag is placed in the front of the balance. The torque meter is used to measure the torque of the rotor, but no interference to the rotor balance is induced.

The static calibration results of the rotor balance shows the precision for all components is better than 0.2% and the accuracy is 1%. The dynamic calibration, except Mx and Mz components, the precision for other components is better than 1.2%.

Rotary Balance

The rotary balance testing technique is developed in CARDC 4m×3m low speed wind tunnel (Fig 17) to measure the overall aerodynamic forces and moments acting on the aircraft rotating round the freestream vector at different angle of attack and side slip wind and then to study and predict of the spinning and spin-recovery behavior of aircraft.

The general arrangement of CARDC rotary balance testing system is composed of model support-attitude mechanism, power and transmission system, six-component balance, data acquisition and reduction system, and setup support. The model support-attitude mechanism consists of a model support strut, a carriage and a arc track.. The angle of attack and side slip of model is obtained by adjusting both the pitching and rolling angle referring to the body-axis-system. The model can be installed in wind tunnel in sting, dorsal and central support, respectively.

The balance for force or moment measurement was specially designed with two attachments to connect it to the model at forward/aft end and to increase the stiffness of model support, see Fig 18.

Rotary balance test is of a dynamic one. In the test structure vibration induced by the dynamic unbalance of model-balance-support system during rotation, inertial forces due to fluctuation of rotating speed and the noise caused by the slipping would introduce incident error and then affect the precision of the test results.

Water-cooling Balance

To decrease the temperature effects on strain gage balances in conventional hypersonic wind tunnel, a series of six -component water-cooling balances were developed in Φ0.5m hypersonic wind tunnel of CARDC, their diameters range from 20 to 28mm and normal forces range from 250 to 2500N, table 5.

A typical six -component water-cooling internal balance is given in Fig 19. It consists of water-cooling system, balance and rear supporting sting. Firstly cooling water goes through metal flexible pipe out of sting into water-cooling pipe, at the heat-insulation joint the sting and the balance are heat-insulated, and the water go then through bellows into water cooling case, the balance itself and the joint part of the balance and the model being heat-insulated and cooled, and finally the water goes out through another bellows and a metal flexible pipe. Under the condition of water-cooling, the temperature of balance body can be controlled within 50°C. But for the cause of reducing temperature effects to output signal temperature compensation is also necessary. The temperature effect of every balance component after temperature compensation is generally less than 0.3% if the temperature of gas flow is within 80 and 600°C.

Medium Temperature Balance

In hypersonic wind tunnel tests, the application of medium temperature balance is one of methods to solve the temperature-related problems. That is taking measures to make the balance elements be heat-insulated. One of the measures is the application of heat-insulating house. A six-Component medium temperature balance used in CARDC Φ0.5m hypersonic wind tunnel is shown in Fig 20.

Microbalance

Recent years, three and two component external microbalances are developed and used in CARDC Φ0.3m low density wind tunnel , which is mostly used to simulate the flight status and condition of space vehicle at high altitude and speed.

A typical external microbalance is given in Fig 21. It uses twisting moment elements through amplification by leverage to increase the balance sensitivity, and uses the signal of force by arm of force to measure aerodynamic load. The mass of sting and model burdened by balance elements can be trimmed to the center of elements, in this way the arm of force is zero and the mass causes no signal under vibration. The balance designed load: normal and axial force components is 0.002N, pitch moment component 0.05Nmm. The balance static calibration accuracy is better than 0.5%.

PIEZOELECTRIC BALANCES

There are two kinds of piezoelectric balances are used in pulse wind tunnels, one kind with elastic elements and the other without. The former has been used in CARDC. The structure is almost

same as strain gage balance except for substituting piezoelectric ceramic strips for strain gages. A typical piezoelectric balance used in CARDC Φ2m shock tunnel is shown in Fig 22. From the structure showed in the figure, it is known that all the polarized vectors of ceramic strips are perpendicular to the silvered strip surface. Different polarities are set for different units, plus piezoelectric effect is adopted to change strain into electricity. The advantages are: simple construction, high rigidity and sensitivity, low nonlinearity, wide load range and high frequency response. The accuracy is low at low frequency or after long time operation, this is the disadvantage.

When the balance is used for force measurement in pulse wind tunnel, the inertia force signals due to vibration of model, balance and supporting system will be mixed with the real output to form actual output signals. Inertia compensation by using an accelerator is necessary for the balance except reducing the altitude and increasing the frequency of inertia force.

For a real system, accurate and full compensation is hardly possible and what can be done is to compensate the frequency within the range of critical frequency. Fig 23 shows the compensation effect on output wave in the force measurement test of CARDC Φ2m shock tunnel. From this Figure, it can be seen that the output wave after compensation is coordinative to the wave of total pressure. At present, the piezoelectric balances have been classified into series, the balances' cross section sizes range from 5mm(width)×10mm(height) to 30mm×30mm, the designed loads of normal force range from 0.1N ~5KN, see table 6.

STRAIN GAGE

The strain gages used for the balances of CARDC are developed by her own staff. There are two kinds of them, which have been classified into series. Except for unusual occasions, strain gage balances are mostly foil-based. According to the temperature, foil strain gages can be divided into two kinds, normal and medium temperature. The former is applied under the temperature of 80 ℃, and their sensitive grids range from 1mm×0.8mm to 6mm× 4.2mm(length by width), and their resistances range from 150~1000Ω. Except single-shaft strain gages, there are double-shaft semi-bridge strain gages, its adhesive can be adjusted without pressure, those make the installation of the strain gages a great convenience. The working temperature of medium temperature strain gage is up to 250 ℃.

BALANCE CALIBRATION

Calibration Machines

There are 13 different calibration machines in service in CARDC. Their designed loads of normal

force components range from 1N to 50kN.

A automatic balance calibration machine used in CARDC 1.2m×1.2m trisonic wind tunnel has been developed recently. This machine is composed of following subsystems: loading, displacing, inspecting, controlling and measuring. Six machine-electrocith force generators in a two-dimensional space compose a definite space force resource system which give load to the six-component balance by means of single component and multi-components. The magnitude of loading is measured by sensors and the resolution is 0.005%. The accuracy is better than 0.02%. The displacement subsystem is mechanism with six degree of freedoms which can fulfill the needs of three line and three angle displacement to ascertain the loading adapter to be positioned in accuracy. The value of displacements are measured by an inspecting system composed of high accuracy vortex probes and the resolution for line displacement is smaller than 0.001mm, for angle less than 1″. The positioning precision for loading adapter is ±0.02mm and ±15″.

The control subsystem works by two microcomputers to execute the six force generators and six degree of freedoms moving mechanism through a closed loop. High accuracy data inspecting device is used in the measurement subsystem for the measurement of loading weights, balance outputs and displacements. One computer is used for the administration of control and measurement subsystems.

Fig 24 shows a full automatic reposition compensation balance calibration machine with six freedoms used in CARDC Φ0.5m hypersonic wind tunnel. The machine is equipped with six air-pressure type of force generators.

Calibration Method

A special kind of loading program, the combination of unit loading and multi-unit loading, is used in CARDC to calibrate balances. In the first, each of six components is loaded by unit loading, then multi-unit loading to all components at the same time is followed. In full scale range, eight loading point s are chosen for each component in unit loading and multi-unit loading. For multi-unit loading the points are separated into two groups, 1, 3, 5, 7 in group one and 2, 4, 6, 8 in the second group. Each group is loaded according to the order of table 7, which is designed according to orthogonality. Every loading point has the same chance to appear in any row and both loading groups present in any two rows, the chance for each group is equal. This loading approach has the advantage of high efficiency in loading and needs less change for loads. Furthermore, all six-component balances are loaded in two directions so that the hysterisis can be illustrated in the procedure.

The general formula of balance calibration can be expressed as

$$F_i = F_{io} + \sum_{j=1}^{6} a_i^j \bullet \Delta U_j + \sum_{j=1}^{6} b_i^j \bullet \left|\Delta U_j\right| + \sum_{j=1}^{6}\sum_{l=1}^{6} c_i^{jl} \bullet \Delta U_j \bullet \Delta U_l + \sum_{j=1}^{6} d_i^j \bullet \Delta U_j^3 \qquad (2)$$

$$(i=1,2.....6)$$

where : a_i^j --the first order coefficient, a is the main coefficient when $i=j$; a is interference coefficient when $i \neq j$;

b_i^j, c_i^{jl}, d_i^j --high order interference coefficient;

F --applied load;

ΔU--output signal increment.

REFERENCES

1. Jiang Jinrong: The Electric Signal of Mechanical Balance in Low Speed Wind Tunnel and the Development of Twin-Ring Strain Gage Element. *Aerodynamic Research and Development,* Nov. 1975.

2. Zhang Xiangming: The Technical Research of Spring Flake Balance. CARDC TR 94-21, Nov. 1994.

3. Lu Wenxiang: Development of External Store Force Balance. CARDC TR 92-203, Aug. 1992.

4. Shen Limin: CARDC Rotary Balance Wind Tunnel Testing System. *Aerodynamic Experiment and Measurement & Control,* vol. 9, no. 1, May. 1995.

5. Liu Yufu: Development of New-Type High Precision External Balance for 8m×6m Wind Tunnel. CARDC TR 96-15, Apr. 1996.

6. Cheng Feng; and Hu Guofeng: Design and Application of High Frequency Dynamic Balance. *Aerodynamic Experiment and Measurement & Control,* vol..9, no.1, May. 1995.

7. Shen Limin: A Wire Type-Support System for High Angle of Attack Test in CARDC Φ3.2m Subsonic Wind Tunnel,.CARDC TR96-26, Aug. 1996.

8. Liu Wei: An Investigation on Temperature Effects of Strain Gauge Balances for Conventional Hypersonic Wind Tunnel.

9. Liu Wei: Development and Application of Internal Six-Component Water-Cooling Balance CARDC TR 92-28, Aug. 1992.

10. Liu Wei: A Kind of Medium Temperature Balances without Water-Cooling for Hypersonic Wind Tunnel. CARDC TR 96-22, May. 1996.

11. Tang Zhigong; and Yang Yanguang: Development and Application of Microbalances in Low-Density Wind Tunnel. CARDC TR 92-52, Aug. 1992.

12. Gu Xingruo; and Hu Jinqing: Development of BFH-Series Strain Gages. NASA CP

13. Gu Xingruo: Balance Calibration Machines and Method for Wind Tunnel in CARDC. CARDC TR 92-46, Jun. 1992.

14. Zhang Yingpei; and Yan Junren: A Fully Automatic Calibration System for Six Component Internal Strain Gauge Balances for High Speed Wind Tunnels.

15. Liu Hongshan; Lu Zhiguo; and Qi Xuequn: Single Load and Multicomponent Balance Calibration System (SL & MBCS) of Piezoelectric Balance in Shock Tunnel. NASA

Table 1. Wind Tunnels and Test Facilities of CARDC

No	Code Name	Facility Name	Test section Dimension [m]	Performance	Built Date
1	FL-11	1.4m×1.4m Low Speed Wind Tunnel	1.4×1.4×2.8	V=15~50m/s Re/m=2.6 × 10^6 N=100kW	1978
2	FL-12	4m × 3m Low Speed Wind Tunnel	4×3×8 4×2.2×15	V=15~80m/s Re/m=5.2×10^6 N=2600kW	1971
3	FL-13	8m×6m/12m×16m Low Speed Wind Tunnel	12×16×25 8×6×15	V_1=5~21m/s V_2=20~85m/s Re/m=5.7×10^6 N=3×2600kW	1978
4	FL-14	Φ3.2m Subsonic Wind Tunnel	Φ3.2×5	V=12~145m/s Re/m=9.5×10^6 N=5200kW	1993
5	Fl-21	0.6m×0.6m Trisonic Wind Tunnel	0.6×0.6×1.775	M=0.5~3.5 Re/m=2.9×10^7 Po=4.9×10^5Pa	1969
6	Fl-23	0.6m×0.6m Trisonic Wind Tunnel	0.6×0.6×2.5	M=0.5~4.5 Re/m=4.3×10^7 Po=7.4×10^5Pa	1975
7	Fl-24	1.2m×1.2m Trisonic Wind Tunnel	1.2×1.2×3.6	M=0.4~3.0 Re/m=3.5×10^7 Po=4.54×10^5Pa	1976
8	FL-26	2.4m×2.4m Transonic Wind Tunnel	2.4×2.4×7	M=0.3~1.4 Re/m=7×10^7 Po=4.5×10^5Pa	under construction
9	FL-31	Φ0.5m Hypersonic Wind Tunnel	Φ0.5	M=5~10 Re/m=5.6×10^7 Po=11.6Mpa To=1073K	1976
10	FD-14	Φ2m Shock Tunnel	Φ0.8 Φ1.2 Φ2.0	M=6~24, t<20ms Re/m=10^4~10^8 Po=67Mpa To=4500K	1978

Table 1(cont). Wind Tunnels and Test Facilities in CARDC

No	Code Name	Facility Name	Test Section Dimension [m]	Performance	Built Date
11	FD-15	Supersonic Arc Heater Wind Tunnel	Φ0.4~0.6	M=5~8 E=4~25MJ/kg H=30~80km t=200~400s	1978
12	FD-17	Φ0.3m Low Density Wind Tunnel	Φ0.3	M=6~24 To=1700K H=60~94km	1977
13	FD-18	200m Free-Flight Ballistic Range	Range Chamber Φ1.5×200	V=2~6.5km/s Po=5×10^5Pa Re/m=10^3~2×10^9 H=0~60km	1979
14	FD-20	Φ0.6m Hypersonic Propulsion Wind Tunnel	Φ0.6	M=4~6, Po=8~10^5Pa H=20~60km t<5s	1988

Table 2. Some Box Strain Gage Balances for Low Speed Wind Tunnels in CARDC

Type	Load Range [N or N.m]						Dimension [mm]		
	Y	Mz	X	Mx	Z	My	L	W	H
TH0701B	3000	400	500	240	700	300	200	70	56
TH1001A	6500	1000	2200	450	1500	700	340	100	80
TH1002A	3400	850	500	150	300	150	340	100	86
TH1301A	10000	3100	4000	700	2700	1100	450	130	104
TH1601A	25000	6000	8000	3000	5000	4000	550	160	130
TH1601B	10000	1500	2500	600	2000	600	400	160	160

Table 3. Some Sting Strain Gage Balances For Low Speed Wind Tunnels in CARDC

Type	Load Range [N or N.m]						Dimension [mm]	
	Y	Mz	X	Mx	Z	My	D	L
TG0101A	30	2	5	1	30	1.5	10	100
TG0151A	60	5	20	2	60	2		130
TG0401A	1500	150	300	80	200	100	40	314
TG0501A	3000	400	1000	200	1000	300	50	410
TG0502A	3000	200	500	100	700	150	50	410
TG0561A	5000	600	1200	500	2000	500	56	430
TG0601A	5200	800	1800	560	1200	560	60	432
TG0701A1	7000	1000	1500	1000	3000	1000	70	554
TG0801A	10000	2000	2000	1500	5000	2000	80	554
TG1201	40000	5500	7000	3000	5000	5000	120	730
TG1202	25000	6000	8000	4000	5000	4000	120	730
TG1203	25000	10000	8000	6000	7000	6000	120	730

Table 4. Some Sting Strain Gage Balances for Trisonic Wind Tunnels in CARDC

Type	Load Range [N or N.m]						Dimension [mm]	
	Y	Mz	X	Mx	Z	My	D	L
2N6-20A	250	20	100	5	150	10	20	163
2N6-22B	600	40	160	10	200	15	22	217
2N6-24A	1200	60	200	15	200	20	24	210
2N6-26A	1200	90	200	15	200	30	26	206
2N6-28B	1600	90	200	20	400	40	28	223
2N6-30A	3000	150	350	35	500	40	30	235
2N6-32A	3000	200	200	50	500	50	32	233
3N6-10A	60	3	50	1.5	100	3	10	95
3N6-26B	1200	80	100	10	300	20	26	220
3N6-28B	3600	120	200	20	500	45	28	240
3N6-30B	2400	150	200	20	500	50	30	246
3N6-32C	5600	250	200	60	900	100	32	275
3N6-34B	5000	120	300	30	400	50	34	300
3N6-36B	3500	120	400	80	350	100	36	280
3N6-45A	6000	500	500	100	1100	250	45	388
3N6-50A	10000	700	1000	150	2000	400	50	378
3N6-60	20000	2000	3000	300	8000	800	60	415

Table 5. Some Sting Strain Gage Balances for Hypersonic Wind Tunnel in CARDC

Type	Load Range [N or N.m]						Dimension [mm]		Note
	Y	Mz	X	Mx	Z	My	D	L	
5N6-20A	250	10	120	2	80	6	20	245	[1]
5N6-22A	294	11.8	196	2	98	4.9	22	215	[2]
5N6-24B	490	29.4	343	2	147	9.8	24	227	[1]
5N6-24D	147	9.8	98	1	49	2.9	24	227	[1]
5N6-24G	980	58.5	98	9.8	196	39.2	24	213	[1]
5N6-26A	1765	98	196	14.7	490	49	26	235	[1]
5N6-28A	3530	118	196	19.6	490	44	28	243	[3]
5N6-28B	1569	108	196	19.6	490	44	28	243	[1]
5N6-28C	2452	49	294	11.8	343	12.7	28	215	[1]

Note: [1] water-cooling balance;
[2] medium temperature balance;
[3] convention balance.

Table 6. Sting Piezoelectric Balances for Shock Tunnel in CARDC

Type	Load Range [N or N.m]						Sting Diameter [mm]
	Y	Mz	X	Mx	Z	My	
YD3-20A	240	530	2000	—	—	—	20
YD6-25A	800	1200	3000	30	250	560	25
YD3-30A	1500	2000	6000	—	—	—	30

Table 7 Orthogonal Loading

order	component number						order	component number					
	1	2	3	4	5	6		1	2	3	4	5	6
0	0	0	0	0	0	0	33	1	2	2	2	2	1
1	1	1	1	1	1	1	34	1	2	2	2	2	2
2	1	1	1	1	1	2	35	1	2	2	2	2	3
3	1	1	1	1	1	3	36	1	2	2	2	2	4
4	1	1	1	1	1	4	37	2	3	4	1	2	4
5	2	1	2	3	4	4	38	2	3	4	1	2	3
6	2	1	2	3	4	3	39	2	3	4	1	2	2
7	2	1	2	3	4	2	40	2	3	4	1	2	1
8	2	1	2	3	4	1	41	3	4	2	1	3	1
9	3	2	4	3	1	1	42	3	4	2	1	3	2
10	3	2	4	3	1	2	43	3	4	2	1	3	3
11	3	2	4	3	1	3	44	3	4	2	1	3	4
12	3	2	4	3	1	4	45	4	1	4	2	3	4
13	4	3	2	4	1	4	46	4	1	4	2	3	3
14	4	3	2	4	1	3	47	4	1	4	2	3	2
15	4	3	2	4	1	2	48	4	1	4	2	3	1
16	4	3	2	4	1	1	49	4	2	3	1	4	1
17	4	4	1	3	2	1	50	4	2	3	1	4	2
18	4	4	1	3	2	2	51	4	2	3	1	4	3
19	4	4	1	3	2	3	52	4	2	3	1	4	4
20	4	4	1	3	2	4	53	3	3	1	2	4	4
21	3	1	3	4	2	4	54	3	3	1	2	4	3
22	3	1	3	4	2	3	55	3	3	1	2	4	2
23	3	1	3	4	2	2	56	3	3	1	2	4	1
24	3	1	3	4	2	1	57	2	4	3	2	1	1
25	2	2	1	4	3	1	58	2	4	3	2	1	2
26	2	2	1	4	3	2	59	2	4	3	2	1	3
27	2	2	1	4	3	3	60	2	4	3	2	1	4
28	2	2	1	4	3	4	61	1	4	4	4	4	4
29	1	3	3	3	3	4	62	1	4	4	4	4	3
30	1	3	3	3	3	3	63	1	4	4	4	4	2
31	1	3	3	3	3	2	64	1	4	4	4	4	1
32	1	3	3	3	3	1	65	0	0	0	0	0	0

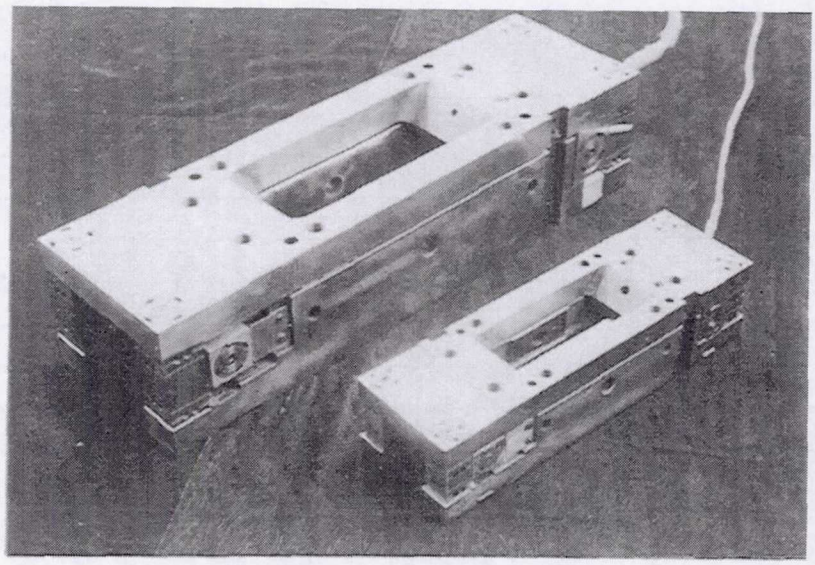

Figure 1. Internal Box Balances Used in 8m×6m Low Speed Wind Tunnel.

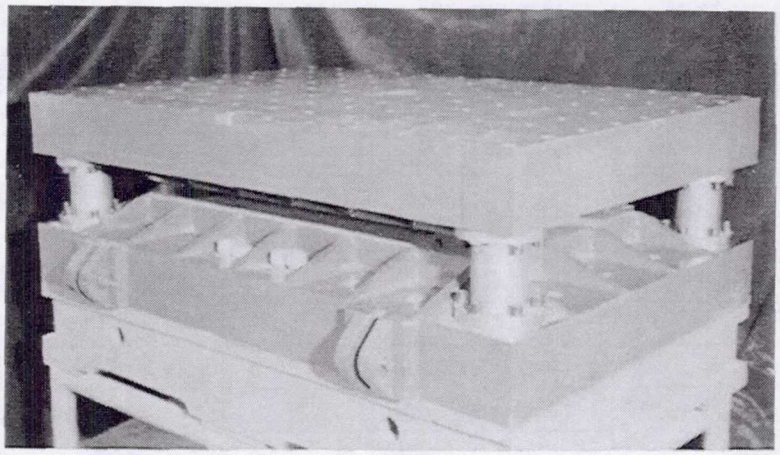

Figure 2. External Box Balance Used in 8m×6m Low Speed Wind Tunnel.

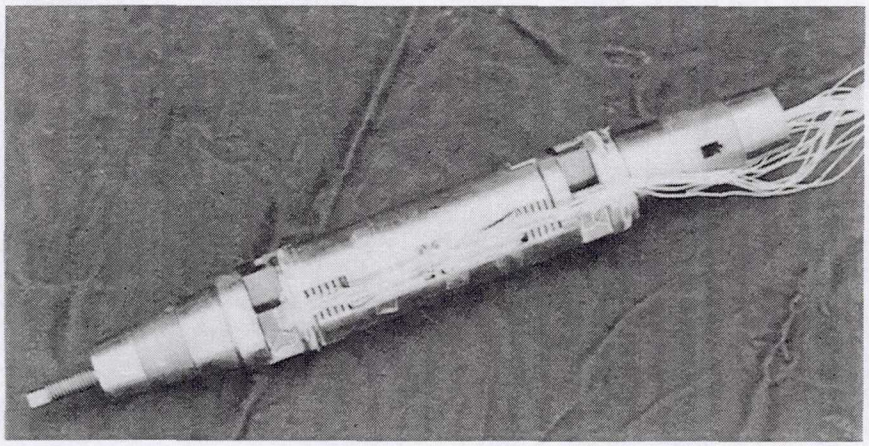

Figure 3. Sting Balance Used in Trisonic Wind Tunnels.

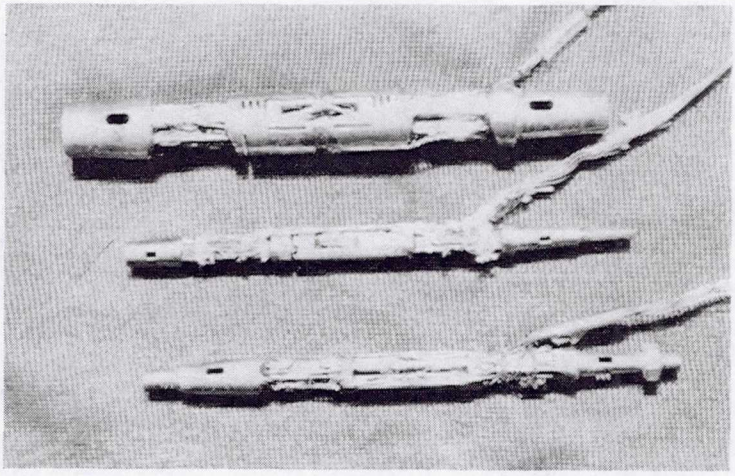

Figure 4. Sting Balances Used for Force Test of Store Model in Trisonic Wind Tunnels.

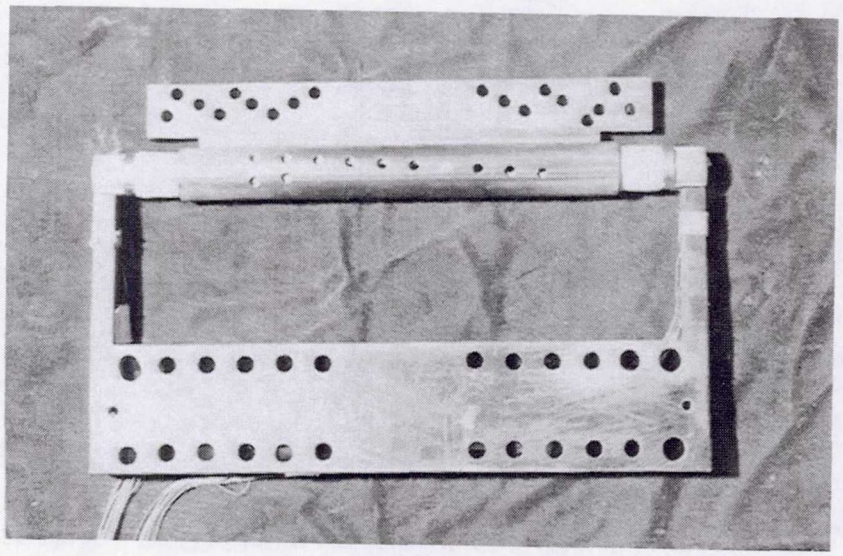

Figure 5. Hinge Moment Balance Used in 8m×6m Low Speed Wind Tunnel.

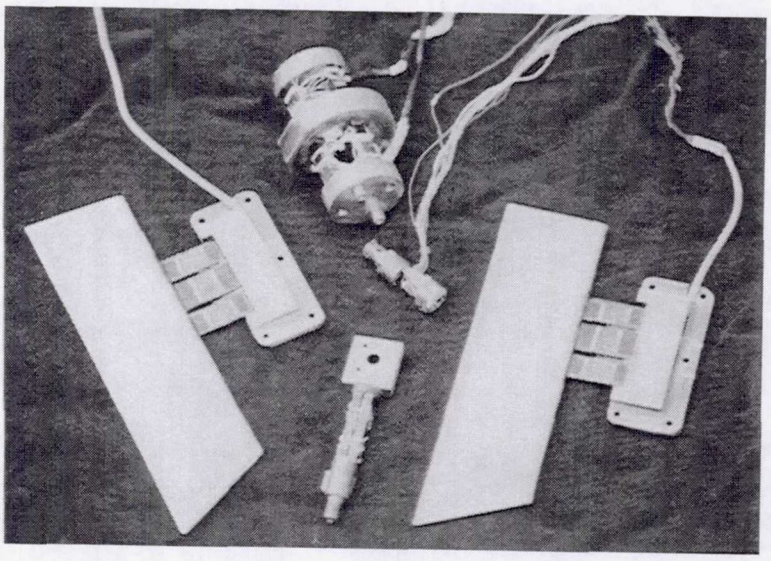

Figure 6. Hinge Moment Balances Used in Trisonic Wind Tunnels.

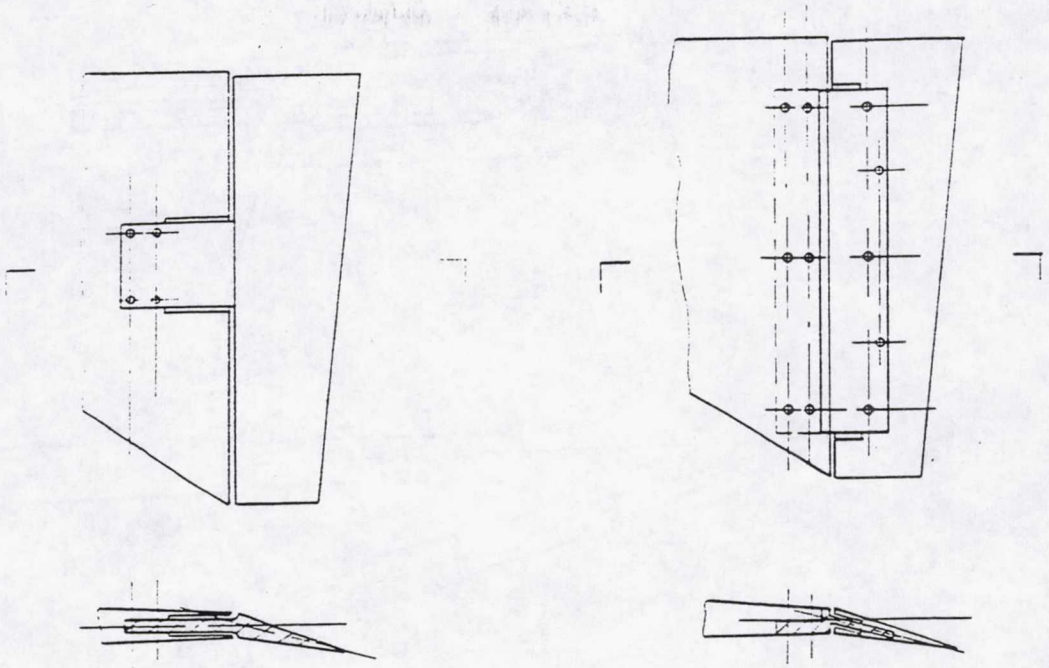

(a) elastic plate type (b) very large elastic plate type

Figure 7. Elastic Plate Type Hinge Moment Balance Used in 1.2m×1.2m Trisonic Wind Tunnel.

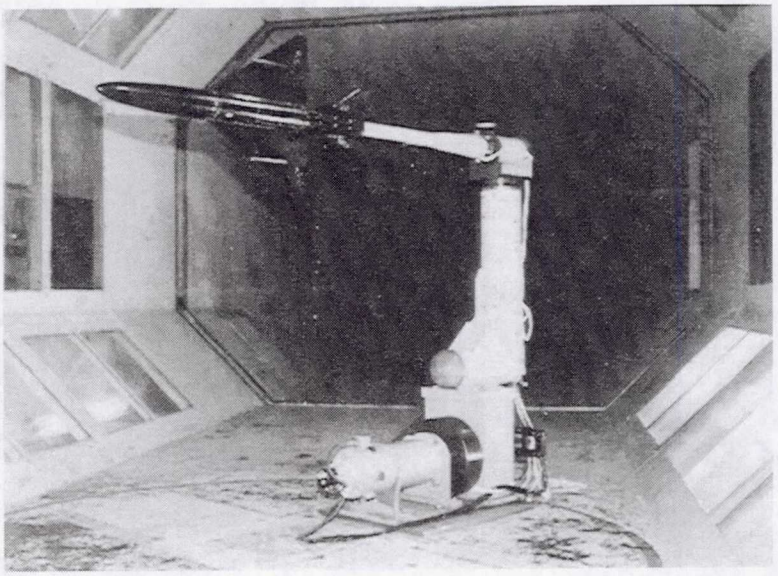

Figure 8. Dynamic Derivative Balance Used in 4m×3m Low Speed Wind Tunnel.

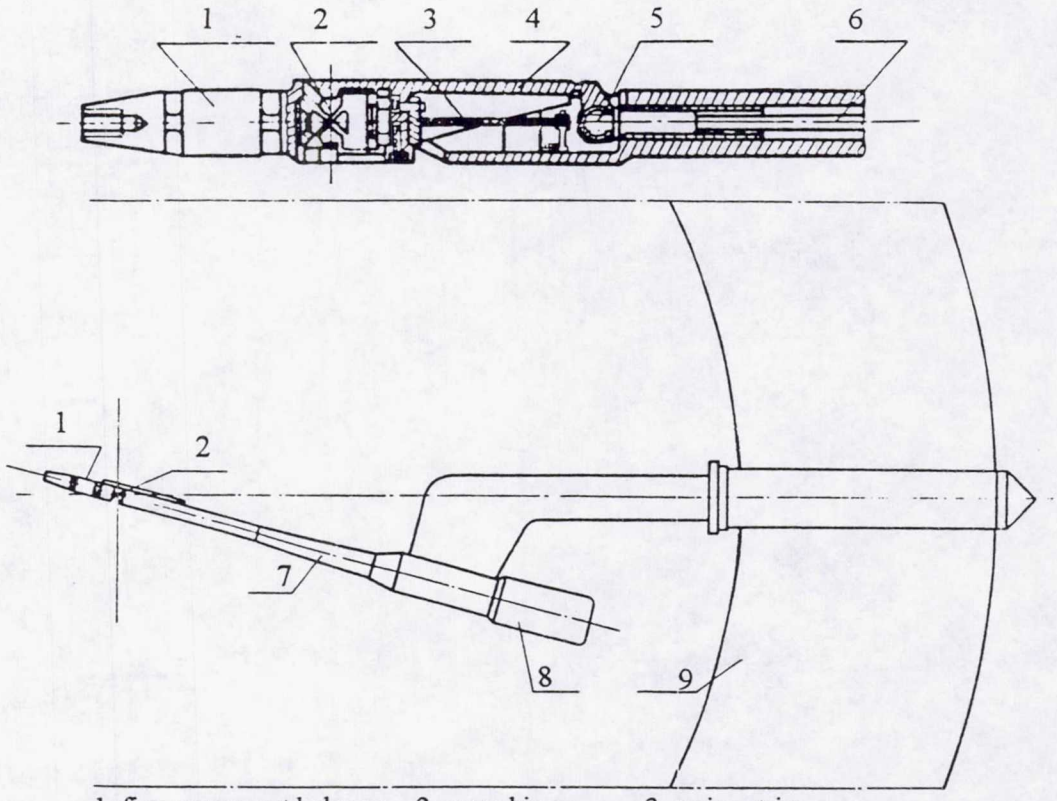

1. five component balance; 2. cross hinge; 3. spring strip;
4. rocker arm; 5. eccentric head; 6. spin shaft;
7.sting; 8. motor; 9. support.

Figure 9. Pitch Dynamic Derivative Balance Used in 1.2m×1.2m Trisonic Wind Tunnel.

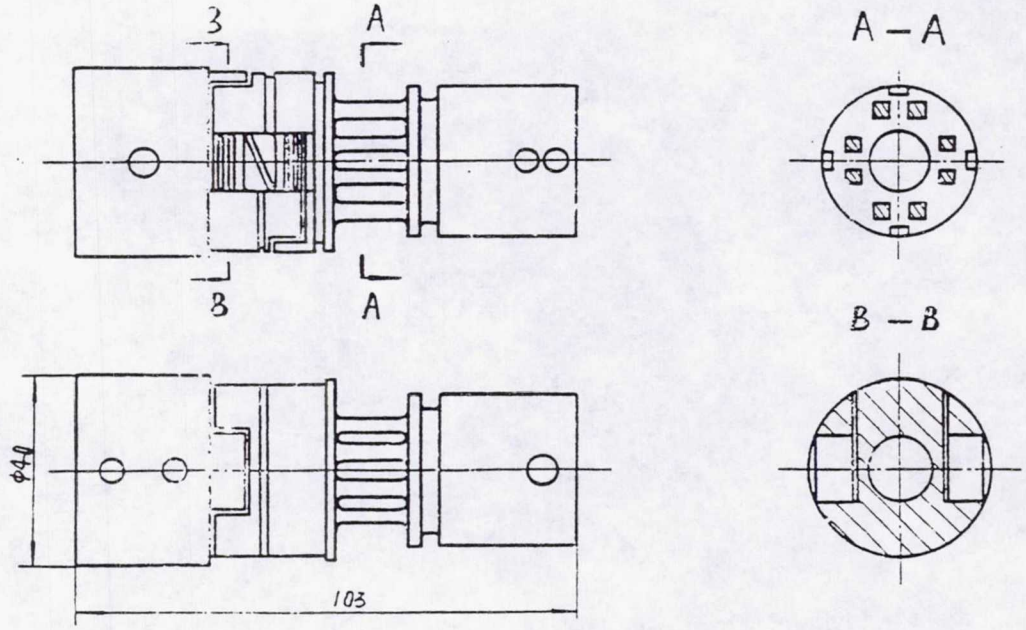

Figure 10. Jet-Flow Balance Used in Trisonic Wind Tunnels.

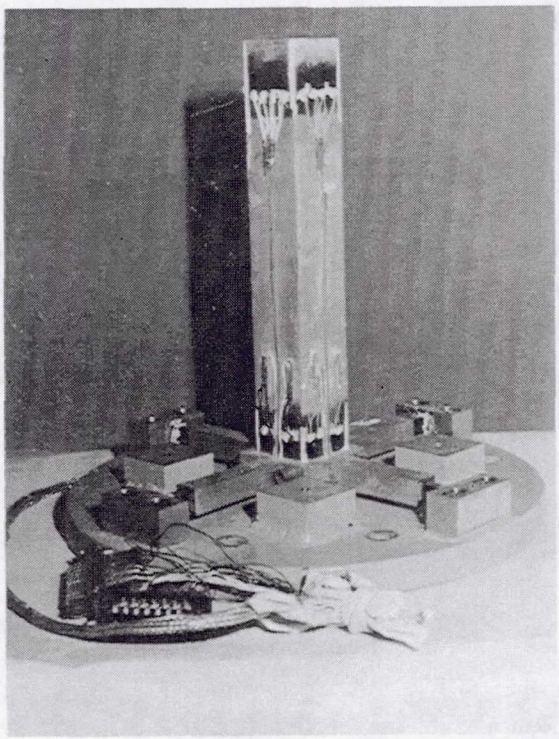

Figure 11. High-Frequency Base Balance Used in 1.4m×1.4m Low Speed Wind Tunnel.

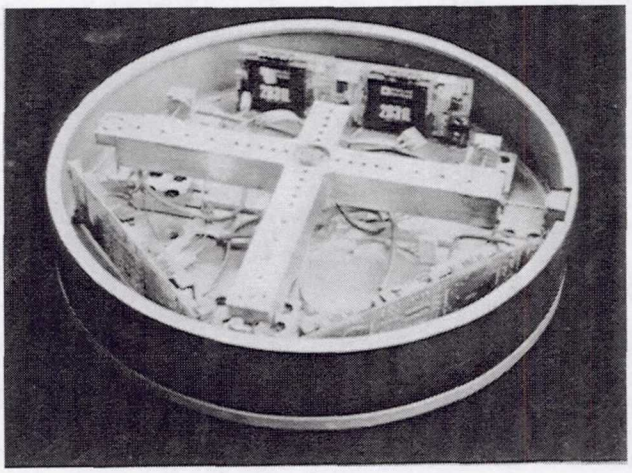

Figure 12. High-Frequency Base Balance Used in 4m×3m Low Speed Wind Tunnel.

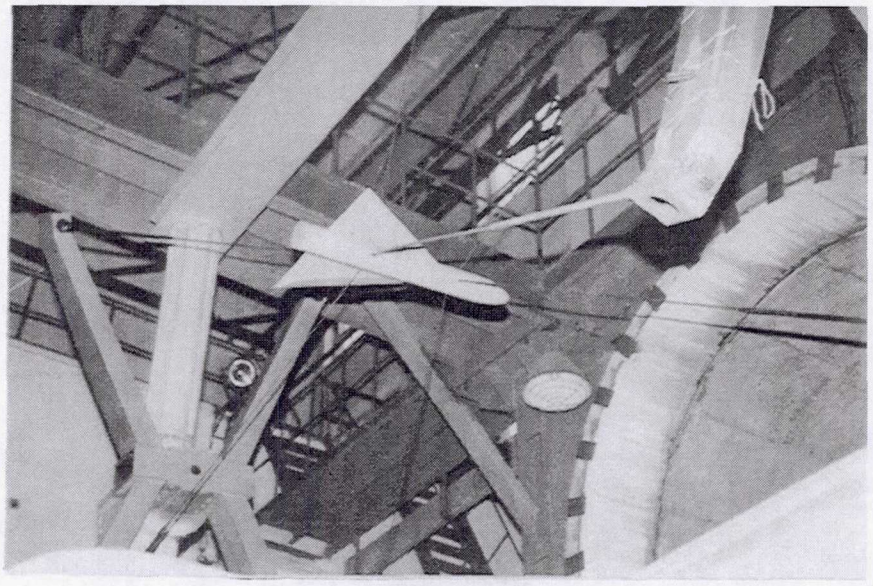

Figure 13. Wire Suspension Balance Used in Φ3.2m Low Speed Wind Tunnel.

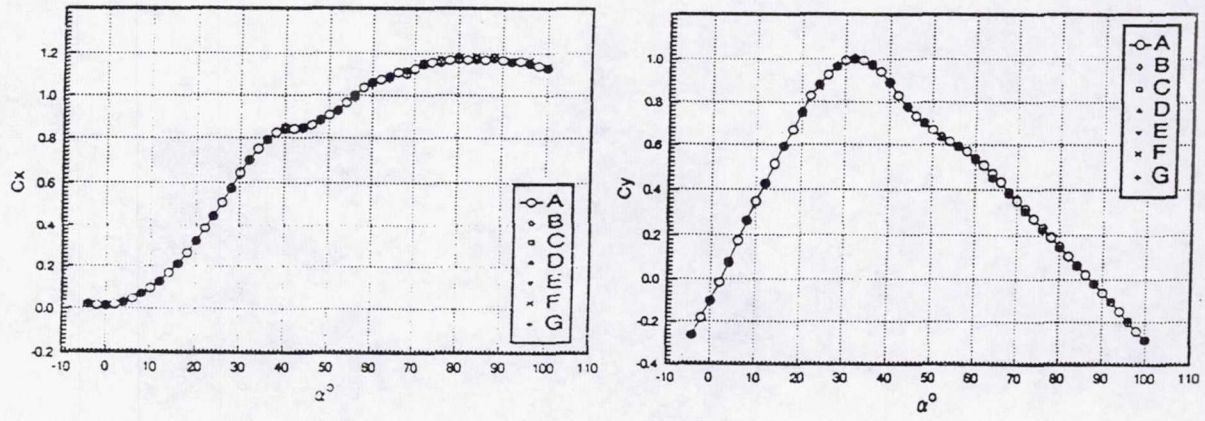

Figure 14. Typical Test Results by Wire Suspension Balance System.

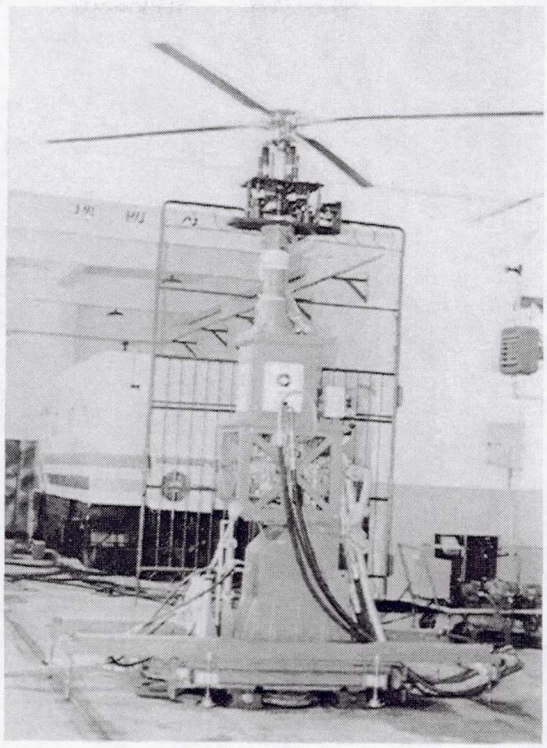

Figure 15. Rotor/Fuselage Combination Test Device.

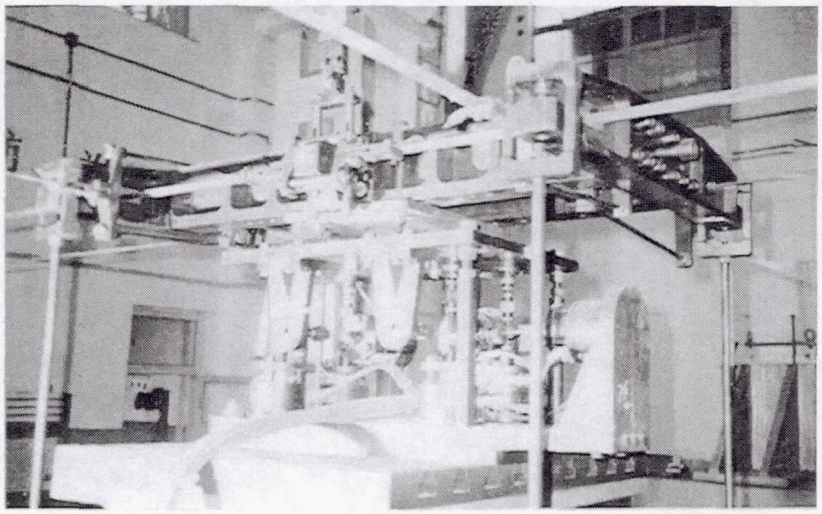

Figure 16. Rotor Balance Being Calibrated.

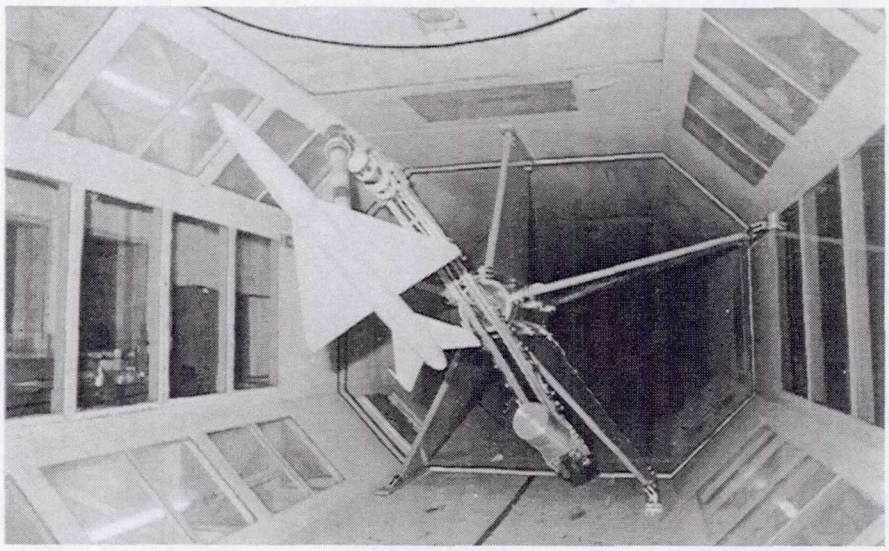

Figure 17. Rotary Balance Measuring Force System Used in 4m×3m Low Speed Wind Tunnel.

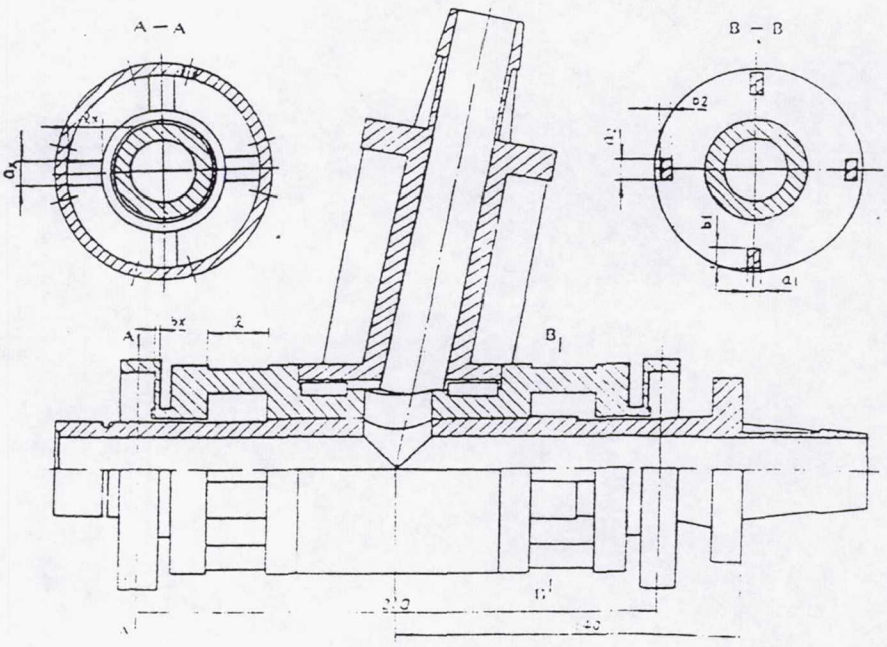

Figure 18. Rotary Balance.

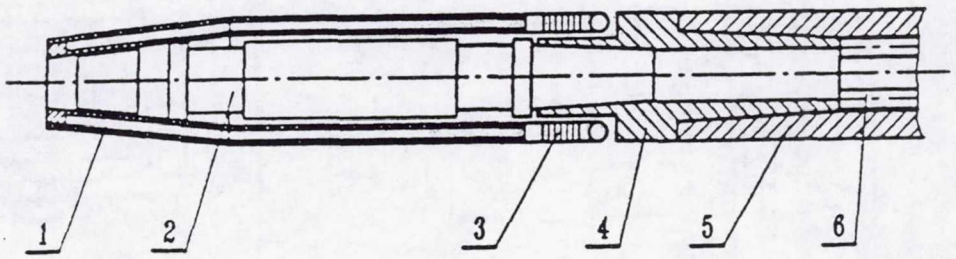

1. water cooling/insulation cover; 2. balance component;
3. bellows; 4. cooling/insulation adapter;
5. sting 6. cooling water tube.

Figure 19. Six Component Water-Cooling Balance Used in Φ0.5m Trisonic Wind Tunnel.

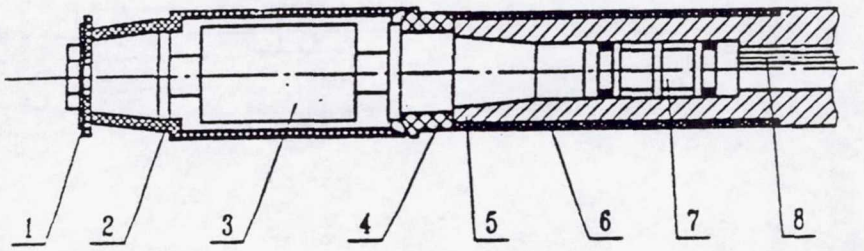

1. Insulation pad; 2. component insulation cover;
3. balance component; 4. Insulation ring;
5. sting; 6. sting insulation cover;
7. cooling cover; 8. cooling water tube.

Figure 20. Medium Temperature Balance Used in Φ0.5m Trisonic Wind Tunnel.

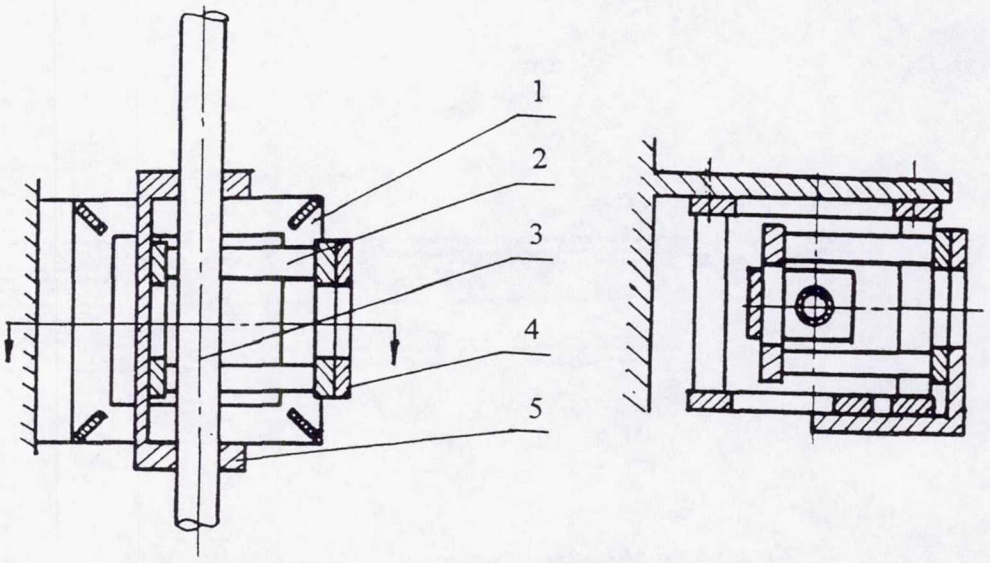

1. external element; 2. internal element; 3. sting;
4. connection of element; 5. connection of sting.

Figure 21. External Microbalance Used in Φ0.3m Low Density Wind Tunnel.

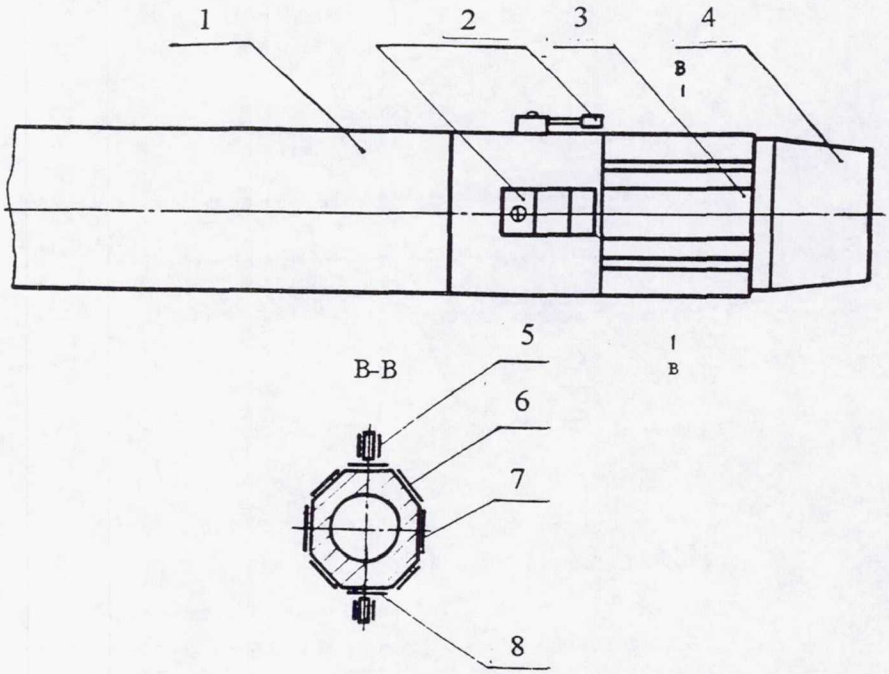

1. sting; 2. accelerometer; 3. elastic element;
4. connecting cone; 5. roll element; 6. axial element;
7. side element; 8. normal element.

Figure 22. A Typical Piezoelectric Balance Used in Φ2m Shock Tunnel.

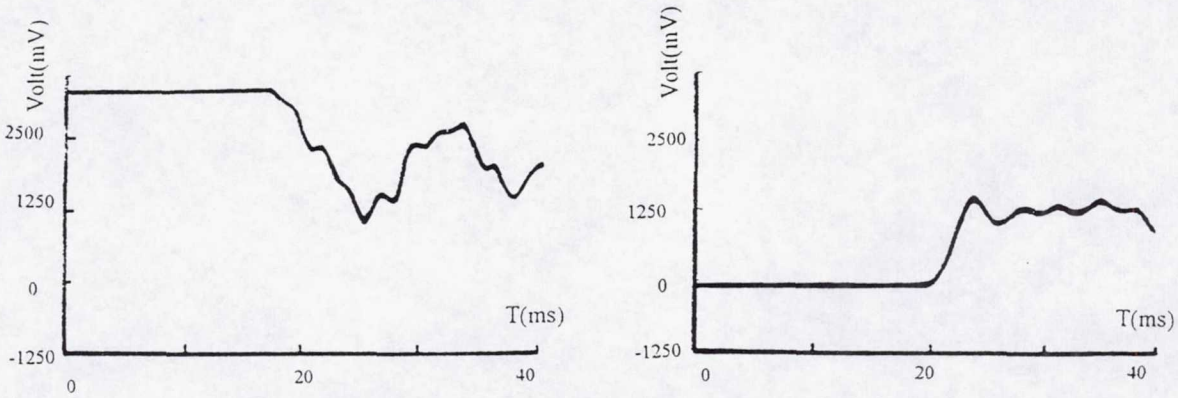

Figure 23. The Inertia Compensation Effect of Piezoelectric Balance.

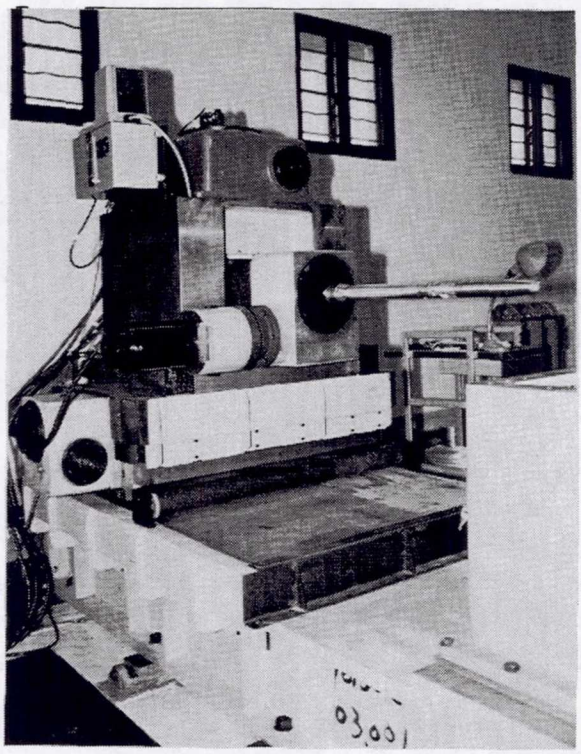

Figure 24. Part of the full automatic calibration machine.

Page intentionally left blank

THE AIAA/GTTC INTERNAL BALANCE TECHNOLOGY WORKING GROUP*

David M. Cahill
Sverdrup Technology Inc., AEDC Group
Arnold Air Force Base, TN 37389-6001

SUMMARY

A working group on internal balance technology has been formed under the auspices of the Ground Testing Technical Committee (GTTC) of the American Institute of Aeronautics and Astronautics (AIAA) to share information on and experiences with all facets of internal balances and develop standards that could be used to allow the facilities to work together to advance the state-of-the-art. The working group's membership consists primarily of individuals from organizations that calibrate and use internal balances. The working group has made excellent progress in three areas: the exchange of information, which requires developing open communications and trust among the member organizations, is flourishing and has had a major impact on the achievements made by the working group; documentation of the balance technology in use at the member organizations; and the establishment of standards for balance nomenclature, axis system, reporting, and an interim standard for a calibration matrix. These efforts will benefit the wind tunnel testing community as a whole through the standardization of balance calibration, usage, terminology, and uncertainty estimation. The standards will improve understanding and communication between facilities as well as the quality of the test data.

INTRODUCTION

Internal balances are the mainstay instrument used by nearly every wind tunnel to measure the aerodynamic loads on the test article. For the most part, each of the facilities designs, fabricates, calibrates, and utilizes internal balances in near seclusion. The time has arrived for collaboration on issues concerning the design, use, calibration, and uncertainty estimation for internal strain-gage balances to begin and become commonplace. To this end, The Internal Balance Technology Working Group was formed under the auspices of the Ground Testing Technical Committee (GTTC) of the American Institute of Aeronautics and Astronautics (AIAA) to share information and experiences and develop standards that could be used to allow the facilities to work together to advance the state-of-the-art. The working group membership consists primarily of individuals from organizations that calibrate and use internal balances.

FORMATION OF THE WORKING GROUP

The concept of forming a working group for internal balances originated from discussions between individuals from the Arnold Engineering Development Center (AEDC), the National Aeronautics and Space Administration (NASA) facility at Langley Research Center (LaRC), and the Boeing Commercial Airplane Group. The discussions also revealed that there was considerable skepticism concerning the

---

* -The research reported herein was performed by the Arnold Engineering Development Center (AEDC), Air Force Materiel Command. Work and analysis for this research were done by personnel of Sverdrup Technology, Inc., AEDC Group, technical services contractor for AEDC. Further reproduction is authorized to satisfy needs of the U. S. Government.

willingness to share information and the ability to reach consensus among the individuals working in the area of internal balances. However, despite the skepticism, it was decided that the time had come for sharing information and the development of standards.

The Ground Testing Technical Committee of the American Institute of Aeronautics and Astronautics was asked to the sponsor a working group on internal balance technology. Sponsorship was unanimously approved, provided that a working group which adequately represented the industry could be formed. Invitations to participate in the working group were sent to 13 wind tunnel facilities in North America in the Spring of 1994 with plans for the first meetings to be held at the AIAA Ground Test Conference in Colorado Springs on June 20 and 21. The response to the invitation was tremendous with all of the facilities agreeing to participate. The current participants in the working group are:

AEDC
NASA Ames Research Center (ARC)
Boeing
Calspan Corp.
Institute for Aerospace Research (IAR)
LaRC
Lockheed-Martin
McDonnell Douglas Aerospace
Micro Craft (San Diego and El Segundo)
NASA Lewis Research Center (LeRC)
Naval Surface Warfare Center
Northrop-Grumman

The first order of business was to acclimate the participants to the idea of sharing information by having each participant provide a short briefing on the status of the balance technology at their facility. As a result of the briefings group's first product was conceived—a document, internal to the group, containing information about each facility and their balance technology (balance design, calibration, and use). This document has been completed and will continue to be updated as necessary.

The second topic was the membership of the working group. Initially, the membership of the working group was limited to individuals from facilities in the U.S. and Canada; however, several European organizations expressed an interest in joining the working group. After considerable discussion, the initial membership agreed that achieving consensus was going to be a difficult task among the current membership and that expanding the membership might impede the group's progres, possibly to the point of being ineffective. Concerns were also expressed over of the willingness of competing airplane manufacturers to share information. After considerable discussion group agreed to form North American and European working groups. Once standards had been set in both groups, representatives of each group could meet to develop mutual standards. However, it is my understanding that a European working group has yet to be formed.

The next task undertaken was the development of a working group charter which includes the group's objectives, structure and operation. The charter that was finally approved is presented in the next section.

WORKING GROUP CHARTER

Scope

Internal strain-gage balances are used extensively to measure the aerodynamic loads on a test article during a wind tunnel test. There has been little collaboration on internal balances; consequently several types of balances, calibration methods, calibration matrices, tare adjustments, and uncertainty evaluations have evolved. The time has arrived at which a collaborative effort is needed to advance the state-of-the-art

for internal strain-gage balance technology. Individuals from wind tunnel facilities will pool their information and experiences to enhance each other's capabilities and to develop standards for their use, calibration, tare adjustment, and uncertainty evaluation. The working group is not an opportunity for an organization to promote their particular balance design, fabrication, and/or calibration services.

Structure

The Internal Balance Technology Working Group was formed under the auspices of the AIAA Ground Testing Technical Committee (GTTC). The working group will be staffed by selected representatives from various wind tunnel facilities and is not limited to members of the AIAA or GTTC. The Chairperson for the working group shall be a member of the GTTC and will be appointed by the GTTC Chairperson. Membership on the working group is currently limited to individuals from facilities operated by government or commercial enterprises in the US and Canada.

Objectives

1. Provide a forum for the members to share information on the methodologies and capabilities for internal strain-gage balances. A document which will remain internal to the working group will be prepared containing a section for each facility.

2. Recommend a calibration matrix format which can be utilized in all of the testing facilities.

3. Develop general guidelines for selecting a balance type and the extent of calibration necessary to meet the objectives of a particular wind tunnel test.

4. Develop a recommended balance calibration uncertainty methodology that is in agreement with existing uncertainty standards (AGARD AR-304 and AIAA S-071-1995)

5. Develop methods of accounting for weight tare adjustments (both calibration and testing) that are accepted by the members.

6. Investigate new methodologies for the design, attachment, and calibration of internal balances.

7. Develop and publish a Recommended Practices document (or documents) for internal strain-gage balance methodologies, including an adjustment methodology for thermal effects on balances.

Operation

1. The working group will meet twice annually at the times and locations concurrent with the scheduled GTTC meetings.

2. Present a formal report on the status of the working group at each GTTC meeting.

3. Accept responsibility for organizing and hosting sessions germane to the scope of the working group as requested by the GTTC.

CALIBRATION STANDARDS

A major milestone has recently been reached with the member's acceptance of a standard terminology, calibration matrix, and calibration file and report structure. The form of the calibration matrix was set to accommodate almost all of the terms currently in use at the individual facilities. It should be noted that this form of the calibration matrix is an interim standard that can be used by all of the facilities for sharing calibrations, calibration data, and for facilitating the analysis of calibration data, various load schemes, and other variables in balance calibration between facilities. As stated above, one of the goals of the working group is to develop a matrix which provides the best model of the balance; however, much work is required before such a matrix can be determined. The information provided here summarizes the agreed-upon standards.

Terminology

Balance Types

One of the first nomenclature problems to be resolved was the terminology used to designate the different types of balances/calibrations that are used by working group members. There are three types used and they have been designated as:

Force - Output from calibration matrix yields forward and aft forces in the normal and side planes along with rolling moment and axial force.

Moment - Output from calibration matrix yields forward and aft moments in the normal and side planes along with rolling moment and axial force.

Direct Read - Output from calibration matrix yields forces and moments in the normal and side planes along with rolling moment and axial force.

Forces and Moments

Every facility involved calibrates balances using various terminology for the six components of the balance, as well as for the gages and their output. After much discussion, group members agreed on the following terminology for applied loads and calculated output:

AF - Axial Force

SF - Side Force

NF - Normal Force

RM - Rolling Moment

PM - Pitching Moment

YM - Yawing Moment

1 - Suffix designating the Forward Gage, if necessary

2 - Suffix designating the Aft Gage, if necessary

r - Prefix designating gage readings in microvolts

The terminology for the gage order, loads, and readings for the three balance types is summarized as follows:

Gage	Force Balance		Moment Balance		Direct Read Balance	
Order	Loads	Readings	Loads	Readings	Loads	Readings
1	NF1	rNF1	PM1	rPM1	NF	rNF
2	NF2	rNF2	PM2	rPM2	PM	rPM
3	SF1	rSF1	YM1	rYM1	SF	rSF
4	SF2	rSF2	YM2	rYM2	YM	rYM
5	RM	rRM	RM	rRM	RM	rRM
6	AF	rAF	AF	rAF	AF	rAF

Balance Axis System and Moment Reference Center

The calibration and use of a balance requires that an axis system and directions of the forces and moments be defined. The same axis system and load directions were used by most of the members while others used systems with some minor variations. The selected standard balance axis system shown in Fig. 1 is oriented such that its origin is at the moment reference center (MRC). The positive directions for the axes, forces, and moments are indicated by the directions of the arrows. The MRC may be at any location along the balance X axis. For force and moment balances the location of the MRC relative to the gage locations is defined by the distances from the MRC to each gage. A positive distance indicates that a gage is located in the positive X direction from (forward of) the MRC. The locations of the gages relative to the MRC are defined as follows:

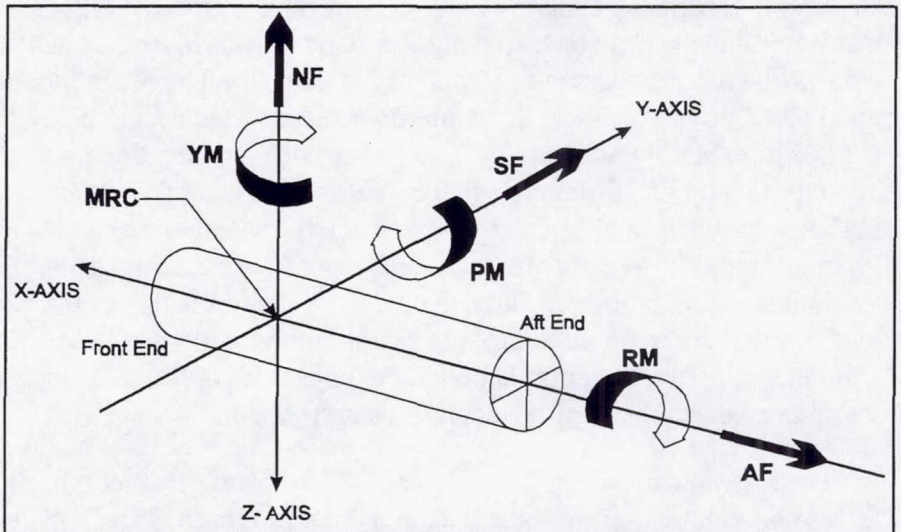

Figure 1. Balance Axis System and Directions of the Forces and Moments

X_1 Distance from the MRC to the forward gage in the normal force plane (X - Z plane)

X_2 Distance from the MRC to the aft gage in the normal force plane (X - Z plane)

X_3 Distance from the MRC to the forward gage in the side force plane (X - Y plane)

X_4 Distance from the MRC to the aft gage in the side force plane (X - Y plane)

Designated Balance Capacity

It was desired that some terminology/methodology be accepted that would allow for a common method for designating the capacity of a balance. The method agreed upon is provided below for the three balance

designations. Note that the designated balance capacity does not necessarily provide the absolute maximum loads that can be applied in any single plane. The designated capacity is for naming conventions and to provide the general capacity of a balance. The absolute capacities must be obtained from the custodian of the balance.

Moment and Force Balances - Maximum NF and SF with no PM or YM, maximum PM and YM with no NF or SF, with maximum AF and RM applied in both cases.

Direct Read Balance - All components fully loaded simultaneously.

Calibration Matrix

Nearly every member of the working group used a calibration matrix that was different in some respect from that used by any other member. Some used a simple 6 by 6 (6 rows by 6 columns) matrix, others used a more "standard" 6 by 27 (or 33) matrix (in either an iterative or direct form in the data reduction process), while still others used a matrix made from various smaller matrices to account for variations in load directions. Not only were there wide variations in the calibration matrices but also in the application of the calibration loads. The loadings varied from applying up to four component loadings to loading only single components by applying loads only at gage locations. With the wide diversity in calibration matrices and loading methodologies, arriving at a standard was indeed a challenge. After considerable debate, a matrix which encompassed nearly all of the terms used by the individual facilities was developed and agreed upon by all of the members as an interim standard which could be used by the individual facilities. Each organization has agreed that it will use or provide a calibration matrix in this form. It was suggested, but not required, that facilities change their calibration matrix to the interim standard. Some members have indicated that they will be changing their matrix generation and data reduction programs to conform to the interim standard. No agreement has been reached concerning the application of calibration loads. The agreement on calibration loadings includes the determination of the type, combinations, and number of loadings that are required to provide a calibration matrix with a specified accuracy. The development of the required calibration loadings is one of the objectives of the working group and will require that extensive set of data be acquired and a full analysis performed.

The interim calibration standard is a 6 by 96 matrix that requires iteration for the calculation of the final forces and moments (i.e., in the data reduction program). The calibration matrix is the result of the curve fit of the calibration data with the applied loads as the independent parameter and the microvolt output as the dependent parameter. The curve fit methodology has not been standardized but is expected to be in the form of a global regression analysis. The coefficients in the matrix have the units of microVolts per engineering unit (EU), EU^2, or EU^3. Forces and moments are expressed in engineering units of pounds and inch-pounds, respectively. The matrix will be normalized to 1 volt (or 1 milliamp) excitation. The matrix will not be normalized by the sensitivity (primary) constants. The transpose of the matrix will normally be used for printing and display purposes. The composition of a transposed matrix is provided in Table 1. Only the first twelve columns of the matrix are shown in the actual transpose form with the remaining 84 columns being provided as column number and column (term) identification. Note that the designation "1.1" means, for a force balance, forward normal force squared ($NF1^2$)and "|5.6|" would mean the absolute value of rolling moment multiplied by axial force (abs(RM*AF)).

Since the matrix is a composite of the matrices from several facilities, only the essential coefficients, as determined by each facility, need to be included in the matrix. It should be noted that the absolute value terms are included to capture the bidirectional behavior associated with the design and manufacturing techniques used for some balances (e.g., shell balances). In cases where these terms are not normally required (e.g. single-piece and the AEDC 3-piece balances) they should be set to zero. The terms which cannot be correctly determined from the calibration loads should also be set to zero.

Matrix File

In order to exchange the calibration information between facilities, a standard file containing the required information needed to be defined. Many items of information were considered for inclusion in the matrix file, along with several possible formats for the file. The standard matrix file which was agreed upon is a comma delimited ASCII text file which will be used to transmit the calibration matrix and the information necessary for its use. The contents and order of the file are shown in Table 2. The calibration matrix will be transmitted in transposed form using the following formats(same as shown in Table 1):

- Include labels for each column and row
- Coefficients in E12.6 format (#.######E±##)

Calibration Report

Since the matrix file provides only the information absolutely necessary for the use of the calibration matrix, a report documenting the balance, calibration process, and calibration results was required. The calibration report fully documents the calibration process and includes the pertinent information relative to the balance. Many items of information were also suggested and considered for inclusion in the calibration report. Again, after considerable discussion, agreement was reached on the information that should be included in the report. The information to be included in the calibration report is provided in Table 3. Some of the parameters included have not yet been completely defined and may be changed. Note that the report need not contain the information in the order shown in Table 3. The document should be transmitted either electronically using the current version of Microsoft Word for Windows™ or in hard copy form.

CONCLUDING REMARKS

The AIAA/GTTC Internal Balance Technology Working Group was formed primarily to provide a means of developing standards and fostering communication between North American organizations that calibrate and use internal balances. The working group's goals are to continue to foster open communications as well as setting standards for internal balance design and fabrication, calibration (including required loadings), usage, uncertainty estimation, and reporting. In the three years since the working group was formed, tremendous progress has been made, particularly in increased communication between member organizations and in the establishment of several key standards regarding the terminology and calibration of internal balances. Ultimately, the working group will develop a formal document describing all of the adopted standards and practices. The results of the working group will benefit the wind tunnel test community as a whole by improving understanding through the use of a common terminology and communications between the participating facilities. The data quality and interpretation of data between facilities should also be enhanced for these same reasons.

Table 1. Interim Standard Calibration Matrix

The example shown is for a force balance. Note that only the first 12 columns are shown in the transposed matrix format. The remaining 84 columns (terms) of the matrix are comprised of various combinations of the first 12 terms and are shown below in their proper order.

Col #	Col/Row ID	rNF1	rNF2	rSF1	rSF2	rRM	rAF
1	1 (NF1)	x.xxxxxxE±xx	x.xxxxxxE±xx	x.xxxxxxE±xx	x.xxxxxxE±xx	x.xxxxxxE±xx	x.xxxxxxE±xx
2	2 (NF2)	x.xxxxxxE±xx	x.xxxxxxE±xx	x.xxxxxxE±xx	x.xxxxxxE±xx	x.xxxxxxE±xx	x.xxxxxxE±xx
3	3 (SF1)	x.xxxxxxE±xx	x.xxxxxxE±xx	x.xxxxxxE±xx	x.xxxxxxE±xx	x.xxxxxxE±xx	x.xxxxxxE±xx
4	4 (SF2)	x.xxxxxxE±xx	x.xxxxxxE±xx	x.xxxxxxE±xx	x.xxxxxxE±xx	x.xxxxxxE±xx	x.xxxxxxE±xx
5	5 (RM)	x.xxxxxxE±xx	x.xxxxxxE±xx	x.xxxxxxE±xx	x.xxxxxxE±xx	x.xxxxxxE±xx	x.xxxxxxE±xx
6	6 (AF)	x.xxxxxxE±xx	x.xxxxxxE±xx	x.xxxxxxE±xx	x.xxxxxxE±xx	x.xxxxxxE±xx	x.xxxxxxE±xx
7	|1|	x.xxxxxxE±xx	x.xxxxxxE±xx	x.xxxxxxE±xx	x.xxxxxxE±xx	x.xxxxxxE±xx	x.xxxxxxE±xx
8	|2|	x.xxxxxxE±xx	x.xxxxxxE±xx	x.xxxxxxE±xx	x.xxxxxxE±xx	x.xxxxxxE±xx	x.xxxxxxE±xx
9	|3|	x.xxxxxxE±xx	x.xxxxxxE±xx	x.xxxxxxE±xx	x.xxxxxxE±xx	x.xxxxxxE±xx	x.xxxxxxE±xx
10	|4|	x.xxxxxxE±xx	x.xxxxxxE±xx	x.xxxxxxE±xx	x.xxxxxxE±xx	x.xxxxxxE±xx	x.xxxxxxE±xx
11	|5|	x.xxxxxxE±xx	x.xxxxxxE±xx	x.xxxxxxE±xx	x.xxxxxxE±xx	x.xxxxxxE±xx	x.xxxxxxE±xx
12	|6|	x.xxxxxxE±xx	x.xxxxxxE±xx	x.xxxxxxE±xx	x.xxxxxxE±xx	x.xxxxxxE±xx	x.xxxxxxE±xx

Col #	Col. ID	Col #	Col. ID	Col #	Col. ID	Col #	Col. ID
13	1.1	34	3.4	55	1.|2|	76	|2|.4
14	2.2	35	3.5	56	1.|3|	77	|2|.5
15	3.3	36	3.6	57	1.|4|	78	|2|.6
16	4.4	37	4.5	58	1.|5|	79	|3|.4
17	5.5	38	4.6	59	1.|6|	80	|3|.5
18	6.6	39	5.6	60	2.|3|	81	|3|.6
19	1.|1|	40	|1.2|	61	2.|4|	82	|4|.5
20	2.|2|	41	|1.3|	62	2.|5|	83	|4|.6
21	3.|3|	42	|1.4|	63	2.|6|	84	|5|.6
22	4.|4|	43	|1.5|	64	3.|4|	85	1.1.1
23	5.|5|	44	|1.6|	65	3.|5|	86	2.2.2
24	6.|6|	45	|2.3|	66	3.|6|	87	3.3.3
25	1.2	46	|2.4|	67	4.|5|	88	4.4.4
26	1.3	47	|2.5|	68	4.|6|	89	5.5.5
27	1.4	48	|2.6|	69	5.|6|	90	6.6.6
28	1.5	49	|3.4|	70	|1|.2	91	|1.1.1|
29	1.6	50	|3.5|	71	|1|.3	92	|2.2.2|
30	2.3	51	|3.6|	72	|1|.4	93	|3.3.3|
31	2.4	52	|4.5|	73	|1|.5	94	|4.4.4|
32	2.5	53	|4.6|	74	|1|.6	95	|5.5.5|
33	2.6	54	|5.6|	75	|2|.3	96	|6.6.6|

Table 2. Contents of the Calibration Matrix File

File Order	Description
1	Facility designation plus calibration number (Not determined)
2	Balance identification
3	Balance calibration type
4	Math model (Not determined)
5	Convergence criteria
6	Maximum rated loads, all 6 components, lbs & in-lbs
7	Calibration temperatures, deg F
8	Temperature correction constants
9	MRC to gage distances, X_1, X_2, X_3, X_4, in
10	Additional comments (10 lines; 80 characters/line)
11	Calibration matrix (96 lines plus header, E12.6)

All items except the calibration matrix and additional comments are 1 line of 80 characters.

Table 3. Contents of the Calibration Report

Item	Description
1	Excitation supply, V
2	Calibration date
3	Calibration temperature, deg F
4	Facility designation (Not defined)
5	± Maximum calibration loads for all 6 components, lbs & in-lbs
6	± Maximum rated loads for all 6 components, lbs & in-lbs
7	Temperature correction constants
8	Balance identification
9	Balance type
10	Balance calibration type
11	Calibration number
12	X_1, X_2, X_3, X_4 distances, in
13	Moment reference center, in
14	Shunts and where used
15	Name of calibration contact
16	Gage resistance, ohms
17	Voltage range of balance, V
18	Which bridges are used
19	Primary constant units
20	Wire color code
21	Balance manufacturer
22	Natural zeros and explanation
23	Pin location, in
24	Balance deflection constants, deg/EU
25	Calibration matrix
26	Identification of calibration body
27	Calibration methodology
28	Balance uncertainties and how obtained
29	Type of temperature sensors
30	Material type
31	Balance electronic sign convention
32	Connector type
33	Balance sketch
34	Load rhombus sketch
35	Is a dummy balance available
36	Wires per gage
37	Wiring diagram
38	Gage manufacturer
39	Gage type
40	Safety factors and basis
41	Attachment methodology
42	Additional comments
43	Math model
44	Convergence criteria

STRAIN GAUGE BALANCE DEVELOPMENT AT NLR

H.B. Vos
National Aerospace Laboratory NLR
Emmeloord, NL

SUMMARY

The National Aerospace Laboratory (NLR) has developed and manufactured strain gauge balances for more than thirty years. All types of balances were developed, not only for NLR tunnels and models but also for many customers and other research institutes.
Through the years new techniques and new materials became available.

In order to raise the overall accuracy of balance measurements the total process of balance design, manufacture and calibration has been reviewed.

Based on extensive investigations many design criteria for the various parts of the balances have been modified and brought in to practice.

This paper summarizes the state of the art of balance technology at NLR.

INTRODUCTION

NLR has developed and manufactured strain gauge balances for more than thirty years. New techniques and new materials allow more predictable and more accurate designs. Review of the balance creation process shows that 'the' accuracy of a balance is not a simple design criterium that can be met by using state of the art means and methods. The achieved accuracy will be the result of a very fragile chain of conditions.
Identifying all of the chain links is difficult because of the variation of conditions during balance use. A few links however are easily identified:

- Design: by adequately choosing the balance concept, and in adequate designing of the several functional parts of the balance, a highly predictable behaviour can be achieved.
- Instrumentation: the use of high quality materials and accurate application ensure long term durability of the measuring instrument.
- Calibration: this makes a complexly shaped piece of steel into a measuring instrument. The accuracy of the calibration equipment and of the calibration procedures determine directly the accuracy of the balance.

Other links vary with the use of a balance, e.g. environmental conditions (temperature, pressure, humidity) or dynamic loading. Although for some conditions some generally applicable compensation techniques are valid, most of these conditions have to be evaluated for specific cases. Adaptation of techniques is then often necessary.

In recent years several investigations have been carried out. They included:

- The relationship between load capacity and measuring hysteresis.
- New connections between model and balance, and between balance and sting/earth

- High load capacity balances.
- The predictability of natural frequencies of balance systems.
- Error causes during application of calibration weights and errors due to the use of elastic hinges.
- Optimized measuring strain levels.
- The effect of surface treatment on strain gauge measurements.
- New temperature compensation techniques.
- Improved predictability of thermal behaviour of the balance system.
- New data processing techniques.
- The use of Finite Element Methods (F.E.M.) in the design phase.

Although the results of the investigations have been incorporated in the design of a new generation of balances, the improvement of the accuracy of balance measurements and of the predictability is an ongoing process.

If accuracy is considered as the difference between applied loads and calculated loads NLR has achieved < 0.1% f.s. typically for the new generation sting balances and < 0.05% f.s. for the new half model balances.

A short description of the design and instrumentation concepts, and the evaluation of balance results is given.

DESIGN AND DESIGN TOOLS

Design tools

The design of balance bodies has been modified to ensure an optimal amount of measuring strain under the strain gauges and to minimize 'parasitic' strain caused by other loadings (interactions from other components, thermal loads, centrifugal loads). In order to improve the accuracy of the strain measurements, and to make the behaviour of the balance more predictable, the use of Finite Element Methods (COSMOS/M, ELFINI) has become indispensable.

The F.E. methods have been used for:
- Stress concentration optimization.
- Strain level optimization.
- Thermal expansion calculations of axial force elements.
- Calculation of thermal stresses.
- Natural frequencies of balance systems.
- Calculation of centrifugal effects on strain gauge bridges of rotating systems.

Also the CAD/CAM system CATIA has increasingly been used for the design and manufacturing of complex balance bodies.

Beside these commercially available software programs, NLR has developed computer programs for special purposes. These programs include F.E.M. postprocessing and algorithms for calculating stress and strain.

Short description of the design process

The predesign of a new balance is based on conventional calculation methods. This predesign should satisfy all conditions and constraints that have been set for the design.
The predesign then is modelled for F.E.M. and analysed. This F.E.M. model consists of BEAM-elements only so that it still can be changed quite easily. Modification of the geometry is usually necessary and is continued until again all conditions are satisfied.
With this BEAM-element model stress and strain are calculated and also thermal expansion of parts of the balance construction is analysed. Sometimes this analysis dictates the changing of the basic concept so radically that a new predesign has to be made.
After this a SOLID-element model is made of the total balance construction. With this F.E.M. model stress concentration effects, plane stress effects and thermal effects on strain gauge bridge output can be analysed. Usually only small dimensional changes are necessary in this phase. With this model a good prediction of the strain gauge bridge output can be given. On basis of these results changing the instrumentation configuration (location of the strain gauges) could be necessary. See figure 1 for an example of a F.E.M.-model.
For an internal six-component balance this process can be very time consuming and the evaluation of the results is very elaborate. For less complex balance bodies however quick reliable results can be obtained within a few days.
After this the balance body can be drawn.
Several balances have been specially gauged after manufacturing to be able to measure at locations where the highest stresses were expected. In this way the calculated stresses can be verified. At this moment calculated values fall within 10% of real values, which is considered sufficient at this moment for design purposes.

Reasons for discrepancies are:
- Physical properties of the used materials not exactly known.
- Exact dimensions of the real balance body not known on all gauge locations; measuring them could be very elaborate and not always possible.
- Exact position of strain gauges not known and often difficult to measure.
- The loads are applied by means of calibration equipment which could influence the load path through the balance; the theoretical loading point (balance centre) as used in the calculations could be different from the real loading point which is determined by the dimensions of the calibration equipment.
  Especially this effect can be found in the interaction output of a certain load on the other strain gauge bridges.
- F.E.M. model can not have the exact geometry of the real balance due to the finite geometry of the elements. Also the element mesh fineness will influence the results.

Of course none of these single reasons will cause the 10% deviation, but all the small contributions add up to this percentage.
Until now the safety factor adopted is four on ultimate strength; in case of small balances with a high loading capacity this factor limits the design possibilities significantly. With the gaining of more experience with F.E.M. and comparing this with experimental results, more confidence in the predictability can be gained. This could mean that in some cases lower safety factors can be accepted.

Connections

The connections of the balance with the model and sting (or some other non metric part of the model support) have been thoroughly investigated in recent years. These connections are of paramount interest to the balance performance. It is shown that the effects of the model/balance interface (but sometimes also of the balance/sting- interface) can jeopardize an otherwise excellent balance behaviour.

It has become clear that there is no type of connection that can be universally used for all balance ranges. Depending on the type and range of the balance a connection has to be evaluated on its merits.

The connections investigated for sting balances were:

- Cone: enhanced by reducing contact area, determinate positioning, modified mounting and dismounting procedures. As model/balance interface this connection has been rejected because of unavoidable hysteresis and bad reproducibility. The matching of the mating cones (male and female) is an important aspect. Especially the female cones are difficult to manufacture and can easily be less accurate than the male cones. This results in large hysteresis and possible damage. The way the loads are transferred in a cone connection can have a significant influence on nearby measuring sections. Due to the slightly varying transfer area (as a result of bad fits or micro movement during external loading) the stress distribution in the measuring section could be influenced. This has led to significant hysteresis in the strain gauge bridge output, and to a sensitivity variation of the bridge in the measuring section. To avoid this a certain minimum distance is necessary between the cone and the measuring section. This distance is dependent on the load range of the balance, the diameter of the measuring section and the dimensions of the cone. It is worthwhile to determine this minimum distance in order to keep the balance as short as possible.
  Cones still are used as balance/sting connection because in most cases the model incidence is directly measured by means of instrumentation inside the model and small position hysteresis in this connection is therefore acceptable.
  The advantages of this connection are its large load carrying capability and yet compact dimensions and robust form.
- Cylindrical bush and cylindrical tap: always a clearance fit with relative movement between the connecting parts. Movement can be avoided by means of expandable elements but this introduces position hysteresis. Vulnerability of joint faces (galling!) is a main problem. The manufacture of cylinders can be very accurate but to have a good clearance fit every balance housing of new models must be matched to the already existing balance. This could give a discrepancy with the calibration model and hence influence the calculated results.
- Flange: two types of flanges have been investigated: so called 'lip' flanges of which the interfaces are parallel to the balance centre line, and 'end face' flanges which are perpendicular to the balance centre line.
  Both types have been used on NLR balances and both show very low hysteresis and very good position reproducibility.
  The disadvantage of lip flanges is that they require much space on both sides of the measuring part of the balance. This type of connection has for this reason only been used for balances for low speed wind tunnel models which have enough space available.
  The end face flanges have been widely used in several shapes. This connection is much more compact in axial direction of the balance and has the same outer diameter as the balance body. For small diameters (e.g. use in slender wind tunnel models) and relatively highly stressed balances this connection is not suitable.
  NLR has developed a hydraulically prestressed end flange connection for the model side of the balance which has the same outer diameter as the balance. This connection is virtually hysteresis

free (< 0,005°) and has a high position accuracy (< 0,015 mm). If possible this type of connection will always be used for new balances. Figure 2 shows a schematic drawing of this connection.

At this moment the general purpose six-component sting balances of the new generation have an enhanced cone at the sting side and an end face flange at the model side.
For other types of balances (external, model parts) only flange connections are used.

Measuring elements

Axial Force Element: Several constructions have been designed to improve the decoupling and to minimize temperature effects. By analysing the deformation of the element due to thermal expansion it is possible to place strain gauge bridges that give output of opposite sign as compared to the axial force bridge thermal output. If such a compensation bridge is used, care must be taken to optimize (in the design phase!) also the strain level for this bridge otherwise the signal will lower the accuracy of the combined signal. NLR has used a compensation bridge on several axial force elements. The design of the axial force element has been adjusted in such a way that a compensation bridge is no longer necessary. Figure 3 shows an axial force with double decoupling beams. This setup copes with most of the thermal expansion problems.
This is the most complex part of the balance which is most sensitive to error causes. Compared to the other strain gauge bridges the axial force bridge gives generally the highest measuring hysteresis. This could be caused by 'heaping up' of material hysteresis in the thin flexures of the element thus giving micro deformation of the measuring flexure.
In the axial force element usually also the rolling moment is measured.

Other measuring elements for the remaining components: Normal setup is the presence of two measuring sections symmetrically placed with respect to the axial force element. These sections could be massive or have a cage form, depending on the desired bridge output and the specified load range.
In each section two strain gauge bridges are placed. These bridges primarily react on the moments (pitching moment, yawing moment) and on the loads due to normal force and side force.
The effect of radial temperature gradients in these sections is partly compensated by measuring also the lateral contraction strain. In this case the strain gauge bridge is self-compensating.

Specific design aspects

Each type of balance has its own specific design problems.

Internal strain gauge balances
Universal six component balances: one piece design with several measuring sections
Problems: quality of model/balance interface; higher order interactions to be determined correctly.
Dedicated compact six component balances with high axial capacity: possible temperature problems when used in small models. By using self-compensating strain gauge bridges the problems can be minimized.

External balances
Half model balances almost completely statically determinate with high accuracy dynamometers, either commercially available load cells or developed in house e.g. if dictated by available space.
Figure 4 shows a photograph of a balance for non-aerospace research.
At this moment the design experience allows excellent balances to be realized.

Problems: Size and accuracy of the calibration equipment

Rotary balances

Compact balances which are able to measure six components in propeller constructions
Problems: Temperature and centrifugal effects on bridge readings, and to avoid damage to the instrumentation due to centrifugal loading.
NLR has gained experience to cope with these problems.
Figure 5 shows a photograph of a rotary balance.

Model part balances

Dedicated balances for use in wind tunnel models of which the loads on model parts have to be measured (fins, rudders, tail plane etc.).
Problems: limited space, low strain gauge bridge output. Often the earth side has to be included in the design and calibration.

INSTRUMENTATION

All used materials (strain gauges, resistances, wiring, coating material) are commercially available.

Description of the procedure

- Definition of instrumentation location: for complex balance bodies optimized with help of F.E.M.

- Surface preparation: all locations where instrumentation material has to be placed (strain gages, compensation resistances) are given a roughness Ra 0,4 - 0,8 μm.
- Bonding strain gauges and compensation resistances: special attention is given to accurate positioning and the required clamping force.
- Wiring: the most time consuming part.
  To have enough slack in the wiring (especially in an axial force element) is essential, but due to complex geometry sometimes difficult to create.
- Checks: electrical measurements and temperature runs must make clear that the gauges are bonded well and that all wiring is correctly.
- Three hardware compensations are applied:
  - Sensitivity shift due to temperature changes.
- Criterium: < 0,003% f.s./°C (0°- 50°C).
  - Zero shift due to temperature changes.
    - Criterium: < 0,01% f.s./°C (0°- 50°C).
  - Bridge (un)balance: < 1000 μV.

  All compensation resistances are placed as close as possible to the bridges, or to the half bridges if compensated per half bridge.
  The resistance values are determined by changing the temperature at a rate that is typical for the NLR wind tunnel conditions. This is done in a computer controlled oven. By recording the bridge outputs almost continuously (triggered by 2°C balance temperature change or half an hour no temperature change) the relation between temperature change and output can be accurately determined. See figure 6 for typical compensation results.
  A great advantage of this procedure is also that the behaviour of the bridge signals can be evaluated during the complete temperature run and in a number of cases faults in the instrumentation have been detected in this way. Also a better understanding of the thermal

expansion behaviour of the balance construction can be obtained.
If no further hardware compensation is possible (for example in case of output due to thermo-mechanical effects) software compensation can be applied on basis of the same temperature run results or based on the temperature distribution as measured by temperature sensors on the balance.

Development of instrumentation techniques

New instrumentation materials or new techniques are investigated with standard test beams. New strain gauges or a new coating material are evaluated on test beams. Completely compensated strain gauge bridges are placed and coated. The beams are tested with dead weight loading.
Instrumentation techniques (e.g. temperature compensation, bonding techniques) are also optimized with these test beams.
If the use of a new balance body material is considered, standard test beams of this new material are made and tested with several types of strain gauges.

EVALUATION OF BALANCE RESULTS

After design and manufacture of a new type of strain gauge balance several tests are performed to determine if the balance satisfies the design requirements:
- Strain measurements on non-bridge locations.
- Bridge output due to nominal loading.
- First order interactions.
- Behaviour at increased temperatures and temperature gradients.
- Quality of the individual bridge signals: hysteresis, mean and maximum deviation of curve fit (second or third order polynoms) through bridge output, zero shift with temperature.
- Difference between measured loads and applied loads and the distribution of deviations.
- Determination of balance deformation due to nominal loading.
- Repeatability of the results.
- Influence of data processing is evaluated: matrix inversion or iteration. At this moment NLR is testing a new processing system (based on an iteration method) which will also improve presentation capabilities and analysis of the calibration results.
- Creep.

The analysis of these test results can be very elaborate due to the many possible error causes as already mentioned in the introduction.
Evaluation of the results is often difficult because of the absence of uniquely defined criteria for several aspects. The determination and/or definition of relevant criteria is one of the main subjects of investigation at this moment. The sum of these criteria must give the maximum *inaccuracy* of the balance in carefully conditioned environments. The definition of such an inaccuracy number (% f.s. or % rated load?, not in dragcounts!) should be done in a way that the value of this number can be determined under reproducible conditions. This inaccuracy number makes direct comparison of balances possible and can be used as design feedback. Essential is that the definition of the number is clear and unique.
The inaccuracy of the load measurements in the wind tunnel is higher than the balance inaccuracy under calibration conditions due to extra possible error causes in tunnel conditions. The balance inaccuracy number therefore can only give information about the *expected* balance behaviour in tunnel conditions.

CONCLUDING REMARKS

The development of a new generation general purpose sting balances was the beginning of a complete review of the balance creation process. This has resulted in a more extensive use of modern computational tools and the adaptation of instrumentation techniques. Predictability of results has improved significantly. The design tools could easily be adopted for other types of balances (external, rotary).
Other aspects (e.g. calibration and calibration equipment) are still being reviewed and investigations are going on.

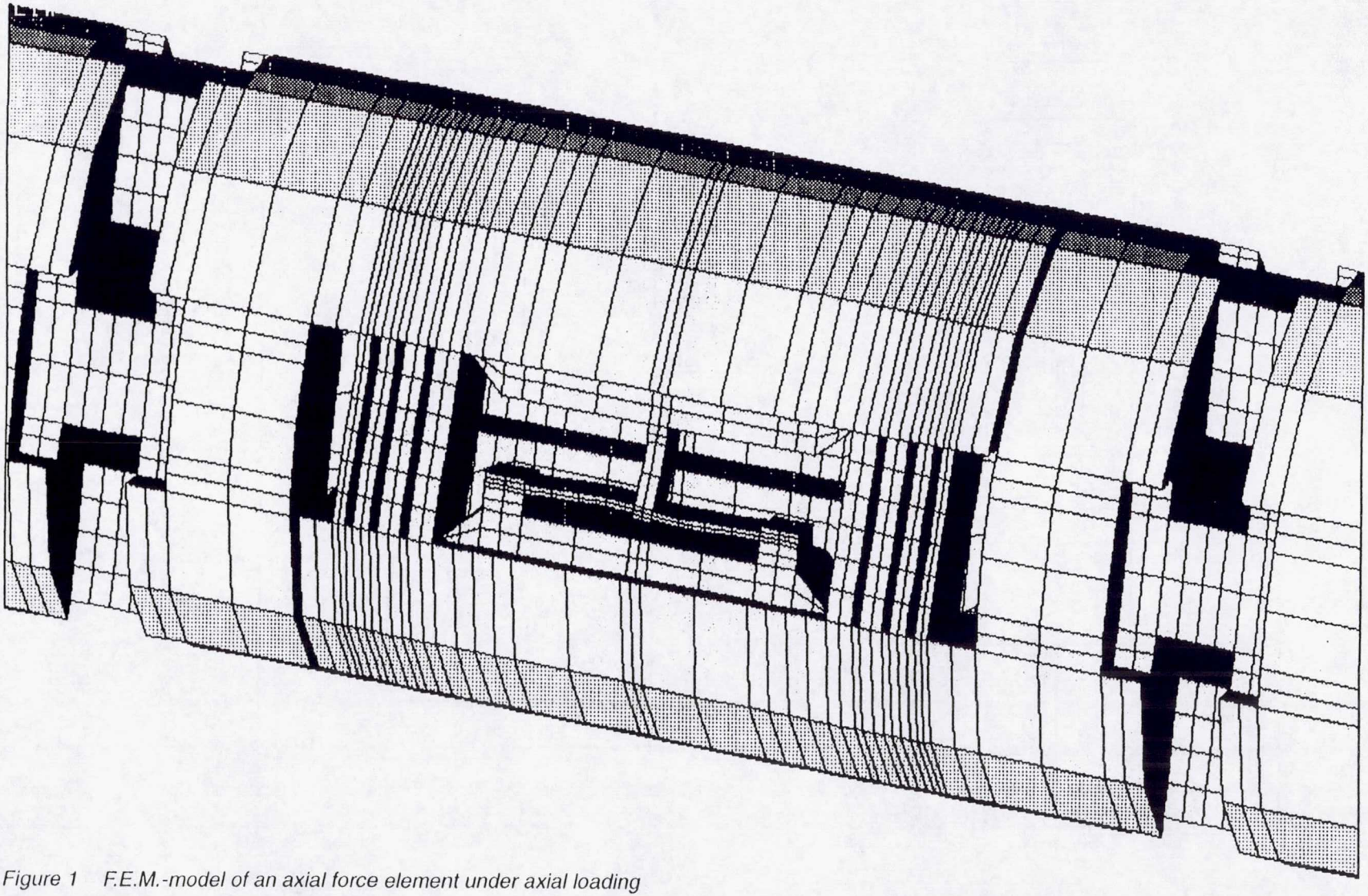

Figure 1 F.E.M.-model of an axial force element under axial loading

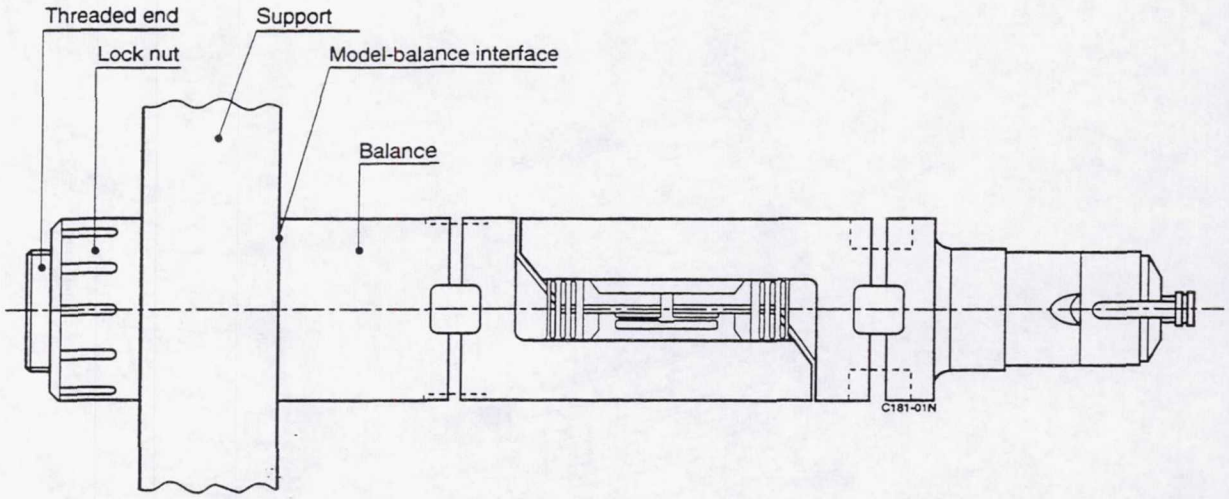

Figure 2 Model/balance connection

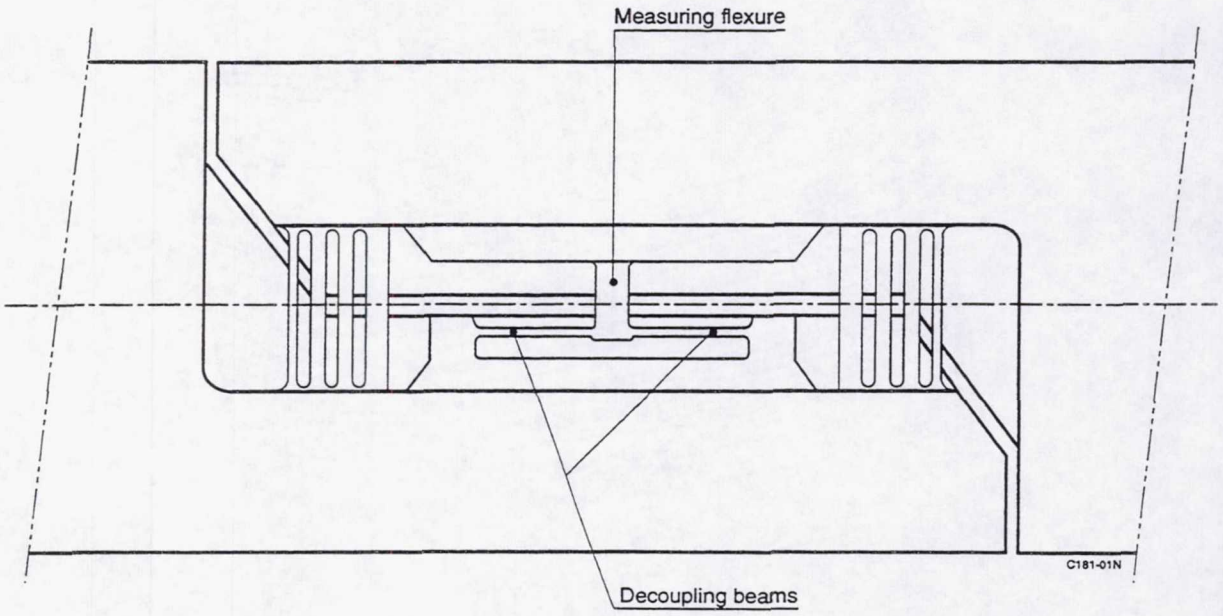

Figure 3 Axial force element with double decoupling beams

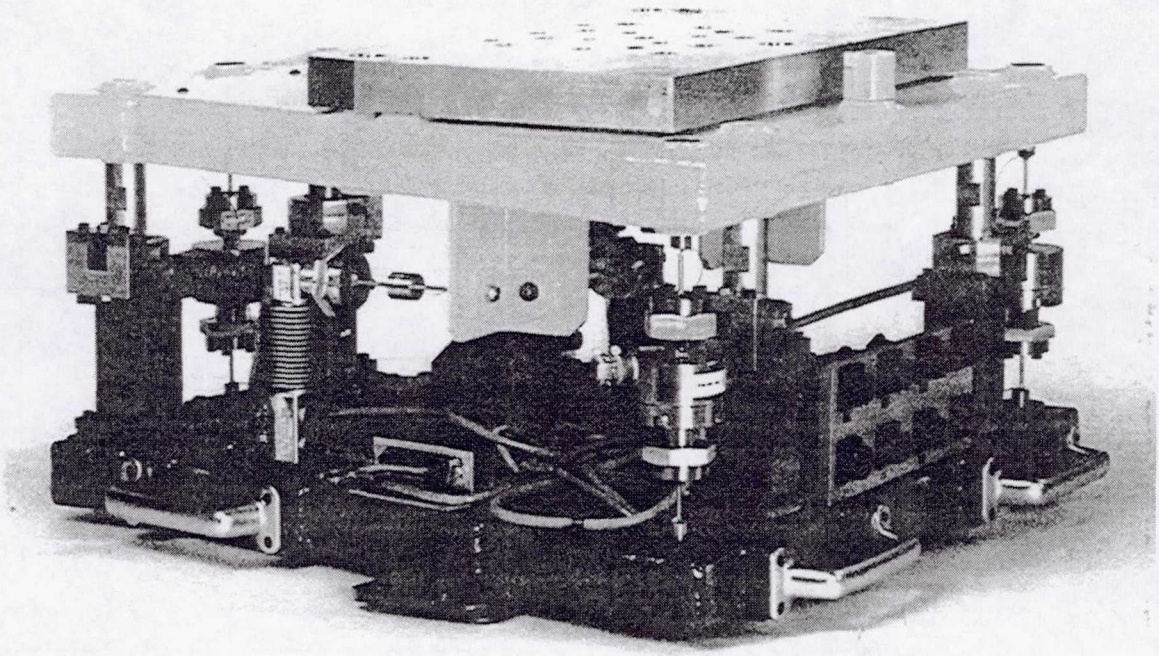

Figure 4 Balance for non-aerospace research

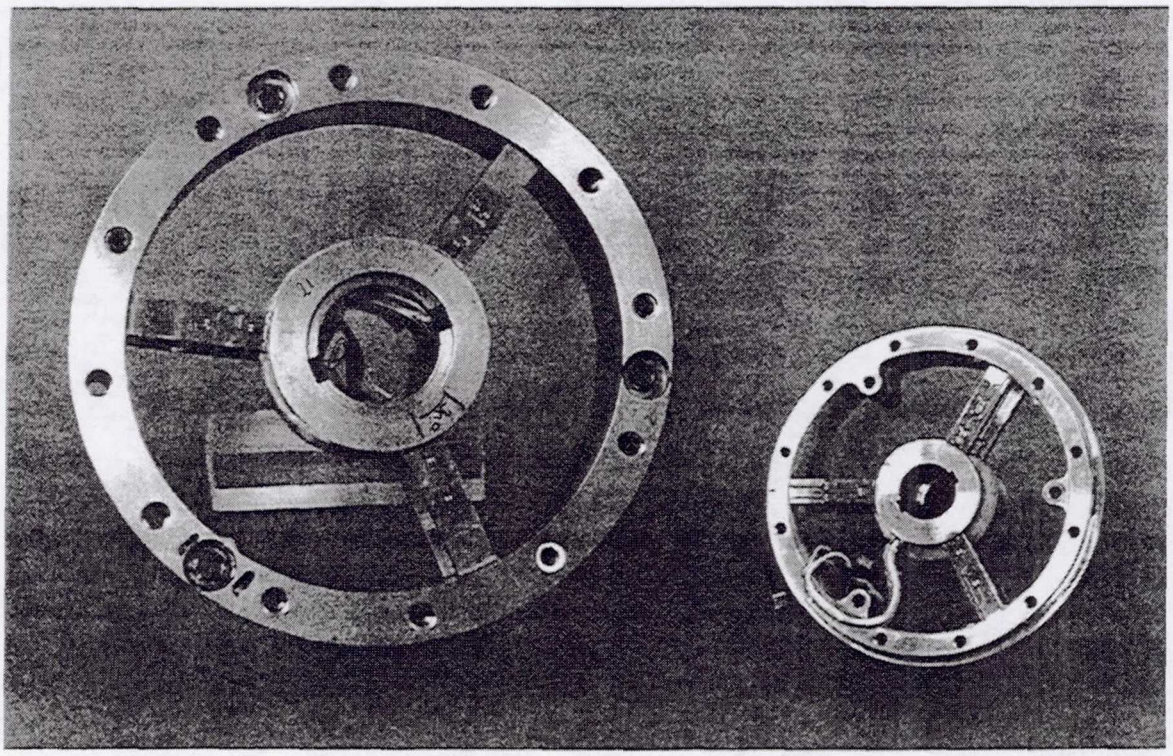

Figure 5 Compact rotary balances

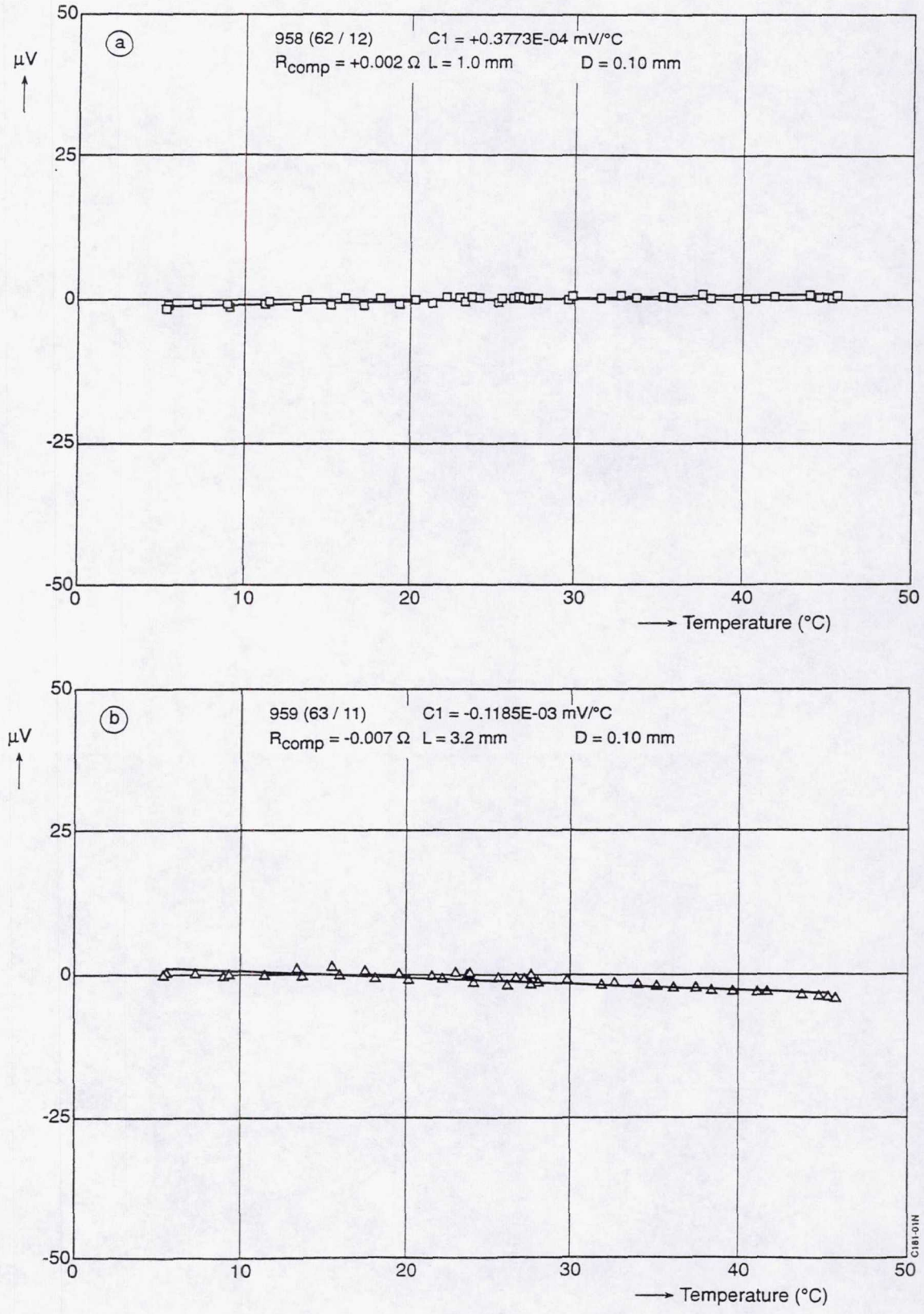

Figure 6 Typical compensation results of a temperature run

NASA Langley Research Center Force and Strain Measurement Capabilities

Roberts, P.W.

NASA Langley Research Center
Experimental Testing Technology Division
Model, Instrumentation, and Systems Branch
Hampton, VA

Abstract

Direct measurements of forces and moments are some of the most important data acquired during aerodynamic testing. This paper deals with the force and strain measurement capabilities at the Langley Research Center (LaRC). It begins with a progressive history of LaRC force measurement developments beginning in the 1940's and ends with the center's current capabilities. Various types of force and moment transducers used at LaRC are discussed including six-component sting mounted balances, semi-span balances, hinge moment balances, flow-through balances, rotor balances, and many other unique transducers. Also discussed are some unique strain-gage applications, such as those used in extreme environments. The final topics deal with the LaRC's ability to perform custom calibrations and our current levels of effort in the area of force and strain measurement.

History

Force and strain measurements are some of the most frequently acquired data in aerodynamic testing. Langley Research Center (LaRC) instrumentation engineers have a long history in this critical area. In 1940, the first LaRC strain gage balance was designed and produced for aerodynamic testing. LaRC balances of the 1940's used multipiece construction techniques with multiple measuring sections. They were physically large, used custom wire strain gages, and were much less accurate than modern balances (figure1).

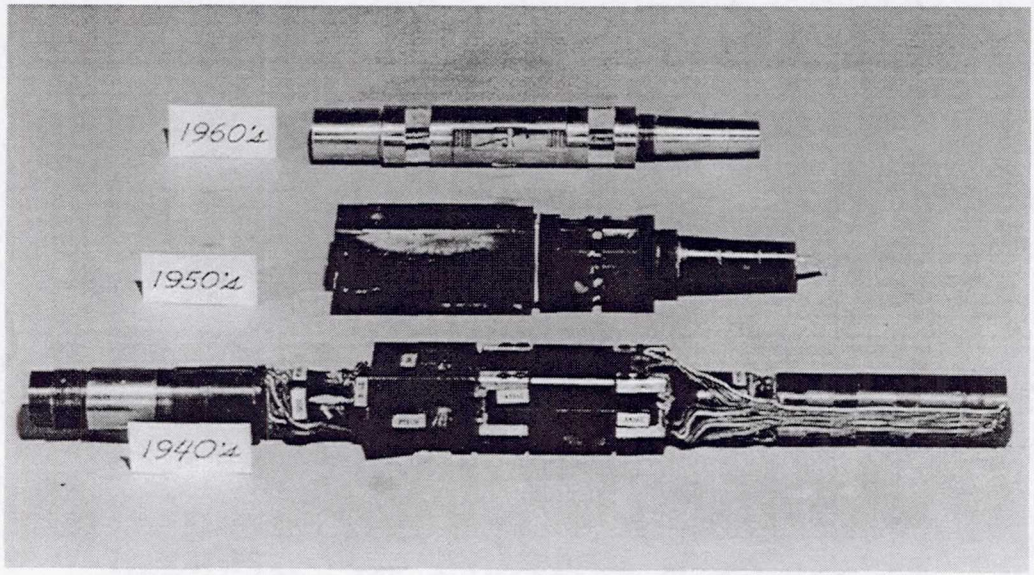

Figure 1 – Langley Historical Balance Photos

In the 1950's, electrical discharge machining was developed. This ability to make smaller, more precise cuts enhanced LaRC's ability to machine complex measuring elements. LaRC engineers were able to design more complex configurations that could be machined with single piece construction. Single piece construction became the preferred production method for all future LaRC force measurement transducers. In the 1950's and 1960's most LaRC balances used either a radius front end fit (fig.2) or a diameter front end fit (fig.3) with taper fits for the mechanical ground and foil strain gages were used.

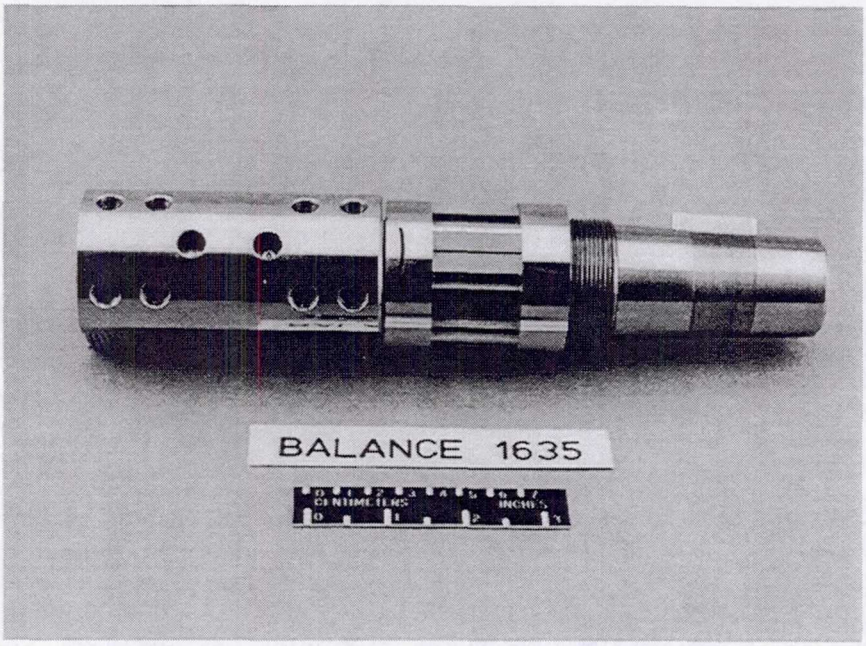

Figure 2 – A LaRC Radius Fit Balance

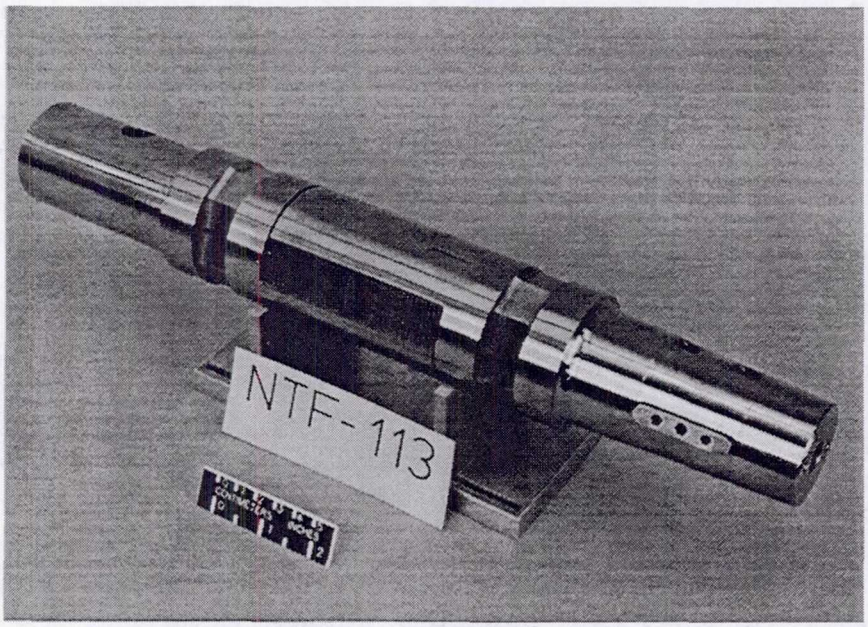

Figure 3 – A LaRC Diameter Fit Balance

In the late 1970's and early 1980's the majority of LaRC balance development effort was concentrated on the development of cryogenic balances. This is a maturing technology and is still a major focus today. The effort to develop the National Aerospace Plane (NASP) was begun in the late 1980's and early 1990's. The NASP project required the ability to more accurately measure high temperature strain (above 100° C). A significant amount of effort was applied to high temperature strain measurement and culminated with the patent of the LaRC High Temperature Strain Gage. Currently, LaRC is focusing on instrumentation uncertainty predictions, thermal compensation techniques, and operational productivity improvements. The development and maintenance of LaRC force and strain measurement instrumentation is the responsibility of the Model, Instrumentation, and Systems Branch (MISB) in the Experimental Test Techniques Division (ETTD). As always, LaRC is constantly looking for future developmental projects that will improve instrumentation accuracies, durability cost effectiveness, and productivity. The MISB currently supports many types of force and strain measurement instrumentation and activities, some of which are discussed below.

Force Transducer Types

LaRC develops, maintains, and operates many unique force transducer types. These include external, hinge moment, flow through and rotor balances. LaRC also has developed many unusual balance systems for use in unique, highly specialized test conditions.

LaRC operates three external balance systems in different environments. The most recent of these is the three component balance in the 8 Ft. High Temperature Tunnel (8'HTT). A photo of this balance is shown in figure 4.

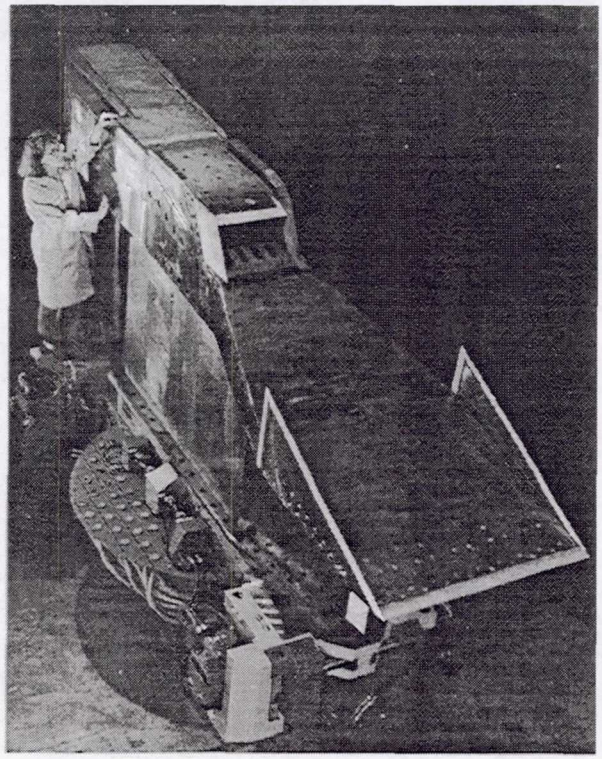

Figure 4 – The 8'HTT External Balance

Here a model of a scramjet engine is mounted on top of the balance. This balance operates in an elevated temperature environment in which thermal gradients across the balance can produce erroneous data. This balance was designed using patented compensation techniques, which theoretically cancel any errors due to thermal expansion differences that may occur within the large balance structure.

Another custom force transducer type that the MISB supports is hinge moment balances. The distinguishing characteristic of these balances are their small size. One such balance is shown in figure 5.

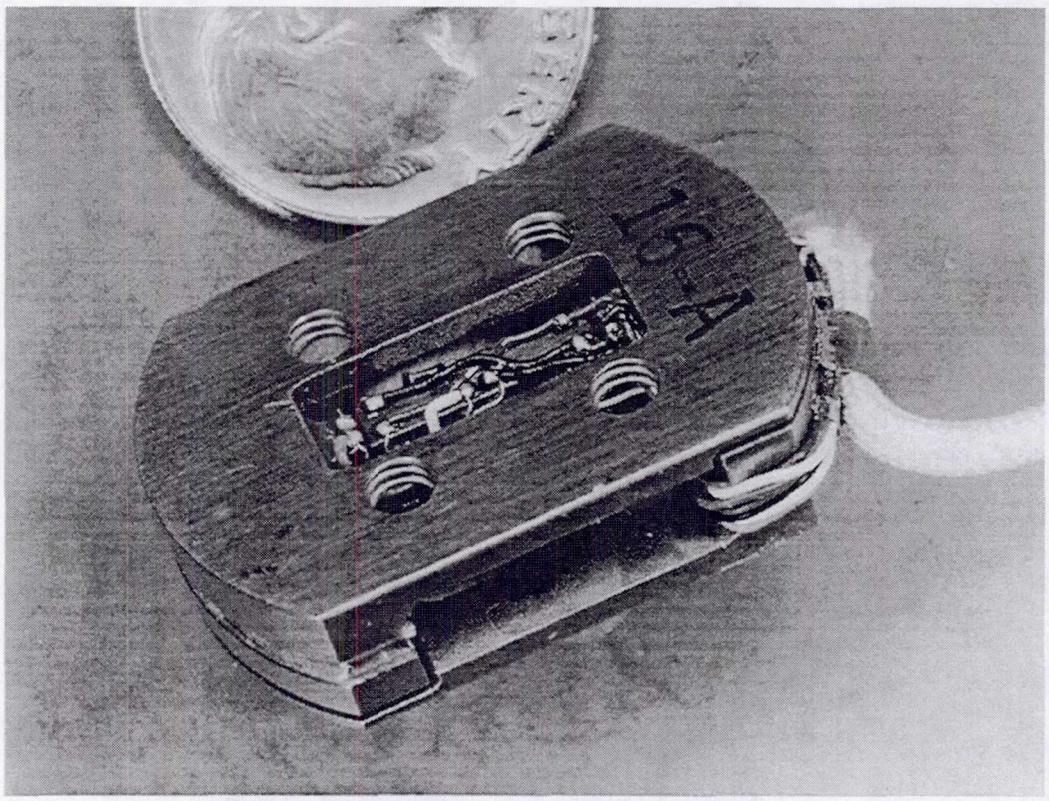

Figure 5 – Hinge Moment Balances

Hinge moment balances are typically used to measure the forces and moments on model control surfaces such as ailerons and elevons. These balances are usually three component transducers that measure two forces and one moment. Often these transducers are designed for specific applications such as the hinge moment balance shown in figure 6.

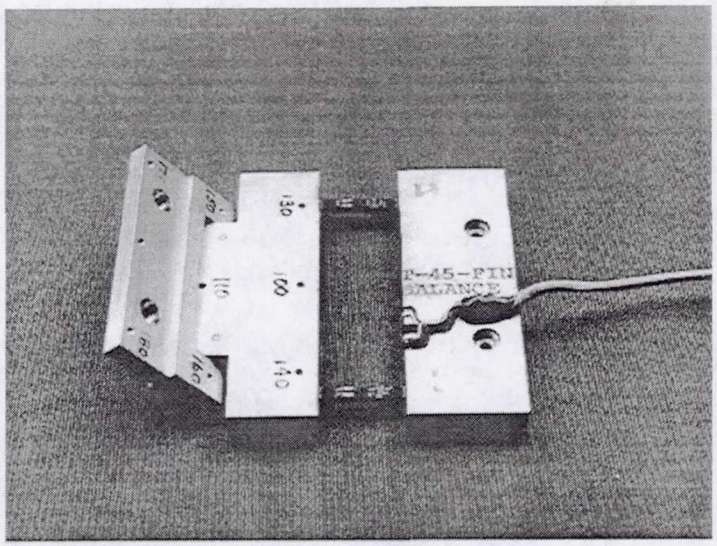

Figure 6 – A Custom Hinge Moment Balance

This balance was designed to measure the aerodynamic loads applied to a vertical tail rudder. It was designed with the unique ability to vary the angular setting of the rudder throughout the wind tunnel test. Also it should be noted that calibration loading points are included as part of the balance design.

The Low Turbulence Pressure Tunnel (LTPT) requested the design of another unique balance system. In this case, the model was a long, two-dimensional airfoil, which spanned the test section and was mounted on rotating drum sidewalls. The model produced high lift and pitching moments relative to the drag. This greatly increased the difficulty of obtaining accurate axial component measurements. The dual balance system, shown in figure 7, was produced for these 2D Eppler tests.

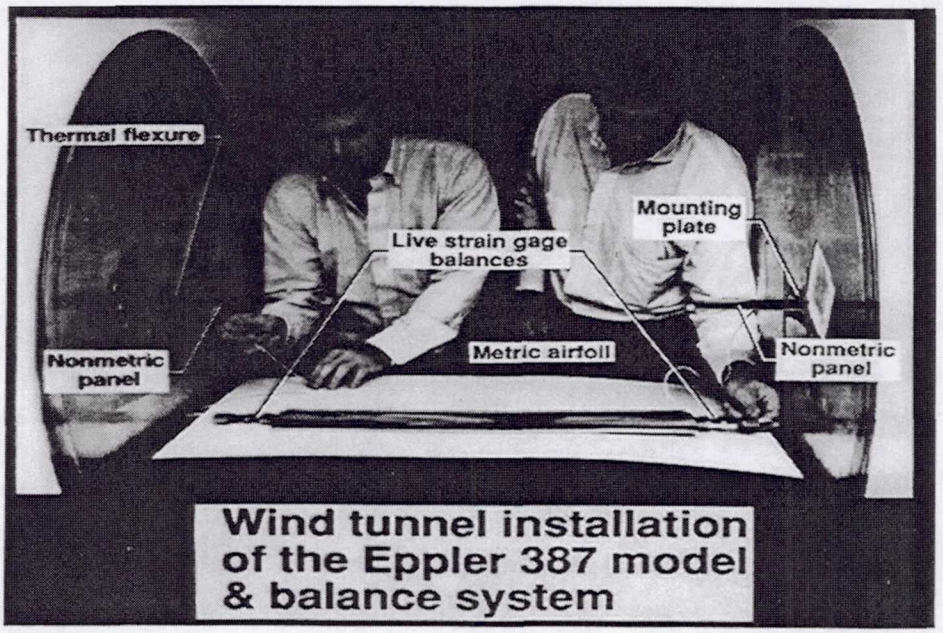

Figure 7 – A Dual Balance System

Results of these aerodynamic tests can be found in reference 1. Perhaps the most unique feature of this balance system was the thermal flexure mounted in one of the sidewalls. This flexure provided relief for the thermal expansion and contraction of the long model and controlled the side forces that otherwise would have overloaded the main balance system. Also included were balance lockouts, which were used during setups and rotation of the entire model and balance system.

Two other unique balance types used at LaRC are flow through balances and rotor balances. A picture of a large flow through balance can be viewed in figure 8.

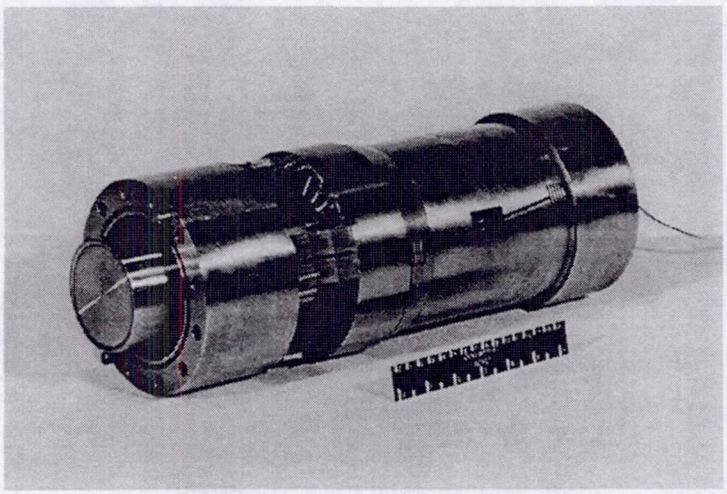

Figure 8 – A LaRC Flow Through Balance

Flow through balances are used in powered wind tunnel tests. The design challenge here is to maintain balance measurement accuracy while paralleling the measuring elements with a bellows arrangement. Calibrations must also provide interaction corrections for pressure and mass flow rates. LaRC has used many types of custom rotor balances. The most complex to date was the 1633CR-balance system (figure 9).

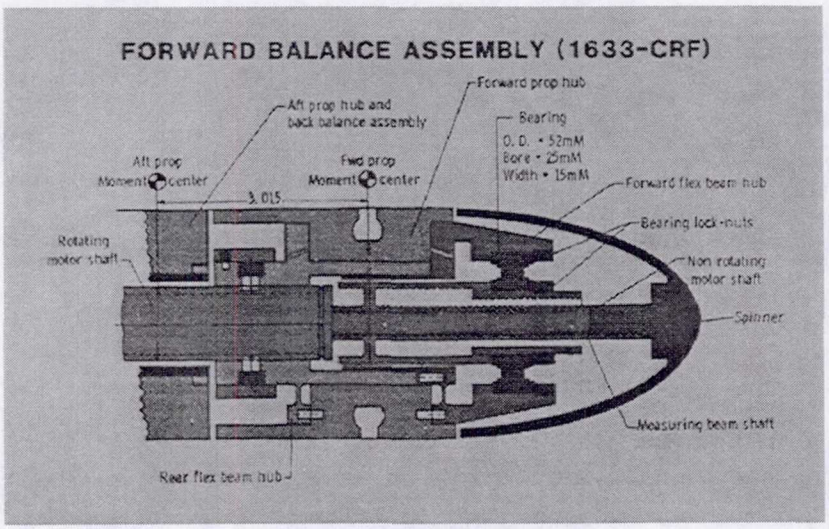

Figure 9 – A Forward Counter Rotating Balance Assembly

This figure shows only the front balance in this counter rotating system. This test was designed to measure the interference effects between a forward and aft propeller propulsion system. The design challenges resulted from not only the system complexity, but also due to thermal issues that were generated by the 16000-RPM propeller speed.

Strain Measurement

Strain measurement is a critical area, which supports force measurement at Langley. In the recent past, this is the area where the greatest balance advancement has taken place. Langley has developed multiple strain measurement application and usage techniques that involve bonding, thermal compensation, moisture barrier, and wiring/connector techniques for many environmental extremes. These strain measurement techniques are not only applied to balances, but also to many structural tests. An example of our high temperature strain gage effort is shown in figure 10.

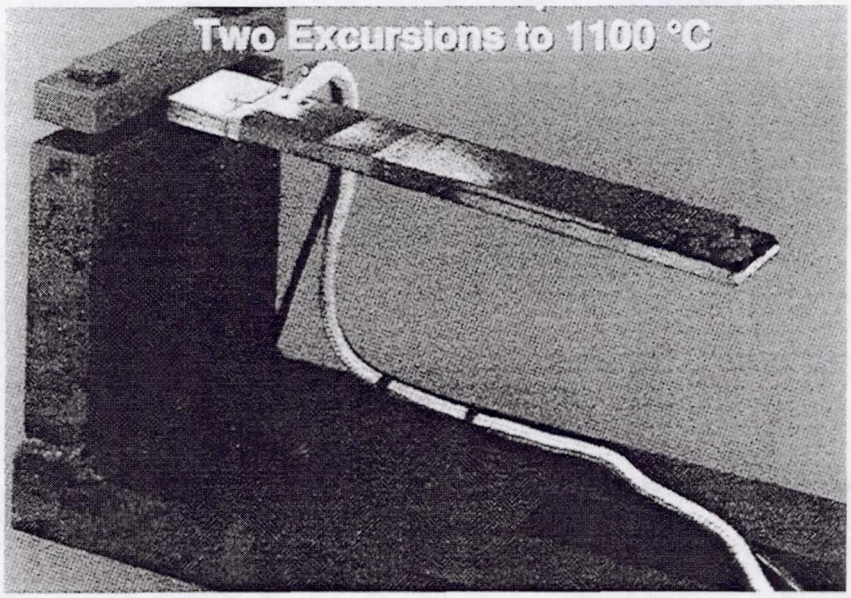

Figure 10 – Carbon/Carbon Test Specimen

The strain gage and application technique shown was developed at LaRC. It can be seen that the strain gage bridge is still operational while the test material is failing due to delamination at 1100° C. At the opposite extreme, a custom force transducer for the CETA experiment is shown successfully operating in space (figure 11).

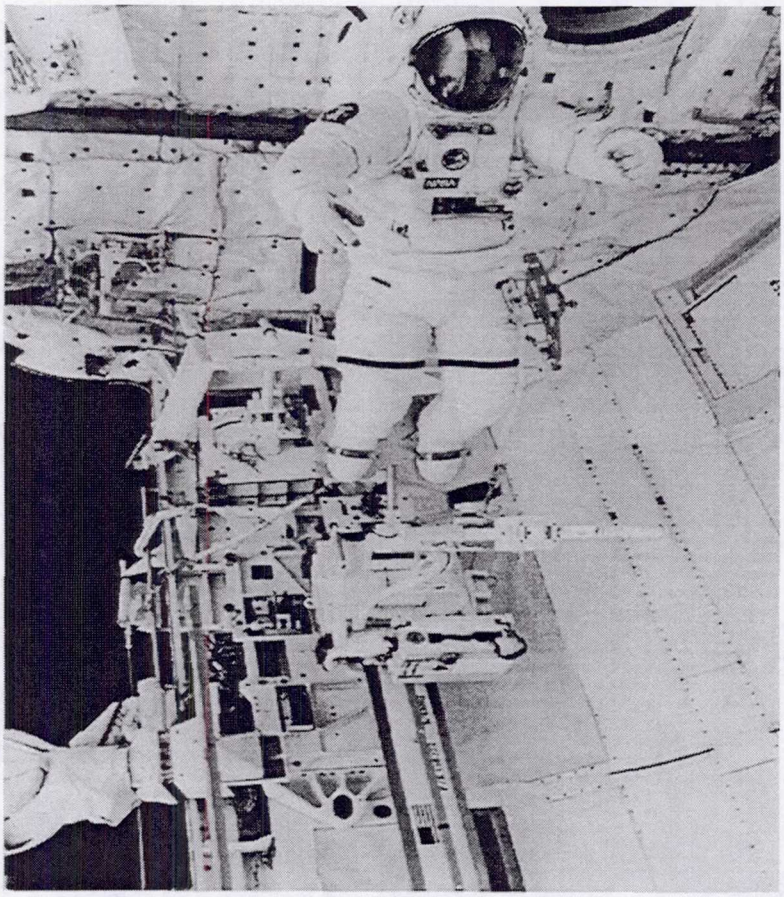

Figure 11 – A Force Transducer Platform in a Space Environment

In a space environment the transducer must perform in extreme cold and vacuum conditions. This test was designed to measure the astronaut's level of effort expended performing various tasks.

Calibration and Data Reduction

Calibration and data reduction are other critical areas for the production of force instrumentation. The LaRC calibration effort begins with the standards lab. This lab maintains our force and mass standards and ensures that they are traceable back to the United States National Institute of Standards and Technology (NIST). The next step in force transducer calibration typically is the application of dead weights and data acquisition. Langley's calibration strategy is to apply calibration loads to simulate test conditions as closely as possible. A more detailed explanation of the LaRC calibration process is given in reference 2. . A loading schedule usually begins with the application of simple single component loadings and progresses into complex sequences of multicomponent check loadings. A photograph of a six component load application can be seen in figure12.

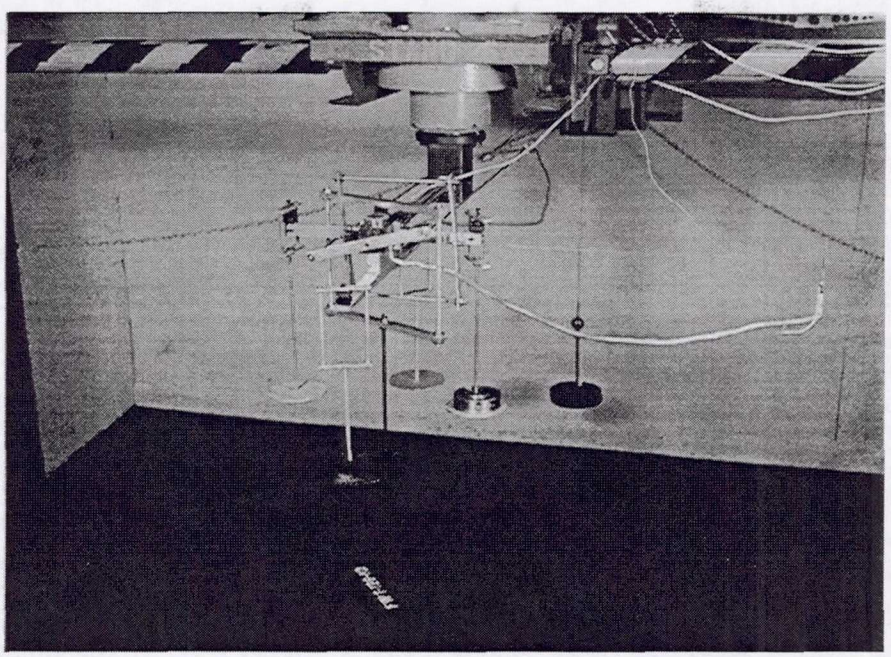

Figure 12 – A Six Component Dead Weight Calibration Loading

Following acquisition, the data is reduced using a least squares curve fit to generate all possible sensitivities, first order, second order, and cross product interaction coefficients (see references 3 and 4). Often, custom calibrations must be performed, such as the on site semi span model calibration shown in figure 13.

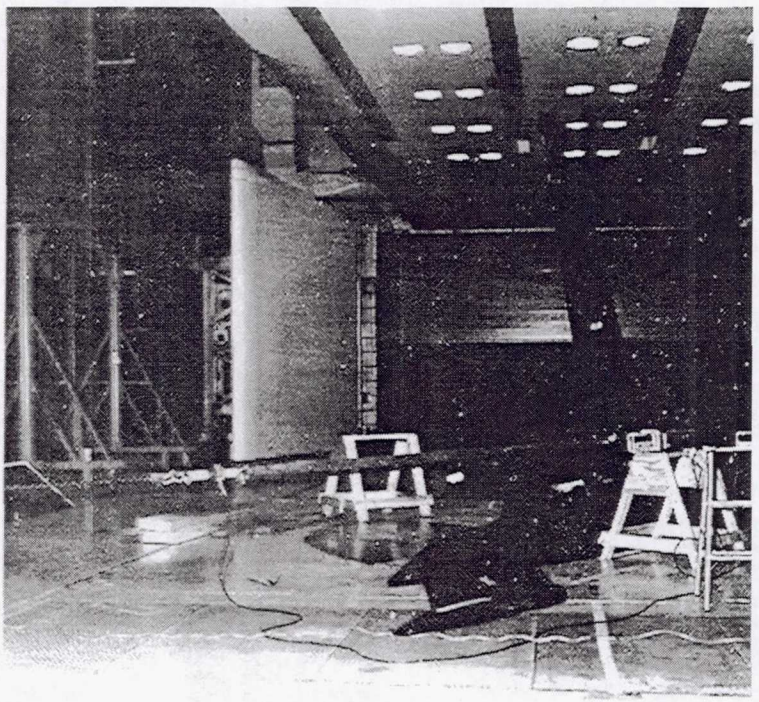

Figure 13 – An On Model Balance Calibration

While the balance was fully calibrated in our lab, the model system required an on model check calibration. A cable load applying axial force and a yawing moment are being shown.

Conclusion

In conclusion, the Model Instrumentation and Systems Branch supports a wide variety of force and strain measurement capabilities. Accurate measurements are required in the presence of many challenging requirements such as: limited physical space, rotating systems, use of exotic materials, and extreme environments. The MISB typically produces about ten new balances per year and supports approximately 300 existing force transducers. There are about 350 tunnel installations and 10,000 strain gage installations performed annually. Our metrology efforts include about 80 six component balance, and 650-load cells/torque wrenches/analytical balance calibrations per year. Hopefully, this broad overview presents a better understanding of the NASA Langley Research Center's force and strain measurement capabilities.

References

1. McGhee, R. J., Walker, B. S., and Millard, B. F.: "Experimental Results for the Eppler 387 Airfoil at Low Reynolds Numbers in the Langley Low-Turbulence Pressure Tunnel," NASA Technical Memorandum 4062, NASA Langley Research Center, Hampton, Virginia, 1988.

2. Hansen, R. H.: "Evaluation and Calibration of Wire-Strain-Gage Wind Tunnel Balances Under Load," Wind Tunnel and Model Test Panel of Advisory Group for Aeronautical Research and Development, Rome, Italy, 1956.

3. Guarino, J. F.: "Calibration and Evaluation of Multicomponent Strain-gage Balances," NASA Interlaboratory Force Measurements Group Meeting, Jet Propulsion Laboratory, April 16-17, 1964.

4. Ferris, A. T.: "An Improved Method for Determining Force Balance Calibration Accuracy," 39th International Instrumentation Symposium, Paper # 93-092, 1993.

THE HALF MODEL BALANCE FOR THE COLOGNE CRYOGENICTUNNEL (KKK)

Prof. Dipl.Ing. B. Ewald, Tech. University of Darmstadt, Germany

Dr.Ing. G. Viehweger, DLR Cologne, Germany

Dip.Ing. R. Rebstock, DLR Cologne, Germany

ABSTRACT

The Cologne Cryogenic Tunnel, better known as KKK, is a Low Speed Atmospheric Wind Tunnel working at temperatures from ambient down to 100 K. The test section size is 2.4 by 2.4 meters. The tunnel has the Reynolds number capability of a highly pressurised tunnel of the same size. The tunnel allows Reynolds number excursions at constant Mach number without change in dynamic pressure, so there are no model deformation effects. With this simulation capability the tunnel will be highly useful for Reynolds Number testing during the high lift system development of transport type airlines. This capability may be improved even more by the use of half models. In conventional tunnels the half model technique is successfully and routinely used in the Airbus development wind tunnel test programmes.

The typical design of compact half model balances leads to a high sensitivity against temperature effects, so a very careful design of the half model mounting system is necessary to get the required high accuracy and repeatability with half models.

In co-operation of the DLR and the Technical University of Darmstadt a half model mounting and measuring system was developed and constructed. The Technical University of Darmstadt was responsible for the balance design and manufacture; on the other hand the DLR designed and constructed the difficult balance installation. To avoid any accuracy degradation due to temperature effects, the complete balance including the angle of attack drive is isolated and conditioned to ambient temperature.

The connections to the cold model at the model side of the balance and to the cold tunnel structure at the earth side created serious design problems. Large forces must be transferred by these connections and heat flow through the connections must be avoided as perfectly as possible. A combination of isolation and local heating was developed to fulfil these requirements.

The half model balance is designed by an interactive computer programme, which analyses the stress distribution in the balance and allows an optimised design for signal strength and stiffness. The half model balance is fabricated from one piece of high strength maraging steel by milling and EDM. Regardless of the fact, that the balance will be conditioned to ambient temperature in the cryogenic environment, gaging and wiring will be done with materials and methods fully qualified for cryogenic conditions. The balance was be calibrated using a third order algorithm.

To allow engine interference testing, in the design of the balance provisions have been made for installation of a compressed air bridge for the engine simulation drive air (resp. nitrogen).

Table of Content

1. INTRODUCTION

Since more than 15 years the half model testing technique is used by Deutsche Airbus, Bremen, with excellent results in the Airbus wind tunnel programme. Especially for the development of the high lift wing configuration the half model technique allows a much larger model scale in a given tunnel and reduces model construction cost. Low speed engine interference, which has a large influence on take off and landing performance, can be studied successfully with half models equipped with turbine driven simulators (TPS).

The Cologne Cryogenic Tunnel is fully developed and qualified for operational testing. The introduction of the half model technique into this tunnel results in a Reynolds Number / Mach Number capability, which is comparable to much larger and highly pressurised conventional tunnels. This capability is achieved with constant dynamic pressure through the Reynolds Number range at a given Mach Number, so there is no interference between model deformation and Reynolds Number effects.

Therefore the DLR decided to provide a half model mounting and balance system for the KKK. The balance is designed and fabricated by the Technical University of Darmstadt while the turntable and the thermal isolation and conditioning system is designed and fabricated by the DLR.

2. THE COLOGNE CRYOGENIC TUNNEL (KKK)

The well known KKK originally was a conventional Low Speed Tunnel, which was modified for cryogenic operation [1,2]. To enable cryogenic test operation, the KKK has some additional systems, which distinguish the cryogenic tunnel from a conventional tunnel. The main features of the KKK are shown in Figure 1 :

- o A closed test section including an access lock and a model conditioning room for model handling, while the tunnel circuit is held at low temperature.
- o A liquid nitrogen injection system to control the gas temperature.
- o An exhaust system to control the tunnel pressure
- o An internal insulation system to protect the concrete shell from the low temperature.

- o A control system to control Mach Number, temperature and pressure with the required accuracy.

The temperature of the test gas can be varied between 300 K and 100 K by injection of liquid nitrogen into the circuit downstream of the second corner. By cooling the obtained Reynolds Number at constant drive power may be increased by a factor of 5.5 to 9,5 Million.

Thus by independent variation of the test parameters the influence of the Mach Number, Reynolds Number and dynamic pressure (strain) on the model results may be considered separately.

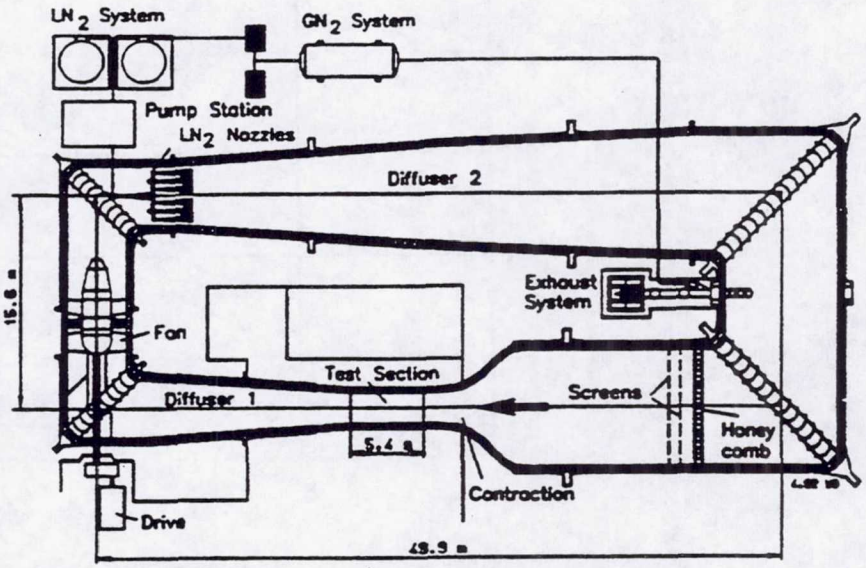

Fig 1 KKK Circuit and Cryogenic Features

The modified tunnel has the following technical characteristics :

Test section dimensions	2.4 m x 2.4 m	Max. Ma-Number (300K)	0.325
Length of test section	5.4 m	Max. Ma-Number (100K)	0.38
Cross section area	5,76 m^2	Max. Re-Number	9.5 x 10^6
Max. model wing span	1,5 m	Fan power	1 MW
Test section static pressure	Atmospheric	Loss coefficient	0.171
Temperature Range	100 K to 300 K		

The Re-Ma-Number capability of the tunnel is shown in Fig. 2.

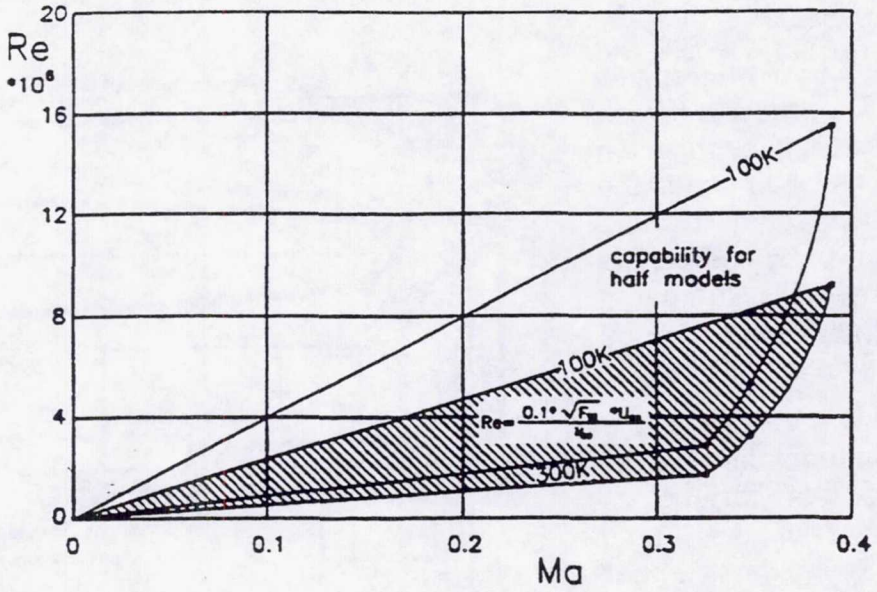

Figure 2 : Full and Half Model Reynolds Number Simulation Capability of the KKK

The test section area consists of the contraction, the test section itself and the transition section to the first diffuser as well as lock and model conditioning room . The test section arrangement of the KKK is shown in Figure 3. Corresponding to the dimensions of the model cart there is an opening measuring 1,5 m in width and 3.1 m in length. The upper cover of the cart serves as test section floor for the duration of the tests.

The access lock and the model conditioning room are below the test section. Both rooms serve for model modifications at ambient temperature while the tunnel is held at low temperature. This ensures economical operation of the tunnel. As the lock and the model conditioning room have individual temperature systems for cooling down and warming up they can be employed as independent cryo-test facilities.

If changes need to be made to the model during low temperature operations, a lift

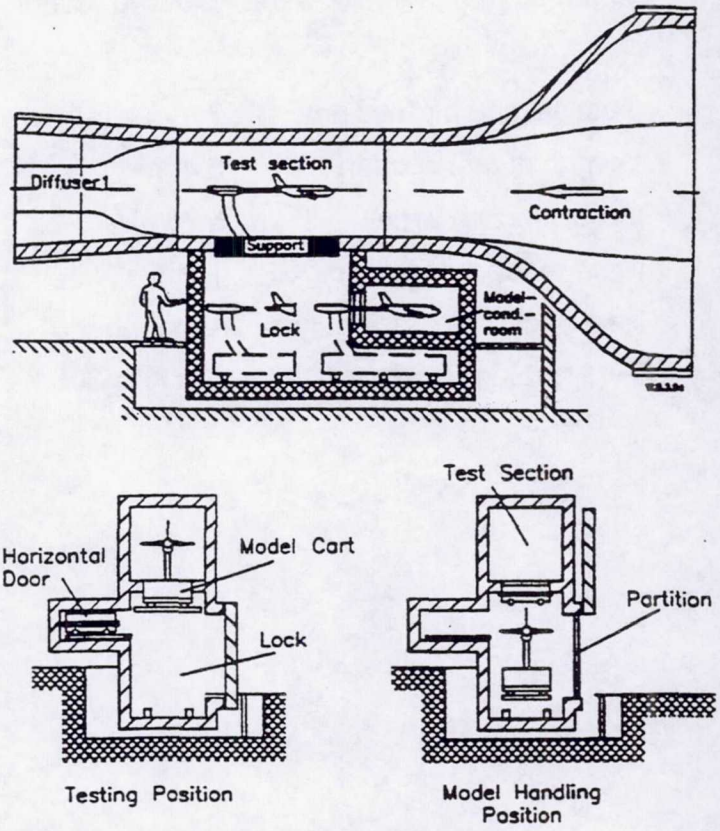

Figure 4. Cart in testing position and in model handling position

system is used to lower the model cart into the lock, which is at the same temperature as the tunnel. The hole in the floor is then sealed with a vapour-tight cover (see Fig. 4) to isolate the lock from the low temperature tunnel.

If major conversions are to be made to the model or if the model is to be changed, the model cart remains parked in the lock. The interior of the lock is gradually warmed up by circulating warm nitrogen gas. Finally, before opening the rig door and before human entry dry air is blown into the lock. Due to the great mass of the steel model support and the lift system the complete operation takes almost four hours.

To achieve shorter model access times in the case of minor changes on the model such as adjusting the flap angle, a model conditioning room (MCR) was installed directly beneath the lock (Fig. 3) The two rooms can be separated by a vertically moving double sliding door. With the door open, the model can be moved into the model conditioning room with the aid of the lift system. The double sliding doors close around the sting. In this case the warm-up process described above can be completed in about 60 minutes as a result of the much smaller volume and the much smaller masses in the model conditioning room. So the conditioning room improves the productivity of the KKK substantially.

3. The Need for Half Model Testing in the KKK

Figure 5 shows an Airbus half model with engine simulation (TPS). The model scale is 1 : 16 with respect to the Airbus A 300.

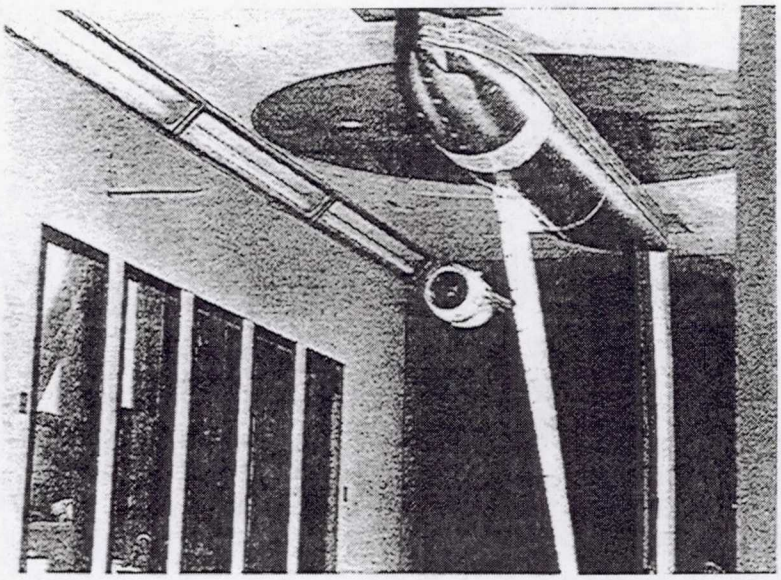

Figure 5. Half model with engine simulation by TPS.

Models of this type are widely used in the Airbus aerodynamic development programme for high lift system pre-development and optimisation and for low speed engine interference testing. Half models of this scale can be tested in the KKK as well. So if the structural design of the models is qualified for cryogenic testing, the same models can be used for conventional routine testing and for Reynolds Number extrapolation in the KKK. The provision of a half model mount and balance in the KKK would qualify the KKK for highly efficient use in the Airbus aerodynamic development programme and in fundamental research on high lift systems.

4. HALF MODEL BALANCE DESIGN

Normally a 'Half Model Balance' is installed on the external side of the test section wall representing the symmetry plane of the model. There are two different design principles for half model balances. One design philosophy follows the idea of a compact 'One-Piece' balance. The other design principle is to assemble the balance from parts (rods, flexures, levers and force sensors) like a very compact external wind tunnel balance. Since the available space for installation in the KKK is very limited, only the 'One Piece Balance' is dealt with in this paper.

Another alternative is the arrangement of the turn table for angle of attack. This turntable may be installed between earth and balance (rotating balance) or between balance and model (fixed balance). For the KKK the principle of the rotating balance was chosen.

An analysis of existing one piece half model balances shows two different arrangements of the sensing beams. What we call the 'Fully Symmetric Cage' is shown in Figure 6 and the 'Half Symmetric Cage' is shown in Figure 7.

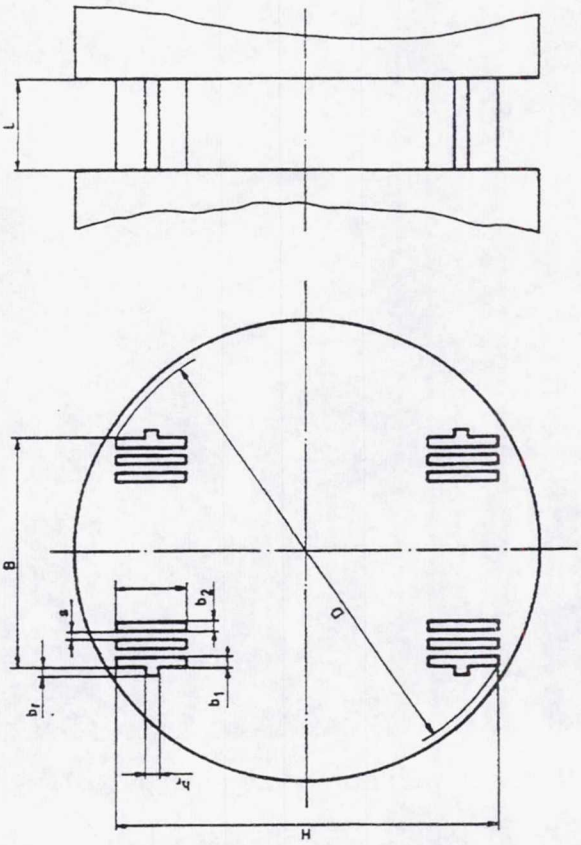

Figure 6 : „Fully Symmetric Cage"

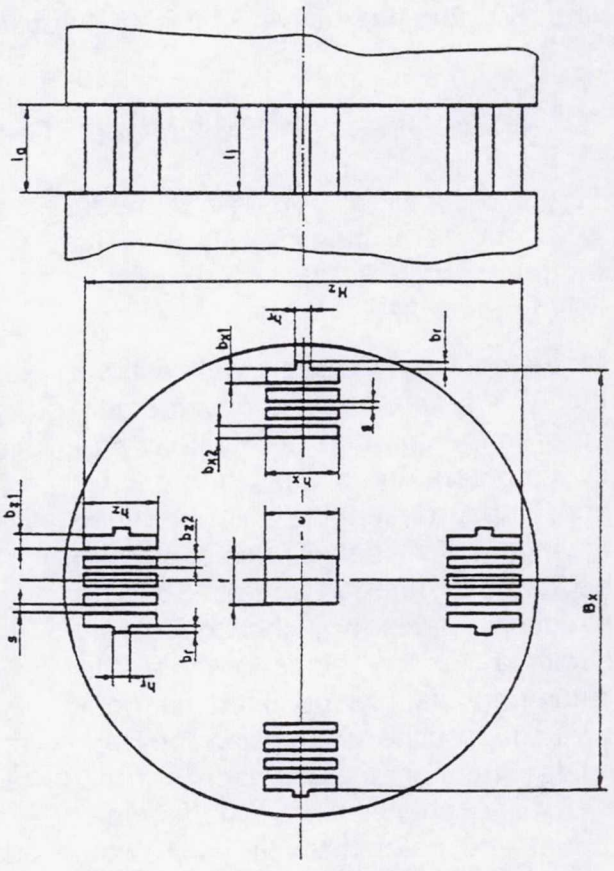

Figure 7 : „Half Symmetric Cage"

From a careful comparison of the two arrangements resulted, that the 'Half Symmetric Cage' (Figure 7) offers more freedom in the adaptation of the sensing beam dimensions to the relative magnitude of the five components X, Z, Mix, My and MSS (the side force Y normally is not measured in the half model case). So this design principle was used for the KKK balance.

In both designs a central beam may be provided as indicated in Figure 7. The central beam gives extra freedom for the individual adaptation of the beams to the desired load range of the components. In the case of the KKK balance design this central beam was not provided to make allowance for a central hole through the balance. Engine interference tests with blown nacelles or with Turbine Powered Simulators (TPS) are an important use of the half model arrangement. This arrangement makes drive air supply to the model much easier than in the case of the complete model. The drive air is supplied to the model via a force free air bridge. For the principle design of such air bridges see [3]. The design of the half model balance for the KKK shall allow to retrofit a force free air bridge. So a relatively large central hole in the balance body was provided.

The key question of a half model balance concept for a cryogenic tunnel is the decision of a 'Cold Balance' or a 'Heated Balances'. For tail sting internal balances in a cryogenic tunnel the author prefers the cold balance. Nevertheless for a half model balance the situation is different. Past experience with compact half model balances demonstrates, that these instruments are very sensitive against temperature changes. Temperature changes create temperature gradients in the balance structure and result in error signals especially in the axial force measurement. Different measures are taken against this problem. One design is a balance completely sealed and filled with oil for better temperature uniformity.

In principle it is no problem to design a balance for cryogenic environment. Nevertheless the large masses of the model, the turntable and the balance itself follow temperature changes in the tunnel very slowly and so temperature gradients in the balance structure exist for long times. The long time waiting periods necessary for sufficient temperature uniformity in the balance deteriorate the tunnels productivity to an unacceptable extent. On the other hand the installation of a half model balance makes heat insulation and heating of the balance for ambient temperature condition much easier than in the case of an Internal Balance. So for the KKK the 'Heated Balance' option was chosen.

One principle design dimension is the diameter of the balance. The balance should be as compact as possible. On the other hand a certain minimum diameter is needed for the large rolling moment (in case of the half model more logically designated a 'Root Bending Moment'). We defined a half model balance load parameter :

$$S_H = {}^{M_X}\!/_{D^3} \qquad [\mathrm{N/cm^2}]$$

For a successful design this Half Model Balance Load Parameter shall be between 15 N/cm^2 and 80 N/cm^2. To avoid any influence of the balance flange screw stresses on the measuring elements, a massive and stiff block is provided between the flange and the bending beam cage in the centre of the balance. These blocks limit the minimum length of the balance. If the stiffness of this part of the balance is not sufficient, the accuracy of the balance is deteriorated by mounting the balance. As a simple design rule a balance length close to the diameter allows a design of sufficient stiffness.

For the design computation an interactive computer programme was written. The dimensions of the balance and the bending beams are fed into the programme and the result is a complete stress analysis of the bending beam cage for the five load components. The balance designer modifies the balance dimensions step by step until a satisfying design is found.

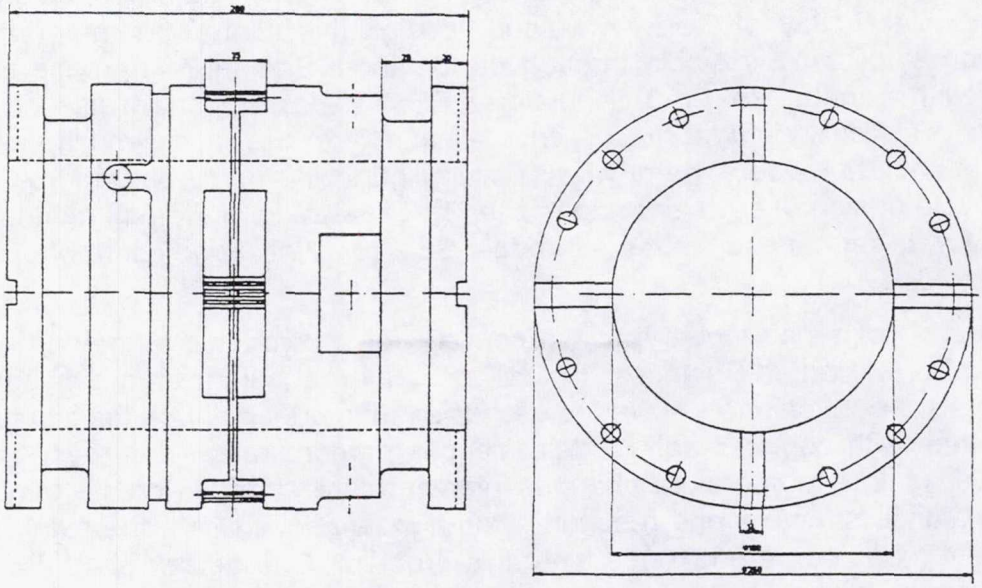

Figure 8. Principle design of the KKK half model balance

The 'Half Symmetrical Balance' design allowed for nearly equal sensitivity of the three main load components Normal Force, Axial Force and Pitching Moment. Figure 8 gives a general impression of the design.

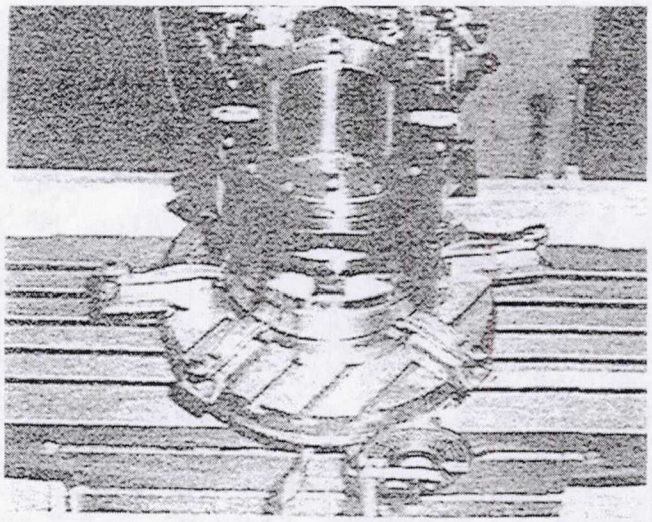

Figure 9 Half Model Balance on Milling Machine

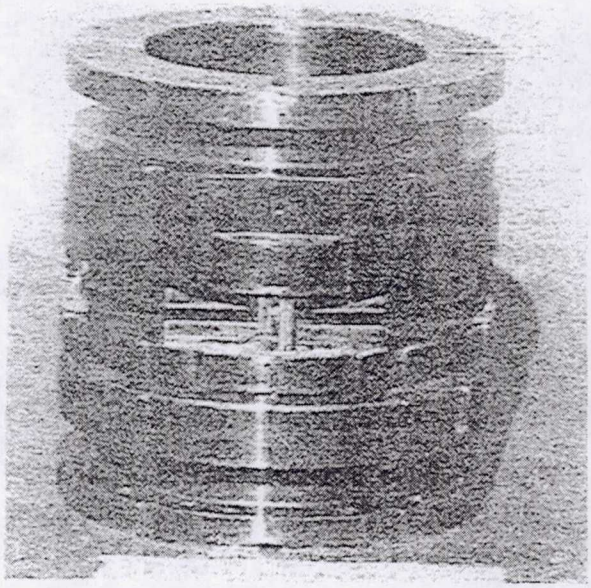

Figure 10 : Balance ready for Gaging

The KKK half model balance was fabricated from a single block of Maraging 250. Careful heat treatment prevented any distortion or cracks during machining of the small bending beams from this block. Figure 9 shows the balance on the milling machine. Figure 10 shows the balance ready for gaging and Figure 11 gives an impression of the final appearance of this balance.

For gaging conventional MM strain gages are used. The wiring is carefully arranged for closely concentrated bridges to minimise temperature effects. For further minimisation of temperature effects some strain gage bridges are wired as Poisson bridges. As an example of the strain gage application a close up of one bending beam is shown in Figure 12.

A sufficient number of PT 100 temperature sensors are installed to monitor the temperature situation of the balance.

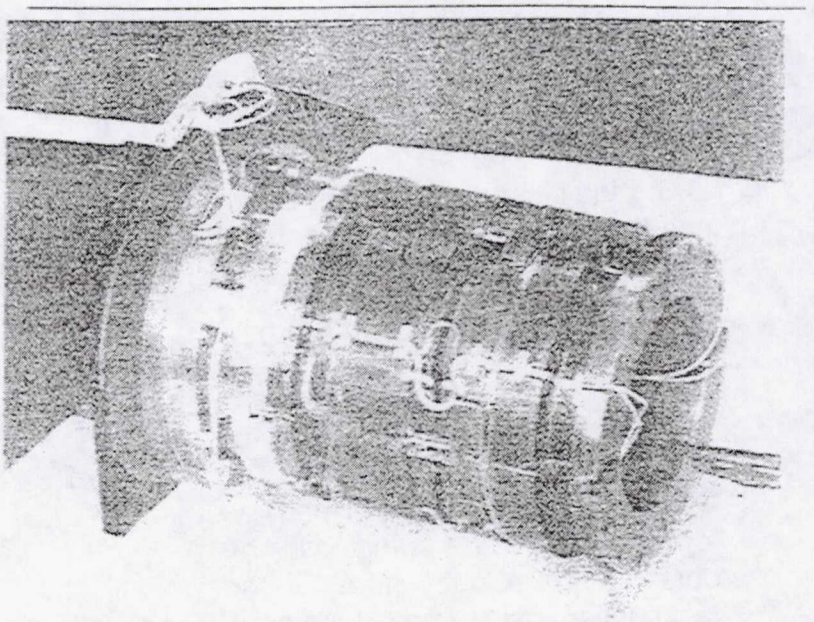

Figure 11 : Half Model Balance Ready for Calibration

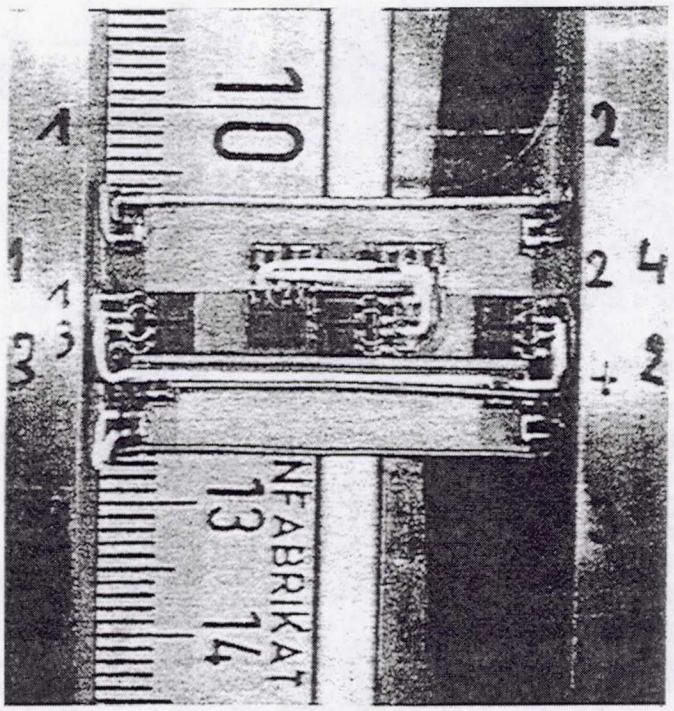

Figure 12 : Gage Application

5. HALF MODEL INSTALLATION IN THE KKK

The half model will be mounted in the test section floor on a turntable, which represents the symmetry plane of the model and allows to set angle of attack. The turntable is mounted on the structure of the 2-D model cart and is connected to the earth frame. The model itself is mounted on the rotating balance.

Using the lift system the model cart can be lowered for model changes from the test section into the lock during cryogenic operation . The equipment of the lock will be completed for drive gas supply to the cart and to the model via a force free air bridge for TPS testing.

During the tests the upper and the lower side of the wing can be observed from both sides of the test section, using special methods for surface flow visualisation. Windows in the ceiling of the test section will allow additional flow field measurements in the slots of high lift configuration elements to investigate the influence of Reynolds Number effects.

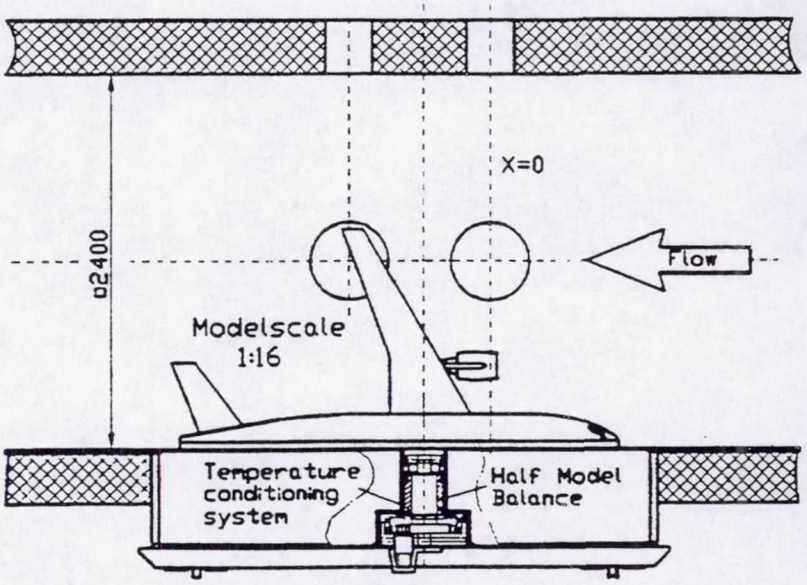

Figure 13 : Predesign of Half Model Arrangement

6. INSULATION AND TEMPERATURE CONDITIONING SYSTEM

Opposite to the internal balances of KKK, which are designed as „cold" balances, the half model balance of KKK is a „warm" balance. One condition for force measurements with an acceptable accuracy and repeatability is a homogeneous temperature distribution in the balance at almost 25° C. To guarantee a homogenous temperature distribution, the balance is surrounded by a super insulation, which prevents a radial heat flow. A heat flow in axial direction is given at the upper model adapter, and at the fixing of the balance at

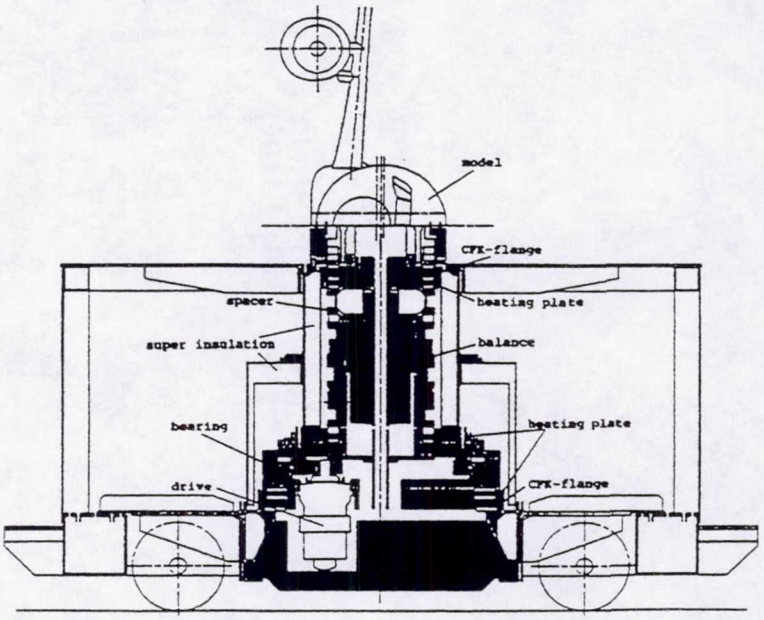

Figure 15 : Balance Installation and Insulation System

the lower structure with bearing. The model side adaptation of the balance is more critical with regard to the amount of heat flow, as here the model with its high surface heat transfer coefficient is responsible for a temperature gradient in axial direction. Therefore, we took much care on the design of the link between balance and model adapter. Beneath the model adapter, there is a CFK layer to reduce heat flux. A heater plate and a spacer is added at the downward side. The spacer is designed with small sectional areas to achieve a low heat transfer rate.

An additional CFK plate at the upper flange of the balance improves the uniform temperature distribution.

The support side flange of the balance temperature conditioned in a similar manner, whereas no spacer is used because of force resistance reasons.

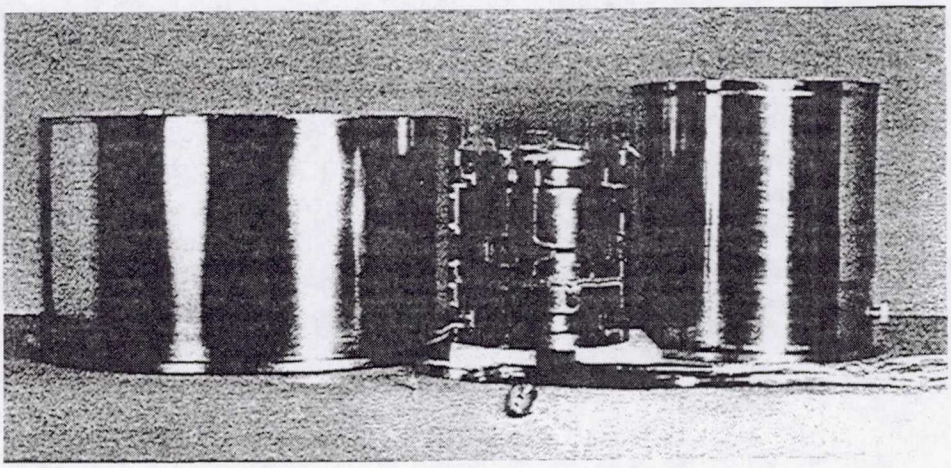

Figure 15 : Balance and Insulation

The various heating layers are temperature adjusted by means of 4 PID control devices. The angle of attack is measured by an angle transmitter connected to the driven part of the bearing and has an accuracy of 1/100 °. Since this device cannot operate in cryogenic conditions, this part of the lower balance adaptation is insulated with an additional super insulation.

7. OPERATIONAL EXPERIENCES

The preliminary tests for half model test runs were carried out in the model access lock of KKK. The test results gave information about the efficiency of the super insulation and heating devices. During the tests the model and support with balance was cooled down in the lock. During the cool down phase the temperatures of the balance (12 temperatures, taken in axial and radial direction in the balance circumference) and the temperatures of the heating layers and insulation layers were registered.

During the cooling tests three non expected effects were obtained, which had a great influence on accuracy and repeatability of the balance :

a) Heat flux via screw joints of the spacer.

b) Convection and gas flow caused by a pressure difference between the inner and outer side of the super insulation tube which surrounds the balance.

c) Interaction of the heating systems and controllers.

These effects resulted in temperature differences at the circumference of the upper balance flange of up to 2 degrees centigrade and influenced the achieved accuracy and repeatability of the balance considerably. To achieve the goal of 2-3 drag counts repeatability for transport measurements in low speed, some improvements were necessary. Between the upper and the

lower flange of the balance similar temperature differences occurred. These temperature differences had no measurable effect on the balance repeatability.

Considerable improvements were achieved already by some counter-measures. The flange screws were replaced by titanium bolts. The much lower heat conductivity of titanium improved the situation.

The gas flow through the balance was prevented by careful sealing of the total balance compartment. Finally some improvements of the temperature controllers were achieved.

In an additional program we studied certain structural modification of the balance design for a drastically reduced sensitivity of the balance against circumferential temperature differences. This seems to be the most promising approach, since during tunnel operations very often conditions may occur, which have not been tested with the insulation and temperature control system and which may cause difficulties. The modification study for a much reduced sensitivity against temperature differences is running just now with the well proven instrument of Finite Element analysis.

8. SUMMARY

The installation of a half model technique in the KKK gives a much increased Mach-Reynolds Number capability for transport aircraft development testing. Maximum MAC Reynolds Numbers of typical transport aeroplane configurations will be Re = 12 x 10^6 at a Mach Number of 0.3. Since the KKK is an atmospheric cryogenic tunnel, Reynolds Number excursions are provided only by temperature excursion with constant total pressure. So Reynolds Number effects are not mixed with model deformation effects.

The concept of a compact one piece half model balance, which is isolated and conditioned to ambient temperature, allows stable and accurate measurements without any need for stabilisation time. So an optimum productivity of the KKK for transport development tests will be achieved. To achieve this goal, a sophisticated temperature conditioning system for the balance compartment is necessary.

The design of the balance allows for engine interference tests. Another useful application of the KKK will be initial low cost testing of models for the ETW, since the size of KKK and ETW allow the use of the same models in both tunnels.

References

[1] Viehweger, G.
"Kryogenisierung des Niedergeschwindigkeits-Windkanals Köln-Porz - Spezifikationsphase -"
DFVLR, WKT 11/80, Köln-Porz (1980)

[2] Viehweger, G.
"THE KRYO-KANAL KÖLN (KKK): DESCRIPTION OF THE TUNNEL CONVERSION. Thermal Insulation, Instrumentation, Operational Experience, Test Results and Operating Costs."
Agard CP-774, Paper 4, June 1989

[3] Prof. Ewald
"Transport Configuration Wind Tunnel Tests with Engine Simulation"
AIAA Aerodynamik Testing Conference, San Diego, März 1984

ON INTERNAL BENDING-BEAM STRAIN-GAUGE WIND-TUNNEL BALANCES*

Knut Fristedt
AB ROLLAB
Solna, Sweden

SUMMARY

A design study of an internal strain-gauge wind-tunnel balance with a force system valid for an airplane model in a transonic 1.5x1.5 m^2 wind-tunnel with a stagnation pressure of 400 kPa is presented. It concerns a "flow-through" model, and the permitted diameter of a balance of type bending-beam is 30 mm. It is shown, that a balance can be designed, if a maximum nominal stress of 600 N/mm^2 is permitted. The 30 mm diameter part of the sting may however be to short from an aerodynamic point of wiev.

As a background a comparison of the relative load carrying capacity of three types of balances is made by use of information found in the litterature. This study shows, that the bending-beam balance is superior, when D<35 mm. The capacity of "Task" balances is equal at larger diameters and the "Two-Shell" balance is a competitor, when D>50 mm.

A discussion of the influence of the numerical value of the diameter on the load carrying capacity at constant stress of the present type of balance is made together with a limited comparison with Task and Two-Shell balances.

A mathematical model of 2:nd degree, which combines the force system loading the balance with the balance signals is finally commented. This model can be used both for calibration and wind-tunnel testing.

INTRODUCTION

The purpose of a wind-tunnel balance is to measure the aerodynamic forces and moments, which load a model during wind-tunnel tests. Both stationary and non-stationary forces may be of interest, and different balance configurations and model support systems are adopted for the different tasks. The present report discusses the design of internal strain-gauge balances for static force and moment measurements.

Internal balances are used within all speed ranges and it is the only balance type used for model testing in transonic and supersonic wind-tunnels. The reason is, that it measures only those forces, which are generated on the model and that the distortion and interference

---

* Based on a report originally written for the Defence Material Administration of Sweden

effects on these forces are small, at least as long as the sting does not require modifications of the external geometry of the afterbody of the model.

The balance must suppress the influences on the output signals from environmental parameters such as temperature and electromagnetic radiation. The influence of periodic mechanical vibrations are eliminated by the signal conditioning equipment or the data evaluation process.

The possibility to manufacture expedient internal balances is a consequence of the development of the cemented resistance strain-gauge and the semiconductor electronics. The former gives small gauges of uniform quality and the latter equipment for reliable conditioning of the small signals from the strain-gauges.

Figure 1 shows, that an internal balance measures the components of a body-fixed force system. A large normal force (N) often 10 to 20 times the axial force (T) characterizes wind-tunnel models of airplanes. The corresponding ratio of missile models can be 3 to 10. The side force (C) of an airplane model is say 30% of the normal force, while most missile models are characterized by equal N and C components. The measured axial force represents practically always a flying condition without engine thrust. A model with open air intakes is also influenced by an internal drag, which must be considered in the evaluation of the measurements.

A strain-gauge balance is an analog transducer, which must be calibrated against known forces and moments. The capacity of the calibration equipment to simulate a correct aerodynamic force system and the ability of the mathematical calibration model to simulate the mechanical and electrical characteristics of the balance are of major importance. They settle the accuracy, by which the aerodynamic forces of a wind-tunnel model can be measured.

An internal balance is normally supported by a sting fixed in the model support of the wind-tunnel. The strength and the stiffness of the sting can be the factors, which limit the load capacity of the balance.

SYMBOLS

N= Normal force.
C= Side force.
T= Axial force.
P= Reaction force.
J= Area moment of inertia.
B= Section modulus in bending.
m= Pitch moment.
n= Yaw moment.
ℓ= Roll moment.
M= Bending moment.
A= Cross-section area.
W,K= Section modulus in torsion.
x y z= Coordinate system with origo in the balance centre.
D= Diameter of balance.
R= Radius of balance.
d= Diameter of sting hole, diameter of balance end support.
E= Modulus of elasticity.
G= Modulus of rigidity.

ν= Poisson´s ratio.
x= Distance along the sting from the balance centre. Relative length in fig 13.
σ= Stress. $\sigma_{0.2}$= Yield stress.
σ_b= Ultimate stress. σ_f= Fatigue stress.
σ_s= Static stress. σ_d= Dynamic stress.
σ_{tot}= Total stress.
τ= Shear stress. τ_b= Ultimate shear stress.
ε= Strain. ε_s= Apparent strain.
R= Electrical resistance. ΔR= Change of resistance.
u= Bridge output signal. V= Power voltage. Wind speed.
g= Linear gauge factor. t= Temperature.
k= Second degree gauge factor. Spring konstant. Coefficient in (214), (215) and (216).
α= Angle of attack. Parameter in figure 13, 20, 21, 22 and 24.
z= Dimension in figure 20, 21, 22 and 24.
β= Angle of yaw. Functions defined in (43), (55) and (69).
$F_1 \rightarrow F_4$= Functions defined in (46) to (49).
$H_1 \rightarrow H_4$= Functions defined in (56) to (61).
S= Function defined in (38). L= Sting length.
V_1= Function defined in (72). r_f= Fillet radius.
$L_1 \rightarrow L_9$= Dimensions defined in figure 10.
a b c d= Dimensions in the N-C-ℓ and N-C elements in figure 10.
t_1 t_2= Length and position of a strain-gauge in (40).
h_1 h_2 b_1 b_2 r_1 r_2 n_1 n_2 s_1 s_2 e_1= T element dimensions. Figure 10.
m_1= Dimension in figure 20 and 21. m_2= Dimension in figure 22.
Cp= Stress control points in figure 10.
m= Model mass. f= Natural frequency.
δ= Symbolic deflection. ψ= Symbolic slope. Relative scale.
Θ= Angle of twist in figure 18. φ= Angle of twist in figure 18.

INTERNAL BALANCES ON THE MARKET

Figure 2 is a summary of the relative load carrying capacities of some internal balances. The information is gathered from brochures and reports and does not lay claim to be complete. Where applicable the forces given are corrected to correspond to force systems with six components, to permit mutual comparisons. The standardizing parameter choosen is

$$N/D^2 \qquad (1)$$

The external forces and moments of a wind-tunnel model exposed to an airflow, can be written (ψ= the relative model scale)

$$N \approx \psi^2 \qquad (2)$$

and

$$m \approx \psi^3 \qquad (3)$$

The bending and torsion resistances of a model are also proportional to ψ^3 and the stresses, which the external forces cause in a given cross-section, are accordingly

$$\sigma = \text{constant} \qquad (4)$$

as long as the models (and the balances) are geometrically similar. The stresses during wind-tunnel testing, in equally located sections of models and balances, are consequently also constant and independent of the model scale as long as the dynamic pressure and the model attitude are unchanged.

Figure 2 includes three types of six-component balances with different geometric layouts.

The Bending-Beam Balance

The bending-beam balance (figure 3) is usually made in one piece. The model is mounted on one end of the balance and the other end fits into a tunnel-fixed support (e.g. a sting). The different measuring elements must carry the whole force system and simultaneously measure their dedicated components. It is impossible from a strength point of view to arbitrarily choose the sensitivities of the different elements.

This type of balance has normally insignificant hysteresis and the different balance signals depend in principle on all force and moment components present. The interactions are proportional to changes in slopes and deflections of the balance with the model as reference. These deformations are relatively large due to the fact, that the balance is a beam fixed in its ends to the sting and the model.

The following comments refer to the numbers in figure 2.

(1) The dots on the curve correspond to the ROLLAB balances tabulated in [1] and a few more. The series begin with a diameter of 6 mm. The relative load carrying capacity increases up to a diameter of 15 to 20 mm. The upper of the three 18 mm balances was provided with an integrated conical sting.

(2) The broken line is a criterion, which so far has been used by ROLLAB as a design limit for bending-beam balances. It can be summarized as

$$N/D^2 = 0.225\ D \qquad \text{when } 0<D<20 \text{ mm} \qquad (5)$$

$$N/D^2 = 4.5 \qquad \text{when } D>20 \text{ mm} \qquad (6)$$

It is obvious in comparison with (18), that "stronger" balances can be made if a maximum nominal stress level of 600 N/mm^2 is permitted.

(3) The dots on the curve correspond to the strongest of the TEM balances tabulated in [1]. Stronger balances can probably be designed.

(4) The curves represent an upper limit for the balance technique given in [2]. The lack of an upper limit for D is confusing.

(5) These data from [2] concern four balances intended for NTF. It is not clear, if it refers to preliminary designs or to manufactured balances.

(6) Data from [3]. The balances are of the same general layout as the TEM balances.

(7) Represents data from [4]. The layout differs from the rest of the examples, it is manufactured of a few pieces screwed together. The relative strength increases rapidly with the diameter up to ~40 mm.

(9) The line represents a criterion given in [7] as a maximum limit for bending-beam balances. It is apparent, that a lower limit of D must be added.

(10) Represents the load carrying capacity of three balances with data from [7]. The curve approaches the criterion [9], when D>70 mm.

(13) Data from [10]. The three balances are only examples. However data from other ONERA balances have not been found in the litterature.

(14) Data from [11].

(15) Data from [12].

(17) Data from [13]. Concerns a balance manufactured by NLR.

(18) Represents the 30 mm balance calculated later in this report. The balance is belived to represent an upper limit for the type of design presented in this paper.

The TASK Balance

The floating-frame balance type "TASK" consists of two coaxial tubes joined by six measuring elements. The model is mounted around the external tube and one end of the internal tube is provided with a taper, which fits into e.g. a sting. The measuring elements are loaded only by single components. The screw joints may cause hysteresis. An uncertain zero-drift can occur if the external tube is squized by the model.

The non-linear interactions are small because all measuring elements are attached to the external tube and consequently deflect only marginaly in relation to the model-fixed force system.

With reference to the numbers in figure 2, the following comments can be made.

(11) Data from [8] and valid for the series D balances. It is presumed,

that the two components N and m load the balances simultaneously, when the relative load carrying capacities are estimated.

12) Data from [9] and valid for the series MK balances. It is believed, that these data represent an upper limit of this balance family. The event of the curve shows, that TASK balances with a diameter >40 mm have large load carrying capacities, but also that this quality drops considerably for D<30 mm.

The Two-Shell Balance

The Two-Shell floating-frame balance is described in [5] and [6]. It consists of an external tube, with the ends soldered to an internal tube. The latter is provided with a taper, which fits into e.g. a sting. Several slits in the external tube near its ends form a number of beams perpendicular to the longitudinal axis of the balance. These beams are the only connections between the soldered ends and the central part of the external tube. The beams are provided with strain-gauges with different functions. The balance can not be designed to measure a force system with arbitrarily choosen components. No screw joints are present and the hysteresis is accordingly small. The model is mounted on the external tube and zero-drift may occur, if the model deforms the tube. The non-linear interactions are small due to small deflections between the external tube and the positions of the strain-gauges. The measuring elements are loaded by all components and linear interactions are present.

With reference to the numbers in figure 2, the following comments can be made.

8) This is a criterion of the maximum load carrying capacity given in [5] and adjusted to correspond to a complete force system.

16) The three balances are calculated in [5]. Similar balances have been manufactured by Convair and by AEDC, but no experimental data have been found in the litterature. The relative load carrying capacity of the design is low, when the diameter is <40 à 50 mm.

THE ELEMENTS OF A STRAIN-GAUGE BALANCE

A strain-gauge balance consists of tree elements, the spring-body, the strain-gauges and the bridge wiring. It is a spring-balance with electric sensing.

The Spring-Body

The metal body is an undamped spring. The external load is balanced by internal stresses distributed in the whole body, and a corresponding

strain distribution excists.

Strain-gauges can only be cemented on the surfaces of the body. The body must consequently be able to carry the external load and simultaneously on its surface produce strains, which permit the strain-gauges to yield suitably large and stable electric signals. The geometry must also permit local changes in the introduction of the external loads without affecting the stress distribution in the cross-sections of the measuring elements.

The ratio between stress and strain in a spring-bady is linear up to a certain value of the stress ($\sigma_{0.2}$). When this limit exceeds the material yields plastically. Only the elastic part of the deformation disappears, when the load is removed. This condition is valid for accuracies typical for wind-tunnel balances.

A one-dimensional stress field always causes a two-dimensional strain field due to the lateral contraction of the spring body (figure 4).

$$\varepsilon_x = \frac{\sigma_x}{E} \tag{7}$$

$$\varepsilon_y = -\nu \cdot \varepsilon_x = -\nu \cdot \frac{\sigma_x}{E} \tag{8}$$

A two-dimensional stress field causes a two-dimensional strain field, which can be described by superimposing the effects of two perpendicular one-dimensional stress fields.

$$\varepsilon_x = \frac{1}{E} \cdot (\sigma_x - \nu \cdot \sigma_y) \tag{9}$$

$$\varepsilon_y = \frac{1}{E} \cdot (\sigma_y - \nu \cdot \sigma_x) \tag{10}$$

Only two types of transducer elements are of interest in bending-beam balances, the bending element and the torsion element.

Figure 5 shows the first type, an element exposed to bending. The stresses under the strain-gauges in point I can be expressed as

$$\sigma = \pm \frac{M}{B} \tag{11}$$

The corresponding strains can be calculated from (7) and (8).

Figure 6 shows the second type, an element exposed to torsion. The principal stresses under the strain-gauges in point I ($\pm 45°$direction) are numerically equivalent with the shear stress or

$$\sigma = \pm \frac{\ell}{W} \tag{12}$$

The corresponding principal strains can be calculated from (9) and (10) and will be

$$\varepsilon = \pm\frac{\ell}{W \cdot E} \cdot (1+\nu) \qquad (13)$$

The sprig-body dimensions are also temperature dependent. A uniform change of the temperature of the body results in an apparent strain without a corresponding stress. Temperature gradients produce local strains with accompanying stresses without the presence of external forces. This means, that only gradients along the spring-body can be accepted.

The Strain-Gauges

Two types of resistance strain-gauges are used in wind-tunnel balances, conventional foil-gauges and semi-conductor gauges. The former type is manufactured of Constantan (Advance) or Karma and the latter of doped silicon. Only conventional gauges are of interest for strongly stressed balances.

The resistance change of a strain-gauge depends on the strain in the sublayer and on the change in temperature. For accuracies of interest to wind-tunnel balances the lateral sensitivity of the gauges can be neglected and one may write

$$\frac{\Delta R}{R} = \left|\frac{\Delta R}{R}\right|_{\varepsilon} + \left|\frac{\Delta R}{R}\right|_{t} = g \cdot \varepsilon + k \cdot \varepsilon^2 + g \cdot \varepsilon_s \qquad (14)$$

The apparent strain ε_s is an expression of the total temperature influence.

Typical values are g=2 and k=10 for conventional strain-gauges. ε_s is non-linear and falls within a bracket of $\sim 10^{-4}$ for self temperature compensating gauges, used on proper sublayers and within proper temperature ranges.

(14) is reduced to the following expression if a non-linear error of 0.5% at $\varepsilon < 10^{-3}$ (200 N/mm^2 in steel) is accepted

$$\frac{\Delta R}{R} = g \cdot (\varepsilon + \varepsilon_s) \qquad (15)$$

The choise between Constantan and Karma is to a great extent a question of strength. To avoid early fatigue of a gauge [15] recommends the following limits of the maximum stress in sublayers of steel

Constantan < 375 N/mm^2 Karma < 575 N/mm^2

A gradual increase in the resistance of the gauge and consequently a corresponding increase of the zero-signal occurs, when a foil gauge is being fatigued. The resistance increase can be watched and used as a fatigue indicator.

The linear gauge factor of Constantan increases with ~1%, for a temperature increase of ~100 K. The corresponding value for Karma is ~-1%. The modulus of elasticity of steel decreasis with ~0.5% within the same

temperature range. At a strain of ε=0.001, the resistance change of a 350Ω gauge is approximately 0.7Ω or 0.2%. To maximize the output signal it is necessary to supply the gauge with highest possible power. The limit is set by the zero-drift of the signal due to self-heating of the gauge. Strain-gauge manufacturers recommend a maximum value of 2 mV per mm^2 effektive gauge area. The power of a 350Ω gauge with a grid surface of 4x4 mm should accordingly be limited to 3.5V or 10mA. The experience says, that double that value often can be used.

The manufacturers recommendations must be followed during cementing and humidity protection of gauge installations. From a physical point of view the strength of a cement layer is settled by the molecular intimacy between the cement, the sublayer and the gauge backing. It is the cleaness of the surfaces and absence of oxides, that give a good bond. The strain in the sublayer is transfered to the strain-gauge through shear forces in the cement layer and it is important, that the latter has sufficient strength. Inadequate ability of the cement layer to transfer the shear forces causes zero-drift due to creep.

The Wheatstone Bridge

The resistance change of a conventional strain-gauge is small. This is one of the reasons for wiring the gauges into bridges. A bridge consisting of active strain-gauges in all four armes is also capable to suppress the influence of a change in the temperature level and in many cases also to suppress the influence of interfering forces and moments.

Figure 7 shows a bridge powered across one of the diagonals. The voltage change across the other diagonal is the output signal. The signal of a bridge consisting of four identical and active gauges is

$$\frac{u}{V} = \frac{R_1}{R_1+R_2} - \frac{R_4}{R_3+R_4} \qquad (16)$$

Application of (16) on the elementary case of figure 7 yields

$$\begin{aligned} R_1 &= R_0(1+g\cdot\varepsilon+g\cdot\varepsilon_s+k\cdot\varepsilon^2) \\ R_2 &= R_0(1-g\cdot\varepsilon+g\cdot\varepsilon_s+k\cdot\varepsilon^2) \\ R_3 &= R_0(1+g\cdot\varepsilon+g\cdot\varepsilon_s+k\cdot\varepsilon^2) \\ R_4 &= R_0(1-g\cdot\varepsilon+g\cdot\varepsilon_s+k\cdot\varepsilon^2) \end{aligned} \qquad (17)$$

and

$$\frac{u}{V} = \frac{g\cdot\varepsilon}{(1+g\cdot\varepsilon_s+k\cdot\varepsilon^2)} \qquad (18)$$

(18) shows that a symmetrical bridge with all gauges exposed to the same numerical strain and with opposite gauges to the same sign linearizes the signal. The second degree terms in the numerator disappears.

(18) shows further that a change in the temperature level does not affect the numerator. The term $k \cdot \varepsilon^2$ is $<<1$. Use of temperature compensated gauges and a temperature range of say 50K causes $\varepsilon_s < 10^{-4}$. Within an accuracy representative of wind-tunnel testing (18) can be replaced by

$$\frac{u}{V} = g \cdot \varepsilon \tag{19}$$

Application of (7) and (11) on the elementary case in figure 5 transforms (19) into

$$\frac{u}{V} = g \cdot \frac{M}{E \cdot B} \tag{20}$$

A corresponding application of (13) on the elementary case in figure 6 results in

$$\frac{u}{V} = g \cdot \frac{\ell}{E \cdot W} \cdot (1+\nu) \tag{21}$$

It may be necessary to compensate a bridge further due to electrical non-symmetries. [16] and [17] describe such processes. It is also necessary to pay attention to the layout of the cable between the balance and the front of the signal-conditioning equipment.

SPRING-BODY MATERIAL

Restricted size and large forces cause large stresses in internal balances. Materials with high yield strength must be used. The machining of the complicated balance geometry is facilitated if no warping occurs during this process. Maraging or precipitation hardening steels meet these demands. Different manufacturers market materials with the $\sigma_{0.2}$ limit within the range

$$1200 < \sigma_{0.2} < 2000 \text{ N/mm}^2 \text{ (MPa)}$$

The following figures present the strength of some materials

a. Armco 17-4PH (see [18] ,[19])

$\sigma_{0.2} = 1200$ N/mm^2
$\sigma_b = 1340\text{-}1550$ N/mm^2
$\sigma_f = 950$ N/mm^2
$\tau_b = 870$ N/mm^2

b. Vascomax 300 (see [5],[20],[21])

$\sigma_{0.2} = 1930$ N/mm^2
$\sigma_b = 2070$ N/mm^2
$\sigma_f = 950$ N/mm^2
$\tau_b = 1170$ N/mm^2

c. Carpenter 455 (see [22])

$\sigma_{0.2}$ = 1370-1410 N/mm²
σ_b = 1440-1480 N/mm²
σ_f = 760 N/mm²

d. Aubert et Duval 819A (see [23])

$\sigma_{0.2}$ = 1550 N/mm²
σ_b = 1950 N/mm²
σ_f = 880 N/mm²

Any material with sufficient strength can be used. However, EDM-machining requires electric conductive materials.

The permitted stress during practical circumstances is influenced not only by the static load but also by the superimposed dynamic load. The permitted limits can be summarized in a Goodman diagram. It is however very seldom, that sufficient information excists to allow a complete diagram to be drawn. Figure 8 shows estimated Goodman diagrams for materials of current type in aged conditions. Data from tension-compression tests and bending tests have been mixed. The full lines are estimated values from catalogue information and from [24] of σ_f at $\sigma_s=0$ and of $\sigma_s=\sigma_{0.2}$ and concerns polished test pieces. The fatigue limit is approximately σ_f=950 N/mm² independent of the $\sigma_{0.2}$ limit. The dotted lines from [24] concern test bars without stress-concentrations and manufactured with EDM technique with the feeding speed limited to 2-4 mm/hour. The surface rawness and as a consequence the σ_f limit are influenced by the feeding speed.

The vertical line B with data from [23] shows measured stress in a balance during wind-tunnel tests with a model. The stress was

σ_{tot} = 550±220 N/mm²

and no fatigue fracture occured. The balance material was Aubert et Duval 819A.

The line A represents tests to destruction reported in [18]. The test pieces were manufactured with EDM technique imitating real axial force (T) elements and including stress concentrations. The nominal stresses were

σ_{tot} = 360±240 N/mm²

The material was Saab 1764-8, which is equivalent with Armco 17-4PH in its hardest condition.

The dot C corresponds to σ_s=600 N/mm² and is recommended in [16] as an upper design limit for balances made by use of EDM technique.

σ_s=900 N/mm² or dot D is a stress limit used at AEDC for balances manufactured of Vascomax 300, see [5].

Figure 8 shows, that the fatigue limits ($\pm\sigma_f$) are approximately the same for all the materials considered and that the permitted value of $\pm\sigma_f$ decreases somewhat with increasing σ_s. It is accordingly important to limit the dynamic loads by use of light models and stiff stings.

No safe information of hysteresis and creep of the current materials valid for stress levels and time periods of interest to wind-tunnel balances was found in the litterature. It is however known, that the hysteresis increases slightly with an increase in the $\sigma_{0.2}$ limit. The experience indicates, that hysteresis and creep of a strain-gauge installation cemented with a two-component, heat-curing cement should be less than 0.1% FS (full scale).

For balance calculation purposes it is permitted to use the following parameter values for steel

Modulus of elasticity	$E=200000\ N/mm^2$
Poisson's ratio	$\nu=0.3$
Modulus of rigidity	$G=77000\ N/mm^2$

From a deflection point of view a higher value of E would be favourable. However usefull alloys and composites with considerably higher values of E than steel and suitable for balance manufacturing do not seem to excist today.

BALANCE FORCE SYSTEM

The force system in figure 9 is based on information obtained from SAAB-SCANIA. It corresponds to tests with an airplane model in a scale adopted to a transonic wind-tunnel with a test section of $1.5x1.5m^2$. The stagnation pressure is 400 kPa and the model scale permits a bending-beam balance of 30 mm diameter.

The two N-m elements of the balance (figure 10) are loaded with the same maximum bending moment if the position of the model in relation to the balance fullfills the following condition (figure 9).

$$x_0 = \frac{L_1}{6} \qquad (22)$$

The condition means, that the moments will be as small as possible.

Earlier experience indicates, that L_1 should not be smaller than $\approx$100mm, when the diameter is 30mm. L_1=108mm corresponds to x_0=18mm. The given load cases are summerized in figure 11, which represents the static force system used in the subsequent calculations of the 30mm balance.

STRESSES IN A BENDING-BEAM BALANCE

The current type of bending-beam balance is manufactured in one piece and the complicated geometry of the T element is made with EDM technique. Figure 1 shows, that four bending moments, one torsion moment and the axial force are used as measuring information.

Figure 10 shows a general layout of the balance and the signification of the different parameters. The positions of the different strain-gauges are shown in figure 30.

Simple engineering theories for bending and torsion are used to calculate stresses and deformations. The resulting mathematical model uses as inputs a force system according to figure 11 and presumed values of the parameters in figure 10. The results are calculated stresses in a number of control points (Cp1 to Cp24 of figure 10). The stresses are nominal, corrections for stress concentrations must be made afterwards.

The following figures are used as a criterion of permitted, nominal static stresses

a. Stress in the balance structure $\sigma < 600$ N/mm^2
b. Stress below the strain-gauges $\sigma < 575$ N/mm^2

From a signal generation point of view the stress below a strain-gauge should not be < 50 N/mm^2.

The N-C-ℓ Element

The forward measuring element or the N-C-ℓ element is in principle a cantilevel beam with a cross-section depending on the magnitudes of the different components.

The moment M_1 (figure 1) causes in the forward N-m bridge a signal (u_1) proportional to the normal force (N) and the pitch moment (m).

$$M_1 = N \cdot \frac{L_1}{2} - m \qquad (23)$$

The moment M_4 gives in the same way a signal (u_4) in the forward C-n bridge proportional to the side force (C) and the yaw moment (n).

$$M_4 = -C \cdot \frac{L_1}{2} - n \qquad (24)$$

The roll moment (ℓ) causes an additional signal (u_6). The strength of the element and the magnitudes of the signals can be estimated by use of (11) and (12), when the bending and torsion stiffnesses of section B-B of figure 10 are known.

Application of the symbols of figure 10 yields

$$J_y = \frac{b \cdot h^3}{12} - \frac{c \cdot a^3}{9} - \frac{a \cdot c}{18} \cdot (3 \cdot h - 2 \cdot a)^2 \tag{25}$$

$$J_z = \frac{b \cdot b^3}{12} - \frac{a \cdot c^3}{9} - \frac{a \cdot c}{18} \cdot (3 \cdot b - 2 \cdot c)^2 \tag{26}$$

$$B_y = \frac{2}{h} \cdot J_y \tag{27}$$

$$B_z = \frac{2}{h} \cdot J_z \tag{28}$$

Application of [26] page 196 case 16 yields further

$$W = \frac{(b \cdot h - 2 \cdot c \cdot a)^4}{40 \cdot b \cdot (J_y + J_z)} \cdot \frac{\left[1 + \frac{0.6169 \cdot b^4}{(b \cdot h - 2 \cdot c \cdot a)^2}\right]}{\left[1 + \frac{0.09253 \cdot b^4}{(b \cdot h - 2 \cdot c \cdot a)^2}\right]} \tag{29}$$

Combination of (12) and (29) is only true, when the cross-section is free to warp. To allow this, the length of the element must not be too short. The experience indicates that $L_6 > 0.8 \cdot h$ is a reasonable choise.

The stresses in the control points of section B-B (figure 10) can be expressed as

$$\sigma_{Cp10} = \frac{(24)}{(28)} \tag{30}$$

$$\sigma_{Cp11} = (23) \cdot \frac{(0.5 \cdot h - a)}{(25)} + \frac{(24)}{(28)} \tag{31}$$

$$\sigma_{Cp12} = \frac{(23)}{(27)} + (24) \cdot \frac{(0.5 \cdot b - c)}{(26)} \tag{32}$$

$$\sigma_{Cp13} = \frac{(23)}{(27)} \tag{33}$$

$$\sigma_{Cp14} = \frac{\ell}{(29)} \tag{34}$$

$$\sigma_{Cp18} = \left[N \cdot \frac{(L_1 + L_6)}{2} - m\right] \cdot \frac{1}{(27)} + \left[-C \cdot \frac{(L_1 + L_6)}{2} - n\right] \cdot \frac{(0.5 \cdot b - c)}{(26)} \tag{35}$$

The N-C Element

The aft measuring element or the N-C element has the same cross-section as the N-C-ℓ element. The balance force system is symmetrical around the centre of the balance and the maximum stresses in the control points except for Cp18 are the same as in the N-C-ℓ element. The length of the N-C element is shorter than the length of the N-C-ℓ element. The

bending moment M_2 causes the signal u_2 and the moment M_5 the signal u_5.

The T Element

The smallest component of the force system is the axial force T, which acts along the longitudinal axis of the balance. The complicated geometry of the element depends on the fact, that it must carry all components to the next element.

The element is in principle a frame consisting of three groups of struts (the primary structure), which join two beams (the secondary structure). The bending of the central struts, when the element is deflected due to T, is used as the measuring information (u_3).

The reason for fixing the central struts in the two beams is to make the frame as stiff as possible in the y- and z-directions. This results in smaller deflections, than with the central struts linked in one of their ends. The draw-back is the tension-compression forces and bending moments, which appear in the central struts due to N and C, and which make demand upon a high degree of geometrical symmetry in the cementing of the T bridge.

The T element is statically indeterminate and all components of the force system contribute to the stresses in the control points Cp1 to Cp9, Cp15 to Cp17 and Cp20 in figure 10. The origo of the force system is supposed to coinside with the centre of the T element during the calculation of the stresses in the control points. This is a small approximation. Figure 19 shows the different force reactions in the primary structure caused by the external force system. The following deductions are a continuation of a work started in [25].

The Influence of T on the T Element

The computation of the distribution of the T component on the external and the central struts is made under the assumption, that the secondary structure is completely stiff. With symbols according to figure 10, the following equations are obtained.

$$T_1 = \frac{T}{2} \cdot \frac{S}{(S+1)} \tag{36}$$

$$T_2 = \frac{T}{(S+1)} \tag{37}$$

with

$$S = \frac{n_1}{n_2} \cdot \frac{b_1}{b_2} \cdot \left|\frac{h_1}{h_2}\right|^2 \cdot \left|\frac{r_2}{r_2}\right|^3 \tag{38}$$

The stresses in the fixed ends of the central struts due to T are

$$\sigma_{Cp2} = \pm \frac{6 \cdot r_2}{n_2 \cdot b_2 \cdot h_2^2} \cdot \frac{T}{(S+1)} \qquad (39)$$

The length and positions of the strain-gauges must be considered, when the usefull stresses (strains) below the gauges of the T bridge are calculated from

$$\sigma_{Cp20k} = \sigma_{Cp20} \frac{(r_2 - o.5 \cdot t_1 - t_2)}{r_2} \qquad (40)$$

The Influence of N on the T Element

The secondary structure can not be regarded as stiff, when the influence of the N component on the stresses in the control points is calculated. This means, that the T element is statically indeterminate and that the central reaction force is directed opposite to the forces in the external struts. The secondary structure is approximated with two beams with a geometry according to figure 13. The area moment of inertia of the cross-section of one of the beams is according to [26] page75 case 10

$$J_y = R^4 \cdot \left[\frac{1}{8} \cdot (2\alpha - \sin 2\alpha) \cdot \left[1 + \frac{2 \cdot \sin 2\alpha \cdot \sin^2 \alpha}{(2\alpha - \sin 2\alpha)}\right] - \frac{8}{9} \cdot \frac{\sin^6 \alpha}{(2\alpha - \sin 2\alpha)}\right] \qquad (41)$$

With a moderate accuracy it is possible to replace (41) along the x-axis with the expression

$$J_y = J_{0y} \cdot (1 + \beta \cdot x^2) \qquad (42)$$

where $\beta = \frac{J_{1y}}{J_{0y}} - 1$ (43)

with J_{0y} = the moment of inertia for x=0

J_{1y} = the moment of inertia for x=1

Application of the differential equation of the elastic curve on figure 14 results in the following expressions of the reaction forces.

$$P_1 = \frac{(F_2 - F_4)}{(F_3 - F_1)} \cdot \frac{N}{\left[1 - 2 \cdot \frac{(F_2 - F_4)}{(F_3 - F_1)}\right]} \qquad (44)$$

$$P_2 = \frac{N}{\left[1 - 2 \cdot \frac{(F_2 - F_4)}{(F_3 - F_1)}\right]} \qquad (45)$$

$$F_1 = \frac{1}{2 \cdot \beta} \cdot \left[\ln(1 + 0.25\beta) - \ln(1 + \beta)\right] - \frac{1}{\beta \sqrt{\beta}} \cdot \left[2 \cdot \tan^{-1} 0.5\sqrt{\beta} - \tan^{-1} \sqrt{\beta}\right] \qquad (46)$$

$$F_2 = \left[\frac{1}{2\sqrt{\beta}} - \frac{1}{\beta\sqrt{\beta}}\right] \cdot \left[\tan^{-1} 0.5\sqrt{\beta} - \tan^{-1}\sqrt{\beta}\right] - \frac{3}{4\cdot\beta} \cdot \left[\ln(1+.25\beta) - \ln(1+\beta)\right] - \frac{1}{2\cdot\beta} \quad ---(47)$$

$$F_3 = \frac{4 \cdot r_1 \cdot J_{0y}}{n_1 \cdot h_1 \cdot b_1 \cdot L^3} \quad (48)$$

$$F_4 = \frac{2 \cdot r_2 \cdot J_{0y}}{n_2 \cdot h_2 \cdot b_2 \cdot L^3} \quad (49)$$

J_{0y} is calculated from (41) with

$$\alpha_0 = \cos^{-1}\left|\frac{r_1 - e_1}{R}\right| \quad (50)$$

The Influence of m on the T Element

The secondary structure can be considered to be stiff, when the influence of m on the stresses in the control points is estimated. The reaction forces will according to figure 15 be

$$P_1 = \frac{m}{L} \quad (51)$$

$$P_2 = 0 \quad (52)$$

The Influence of C on the T Element

The secondary structure can not be considered to be stiff, when the influence of the C component on the stresses in the control points is calculated. The T element is a statically indeterminate frame and the central reaction force is directed opposite to the forces in the external struts. The secondary structure consists of two beams with a geometry according to figure 13. The area moment of inertia of the cross-section of the beams is ([26] page 75 case 10)

$$J_z = R^4 \cdot \left[\frac{1}{8} \cdot (2\alpha - \sin 2\alpha) - \frac{1}{12} \cdot \sin 2\alpha \cdot \sin^2 \alpha\right] \quad (53)$$

With a moderate accuracy it is possible to replace (53) along the x-axis with the expression

$$J_z = J_{0z} \cdot (1 + \beta \cdot x) \quad (54)$$

and $$\beta = \frac{J_{1z}}{J_{0z}} - 1 \quad (55)$$

with J_{0y} = the moment of inertia for x=0 and J_{1y} for x=1.

Application of the differential equation of the elastic curve on figure 16 results in the reaction forces

$$P_1 = \frac{(H_2-H_4)}{(H_3-H_1)} \cdot \frac{C}{\left[1-2\cdot\frac{(H_2-H_4)}{(H_3-H_1)}\right]} \tag{56}$$

$$P_2 = \frac{C}{\left[1-2\cdot\frac{(H_2-H_4)}{(H_3-H_1)}\right]} \tag{57}$$

with

$$H_1 = \frac{1}{\beta^2} - \frac{1}{4\cdot\beta} + \frac{1}{\beta^3}\cdot\left[(1+\beta)\cdot\ln(1+\beta)-2\cdot(1+0.5\beta)\cdot\ln(1+0.5\beta)\right] \tag{58}$$

$$H_2 = \frac{1}{2\cdot\beta^2} - \frac{5}{8\cdot\beta} + \left[\frac{1}{2\cdot\beta}+\frac{3}{2\cdot\beta^2}+\frac{1}{\beta^3}\right]\cdot\left[\ln(1+0.5\beta)-\ln(1+\beta)\right] \tag{59}$$

$$H_3 = \frac{8\cdot r_1^3\cdot J_{0z}}{n_1\cdot h_1\cdot b_1^3\cdot L^3} \tag{60}$$

$$H_4 = \frac{4\cdot r_2^3\cdot J_{0z}}{n_2\cdot h_2\cdot b_2^3\cdot L^3} \tag{61}$$

J_{0z} is calculated from (53) with

$$\alpha_0 = \cos^{-1}\left|\frac{r_1-e_1}{R}\right| \tag{62}$$

The Influence of n on the T Element

The secondary structure can be considered to be stiff, when the influence of n on the stresses in the control points is estimated. The reaction forces will be (figure 17)

$$P_1 = \frac{n}{L} \tag{63}$$

$$P = 0 \tag{64}$$

The Influence of ℓ on the T Element

The limited stiffness of the secondary structure should also be con-

sidered, when the contributions of the ℓ component on the reaction forces are estimated. The section modulus in torsion of the beam in figure 13 is ([26] page 197 case 16)

$$K = \frac{A^4}{40 \cdot J} \tag{65}$$

with

$$A = \frac{R^2}{2} \cdot (2\alpha - \sin 2\alpha) \tag{66}$$

and

$$J = J_y + J_z \tag{67}$$

With a moderate accuracy it is possible to replace (65) with the expression

$$K = K_0 \cdot (1 + \beta \cdot x^2) \tag{68}$$

and

$$\beta = \frac{K_1}{K_0} - 1 \tag{69}$$

where K_0 = the section modulus in torsion for x=0

K_1 = the section modulus in torsion for x=1

The distorsion in figure 18 corresponds to the following reaction forces in the primary structure

$$P_1 = \frac{\ell}{4 \cdot y_1} \cdot \frac{V_1}{(V_1 + 0.5)} \tag{70}$$

$$P_2 = \frac{\ell}{4 \cdot y_2} \cdot \frac{1}{(V_1 + 0.5)} \tag{71}$$

$$V_1 = \frac{\frac{L}{K_0 \cdot G \cdot \sqrt{\beta}} \cdot \left[\tan^{-1}\sqrt{\beta} - \tan^{-1} 0.5\sqrt{\beta}\right] + \frac{2 \cdot r_2}{n_2 \cdot b_2 \cdot h_2 \cdot E \cdot y_2^2}}{\frac{L}{K_0 \cdot G \cdot \sqrt{\beta}} \cdot \left[2 \cdot \tan^{-1} 0.5\sqrt{\beta} - \tan^{-1}\sqrt{\beta}\right]} \tag{72}$$

K_0 is computed by use of (65), (66) and (67) with

$$\alpha_0 = \cos^{-1}\left|\frac{r_1 - e_1}{R}\right| \tag{73}$$

The following expression can be used if G is unknown

$$G = \frac{E}{2 \cdot (1 + \nu)} \tag{74}$$

The Stresses in the Primary structure of the T Element

The reaction forces in the primary structure are shown in figure 19. The maximum stresses in the primary structure occur in the roots of the struts or the control points Cp1 and Cp2 in figure 10.

$$\sigma_{Cp1} = T_1 \cdot \frac{12 \cdot r_1}{n_1 \cdot b_1 \cdot h_1^2} + (P_{1C} - P_{1n}) \cdot \frac{12 \cdot r_1}{n_1 \cdot b_1^2 \cdot h_1} + (P_{1N} + P_{1m} + P_{1\ell}) \cdot \frac{2}{n_1 \cdot b_1 \cdot h_1} \qquad (75)$$

$$\sigma_{Cp2} = T_2 \cdot \frac{6 \cdot r_2}{n_2 \cdot b_2 \cdot h_2^2} + P_{2C} \cdot \frac{6 \cdot r_2}{n_2 \cdot b_2^2 \cdot h_2} + (P_{2N} + P_{2\ell}) \cdot \frac{1}{n_2 \cdot b_2 \cdot h_2} \qquad (76)$$

It is presupposed, that the components of the force system can be both positive and negative and it is necessary to take this into account to get the maximum values of (75) and (76). The influence of the fillets (stress concentrations) can be considered after the computation of the nominal stresses.

The Stresses in the Secondary Structure of the T Element

The strength of the secondary structure is checked in the four cross-sections C-C, D-D, E-E and F-F in figure 10.

The Cross-Section C-C

The geometry of the cross-section C-C is different for positive and negative value of the parameter e_1. Different expressions of the area moments of inertia (J_y and J_z) must be deduced before the stresses in the control points Cp3, Cp4 and Cp5 can be calculated. The expressions (77) to (94) below with designations from figure 10 and 20 must be known before J_y and J_z can be calculated.

$$z_1 = R \cdot \left[1 - \frac{4}{3} \cdot \frac{\sin^3 \alpha_1}{(2\alpha_1 - \sin 2\alpha_1)} \right] \qquad (77)$$

$$A_1 = \frac{R^2}{2} \cdot (2\alpha_1 - \sin 2\alpha_1) \qquad (78)$$

$$z_2 = R \cdot \left[1 - \frac{1}{2} \cdot (\cos \alpha_1 - \cos \alpha_2) \right] \qquad (79)$$

$$A_2 = 2 \cdot R^2 \cdot \sin \alpha_2 \cdot (\sin \alpha_1 + \cos \alpha_2) \qquad (80)$$

$$z_3 = R \cdot \left[1 - \frac{4}{3} \cdot \frac{\sin^3 \alpha_2}{(2\alpha_2 - \sin 2\alpha_2)} \right] \tag{81}$$

$$A_3 = \frac{R^2}{2} \cdot (2\alpha_2 - \sin 2\alpha_2) \tag{82}$$

$$z_4 = R \cdot (1 - \cos\alpha_1) - e_1 \tag{83}$$

$$A_4 = -4 \cdot e_1 \cdot R \cdot (\sin\alpha_1 - \sin\alpha_2) \tag{84}$$

$$J_{1y} = R^4 \cdot \left[\frac{1}{8} \cdot (2\alpha_1 - \sin 2\alpha_1) \cdot \left[1 + \frac{2 \cdot \sin 2\alpha_1 \cdot \sin^2 \alpha_1}{(2\alpha_1 - \sin 2\alpha_1)} \right] - \frac{8}{9} \cdot \frac{\sin^6 \alpha_1}{(2\alpha_1 - \sin 2\alpha_1)} \right] \tag{85}$$

$$J_{2y} = \frac{R^4}{6} \cdot \sin\alpha_2 \cdot (\cos\alpha_1 + \cos\alpha_2)^3 \tag{86}$$

$$J_{3y} = R^4 \cdot \left[\frac{1}{8} \cdot (2\alpha_2 - \sin 2\alpha_2) \cdot \left[1 + \frac{2 \cdot \sin 2\alpha_2 \cdot \sin^2 \alpha_2}{(2\alpha_2 - \sin 2\alpha_2)} \right] - \frac{8}{9} \cdot \frac{\sin^6 \alpha_2}{(2\alpha_2 - \sin 2\alpha_2)} \right] \tag{87}$$

$$J_{4y} = -\frac{4}{3} \cdot R \cdot e_1^3 \cdot (\sin\alpha_1 - \sin\alpha_2) \tag{88}$$

$$J_{1z} = R^4 \cdot \left[\frac{1}{8} \cdot (2\alpha_1 - \sin 2\alpha_1) - \frac{1}{12} \cdot \sin 2\alpha_1 \cdot \sin^2 \alpha_1 \right] \tag{89}$$

$$J_{2z} = \frac{2}{3} \cdot R^4 \cdot \sin^3 \alpha_2 \cdot (\cos\alpha_1 + \cos\alpha_2) \tag{90}$$

$$J_{3z} = R^4 \cdot \left[\frac{1}{8} \cdot (2\alpha_2 - \sin 2\alpha_2) - \frac{1}{12} \cdot \sin 2\alpha_2 \cdot \sin^2 \alpha_2 \right] \tag{91}$$

$$J_{4z} = -\frac{4}{3} \cdot R^3 \cdot e_1 \cdot (\sin^3 \alpha_1 - \sin^3 \alpha_2) \tag{92}$$

The bending moments in the cross section C-C are according to figure 10 and 19

$$M_y = \frac{1}{2} \cdot \left[P_{2N} \cdot (L_2 - s_1) - (P_{1N} - P_{1m}) \cdot (L_5 - s_1) - (P_{1N} - P_{1m}) \cdot (2 \cdot L_2 - L_5 - s_1) \right] \tag{93}$$

$$M_z = \frac{1}{2} \cdot \left[-P_{2C} \cdot (L_2 - s_1) + (P_{1C} + P_{1n}) \cdot (L_5 - s_1) - (P_{1C} - P_{1n}) \cdot (2 \cdot L_2 - L_5 - s_1) \right] \tag{94}$$

To get maximum values of (93) and (94) it is necessary to consider, that the components of the force system can be positive and negative.

$e_1 > 0$

$$\cos\alpha_1 = \frac{r_1 + e_1}{R} \tag{95}$$

$$\sin\alpha_2 = \frac{m_1}{2 \cdot R} \tag{96}$$

The moments of inertia J_y and J_z are calculated from the equations

$$A= (78)+(80)+(82) \tag{97}$$

$$z= \frac{(77)\cdot(78)+(79)\cdot(80)+(81)\cdot(82)}{(97)} \tag{98}$$

$$J_y=(85)+(86)+(87)+(78)\cdot\left[(98)-(77)\right]^2+(80)\cdot\left[(98)-(79)\right]^2+ (82)\cdot\left[(98)-(81)\right]^2 \tag{99}$$

$$J_z=(89)+(90)+(91) \tag{100}$$

The stresses in the control points of the cross-section are

$$\sigma_{Cp3}= (93)\cdot\frac{\left[2\cdot R-(98)\right]}{(99)} \tag{101}$$

$$\sigma_{Cp4}= (93)\cdot\frac{\left[R\cdot(1+\cos\alpha_2)-(98)\right]}{(99)}+(94)\cdot\frac{R\cdot\sin\alpha_2}{(100)} \tag{102}$$

$$\sigma_{Cp5}= (93)\cdot\frac{\left[(98)-R\cdot(1-\cos\alpha_1)\right]}{(99)}+(94)\cdot\frac{R\cdot\sin\alpha_1}{(100)} \tag{103}$$

$e_1<0$

$$\cos\alpha_1= \frac{r_1-e_1}{R} \tag{104}$$

$$\sin\alpha_2= \frac{m_1}{2\cdot R} \tag{105}$$

The moments of inertia J_y and J_z are calculated from the equations

$$A= (78)+(80)+(82)+(84) \tag{106}$$

$$z= \frac{(77)\cdot(78)+(79)\cdot(80)+(81)\cdot(82)+(83)\cdot(84)}{(106)}$$

$$J_y=(85)+(86)+(87)+(88)+(78)\cdot\left[(107)-(77)\right]^2+(80)\cdot\left[(107)-(79)\right]^2+ (82)\cdot\left[(107)-(81)\right]^2+(84)\cdot\left[(107)-(83)\right]^2 \tag{108}$$

$$J_z=(89)+(90)+(91)+(92) \tag{109}$$

The stresses in the control points of the cross-section are

$$\sigma_{Cp3}= (93)\cdot\frac{\left[2\cdot R-(107)\right]}{(108)} \tag{110}$$

$$\sigma_{Cp4}= (93)\cdot\frac{\left[R\cdot(1+\cos\alpha_2)-(107)\right]}{(108)}+(94)\cdot\frac{R\cdot\sin\alpha_2}{(109)} \tag{111}$$

$$\sigma_{Cp5}= (93)\cdot\frac{\left[(107)-R\cdot(1-\cos\alpha_1)\right]}{(108)}+(94)\cdot\frac{R\cdot\sin\alpha_1}{(109)} \tag{112}$$

The Cross-section D-D

The geometry of the cross-section D-D is different for positive and negative value of the parameter e_1. Different equations for the area moment of inertia (J_y and J_z) must be deduced before the stresses in the control points Cp6 and Cp7 can be calculated. The equations (113) to (122) below, with designations from figure 10 and 21, must be known before J_y and J_z can be computed

z_1=(77), A_1=(78), z_4=(83), A_4=(84), J_{1y}=(85), J_{4y}=(88), J_{1z}=(89), J_{4z}=(92)

$$z_5 = \frac{(2 \cdot r_1 - s_1)}{2} + R \cdot (1 - \cos\alpha_1) \qquad (113)$$

$$A_5 = 2 \cdot (2 \cdot r_1 - s_1) \cdot R \cdot \sin\alpha_2 \qquad (114)$$

$$z_6 = \frac{(2 \cdot r_1 - 2 \cdot e_1 - s_1)}{2} + R \cdot (1 - \cos\alpha_1) \qquad (115)$$

$$A_6 = 2 \cdot (2 \cdot r_1 - 2 \cdot e_1 - s_1) \cdot R \cdot \sin\alpha_2 \qquad (116)$$

$$J_{5y} = \frac{R}{6} \cdot (2 \cdot r_1 - s_1)^3 \cdot \sin\alpha_2 \qquad (117)$$

$$J_{6y} = \frac{R}{6} \cdot (2 \cdot r_1 - 2 \cdot e_1 - s_1)^3 \cdot \sin\alpha_2 \qquad (118)$$

$$J_{5z} = \frac{2}{3} \cdot R^3 \cdot (2 \cdot r_1 - s_1) \cdot \sin^3\alpha_2 \qquad (119)$$

$$J_{6z} = \frac{2}{3} \cdot R^3 \cdot (2 \cdot r_1 - 2 \cdot e_1 - s_1) \cdot \sin^3\alpha_2 \qquad (120)$$

The bending moments in the cross-section D-D are according to figure 10 and 19.

$$M_y = \frac{1}{2} \cdot \left[P_{2N} \cdot (L_2 - 2 \cdot L_5 + 2 \cdot s_1) - (P_{1N} + P_{1m}) \cdot (2 \cdot L_2 - 3 \cdot L_5 + 2 \cdot s_1) \right] \qquad (121)$$

$$M_z = \frac{1}{2} \left[-P_{2C} \cdot (L_2 - 2 \cdot L_5 + 2 \cdot s_1) + (P_{1C} - P_{1n}) \cdot (2 \cdot L_2 - 3 \cdot L_5 + 2 \cdot s_1) \right] \qquad (122)$$

To get the maximum values of (121) and (122) it is necessary to observe, that the components can be both positive and negative.

$e_1 > 0$

$\cos\alpha_1$= (95)

$\sin\alpha_2$= (96)

The moments of inertia J_y and J_z are calculated from

A= (78)+(114) (123)

$$z = \frac{(77)\cdot(78)+(113)\cdot(114)}{(123)} \tag{124}$$

$$J_y = (85)+(117)+(78)\cdot\left[(124)-(77)\right]^2+(114)\cdot\left[(124)-(115)\right]^2 \tag{125}$$

$$J_z = (89)+(119) \tag{126}$$

The stresses in the control points of the cross-section are

$$\sigma_{Cp6} = (121)\cdot\frac{\left[R\cdot(1-\cos\alpha_1)+(2\cdot r_1-s_1)-(124)\right]}{(125)}+(122)\cdot\frac{R\cdot\sin\alpha_2}{(126)} \tag{127}$$

$$\sigma_{Cp7} = (121)\cdot\frac{\left[(124)-R\cdot(1-\cos\alpha_1)\right]}{(125)}+(122)\cdot\frac{R\cdot\sin\alpha_1}{(126)} \tag{128}$$

$e_1 < 0$

$\cos\alpha_1 = (104)$

$\sin\alpha_2 = (105)$

The moments of inertia J_y and J_z are calculated from

$$A = (78)+(116)+(84) \tag{129}$$

$$z = \frac{(77)\cdot(78)+(115)\cdot(116)+(83)\cdot(84)}{(129)} \tag{130}$$

$$J_y = (85)+(118)+(88)+(78)\cdot\left[(130)-(77)\right]^2+(116)\cdot\left[(130)-(115)\right]^2+(84)\cdot\left[(130)-(83)\right]^2 \tag{131}$$

$$J_z = (89)+(120)+(92) \tag{132}$$

The stresses in the control points of the cross-section are

$$\sigma_{Cp6} = (121)\cdot\frac{\left[R\cdot(1-\cos\alpha_1)+(2\cdot r_1-2\cdot e_1-s_1)-(130)\right]}{(131)}+(122)\cdot\frac{R\cdot\sin\alpha_2}{(132)} \tag{133}$$

$$\sigma_{Cp7} = (121)\cdot\frac{\left[(130)-R\cdot(1-\cos\alpha_1)\right]}{(131)}+(122)\cdot\frac{R\cdot\sin\alpha_1}{(132)} \tag{134}$$

The Cross-Section E-E

The expressions (135) to (146) below with designations from figure 10 and 22 must be known before J_y and J_z can be computed.

$$\cos\alpha_3 = \frac{r_2}{R} \tag{135}$$

$$\sin\alpha_4 = \frac{m_2}{2\cdot R} \tag{136}$$

$$z_7 = R\cdot\left[1-\frac{4}{3}\cdot\frac{\sin^3\alpha_3}{(2\alpha_3-\sin 2\alpha_3)}\right] \tag{137}$$

$$A_7 = \frac{1}{2}\cdot R^2\cdot(2\alpha_3 - \sin 2\alpha_3) \tag{138}$$

$$z_8 = R\cdot\left(1 - \frac{1}{2}\cdot\cos\alpha_3\right) - \frac{1}{4}\cdot s_1 \tag{139}$$

$$A_8 = 2\cdot R\cdot\sin\alpha_4\cdot\left(R\cdot\cos\alpha_3 - \frac{1}{2}\cdot s_1\right) \tag{140}$$

$$J_{7y} = R^4\cdot\left[\frac{1}{8}\cdot(2\alpha_3 - \sin 2\alpha_3)\cdot\left[1 + \frac{2\cdot\sin 2\alpha_3\cdot\sin^2\alpha_3}{(2\alpha_3 - \sin 2\alpha_3)}\right] - \frac{8}{9}\cdot\frac{\sin^6\alpha_3}{(2\alpha_3 - \sin 2\alpha_3)}\right] \tag{141}$$

$$J_{8y} = \frac{R}{6}\cdot\left[R\cdot\cos\alpha_3 - \frac{1}{2}\cdot s_1\right]^3\cdot\sin\alpha_4 \tag{142}$$

$$J_{7z} = R^4\cdot\left[\frac{1}{8}\cdot(2\alpha_3 - \sin 2\alpha_3) - \frac{1}{12}\cdot\sin 2\alpha_3\cdot\sin^2\alpha_3\right] \tag{143}$$

$$J_{8z} = \frac{4}{3}\cdot R^3\cdot\left(R\cdot\cos\alpha_3 - \frac{1}{2}\cdot s_1\right)\cdot\sin^3\alpha_4 \tag{144}$$

The bending moments in the cross-section E-E are according to figure 10 and 19.

$$M_y = -\frac{1}{2}\cdot(P_{1N} + P_{1m})\cdot(L_2 - L_5) \tag{145}$$

$$M_z = \frac{1}{2}\cdot(P_{1C} - P_{1n})\cdot(L_2 - L_5) \tag{146}$$

To get the maximum values of (145) and (146) it is necessary to observe, that the force components can be both positive and negative.

The moments of inertia J_y and J_z are calculated from

$$A = (138) + (140) \tag{147}$$

$$z = \frac{(137)\cdot(138) + (139)\cdot(140)}{(147)} \tag{148}$$

$$J_y = (141) + (142) + (138)\cdot[(148) - (137)]^2 + (140)\cdot[(148) - (139)]^2 \tag{149}$$

$$J_z = (143) + (144) \tag{150}$$

The stresses in the control points of the cross-section are

$$\sigma_{Cp15} = (145)\cdot\frac{[R - 0.5\cdot s_1 - (148)]}{(149)} + (146)\cdot\frac{R\cdot\sin\alpha_4}{(150)} \tag{151}$$

$$\sigma_{Cp16} = (145)\cdot\frac{[(148) - R\cdot(1 - \cos\alpha_3)]}{(149)} + (146)\,\frac{R\cdot\sin\alpha_3}{(150)} \tag{152}$$

$$\sigma_{Cp17} = (145)\cdot\frac{(148)}{(149)} \tag{153}$$

The Cross-Section F-F

The geometry of the cross-section F-F is different for positive and negative value of the parameter e_1. The control points are Cp8 and Cp9. When the external struts in section D-D are displaced upwards, the corresponding struts in section F-F will be displaced downwards. The expressions (154) to (170) below with designations from figure 10 and 24 must be known before the moments of inertia J_y and J_z can be computed.

z_1=(77), A_1=(78), J_{1y}=(85), J_{1z}=(89)

$$z_9 = R\cdot(1-\cos\alpha_1 - \frac{1}{2}\cdot\cos\alpha_5) \tag{154}$$

$$A_9 = 2\cdot R^2\cdot(\cos\alpha_5-\cos\alpha_1)\cdot\sin\alpha_5 \tag{155}$$

$$z_{10}=R\cdot\left[1- \frac{4}{3}\cdot\frac{\sin^3\alpha_5}{(2\alpha_5-\sin2\alpha_5)}\right] \tag{156}$$

$$A_{10}=\frac{1}{2}\cdot R^2\cdot(2\alpha_5-\sin2\alpha_5) \tag{157}$$

$$z_{11}=R\cdot(1-\cos\alpha_1)+e_1 \tag{158}$$

$$y_{11}=\frac{1}{2}\cdot R\cdot(\sin\alpha_1+\sin\alpha_5) \tag{159}$$

$$A_{11}=4\cdot e_1\cdot R\cdot(\sin\alpha_1-\sin\alpha_5) \tag{160}$$

$$y_{12}=\frac{R^3}{(162)}\cdot\left[-\frac{1}{3}\cdot(\cos^3\alpha_1-\cos^3\alpha_5)+\frac{\cos\alpha_1}{2}\cdot(\cos^2\alpha_1-\cos^2\alpha_5)\right] \tag{161}$$

$$A_{12}=2\cdot R^2\cdot\left[\frac{1}{2}\cdot(\alpha_1-\alpha_5)+\frac{1}{4}\cdot(\sin2\alpha_1-\sin2\alpha_5)-\cos\alpha_1\cdot(\sin\alpha_1-\sin\alpha_5)\right] \tag{162}$$

$$J_{9y}=\frac{1}{6}\cdot R^4\cdot(\cos\alpha_5-\cos\alpha_1)^3\cdot\sin\alpha_5 \tag{163}$$

$$J_{10y}=R^4\cdot\left[\frac{1}{8}\cdot(2\alpha_5-\sin2\alpha_5)\cdot\left[1+\frac{2\cdot\sin2\alpha_5\cdot\sin^2\alpha_5}{(2\alpha_5-\sin2\alpha_5)}\right]-\frac{8}{9}\cdot\frac{\sin^6\alpha_5}{(2\alpha_5-\sin2\alpha_5)}\right] \tag{164}$$

$$J_{11y}=\frac{4}{3}\cdot R\cdot e_1^3\cdot(\sin\alpha_1-\sin\alpha_5) \tag{165}$$

$$J_{9z}= \frac{2}{3}\cdot R^4\cdot(\cos\alpha_5-\cos\alpha_1)\cdot\sin^3\alpha_5 \tag{166}$$

$$J_{10z}=R^4\cdot\left[\frac{1}{8}\cdot(2\alpha_5-\sin2\alpha_5)-\frac{1}{12}\cdot\sin2\alpha_5\cdot\sin^2\alpha_5\right] \tag{167}$$

$$J_{11z}=\frac{4}{3}\cdot R^3\cdot e_1\cdot(\sin^3\alpha_1-\sin^3\alpha_5) \tag{168}$$

The bending moments in the cross-section F-F are according to figure 10 and 19.

$$M_y = -\frac{1}{2}\cdot(P_{1N}+P_{1m})\cdot L_5 \qquad (169)$$

$$M_z = \frac{1}{2}\cdot(P_{1C}-P_{1n})\cdot L_5 \qquad (170)$$

To get the maximum values of (169) and (170) it is necessary to observe, that the components of the force system can be both positive and negative.

$e_1 > 0$

$\cos\alpha_1 = (95)$

$$\sin\alpha_5 = \frac{m_1+2\cdot r_1}{2\cdot R} \qquad (171)$$

The moments of inertia J_y and J_z are calculated from

$$A = (78)-(155)-(157)+(160) \qquad (172)$$

$$z = \frac{(77)\cdot(78)-(154)\cdot(155)-(156)\cdot(157)+(158)\cdot(160)}{(172)} \qquad (173)$$

$$J_y = (85)-(163)-(164)+(165)+(78)\cdot[(172)-(77)]^2-(155)\cdot[(172)-(154)]^2-(157)\cdot[(172)-(156)]^2+(160)\cdot[(172)-(158)]^2 \qquad (174)$$

$$y = \frac{(159)\cdot(160)+(161)\cdot(162)}{(160)+(162)} \qquad (175)$$

$$J_z = (89)-(166)-(167)+(168)-[(162)+(160)]\cdot(175)^2 \qquad (176)$$

The stresses in the control points of the cross-section are

$$\sigma_{Cp8} = (169)\cdot\frac{[(173)-R\cdot(1-\cos\alpha_5)]}{(174)}+(170)\cdot\frac{[(175)-R\cdot\sin\alpha_5]}{(176)} \qquad (177)$$

$$\sigma_{Cp9} = (169)\cdot\frac{[R\cdot(1-\cos\alpha_1)+2\cdot e_1-(173)]}{(174)}+(170)\cdot\frac{[R\cdot\sin\alpha_1-(175)]}{(176)} \qquad (178)$$

$e_1 < 0$

$\cos\alpha_1 = (95)$

$\sin\alpha_5 = (171)$

The moments of inertia are calculated from

$$A = (78)-(155)-(157) \qquad (179)$$

$$z = \frac{(77)\cdot(78)-(154)\cdot(155)-(156)\cdot(157)}{(179)} \qquad (180)$$

$$J_y = (85)-(163)-(164)-(78)\cdot[(173)-(77)]^2-(155)\cdot[(173)-(154)]^2 \qquad (181)$$

$$y = (161)$$

$$J_z = (89)-(166)-(167)-(162)\cdot(161)^2 \qquad (182)$$

The stresses in the control points of the cross-section are

$$\sigma_{Cp8} = (169)\cdot\frac{[(180)-R\cdot\cos\alpha_5]}{(181)}+(170)\cdot\frac{[(161)-R\cdot\sin\alpha_5]}{(182)} \qquad (183)$$

$$\sigma_{Cp9} = (169)\cdot\frac{[R\cdot(1-\cos\alpha_1)-(180)]}{(181)}+(170)\cdot\frac{[R\sin\alpha_1-(161)]}{(182)} \qquad (184)$$

The Model Support End

The model support end can be cylindrical or conical. The maximum bending stress occurs in the control point Cp19 in figure 10.

$$\sigma_{Cp19} = \frac{32}{\pi\cdot d^3}\cdot(M_y^2+M_z^2)^{1/2} \qquad (185)$$

with

$$M_y = N\cdot L_8 - m \qquad (186)$$

$$M_z = C\cdot L_8 + n \qquad (187)$$

The Sting End

The stress in the sting end of the balance is calculated analogous to the model support end. The sting end is often made conical and it must transfer all forces and moments, which load the balance. The request of freedom from play is not as rigorous as for the model end. The stress control point is designated Cp23.

The Sting

The balance is carried by a sting fixed in the model support of the wind-tunnel. For aerodynamic reasons the sting must be long and slender. This causes strength problems. The sting must also be provided with a longitudinal cavity for the balance cable and a base pressure tube.

The static stress in the sting is

$$\sigma_x = \frac{M}{B_x} \qquad (188)$$

with

$$M = \left[(N \cdot x + m)^2 + (C \cdot x - n)^2\right]^{1/2} \qquad (189)$$

$$B_x = \frac{\pi}{32} \cdot \frac{(D_x^4 - d_x^4)}{D_x} \qquad (190)$$

The influence of the local cavity on the stress and deflection of the sting is shown in figure 23. A hole with a relative diameter of 55% causes an stress increase of approximately 10%.

The material in the sting is often a high alloy steel with qualities comparable with figure 8. It is however a pronounced need to find materials with higher modulus of elasticity.

An internal, sting mounted, bending-beam balance is an undamped string. The spring constant and the mass of the model determine the dynamic loads in the y-z-plane, which the balance and the sting are exposed to. The natural frequency of the model-sting combination is in principle

$$f = \frac{1}{2 \cdot \pi} \left|\frac{k}{m}\right|^{1/2} \qquad (191)$$

(191) neglects the influence of the mass of the sting and overestimates the value of the natural frequency. A more reliable, but more complicated computation method in which the distributed mass along the sting is considered, is discussed in [28].

The diameter of the sting increases normally along its length and this complicates the calculation of the slope and deflection of the loaded sting. An estimation of these quantities can be made by use of the area-moment method illustrated in figure 25.

STRAIN-GAUGE INSTALLATIONS

All strain-gauges are cemented on the balance body and wired into full bridges. One motive for full bridges is to reduce the influence of the internal wiring on the internal resistance of the bridges. Enamelled copper wire with a core diameter of >0.1mm can be used.

The N-m Bridges

The two N-m bridges can be "moment-moment" wired or "force-moment" wired. The signals u_1 and u_2 are in the first case dependent of both N and m. The wiring in the second case causes u_1 to be proportional to N and u_2 to m.

Moment-Moment Wiring of the N-m Bridges

Figure 26a shows the wiring

$$\frac{u_1}{V} = g \cdot \varepsilon_{13} = \frac{g}{E \cdot B_y} \cdot \left[\frac{N \cdot L_1}{2} - m \right] \tag{194}$$

$$\frac{u_2}{V} = g \cdot \varepsilon_{21} = \frac{g}{E \cdot B_y} \cdot \left[\frac{N \cdot L_1}{2} + m \right] \tag{195}$$

Force-Moment Wiring of the N-m Bridges

The wiring of figure 26b results in

$$\frac{u_1}{V} = \frac{g}{2} \cdot (\varepsilon_{13} - \varepsilon_{21}) = \frac{g \cdot N \cdot L_1}{2 \cdot E \cdot B_y} \tag{196}$$

$$\frac{u_2}{V} = \frac{g}{2} \cdot (\varepsilon_{13} + \varepsilon_{21}) = \frac{g \cdot m}{E \cdot B_y} \tag{197}$$

The advantage of the latter wiring is, that each signal is dependent on only one component of the force system. The draw-back is, that each half bridge must be individually temperature compensated before a full bridge can be wired.

Moment-Moment Wiring of the C-n Bridges

$$\frac{u_4}{V} = g \cdot \varepsilon_{10} = \frac{g}{E\ B_z} \cdot \left[\frac{C \cdot L_1}{2} + n \right] \tag{198}$$

$$\frac{u_5}{V} = g \cdot \varepsilon_{22} = \frac{g}{E\ B_z} \cdot \left[- \frac{C \cdot L_1}{2} + n \right] \tag{199}$$

Force-Moment Wiring of the C-n Bridges

$$\frac{u_4}{V} = \frac{g}{2} \cdot (\varepsilon_{10} - \varepsilon_{22}) = \frac{g \cdot C \cdot L_1}{2 \cdot E \cdot B_z} \tag{200}$$

$$\frac{u_5}{V} = \frac{g}{2} \cdot (\varepsilon_{10} + \varepsilon_{22}) = \frac{g \cdot n}{E \cdot B_z} \tag{201}$$

The T Bridge

The resistance change in a strain-gauge is proportional to the middle value of the strain along the length of the active part of the gauge. The strain due to T along the primary struts of the T-element changes from $-\varepsilon$ to $+\varepsilon$. It is consequently favourable from a signal point of view to use short gauges positioned close to the ends of the struts. The influence on the strain below the gauges due to other components necessitates a high degree of symmetry in the positioning of the gauges.

The T bridge in figure 27 consists of 8 gauges, which form two half-bridges. Each half-bridge must be individually temperature compensated before the full-bridge is wired. The sensitivity of the bridge is

$$\frac{u_3}{V} = g \cdot \varepsilon_{20k} \qquad (202)$$

The ℓ Bridge

The ℓ-bridge measures the principal strains $\pm\varepsilon_{14}$ due to the roll moment. The maximum values of these strains occur in the ±45° directions in the middle of the vertical sides of the N-C-ℓ element. These values will be somewhat lower than the calculated values because the cross-section can not warp freely.

The sensitivity of the bridge (see figure 28) will according to (13) be

$$\frac{u_6}{V} = g \cdot \varepsilon_{14} \cdot (1+\nu) \qquad (203)$$

LAYOUT OF A 30mm DIAMETER BALANCE

The stresses in the control points (figure 10) are calculated with the force system of figure 11 and a presumed value of the distance between the N-C-ℓ and the N-C elements of L_1=108 mm. The choosen value of L_1 means, that $N_1 m_1$ and $N_2 m_2$ in figure 11 causes the same numerical values of stress in Cp13 and Cp21. L_1=108 mm is an initial value, which usefullness must be confirmed during the computation of the T element. It is also necessary, that the cross-sections of the N-C-ℓ and the N-C elements fit within a diameter of say 28 mm.

The following parameter values (see figure 10)

h= 26.2mm, b= 16.6mm, a=c= 4.0mm and L_6= 26mm

result in (see figure 10)

Stress due to C-n	$\sigma_{Cp10} = 156$ N/mm²
Stress due to N-m	$\sigma_{Cp13} = 416$ "
Principal stress due to ℓ	$\sigma_{Cp14} = 103$ "
Combined stress	$\sigma_{Cp11} = 444$ "
Combined stress	$\sigma_{Cp12} = 496$ "
Maximum stress	$\sigma_{Cp18} = 588$ "

The influence of the stress concentration on Cp18 causes according to figure 73 of [27] a stress concentration factor of K=1.65 at a fillet radius of 2.5 mm.

$\sigma_{Cp18k} = 970$ N/mm²

The positions of the fillets in the x-y and the x-z planes should be displaced (~0.5 mm) to avoid a combined influence on the stress in Cp18.

The T Element

The stresses in the control points (figure 10) are calculated with the force system of figure 11, and with the following parameter values.

$L_1 = 108$mm, $L_3 = 15$ mm, $L_4 = 15$mm, $L_6 = 25$mm, $L_7 = 16$mm, $n_1 = 4$, $n_2 = 2$,
$s_1 = 0.8$mm, $s_2 = 1.0$mm, $h_1 = 1.5$mm, $h_2 = 4.2$mm, $b_1 = 7.7$mm, $b_2 = 4.5$mm,
$r_1 = 4.0$mm, $r_2 = 6.0$mm, $e_1 = -1.5$mm.

The following control points are of primary interest from a strength point of view.

The maximum stress in the external struts of the primary structure
$\sigma_{Cp1} = 516$ N/mm²

The maximum stress in the central struts of the primary structure
$\sigma_{Cp2} = 527$ N/mm²

The maximum stress in section D-D of the secondary structure
$\sigma_{Cp6} = 596$ N/mm²

The maximum stress in section F-F of the secondary structure
$\sigma_{Cp8} = 561$ N/mm²

The maximum stress in the central struts of the primary structure due to T alone $\sigma_{Cp20} = 110$ N/mm

The effects of the fillets are estimated to be ([27] figure 73)

$r_f = 0.4$mm	$\sigma_{Cp1k} = 1.44 \cdot 516 = 743$ N/mm²
$r_f = 1.0$mm	$\sigma_{Cp2k} = 1.44 \cdot 527 = 759$ N/mm²
$r_f = 0.4$mm	$\sigma_{Cp6k} = \sim 1.4 \cdot 596 = 834$ N/mm²
$r_f = 0.4$mm	$\sigma_{Cp8k} = \sim 1.4 \cdot 561 = 785$ N/mm²

Application of (40) to Cp20 with t_1=1.0mm and t_2=0.5mm results in σ_{Cp20k}= 0.83·110= 92 N/mm²

The bridge sensitivities

All components of the force system are present with their maximum values, when the bridge sensitivities are calculated.

The sensitivities of the N-m bridges. Equations (194) and (195)

$$\frac{u_1}{V}= \frac{u_2}{V}= 4.16\cdot10^{-3}= 4.16 \text{ mV/V}$$

The sensitivities of the C-n bridges. Equations (198) and (199)

$$\frac{u_4}{V}= \frac{u_5}{V}= 1.56\cdot10^{-3}= 1.56 \text{ mV/V}$$

The sensitivity of the T bridge. Equation (202)

$$\frac{u_3}{V}= 0.92\cdot10^{-3}= 0.92 \text{ mV/V}$$

The sensitivity of the ℓ bridge. Equation (203)

$$\frac{u_6}{V}= 1.34\cdot10^{-3}= 1.34 \text{ mV/V}$$

The Model Support End

It is advantageous from a deflection point of view (an interaction point of view) to use as low stresses as possible in the model end of the balance. The stress in the control point Cp19 is computed with (185), (186) and (187). With L_8=91.5mm and using the full diameter the result is σ_{Cp19}= 426 N/mm².

The model end can be a cylinder or a cone. Available manufacturing methods result in plays smaller than uncertanties normally found in the attitude mechanism of a wind-tunnel. A different situation excists during the balance calibration, where even a small play introduces false interactions and must be eliminated. However, The calibration model can be provided with a clamping device around the model end of the balance and eliminate such plays. The roll moment is balanced with a key at the model end. This connection must also be free from play during the calibration process.

The Sting End

The stress in the sting end is calculated by use of (185) and (189). With $x=L_9=$ 84mm and d= 26mm the maximun stress in Cp23 is $\sigma_{Cp23}=585$ N/mm². The fillet increases this value. Figure 73 in [27] and $r_f=$ 5mm give $\sigma_{Cp23k}=$ 1.42 585= 830 N/mm². The sting end of the balance must be conical due to the required strength of the sting. Cone angle >6.5°.

The Sting

The static stress of the cross-sections of the sting is calculated with (188), (189) and (180). Figure 29 shows the necessary dimensions if $\sigma_{Cp24}=600$ N/mm². The angle deflection ψ of the sting calculated by use of figure 25 is also shown in figure29. The stiffness at a sting length of 1.5 m and a load of N=12000 (N) is 51000 N/rad. The aerodynamic stiffness of a model comparable with the force system is approximately 27500 N/rad. No risk of sting divergence is present.

Comments

Figure 30 shows a layout of the 30mm balance. The load carrying capacity expressed as N/D^2 is 6.67 for the combination $N_2=6000$ (N) and $m_2=324$ (Nm). This value is introduced in figure 2 as (18). The dot falls above (9), which is a limit for bending-beam balances stated in [7], and (8) which is a limit for Two-Shell balances quoted in [5].

The balance carries the force system of figure 11, if a maximum nominal stress of 600 N/mm² is permitted. When stress concentration factors are considered a calculated value of 834 N/mm must be allowed.

The expected deflection of the balance, calculated with the equation of the elastic curve, is shown in figure 31. From this figure the necessary open base diameter of the model can be estimated.

The N-C-ℓ and the N-C elements can change places. The result will be a slight modification of the non-linear interactions on T and ℓ.

The necessary channels for the wiring on the balance are not shown in figure 30.

INFLUENCE OF THE SCALE

The load carrying capacity of geometrically similar balances with diameters ≠ 30 mm and with the same stress levels can be estimated by use of (2) and (3). Application of the force system of figure 11 gives

$$N_1 = 12000 \cdot \left|\frac{D}{30}\right|^2 \text{ (N)} \qquad (204) \qquad m_1 = 0 \cdot \left|\frac{D}{30}\right|^3 \text{ (Nm)} \qquad (205)$$

$$N_2 = 6000 \cdot \left|\frac{D}{30}\right|^2 \text{ (N)} \qquad (206) \qquad m_2 = 324 \cdot \left|\frac{D}{30}\right|^3 \text{ (Nm)} \qquad (207)$$

$$C_1 = 2917 \cdot \left|\frac{D}{30}\right|^2 \text{ (N)} \qquad (208) \qquad n_1 = 0 \cdot \left|\frac{D}{30}\right|^3 \text{ (Nm)} \qquad (209)$$

$$C_2 = 1500 \cdot \left|\frac{D}{30}\right|^2 \text{ (N)} \qquad (210) \qquad n_2 = 76.5 \cdot \left|\frac{D}{30}\right|^3 \text{ (Nm)} \qquad (211)$$

$$T = 1000 \cdot \left|\frac{D}{30}\right|^2 \text{ (N)} \qquad (212) \qquad \ell = 180 \cdot \left|\frac{D}{30}\right|^3 \text{ (Nm)} \qquad (213)$$

Figure 32 shows N.m and C-n envelopes for a number of balance diameters. Data from three Task balances [9] and a pair of Two-Shell balances [5] are added as a comparison. The influences of the diameter on T and ℓ are shown in figure 33.

A MATHEMATICAL CALIBRATION MODEL

It is shown in the preceding text how full-bridges of strain-gauges can be arranged on a multi-component balance to measure forces and moments and simultaneously suppress the influences from secondary components. In practice these suppressions will be incomplete and the remainders are designated interactions.

A mathematical modell, which combines the signals of the balance with the load system in an unambigous way and which can be used for both calibration and wind-tunnel testing is described in [29]. The model is not new, it has been used earlier by many research establishments. It is based on the following presumptions.

A. The strains below the strain-gauges of a bridge and caused by the external load are directly proportional to the moments (bending or torsion) in the measuring elements.

B. The signal from a bridge is directly propertional to the combined effect of the strains below the strain-gauges.

C. The different signals are primarily dependent on one or two of the components of the force system.

D. Linear interactions are present due to mechanical and electrical non-symmetries.

E. Non-linear interactions are present due to the elasticity of the balance, which causes the force system in the model to be displaced (translations and rotations) in relation to the measuring elements of the balance.

F. The non-linear interactions must be small compared with the primary sensitivities.

G. The displacements (translations and rotations) of the balance elements must be small and directly proportional to the different components. The principle of superposition must be applicable. This means, that the equation of the elastic curve can be applied.

H. Each sub-displacement depends only on one component at a time and is consequently of the type

$$\delta \text{ or } \psi = k \cdot P \tag{214}$$

with k= a constant coefficient.
P= a component of the force system.
δ= a deflection.
ψ= a change of slope.

I. Each sub-displacement causes a moment contribution of type δ or ψ times R (a component) in each measuring element.

$$\Delta M_R = (k \cdot P) \cdot R = k \cdot (P \cdot R) \tag{215}$$

R= a component of the force system.

K. The conditions above mean, that the balance signals are considered as dependent and the components of the force system as independent variables. A necessary and sufficient mathematical model, which has reference to the type of balances and applications in question, must consequently be of second degree. It can be expressed as

$$u_i = \sum_{n=1}^{6} k_{in} \cdot P_n + \sum_{n=1}^{6} \cdot \sum_{m=n}^{6} k_{inm} \cdot P_n \cdot P_m \tag{216}$$

with u_i = the different balance signals.
k_{in} = primary sensitivity coefficients and linear interaction koefficients.
k_{inm} = non-linear interaction koefficients.
P_n, P_m = components of the force system

(216) consists in the general case of 6x6 linear terms and 6x21 non-linear terms of second degree. How many of these terms, which must be considered in practice, depends on the symmetry of the balance, the stiffnesses, the mutual sizes of the components of the force system and the required accuracy.

REFERENCES

[1] Multicomponent Strain-Gauge Balances. TEM-ROLLAB Brochure.

[2] Ferris,A.T.: Strain Gauge Balances and Buffet Gauges.NASA CP 2262, 1982.

[3] Moss,G.F.: A Compact Design of Six-Component Internal Strain Gauge Balances. RAE TN AERO 2764.

[4] Test Instrumentation. Vought Aeronautics Brochure, 1970.

[5] Griffin,S.A.: Study of Six-Component Strain Gauge Balances for use in the HIRT Facility. AEDC-TR-75-63, July 1975.

[6] Dimeff,J.: Characteristics of a New Type Balance for Wind Tunnel Models. NASN-TM-X-1278, Aug 1966.

[7] Hypersonic Research Facilities Study. NASA CR 114323, Oct 1970.

[8] Strain Gauge Balances. Series D. TASK Brochure.

[9] Strain Gauge Balances. Series MK. TASK Brochure.

[10] Broussaud,P.: Balances et dynamomètres utilisés au centre de Modane-Avrieux. ONERA Note Tech 122, 1968.

[11] Pollok,N.: An Improved Design of Strain Gauge Sting Balance for Small Wind Tunnel Models. ARL Aero Rep 331.

[12] Wind Tunnel Model Force Balances. Micro Craft Inc. Brochure.

[13] Boyden,P.: Aerodynamic Measurements and Thermal Tests of a Strain-Gauge Balance in a Cryogenic Wind Tunnel. NASA TM 89039, Apr 1987.

[14] Blake,A.: Practical Stress Analysis in Engineering Design. Marcel Dekker Inc, New York 1982.

[15] Data Sheets FR-22 and FR-35. MM Tech Note TN-130-2. Vishey Intertechnology Inc, 1968.

[16] Dubois,M.: Six Component Strain Gauge Balances for Large Wind-Tunnels. ONERA TP no 1980-94.

[17] Fristedt,K.: Force Measurements in Wind Tunnels. 1:st Conf on Aero Sci & Avi Tech, Cairo May 1985. Also ROLLAB REP 041.

[18] Jarfall,L.: Utmattningshållfasthet hos gnistbearbetade detaljer. FFA Rapport DU-1440, 1974.

[19] Saab Normblad AS 111624, Stål 1624.

[20] Griffin,S.A.: Wind Tunnel Parametric Study for use in the Proposed 8x10 ft HIRT Tunnel at AEDC. AEDC-TR-73-47, 1973.

[21] Vascomax Catalogue Regarding 18% Ni Maraging Steel.

[22] Carpenter 455 Catalouge.

[23] Brocard,J.: Study of a Balance for the Airbus Model. ONERA Note no 74-28.

[24] Cooksey,J.M.; and Roy,J.F.: Effects of Processing Techniques on the Fatigue Properties of Strain Gauge Balance Material. Vought Aeronautics, 1973.

[25] Björk,A.: A Computer Program for the Design and Strength Calculation of 3 or 6 Component Internal Strain Gauge Balances. ROLLAB REP RR 046.

[26] Roark,R.J.: Formulas for Stress and Strain. McGraw Hill, 4th Edition 1965.

[27] Peterson,R.E.: Stress Concentration Factors.John Wiley and Sons, 1974.

[28] Billingsley,J.P.: Sting Dynamics of Wind Tunnel Models. AEDC-TR-76-41, 1976.

[29] Fristedt,K.: A Calibration Model of a Six-Component Internal Wind-Tunnel Balance of the Bending-Beam Type. Measurement 11 (1993), page 107-118.

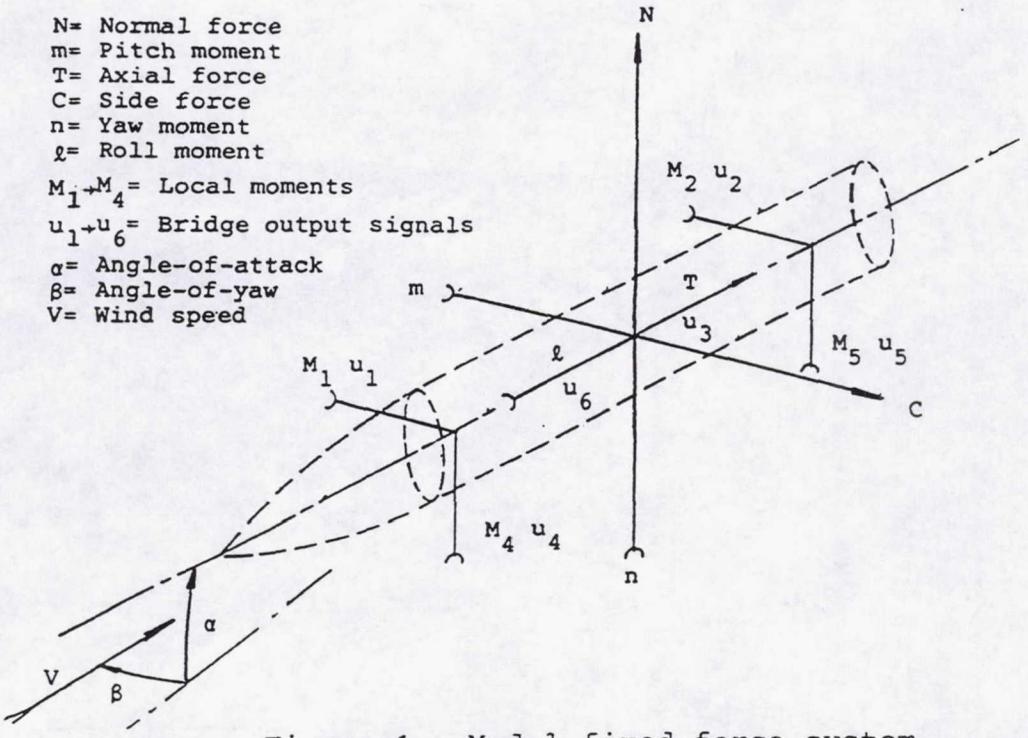

Figure 1. Model fixed force system

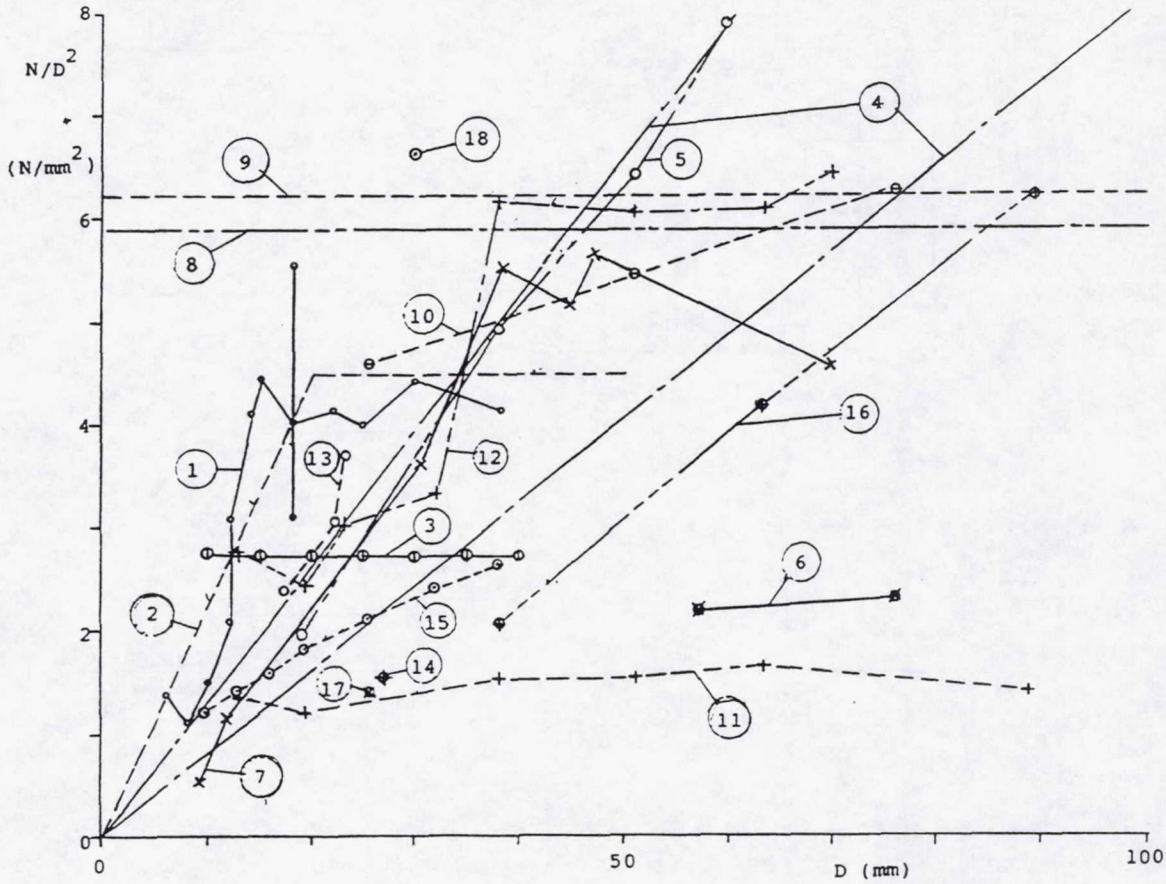

Figure 2. The relative load carrying capacity of internal wind tunnel balances.

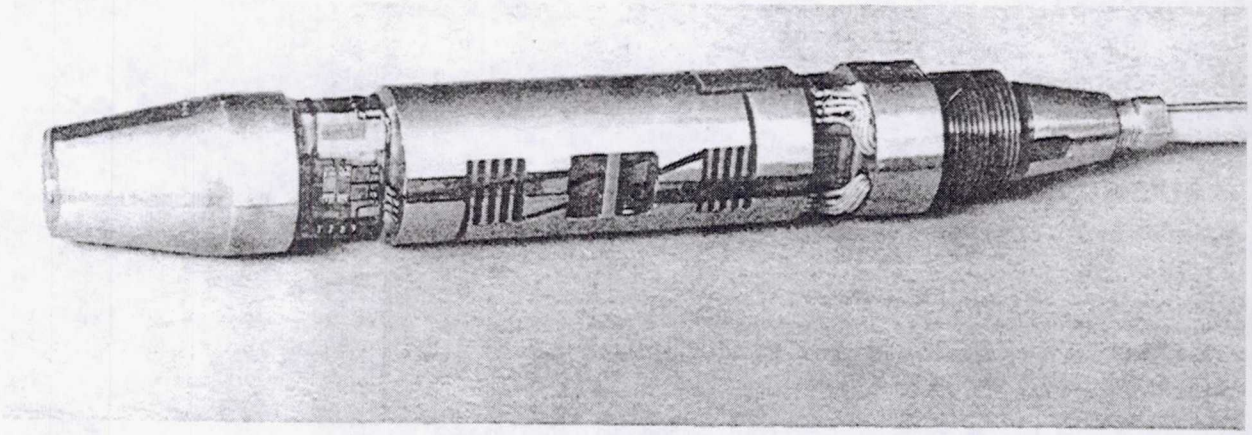

Figure 3. A 16 mm diameter balance of the current type.

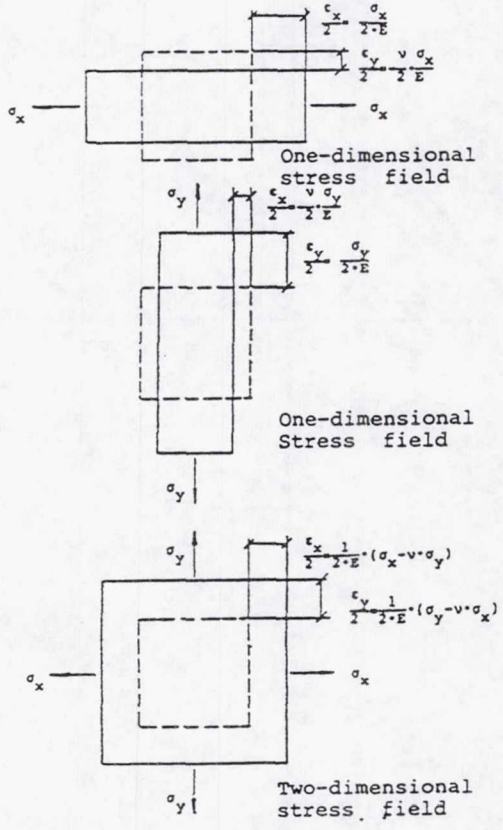

Figure 4. One- and two-dimensional stress fields and corresponding strain fields.

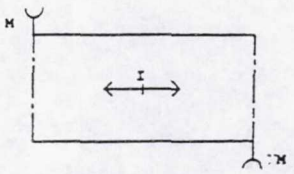

Figure 5. A spring element in bending.

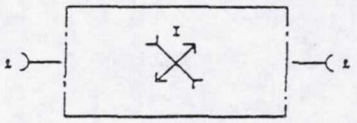

Figure 6. A spring element in torsion

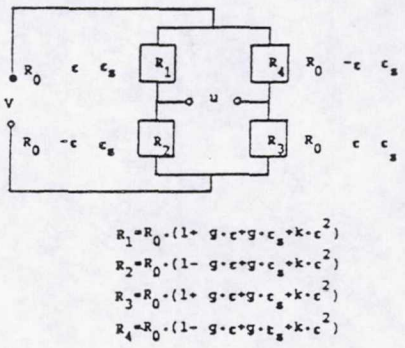

Figure 7. The Weatstone bridge with four identical arms.

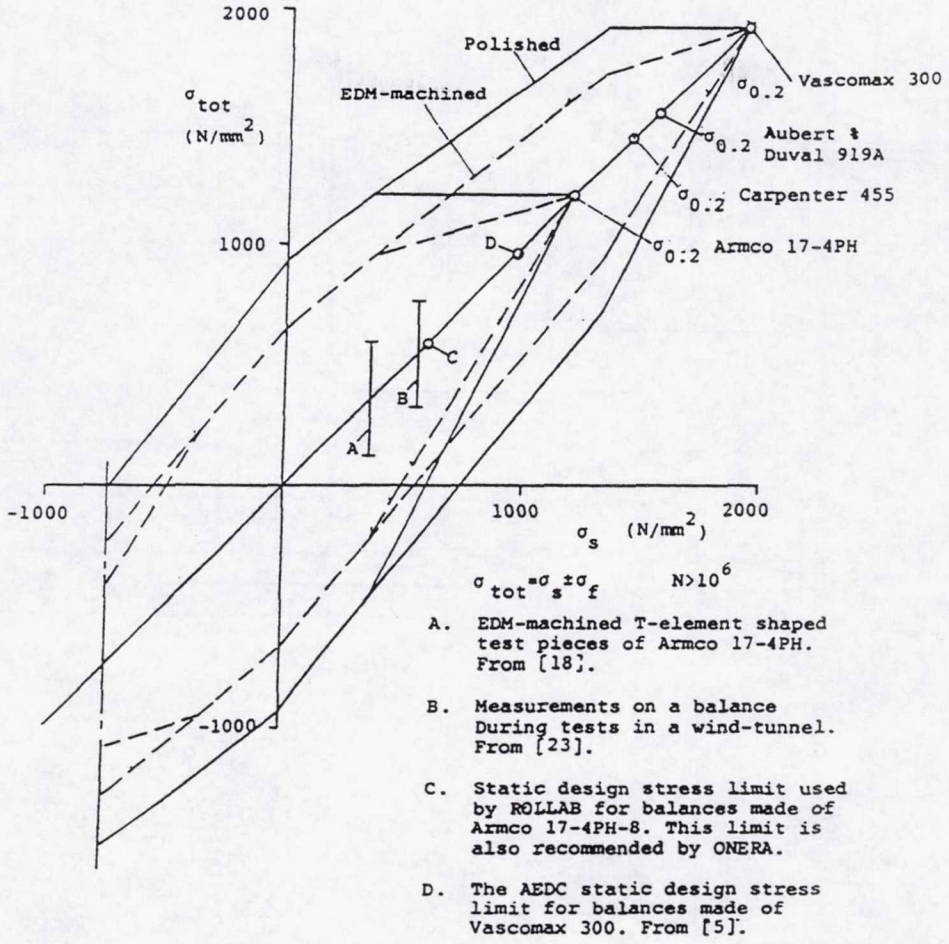

Figure 8. Estimated Goodman diagrams for materials similar to Wascomax 300 and Armco 17-4PH.

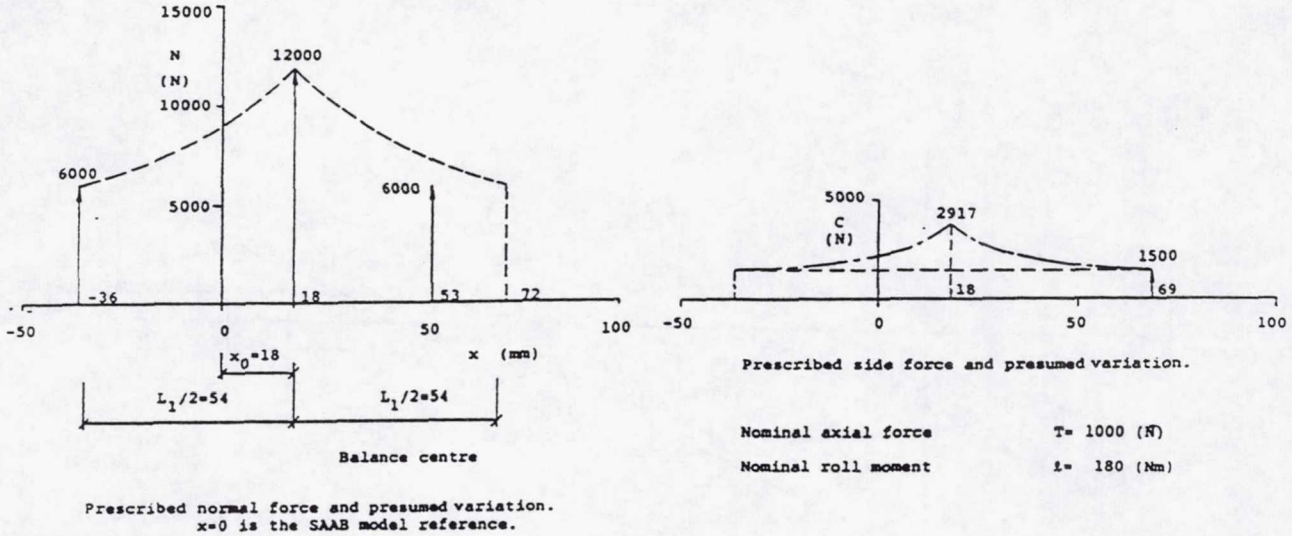

Figure 9. The nominal force system of the 30 mm balance based on information from SAAB-SCANIA.

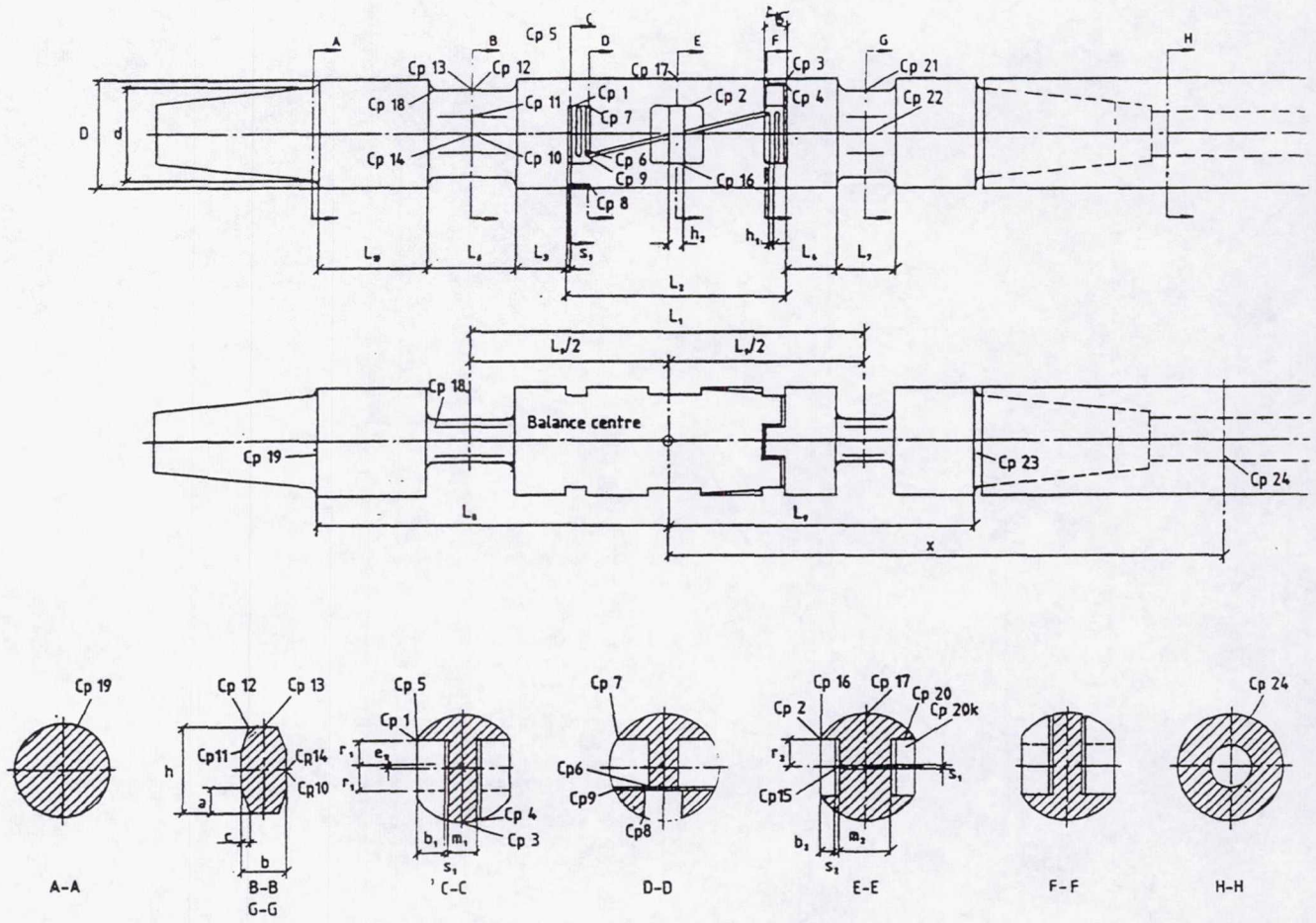

Figure 10. Balance parameters and positions of the different stress control points.

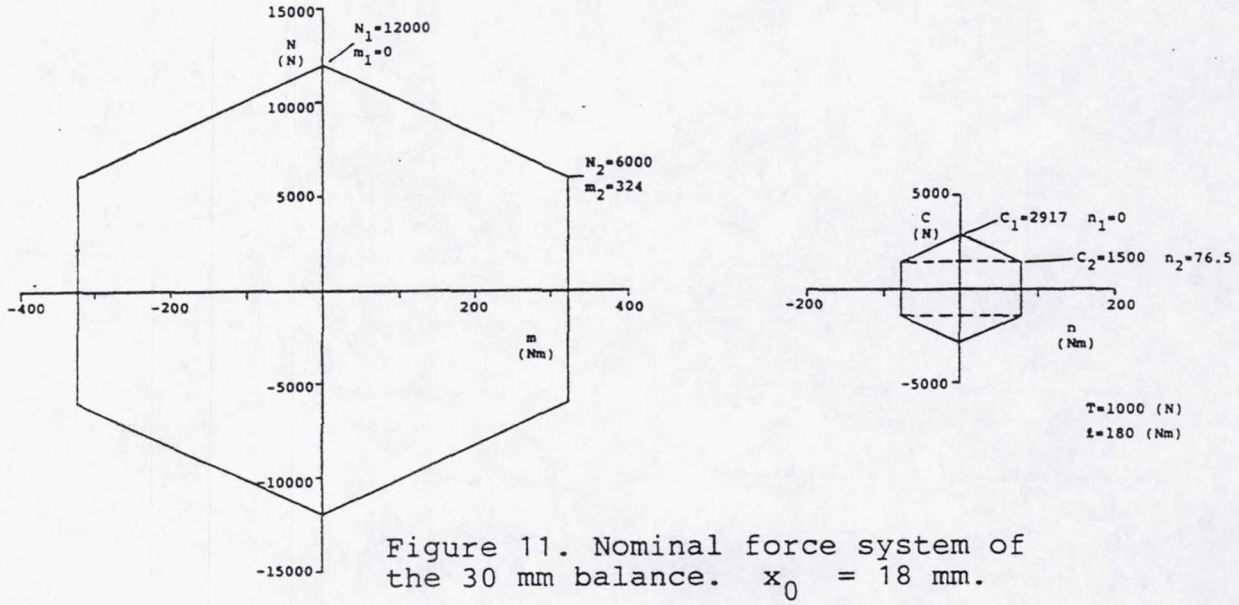

Figure 11. Nominal force system of the 30 mm balance. x_0 = 18 mm.

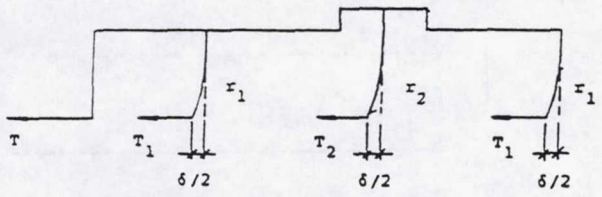

T_1= The reaction force from $n_1/2$ external struts.
T_2= The reaction force from n_2 central struts.

Figure 12. The T-element or axial force balance.

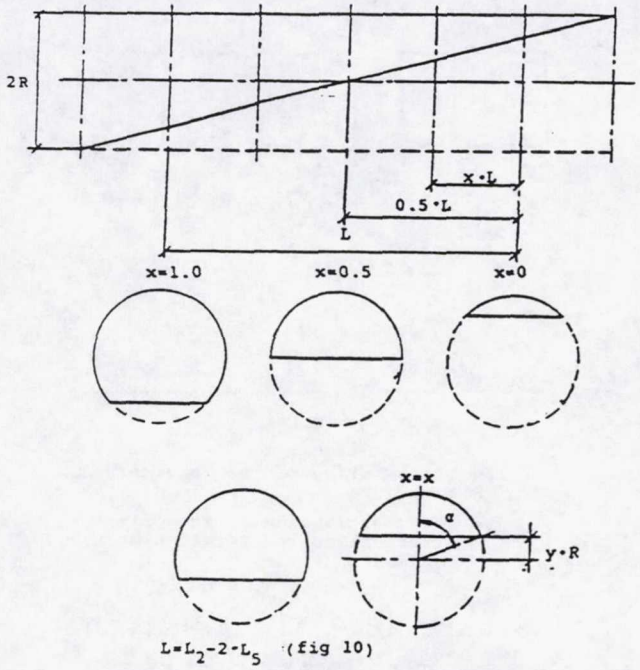

$L=L_2-2\cdot L_5$ (fig 10)

x= The relative length between the end of the approximated secondary structure and a cross-section.

Figure 13. The approximated geometry of the secondary structure of the T-element.

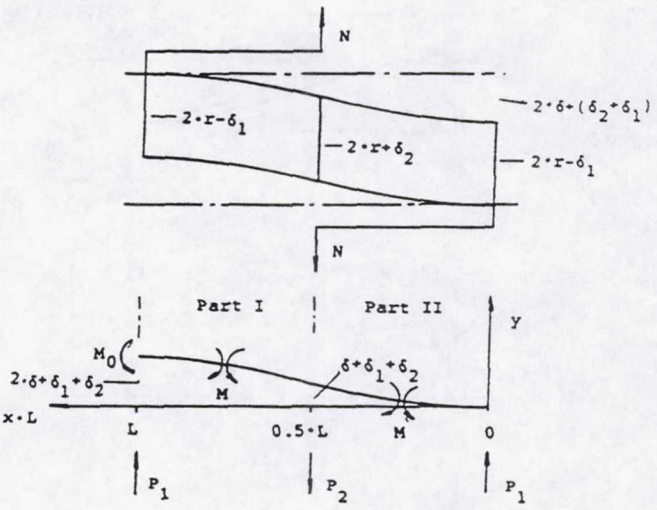

Figure 14. The deflection of the T-element due to N.

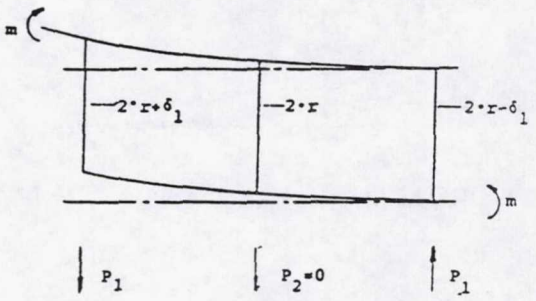

Figure 15. The deflection of the T-element due to m.

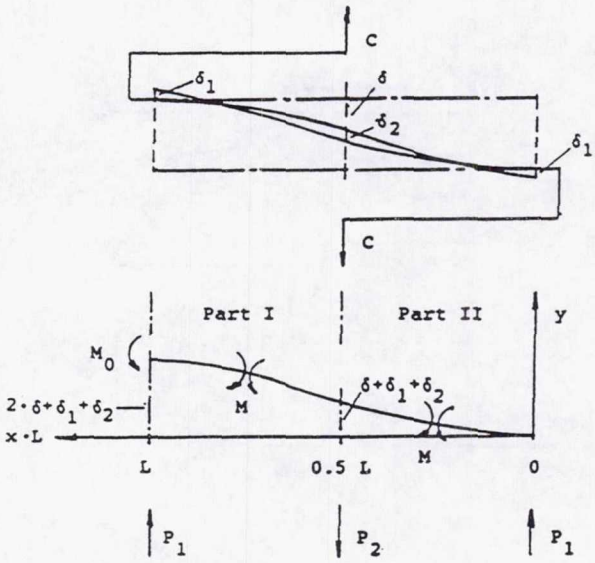

Figure 16. The deflection of the T-element due to C.

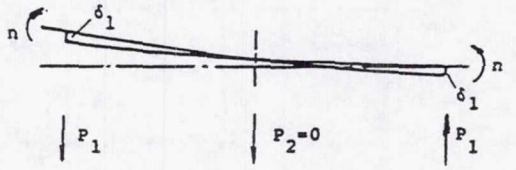

Figure 17. The deflection of the T-element due to n.

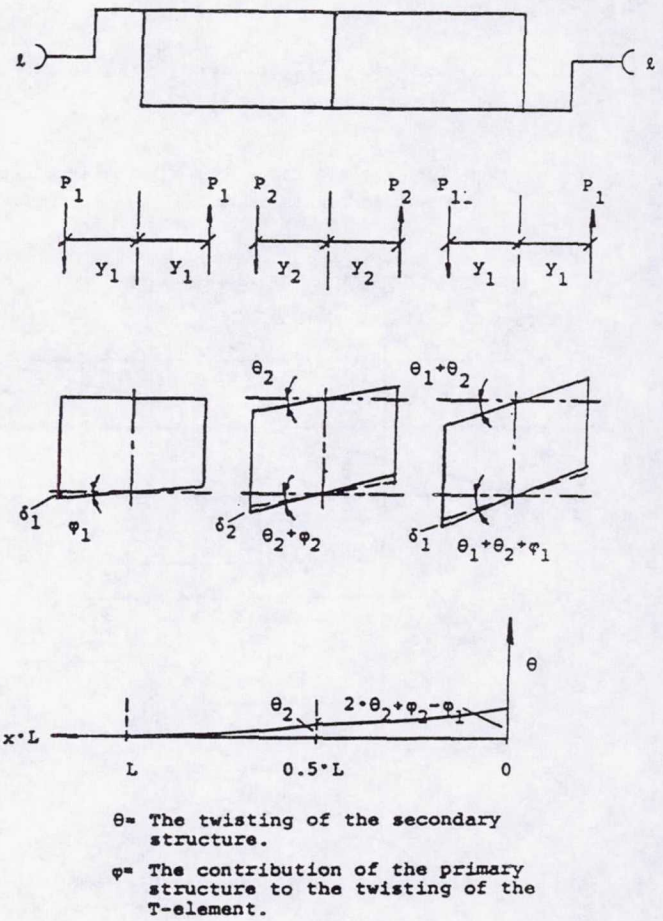

θ= The twisting of the secondary structure.

φ= The contribution of the primary structure to the twisting of the T-element.

Figure 18. The twisting of the T-element due to ℓ.

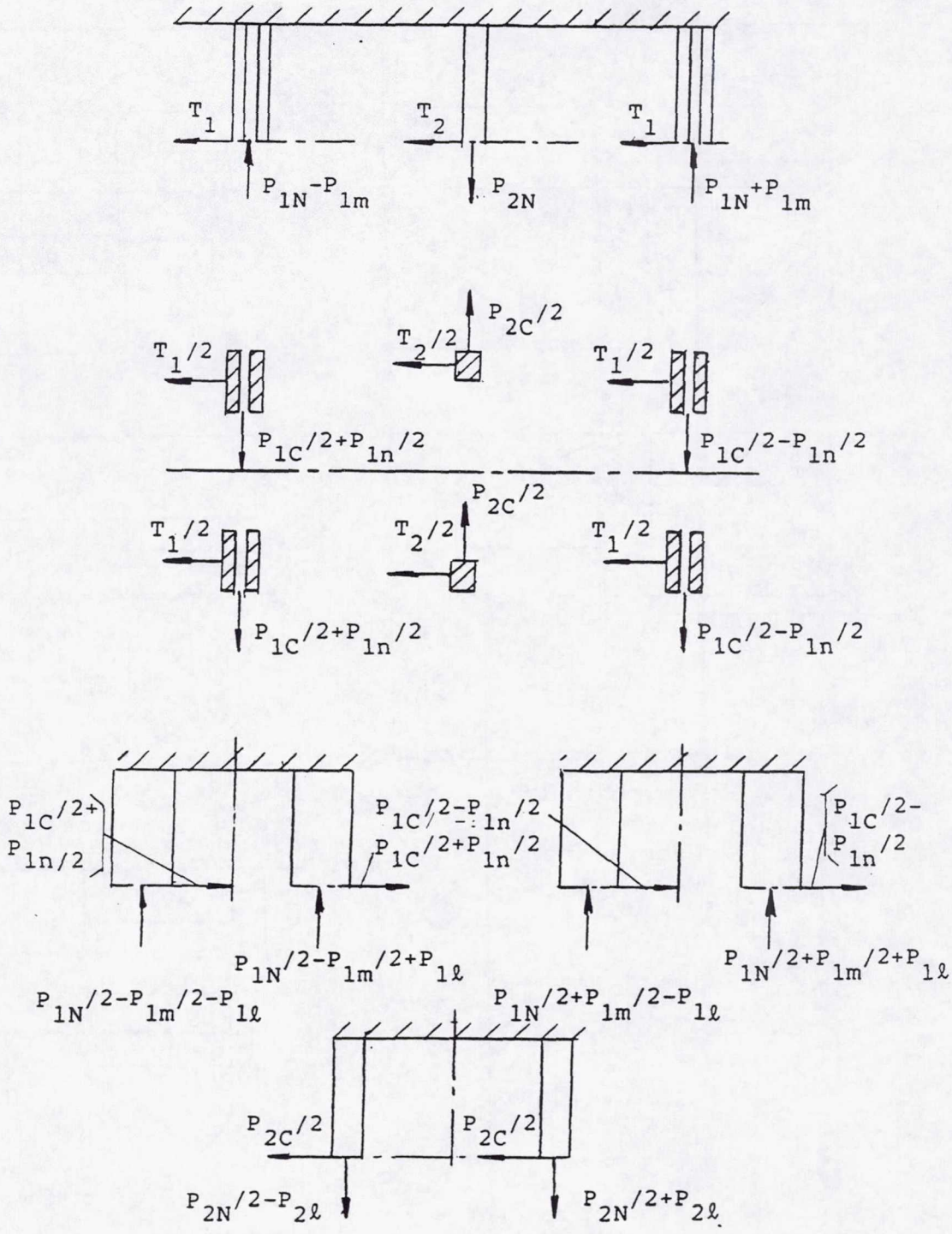

Figure 19. Reaction forces on the primary structure of the T-element.

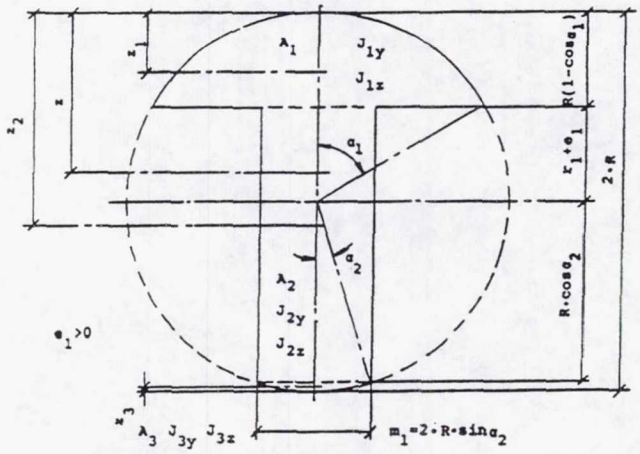

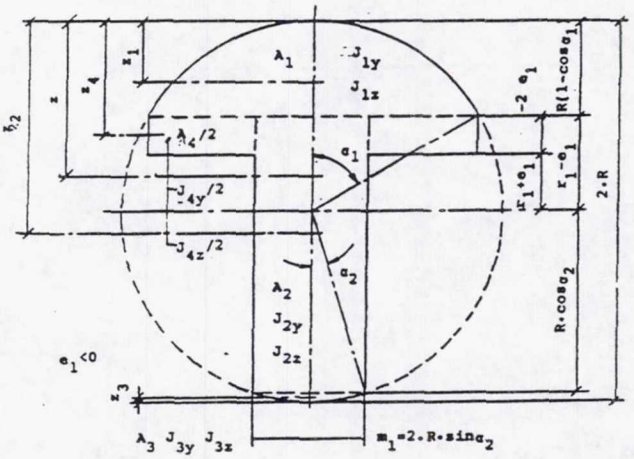

Figure 20. Cross section C-C of figure 10.

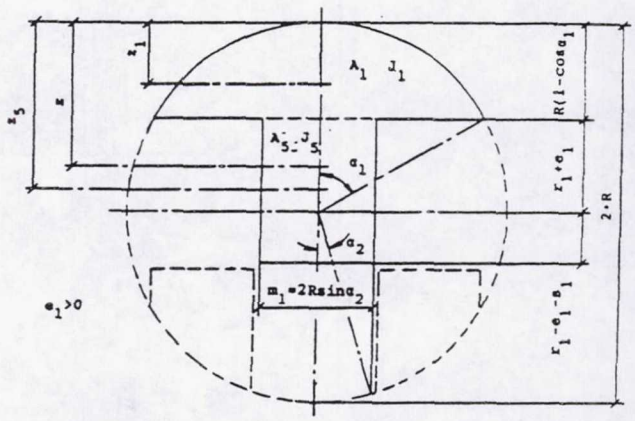

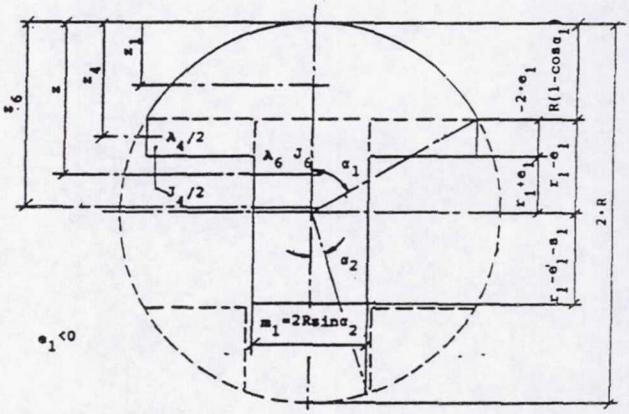

Figure 21. Cross section D-D

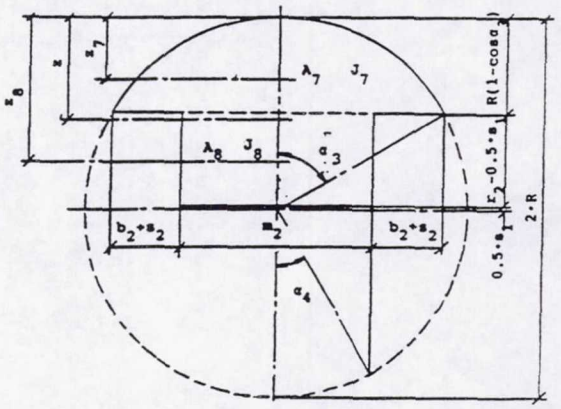

Figure 22. Cross section E-E of figure 10.

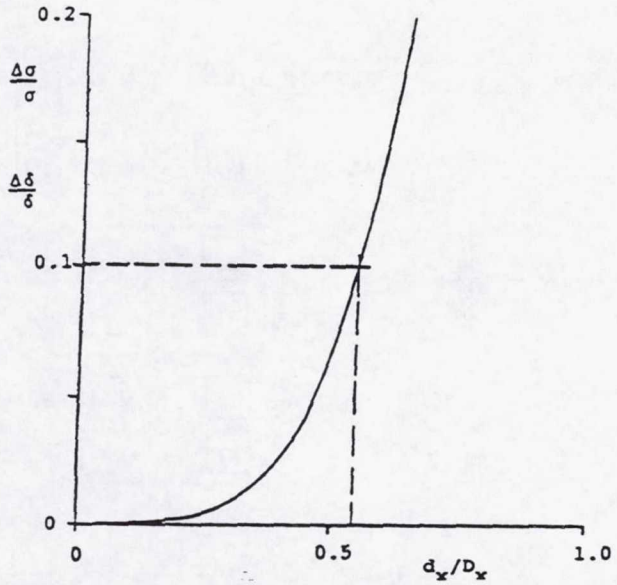

Figure 23. The influence of a longitudinal hole in the sting on the stress and deflection.

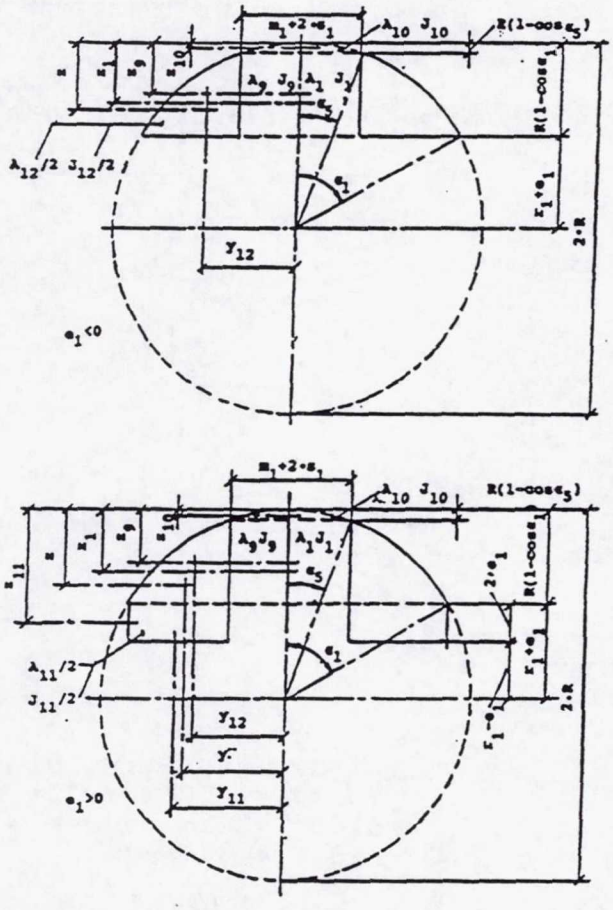

Figure 24. Cross section F-F of figure 10.

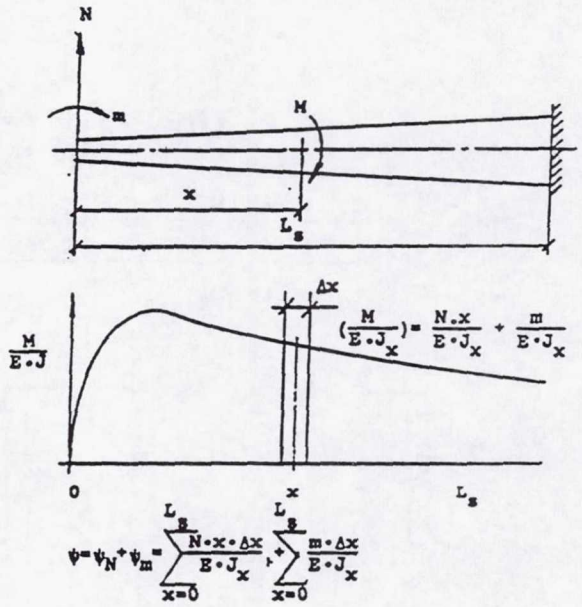

$$\left(\frac{M}{E \cdot J_x}\right) = \frac{N \cdot x}{E \cdot J_x} + \frac{m}{E \cdot J_x}$$

$$\psi = \psi_N + \psi_m = \sum_{x=0}^{L_s} \frac{N \cdot x \cdot \Delta x}{E \cdot J_x} + \sum_{x=0}^{L_s} \frac{m \cdot \Delta x}{E \cdot J_x}$$

ψ= the slope of the sting at x=0.

$$\delta = \delta_N + \delta_m = \sum_{x=0}^{L_s} \frac{N \cdot x^2 \cdot \Delta x}{E \cdot J_x} + \sum_{x=0}^{L_s} \frac{m \cdot x \cdot \Delta x}{E \cdot J_x}$$

δ= the deflection of the sting at x=0.

E= modulus of elasticity.

J_x= the local value of the moment of inertia of the sting.

Figure 25. Application of the area-moment method.

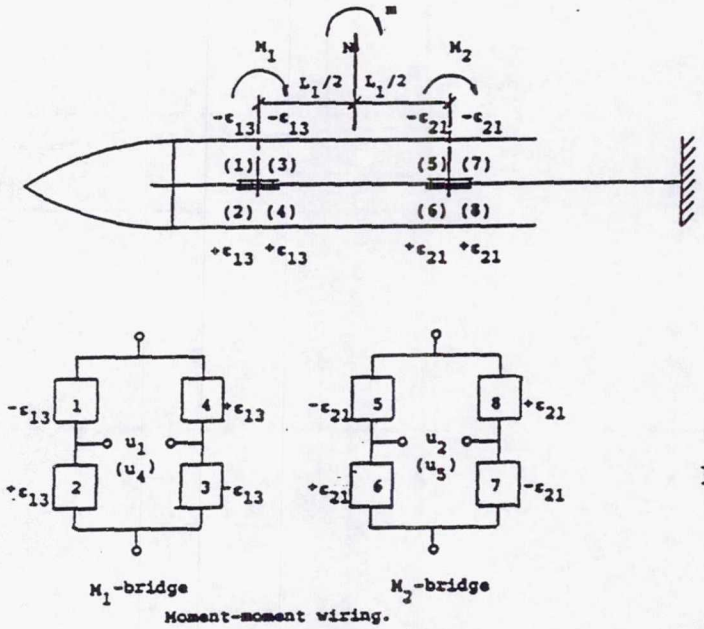

Figure 26. Wiring of the N-m bridges.

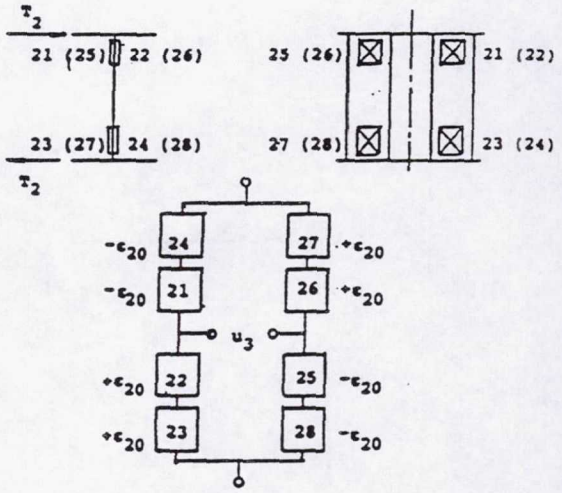

Figure 27. Wiring of the T bridge

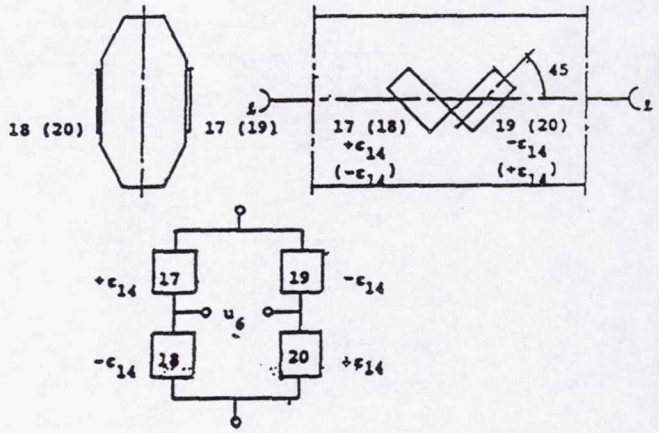

Figure 28. Wiring of the bridge.

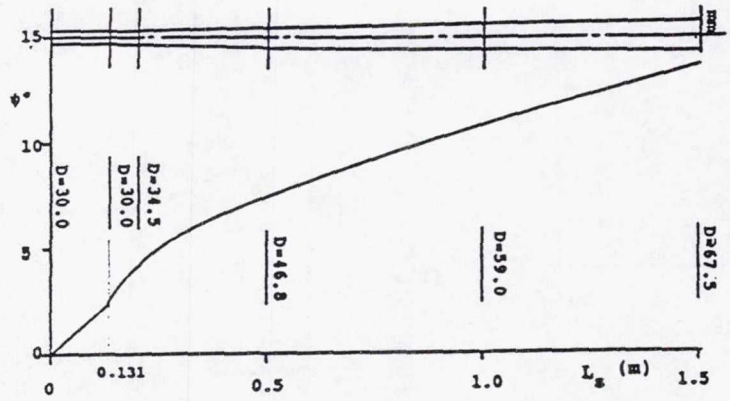

Figure 29. Sting dimensions for σ_s = 600 N/mm^2. Change of slope. Load case N_1=12000(N) and m_1= 0 (Nm)

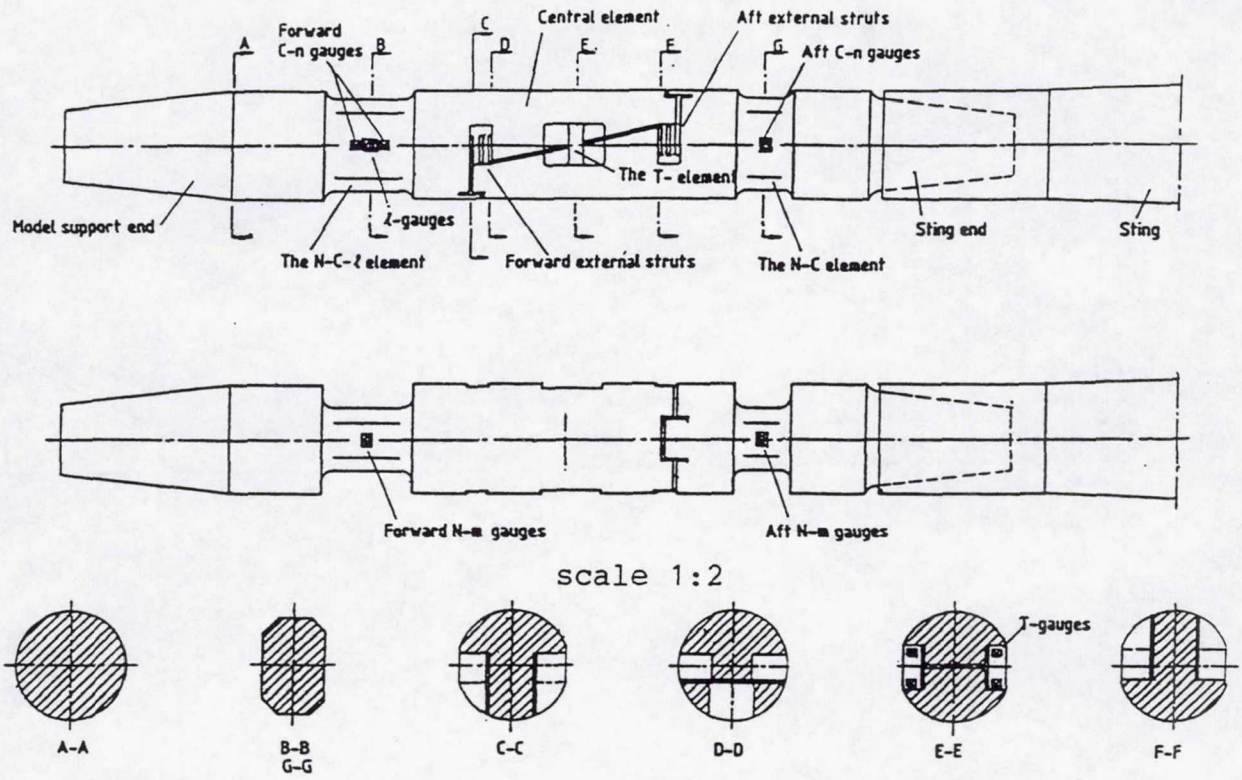

Figure 30. Layout of the calculated 30 mm diameter balance.

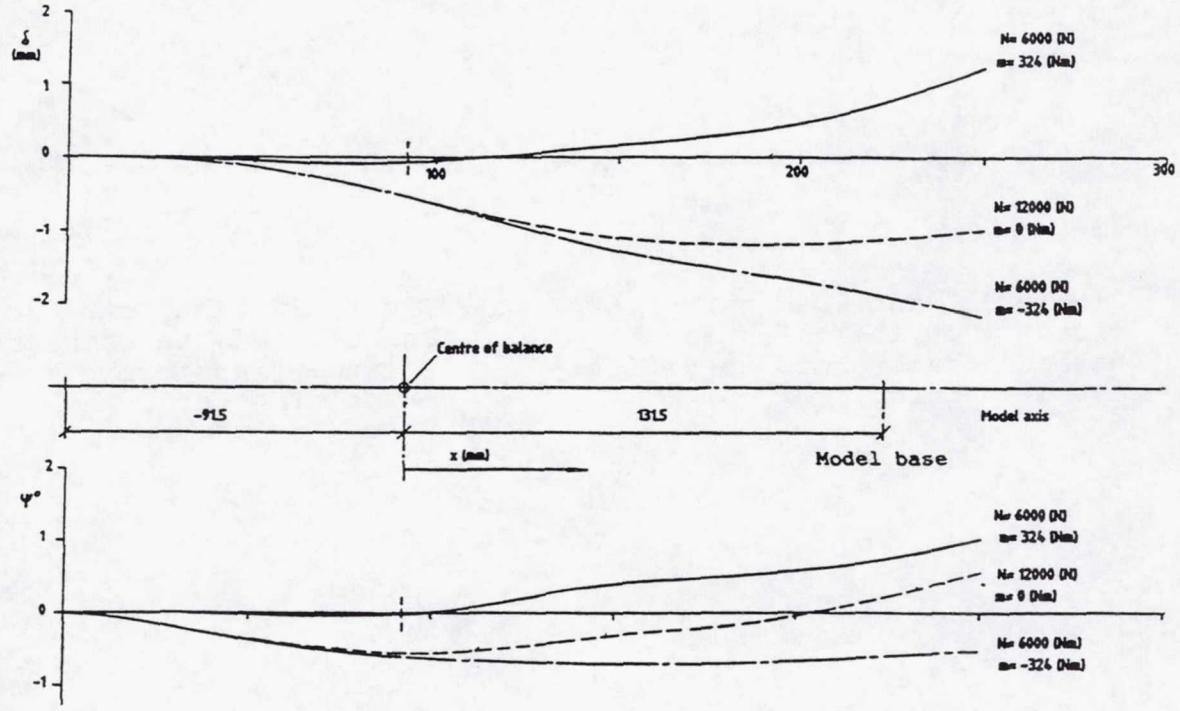

Figure 31. The deflection and the change of slope of the 30 mm balance at different N and m.

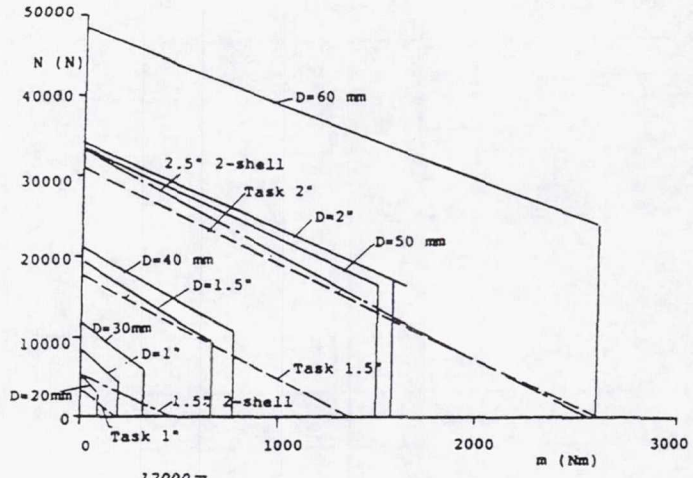

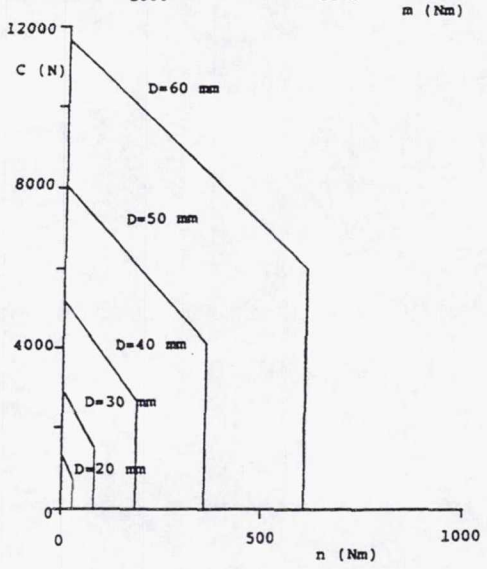

Figure 32. The load carrying capacity of the calculated balance transformed to different diameterś.

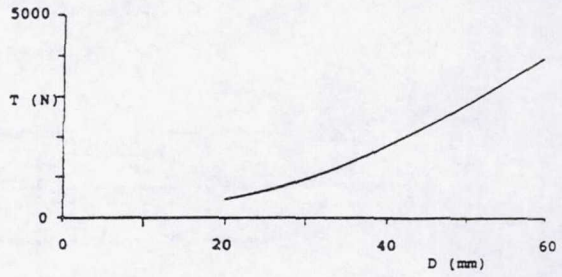

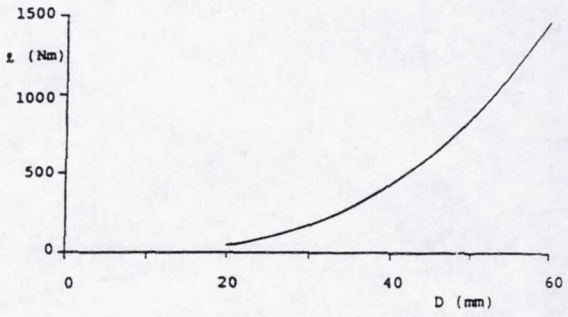

Figure 33. The load carrying capacity of the calculated balance transformed to different diameters.

Hinge Moment Balance For Complete Model

Kaike, Guo
Beijing Institute of Aerodynamics
1996, 3, 31

Abstract
The structure, reference center, measurement range, bridges, static and dynamic calibration of hinge moment balance for complete models are discussed in this paper.

Symbols

M_H	Hinge Moment	N.M
y	Normal Force	N
Q	Axial Force	N
Mx	Roll Moment	N.M
My	Yaw Moment	N.M
Z	Side Force	N
M_H; y; Q; Mx; My; Z;	Represent for Each Component Measuring Bridges	
O.xyz	Measurement Coordinate System	
O	Measurement Reference Center, Origin of Coordinate	
α	Angle of Attack	degree
δ	Deflection Angle	degree
γ	Roll Angle	degree
$M\infty$	Mach Number	
v	Bridge Voltage	volt
μv	Signal	$1x10^{-6}$ volt
k	Amplify Coefficient	

1. Introduction

In this paper, balance used for measuring hinge moment and other aerodynamic characteristics of a rudder or a moving wing of complete model of a winged vehicle by wind tunnel tests is discussed.

The property of hinge moment is quite important for aerodynamic design, for it is required by maneuverability, controllability, selection of rudder motor power, control system. constriction and strength of a vehicle. Usually, higher rudder effect and smaller hinge moment are needed. Therefore, the axes of rudder or wing should be arranged as close as possible to the center of pressure. Compared with other five components, hinge moment is really a small one. In a small wind tunnel (such as 0.6m*0.6m test section), the measurement of a hinge moment is difficult indeed. We have applied several techniques in hinge moment measurement:

1. By using of an external balance, a separate rudder or wing could be mounted on the front sting and the loads on the rudder or wing could be measured directly. But the basic simulation could not be achieved and the interaction between rudder and body, wing and body could not be obtained either.

2. Using half model

a. To avoid wind tunnel choked, half model enables to use a larger model, so that the hinge moment could be measured.

b. Hinge moment of plane aileron, elevating rudder of tail planes and rudder of vertical tail, especially of that with oblique axis will be much more convenient measured by half model.

c. By using of half model hinge moment balance, it could change deflection and angle of attack in one wind tunnel run. That means a higher efficiency and lower consumption.

d. The half model balance could roll from 0 through 360 degrees, and so that it had a big convenience for higher deflection tests.

e. Some problems exist with half model test, such as the interaction of boundary layer with wind tunnel wall, the space piece or the reflection plate.

f. Mounted in the wind tunnel, half model could not simulate side rolling and side slipping of a vehicle.

C. Complete model hinge moment test technique

Complete model hinge moment test technique could simulate the flow pattern around the whole vehicle, such as with canard, complete moving wing of tail, and change the attitude of the model by rolling or slipping. So, it could simulate the cross interaction between wing and body, wing and rudder, rudder and another rudder. Also, the influence of body vortices, velocity reduction at rudder by front wing and of downwash could be incorporated.

There are two types hinge moment balances for complete model: transverse and longitudinal. For the transverse hinge moment balance for complete model, the wing and rudder is connected with the balance by "changing deflection lock". While the deflection changed, the normal force will always be vertical to the chord plane, so the normal force read from the balance is the normal force of the wing or rudder. This kind of balance is simple in structure and easy for manufacturing. However, the space of a traverse balance for transverse movement is much less than that of a longitudinal balance for longitudinal movement. Besides, the sensitivity of the transverse balance is confined by the requirement of strength for normal force and other components. At high angle of attack or high deflection, the normal force is quite large, and the sensitivity of the hinge moment must be scarified.

The longitudinal hinge moment balance for complete model , consisting of sing support balance and a so-called "nut" is of high sensitivity. It has several advantages:

First, the six aerodynamic components will be measured simultaneously. The interaction between different components could be corrected, especially when the hinge moment is much less than other components. So it raises the precision.

Second, the inconsistency of requirements by sensitivity and strength will be solved by

separating flexure pivot for hinge moment from those for other components. The balance is sensitive enough for hinge moment and strange enough for shocks by other components.

Third, this method of add a "cap" on a common strain-gage balance is simple as well as economical and very special:

- Hinge moment balance for special purposes is not needed.
- Costs are saved greatly.
- According to existing conventional balances, design various kinds of "hinge cap". Then assemble them to the balances. In this way, different sensitivity and measurement range hinge balances are formed to measure hinge moment of rudder or wing.

Fourth, the sting balances listed in this paper not only can be used to connect :hinge cap", are high quality conventional balance themselves. their axial components is of integrate "horizontal " structure. And two pieces of half-bridge strain gauges are used to for a whole Wheatstone bridge. It of the feature of low temperature effect and high ability to stand shock.

2. Structure of the Balance

2.1 Structure of Hinge Mount Element-Hinge Cap Consists of Five Elements (see Figure 1)

1. The elastic element of hinge moment component (see Figure 1 and 2)
2. Rigid cylinder body relative to elastic thin piece beam (see Figure 2 and 3)
3. Pin holes of fixed position
4. Fastening screws
5. High-precision bearing

Measuring range can be changed by elastic element (Figure 2) of hinge moment component. But even if a high-precision bearing were used, mechanical friction would seriously affect measuring precision. Substituting mechanical bearing with air floating bearing can improve the precision, but result in a larger size. Has now been substituted by integral hinge cap.

The integral cap of hub type as shown in Figure 4A and Figure 4B, has been carved and manufactured from an integral high-strength F141(18Ni) Maraging steel by wire working (spark) and electric corrosion technology.

In Figure 4A and Figure 4B,

1. Four thin pieces of elastic beams for measuring hinge moment.
2. High-strength cylinder opposite to elastic beam.
3. The fitting face of inside taper ($\triangleleft$ 1:5) connected with the sting conventional balance for measuring other five components.
4. A wedge slot for tightening up the hinge cap with sting balance
5. An inside taper hole for fitting of shaft of rudder
6. Two protruding keys used for being locked with another one to change the deflection angle ($\delta°$) and obtain test attitude of measured complete moving wing or rudder.

2.2 Structure of Singe Balance

The sting balance for measuring other five component is actually a conventional balance used in wind tunnel (see Figure 5 and Figure 7). Here on following are explanations for Figure 5.

(1). The structure design: Separate force measuring elements from transitive force element. The elastic beam of "cross horizontal type" on central k-k section (Figure 5) take charge of force of axial direction. Front, rear, left, right groups (4x4=16 pieces) of vertical thin elastic pieces symmetrical to the center of k-k section bear and transfer other five component (y, Q, Mx, My, Z) loads.

(2). On the front and back side of axial force measuring beam, bond one pieces of stain-gage respectively. They are specifically designed half bridge strain-gage (see Figure 6_ used for forming a Wheatstone four arm complete bridges and measuring axial force "Q". Advantages of this design are:

- Integral carves; compact structure; no mechanical hysteresis; return to zero; data repeatability
- Separation of force-measuring elements from force transmitting once results in small interaction and high shock-resistance.
- In bridge line of axial force measuring there are all together. Two pieces of strain-gage only 2mm away from each other. They are nearly in a same temperature filed with small temperature gradient therefore temperature of axial for measuring bridge influences little.

(3). On the front taper part of the balance (see Figure 5) there are key slot and wedge slot. These enable the balance for both conventional use and special conjunction with the hinge cap.

Use one positive wedge for tightening hinge cap and sting balance. The key is for roll direction positing on the design for both conventional and specific use is economic and ingenious.

3. Reference Center, Measureng Coordination System

General, reference center of conventional balance is at central position of each elastic element of balance. It is often put at symmetry center of axial force element, such as in the k-k section center shown in Figure 5. Our hinge moment balance is for measuring hinge moment of revolving on rudder axis. Therefore, its reference center is on the internal cone hole axial line. That is at the intersection of axial line of turning center of the rudder and longitudinal axis of sting balance. This intersect is selected as origin point of coordinates system. From which three mutually vertical right angle coordinates system. "Oxyz" are drawn (see Figure 8).

"Ox' axis coincides with longitudinal center axis of balance and points to head of the balance.

"Oy" axis is vertical to "Ox" and directs downward.

"Oxy" plane is symmetric longitudinal plane of balance

"Oz" axis is vertical to "Oxy" plane and according to right-hand coordination method.

The thumb points to "Ox" axis, fore finger to "Oy" axis and middle finger to positive direction of "Oz" axis.
Three force positive directions are defined as follows:
Direction of positive axial force "Q" is negative of "Ox" axial direction;
Direction of positive normal force "y" is same as that of "Oy" axis;
Direction of side force "Z" is same as "Oz" axial positive direction.
Positive direction of three moments are defined as follows:
About the hinge moment (M_H), according to right hand spiral method, the thumb directs to "Oz" axis, and spiral direction of other fingers are positive direction of the hinge moment. The same principal is applicable to "Mx" and "My" ("Mx" revolves round "Ox" axis and "My" revolves round "Oy" axis).
It should be stated that the hinge moment is moment revolving round the rudder axis.

4. Measurement Range

We have developed kinds of hinge cap of hub type and many have been installed on sting balances with different diameters. Thereupon, we have obtained the hinge moment combination meeting the needs for measuring in fact the range of balance can be permuted, combined and chosen.
Arbitrary selections in table 1 are examples of ranges permutations and combinations. H-24 in table 1 references to Figure 4A and Figure 5. I-18 in table 1, references to Figure 4A and Figure 7.

5. Bridges

On the four elastic elements of radiate hub-type hinge moment (hinge cap) bond strain-gauges forming a Wheastone bridge (see Figure 9). They are bridges for measuring hinge moment component.
Sensitive elements (except axial force element) of the sting balance bonded strain-gages produced by Beijing Institute of Aerodynamics (BIA). Brand number is BF600-2.5AA and BF550-2.5AA. These strain-gages are composed of component measuring bridge. See Figure 10A and 10B.
As mentioned above, in Figure 5, on the axial force element of the sting balance bonded special half-bridge strain-gages (see Figure 8) brand number is "BF-600-14BB"
The two half-bridge strain gages is composed of axial force measurement bridge as indicated in Figure 10A.

6. Static Calibration

6.1 Preparation

- Check machine hysteresis
- Check drift of each measuring bridges and lines
- Do temperature effect compensation to each measuring bridges and lines on the ground until output voltages of each component bridges are $\leq 40\ \mu v$

- Simulate shock of the wind tunnel on the ground and observe the resetting of zero

If normal with listed tests and the static stability of balance components examined, a static calibration can start.

6.2 Static Calibration Devices

Static calibration devices of hinge moment balance are different from those of conventional balance. They must be specifically produced. Figure 11 gives the new loading device for hinge cap six component loads. Center of the loading device is the reference center, also the intersection point of longitudinal axis and rudder axis of the hinge cap.

6.3 Static Calibration Method and Contents

6.3.1 Single-component calibration

Apply loads to each component and no loads to other components count main coefficient of single-component and interference coefficient of first-order term.

Apply loads to second-order component alternately and do static calibration. Count the cross interference coefficients.

After finishing the steps listed, for each component, the main coefficient, five interference coefficient of first-order degree, six interference coefficients of square degree and fifteen compound cross interference coefficients can be obtained.

We obtain altogether 27 coefficients for each component, that is 162 coefficients for six components. They form the balance formula.

6.3.2 Multi-component calibration

According to the six component load range required by complete model hinge moment test, select maximum loading value that can cover the measuring range for each component combine sixty groups of combinative loads by permutation then apply load calibrations to each group one by one. Count and determine the 162 balance formula coefficients by the optimum approach method according to the load values applied to each component and the increments of corresponding outputs. Formula of hinge moment balance H-24 is as shown in table 2 and that of I-18 in table 3.

7. Dynamic Calibration

Dynamic calibration means to fit known-data model on hinge moment balance in wind tunnel and applied blowing wind test to it to examine its dynamic stability in blowing wind.

7.1 Impact test

- Model attitude: $\alpha=\beta=\gamma=0°$ without change
- Mach number: $M\infty=3.0$
- Start the wind tunnel and stop it when airflow is stable (the shorter, the better) to observe reading condition of resetting of zero

7.2 Temperature effect and compensation test

- Model attitude: $\alpha=\beta=\gamma=0°$ without change
- Mach number: transonic speed, $M\infty=0.8$
- Mach number: supersonic speed, $M\infty=2.0$

Start the wind tunnel and collect data every twenty sections after airflow is stable: supersonic speed, 100 seconds; and transonic speed, collect 360 seconds. observe influence to output reading. When a components output voltage over 21μv.

7.3 Repeatability Test

- Model attitude: change angle of attack(α), remain "β" and "γ" unchanged. $\alpha°=-4,-2,-1,0,1,2,4,6,8,10$
- Mach number: transonic speed, $M\infty=0.8$
  supersonic speed, $M\infty=2.0$
- Under each Mach number, repeat seven wind blowing, compute aerodynamic coefficient mean-square root repeatability deviation.

8 Conclusions

The hinge moment balance for complete model given in table 1 have all passed static calibration, dynamic calibration, and other tests. Results are as following: static calibration precision within 0.1~0.5%; dynamic calibration shock resetting of zero; output reading of temperature influence less tan 20 μv; and repeatability is very good. These balances have all accomplished a large quantity of aerodynamic characteristics tests of hinge moment for complete model.

Techniques discussed in this paper are unique in the following three aspects:

Put cap on head of the sting balance

Adopt :"cross horizontal integral" axial force element in the sting balance structure

Adopt half-bridge strain -gage

Reference

(1). Kaike, Guo "Hinge moment Balance"
The Forth National Wind Tunnel Balance Technical Meeting
P.R. China, September, 1989
(2). The Wind Tunnel Strain-Gage
GJB, P.R. China, 1989.

Tables

Figures

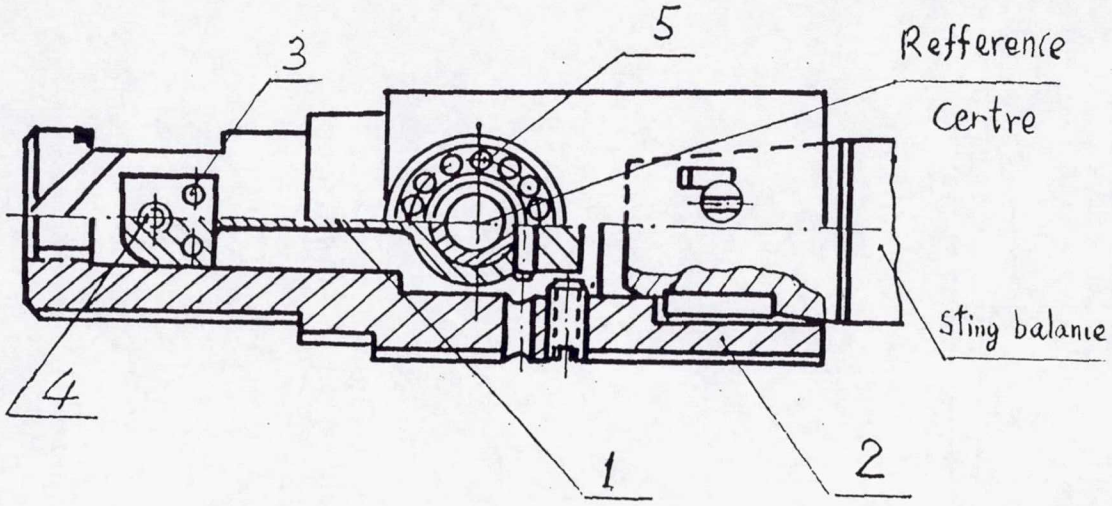

Figure 1

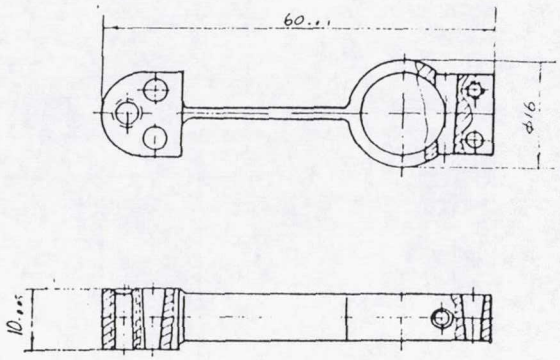

Figure 2

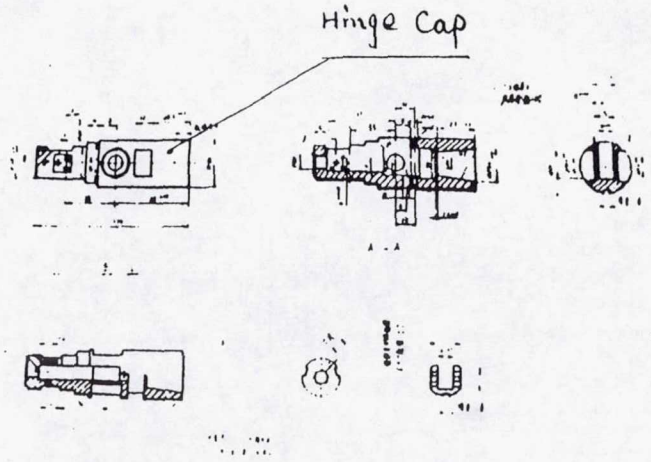

Figure 3

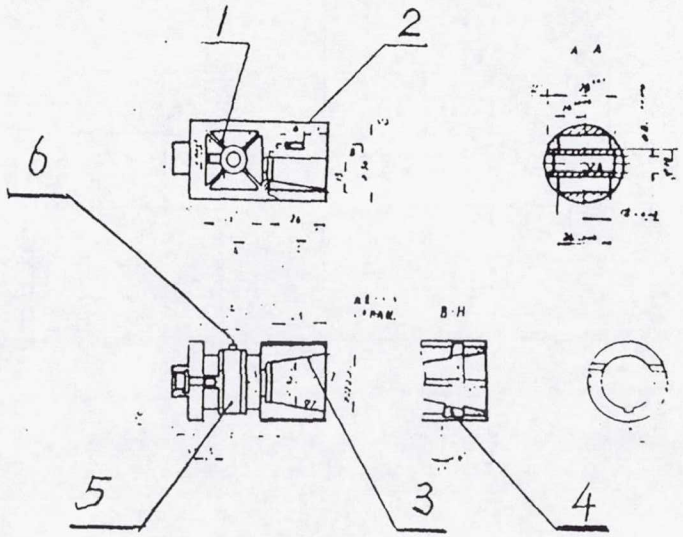

Figure 4A

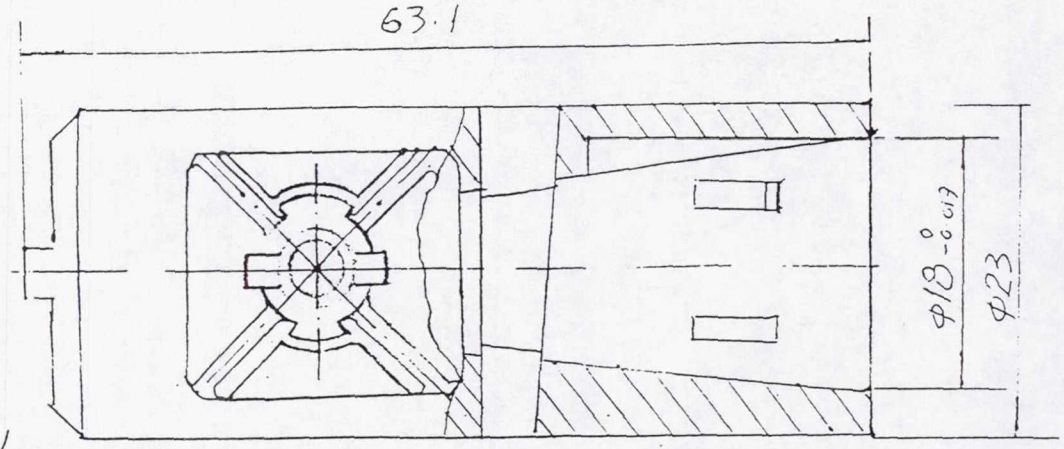

Figur 4B

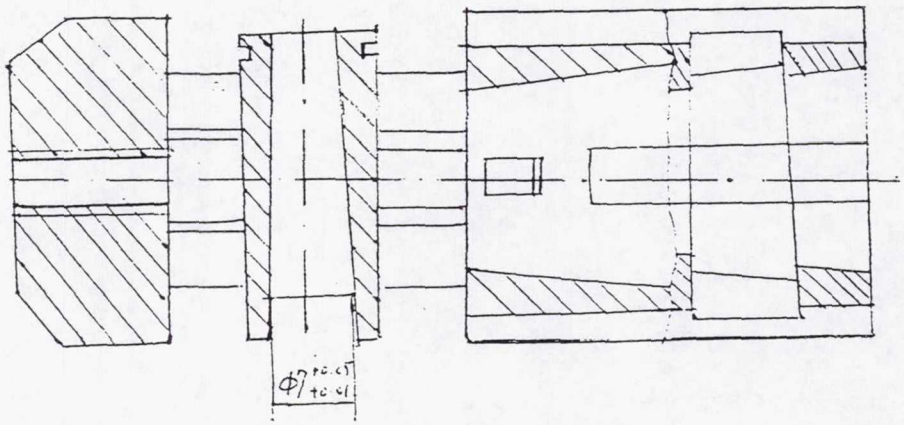

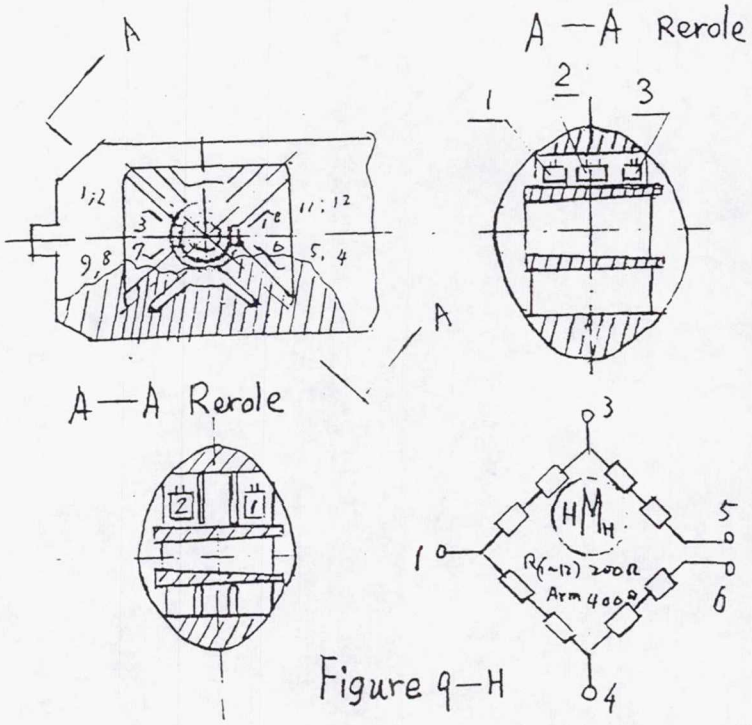

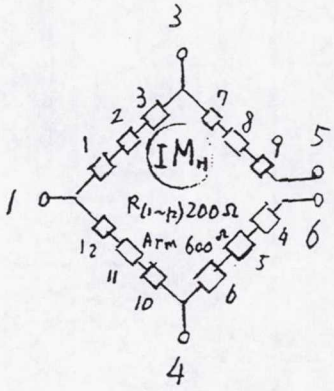

Figureq — I

Figure 9—H

Figure 9

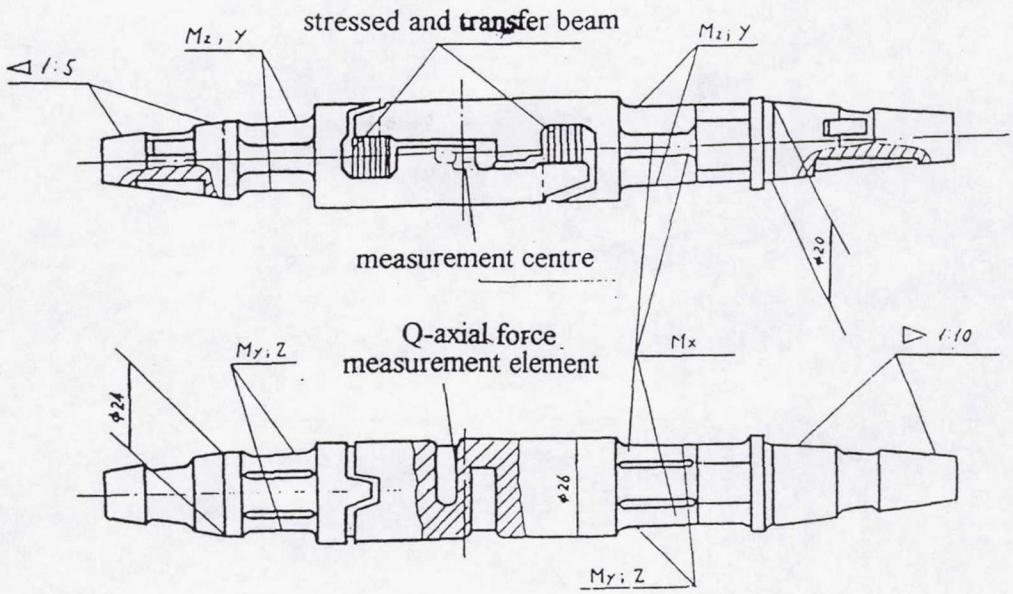

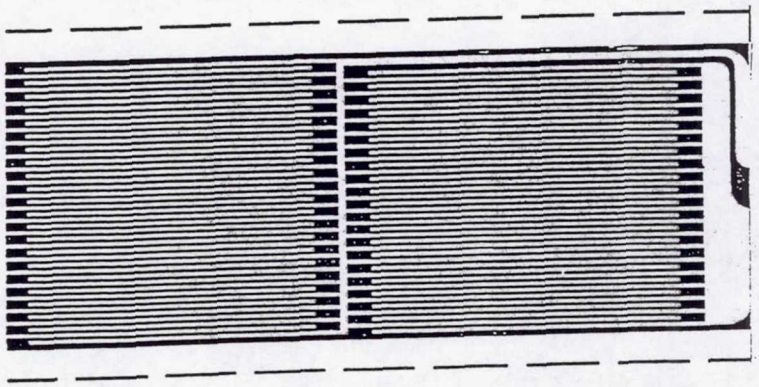

Strain gaiv — BIA Figure 6

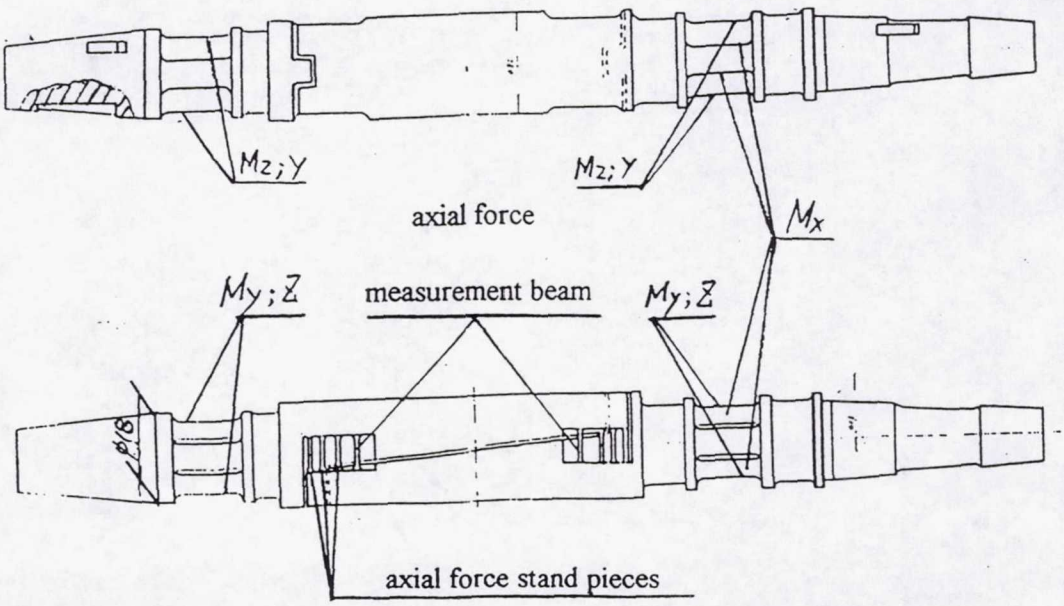

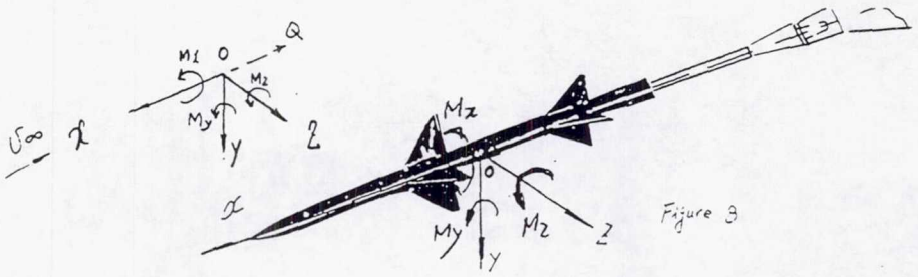

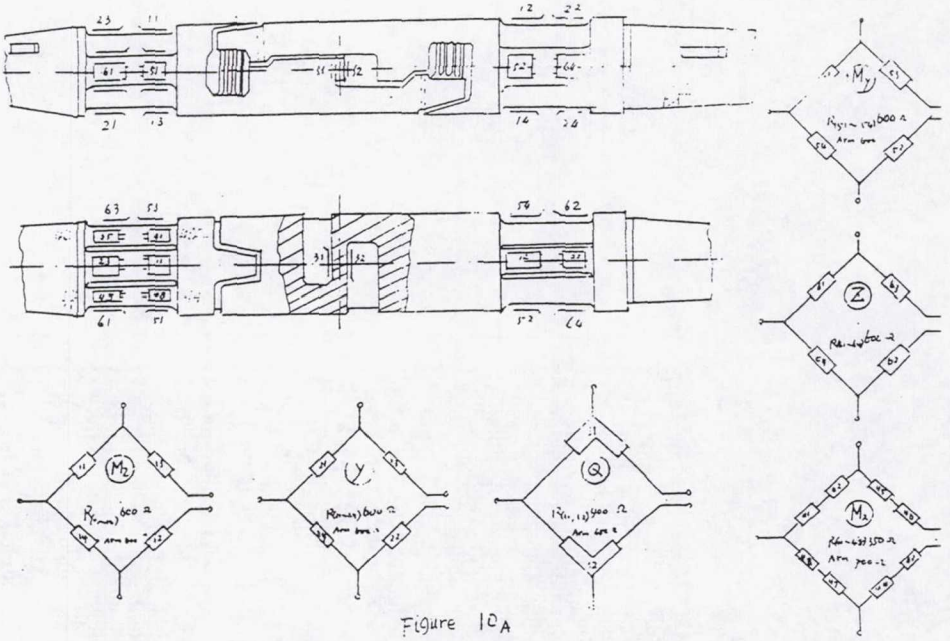

Figure 10A

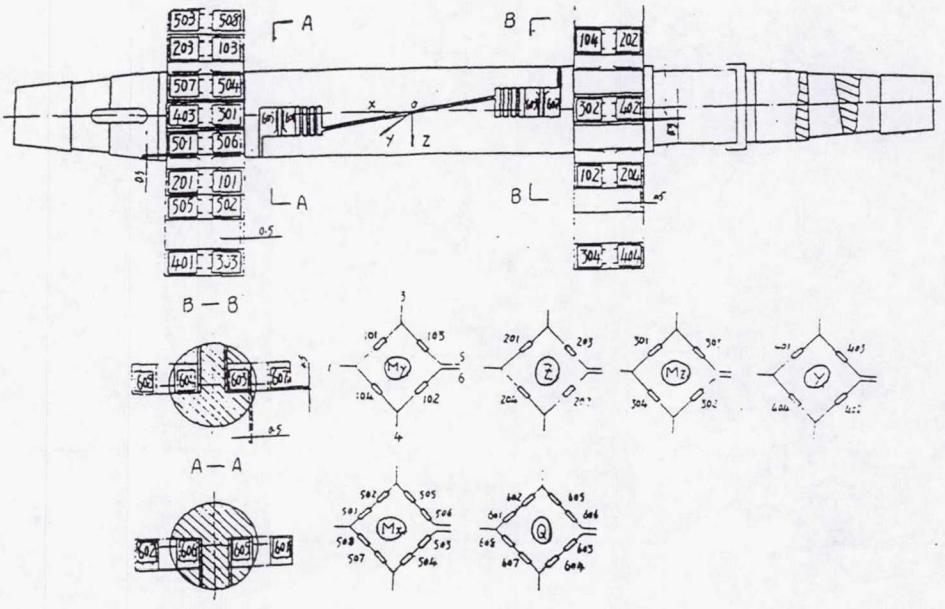

figure 10 B

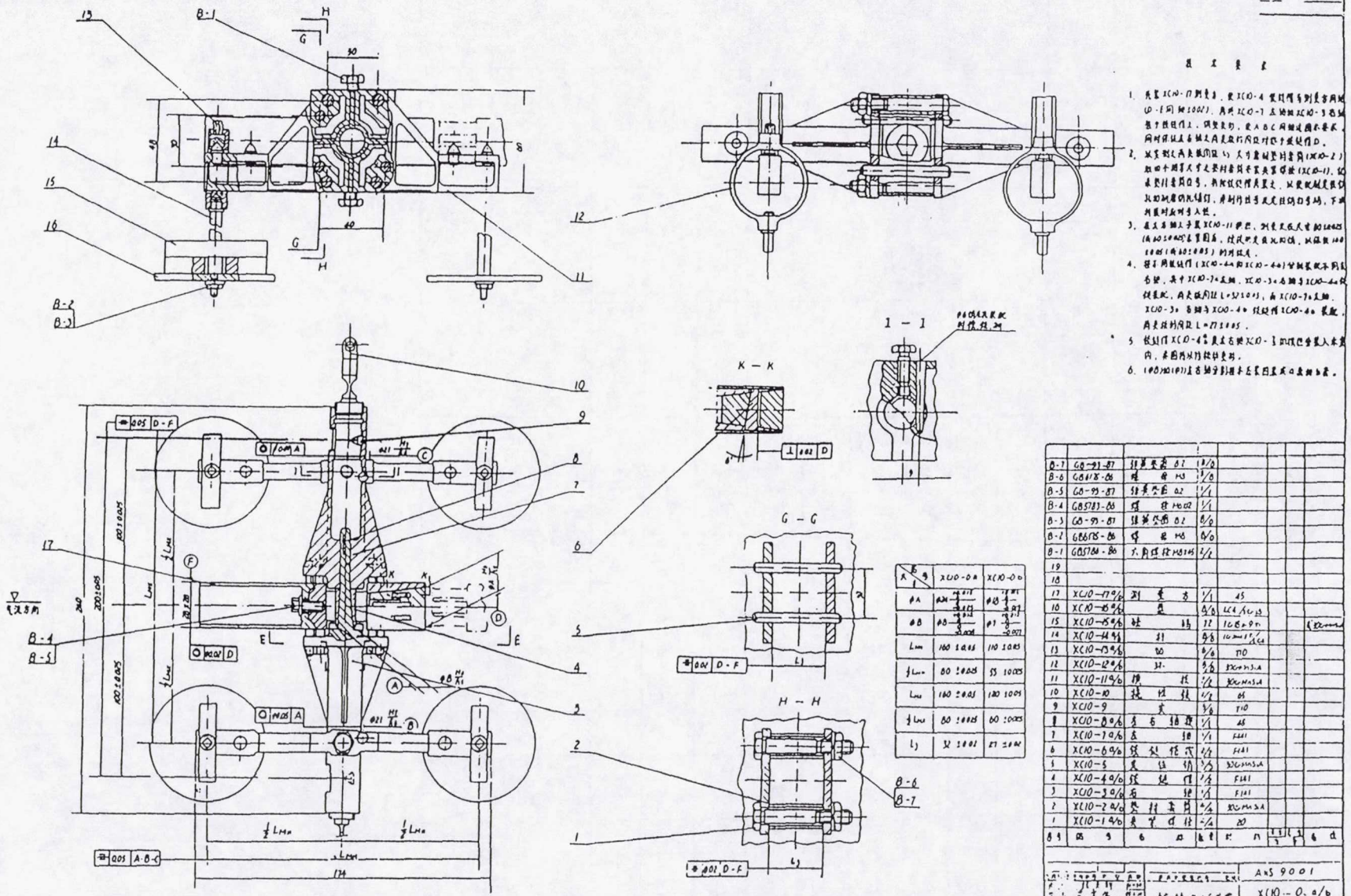

序号	代号	名称	数量	材料	备注
B-7	GB-93-87	弹簧垫圈 B7	1/0		
B-6	GB6178-86	螺母 M5	1/0		
B-5	GB-93-87	弹簧垫圈 B2	1/1		
B-4	GB5783-86	螺钉 M6×12	1/1		
B-3	GB-93-87	弹簧垫圈 B2	6/0		
B-2	GB6175-86	螺母 M5	6/0		
B-1	GB5780-86	六角螺栓 M5×16	1/1		
19					
18					
17	XC10-17	对定支承	1/1	45	
16	XC10-16	垫圈	6/6	65Mn 淬火 43	
15	XC10-15	螺柱 M8	12	10B21 渗碳淬火	
14	XC10-14	对定销	6/6	20Mn2B 渗碳淬火	
13	XC10-13	支架	6/6	T10	
12	XC10-12	支承头	6/6	20CrMnTi 渗碳淬火	
11	XC10-11	压盖	1/1	20CrMnTi 渗碳淬火	
10	XC10-10	铰链销轴	1/1	45	
9	XC10-9	支承	3/6	T10	
8	XC10-8	夹紧螺钉	1/1	45	
7	XC10-7	左轴	1/1	HT200	
6	XC10-6	铰链销支承	1/1	HT200	
5	XC10-5	支承轴	1/1	20CrMnTi 渗碳淬火	
4	XC10-4	铰链支承	1/1	HT200	
3	XC10-3	右轴	1/1	HT200	
2	XC10-2	夹具支架	1/1	20CrMnTi 渗碳淬火	
1	XC10-1	夹具体	1/1	20	

序号	图号	名称	数量	材料	重量	备注

标记	处数	分区	更改文件号	签字	年月日
设计	审核	工艺	标准化	批准	

ANS 9001

铣键槽专用夹具

XC10-0.a/b

1:1

Figure 11

Table 1 Combinatorial the hinge moment balance range

Range / Sting balance No. / Hinge Cap No.	Hinge moment Component	Other five component				
	M_H	Y	G	M_x	M_y	Z
	Newton. meter	N	N	N.M	N.M	N
A — 14	± 0.170	±400	300	±20	±30	±300
B — 19	± 0.350	±800				
C — 19	± 0.750	±800				
D — 19	± 2.000	±800				
E — 19	± 4.000	±800				
F — 19	± 6.500	±800				
G — 21	± 1.000	±350	240	±10	±10	±80
H — 24	± 1.280	±800	250	±18	±26	±360
I — 18	± 0.640	±580	200	±16	±19	±300
⋮	⋮	⋮	⋮	⋮	⋮	⋮
M — N618C	± 0.100	±250	125	±12.5	±7.5	±50

Table 2

```
\:624y1yyb.kkk                94418
fy            z            Mz            y            Mx            Q

fy=0.001349(12V K=500)*nmy+ .120132 *z+ .048801 *Mz+ .003369 *y-.041948 *Mx-.00003 *Q-.000905 *My^2-.000134 *z^2-.028884 *Mz^2
.000008 *y^2-.001322 *Mx^2+ 9.999999E-06 *Q^2+ .000887 *My*z-.021121 *My*Mz-.000202 *My*y+ .00091 *My*Mx-.000289 *My*Q-.005129 *
:*Mz-.000051 *z*y-.000029 *z*Mx+ .000067 *z*Q+ .00008 *Mz*y-.014417 *Mz*Mx+ .000328 *Mz*Q+ .000018 *y*Mx+ 9.999999E-06 *y*Q+
.000197 *Mx*Q


:=-.64307 *My+0.01800(12V K=500)*nz + .176251 *Mz+ .006679 *y+ .341643 *Mx-.002435 *Q-.041367 *My^2-.000123 *z^2+ .159913 *Mz^2+
.000082 *y^2-.005831 *Mx^2+ .00007 *Q^2-.001346 *My*z+ .291649 *My*Mz+ .000605 *My*y+ .011417 *My*Mx+ .002378 *My*Q+ .019351 *z*Mz
.000107 *z*y-.001602 *z*Mx-.000621 *z*Q+ .001145 *Mz*y-.210624 *Mz*Mx-.004022 *Mz*Q+ .001354 *y*Mx-.000024 *y*Q-.001136 *Mx*Q


z=-.000961 *My-.000022 *z+0.0001621(12V K=250)*nmz+ .000805 *y-.01654 *Mx-.000019 *Q+ 0 *My^2+-.000001 *z^2-.002728 *Mz^2+ .000001
y^2+ .00022 *Mx^2+ .000001 *Q^2+ .000014 *My*z+ .001128 *My*Mz-.000031 *My*y-.000531 *My*Mx+ .000017 *My*Q-.000022 *z*Mz+ 0 *z*y+
.00003 *z*Mx+ .000001 *z*Q+ .000033 *Mz*y+ .000554 *Mz*Mx+ .000015 *Mz*Q+ .000018 *y*Mx+ .000001 *y*Q+ .000006 *Mx*Q


=-.397677 *My+ 8.681699E-02 *z+ .342342 *Mz+0.04012(12V K=250)*ny + .374125 *Mx-.003648 *Q+ .006564 *My^2-.000039 *z^2+ 0 *Mz^2+
.000004 *y^2-.021254 *Mx^2+ .000105 *Q^2-.001185 *My*z+ .063506 *My*Mz+ .001385 *My*y-.006039 *My*Mx+ .000717 *My*Q+ .01936 *z*Mz+
.000233 *z*y-.00103 *z*Mx-.000275 *z*Q+ .005109 *Mz*y+ .11517 *Mz*Mx-.004342 *Mz*Q-.000382 *y*Mx-.000402 *y*Q+ .000246 *Mx*Q


x=-.102336 *My+ .008757 *z+ .007357 *Mz-.000163 *y+0.0009428(12V K=500)*nmx-.000068 *Q+ .000287 *My^2-.00004 *z^2+ .00319 *Mz^2+
.000001 *y^2-.00087 *Mx^2+ .000006 *Q^2+ .000032 *My*z-.007634 *My*Mz-.000596 *My*y+ 0 *My*Mx-.000008 *My*Q-.001174 *z*Mz-.000033 *
*y+ .00087 *z*Mx+ .000005 *z*Q-.000056 *Mz*y-.001596 *Mz*Mx-.000413 *Mz*Q-.000047 *y*Mx+ .000001 *y*Q+ .000083 *Mx*Q


= .123331 *My+ .211683 *z-.598559 *Mz+ .030827 *y-.568881 *Mx+0.01769(12V K=500)*nQ + .005901 *My^2+ .001091 *z^2-.12948 *Mz^2+
.00039 *y^2-.058577 *Mx^2-.00011 *Q^2-.003223 *My*z-.065251 *My*Mz+ .000778 *My*y+ .056573 *My*Mx-.000736 *My*Q-.027787 *z*Mz+
.00017 *z*y-.003969 *z*Mx+ .000497 *z*Q+ .012865 *Mz*y-.116613 *Mz*Mx+ .004533 *Mz*Q-.005055 *y*Mx+ 0 *y*Q-.000305 *Mx*Q
```

Table 3

```
18y1yyb.kkk                94420
          z              Mz              y              Mx              Q

J.0009959(9V K=500)*nmy+ .100912 *z+ .011314 *Mz+ .001264 *y+ 8.999999E-03 *Mx+ .00054 *Q+ .001391 *My^2-.000309 *z^2+ 0 *Mz
)0001 *y^2+ .001682 *Mx^2+-.000002 *Q^2+ .001597 *My*z+ .003094 *My*Mz+ .000044 *My*y+ .000546 *My*Mx-.000725 *My*Q+ .000613
z+ .000024 *z*y+ .000152 *z*Mx+ .000143 *z*Q+ .000059 *Mz*y-.004394 *Mz*Mx-.000068 *Mz*Q+ .000478 *y*Mx-.000018 *y*Q-.000087
]


.772768 *My+0.01504(9V K=500)*nz -.468203 *Mz-.002003 *y+ .460796 *Mx-.021923 *Q-.026669 *My^2-.001584 *z^2+ 2.810175 *Mz^2
)0539 *y^2-.030134 *Mx^2+ .000631 *Q^2+ .006827 *My*z+ .219534 *My*Mz-.004716 *My*y+ .029177 *My*Mx+ .003557 *My*Q+ .007056
00961 *z*y-.000653 *z*Mx-.000976 *z*Q+ .032871 *Mz*y+ 0 *Mz*Mx+ .009903 *Mz*Q+ .009943 *y*Mx+ .001005 *y*Q+ .004484 *Mx*Q


 .002762 *My+ .000022 *z+0.00009842(9V K=250)*nmz+ .000773 *y-.002113 *Mx-.000017 *Q+ .00017 *My^2+ .000006 *z^2+ .005664 *M
*y^2-.00005 *Mx^2+ .000006 *Q^2-.000103 *My*z+ .000681 *My*Mz+ .000028 *My*y-.000116 *My*Mx-.000014 *My*Q+ .000032 *z*Mz+
00002 *z*y+ .000034 *z*Mx+ 0 *z*Q+ 0 *Mz*y-.001116 *Mz*Mx+ .000179 *Mz*Q+ 9.699999E-05 *y*Mx+ .000002 *y*Q-9.999999E-06 *Mx*


.0821 *My-.021327 *z+ 1.154885 *Mz+0.02914(9V K=250)*ny -.350626 *Mx+ .00163 *Q+ .013071 *My^2+ .001208 *z^2-1.003951 *Mz^2+
00088 *y^2-.013643 *Mx^2-.00029 *Q^2+ 0 *My*z-.292925 *My*Mz+ .0018 *My*y-.031074 *My*Mx+ .001322 *My*Q+ .00842 *z*Mz+ .0003
-.008565 *z*Mx-.000366 *z*Q-.012508 *Mz*y+ .151461 *Mz*Mx+ .004916 *Mz*Q-.002476 *y*Mx-.001321 *y*Q-.002452 *Mx*Q


-.005887 *My+ .000263 *z-.024859 *Mz-.001341 *y+0.0008538(9V K=500)*nmx-.000057 *Q+ 0 *My^2+ .000033 *z^2-.025893 *Mz^2-.000
+ .000207 *Mx^2+ .000006 *Q^2+ .000133 *My*z-.008085 *My*Mz-.001536 *My*y-.000468 *My*Mx-.000056 *My*Q-.000852 *z*Mz-.000019
002138 *z*Mx-.000007 *z*Q+ .000817 *Mz*y+ .002438 *Mz*Mx+ .000814 *Mz*Q-9.999999E-06 *y*Mx+ .000008 *y*Q+ .000015 *Mx*Q


1.632806 *My+ .197712 *z+ .173315 *Mz+ .035241 *y-.698896 *Mx+0.01185(9V K=1000)*nQ -.035557 *My^2+ .001199 *z^2-.669683 *M
01736 *y^2-.106788 *Mx^2+ .000286 *Q^2-.004628 *My*z-.022506 *My*Mz+ .004697 *My*y+ .008127 *My*Mx+ .004901 *My*Q+ .002817 *
00639 *z*y+ .004095 *z*Mx+ .000374 *z*Q-.006134 *Mz*y+ .071897 *Mz*Mx-.003695 *Mz*Q-.00609 *y*Mx+ .000262 *y*Q+ .002631 *Mx*
```

DEVELOPMENTS TO IMPROVE THE ACCURACY OF HALF-MODEL BALANCE MEASUREMENTS IN THE ARA 2.74 m x 2.44 m (9 ft x 8 ft) TRANSONIC WIND TUNNEL

Adrian J. Day, Nigel Corby
Aircraft Research Association Ltd,
Manton Lane, Bedford MK41 7PF, England

SUMMARY

Tests on half span models provide a significant contribution to the programme of work performed in the ARA Transonic Wind Tunnel. The half model concept is considered mainly as a means of obtaining high quality incremental aerodynamic data. To achieve this objective, balance performance has to be maximised. Details of an evolutionary programme of work undertaken at ARA to improve balance quality is presented.

INTRODUCTION

Tests on half span models provide a significant contribution to the programme of work performed in the ARA 2.74 m x 2.44 m (9 ft x 8 ft) Transonic Wind Tunnel (TWT). The increased model scale compared to a full span model allows testing at higher chordal Reynolds numbers and more detailed representation of model components. In addition to military applications, half span models are extensively used for transport aircraft testing as a means of obtaining propulsion installation effects, using either through-flow nacelles (TFN) or turbine-powered simulators (TPS), and to investigate incremental effects associated with detailed design modifications to small components such as winglets, pylons and flap-track fairings. Figure 1 shows a typical half span model installed in the working section of the TWT.

With the ever increasing demand for greater precision, an ongoing improvement programme was initiated in 1990 and this has highlighted a number of areas associated with the balances themselves, the air feed assembly and the calibration techniques that have had the potential to degrade data quality. This paper provides details of the half model balances at ARA and recent developments of the balance assembly and calibration techniques that have lead to improved accuracy and repeatability of half model data measured in the ARA TWT.

GENERAL DESCRIPTION

Half span models are installed in the TWT mounted on an underfloor five-component strain gauge balance. A general arrangement of the tunnel installation is shown in Figure 2. The balance is immersed in an oil-filled chamber and maintained at a constant temperature of approximately 310 /K using a thermostatically controlled heating element.

Two half model balances are available for half span model testing at ARA. A high load range unit, commissioned in 1968, is used primarily for testing beyond buffet onset. This is complimented by a low load range unit used for high accuracy drag measurement. The original low range half model balance, commissioned in 1972, has recently been replaced by a new balance commissioned in 1994. Details of the capacities of the half model balances are given in Table 1.

Each balance consists of a 4-bar cage measuring five load components (excluding Side force). Figure 3 shows a half model balance prior to installation in the half model cart balance housing. Each balance beam is instrumented with two sets of strain gauges measuring each load component. The output from these strain gauge bridges effectively gives two separate outputs for each component.

Both balances have the ability to carry high pressure air to the model to power Turbine Powered Simulators (TPS), air motors or for blown nozzles. Two independent supplies are available. Each supply is capable of delivering accurately metered flow at rates of up to 3.5 kg/sec (7.7 lb/sec).

The underfloor balance lends itself particularly well to the TPS technique since the air transfer system from earth to live is perpendicular to the balance Normal and Axial force axes. This means that the interaction and redundancy of the relatively flexible air feed pipes on the balance signals are both low and repeatable. Details of the balance and air feed assembly are given in Figure 4.

LOW RANGE BALANCE

In order to measure the incremental differences due to small changes in configuration, it is necessary to discriminate very small changes in the aerodynamic forces on the model and this is only possible with a high standard of repeatability within a given test series. During the 1980s the Association developed a technique for half model testing that gave a drag repeatability within a given test series of approximately one count ($\Delta C_D = 0.0001$) for a typical transport aircraft model.

During a series of half model tests using the low-range balance early in 1990, it was noted that drag repeatability fell outside of acceptable limits with repeat tests on a given configuration showing a variation of 2-3 drag counts. A detailed investigation was therefore implemented to re-establish the standard. During the course of this investigation a diurnal variation of drag was

identified which could be attributed to the small changes in temperature difference between the tunnel plenum shell and the freestream (Reference 1). However, while significant, the buoyancy effect induced by the thermal effects did not account for all of the non-repeatability.

It was initially considered that the balance fixation might be suspect. As a result, the number of fixation bolts and dowels in the base of the balance were significantly increased. In addition, a 0.125 mm (0.005") dished seating ring was fitted under the balance in the housing to reduce the distortion of the base thought to arise due to balance loading.

Subsequent re-calibration of the modified balance assembly revealed that one of the Normal force gauges exhibited notable hysteresis and zero shifts during loading while all other components were considered to be satisfactory. The balance was then removed from its housing to allow for the inspection of a possible crack in the region of the Normal force flexures and to check for any strain gauge faults.

After repeated loadings of the balance in isolation and consultation with metallurgists, it was concluded that the fault may be due to a crack or some other form of metallic degradation in the region of the gauges on one of the Normal force flexures. As part of the investigation, a photoelastic strip was bonded to one of the flexures to monitor the stress levels during loadings. These investigations were inconclusive and gave no clear indication of the nature of the fault.

A series of material hardness checks were then conducted on the balance with surprising results. The original EN24 steel billet was scrapped during manufacture by a sub-contractor and replaced by them with one of 'similar quality'. However, the hardness tests indicated that the heat treatment process may not have been successful or that an inferior quality steel was used as a replacement.

With the low range balance effectively out of service (good quality data could only be obtained up to a maximum normal force of 2kN), the high range balance was pressed into use for drag measurements on half span model tests. It was demonstrated that the balance did, with the application of stringently adhered to test technique, provide adequate results.

The decision to procure a replacement low range balance was made early in 1992. There however still existed an interim requirement for a sensitive axial force half model balance for isolated TPS calibrations. Bearing in mind that only one of the two available normal force bridges seemed to be affected, the low range balance was reinstalled, calibrated and certified for use over a low load range.

HIGH RANGE BALANCE

The high range balance has been used since 1968 for tests of half span military models at high incidence and for tests of civil transport models beyond buffet onset. However, following problems with the low range balance and the subsequent reduction of its permissible load range, the high range balance was utilised for model drag tests until the new low range balance was commissioned. During this time, the balance fixation was modified in line with the low range balance.

However, it became apparent during a model test series that there was unacceptable data repeatability when the air-feed pipes were pressurised. Wind-off balance pressurisation showed that this was most apparent on the Normal force, Pitching moment and Rolling moment bridges, Figure 5. Significant hysteresis loops and offsets in the component reading were evident as the pressure in the air-feed pipes was cycled.

It was thought that the problems were caused by movement in the earthed end of the air-feed assembly which effectively induced a moment into the balance. The earthed part of the air-feed assembly was different to that shown in Figure 4. The air tube support housing was originally a two piece splined arrangement held together by a large locking nut. Although this was an elegant engineering arrangement, it was overly complicated with many joints that were susceptible to wear. A simpler, single piece structure that bolted directly to the balance housing was designed and installed on the balance assembly. Subsequent pressure cycling of the air-feed system showed that the hysteresis loops and offsets had been removed, as can be seen in Figure 6.

This modified air-feed assembly was then installed onto the low range half model balance.

NEW LOW RANGE BALANCE

The design of the replacement low range balance was essentially the same as its forebear. The use of increasingly larger half span models for drag measurement work prompted the decision to thicken the flexures slightly to cater for the associated higher loads. A slightly stiffer balance would also lend itself for occasional buffet onset investigations. The use of previously unavailable finite element analysis methods allowed the effect of small modifications to the original design to be assessed. The new balance design incorporates an integrated seating ring similar to those fitted to the high range and original low range balances.

A suitable EN25V steel billet was procured and sent for ultrasonic scanning. The scanning process highlighted three small inclusions within the material. Careful alignment of the billet prior to machining allowed the inclusions to be removed during the machining operation to cut the flexures.

Due mainly to its large size and the inability to perform all of the tooling operations in-house, manufacture of the balance was placed in the hands of a sub-contractor. Towards the end of manufacture, an unfortunate machining error occurred in the form of severe undercutting of the webs, at the top and bottom of the aft Normal force flexure. Significant delays during balance design and manufacture combined with an ever increasing requirement for a replacement low load range balance resulted in the decision to remove the undercuts by thinning the flexure and to accept the balance in this modified form. The thinner Normal force flexures effectively reduce the maximum balance loads by approximately 20%. This precludes its use for buffet onset investigations as originally intended.

Commissioning Trials

The new low range balance was fitted with strain gauges and mounted in the model cart. Prior to calibration extensive static loadings were applied to the balance to ensure that the balance characteristics remained constant. The balance was then calibrated over its full load range. The gauge sensitivities for all components compared well with theoretical values and residual errors fell well within acceptable limits.

A half span civil aircraft model, typical of those normally tested, was then mounted on the balance and the model cart installed in the TWT working section. Repeat incidence traverses were performed over a range of Mach numbers using ARA's standard test technique for civil half model testing. The data thus obtained could then be used for a direct comparison with data from an identical configuration tested previously on the high range half model balance.

Force and moment data from the new low range balance, Figure 7, displays good quality with run to run drag repeatability generally falling within $\Delta C_D = \pm 0.00003$ about a mean. Comparisons of Mach number smoothed, averaged data, Figure 8, measured using the high range and low range balances are again very good with test to test drag repeatability generally falling within $\Delta C_D = \pm 0.00005$ about a mean. It should, however, be noted that long term test to test repeatability using the high range balance has previously been shown, by a relatively large sample of data, to be within $\Delta C_D = \pm 0.0003$ about a mean.

BALANCE CALIBRATION

ARA's half model balances are calibrated whilst installed within the model cart. A loading tongue is mounted to the balance in a similar manner to a normal model wing fixation. A rigid steel loading frame is then lowered over the tongue and fixed to the non-metric (earthed) balance housing. Figure 9 shows the loading frame assembly mounted on a half model cart.

Force loads are applied to the balance using a pair of dedicated load cells. A 22 kN (5000 lb) device is used to apply Normal force, Pitching moment and Rolling moment whilst a 4.5 kN (1000 lb) device is used to apply Axial force and Yawing moment. Both load cells attach to the loading

frame with the loads hydraulically applied to the loading tongue via a solid linkage fitted with a flexure.

Normal Force Loadings

Following the improvements in the fixation of the air-feed assembly, the high range half model balance was calibrated prior to the commencement of a wind tunnel test campaign. Force loads were applied using the ARA half cart loading frame. A sample of the balance component residual load errors due to Normal forces applied at three different loading points are presented in figure 10. It can be seen that there were not only differences in the residual errors when loads were applied at different load points (errors that could not be removed by a modification to the mathematical model), but also clear evidence of non-repeatability from repeat loadings. At the time it was thought that this was the limit of the balance capabilities when point loads were applied.

The wind tunnel tests following the calibration included a significant amount of repeat testing and results from these tests suggested that the balance measurement repeatability was considerably better than had been shown by the calibration results. Therefore, after the wind tunnel tests had been completed, the model was removed from the balance and the loading frame reinstalled. Once again, residual errors from repeat Normal force loadings showed significant levels of non-repeatability. These errors suggested that the load application method was probably introducing spurious errors into the data. The loads were applied via the double knife-edge linkage arrangement shown in Figure 11. This had been designed to allow for any deflection of the loading tongue under load. However, it was found that the computed Axial force residual errors associated with Normal force loadings were influenced by the orientation of the knife-edges. The knife-edges were locking under load preventing them from acting in the intended manner.

The knife-edges were removed and replaced with the simple linkage shown in Figure 12. A sample of the residual errors measured using this linkage are presented in Figure 13 and it can be seen that these are significantly reduced from those measured using the knife-edge arrangement.

The data from the wind tunnel tests were then re-computed using the balance matrices derived from these post-test loadings. The computed drag data were generally shifted by up to 2 counts compared with data computed using matrices derived from the previous loadings.

The modified loading assembly was later used to perform initial Normal force loadings on the new low range balance. A sample of the balance component residual errors due to applied Normal force are presented in Figure 14. The non-linearity evident in the Axial force and Pitching moment residuals at low load was found to be due to the excessive stiffness of the flexure within the Normal force load cell assembly. Reducing the diameter of the linkage connecting the load cell to the loading tongue, thus allowing the linkage itself to act as a flexure, produced significant improvements in the residual errors, shown in Figure 15.

The modifications made to the loading assembly suggest that further improvements may be made if greater flexibility is introduced to the linkage. Development work currently in progress is centred around replacing the solid linkage with a flexible wire rope.

Axial Force Loadings

During a calibration of the high range balance, residual loads from a series of Axial force loadings were consistently larger than expected. This was thought to be due to some form of deformation or misalignment of the linkage within the Axial force load cell assembly. An alternative loading assembly consisting of a 2.2 kN (500 lb) load cell mounted on a frame secured at one end of the model cart was designed. A thin wire rope is used to connect the load cell to the loading tongue. Force loads are applied by inducing tension in the rope using a turnbuckle. This method of load application has proven to be very successful for the application of loads up to 1.1 kN (250 lb) on the high range balance reducing axial force residual errors from typically ±0.9 N (±0.2 lb) to ±0.25 N (±0.05 lb). This technique has been adopted for calibration of the new low range balance.

CONCLUDING REMARKS

In order to meet customer demands for highly accurate balance measurements on half span models at transonic test Mach numbers, ARA has focused resources onto the further development of underfloor strain gauge balances. In addition to procuring a new more sensitive balance, detailed development activities have enabled the data quality from existing balances to be significantly enhanced. It would now seem that the excellent repeatability of aerodynamic data from the execution of repeat polars is to a higher standard than that achieved during the calibration process. Efforts have, and are being directed towards improving the balance loading techniques. However, since relatively small balance residual errors are currently being achieved, it is considered that further progress will only be made by addressing a number of detailed elements in the whole of the balance calibration process.

Commissioning of a new half span model balance with a high pressure air transfer system and relatively high sensitivities is almost complete. This has considerably benefited from the experience gained with the existing ARA half model balances and promises to be a tool for high quality aerodynamic wind tunnel research.

REFERENCES

1. Stanniland, D.R., Burns, I.F., Green, Dr J.E. : Investigation of a Thermal Buoyancy Effect on the Drag of Half Models Tested in the ARA Transonic Wind Tunnel. ARA Technical Memo 407. May 1994.

Table 1. Capacity of ARA Half Model Balances

COMPONENT	HIGH RANGE		NEW LOW RANGE		OLD LOW RANGE	
SIDE FORCE N (lb)	-		-		-	
NORMAL FORCE N (lb)	27579	(6200)	11466	(2577)	1779	(400)
AXIAL FORCE N (lb)	3781	(850)	1093	(246)	578	(130)
PITCHING MOMENT Nm (lbft)	2712	(2000)	699	(516)	176	(130)
ROLLING MOMENT Nm (lbft)	20340	(15000)	9715	(7165)	2712	(2000)
YAWING MOMENT Nm (lbft)	2848	(2100)	1333	(982)	881	(650)

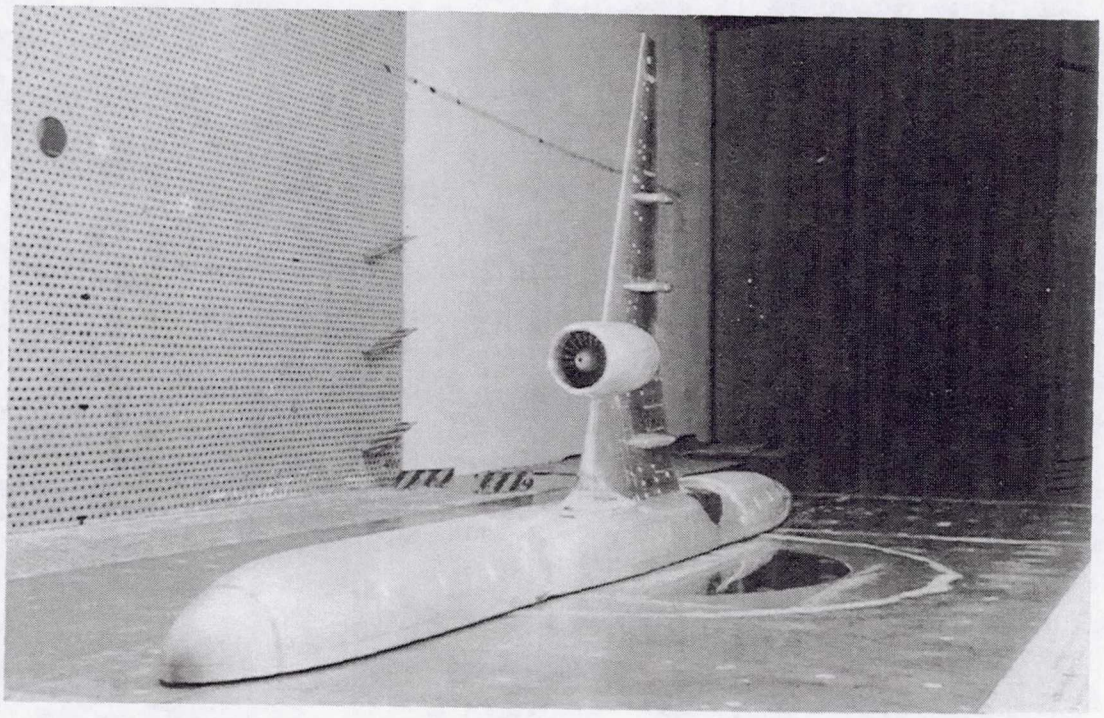

Fig.1 Typical Semi-Span Model In The ARA Transonic Wind Tunnel

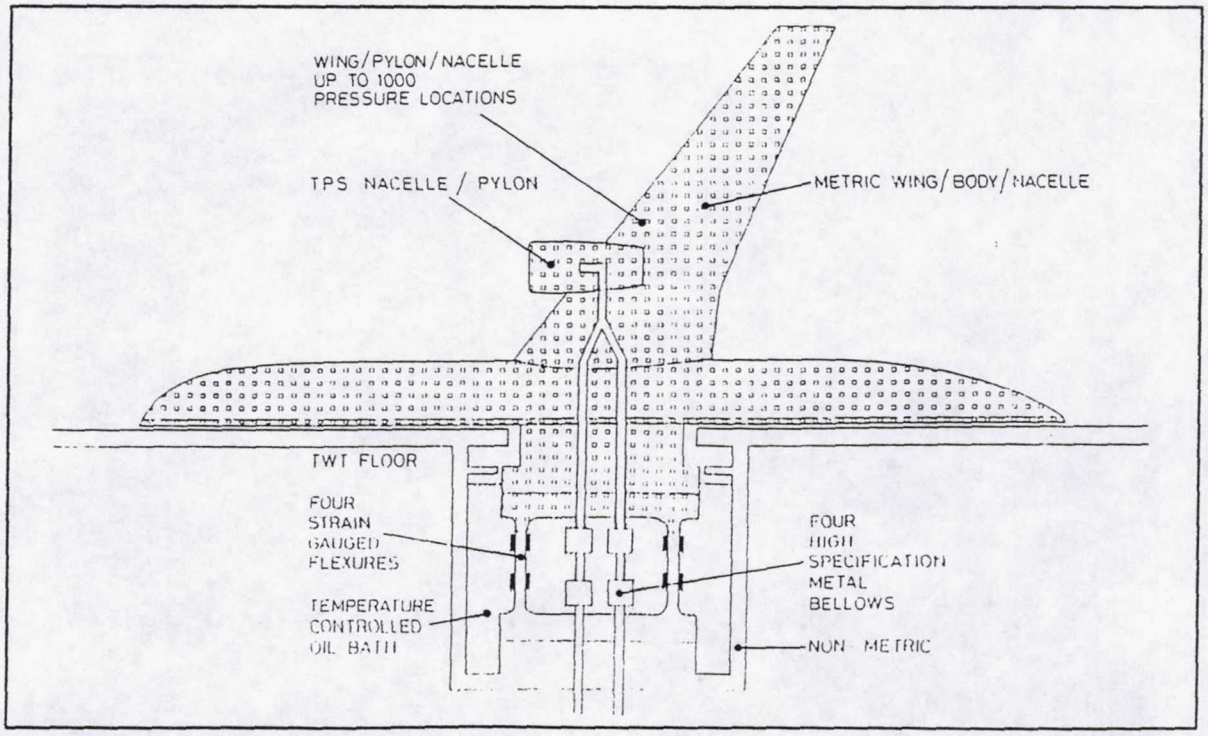

Fig.2 General Arrangement Of Semi-Span Model And Underfloor Balance In The ARA Transonic Wind Tunnel.

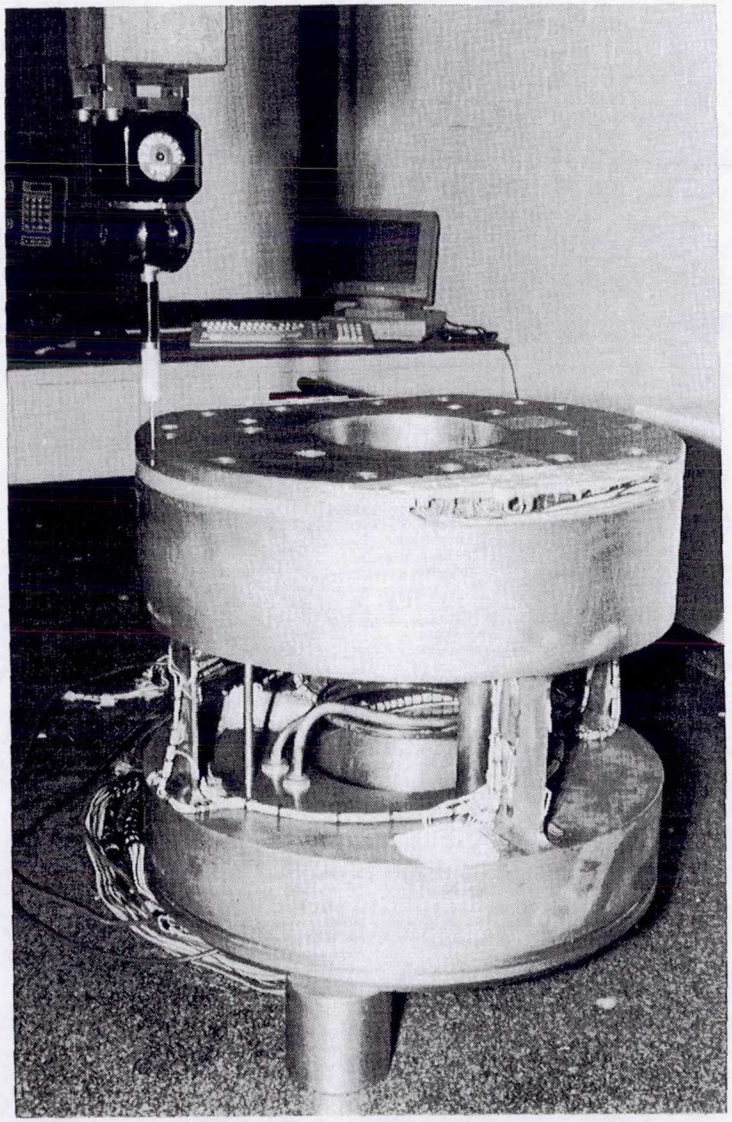

Fig.3 ARA Half Model Balance

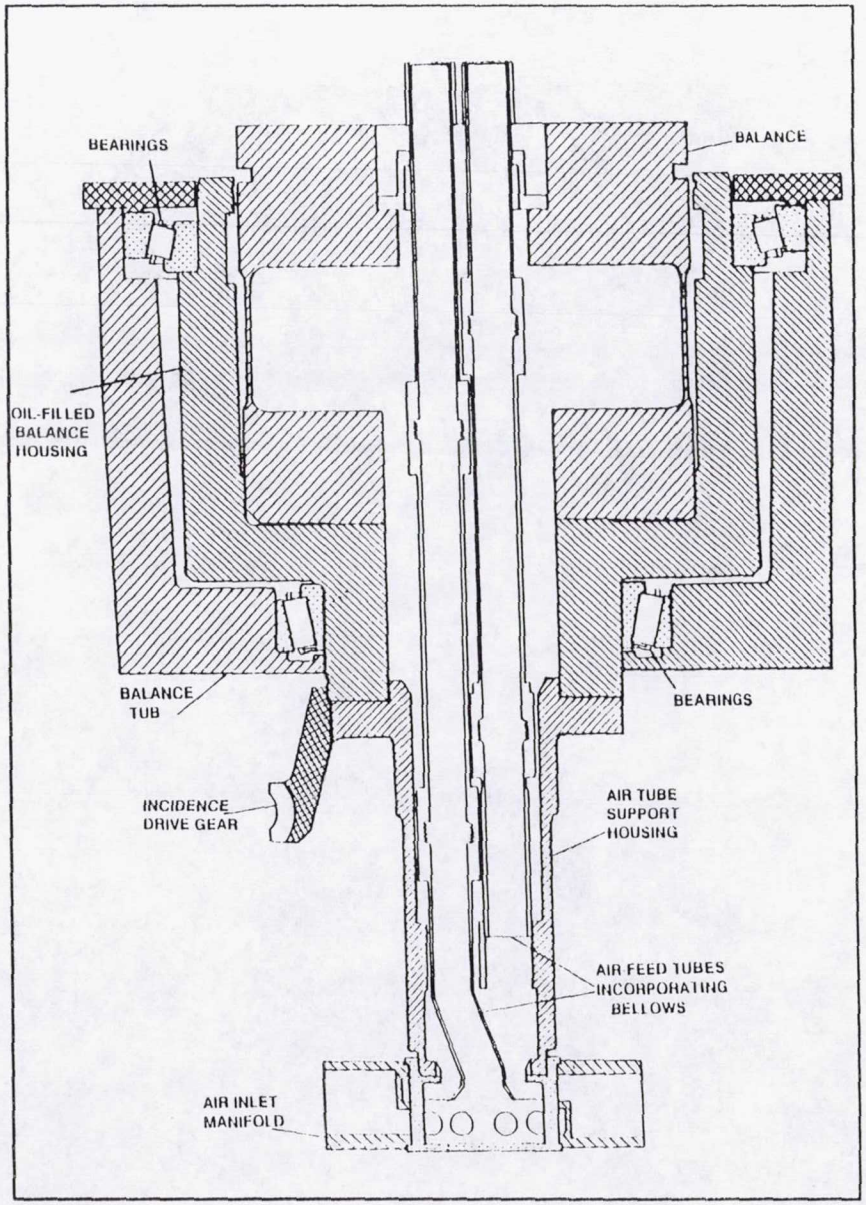

Fig.4 Half Model Balance And Air Feed Assembly

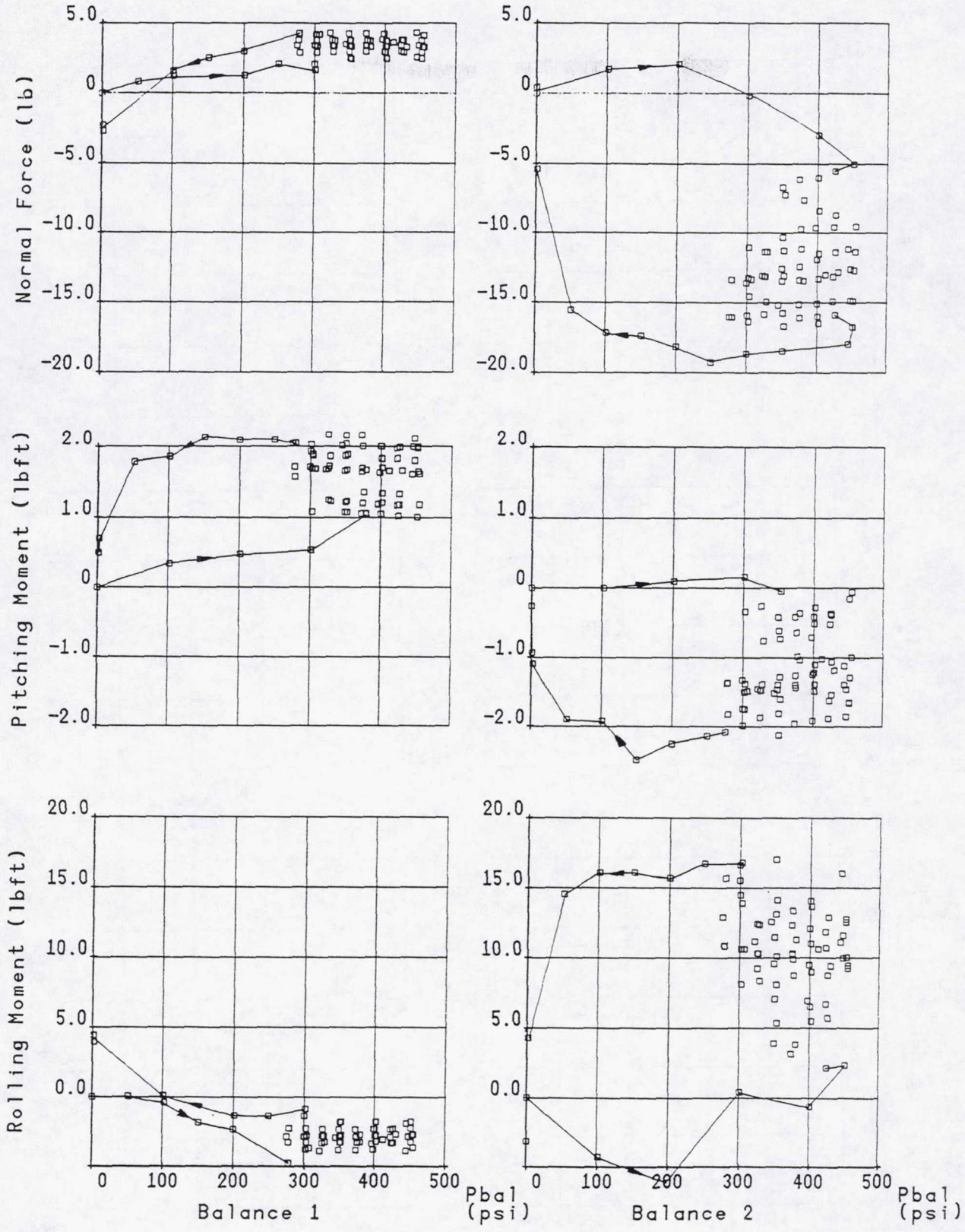

Fig. 5 Balance Residual Loads Due To Applied Pressure. Original Air-Feed Assembly.

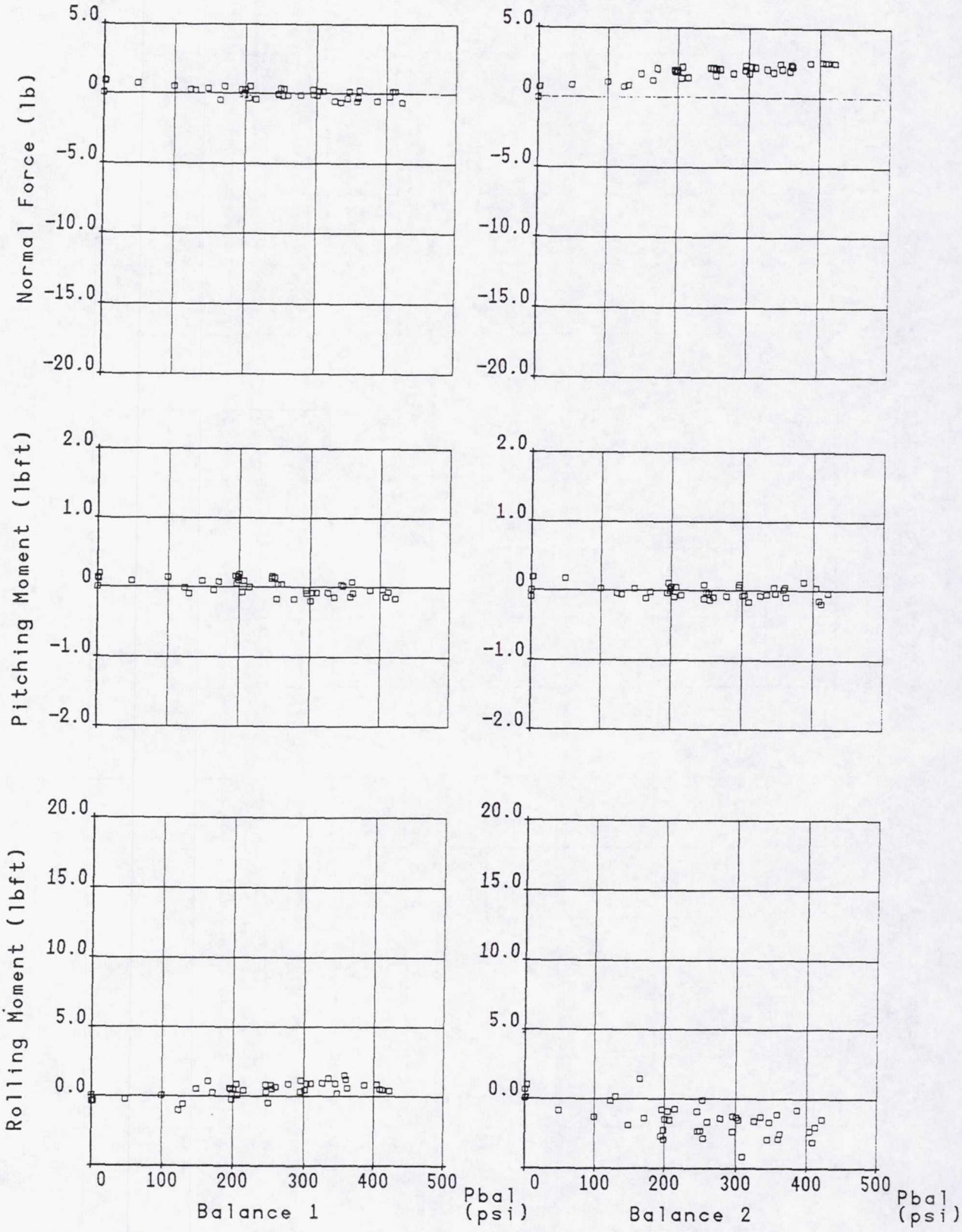

Fig.6 Balance Residual Loads Due To Applied Pressure. Modified Air-Feed Assembly.

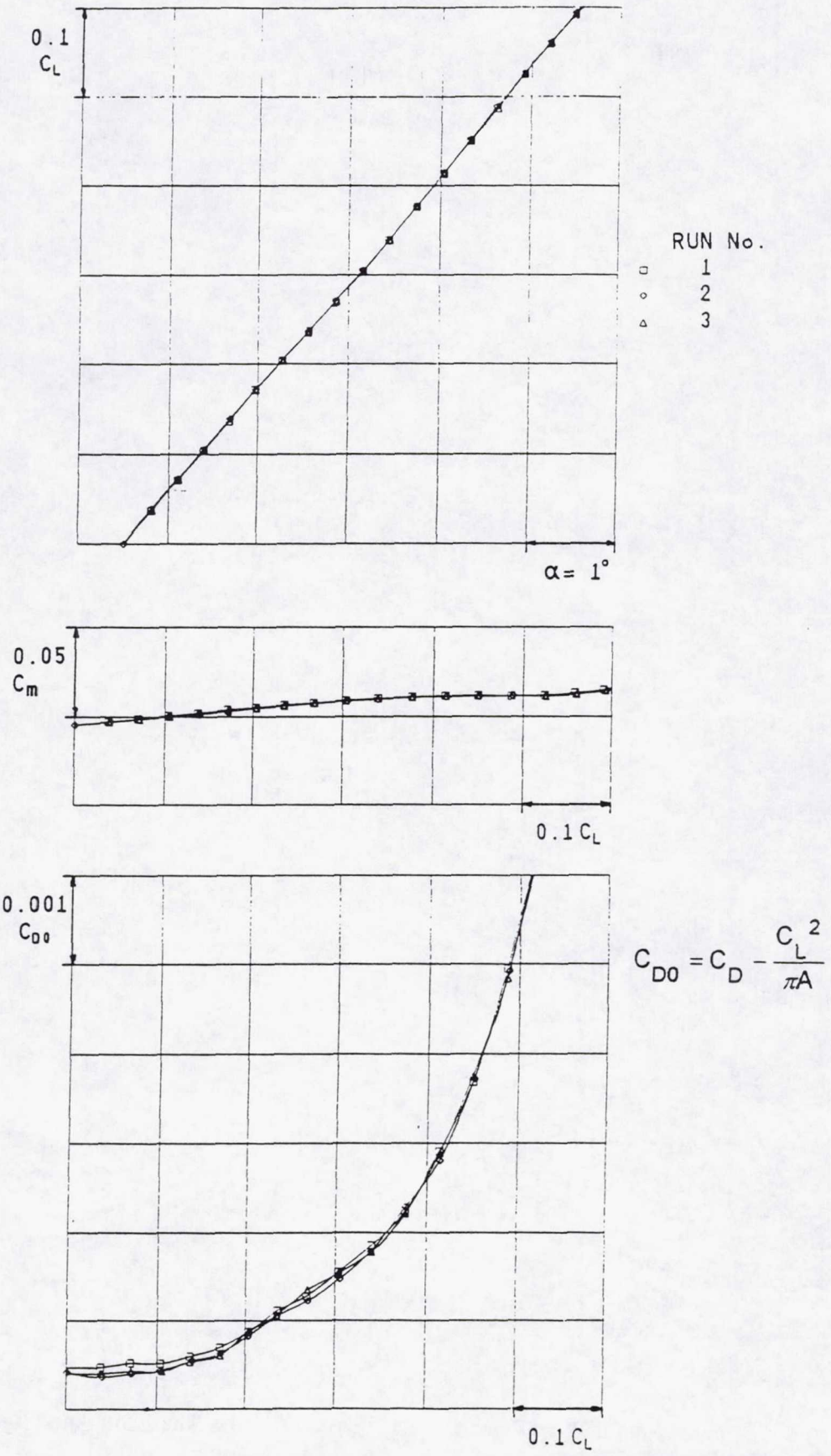

Fig.7 Comparison Of Wind Tunnel Data Measured Using The New Load Range Half Model Balance.

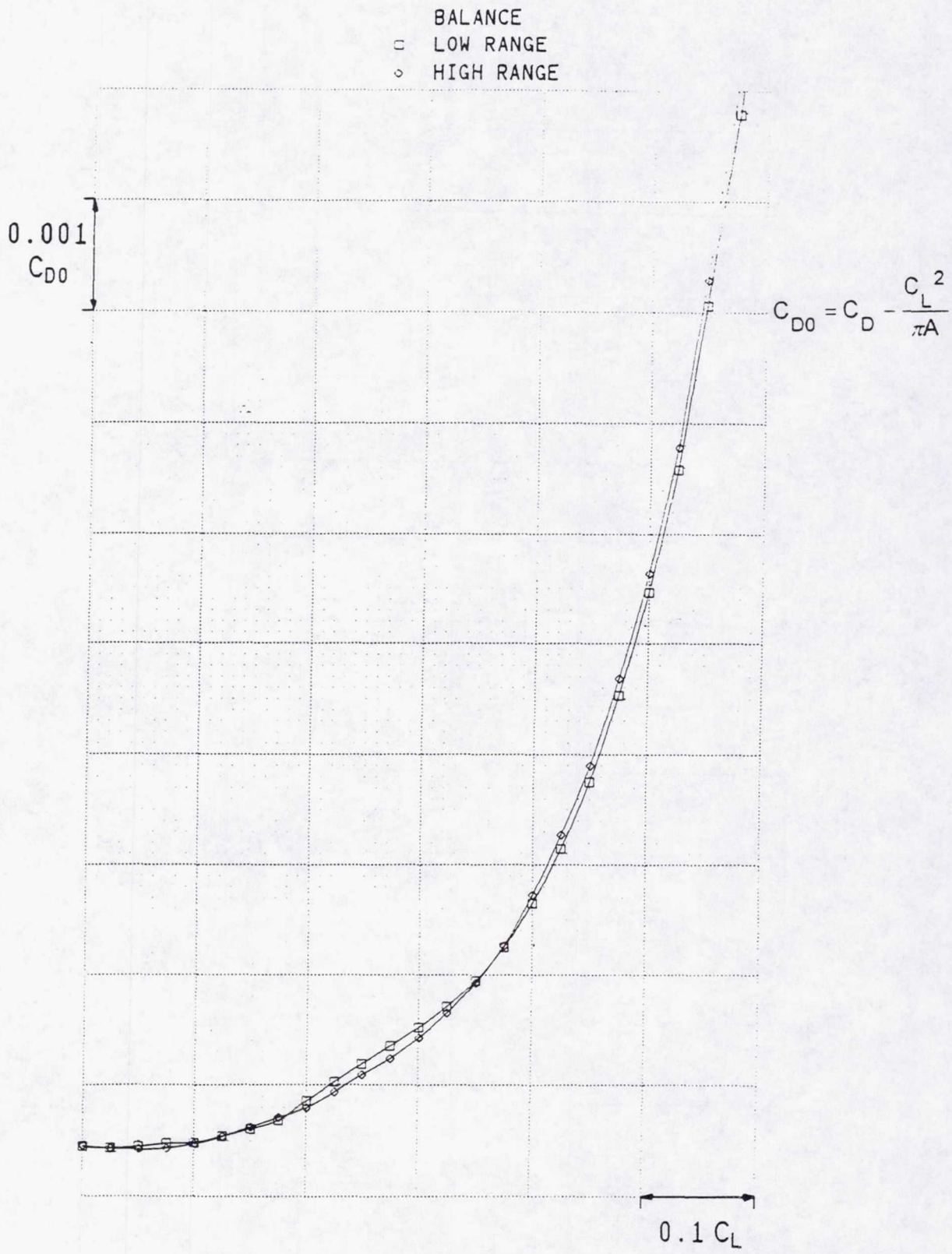

Fig.8 Comparison Of Wind Tunnel Data Measured Using The Low And High Range Half Cart Balances.

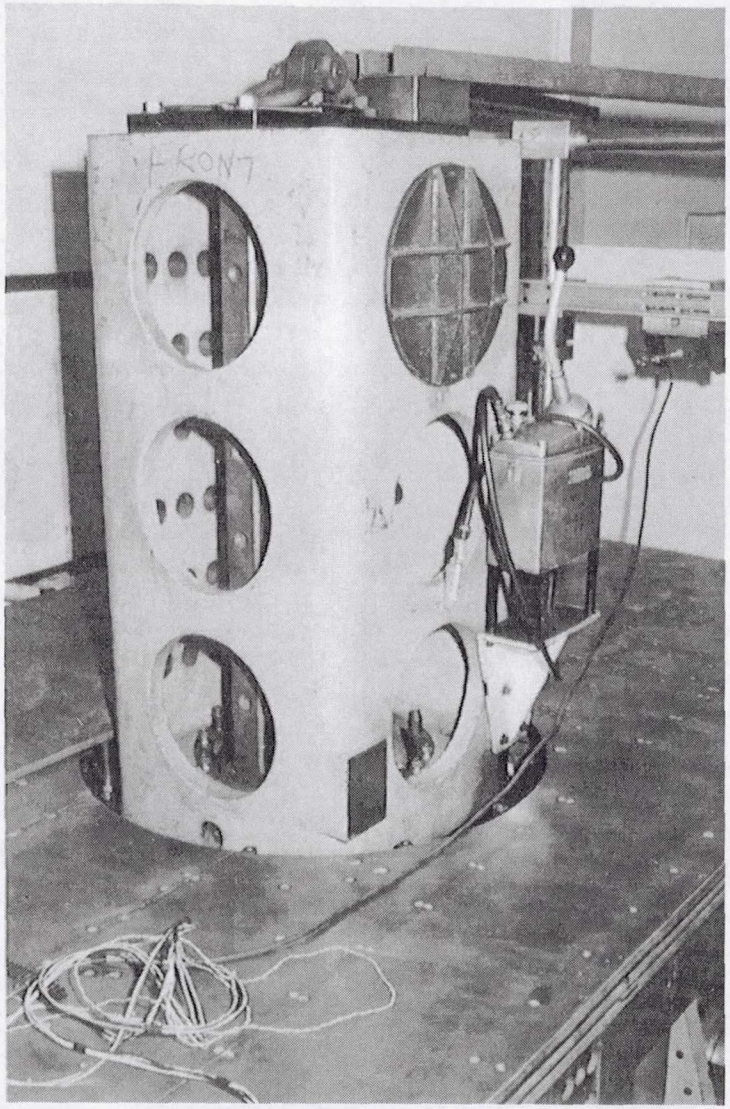

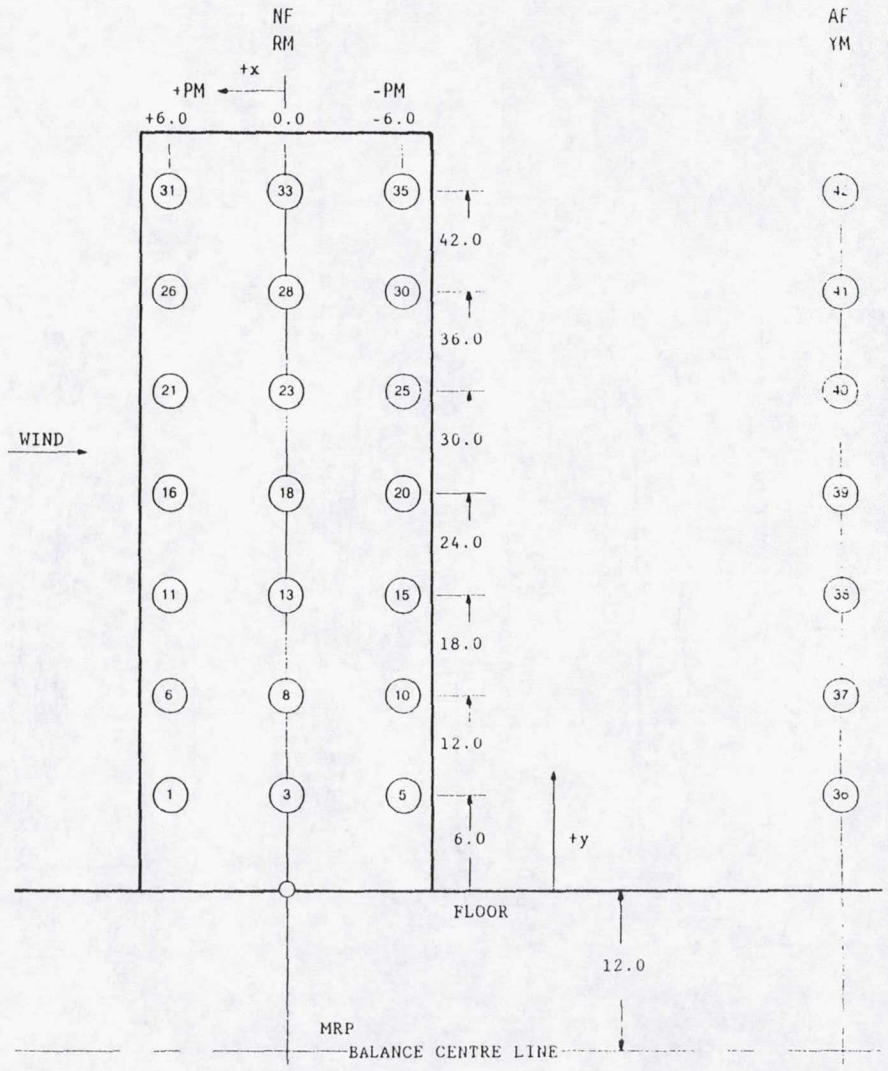

Fig.9 ARA Half Model Balance Loading Frame And Load Application Points.

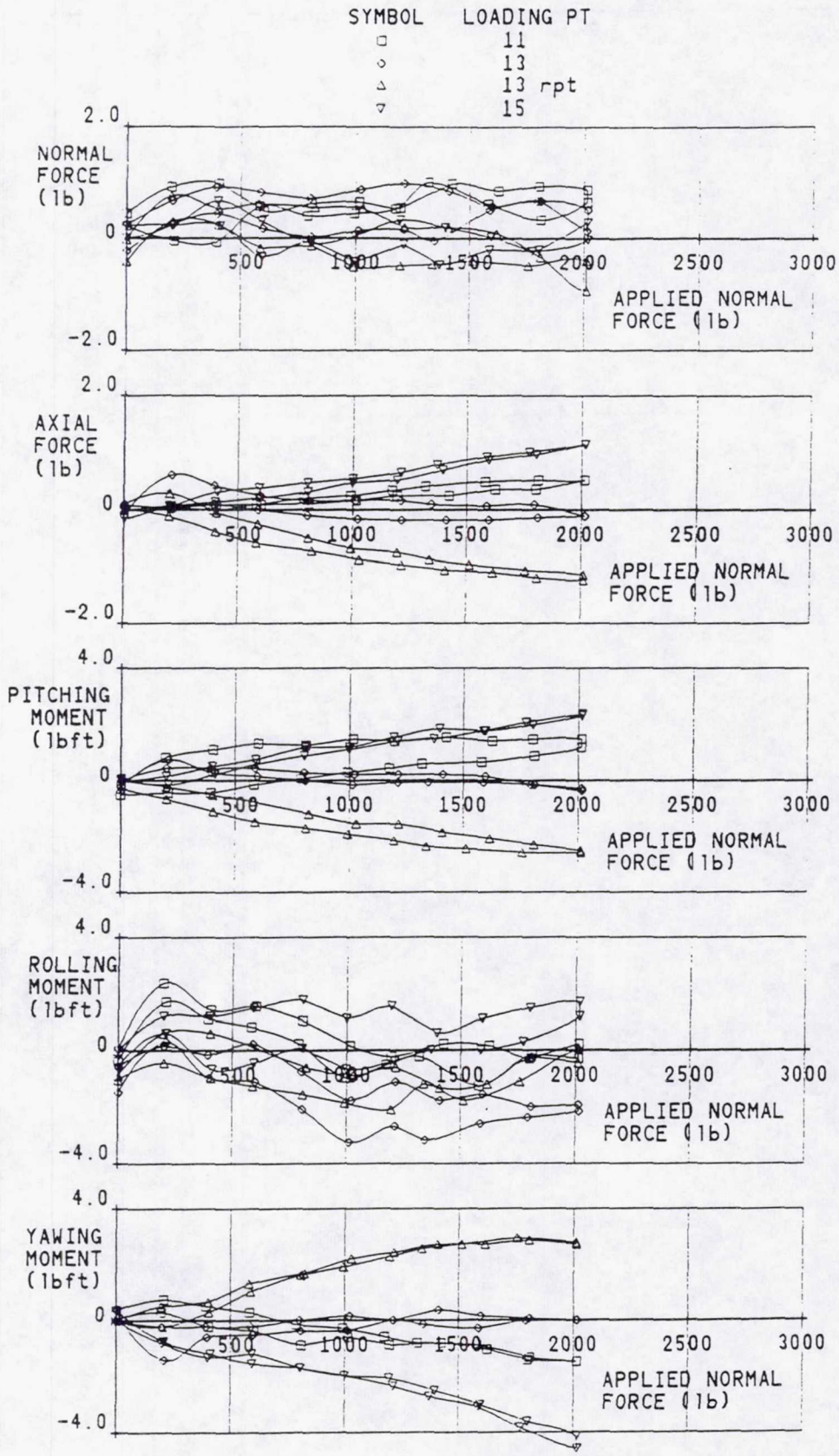

Fig. 10 Balance Residuals Due To Applied Normal Force From Loadings Using The Knife-Edge Assembly.

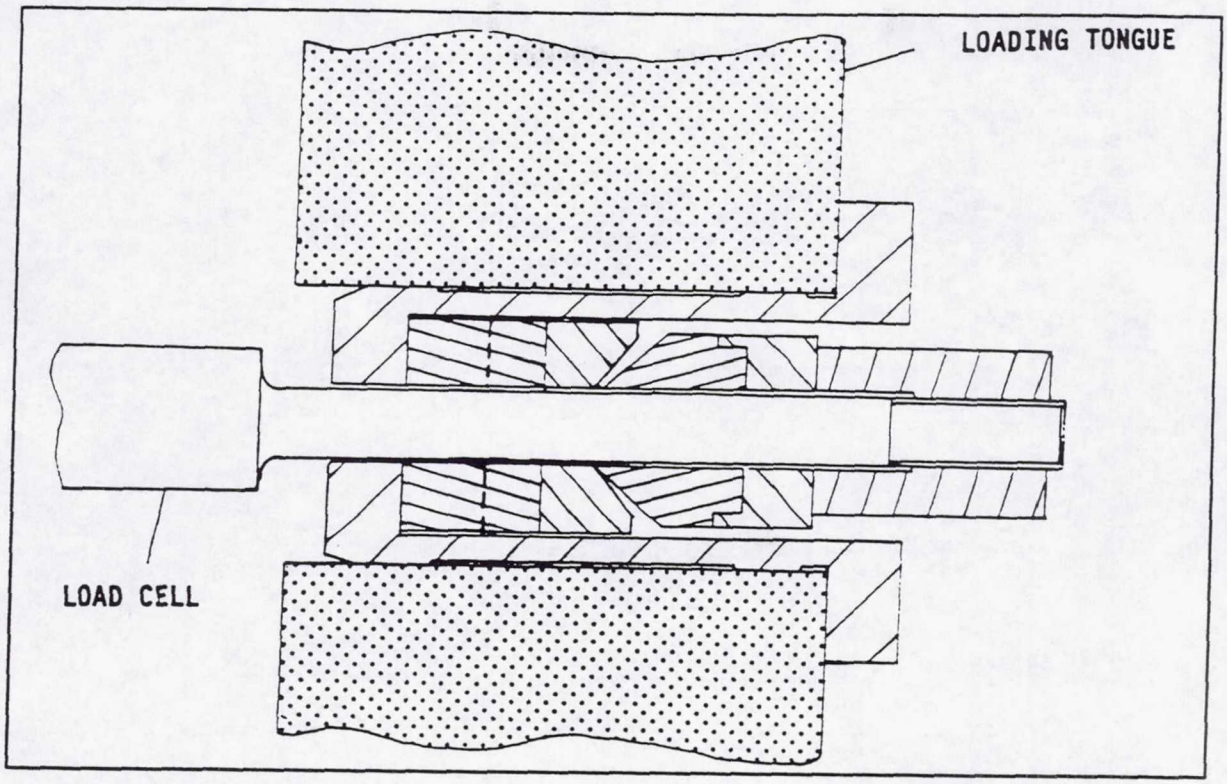

Fig.11 Normal Force Loading Arrangement Using Knife-Edge Assembly.

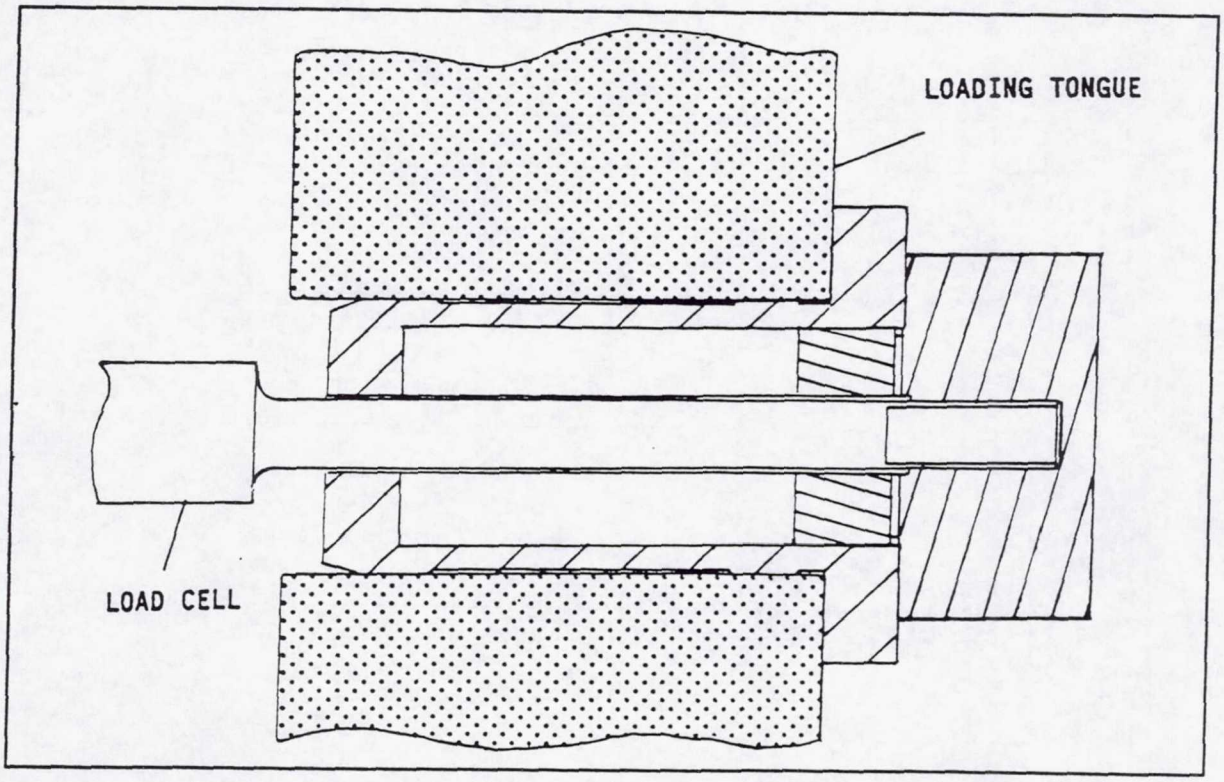

Fig.12 Normal Force Loading Arrangement Using Simple Linkage.

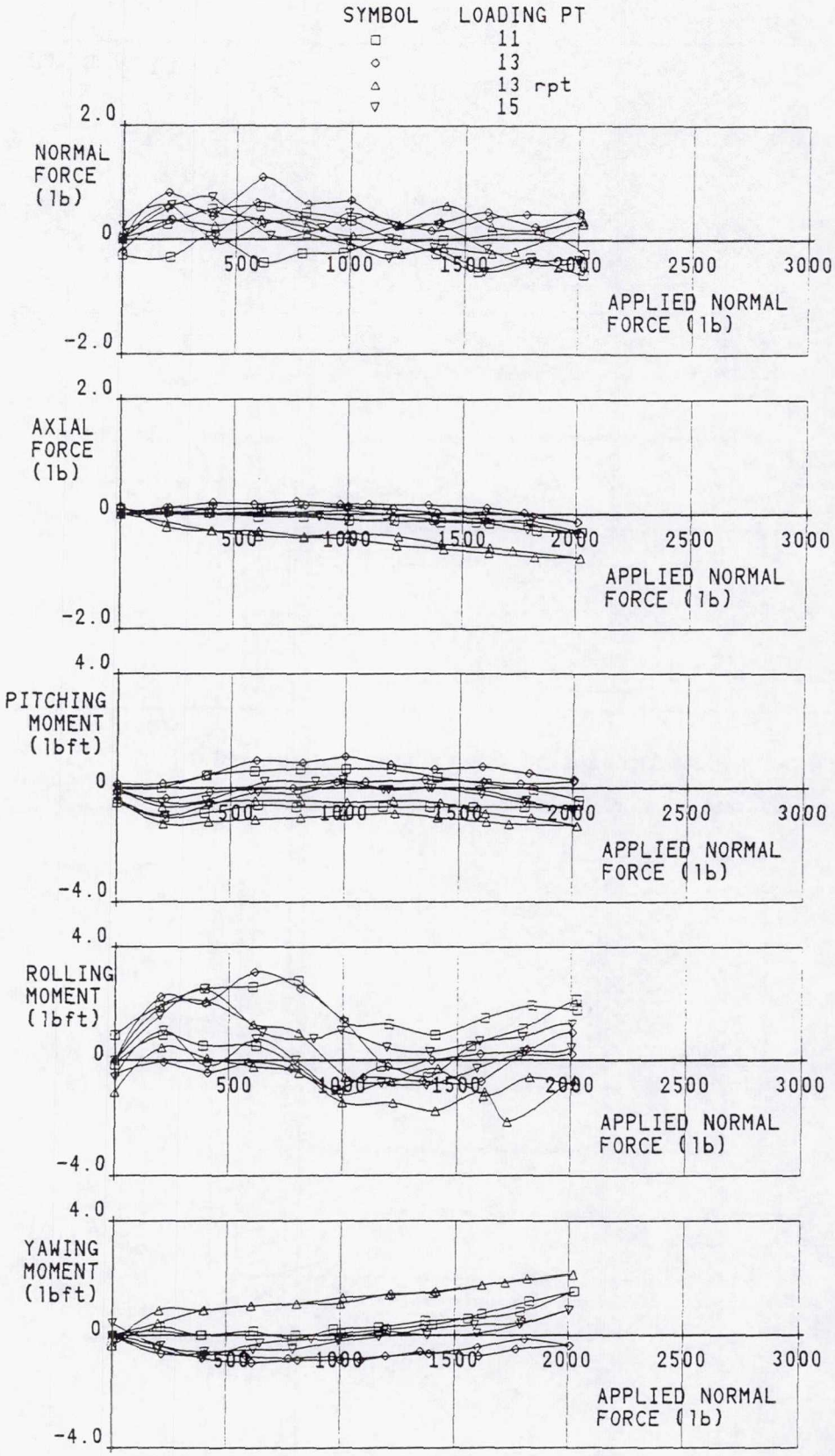

Fig.13 Balance Residuals Due To Applied Normal Force From Loadings Using The Simple Linkage.

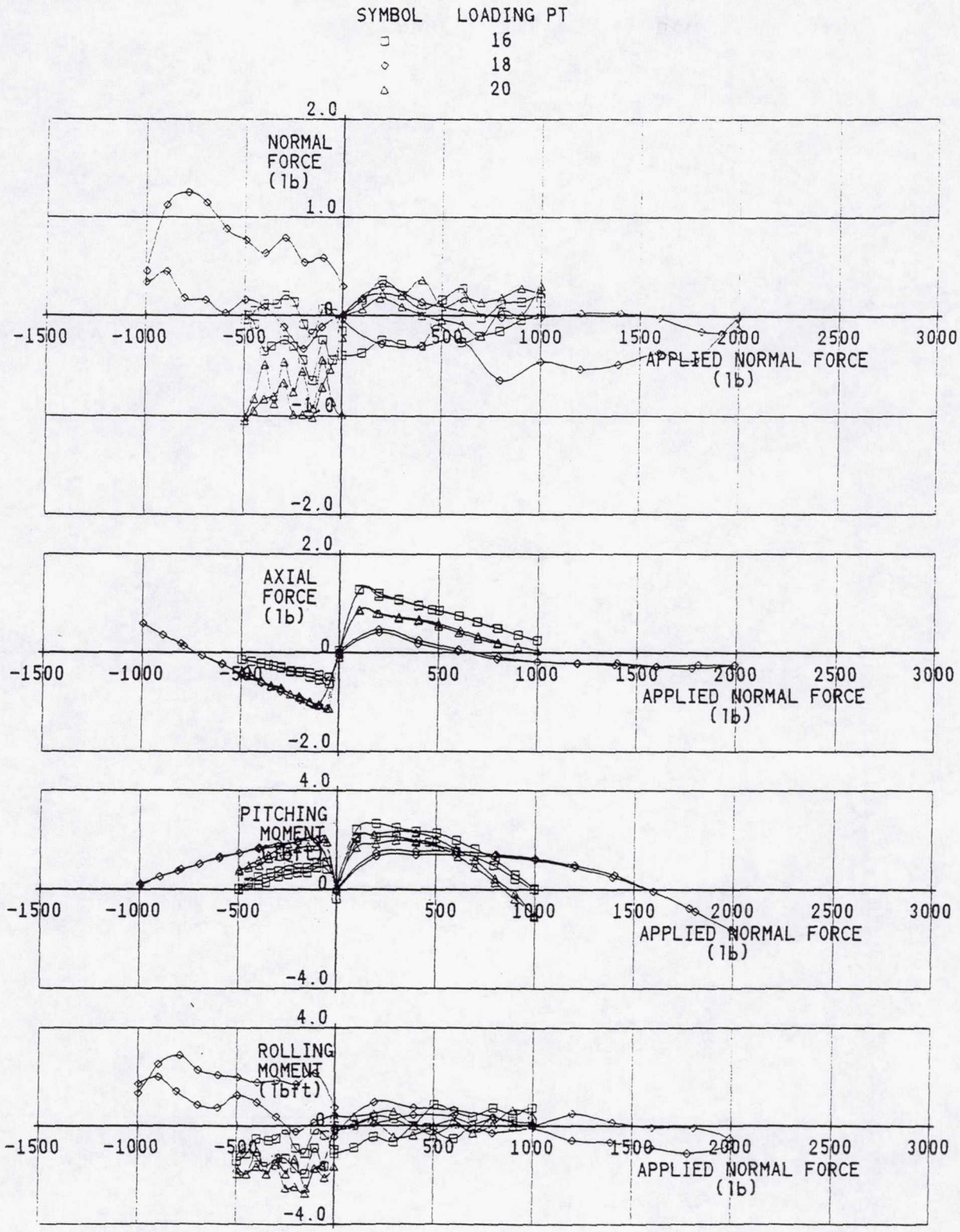

Fig.14 Balance Residuals Due To Applied Normal Force On The New Low-Range Half-Model Balance, Using The Simple Linkage.

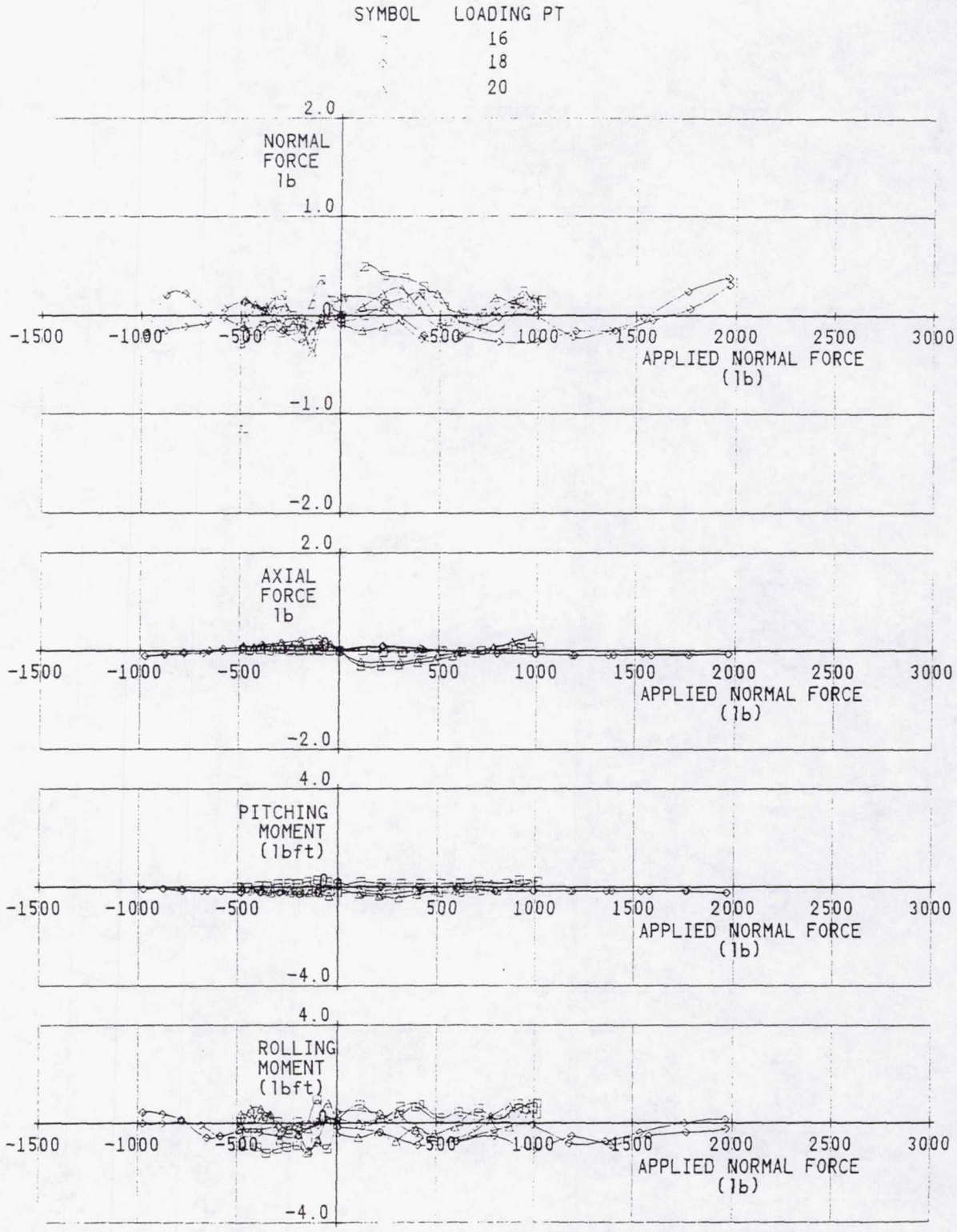

Fig. 15 Balance Residuals Due To Applied Normal Force On The New Low-Range Half-Model Balance, Using The Modified Simple Linkage.

LOOKING FOR THE LAST DRAGCOUNT
- MODEL VIBRATIONS VS. DRAG ACCURACY -

P.H. Fuijkschot
National Aerospace Laboratory NLR
Amsterdam, NL

SUMMARY

The paper investigates the influence which vibrations of a windtunnel model have on the reading of the axial force as measured by an internal strain-gage balance. When the model vibration modes exhibit a finite bending radius - as they usually do - centrifugal accelerations are generated. These will act on the model mass and thus cause a bias on the axial force or drag reading of the balance. Though this effect is not spectacular, it is certainly not always negligible: errors can be up to five dragcounts.
The paper is an extension of an earlier study on the compensation of comparable effects in gravity sensing angle-of-attack inclinometers. It presents a theoretical analysis and some typical quantitative results. Based on this analysis a simple but effective compensation scheme is proposed: it uses only four signals from the inclinometer signal conditioning and some model data such as mass and center of gravity location.

SYMBOLS

AOA	Angle of attack
c.g.	Center of gravity
C_D	Drag Coefficient
ε	Centrifugal Acceleration
F_ε	Bias on Axial Force of SGB
kg	kilogram mass
ℓ	Model length
m	meter
M	Model mass
N	Newton
ν	Frequency
Q	Dynamic Pressure
r	Distance between Accelerometers
R	Bending radius
$\dot{\rho}$	Angular rate
s	second
S	Reference Surface of Model
SGB	Strain Gage Balance
$\dot{\tau}$	Tangential Speed
x	Distance from inclinometer
z	Vibration amplitude

INTRODUCTION

It is generally recognized that model vibrations involving a finite bending radius can severely affect the accuracy of gravity-vector sensing inclinometers in windtunnel models. Due to 'sting whip' and other related motions - e.g. around the balance center - centrifugal accelerations are generated which can easily cause errors of up to .5 deg in angle-of-attack (AOA). Although equally obvious, it is much less appreciated that (part of) these centrifugal accelerations will also act on the model mass and will therefore cause a deviation in the axial force reading of an internal strain-gage balance (SGB). The errors created by this effect may not be spectacular - they are certainly not always negligible as illustrated by the example below.

For a typical model on a Z-sting in the NLR HST Transonic Windtunnel the following figures apply:

Model mass	:	$M = 50$	kg
Pitch frequency	:	$\nu = 16$	Hz
Bending radius	:	$R = 1.1$	m
Vibration Amplitude	:	$z = 2$	mm

The peak centrifugal acceleration under these conditions is .036 m/s^2, the relevant average value is half of that or .018 m/s^2. With the model mass of 50 kg this acceleration causes an axial force of .9 N. The aerodynamic parameters for this model would be:

Dynamic pressure $Q = 30000\ N/m^2$
Reference surface $S = 0.15\ m^2$

This means that one 'dragcount' or .0001 in C_D is equivalent to .45 N and that the bias in this case is two dragcounts! It should be reminded that this figure applies for a single mode and that many more modes (in pitch and yaw) can contribute. In an era where a reproducibility of .5 dragcounts in C_D is desired this error source obviously cannot always be neglected.

Another approach to illustrate the point is to look at the bias on the inclinometer readings. For the values given above the error in AOA would be .1 deg, which is not unusual. In practice AOA errors up to .5 deg are encountered, but fortunately mostly under buffet conditions, where the requirements on drag-accuracy are relaxed. The errors on AOA and the compensation of these have been discussed extensively in reference 1, from which figure 1 is taken. It gives the bias on AOA during a polar and thereby implicitly the order if magnitude of potential errors (depending on the mode) on drag. For this model .1 deg $\Delta\alpha$ in AOA could be equivalent to 2 dragcounts, the error in drag being proportional to the error in AOA for this mode.

The nature of the bias is such that it will apparently reduce the drag - the centrifugal acceleration vector points outward. Its amplitude will have a stochastic character, causing a small constant bias plus some scatter on axial force. The point should be stressed that the bias increases quadratically with model vibration amplitude - another reason to keep model vibration levels low!

The conclusion of the above is that a correction on axial force is desirable and worthwhile, but since it is relatively small the absolute accuracy of the correction can be limited to some 10 %.

ANALYSIS

Any quantitative correction scheme must be based on a kinematic analysis of the actual model vibrations involving all simultaneous vibration modes. The basis for this is provided by reference 1, which does exactly that for the influence of model vibrations on inclinometers for AOA measurement. The compensation proposed therein has been fully validated in actual windtunnel use.
At first sight the calculation of the influence on drag might look simple: multiply the bias on the inclinometer by the model mass, et voilà. Unfortunately real life is more complicated than that: not all vibration modes produce a net contribution to the axial force bias. A vibration around the c.g. of the model for instance might create opposite forces fore and aft of the c.g. and have near zero net effect. An inclinometer (not mounted in the c.g.) however would be affected.

In reference 1 it was proven that for any arbitrary point on the model (including the location of the inclinometer) the centrifugal acceleration ε is given by the product of the local tangential speed $\dot{\tau}$ and the angular rate $\dot{\rho}$ (Fig. 2), or:

$$\varepsilon = \dot{\tau} \cdot \dot{\rho} \tag{1}$$

This expression is valid for any combination of simultaneous vibration modes. It must be applied twice: in the x-z plane and in the x-y plane of the model.

The total net axial force bias F_ε is obtained by multiplying the local ε_x by the local mass M_x for that particular 'slice' of the model and integrating the product over the length of the model, or:

$$F_\varepsilon = \int_0^\ell \varepsilon_x \cdot M_x \, dx \tag{2}$$

This expression looks simple, but is not very convenient to work with - even more so because ε_x relates to momentary local values.

COMPENSATION

The compensation of course is equal to F_ε as given by equation (2). The big challenge is to find a user-friendly expression for ε_x - in order to avoid an array of accelerometers over the length of the model! The constituents of ε are $\dot{\tau}$ and $\dot{\rho}$, as given by equation (1). The angular rate $\dot{\rho}$ is constant over the length of the model. It can either be measured directly or be derived from two linear accelerometers as sketched in figure 3:

$$\dot{\rho} = \frac{\dot{\tau}_1 - \dot{\tau}_2}{r} \tag{3}$$

It should be reminded that it is not possible to measure or assess the momentary bending radius R directly, but it can be deduced from measurable quantities as:

$$R = \frac{\dot{\tau}_1}{\dot{\rho}} \tag{4}$$

Assuming $\dot{\tau}_1$ and $\dot{\rho}$ are known because they are required for the inclinometer compensation, $\dot{\tau}_x$ at an arbitrary distance x from $\dot{\tau}_1$, (Fig. 3) is given by:

$$\dot{\tau}_x = \dot{\tau}_1 + \dot{\rho} \cdot x \tag{5}$$

Note: x can be positive or negative.

The local centrifugal acceleration ε_x at a distance x from the reference location of $\dot{\tau}_1$ then becomes:

$$\varepsilon_x = \dot{\rho} \cdot \dot{\tau}_x = \dot{\rho} \cdot \dot{\tau}_1 + \dot{\rho}^2 \cdot x \tag{6}$$

The first right-hand term is the original inclinometer compensation from reference 1 and is independent of x. Thus, for axial force bias compensation purposes, it can be directly multiplied by the total model mass M. The second term can be regarded as a correction on the first one. Depending on the direction of x its contribution can be positive or negative.

Combining equation (2) and equation (6) the complete expression for the axial force bias thus becomes:

$$F_\varepsilon = M \cdot \dot{\rho} \cdot \dot{\tau}_1 + \dot{\rho}^2 \int_0^\ell M_x \cdot x \cdot dx \tag{7}$$

in which ℓ is the length of the model.

The integral term represents a moment with respect to the position where $\dot{\tau}_1$ is measured, i.e. the inclinometer location. The mass is the model mass M and the arm is the distance x_{cg} between the center of gravity of the model and the inclinometer location. Expression (7) can thus be simplified to:

$$F_\varepsilon = M \left(\dot{\rho} \cdot \dot{\tau}_1 + \dot{\rho}^2 \cdot x_{cg} \right) \tag{8}$$

This result is in-line with what one would intuitively expect. It is relatively simple and all quantities can be measured or assessed. Normally the c.g. of the model will be located aft of the inclinometer, so x_{cg} will be negative. It should be emphasized that all of the above reasoning is based on the assumption that the models, including their built-in instrumentation, are sufficiently stiff: i.e. have no resonances in the vicinity of the compensated modes.

IMPLEMENTATION

The correction for bias on axial force as proposed in this paper is - not surprisingly - closely related to the compensation of the AOA inclinometer for the same centrifugal acceleration effects. For the latter application a dedicated and validated 'Inclinometer Conditioning Unit' is available at NLR. It provides a fully corrected AOA output with a resolution of .001 deg. The compensations functions are realized with analog techniques, as shown on the block diagram of figure 4.
For each plane of the axial force bias compensation two extra output signals are required: $\dot{\rho} \cdot \dot{\tau}_1$ and $\dot{\rho}^2$. They are made available, as indicated in figure 4, for digitization by the regular data acquisition system. The model mass - including the weighed part of the balance - can be weighed directly or can be obtained from the usual wind-off 'weight polar' in the windtunnel. The same applies to the distance x_{cg}. With all variables known the processing (in two planes!) according to equation (8) is elementary.

CONCLUSION

The paper presents a compensation for the small, but not negligible, bias effect on drag of windtunnel models due to model vibrations. The proposed scheme is simple, transparent and accurate and can be applied in real time.
Admittedly it is based on a theoretical analysis and has not yet been validated during real windtunnel testing. A comparable compensation for AOA Inclinometers however has been proven in practice and has shown to be extremely accurate, leaving no doubt as to the applicability of the scheme proposed here.

REFERENCE

1. Fuijkschot, P.H., National Aerospace Laboratory NLR, *Vibration Compensation of Gravity Sensing Inclinometers in Windtunnel Models*, Proceedings ISA 42nd International Instrumentation Symposium, pp. 493-503, May 1996, San Diego, NLR Report TP 96003 L.

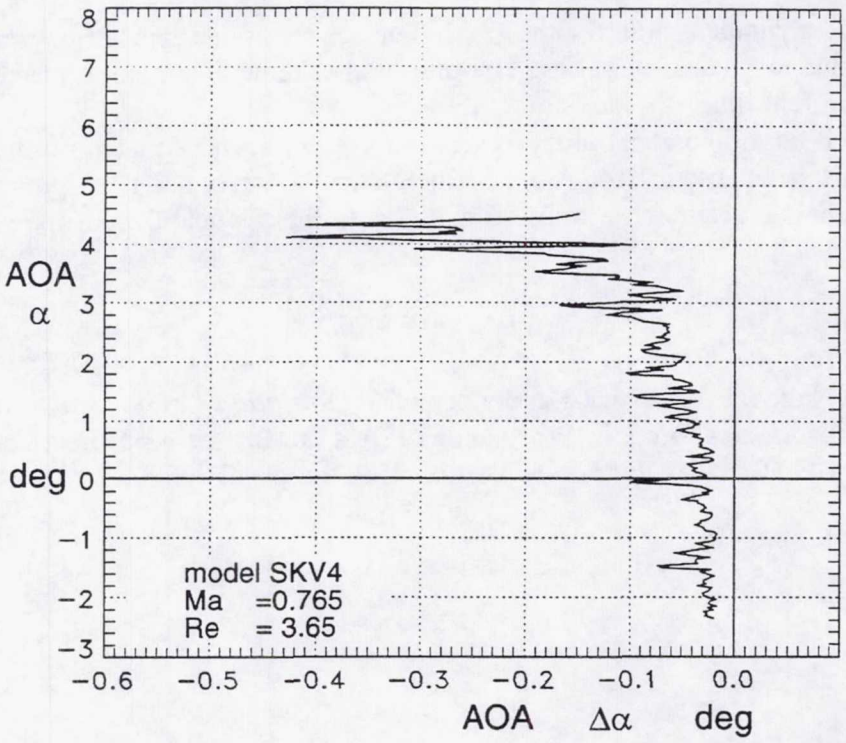

Figure 1. Bias on Inclinometer AOA.

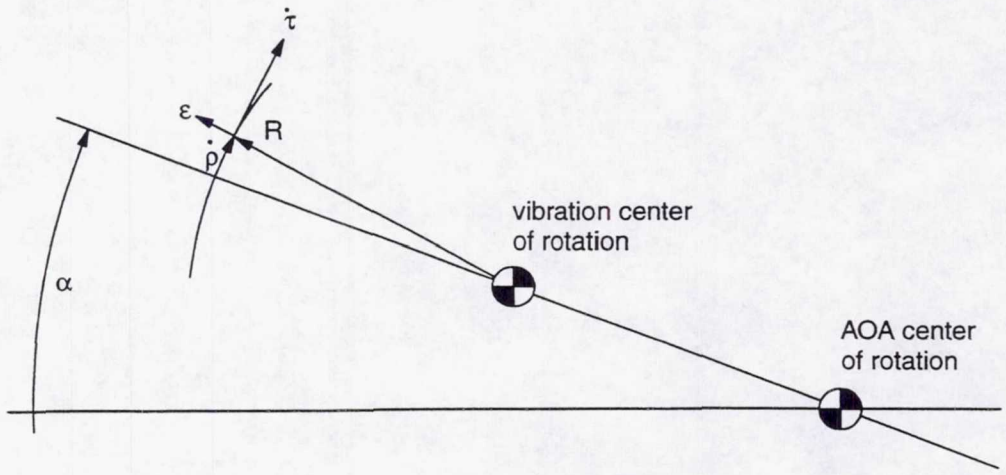

Figure 2. Centrifugal Acceleration ε.

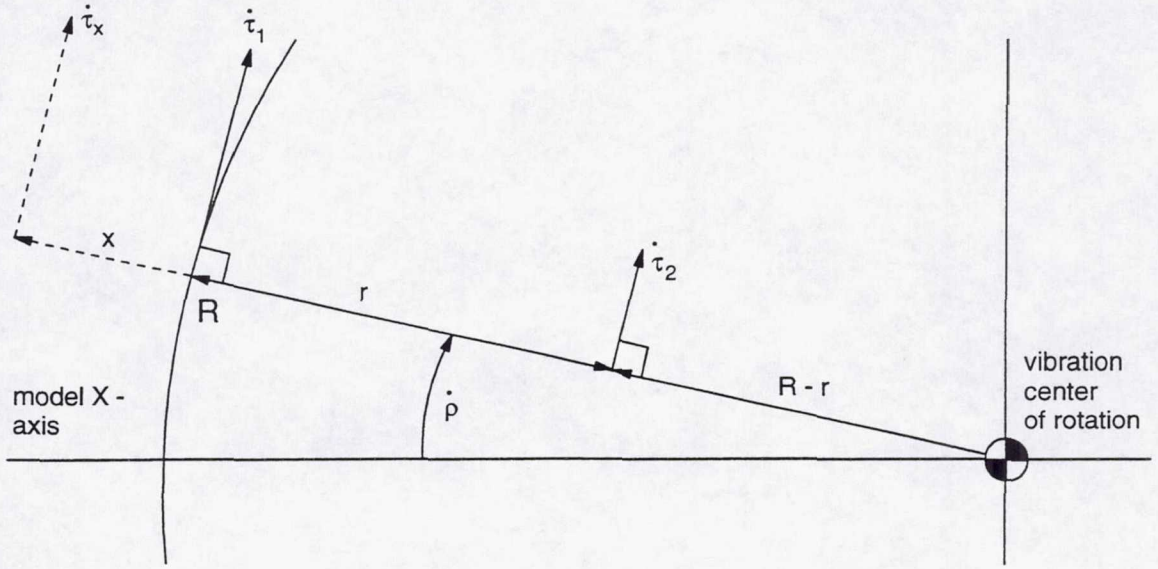

Figure 3. Angular Rate from two linear Accelerometers.

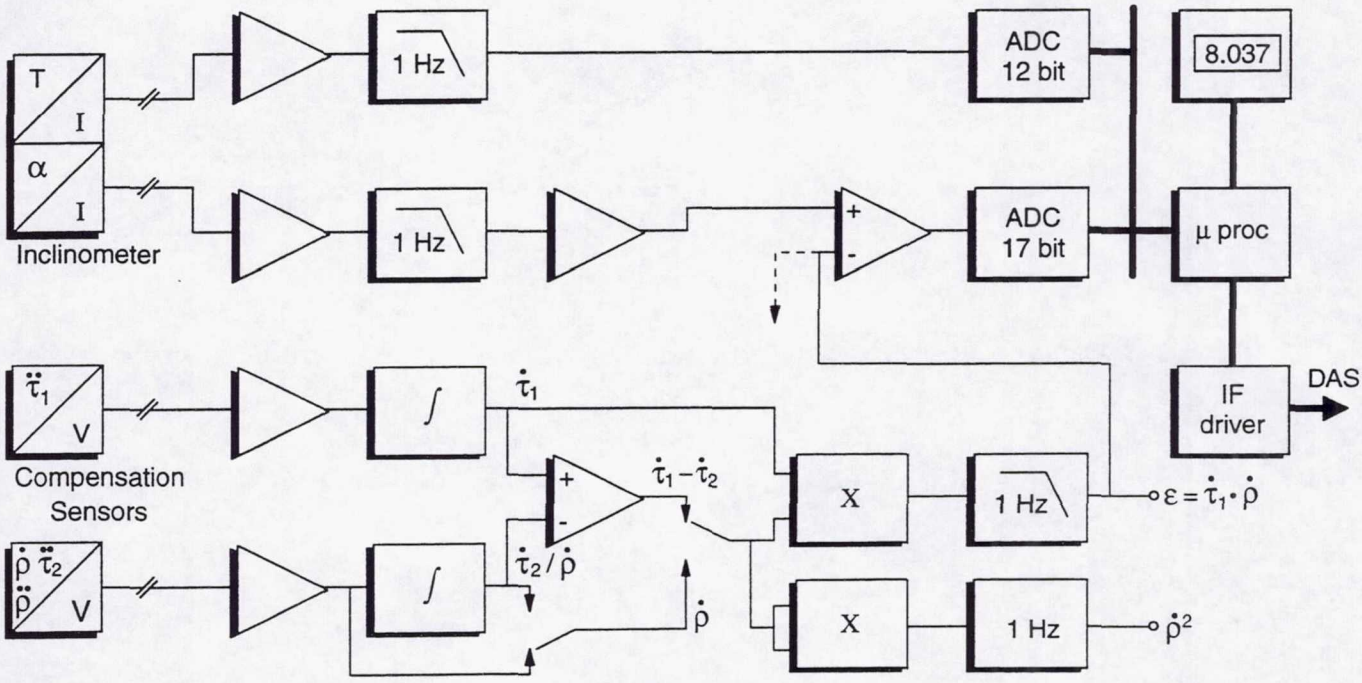

Figure 4. Inclinometer Conditioning Unit with extra Outputs.

Page intentionally left blank

UNCERTAINTY ANALYSIS FOR FORCE TESTING IN PRODUCTION WIND TUNNELS

Mark E. Kammeyer*
Hypervelocity Wind Tunnel 9
Naval Surface Warfare Center Dahlgren Division
Silver Spring, MD

SUMMARY

This paper documents the implementation of measurement uncertainty analysis for aerodynamic force testing at the Naval Surface Warfare Center (NSWC) Hypervelocity Wind Tunnel 9. The general uncertainty methodology as presented in several published standards is reviewed, highlighting the general approach in use at Tunnel 9. A detailed application to static stability and drag testing is presented. The emphasis is not on estimating precision and bias errors for force balances. Rather, the focus is on the automation of procedures and the propagation of errors to provide the maximum understanding of the data flow. The techniques and approach discussed should have application to other wind tunnel facilities.

INTRODUCTION

An accepted measurement uncertainty methodology for wind tunnel testing is needed to allow meaningful comparisons between facilities, proper validation of computational fluid dynamic models, and ultimately, rational design decisions. The growing acceptance of a standard method is evidenced by the publication of several standards and text books in the past decade.[1–5] These documents define a consistent methodology and present a variety of examples to serve as illustrations. AIAA Standard S-071-1995 in particular provides simplified examples of the assessment of uncertainty for force measurements in a transonic wind tunnel. However, these references

* Currently with McDonnell Douglas Corp., St. Louis, MO.

do not present a universal strategy for the *implementation* of the methodology for a specific test facility.

Wind tunnel stability and drag measurements present a special challenge to the experimenter in at least two respects. First, the force balance itself is a complex instrument with multiple inputs and outputs. In particular, the assessment of the balance calibration uncertainty merits special attention. Second, the desired test results, the nondimensional coefficients, are complex functions of a large number of measured inputs. A typical analysis for a single angle-of-attack encompasses:

- 35 measured inputs: supply pressure and temperature and test cell Pitot pressure, model support system position, 6 balance loads, integrated base pressure, 2 reference areas, 1 reference length, the relative position of the model and balance moment reference centers, and 3 angles for each of 5 coordinate system transformations and sting/balance deflections.
- 46 correlated bias pairs, primarily from the coordinate system transformation angles.
- 20 computed results: angle-of-attack, angle-of-sideslip and 6 force/moment coefficients in each of the body and stability axis systems, base pressure coefficient, axial force coefficient corrected for base pressure, lift-to-drag ratio, and the pitch and yaw center-of-pressure locations.

The complete angle-of-attack range must be considered since sensitivities vary with model attitude. This is especially important when angle-of-attack passes through zero. The estimation of so many uncertainties and the propagation to so many desired results, over a range of test conditions and model attitudes, in a production environment, can be intimidating. For these reasons there is a strong incentive to standardize and automate the process as much as possible.

This paper will present a synthesis of the published standards on measurement uncertainty for aerodynamic force measurements. The implementation is for a particular facility, the Naval Surface Warfare Center's Hypervelocity Wind Tunnel 9 (Tunnel 9). However, the approach was kept as general as possible to cover the wide array of test conditions, balance designs, load capacities, and measurement techniques typically encountered. Standardization and integration with pressure and heat transfer measurements was also a consideration. The general approach will have application to other test facilities.

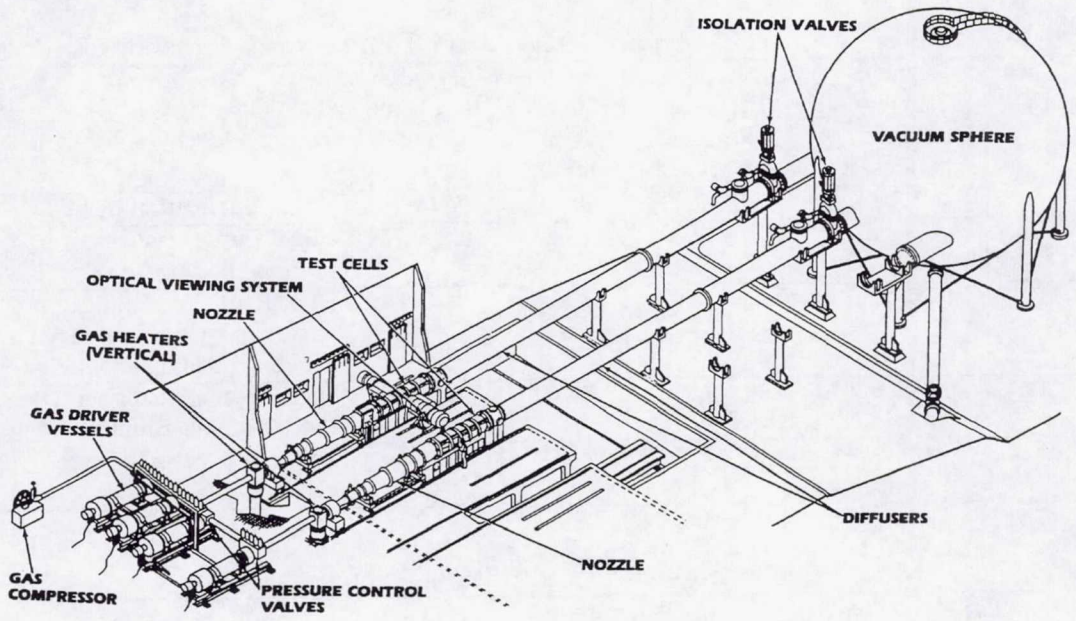

Figure 1: The NSWC Hypervelocity Wind Tunnel 9.

FACILITY DESCRIPTION

Tunnel 9 is a blowdown facility which uses pure nitrogen as the working fluid and operates at Mach numbers of 7, 8, 10, 14, and 16.5. Supply pressures up to 21,000 psia (1430 atm) and total temperatures up to 3500 R (1950 K) are currently available. Mach numbers 8–16.5 operate "cold" in that the gas is expanded to just above the saturation line, producing a high Reynolds number environment. Mach 7 operates "hot" in that the gas is expanded to ambient atmospheric conditions producing full velocity, enthalpy, pressure, and temperature duplication between flight altitudes of 38,000 ft (11.5 km) and 68,000 ft (20.5 km). The test cells are five feet in diameter and are over twelve feet long. A schematic of the facility is shown in figure 1. Ranges for facility operation for all currently calibrated test conditions are listed in table 1. References 6–10 provide a complete discussion of Tunnel 9 operation and calibration.

Aerodynamic tests at Mach numbers 8–16.5 are typically one second or less in duration. The test cell for Mach numbers 10 and above is equipped with a hydraulic sector mechanism for pitching models through an angle-of-attack sweep. The maximum attainable pitch rate is 80 deg/s. The short test time and the fast pitch sweep require fast instrumentation response times and proper accounting for inertial loads. These issues have implications for the uncertainty analysis, which will be addressed in later sections. The short run times also preclude significant increases in model internal temperature. Therefore, active cooling of the model or instrumentation is

Table 1: NSWCDD Hypervelocity Wind Tunnel No. 9 Capabilities

Mach	Reynolds Number Range (millions/ft)	Supply Pressure Range (psia)	Nominal Supply Temp. (deg R)	Useable Run Time Range (s)	Comment
7	3.7–15.8	2,000–12,000	3,460	1.75–5	Flight duplication of P, T
8	8.7–55.7	2,000–12,000	1,660	0.2–0.75	Flight duplication of dynamic pressure
10	0.86–21.9	500–14,000	1,810	0.23–15	High Reynolds number naturally turb. boundary layers with pitch capability
14	0.072–6.2	100–19,000	3,160	0.7–15	High Reynolds number/High Mach number simulation with long run times and pitch capability
16.5	2.65–3.2	19,000–21,000	3,260	3.0–3.5	

Table 2: Tares recorded in tunnel run sequence.

Type	No. recorded	Purpose	Comment
Static	5–6	P_0 shunt calibration	Driver vessel pressurization
Static	10–20	Test cell pressure calibration	Driver vessel pressurization, test cell evacuation
Static Dynamic	1 1	Used to subtract inertial loads	Immediately prior to heating cycle
Static	1	Used to eliminate zero shifts	$\approx$ 2 minutes before run initiation
Dynamic	1	Run	Wind-on data

almost never required.

The current data acquisition system allows over two hundred model and facility inputs to be simultaneously recorded. Sampling rates are typically 250 or 500 samples/s per instrumentation channel. Data acquisition for a typical test consists of a number of wind-off data snapshots, or tares followed by the wind-on run data record. The tares are outlined in table 2 and are of two types: static and dynamic. A static tare is usually one or two seconds in duration (250–500 points), taken when the tunnel is quiescent. These tares are used to provide data for instrument calibrations and a reference point for force balance and thermocouple data reduction. For example, model and test cell pressure transducers are calibrated during the pump down of the test cell. The evacuation is briefly halted while the tare data are recorded. A dynamic tare is a wind-off duplicate of the run, with the model pitching. It is used to subtract the inertial forces, which arise from the pitch sweep, from the wind-on data. These tares are utilized for the determination of various precision limits, and are referenced throughout the paper.

MEASUREMENT UNCERTAINTY METHODOLOGY

The measurement uncertainty methodology, taken from reference 5 and consistent with references 1–4, will now be presented, and the case made for an implementation strategy that emphasizes a production environment. Implicit in this entire discussion is the requirement that the instrumentation system measure the intended physical quantity. This means that error sources from the transducer response, its installation, signal conditioning, etc. have been made negligible by design.[11] The referenced works on uncertainty refer to this as the elimination of blunders. The methodology is as follows:

1. *Define the measurement system and determine the data reduction equations.* Some experimental data reduction equations used in Tunnel 9, such as pressure ratios and force coefficients, are simply algebraic. Others are not so straightforward. For example, supply conditions span three orders of magnitude in pressure and a factor of two in temperature. The data reduction equations defining tunnel conditions, to which all test results are referenced, include real gas thermodynamics and are solved iteratively.

2. *Identify the sources of uncertainty for each individual measurement.*

3. *Assess the relative significance of the uncertainty sources.*

4. *Estimate the precision, P, and bias, B, for each significant error source. The total bias and precision are then obtained as the root-sum-square of each contributor.* Reference 5 provides a partial, ranked list of 57 error sources specific to wind tunnel testing. With the wide variations in dynamic pressure and temperature possible in Tunnel 9, the significant error sources will vary within and between tests. An elemental approach to uncertainty that examines each contributor individually would entail a formidable bookkeeping task, which is not ideal in a production environment. Therefore, a "black box" approach is used wherever possible. This approach lumps individual contributors into one contributor which is then assessed by examining its input and output response. For example, pressure transducers are calibrated in-situ prior to every run with a working standard using the same wiring, power supply voltage, amplifiers, filters, etc. There is no need to individually assess the errors due to wiring, amplifier noise, power supply voltage, and filter noise because these contributors are lumped into the overall calibration curve uncertainty.

5. *Propagate the precision and bias limits into the test results, combine into total uncertainties, and document.* Propagation of input uncertainties to the final

results is accomplished using a Taylor series expansion with the inclusion of terms to account for correlated biases, B':

$$B_R^2 = \sum_i \left(\frac{\partial R}{\partial x_i} B_{x_i}\right)^2 + \sum_{i,j;i\neq j} \frac{\partial R}{\partial x_i}\frac{\partial R}{\partial x_j} B'_{x_i} B'_{x_j} \quad (1)$$

$$P_R^2 = \sum_i \left(\frac{\partial R}{\partial x_i} P_{x_i}\right)^2 \quad (2)$$

$$U_R = \left(B_R^2 + P_R^2\right)^{1/2} \quad (3)$$

The total uncertainty U for result R is the root-sum-square of the bias and precision. The partial derivatives represent the sensitivity of the result to each measured input, x_i. For the reasons cited in item 1, this is difficult, if not impossible, to do analytically for Tunnel 9 instrumentation. Therefore, a "jitter" approach is typically used to propagate the precision and bias limits into the test results.

IMPLEMENTATION STRATEGY

In order to apply this methodology consistently and routinely to all Tunnel 9 measurements, the following general procedures have been implemented:

Bias limits

Two contributors to bias for each measurement are considered. The first contributor is the working standard against which the instrument is calibrated, B_{ws}. The second is the bias of the calibration as determined in situ through the test measurement system, B_{cal}. Any precision errors from these two sources become fossilized in the calibration constants. For least-squares fits to calibration data, the calibration bias is taken as $B_{cal} = 2SEE$, where SEE is the standard error of the estimate. If measurements are made outside of the calibration range, the total bias should be increased by an extrapolation factor, C:

$$B = C\left[B_{ws}^2 + (2SEE)^2\right]^{1/2} \quad (4)$$

When measurements are beyond the calibration range, C is set equal to the ratio of the measured value to the maximum calibration point. If the measurement is below the minimum calibration point, the value of C is based on engineering judgement.

Some instruments are not calibrated in place for each test, for example, force balances. In these cases, "check loads" are applied to the instrument and special tare data are recorded and reduced. The results are then compared with the calibration for consistency. The value of B_{cal} is adjusted if necessary, based on engineering judgement.

Precision limits

Precision limits are estimated from in-place readings using the entire measurement system as $P = t_{95}S$. Here, S is the standard deviation and t_{95} is the 95th percentile point for the two-tailed Student's "t" distribution. References 12 and 5 indicate that $t_{95} = 2$ is valid for as few as 9 degrees of freedom. The standard deviations are computed from the static and dynamic tare data recorded prior to each run. The dynamic tares include noise sources generated by the pitch sweep.

Automation of computations

The *SEE* and standard deviation computations are performed automatically as part of the data reduction process. The results are written to the log file detailing the parameters for each run. Separate sections are displayed for each type of instrumentation. Within the pressure section, the details for each transducer are displayed followed by a summary. Figure 2 presents the calibration details for a typical transducer, while figure 3 illustrates the summary section. For each individual transducer, precision limits are computed for each pressure set point in the calibration and the largest one is reported. The summary groups transducers by their pressure capacity. Within each group, the maximum *SEE* and maximum P are identified. In this way, a conservative value can be applied to all similar transducers, or the gauges can be treated individually if desired. The summary also notes the calibration set points that determined each precision, in order to identify and eliminate possible unsteady points.

Propagation to results

References 1–5 point out that propagation can be accomplished numerically using finite differences, but the recommendations among the sources differ. Coleman and Steele's[2] methodology and flowchart were adopted for the propagation of errors. This

```
Calibration Run   25:  Step135:  Dare Chan 198:   PTN

PTN: SLOPE(  2)= 5.0671E-02   INTERCEPT(  2)=-1.9617E+00

X COUNTS     Y INPUT      Y CALC       DIFF
     (BARH=1000 mmHg)
   7946.     399.625     400.662     -1.0368
   5947.     299.432     299.389      0.0432
   4955.     249.497     249.109      0.3871
   3965.     199.552     198.942      0.6093
   2991.     150.273     149.614      0.6588
   1994.      99.577      99.063      0.5134
   1597.      79.336      78.937      0.3987
   1211.      59.693      59.423      0.2708
    800.      38.594      38.566      0.0274
    627.      29.773      29.801     -0.0275
    428.      19.583      19.744     -0.1614
    238.       9.997      10.076     -0.0789
    201.       8.052       8.229     -0.1779
    179.       6.871       7.092     -0.2213
    161.       5.957       6.181     -0.2233
    146.       5.158       5.439     -0.2802
    128.       4.247       4.541     -0.2942
     97.       2.521       2.929     -0.4073

STD ERROR OF ESTIMATE =  4.3467E-01
PRECISION             =  9.0650E-02
```

Figure 2: Log file display of pressure transducer calibration details.

GAGE	RANGE psi	SLOPE mmHg/COUNTS	STD.E.E. mm Hg	PRECISION mm Hg	CALIB PT. mmHg
PB1	5.	1.524E-03	3.6657E-02	1.0311E-02	2.48
PB2	5.	1.462E-03	2.7438E-02	6.8332E-03	2.48
PB4	5.	1.187E-03	2.1574E-02	6.1021E-03	2.48
PB5	5.	1.506E-03	2.0930E-02	6.6187E-03	2.48
PB6	5.	1.480E-03	1.1735E-02	6.7250E-03	2.48
PB7	5.	1.538E-03	1.6415E-02	6.6791E-03	2.48
P1A	5.	6.177E-03	1.0346E-01	8.1294E-02	79.34
P1G	5.	2.517E-02	2.0646E-01	9.0200E-02	399.62
P2A	5.	6.275E-03	9.3231E-02	7.8224E-02	79.34
.					
.					
.					
MAX. STD.E.E.		P5B	3.9926E-01		
MAX. PRECISION		P7E	1.3148E-01		
PTN	15.	5.067E-02	4.3467E-01	9.0650E-02	79.34
PTS	15.	5.055E-02	5.2176E-01	9.2560E-02	399.62
P3G	15.	3.488E-02	1.5095E-01	8.7201E-02	399.62
P9G	15.	3.497E-02	3.5215E-01	8.4486E-02	79.34
MAX. STD.E.E.		PTS	5.2176E-01		
MAX. PRECISION		PTS	9.2560E-02		

Figure 3: Log file summary of pressure transducer calibrations.

method uses a jitter program where the partial derivatives are calculated using finite differences by calling the data reduction computer program as a subroutine. All data reduction software is written in FORTRAN, therefore FORTRAN was also used for the jitter code. The input/output and actual jittering engine were coded in a generic way to allow their application to any problem. A specific implementation then consists of a main program that defines the measured inputs and desired calculated parameters along with a subroutine called `RESULTS` which serves as a gateway to the actual data reduction codes. Equivalence statements associate the variable names in the jitter program to their counterparts in the production code. Advantages of this technique are as follows:

- Makes use of existing data reduction codes, reducing the potential for typographical error.
- Rapid implementation.
- Automatic process, handles both bias and precision limits simultaneously.
- Removes the temptation to perform the analysis with respect to anything other than the independent, measured inputs.

The Tunnel 9 version of the methodology generates two output files. One is a summary of the precision, bias, and total uncertainty for each result. This file is written in comma-delimited format to facilitate import into word processing and spreadsheet programs for documentation or further analysis. The second file is in a format suggested by Coleman and Steele. This shows the results in engineering units and percentages of nominal value which is particularly useful for comprehending the results. It also includes an array of normalized values of the individual contributors to the total bias and precision. The numerical values of the partial derivatives are hidden from the analyst since they are not in obviously meaningful engineering units. Retention of sign for correlated bias terms immediately shows whether the correlation is beneficial or detrimental to the final uncertainty.

To summarize, this general strategy has the following advantages:

- Evaluation of B_{cal} and P from in-situ data automatically includes all data acquisition and reduction components.
- Computation of B_{cal} and P in the primary data reduction program automates the process and ensures consistency across test programs.
- The number of separate error sources to track has been minimized.

- Use of jitter programs automates propagation across the entire tunnel operational map without sacrificing generality when closed form solutions do not exist.

The following sections present the application of the general methodology to the calculation of uncertainties in aerodynamic angles and force coefficients. A waverider configuration tested at Mach 10 and 14 conditions serves to illustrate a typical test situation.[13] Cases where extra effort is needed in the evaluation of precision and bias indices are elaborated upon, and typical results are presented.

AERODYNAMIC ANGLES AND FORCE COEFFICIENTS FOR A HYPERSONIC WAVERIDER

As noted above, the data reduction equations for force testing require 35 measured inputs to compute 20 results. Estimation of the precision and bias for each input will be addressed in turn.

Tunnel conditions

One supply pressure (P_0) transducer, two supply temperature (T_0) thermocouples, and one or two test cell Pitot pressure probes (PT) are used to determine the freestream environment.

The supply pressure (P_0) transducers are piezoresistive bridge-type instruments. For each run, the transducer is calibrated in-place by the application of external shunt resistances to simulate a range of pressure levels. The bias and precision are estimated in the main data reduction program as described above. The shunt resistances are determined on an annual basis for each transducer. To ensure the validity of the pressure-resistance pairs, "check loads" are performed at the start of each test program. The transducer is physically removed from the tunnel and manifolded to the laboratory working standard, retaining the same cabling, signal path, and mounting technique as used for the test. A shunt calibration is then performed using standard test procedures, and a series of physical pressures applied covering the anticipated test levels. Data are recorded and reduced using the production routines. Comparison with the working standard then confirms the adequacy of the bias and precision limits.

The supply temperature, T_0, is measured by two bare-wire beaded thermocouples

fabricated in-house. For Mach 8 and 10 operation the thermocouple materials are chromel versus alumel (type K), while for Mach 7, 14, and 16.5 operation the materials are tungsten-5% rhenium versus tungsten-26% rhenium. Tables from references 14 and 15 convert the millivolt output to temperature. The errors due to conduction and radiation are negligible in the high-density low Mach number plenum area. Bias limits are estimated to be 0.75% of measured value for the letter-designated series and 1% of measured value for the tungsten-rhenium series.[16] Precision limits ($P = t_{95}S$) are computed from the pre-heat static tare where S is the standard deviation of the measurement during the tare. Two thermocouples are used for redundancy. When both thermocouples are functioning properly, the average of the two readings is used as the measured T_0 value, and the bias reduced by a factor $1/\sqrt{2}$.

The Pitot pressure is measured using a variety of piezoresistive transducers. Precision and bias limits are estimated from in-place calibration as described above.

Balance forces and moments

The biases for the six measured loads are computed from the usual two components: B_{ws} and B_{cal}. The working standards are calibrated weight sets. For most of the weight sets, the reported weights are very close to the nominal values. Therefore, the nominal values are used to calculate the calibration coefficients and B_{ws} is taken to be equal to $NDev$, where N is the maximum number of weights hung simultaneously and Dev is the maximum deviation from the nominal for the entire set. This is typically negligible compared to B_{cal}. When using the heaviest weight set (up to 2500 lbf), the reported values are used to calculate the coefficients and B_{ws} is taken directly from the metrology report.

Estimates for the $(B_{cal})_i$ are derived from the residuals $R =$ *(calculated load − applied load)*, which are computed for each loading in the calibration. Specifically,

$$(B_{cal})_i = RSS_j\,[RMS_j(R_{ij})] \tag{5}$$

where $(B_{cal})_i$ is the calibration bias for load component i, R_{ij} are the residuals for load component i computed for calibration loading series j, and RSS_j and RMS_j are the root-sum-square and root-mean-square, respectively, where the sums are performed over each loading series j. The calibration loading series refers to a particular type of loading, e.g. normal, side, axial, etc. The adequacy of the resulting bias estimates are verified by hanging check loads upon installation of the balance in the tunnel.

The estimate of the precision limit must include the dynamics of the pitch sweep.

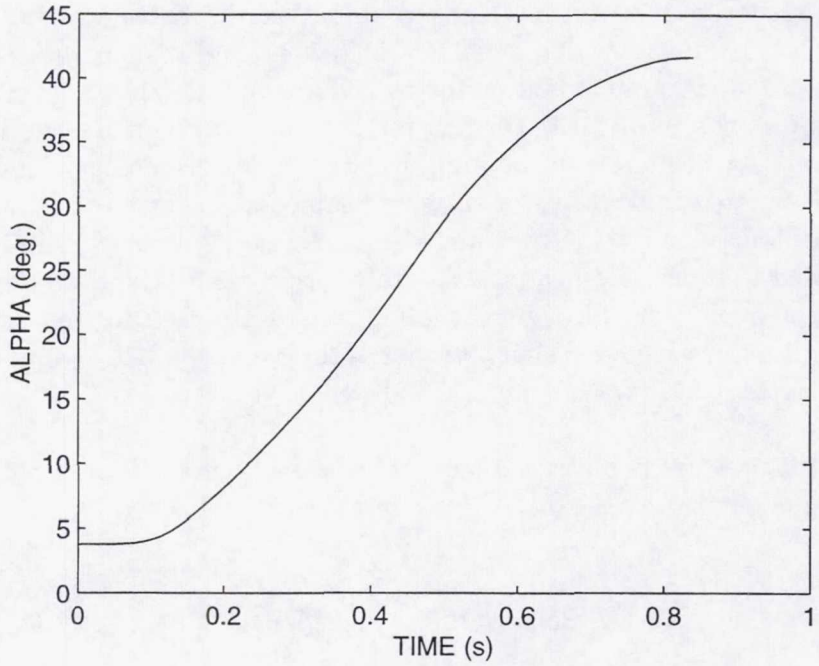

Figure 4: Typical pitch trajectory.

The basic equation for obtaining the aerodynamic loads is given by:

$$\begin{aligned} &\textit{Aerodynamic load} = \\ &\quad \textit{(Wind-on data} - \textit{pre-run static tare)} \\ &\quad -\textit{(Wind-off dynamic tare} - \textit{pre-heat static tare)} \end{aligned} \tag{6}$$

The dynamic tare measures the inertial loads of the sweep, which are subtracted out of the wind-on data. The precision is intimately tied to the repeatability of the hydraulic sector mechanism. Therefore, the precision is estimated statistically from a minimum of 10 repeat dynamic tares. The balance loads are computed for each tare and interpolated at integer increments in angle-of-attack. This allows the computation of standard deviations at each interpolated angle. The largest standard deviation value for each force component is a measure of the precision of the system. This method takes into account the model/balance installation, the cabling and signal conditioning, hydraulic system-induced noise, and digital filtering to remove sting vibrations. Figures 4 and 5 show a nominal pitch trajectory and the normal force results and precision estimate for 10 dynamic tares. When the model is not pitched, the standard deviation from a static tare is used. The overall balance uncertainty estimates are presented in table 3.

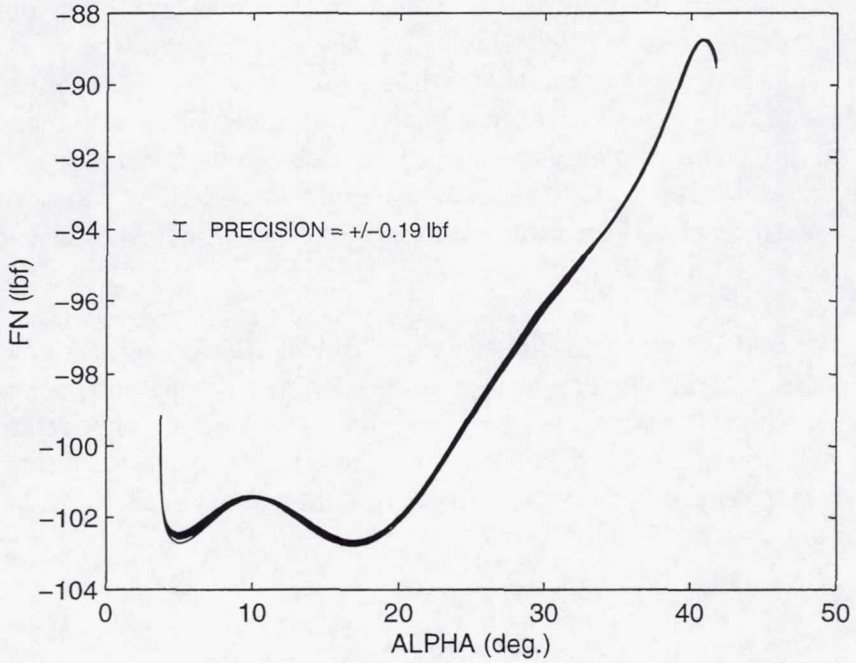

Figure 5: Normal force results from 10 repeat dynamic tares.

Table 3: Force balance uncertainties for the sweep profile of figure 4.

Component units	Capacity	B	S	dof	U_{rss}
FN, lbf	2000	6.48	0.093	10	6.48
FY, lbf	500	2.05	0.177	10	2.08
MY, in-lbf	—	6.59	6.590	10	14.74
MZ, in-lbf	—	5.96	0.288	10	5.99
MX, in-lbf	800	1.13	0.050	10	1.13
FA, lbf	600	0.41	0.275	10	0.69

Reference dimensions

A number of reference lengths and areas need to be measured. The model reference length and area are typically obtained from the acceptance inspection of the model hardware. The base area of models with irregular base geometry but a well-defined base plane can sometimes be measured by tracing the outline on paper, then using a mechanical integrator or planimeter. The precision can be taken as zero, or calculated from the standard deviation of repeat measurements. If the geometry is not suited to direct measurement, these values are sometimes assumed as exact from the model design.

Also required is the three-dimensional offset of the model and balance moment reference centers. These three lengths are obtained during model build up. The procedure involves relative measurements between a temporary reference surface, typically a machinist V-block mounted to the sting, and the calibration body and model mounted on the balance. Gage blocks, calipers, and scales are used to suit the particular geometry.

Model aerodynamic angles

In Tunnel 9, five coordinate system transformations have been defined to determine the model attitude relative to the tunnel freestream velocity. Three angles are required for each transformation, (θ, ψ, ϕ), which correspond to the sequence pitch-yaw-roll. The data reduction program constructs a transformation matrix from each set of angles. The transformations, in order of application, relate the wind to the tunnel, tunnel to the sting, sting to the balance, balance to the model, and finally, model misalignments. The first four systems are illustrated in figure 6.

Each angle for the tunnel-to-sting and sting-to-balance transformations is represented by the sum of two angles, one constant and one variable. In the tunnel-to-sting transformation, the constant angles are used to account for dog-leg geometries while the variable component handles the pitching of the support system. The constant angles are typically measured with a pendulum inclinometer or set identically to zero. The variable sector position is measured as a least-squares fit against the output of a real-type potentiometer. In the sting-to-balance transformation, the variable terms are angular deflections of the sting/balance assembly due to the applied loads, while the constant terms represent any fixed offset. The variable sting/balance deflections are calibrated as a linear combination of load and moment as measured by the balance. For example, pitch deflections are a function of balance normal force

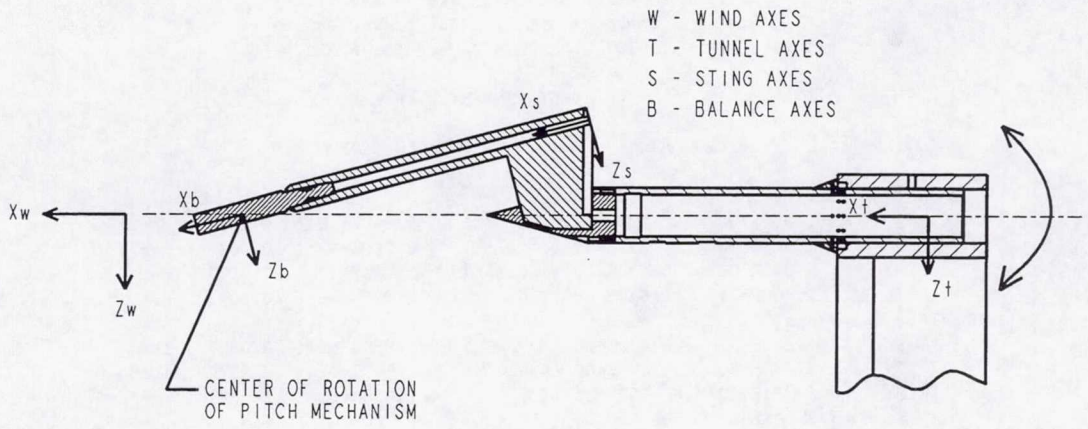

Figure 6: Coordinate systems used in balance transformations.

and pitching moment. All measurements and calibrations are typically made against the same working standard, which results in a large number of correlated biases. Precision errors for the constant angles are set to zero, while those for the variable angles are treated as fossilized in the calibration constants.

Results

Results for a waverider configuration tested at Mach 10 will now be presented. The jitter program input summary is presented in figure 7. For each input, the program requires the nominal value, a delta for use in the finite-difference computation, and the precision and bias. The delta values are arbitrarily chosen to be small compared to the precision and bias values. Next, the correlated bias pairs, if any, are provided, with the correlated bias being equal to the bias of the common working standard. Execution of the program, including the iterative tunnel conditions computations and propagations for all 20 results, requires a fraction of a second per analysis on a 100 MHz MIPS R4000 class Unix workstation. Figure 8 shows the summary, while figures 9 and 10 present detailed results for the axial force coefficient in the body axis system and the drag coefficient in the stability axis system. The result summaries are the most revealing. Only those inputs with a finite contribution are included in the listings. Notice that the uncertainties in the balance loads are by far the dominant contributors. In the body axes (figure 9), for this particular case, the uncertainty in axial force coefficient is driven by the precision in the balance axial force. However, this is true only for axial force. Precision errors are insignificant for the other balance load components, where the bias errors dominate. In the stability axes (figure 10),

TUNNEL 9 FORCE DATA UNCERTAINTY PROPAGATION
Real gas thermodynamics, Pitot pressure measured.
Waverider WTR 1610, Run 2393, Mach 10, ALPHA = 10

INPUT SUMMARY

INPUT	NOM. VALUE	BIAS	PRECISION	
Tunnel conditions and sector position				
P0	1.355E+03	1.300E+01 (0.96%)	2.000E+00 (0.15%)	psia
T0	1.389E+03	1.820E+01 (1.31%)	3.000E-02 (0.00%)	degF
PT	4.940E+00	1.400E-02 (0.28%)	1.400E-02 (0.28%)	psia
THETAS	2.466E+01	1.680E-02 (0.07%)	2.000E-06 (0.00%)	deg
Model measurements				
FN	2.402E+02	6.480E+00 (2.70%)	1.860E-01 (0.08%)	lbf
FY	1.090E+00	2.050E+00 (188.07%)	3.540E-01 (32.48%)	lbf
MY	3.587E+02	6.590E+00 (1.84%)	1.318E+01 (3.67%)	in-lbf
MZ	8.685E+00	5.960E+00 (68.62%)	5.760E-01 (6.63%)	in-lbf
MX	1.413E+01	1.130E+00 (8.00%)	1.000E-01 (0.71%)	in-lbf
FA	4.805E+01	4.100E-01 (0.85%)	5.500E-01 (1.14%)	lbf
PBASE	1.100E-02	4.000E-03 (36.36%)	8.000E-04 (7.27%)	psia
Reference dimensions and moment reference center offsets				
RFAREA	3.753E+02	0.000E+00 (0.00%)	0.000E+00 (0.00%)	in^2
RFLT	3.900E+01	0.000E+00 (0.00%)	0.000E+00 (0.00%)	in
ABASE	6.460E+01	0.000E+00 (0.00%)	0.000E+00 (0.00%)	in^2
DXMC	2.623E+01	1.000E-02 (0.04%)	0.000E+00 (0.00%)	in
DYMC	0.000E+00	5.000E-03 (-- %)	0.000E+00 (-- %)	in
DZMC	-2.113E+00	5.000E-03 (-0.24%)	0.000E+00 (0.00%)	in
Coordinate system transformation angles				
DELVTH	0.000E+00	0.000E+00 (-- %)	0.000E+00 (-- %)	deg
DELVPS	0.000E+00	0.000E+00 (-- %)	0.000E+00 (-- %)	deg
DELVPH	0.000E+00	0.000E+00 (-- %)	0.000E+00 (-- %)	deg
THETAST	-1.493E+01	1.670E-02 (-0.11%)	1.670E-02 (-0.11%)	deg
PSIST	9.500E-01	1.670E-02 (1.76%)	1.670E-02 (1.76%)	deg
PHIST	0.000E+00	1.670E-02 (-- %)	1.670E-02 (-- %)	deg
DELTA	1.840E-01	3.280E-02 (17.83%)	1.000E-03 (0.54%)	deg
GAMA	0.000E+00	0.000E+00 (-- %)	0.000E+00 (-- %)	deg
EPSIL	0.000E+00	0.000E+00 (-- %)	0.000E+00 (-- %)	deg
THETABS	0.000E+00	0.000E+00 (-- %)	0.000E+00 (-- %)	deg
PSIBS	0.000E+00	0.000E+00 (-- %)	0.000E+00 (-- %)	deg
PHIBS	0.000E+00	0.000E+00 (-- %)	0.000E+00 (-- %)	deg
THETAMB	0.000E+00	1.670E-02 (-- %)	1.670E-02 (-- %)	deg
PSIMB	0.000E+00	0.000E+00 (-- %)	0.000E+00 (-- %)	deg
PHIMB	0.000E+00	1.670E-02 (-- %)	1.670E-02 (-- %)	deg
DTHETAM	0.000E+00	1.670E-02 (-- %)	1.670E-02 (-- %)	deg
DPSIM	1.000E-01	1.670E-02 (16.70%)	1.670E-02 (16.70%)	deg
DPHIM	1.700E-02	1.670E-02 (98.24%)	1.670E-02 (98.24%)	deg

CORRELATED BIASES:

FN	,MY	6.250E+00	in-lbf
FY	,FA	1.000E-01	lbf
THETAS	,THETAST	1.670E-02	deg
THETAS	,PHIST	1.670E-02	deg
THETAS	,DELTA	1.670E-02	deg
THETAS	,GAMA	1.670E-02	deg

.
.
.

Figure 7: Jitter program input summary.

TUNNEL 9 FORCE DATA UNCERTAINTY PROPAGATION
Real gas thermodynamics, Pitot pressure measured.
Waverider WTR 1610, Run 2393, Mach 10, ALPHA = 10

RESULT	NOM. VALUE	BIAS	PRECISION	UNCERTAINTY	UNITS
ALPHA ,	9.913E+00,	8.907E-02,	2.895E-02,	9.365E-02,	deg
BETAP ,	-1.048E+00,	2.480E-02,	2.415E-02,	3.462E-02,	deg
NFC ,	2.390E-01,	6.485E-03,	7.002E-04,	6.522E-03,	
PMC ,	-1.542E-01,	4.208E-03,	5.647E-04,	4.245E-03,	
YFC ,	1.097E-03,	2.044E-03,	3.661E-04,	2.077E-03,	
YMC ,	-5.191E-04,	1.383E-03,	2.457E-04,	1.404E-03,	
RMC ,	3.171E-04,	1.187E-04,	2.010E-05,	1.203E-04,	
AFC ,	4.782E-02,	4.519E-04,	5.723E-04,	7.292E-04,	
CPB ,	-1.140E-02,	1.495E-03,	3.011E-04,	1.525E-03,	
CAFC ,	4.586E-02,	5.216E-04,	5.761E-04,	7.772E-04,	
XCPP ,	-6.451E-01,	4.076E-04,	1.412E-03,	1.470E-03,	
XCPY ,	-4.730E-01,	3.678E-01,	6.213E-02,	3.730E-01,	
CLS ,	2.272E-01,	6.387E-03,	6.742E-04,	6.422E-03,	
PMCS ,	-1.542E-01,	4.208E-03,	5.647E-04,	4.245E-03,	
YFCS ,	1.097E-03,	2.044E-03,	3.661E-04,	2.077E-03,	
YMCS ,	-5.659E-04,	1.343E-03,	2.386E-04,	1.364E-03,	
RMCS ,	2.230E-04,	3.492E-04,	6.182E-05,	3.546E-04,	
CDS ,	8.826E-02,	1.229E-03,	5.986E-04,	1.367E-03,	
BETA ,	-1.032E+00,	2.420E-02,	2.379E-02,	3.393E-02,	deg
L/D ,	2.575E+00,	4.225E-02,	1.696E-02,	4.552E-02,	

Figure 8: Jitter program output summary.

the drag coefficient at 10 deg angle-of-attack is driven by the bias in the normal force, with significant contributions from the axial force uncertainties. Attempts to improve the measurements should focus on the balance calibration to reduce the biases and on the dynamics of the pitch sweep to reduce the precision in axial force. The order in which these steps are taken would depend on which results are more important. If the stability axis data are primary, then the bias errors should receive the most attention. If the body axes data are critical, resources should be concentrated on improving the pitch system repeatability.

The analysis was performed over the entire angle-of-attack range. The changes to the input data are confined to changes in the nominal values; the precision and bias estimates were left unchanged. For most computed parameters, the resulting uncertainties vary only a small amount, allowing one uncertainty value to be applied to the entire range of data. This is the case in figure 11, which shows the lift and drag coefficients in the stability axes for three runs at Mach 10, Re=2.0e6/ft. The lift-to-drag ratio is an example where the uncertainty varies significantly over the pitch sweep due to the functional dependence on normal force, axial force, and angle of attack. This is illustrated in figure 12. The result is particularly sensitive to normal force at $L/D = 0$.

Three runs are shown in figures 11 and 12. Data represented by an X are for a run in which the model was swept from -10 to $+25$ degrees. Plus signs $(+)$ represent

```
TUNNEL 9 FORCE DATA UNCERTAINTY PROPAGATION
 Real gas thermodynamics, Pitot pressure measured.
Waverider WTR 1610, Run 2393, Mach 10, ALPHA = 10


          RESULT SUMMARY


     AFC    =  4.782E-02

     Urss =  7.292E-04          ;   1.52%
     B    =  4.519E-04          ;   0.94%
     P    =  5.723E-04          ;   1.20%


     CONTRIBUTION COMPARISON
AS % OF MAX CONTRIBUTOR OF  5.474E-04

INPUT      BIAS TERM     PRECISION TERM

PO                 0                  0
TO                 0                  0
PT                 6                  6
FY                 0                  0
FA                55                100
THETAMB            1                  1
PHIMB              0                  0
DTHETAM            1                  1
DPSIM              0                  0

CORRELATED BIAS TERMS:
FY     ,FA          0
THETAMB,PHIMB       0
THETAMB,DTHETAM     3
THETAMB,DPSIM       0
PHIMB  ,DTHETAM     0
PHIMB  ,DPSIM       0
DTHETAM,DPSIM       0
```

Figure 9: Jitter program output — Axial force coefficient in body axes.

```
TUNNEL 9 FORCE DATA UNCERTAINTY PROPAGATION
  Real gas thermodynamics, Pitot pressure measured.
Waverider WTR 1610, Run 2393, Mach 10, ALPHA = 10

                RESULT SUMMARY


     CDS    =  8.826E-02

     Urss =  1.367E-03          ;   1.55%
     B    =  1.229E-03          ;   1.39%
     P    =  5.986E-04          ;   0.68%


     CONTRIBUTION COMPARISON
AS % OF MAX CONTRIBUTOR OF  1.110E-03

INPUT      BIAS TERM     PRECISION TERM

PO                0                  0
TO                0                  0
PT                5                  5
THETAS            0                  0
FN              100                  0
FY                0                  0
FA               13                 23
THETAST           0                  0
PSIST             0                  0
PHIST             0                  0
DELTA             1                  0
PHIMB             0                  0
DPSIM             0                  0
DPHIM             0                  0

CORRELATED BIAS TERMS:
FY     ,FA          0
THETAS ,THETAST     0
THETAS ,PHIST       0
THETAS ,DELTA       0
THETAS ,GAMA        0
  .
  .
  .
```

Figure 10: Jitter program output — Drag coefficient in stability axes.

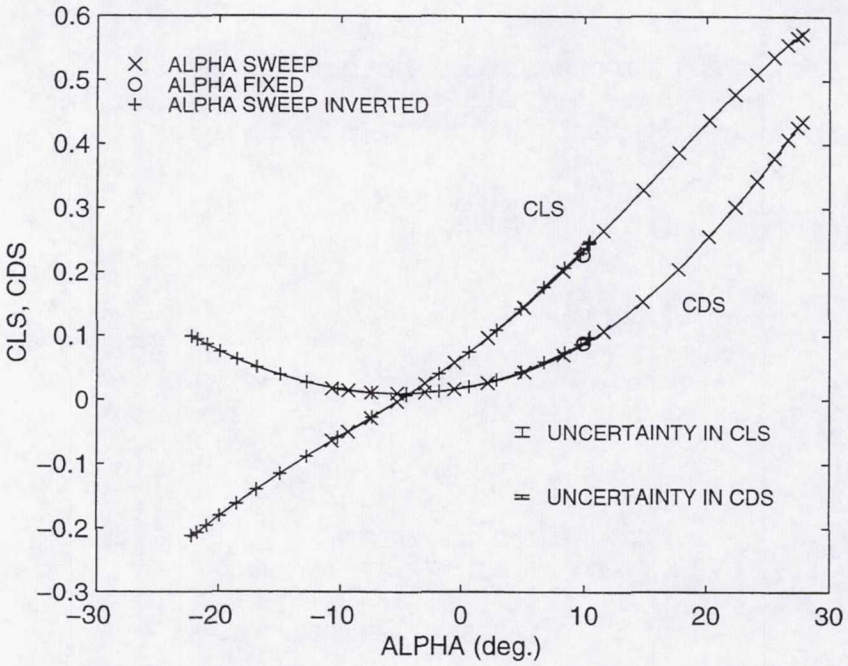

Figure 11: Lift and drag on a waverider configuration at Mach 10.

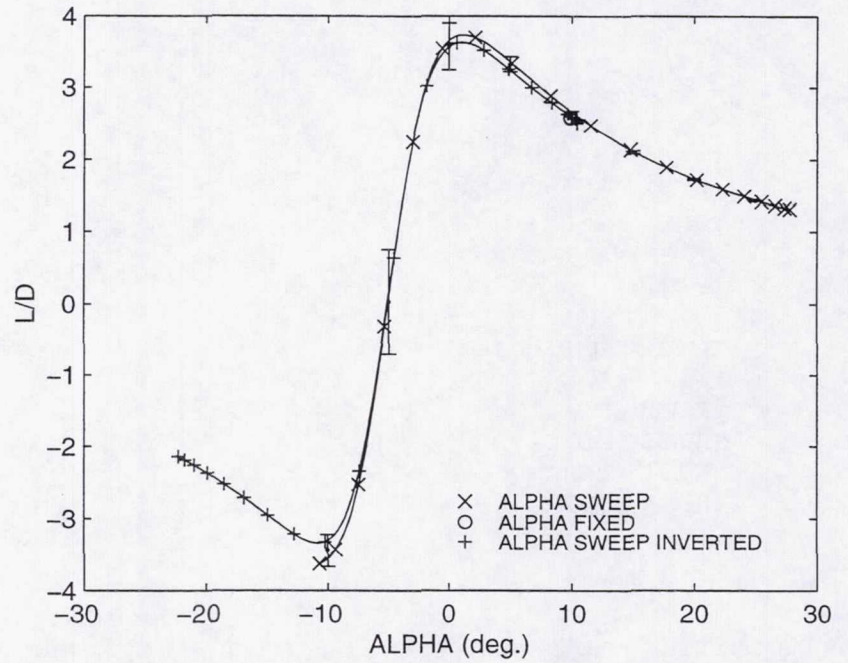

Figure 12: Lift-to-drag ratio on a waverider configuration at Mach 10.

data in which the model/sting combination was rolled 180 deg, thus producing an equivalent +10 to −25 degree sweep. The circles represent data in which the model is held fixed at an angle of +10 degrees throughout the run. The agreement between the dynamic and fixed-angle runs at ALPHA = +10 deg, as well as the agreement between the upright and inverted runs at zero lift/minimum drag at ALPHA = −5 deg, indicates that the inertial effects, sting bending, and model misalignments were being properly accounted for.

CONCLUSIONS

The assessment of experimental uncertainty force measurements as implemented in the NSWC Hypervelocity Tunnel 9 facility has been discussed. The general approach, which is in accordance with AIAA Standard S-071-1995, seeks to account for all significant error sources while reducing the bookkeeping to a manageable level. Wherever possible, precision and bias components are computed automatically by the standard data reduction program, ensuring consistency across test programs. Propagation of errors in measured quantities to computed results is accomplished with a jitter program, This approach maintains generality across a very wide range of tunnel operating conditions and measured loads, while requiring a minimum of programming maintenance. Human involvement is still required to assess the adequacy of bias estimates and interpret the results. However, the overall approach works well in a production testing environment, and may have application to other testing facilities.

References

[1] ANSI/ASME. *Measurement Uncertainty*, volume 19.1 of *Performance Test Codes*. American Society of Mechanical Engineers, 1985.

[2] H. W. Coleman and W. G. Steele, Jr. *Experimentation and Uncertainty Analysis for Engineers*. John Wiley & Sons, 1989.

[3] Ronald H. Dieck. *Measurement Uncertainty: Methods and Applications*. Instrument Society of America, 1992.

[4] ISO/TAG/WG3. *Guide to the Expression of Uncertainty in Measurement*. First edition 1995. International Organization for Standardization, 1993. ISBN 92-67-10188-9.

[5] AIAA. *Assessment of Wind Tunnel Data Uncertainty*. Standard S-071-1995. American Institute of Aeronautics and Astronautics, 1995.

[6] William C. Ragsdale and Christopher F. Boyd. Hypervelocity Wind Tunnel 9 facility handbook, third edition. Technical Report NAVSWC TR 91-616, Naval Surface Warfare Center, Silver Spring, MD 20903-5640, Jul 1993.

[7] John F. Lafferty and Dan E. Marren. NSWC Hypervelocity Tunnel No. 9 Mach 7 thermal structural facility verification and calibration, Jan 1995. AIAA Paper 95-0237, 33rd Aerospace Sciences Meeting, Reno, NV.

[8] Dan E. Marren. Hypervelocity Wind Tunnel 9 Mach 10/14 calibration. Technical Report NSWCDD/TR-92/160, Naval Surface Warfare Center, Silver Spring, MD 20903-5640, Jan 1994.

[9] Nancy F. Swinford. Hypervelocity Wind Tunnel 9 Mach 8 calibration. Technical Report NSWCDD/TR-93/40, Naval Surface Warfare Center, Silver Spring, MD 20903-5640, Mar 1994.

[10] Melissa A. Lederer. Hypervelocity Wind Tunnel Number 9 high Mach number development. Technical Report NSWCDD/TR-94/96, Naval Surface Warfare Center, Silver Spring, MD 20903-5640, Dec 1994.

[11] Charles P. Wright. *Applied Measurement Engineering: How to Design Effective Mechanical Measurement Systems.* Prentice-Hall, 1995.

[12] W. G. Steele, R. A. Ferguson, R. P. Taylor, and H. W. Coleman. Comparison of ANSI/ASME and ISO models for calculation of uncertainty, 1994. ISA Paper 94-1014.

[13] M. E. Kammeyer and M. J. Gillum. Design validation tests on a realistic hypersonic waverider at Mach 10, 14, and 16.5 in the Naval Surface Warfare Center Hypervelocity Wind Tunnel No. 9. Technical Report NSWCDD/TR-93/198, Naval Surface Warfare Center, Silver Spring, MD 20903-5640, 1994.

[14] G. W. Burns, M. G. Scroger, G. F. Strouse, M. C. Croarkin, and W. F. Guthrie. Temperature-electromotive force reference functions and tables for the letter-designated thermocouple types based on the ITS-90, Apr 1993. NIST Monograph 175.

[15] National Institute of Standards and Technology. Temperature-electromotive force reference functions and tables for the tungsten-5% rhenium versus tungsten-26% rhenium thermocouple type based on the ITS-90, Sep 1995. Private communication.

[16] G. W. Burns and D. Ripple. National Institute of Standards and Technology. Private communication, Nov 1994.

EXPERIENCES RELATIVE TO THE INTERACTION BETWEEN THE BALANCE ENGINEER AND THE PROJECT ENGINEER WITH REGARD TO MEASUREMENT UNCERTAINTY

Frank L. Wright
Senior Principal Engineer
Boeing Commercial Airplane Group
Seattle, WA

ABSTRACT

When conducting ground based testing to measure forces and moments on a model, the balance is a key, but not the only component of the measurement system. The data acquisition system is also an important part of the overall measurement system. In the case of a balance which rotates with the model as it is pitched, the measurement of the pitch angle of the balance relative to the freestream velocity vector (angle of attack) is critical in resolving the balance force components into the model stability axes. Many balance engineers tend to view test measurement uncertainty requirements in terms of the forces and moments of the balance. On the other hand, the project engineer who uses the test results views the measurement uncertainty requirements in terms of corrected force and moment coefficients. The uncertainty of these coefficients is not only a function of balance uncertainty, but also of the data acquisition system uncertainty, the angle of attack uncertainty, the dynamic pressure uncertainty, and the uncertainty of any corrections applied to obtain the final results. This paper gives some experiences relative to the measurement uncertainty interaction between balance and project engineers. In addition, statistical analysis techniques and uncertainty analysis methodology are described which can be used to facilitate a productive interchange between balance and project engineers regarding measurement uncertainty requirements.

SUMMARY

Internationally accepted definitions for uncertainty, bias, confidence level and precision are used to define uncertainty budgets for balance requirements. Equations are derived that relate uncertainty budget requirements in lift coefficient, drag coefficient and angle of attack to achievable uncertainty budgets in internal balance normal force, axial force and angle of attack. These expressions will allow the balance engineer (or the project engineer) to determine what balance uncertainties are allowed in meeting lift and drag coefficient and angle of attack uncertainty requirements. More information and knowledge is available to estimate the repeatability (precision) of a internal strain gage balance than its bias (systematic error), so it is recommended that the balance engineer spend most of his uncertainty estimate effort in determining balance precision. Three classes of repeatability are defined as short term, near term and long term, and definitions are provided. The use of statistical analysis of repeat load residuals, balance calibration residuals and historical end zero shifts to estimate the balance repeatability is discussed and results are shown. Some are used to estimate drag coefficient repeatability and compared with that measured during a wind tunnel test. The use of the standard deviation of all of the residuals from a balance calibration appears to provide a reasonable estimate of the balance repeatability during a test. A conservative estimate is obtained if the standard deviation of historical wind-off zero shift data is used. It is seen that

the achievable drag coefficient repeatability using an internal strain gage balance is a strong function of the repeatability of the angle of attack measurement which relates balance axes to stability axes. Two examples of the measured loads experienced during a drag test to the calibration loads are given which show that a better selection of the calibration loads is needed to reduce the uncertainty in the calibration results. The range and spacing of the balance calibration loads significantly exceed those obtained in the test. Perhaps two calibrations are needed, one for drag tests and one for stability and control tests. Additional study is needed relative to this matter and to the math model used to describe the balance performance. Additional work is needed to provide the methodology and data to enable the performance of an internal strain gage balance, both precision and bias, to be realistically and adequately estimated.

INTRODUCTION

As is well known within companies who design, build and sell subsonic commercial jet transports, risk reduction processes are being implemented to assure that guarantees are met without the need to conduct additional extensive and expensive wind tunnel and flight tests after airplane rollout. The one flight performance parameter which commands the most attention is the cruise drag coefficient. Although other performance parameters are also important, the cruise drag coefficient has a major impact on the success of a commercial transport. The total cruise drag coefficient is determined from a buildup such as the following one:

$$\mathbf{CD_{Full\ Scale}} = CD_{\text{Wind Tunnel}} + CD_{\text{Full Scale Adjustments}} \quad (1)$$

$$\mathbf{CD_{Wind\ Tunnel}} = CD_{\text{Balance}} + \Delta CD_{\text{Upflow}} + \Delta CD_{\text{Wall Interference}} + \Delta CD_{\text{Mount}} + \Delta CD_{\text{Buoyancy}} + \Delta CD_{\text{Internal Drag}} + \Delta CD_{\text{Thrust}} + \Delta CD_{\text{Trim}} + \Delta CD_{\text{Trip}} + \Delta CD_{\text{Laminar Run}} \quad (2)$$

The drag coefficient terms which usually involve balance measurements are:

$\mathbf{CD_{Balance}}$ = Drag coefficient from the balance corrected for weight tare.
$\mathbf{\Delta CD_{Upflow}}$ = Drag coefficient correction due to integrated clear tunnel flow angularity angle. It is usually determined by testing the model upright and inverted, and derived from balance normal force coefficient versus angle of attack curves.
$\mathbf{\Delta CD_{Mount}}$ = Drag coefficient correction due to model mounting system. It is usually determined by testing the model on two different mounting systems with and without dummy representations of the mounting systems and taking the difference in the balance drag coefficient readings.
$\mathbf{\Delta CD_{Thrust}}$ = Drag coefficient correction due to thrust effects. It is usually determined from balance readings by testing the model at ram pressure ratio and some other pressure ratio, correcting both sets of data for their respective thrusts, and then taking the difference in the resulting drag coefficients. May or may not be determined with the gross thrust vectored with angle of attack.
$\mathbf{\Delta CD_{Trim}}$ = Drag coefficient correction due to trimming the pitching moment to zero. It is usually determined from balance readings by testing the model with the horizontal tail, elevators or canards off and with them installed at several deflection angles.
$\mathbf{\Delta CD_{Trip}}$ = Drag coefficient correction due to boundary layer transition devices. It is usually determined from balance readings by testing the model with various heights of the devices and extrapolating drag coefficients back to zero height.

In this paper only the $CD_{Balance}$ term will be addressed.

For some wind tunnel models, an internal strain gage balance is used, installed inside the model and rotating with the model when it is pitched. In other cases, the model is attached to an external balance which remains stationary when the model is pitched. Additionally, for some semi-span model installations, the external balance rotates with the model. *Hence, the resolution of the balance normal and axial forces into lift and drag forces is dependent upon the balance attitude for many model installations.*

DISCUSSION

Interaction Between the Project and Balance Engineer

Project Engineer Accuracy Requirements

Even among the project engineers there has not been a clear understanding of "accuracy" requirements or commonly agreed to definitions for specifying them. Over the years, the author has heard these types of "accuracy" requirement statements used among the project engineers:

1. ±**XX** percent data are needed to meet performance guarantees.
2. Data are needed that are repeatable to ±**XX** percent.
3. The scatter in the data should be less than ±**XX** percent.
4. Data should be accurate to within ±**XX** percent.
5. The maximum error in the data should be ±**XX** percent.
6. The data should be better than ±**XX** percent.
7. The tolerance for the data should be ±**XX** percent.
8. The error band for the data should be ±**XX** percent.

Needless to say, these kind of statements have provoked considerable discussions among the engineers as to what they mean and which one(s) are or are not correct. With these kind of definitions, it is no wonder that the project engineers had a difficult time in conveying their accuracy requirements to anyone, much less to the balance engineers. However, in the last few years the project engineers have made progress in their ability to specify their accuracy requirements in terms that can be understood by all. This improvement has involved the use of internationally accepted statistical and uncertainty definitions (Reference 1 and 2) such as uncertainty, bias, precision, confidence level and degrees of freedom (number of points). However, these accuracy specifications tend to be for stability axes force and moment coefficients for only certain test conditions. The specifications are often supplied without the test conditions being provided.

Balance Engineer Accuracy Requirements

The recent (1991) Boeing exploration of designing and building a new pressure wind tunnel complex provided some experiences of the communication difficulties between the balance and project engineers in regard to "accuracy" requirements. The balance engineers were to provide one or more external balances and a family of internal balances for low speed and transonic testing of full and semi-span models. The

balance engineers prepared a balance accuracy requirements survey form to be distributed to several project engineers to be completed by them. The form asked for the maximum expected loads (in pounds and inch-pounds) for normal force, axial force, side force, pitching moment, yawing moment and rolling moment for the external and internal balances at various test conditions, usually Mach number, dynamic pressure and tunnel total pressure. Also, the form asked for the required "accuracies" (in pounds and inch-pounds) for the six balance components for the external and internal balances. Prior to the form being distributed, the author was asked to review it. This engineer pointed out that if this survey form was sent to the project engineers very few of them would be returned. This result would occur because the project engineer views the measurement accuracy requirements in terms of corrected force and moment coefficients. And the accuracy of these coefficients is not only a function of balance uncertainty, but also of the data acquisition system uncertainty, the angle of attack uncertainty, the dynamic pressure uncertainty, and the uncertainty of any corrections applied to obtain the final results. Consequently, even if a form was completed and returned, for all of the blanks to be filled in requiring pounds and inch-pounds, the pounds and inch-pounds would be crossed out and coefficients used. In addition, the moment requirements depend upon the moment reference center, and this information was not requested for either maximum expected moments or accuracies. The author suggested that the following accuracy (uncertainty) requirement specifications be incorporated into the form.

1. The confidence level. In accordance with accepted international practice (Reference 1 and 2), it is suggested that the confidence level be 95 percent.
2. A statement as to how much of the accuracy specification is bias and how much is precision. Assuming a root-sum-square addition for combining bias and precision to obtain accuracy (uncertainty), any two of the three can be provided and the other determined.

$$U_{RSS} = \pm [(\text{Bias})^2 + (\text{Precision})^2]^{1/2} \qquad \text{(95 percent confidence level)}$$

3. If the specification is given as a percent, a statement that it is percent of value or reading, unless for some reason it is given in percent of some other value.
4. A statement if the specification applies to absolute levels or to increments or to both.
5. A statement as to the number of runs and/or data points assumed in determining the specification.
6. The test conditions for which the specification applies:
   - The model pitch attitude (angle of attack) and the axis system used to define it. The relationship between the model angle of attack and the balance angle of attack, if different. The model yaw attitude (yaw angle) and the axis system used to define it. The relationship between the model yaw angle and the balance yaw angle, if different. The specification could be a range of model attitudes.
   - The test Mach number and dynamic pressure. The specification could be a range of values.
   - The test Reynolds number per foot. The specification could be a range of values.
7. The moment reference center for all moment requirements.

Most of these suggested changes were incorporated into the form and it was distributed to the project engineers. Several of them were returned with most of the form completed. However, the balance engineers were unsure as to what to do with the coefficient information the forms contained and how to translate it into the familiar terms of pounds and inch-pounds. The author assisted the balance engineers by helping them to perform a preliminary, first order uncertainty analysis, especially for drag. Assumptions for this first order uncertainty analysis were:

1. Since the uncertainty introduced by data acquisition systems tends to be 3 to 5 times less than that of the balance, its contribution was neglected.
2. The uncertainty of the dynamic pressure is much less than that for drag so its contribution was neglected.
3. The project engineer's requirements tend to be specified in terms of repeatability (precision) since the engineer assumes that there will be no significant biases. Hence, the first order uncertainty analysis dealt with repeatability (precision) at a 95 percent confidence level (2 sigma).
4. A generalized ratio of the absolute level uncertainty of the balance to its repeatability (precision) is often specified as 3 to 1 (Reference 3). This ratio from Reference 3 is the same ratio which was specified by a senior balance engineer at the Boeing Aerodynamics Laboratory many years ago and often has been used for uncertainty analysis. The author felt that this ratio had been determined by a direct addition of the estimated balance bias and precision. If a root-sum-square approach is used, this ratio becomes:

$$U_{ADD} = [(\text{Bias}) + (\text{Precision})] = [(\text{Bias}) + (2\ \text{Sigma})]$$
$$\text{Bias} = U_{ADD} - \text{Precision} = (3)(2\ \text{Sigma}) - (2\ \text{Sigma}) = (2)(2\ \text{Sigma})$$
$$U_{RSS} = [(\text{Bias})^2 + (\text{Precision})^2]^{1/2}$$
$$U_{RSS} = \{[(2)(2\text{Sigma})]^2 + (2\text{Sigma})^2\}^{1/2} = (2\text{Sigma})(5)^{0.5} = 2.236\ (2\text{Sigma})$$
$$U_{RSS} / \text{Precision} = 2.236$$

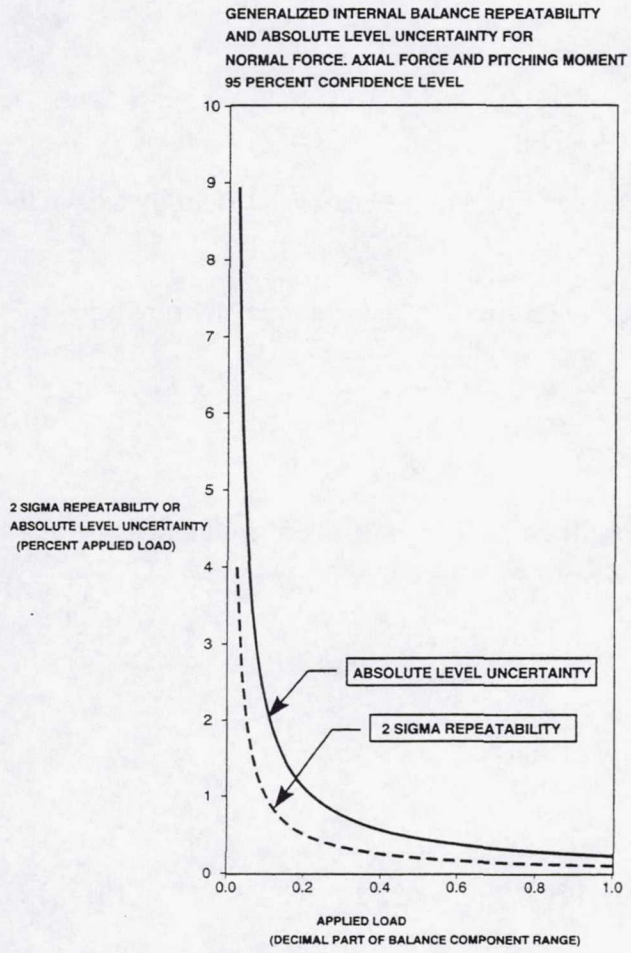

Figure 1. Percentage of Balance Range Values.

The author suggests that, in the absence of more complete information about the balance bias, estimating the **precision** uncertainty requirements for balance normal and axial force and multiplying them by 2.236 to obtain an estimate for the **absolute level** uncertainty. A plot of the generalized 2 sigma repeatability (precision) and the absolute level uncertainty in percent of load as a function of the load (the ratio of the load to the range of the balance) used at the Boeing Aerodynamics Laboratory for internal balance normal force, axial force and pitching moment is provided in Figure 1. The load range for normal force, axial force and pitching moment for an internal balance often used for drag testing at Boeing is:

Normal Force = 3,200 lb.
Axial Force = 240 lb.
Pitching Moment = 9,000 in-lb.

Lift and Drag Coefficient Uncertainty Analysis Equation Derivation

Basic Stability Axis Lift and Drag Coefficient Equations

$$C_L = (L)/[(Q)(S_{REF})] \quad (3)$$
$$C_D = (D)/[(Q)(SREF)] \quad (4)$$

C_D = Drag coefficient
C_L = Lift coefficient
D = Drag ~ lb.
L = Lift ~ lb.
Q = Dynamic pressure ~ pounds per square foot
S_{REF} = Reference area ~ square feet

Internal Balance Lift, Drag, Normal Force and Axial Force Coefficient Relationships

The basic lift and drag force equations for an internal strain gage balance which rotates with the model are:

$$L = (NF)\ (COS\ \alpha) - (AF)\ (SIN\ \alpha) \quad (5)$$
$$D = (AF)\ (COS\ \alpha) + (NF)\ (SIN\ \alpha) \quad (6)$$

AF = Balance axis axial force ~ lb.
D = Stability axis drag ~ lb.
L = Stability axis lift ~ lb
NF = Balance axis normal force ~ lb.
α = Angle of attack. Angle between the horizontal balance axis and the horizontal stability axis in the pitch plane ~ deg.

Dividing the left and right hand sides of the equation 5 and 6 by the dynamic pressure times the reference area $(Q)(S_{REF})$ gives

$$C_L = (C_{NF})\ (COS\ \alpha) - (C_{AF})\ (SIN\ \alpha) \quad (7)$$
$$C_D = (C_{AF})\ (COS\ \alpha) + (C_{NF})\ (SIN\ \alpha) \quad (8)$$

Since the project engineer will provide values of lift coefficient, drag coefficient and angle of attack for each test condition of interest, the above represents two equations in two unknowns (C_{NF} and C_{AF}) which can be solved for each of the unknowns.

Solving equation 7 for C_{AF}:

$$C_{AF} = \{[(CNF)\ (COS\ \alpha) - (C_L)] / (SIN\ \alpha)\} \quad (9)$$

Substituting equation 9 into equation 8 gives:

$$C_D = \{[(C_L) - (C_{NF})\ (COS\ \alpha)] / (SIN\ \alpha)\}\ (COS\ \alpha) + (C_{NF})\ (SIN\ \alpha) \quad (10)$$

Solving equation 10 for C_{NF}:

$$C_{NF} = \{[C_D + (C_L)(\cos \alpha) / (\sin \alpha)] / [(\cos \alpha)^2 / (\sin \alpha) + (\sin \alpha)]\} \quad (11)$$
$$C_{NF} = \{[C_D + (C_L) / (\tan \alpha)] [\sin \alpha]\} \quad (12)$$

An example of the use of these equations, if the project engineer provides the following for the cruise test condition and states that the coefficients represent the balance loads corrected for weight tares, but without additional corrections:

Reference area = S_{REF} = 4.0 sq. ft.
Mach No. = 0.8
Dynamic pressure = 625 pounds per square foot (psf)
Angle of attack = 2 degrees (in stability axis)
Lift coefficient (C_L) = 0.5
Drag coefficient (C_D) = 0.0250

Then, the balance normal and axial force coefficients would be:

$$C_{NF} = \{[C_D + (C_L) / (\tan \alpha)] [\sin \alpha]\} \quad (12)$$
$$C_{NF} = 0.500568$$
$$C_{AF} = \{[(C_{NF}) (\cos 2) - (0.5)] / (\sin 2)\} \quad (9)$$
$$C_{AF} = 0.00754$$

And the loads would be:

$$AF = (C_{AF})(Q)(S_{REF}) \sim \text{pounds}$$
$$AF = (0.00754)(625)(4.0) = 18.85 \sim \text{pounds}$$
$$NF = (C_{NF})(Q)(S_{REF}) \sim \text{pounds}$$
$$NF = (0.50057)(625)(4.0) = 1251.425 \sim \text{pounds}$$

Derivation of Basic Lift and Drag Coefficient Uncertainty Equations

$$C_L = (L)/[(Q)(S_{REF})] \quad (13)$$
$$C_D = (D)/[(Q)(S_{REF})] \quad (14)$$

An uncertainty (error) propagation technique is given in Reference 4. For a result, r, which is a function of several variables X1, X2.....XJ, the uncertainty propagation equation is:

$$(U_r)^2 = \{[(\partial r / \partial X1) (U_{X1})]^2 + ... + [\partial r / \partial XJ) (U_{XJ})]^2\}$$

Applying this technique to equations 13 and 14 gives:

$$[U_{CL}] = \{ [(U_L)]^2 + [- (U_Q)]^2\}^{0.5} \quad (15)$$
$$[U_{CD}] = \{ [(U_D)]^2 + [- (U_Q)]^2\}^{0.5} \quad (16)$$

For this derivation, Ux is the ratio of the uncertainty in a parameter to the value of the parameter. Making the uncertainty terms equal to 2 sigma or 2σ values, equations (15) and (16) become:

$$2\sigma\, C_L / C_L = \{ [(2\sigma\, L) / (L)]^2 + [- (2\sigma\, Q) / (Q)]^2 \}^{0.5} \quad (17)$$
$$2\sigma\, C_D / C_D = \{ [(2\sigma\, D) / (D)]^2 + [- (2\sigma\, Q) / (Q)]^2 \}^{0.5} \quad (18)$$

At this stage it will be assumed that the accuracy in dynamic pressure is much better than that for drag and about the same for lift. For example, for the Boeing Transonic Wind Tunnel (BTWT), a typical comparison of the lift and drag repeatability versus the dynamic pressure repeatability is:

Mach No.	$[(2\sigma L) / (L)]$	$[(2\sigma D) / (D)]$	$[(2\sigma Q) / (Q)]$
0.7	0.0068	0.012	0.0025
0.8	0.0024	0.006	0.0025

Since the uncertainty in dynamic pressure is significantly smaller than that for drag, and since the uncertainty analyses which follow will be focussed on drag, the dynamic pressure uncertainty will be dropped in both the lift and drag uncertainty analysis equations.

$$2\sigma C_L / C_L = \{ [(2\sigma L) / (L)]^2 \}^{0.5} \quad (19)$$
$$2\sigma C_D / C_D = \{ [(2\sigma D) / (D)]^2 \}^{0.5} \quad (20)$$

Derivation of Lift, Drag, Normal Force and Axial Force Coefficient Uncertainty Equations for an Internal Balance

The lift and drag force equations for an internal strain gage balance which rotates with the model are:

$$L = (NF)(\cos\alpha) - (AF)(\sin\alpha) \quad (21)$$
$$D = (AF)(\cos\alpha) + (NF)(\sin\alpha) \quad (22)$$

Dividing both sides of the above equations by the product of the reference area (SREF) and the dynamic pressure (Q) gives:

$$C_L = (C_{NF})(\cos\alpha) - (C_{AF})(\sin\alpha) \quad (23)$$
$$C_D = (C_{AF})(\cos\alpha) + (C_{NF})(\sin\alpha) \quad (24)$$

Substituting the small angle assumptions ($\cos\alpha = 1$, $\sin\alpha = \tan\alpha = \alpha$ in radians) into equation 23 and 24 yields:

$$C_L = (C_{NF}) - (C_{AF})(\alpha) \quad (25)$$
$$C_D = (C_{AF}) + (C_{NF})(\alpha) \quad (26)$$

The small angle assumptions are used to make the following mathematical derivations easier to follow. These small angle assumptions are valid in the angle of attack range of ± 10 degrees which includes the minimum and cruise drag angles of attack. A derivation without the small angle assumptions is provided in Appendix A. Results obtained with and without making the small angle assumptions were compared and there was no significant difference between them. Also, the small angle assumptions could be made after the uncertainty propagation equations have been derived. However, no significant difference in the uncertainty estimates are obtained whether the small angle assumptions are made initially or later in the uncertainty propagation equations.

An uncertainty (error) propagation technique is given in Reference 4. For a result, r, which is a function of several variables X1, X2.....XJ, the uncertainty propagation equation is:

$$(U_r)^2 = \{[(\partial r / \partial X1)(U_{X1})]^2 + ... + [\partial r / \partial XJ)(U_{XJ})]^2\}$$

Applying this technique to equations 25 and 26 and assuming the uncertainty contribution of the dynamic pressure is much less than that of the other parameters:

$$(U_{CL})^2 = (U_{CNF})^2 + (-\alpha U_{CAF})^2 + (-C_{AF} U_\alpha)^2 \quad (27)$$
$$(U_{CD})^2 = (U_{CAF})^2 + (\alpha U_{CNF})^2 + (C_{NF} U_\alpha)^2 \quad (28)$$

The α and U_α terms must be in radians.

Now, if the balance engineer has U_{CNF} and U_{CAF} for his balance and has an estimate for $U\alpha$ from an instrumentation or test engineer, then he can estimate the resulting uncertainties in C_L and and C_D using the previous two equations. However, it may be more useful to be able to estimate the U_{CNF} and U_{CAF} of a balance needed to obtain the project engineer's requirements for U_{CL} and U_{CD}.

Solving equations 27 and 28 simultaneously for UC_{AF} and UC_{NF} :

$$[UC_{AF}]^2 = \{-[UC_D]^2 + [(\alpha)(UC_L)]^2 + [(C_{NF})(U\alpha)]^2 - [(C_{AF})(\alpha)(U\alpha)]^2\}/[(\alpha)^4 - 1] \quad (29)$$
$$[UC_{NF}]^2 = \{-[UC_L]^2 + [(\alpha)(UC_D)]^2 + [(C_{AF})(U\alpha)]^2 - [(C_{NF})(\alpha)(U\alpha)]^2\}/[(\alpha)^4 - 1] \quad (30)$$

Example Calculation Process To Determine C_{NF} and C_{AF} Uncertainty Requirements

Assume that the project engineer supplies lift coefficient, drag coefficient and angle of attack repeatabilities and accuracies at a 95 percent confidence level. Assume that the following 2σ repeatabilities for the cruise and minimum drag cases are provided.

$U_{CL} = 2\sigma C_L = 0.005$
$U_{CD} = 2\sigma C_D = 0.0001$ (one drag count)
$U_\alpha = 2\sigma(\alpha) = 0.01$ degrees or 0.00017452 radians

Assume that the instrumentation engineer supplies angle of attack repeatability and accuracy at a 95 percent confidence level, and that the following 2σ repeatability is provided:

$U_\alpha = 2\sigma(\alpha) = 0.01$ degrees or 0.00017452 radians

Assume the project engineer provides the following information for the cruise and minimum drag test condition and states that the coefficients represent the balance loads corrected for weight tares, but without additional corrections.

Reference area = S_{REF} = 4.0 sq. ft.
Mach No. = 0.8
Dynamic pressure = 625 pounds per square foot (psf)

Cruise drag case:

Angle of attack = 2 degrees (in stability axes)
Lift coefficient (C_L) = 0.5
Drag coefficient (C_D) = 0.0250

Minimum drag case:

Angle of attack = - 0.5 degrees (in stability axes)
Lift coefficient (C_L) = 0.1
Drag coefficient (C_D) = 0.0175

Cruise Drag Coefficient Condition

Then, the balance normal and axial force coefficients would be for the cruise drag case:

$C_{NF} = \{[C_D + (C_L) / (TAN\ \alpha)]\ [SIN\ \alpha)$
$C_{NF} = 0.500568$
$C_{AF} = \{[\ (C_{NF})\ (COS\ 2) - (0.5\ )] / (SIN\ 2)\}$
$C_{AF} = 0.00754$

$$[UC_{AF}]^2 = \{-[UC_D]^2 + [(\alpha)(UC_L)]^2 + [(C_{NF})(U\alpha)]^2 - [(C_{AF})(\alpha)(U\alpha)]^2\}/[(\alpha)^4 - 1] \quad (29)$$
$$[UC_{NF}]^2 = \{-[UC_L]^2 + [(\alpha)(UC_D)]^2 + [(C_{AF})(U\alpha)]^2 - [(C_{NF})(\alpha)(U\alpha)]^2\}/[(\alpha)^4 - 1] \quad (30)$$

All of the variables on the right side of the equation 29 and 30 are known so that UC_{AF} and UC_{NF} can be computed.

$[2\alpha C_{AF}]^2 = \{-[2\alpha C_D]^2 + [(\alpha)(2\sigma CL)]^2 + [(C_{NF})(2\sigma\alpha)]^2 - [(C_{AF})(\alpha)(2\sigma\alpha)]^2\}/[(\alpha)^4 - 1]$
$[2\sigma CAF]^2 = \{-[0.0001]^2 + [(0.0349)(0.002)]^2 + [(0.50057)(0.00017453)]^2$
$\quad - [(0.00754)(0.0349)(0.00017453)]^2\}/[(0.0349)^4 - 1]$
$[2\sigma C_{AF}]^2 = [\ 2.506 \times 10^{-9}\ ] / [\ - 0.999998517] = [\ - 2.506 \times 10^{-9}\ ]$

Since we can't take the square root of a negative number, we can get no answer for $2\sigma C_{AF}$ for this combination of α, C_{AF} , C_{NF} , C_L and C_D with the requested 2σ uncertainty budgets for C_L , C_D , and α.

If the $(2\sigma\alpha)$ uncertainty budget is reduced to 0.005 degrees (0.00008726 radians) we get:

$(2\sigma C_{AF})^2 = (3.217 \times 10\text{-}9)$
$2\sigma C_{AF} = 0.000057$

We now have a solution for $2\sigma C_{AF}$.

Solving for $2\sigma C_{NF}$:

$[2\sigma C_{NF}]^2 = \{-[2\sigma C_L]^2 + [(\alpha)(2\sigma C_D)]^2 + [(C_{AF})(2\sigma\alpha)]^2 - [(C_{NF})(\alpha)(2\sigma\alpha)]^2\}/[(\alpha)^4 - 1]$
$[2\sigma C_{NF}]^2 = \{-[0.002]^2 + [(0.0349)(0.0001)]^2 + [(0.00754)(0.00017453)]^2$
$\quad - [(0.50057)(0.0349)(0.00017453)]^2\}/[(\alpha)^4 - 1]$
$2\sigma C_{NF} = 0.001999$

Minimum Drag Coefficient Condition

The balance normal and axial force coefficients would be for the **minimum drag case**:

$C_{NF} = \{[C_D + (C_L) / (\text{TAN } \alpha)] [\text{SIN } \alpha)$
$C_{NF} = 0.09984$
$C_{AF} = \{[(C_{NF}) (\text{COS } -0.5) - (0.1)] / (\text{SIN } -0.5)\}$
$C_{AF} = 0.01837$

$$[UC_{AF}]^2 = \{-[U_{CD}]^2 + [(\alpha)(U_{CL})]^2 + [(C_{NF})(U\alpha)]^2 - [(C_{AF})(\alpha)(U\alpha)]^2\}/[(\alpha)^4 - 1] \quad (29)$$
$$[UC_{NF}]^2 = \{-[U_{CL}]^2 + [(\alpha)(U_{CD})]^2 + [(C_{AF})(U\alpha)]^2 - [(C_{NF})(\alpha)(U\alpha)]^2\}/[(\alpha)^4 - 1] \quad (30)$$

Computing U_{CAF} and U_{CNF} :

$$[2\sigma C_{AF}]^2 = \{-[2\sigma_{CD}]^2 + [(\alpha)(2\sigma C_L)]^2 + [(C_{NF})(2\sigma\alpha)]^2 - [(C_{AF})(\alpha)(2\sigma\alpha)]^2\}/[(\alpha)^4 - 1]$$
$$[2\sigma C_{AF}]^2 = \{-[0.0001]^2 + [(-0.0087)(0.005)]^2 + [(0.09984)(0.00017453)]^2$$
$$- [(0.01837)(-0.0087)(0.00017453)]^2\}/[(-0.0087)^4 - 1]$$
$$[2\sigma C_{AF}]^2 = [\ 7.7937 \times 10^{-9}\ ]$$
$$[2\sigma C_{AF}] = 0.000088$$
$$[2\sigma C_{NF}]^2 = \{-[2\sigma C_L]^2 + [(\alpha)(2\sigma C_D)]^2 + [(C_{AF})(2\sigma\alpha)]^2 - [(C_{NF})(\alpha)(2\sigma\alpha)]^2\}/[(\alpha)^4 - 1]$$
$$[2\sigma C_{NF}]^2 = \{-[0.005]^2 + [(-0.0087)(0.0001)]^2 + [(0.01837)(0.00017453)]^2$$
$$- [(0.09984))(-0.0087)(0.00017453)]^2\}/[(-0.0087)^4 - 1]$$
$$2\sigma C_{NF} = 0.005$$

For these cruise and minimum drag coefficient calculation cases, it becomes apparent that $2\sigma C_L$ and $2\sigma C_{NF}$ are, for all intents and purposes, the same.

The example calculation process was programmed into a spread sheet so that the sensitivity of the calculated uncertainty budgets $2\sigma C_{AF}$ and $2\sigma C_{NF}$ to various combinations of α, C_{AF} , C_{NF} , C_L and C_D with various 2σ uncertainty budgets for C_L , C_D , and α could be investigated. In addition, unrealistic combinations of test conditions and uncertainty budgets which have no solution for $2\sigma C_{AF}$ and $2\sigma C_{NF}$ could be identified. An example of the spread sheet output is presented in Figure 2 for four **cruise drag** cases and in Figure 3 for four **minimum drag** cases. The load range for normal force, axial force and pitching moment for an internal balance often used for cruise drag testing at Boeing is:

Normal Force = 3,200 lb. Axial Force = 240 lb. Pitching Moment = 9,000 in-lb.

The normal and axial force coefficients corresponding to these load ranges at the cruise and minimum drag conditions of Figure 2 and 3 are $C_{NF} = 1.28$ and $C_{AF} = 0.096$. The two sigma uncertainties for normal and axial force coefficients calculated in Figure 2 and 3 are expressed as a percent of both balance range and of reading and are presented in the table on page 13. Also, the percent of the balance range values are compared with the generalized percent from Figure 1. The generalized percent agrees with the estimated percent for axial force,in most cases, but is too low for the normal force percent.

CASE 1

SREF (SQ FT)	MACH	Q (PSF)	ALPHA (DEG)	CL	CD	CNF	CAF	UCL (2 Sigma)	UCD (2 Sigma)	UALPHA (2 Sigma Radians)
4	0.8	625	2	0.5	0.025	0.500568	0.75400	0.005	0.0001	0.000174532 (0.01 Degrees)

(UCAF)^2	UCAF (2 Sigma)	(UCNF)^2	UCNF (2 Sigma)	UAF (LB-2 Sigma)	UNF (LB-2 Sigma)
-2.8090E-08					

CASE 2

SREF (SQ FT)	MACH	Q (PSF)	ALPHA (DEG)	CL	CD	CNF	CAF	UCL (2 Sigma)	UCD (2 Sigma)	UALPHA (2 Sigma Radians)
4	0.8	625	2	0.5	0.025	0.50057	0.75400	0.002	0.0001	0.000174532 (0.01 Degrees)

(UCAF)^2	UCAF (2 Sigma)	(UCNF)^2	UCNF (2 Sigma)	UAF (LB-2 Sigma)	UNF (LB-2 Sigma)
-2.505830E-09					

CASE 3

SREF (SQ FT)	MACH	Q (PSF)	ALPHA (DEG)	CL	CD	CNF	CAF	UCL (2 Sigma)	UCD (2 Sigma)	UALPHA (2 Sigma Radians)
4	0.8	625	2	0.5	0.025	0.50057	0.75400	0.002	0.0001	8.72660E-05 (0.005 Degrees)

(UCAF)^2	UCAF (2 Sigma)	(UCNF)^2	UCNF (2 Sigma)	UAF (LB-2 Sigma)	UNF (LB-2 Sigma)
3.218680E-09	0.570000	4.0E-06	0.200000	0.14	5.00

CASE 4

SREF (SQ FT)	MACH	Q (PSF)	ALPHA (DEG)	CL	CD	CNF	CAF	UCL (2 Sigma)	UCD (2 Sigma)	UALPHA (2 Sigma Radians)
4	0.8	625	2	0.5	0.025	0.50057	0.75400	0.002	0.00015	0.000174532 (0.01 Degrees)

(UCAF)^2	UCAF (2 Sigma)	(UCNF)^2	UCNF (2 Sigma)	UAF (LB-2 Sigma)	UNF (LB-2 Sigma)
9.994190E-09	0.100000	4.0E-06	0.200000	0.25	5.00

Figure 2. Cruise Drag Condition.

The spread sheet was used to generate results for various combinations of uncertainty budgets for the cruise and minimum drag coefficient cases so that the sensitivity of the achievable drag coefficient repeatability (2 sigma) could be examined. Some of these results are presented in Figure 4 as attainable two sigma drag coefficient versus two sigma angle of attack uncertainty with two sigma uncertainty budgets of 0.00005, 0.0001 and 0.0003 for axial force coefficient, and two sigma uncertainty budgets of 0.002, 0.005 and 0.01 for normal force coefficient. Three plots are provided for the cruise drag case and one for the minimum drag case. For the minimum drag case, the attainable two sigma drag coefficient is not sensitive to the two sigma angle of attack uncertainty even at a value of 0.03 degrees. The explanation for this result is that almost all of the drag coefficient is coming from balance axial force. However, for the cruise drag case, the attainable two sigma drag coefficient is sensitive to the two sigma angle of attack uncertainty since a significant part of the drag coefficient is coming from the balance normal force. Also, the variation is seen to depend on the uncertainty budget for the normal force coefficient with the slope decreasing as the value of two sigma normal force coefficient is increased.

CASE 5

SREF (SQ FT)	MACH	Q (PSF)	ALPHA (DEG)	CL	CD	CNF	CAF	UCL (2 Sigma)	UCD (2 Sigma)	UALPHA (2 Sigma Radians)
4	0.8	625	-0.5	0.1	0.0175	0.99840	0.18370	0.005	0.0001	0.000174532 (0.01 Degrees)
				(UCAF)^2	UCAF (2 Sigma)	(UCNF)^2	UCNF (2 Sigma)	**UAF** (LB-2 Sigma)	**UNF** (LB-2 Sigma)	
				7.79280E-09	0.880000	2.50E-05	0.500000	0.22	12.50	

CASE 6

SREF (SQ FT)	MACH	Q (PSF)	ALPHA (DEG)	CL	CD	CNF	CAF	UCL (2 Sigma)	UCD (2 Sigma)	UALPHA (2 Sigma Radians)
4	0.8	625	-0.5	0.1	0.0175	0.99840	0.18370	0.002	0.0001	0.000174532 (0.01 Degrees)
				(UCAF)^2	UCAF (2 Sigma)	(UCNF)^2	UCNF (2 Sigma)	**UAF** (LB-2 Sigma)	**UNF** (LB-2 Sigma)	
				9.39180E-09	0.970000	4.0E-06	0.200000	0.24	5.00	

CASE 7

SREF (SQ FT)	MACH	Q (PSF)	ALPHA (DEG)	CL	CD	CNF	CAF	UCL (2 Sigma)	UCD (2 Sigma)	UALPHA (2 Sigma Radians)
4	0.8	625	-0.5	0.1	0.0175	0.99840	0.18370	0.002	0.0001	8.72660E-05 (0.005 Degrees)
				(UCAF)^2	UCAF (2 Sigma)	(UCNF)^2	UCNF (2 Sigma)	**UAF** (LB-2 Sigma)	**UNF** (LB-2 Sigma)	
				9.61950E-09	0.980000	4.0E-06	0.200000	0.25	5.00	

CASE 8

SREF (SQ FT)	MACH	Q (PSF)	ALPHA (DEG)	CL	CD	CNF	CAF	UCL (2 Sigma)	UCD (2 Sigma)	UALPHA (2 Sigma Radians)
4	0.8	625	-0.5	0.1	0.0175	0.99840	0.18370	0.002	5.0E-05	0.000174532 (0.01 Degrees)
				(UCAF)^2	UCAF (2 Sigma)	(UCNF)^2	UCNF (2 Sigma)	**UAF** (LB-2 Sigma)	**UNF** (LB-2 Sigma)	
				1.89180E-09	0.430000	4.0E-06	0.200000	0.11	5.00	

Figure 3. Minimum Drag Condition.

95 percent confidence level (2 sigma)

CASE NO. Figure 2 and 3	UCNF % of Range	UCAF % of Range	Generalized UCNF &UCAF From Figure 1 % of Range	UCNF % of Reading	UCAF % ofReading
1	Undefined	Undefined	0.10	Undefined	Undefined
2	Undefined	Undefined	0.10	Undefined	Undefined
3	0.156	0.059	0.10	0.399	0.756
4	0.156	0.104	0.10	0.399	1.326
5	0.391	0.092	0.10	5.008	0.479
6	0.156	0.101	0.10	2.003	0.528
7	0.156	0.102	0.10	2.003	0.533
8	0.156	0.046	0.10	2.003	0.239

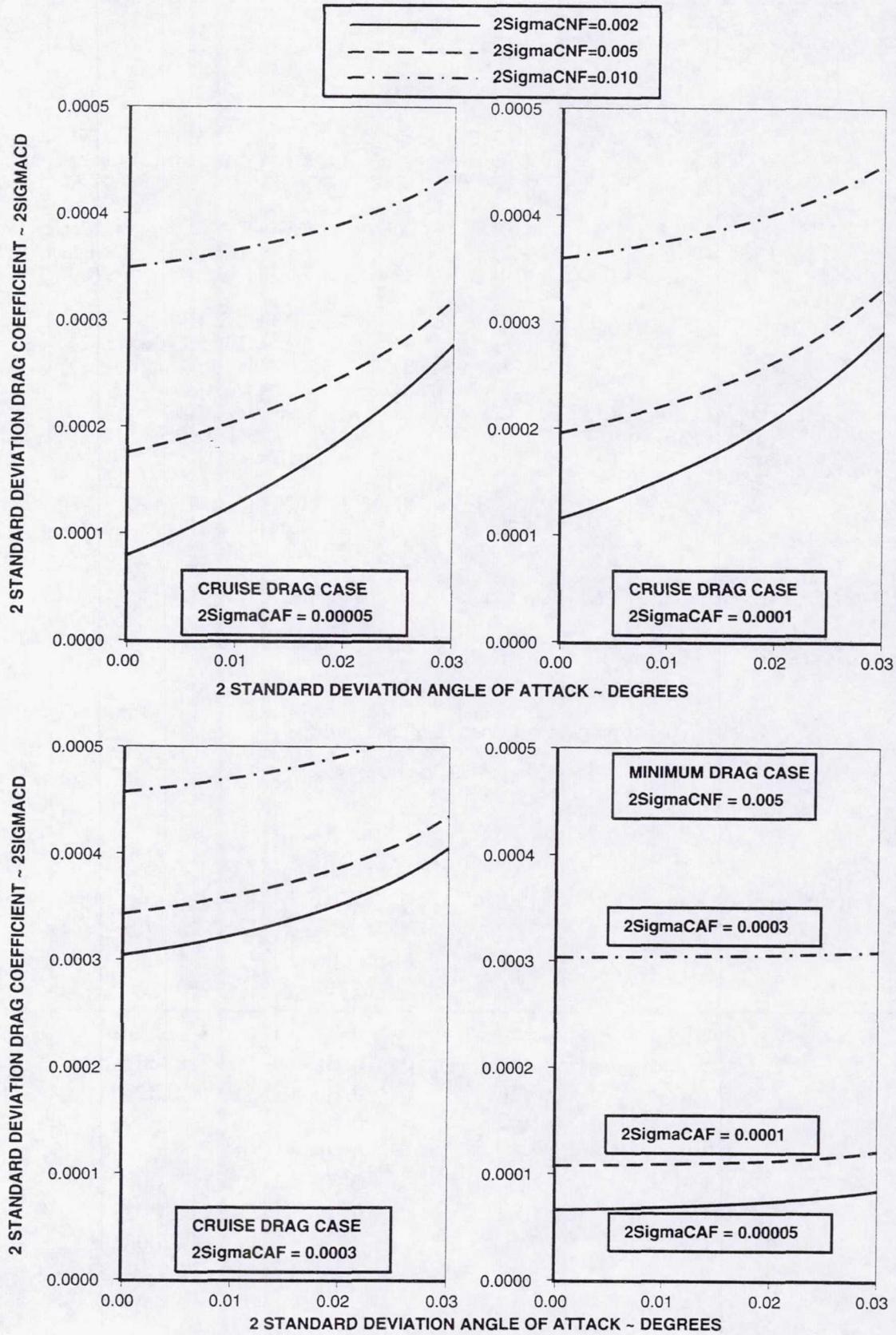

Figure 4. Sensitivity of Drag Coefficient Repeatability to Uncertainty Budgets.

Project engineers are now asking for an attainable two sigma drag coefficient of 0.00005 (half a drag count) for the cruise condition. What attainable uncertainty budgets in α, C_{AF}, C_{NF} and C_L are needed to achieve this goal in C_D ? The attainable two sigma drag coefficient for various uncertainty budgets in α, C_{AF}, C_{NF} and C_L are tabulated below to show the difficulty in achieving a half a drag count two sigma value for the cruise drag coefficient.

All values in the table are two sigma for a cruise condition.

UAlpha (degrees)	UCL	UNF (lb.)	UNAF % of Value	UAF (lb.)	UAF % of Value	Attainable UCD
0.005	0.002	5.0	0.4	0.09	0.48	0.00009
0.005	0.0015	3.75	0.3	0.04	0.21	0.00007
0.005	0.001	2.5	0.29	0.05	0.28	0.00006
0.002	0.001	2.5	0.2	0.08	0.42	0.00005

Using a current technology internal balance and angle of attack device, the half a drag count, two sigma, cruise drag coefficient requirement does not appear to be achievable. Repeatability for three current angle of attack devices is described in Reference 5.

Takeoff and Approach Drag Coefficient Conditions

Much of low speed testing is done with the model mounted on an external balance. However, the required uncertainty budgets requested by the project engineer are the same although the required angle of attack uncertainty for the model mounted on an external balance often is not supplied by the project engineer. The following analysis is for a low speed model which utilizes an internal strain gage balance.

Some representative test conditions for takeoff and approach are:

Reference area = S_{REF} = 9.5 sq. ft.
Dynamic pressure = 60 pounds per square foot (psf)
Takeoff drag case:
Angle of attack = 10 degrees (in stability axes)
Lift coefficient (C_L) = 1.75
Drag coefficient (C_D) = 0.1875Mach No. = 0.26
Approach drag case:
Angle of attack = 6 degrees (in stability axes)
Lift coefficient (C_L) = 1.8
Drag coefficient (C_D) = 0.2490
Mach No. = 0.2

The balance normal and axial force coefficients would be:

Takeoff drag case:	Approach drag case:
CNF = 1.756	CNF = 1.816
CAF = -0.1192	CAF = 0.0595

Assume that the project engineer supplies lift coefficient, drag coefficient and angle of attack repeatabilities at a 95 percent confidence level. Typical 2σ repeatabilities for the takeoff and approach drag cases might be:

Takeoff drag case:

$U_{CL} = 2\sigma C_L = 0.005$

$U_{CD} = 2\sigma C_D = 0.0005$ (five drag counts)

$U\alpha = 2\sigma(\alpha) = 0.03$ degrees or 0.000523596 radians

Approach drag case:

$U_{CL} = 2\sigma_{CL} = 0.01$

$U_{CD} = 2\sigma_{CD} = 0.0010$ (ten drag counts)

$U\alpha = 2\sigma(\alpha) = 0.03$ degrees or 0.000523596 radians

The same example calculation process spread sheet described previously was used to calculate uncertainty budgets $2\sigma C_{AF}$ and $2\sigma C_{NF}$ needed for various combinations of α, C_{AF}, C_{NF}, C_L and C_D with various 2σ uncertainty budgets for C_L, C_D, and α. Spread sheet output is presented in Figure 5 for the **takeoff drag** case and in Figure 6 for the **approach drag** case. The load range for normal force, axial force and pitching moment for an internal balance often used for low speed drag testing at Boeing is:

Normal Force = 2,500 lb. Axial Force = 300 lb. Pitching Moment = 12,000 in-lb.

CASE 1

SREF (SQ FT)	MACH	Q (PSF)	ALPHA (DEG)	CL	CD	CNF	CAF	UCL (2 Sigma)	UCD (2 Sigma)	UALPHA (2 Sigma Radians)
9.5	0.26	60	10	1.75	0.1875	1.755974	-0.11921	0.005	0.0005	0.000523596 (0.03 Degrees)

(UCAF)^2	UCAF (2 Sigma)	(UCNF)^2	UCNF (2 Sigma)	UAF (LB-2 Sigma)	UNF (LB-2 Sigma)
-1.357910E-06					

CASE 2

SREF (SQ FT)	MACH	Q (PSF)	ALPHA (DEG)	CL	CD	CNF	CAF	UCL (2 Sigma)	UCD (2 Sigma)	UALPHA (2 Sigma Radians)
9.5	0.26	60	10	1.75	0.1875	1.75597	-0.11921	0.002	0.001	0.000523596 (0.03 Degrees)

(UCAF)^2	UCAF (2 Sigma)	(UCNF)^2	UCNF (2 Sigma)	UAF (LB-2 Sigma)	UNF (LB-2 Sigma)
3.298520E-08	0.182000	4.0E-06	0.199200	0.10	1.14

CASE 3

SREF (SQ FT)	MACH	Q (PSF)	ALPHA (DEG)	CL (2 Sigma)	CD (2 Sigma)	CNF (2 Sigma Radians)	CAF	UCL	UCD	UALPHA
9.5	0.26	60	10	1.75	0.1875	1.75597	-0.11921	0.0044	0.001	0.000349064 (0.02 Degrees)

(UCAF)^2	UCAF (2 Sigma)	(UCNF)^2	UCNF (2 Sigma)	UAF (LB-2 Sigma)	UNF (LB-2 Sigma)
3.47280E-08	0.186000	1.90E-05	0.439800	0.11	2.51

CASE 4

SREF (SQ FT)	MACH	Q (PSF)	ALPHA (DEG)	CL (2 Sigma)	CD (2 Sigma)	CNF (2 Sigma Radians)	CAF	UCL	UCD	UALPHA
9.5	0.26	60	10	1.75	0.1875	1.75597	-0.11921	0.002	0.0005	0.000174532 (0.01 Degrees)

(UCAF)^2	UCAF (2 Sigma)	(UCNF)^2	UCNF (2 Sigma)	UAF (LB-2 Sigma)	UNF (LB-2 Sigma)
3.428990E-08	0.185000	4.0E-06	0.199900	0.11	1.14

Figure 5. Takeoff Drag Condition.

CASE 5

SREF (SQ FT)	MACH	Q (PSF)	ALPHA (DEG)	CL	CD	CNF	CAF	UCL (2 Sigma)	UCD (2 Sigma)	UALPHA (2 Sigma Radians)
9.5	0.2	60	6	1.8	0.249	1.81617	0.05950	0.01	0.001	0.000523596 (0.03 Degrees)

(UCAF)^2	UCAF (2 Sigma)	(UCNF)^2	UCNF (2 Sigma)	UAF (LB-2 Sigma)	UNF (LB-2 Sigma)
-1.00085E-06					

CASE 6

SREF (SQ FT)	MACH	Q (PSF)	ALPHA (DEG)	CL	CD	CNF	CAF	UCL (2 Sigma)	UCD (2 Sigma)	UALPHA (2 Sigma Radians)
9.5	0.2	60	6	1.8	0.249	1.816167	0.05950	0.002	0.001	0.000523596 (0.03 Degrees)

(UCAF)^2	UCAF (2 Sigma)	(UCNF)^2	UCNF (2 Sigma)	UAF (LB-2 Sigma)	UNF (LB-2 Sigma)
5.18762E-08	0.000228	3.99E-06	0.001997	0.13	1.14

CASE 7

SREF (SQ FT)	MACH	Q (PSF)	ALPHA (DEG)	CL	CD	CNF	CAF	UCL (2 Sigma)	UCD (2 Sigma)	UALPHA (2 Sigma Radians)
9.5	0.2	60	6	1.8	0.249	1.81617	0.05950	0.0071	0.001	0.000349064 (0.02 Degrees)

(UCAF)^2	UCAF (2 Sigma)	(UCNF)^2	UCNF (2 Sigma)	UAF (LB-2 Sigma)	UNF (LB-2 Sigma)
4.53809E-08	0.000213	5.04E-05	0.007100	0.12	4.05

CASE 8

SREF (SQ FT)	MACH	Q (PSF)	ALPHA (DEG)	CL	CD	CNF	CAF	UCL (2 Sigma)	UCD (2 Sigma)	UALPHA (2 Sigma Radians)
9.5	0.2	60	6	1.8	0.249	1.81617	0.05950	0.0088	0.001	0.000174532 (0.01 Degrees)

(UCAF)^2	UCAF (2 Sigma)	(UCNF)^2	UCNF (2 Sigma)	UAF (LB-2 Sigma)	UNF (LB-2 Sigma)
5.04319E-08	0.000225	7.74E-05	0.008800	0.13	5.02

Figure 6. Approach Drag Condition.

The normal and axial force coefficients corresponding to these load ranges at the takeoff and approach drag conditions are $C_{NF} = 4.386$ and $C_{AF} = 0.5263$. The two sigma uncertainties for normal and axial force coefficients calculated in Figures 5 and 6 are expressed as a percent of both the balance range normal and axial force coefficients and the normal and axial force coefficient readings and are tabulated below. Cases 1 and 5 are for the typical 2σ repeatabilities for the takeoff and approach drag cases tabulated above which result in no solution for $2\sigma C_{AF}$ and $2\sigma C_{NF}$. The author has met some engineers who maintain that an uncertainty budget for angle of attack of $2\sigma(\alpha) = 0.10$ degrees is adequate for low speed testing even for commercial transports. This analysis clearly shows that this magnitude of uncertainty budget for angle of attack is totally inadequate for low speed testing of commercial transports from the project engineer's perspective.

95 percent confidence level (2 sigma)

CASE NO. Figure 5 and 6	UCNF % of Range	UCAF % of Range	UCNF % of Reading	UCAF % of Reading
1	Undefined	Undefined	Undefined	Undefined
2	0.040	0.035	0.101	-0.152
3	0.100	0.035	0.248	-0.156
4	0.045	0.035	0.112	-0.155
5	Undefined	Undefined	Undefined	Undefined
6	0.043	0.040	0.097	0.383
7	0.161	0.040	0.389	0.358

Categories of Repeatability

The project engineer may specify different repeatability requirements for the stability axes coefficients, especially drag coefficient. Four types of repeatability which interest the project engineer are:

1. The repeatability of several back-to-back runs. A run involves changing only one test parameter during the run. Define this testing as short term repeatability.
2. The repeatability of runs separated by a change in wind tunnel test conditions, such as repeat runs within a Mach number series. Define this testing also as short term repeatability.
3. The repeatability of repeat builds of a given configuration within a test. Define this testing as near term repeatability.
4. The repeatability of repeat builds of a given configuration between tests. Define this testing as long term repeatability.

The corresponding repeatabilities for the balance engineer might be:

1. The repeatability of several back-to-back applied calibration loads during the balance calibration period. Define this calibrating as short term repeatability.
2. The repeatability of several applied calibration loads separated by a change in calibration conditions, such as combined loads, change in calibration hardware, etc. Define this calibrating also as short term repeatability.
3. The repeatability of repeat calibrations of a given balance within the same calibration period. Define this calibrating as near term repeatability.
4. The repeatability of repeat calibrations of a given balance between different calibration periods. Define this calibrating as long term repeatability.

The repeatabilities for the balance engineer might involve the application of check loads rather than calibrating the balance. The same repeatability definitions would be used.

Uncertainty for Mean Values.

In the discussions that follow, it will be seen that specifying the uncertainty for mean values involves the use of statistical confidence intervals based on the precision of the measurements and their number. Hence, if the project engineer provides a requirement that is a confidence interval, the number of measurements or runs associated with the interval needs to be given.

Single Sample with Independent Variable Constant

Although the project engineer is interested in repeatabilities, mean values of the stability axes coefficients are used for the description of the airplane characteristics and for performance calculations. The project engineer needs an estimate of the uncertainty in the mean values of C_L, C_D and C_M. The uncertainty of a mean value is given by the following expression (Reference 1 and 2):

$$U_{RSS} = \pm [(\text{Bias})^2 + (\text{Precision})^2]^{1/2} \qquad \text{(95 percent confidence level)}$$
$$U_{RSS} = \pm \{(\text{Bias})^2 + [(t95)(S)/(N)^{0.5}]^2\}^{1/2}$$

N = the number of measurements used to calculate the mean value.
S = the sample standard deviation computed from the N values.
(t_{95}) = the student-t value for a 95 percent confidence level and N -1 degrees of freedom.

If the bias term is negligible, then:

$$U_{RSS} = \pm [(t_{95})(S)/(N)^{0.5}] \qquad \text{(commonly known as a confidence interval)}$$

Note that, in the absence of significant bias, the uncertainty in the mean value can be reduced by taking more repeat measurements (N), since the interval is a function of the reciprocal of the square root of the number of measurements.

Curve Fit with Independent Variable Not Constant

Least squares curves are often fit to a set of measurements to provide mean values of the stability axes coefficients for describing airplane characteristics, calculating airplane performance, and to provide curve fits or tables to represent the results of instrument calibrations. From Reference 6, the confidence interval for a least squares curve fit is:

$$U_{RSS} = \pm [(t_{95})(SE)(\text{Hat Matrix})] \qquad \text{(95 percent confidence level)}$$

Hat Matrix = the hat matrix, a dispersion matrix which is a measure of the data density for a given value of the independent variable. It effectively adjusts the value of the standard error of estimate depending upon the distance from the centroid of the data.

N = the number of measurements used to determine the curve fit.

SE = the standard error of estimate computed from the N values.

(t95) = the student-t value for a 95 percent confidence level and (N - curve fit order - 1) degrees of freedom.

The uncertainty in the mean value can be reduced by taking more repeat measurements (N), since the interval is a function of the reciprocal of the square root of the number of measurements.

The uncertainty methodology for least squares curve fits (regressions) provided in Reference 6 is not comprehensive. The proper estimation of the uncertainty associated with a regression is a careful comprehensive accounting of systematic and correlated systematic uncertainties. One approach in the development of a methodology by applying uncertainty propagation techniques to the linear regression analysis equations is presented in Reference 7.

Uncertainty Associated with Increments

Single Sample - Independent Variable Constant.

Much of the project engineer's wind tunnel testing involves the measurement of increments. These increments are often determined by back-to-back tests of a configuration with a change in test conditions or the configuration. If the biases in the results for the back-to-back tests are totally correlated, then they will cancel when the difference is computed (Reference 8). This situation is often the case for incremental wind tunnel testing. Hence, the uncertainty of the increments is largely dependent upon the precision (repeatability) of the two sets of data. A methodology for computing a confidence interval for an increment with totally correlated biases is given in Reference 9. The methodology is outlined below and involves testing, statistically, whether the increment or difference is statistically significant at a stated confidence level. Statistically significant means whether the difference is greater that what might be expected from just the random scatter (precision) in the two data sets.

Confidence Interval for the Difference between Two Means (Two-sided t-test)

Two sets of data designated Set A and Set B. The number of data points in Set A is NA, and the number in Set B is NB. The mean values computed for Set A and Set B are XbarA and XbarB, respectively, and the corresponding sample standard deviations are SA and SB, respectively.

PROCEDURE

1. Choose α the significance level of the test. For 95 percent confidence pick $\alpha = 0.05$.
2. Look up $t_{1-\alpha/2}$ for $\nu = (NA + NB - 2)$ degrees of freedom in a one-sided student-t table.
3. Compute XbarA and XbarB, and SA and SB.
4. Compute a pooled sample standard deviation:
$$SP = \{[(NA-1)(SA)^2 + (NB-1)(SB)^2]/ (NA + NB - 2)\}^{0.5}$$
5. Compute the t-test interval, $u = (t_{1-\alpha/2}) (SP) [(NA + NB) / (NA)(NB)]^{0.5}$
6. If $| XbarA - XbarB | > u$, decide that SetA and SetB differ.
7. It is worth noting that the interval $(XbarA - XbarB) \pm u$ is a $100(1 - \alpha)$ percent confidence interval estimate. For $\alpha = 0.05$, it is a 95 percent confidence interval estimate.

EXAMPLE

The number of drag coefficient data points for Configuration A is NA = 6, and the number for Configuration B is NB = 4. The mean values computed for Configuration A and Configuration B are CDbarA = 0.0300 and CDbarB = 0.0310, respectively, and the corresponding sample standard deviations are SA = 0.0003 and SB = 0.0004, respectively.

1. Choose α the significance level of the test. For 95 percent confidence pick $\alpha = 0.05$.
2. Look up $t_{1-\alpha/2}$ for $\nu = (NA + NB - 2)$ degrees of freedom in a one-sided student-t table. $\nu = 8$, $t_{1-\alpha/2} = 2.306$
3. CDbarA = 0.0300 and CDbarB = 0.0310, and SA = 0.0003 and SB 0.0004.
4. Compute a pooled sample standard deviation:
$SP = \{[(5)(0.0003)^2 + (3)(0.0004)^2] / (8)\}^{0.5}$
$SP = 0.00034$

5. Compute the t-test interval, $u = (t_{1-\alpha/2}) (SP) [(NA + NB) / (NA)(NB)]^{0.5}$
   $u = (2.306) (0.00034) [(10) / (24)]^{0.5}$
   $u = 0.00051$
6. If $| XbarA - XbarB | > u$, decide that SetA and SetB differ.
   $| 0.0300 - 0.0310 | > 0.00051$, $0.0010 > 0.00051$. Conclude that the means of Configuration A and B differ at the 95 percent confidence level.
7. It is worth noting that the interval $(XbarA - XbarB) \pm u$ is a $100(1 - \alpha)$ percent confidence interval estimate. For $\alpha = 0.05$, it is a 95 percent confidence interval estimate.

The 95 percent confidence level confidence interval estimate for the difference between the CD of configuration A and B is:

$$U\Delta C_D = 0.0010 \pm u$$
$$U\Delta C_D = 0.0010 \pm 0.00051 \qquad \text{(95 percent confidence level)}$$

The confidence interval for the difference between two configurations, when their repeatability in drag coefficient (SC_D) is the same and the number of data points or runs for each is the same, can be easily computed and plotted as a function of the number of data points or runs for constant values of SC_D (see Figure 7). Note to obtain a 95 percent confidence level confidence interval equal to the repeatability in drag coefficient (SC_D), **each configuration must be tested 9 times!**

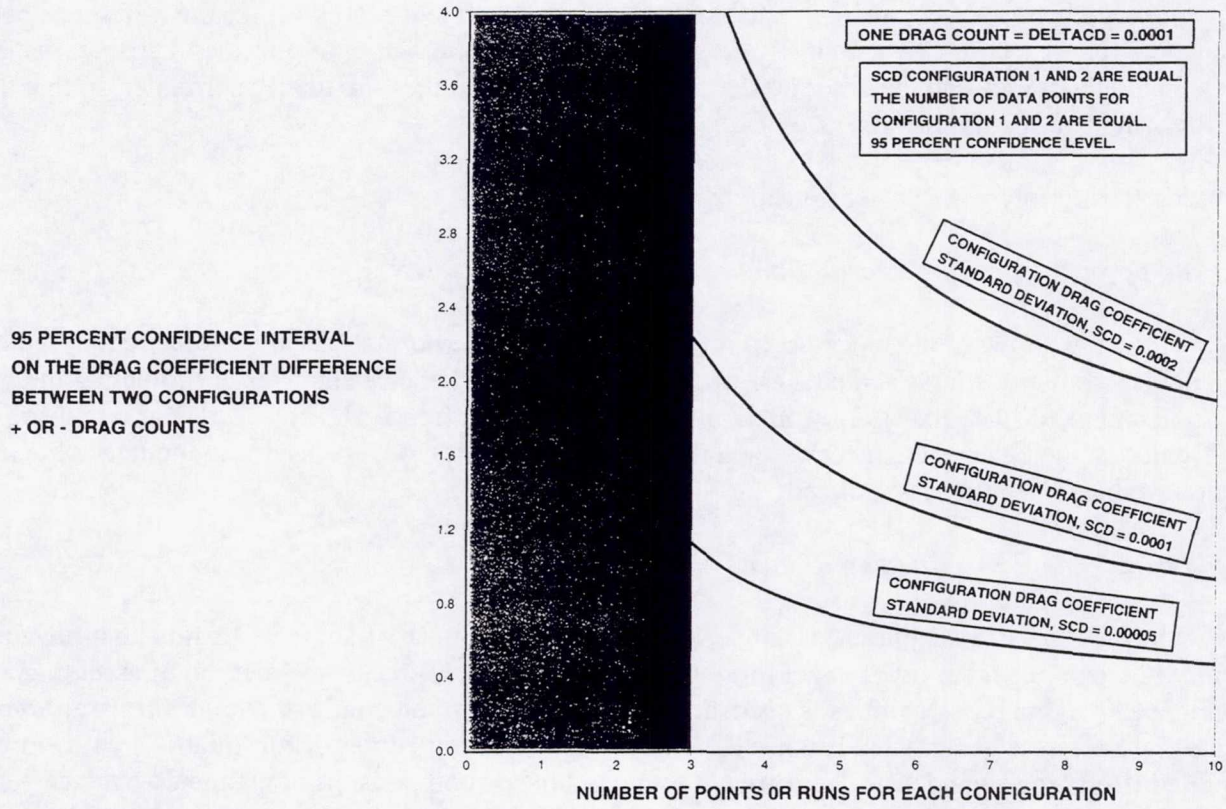

Figure 7. Variation in Confidence Interval on Drag Coefficient Increment as the Number of Data Points is Increased.

Curve Fit - Independent Variable Not Constant.

The author has not found any published and totally statistically defensible method for computing the confidence interval for the difference between least squares curve fits. The author's approach is to base it on the calculated confidence interval for each curve fit (Reference 6) in the following manner. For example, the confidence interval for the difference between two drag curve fits (configuration A and B) is defined as:

$C_{DA} - C_{DB} = \Delta C_D$

Confidence Interval for curve fit A = $\mathbf{CIC}_{DA}$ = Total bandwidth
Confidence Interval for curve fit B = $\mathbf{CIC}_{DB}$ = Total bandwidth
One half of Confidence Interval for curve fit A = $\mathbf{CIC}_{DA}/2$
One half of Confidence Interval for curve fit B = $\mathbf{CIC}_{DB}/2$

The confidence interval for the difference between the two drag curve fits is given by:

$$\mathbf{CI}\Delta C_D = \pm [(\mathbf{CIC}_{DA}/2)^2 + (\mathbf{CIC}_{DB}/2)^2]^{0.5}$$

Since the curve fit confidence interval represents an interval in which the true mean is expected to lie, it represents a bias distribution estimate for the mean. Since the curve fit confidence interval represents a bias distribution estimate, the author believes the two confidence interval halves should be root-sum-squared together to obtain the bias distribution estimate (confidence interval) for the difference between the curve fits in accordance with the Reference 1 method of combining uncertainty distributions. Note that this method assumes that the other biases are negligible or that they are totally correlated so that they cancel when taking the increment.

Characterizing Internal Balance Uncertainty

Some Approaches to Characterize Balance Uncertainty

Now that a methodology for determining internal balance normal and axial force requirements is available, what procedures and data are available to assist the balance engineer in estimating the balance normal and axial force uncertainty, in particular, the precision (repeatability)? This task is one of the most difficult that the balance engineer has and the author decided it would be useful to include some results that have been and might be utilized.

Calibration and Check Loading Residuals

Once the balance engineer has converted the project engineer's requirements into an allowable uncertainty (2 sigma repeatability) budget for normal force and axial force, some method of assessing the attainable 2 sigma repeatabilities is needed. This assessment is not simple or straightforward. Some balance engineers use generalized balance uncertainty specification curves or formulations with empiricism applied (Reference 3 and 10). There are not many published comparisons of estimated balance performance compared to that achieved Some comparisons of the generalized formulations with the demonstrated absolute uncertainty for **external balances** are provided in Reference 10. In Reference 11, a generalized balance uncertainty (accuracy) formulation is used to estimate balance uncertainties for three balances used for three tests. Although no direct comparisons are made between the estimated balance

uncertainties and the repeatability of the measured forces and moments in the wind tunnel, the authors of Reference 11 indicate that the estimates correspond very well with their experiences in the wind tunnels mentioned. Direct correlations relating balance uncertainty budgets to uncertainty assessments of measured data in the wind tunnel are extremely difficult to find.

One method that the balance engineer uses to provide an estimate of balance performance is to perform a statistical analysis on the balance calibration residuals. In this case the residual is the difference between the applied load and the load indicated by the balance. Generally, all of the residuals from all of the loadings (including combined loadings) are used to compute a standard deviation for each of the balance components. This procedure includes residuals for balance components which were not loaded at all, but the residuals are produced by the imprecision of the derived interaction terms. An example of this type of statistical evaluation is given below for three Boeing **blowing** balances of the same design and range which were calibrated at the Arnold Engineering Development Center in 1987.

2 STANDARD DEVIATION CALCULATIONS FROM ALL BALANCE CALIBRATION RESIDUALS

BALANCE	NO. OF LOADINGS	COMPONENT	2 STANDARD DEVIATIONS (LB OR IN-LB)	2 STANDARD DEVIATIONS (% OF RANGE)
6231A	926	NORMAL FORCE	1.14 LB	0.046
	926	AXIAL FORCE	0.72 LB	0.24
	926	PITCHING MOMENT	14.4 IN-LB	0.12
6231C	926	NORMAL FORCE	1.22 LB	0.048
	926	AXIAL FORCE	0.52 LB	0.17
	926	PITCHING MOMENT	15.4 IN-LB	0.13
6231D	926	NORMAL FORCE	1.27 LB	0.051
	926	AXIAL FORCE	0.41 LB	0.18
	926	PITCHING MOMENT	14.9 IN-LB	0.13

These results are nearly the same for all three of the balances which indicates that using the balance calibration residuals may be a consistent way of describing the repeatability of an internal strain gage balance. Another comparison for a drag-type internal balance is provided in the following table. The normal force and axial force ranges for this balance are 3200 and 240 pounds, respectively. Two standard deviation values for normal and axial force were computed from three different sets of residuals. The first set of residuals was obtained by doing ten cycles of back-to-back pure normal and axial force loadings of the balance. A loading cycle for normal force was from 0.0 to +1600 to -1600 to 0.0 pounds in 200 pound increments, and for axial force it was 0.0 to +70 to 0.0 pounds in 5 pound increments. The second set of residuals was acquired during the usual calibration of the balance. Ten cycles of pure normal and axial force loadings of the balance were interspersed throughout the calibration period (about 5 days). A loading cycle for normal force was from 0.0 to -3200 to 0.0 pounds in 1600 pound increments, and for axial force it was 0.0 to +240 to 0.0 pounds in 120 pound increments. The third set of residuals are from the same calibration period and consists of all of the residuals for normal and axial force, even when they weren't loaded or when combined loads were applied in both the longitudinal and lateral-directional balance axes.

2 STANDARD DEVIATION CALCULATIONS FROM BALANCE LOADING AND CALIBRATION RESIDUALS

BALANCE	NO. OF LOADINGS	COMPONENT	2 STANDARD DEVIATIONS (LB OR IN-LB)	2 STANDARD DEVIATIONS (% OF RANGE)
BACK-T0-BACK LOADS				
635	150	NORMAL FORCE	0.6 LB	0.019
	140	AXIAL FORCE	0.04 LB	0.017
CALIBRATION REPEAT LOADS				
635	50	NORMAL FORCE	0.6 LB	0.019
	45	AXIAL FORCE	0.10 LB	0.04
CALIBRATION ALL LOADS				
635	522	NORMAL FORCE	0.7 LB	0.022
	527	AXIAL FORCE	0.4 LB	0.125

The largest two standard deviation values for normal and axial force are obtained when all of the calibration residuals are used; the next largest values are obtained when only the calibration residuals from the pure, repeat calibration loads are used; and the smallest values are produced from the pure, back-to-back non-calibration loads. However, for normal force, the two standard deviation values for all three types of loadings are nearly the same. It is in axial force that a large variation in the two standard deviation values for all three types of loadings is seen. The two standard deviation value for the calibration residuals from the pure, repeat calibration loads is two and half times the value produced by the pure, back-to-back non-calibration loads, and the two standard deviation value for the calibration residuals from all of the calibration loads is ten times the value produced by the pure, back-to-back non-calibration loads.

Yet another set of residuals for two balances (6118D and 6118E) are provided in the following table. Ten cycles of pure normal and axial force loadings of the balance were interspersed throughout the calibration period (about 5 days).

2 STANDARD DEVIATION CALCULATIONS FROM PURE BALANCE CALIBRATION RESIDUALS

BALANCE	NO. OF LOADINGS	COMPONENT	2 STANDARD DEVIATIONS (LB OR IN-LB)	2 STANDARD DEVIATIONS (% OF RANGE)
CALIBRATION REPEAT LOADS				
6118D	67	NORMAL FORCE	0.18 LB	0.045
	60	AXIAL FORCE	0.05 LB	0.10
CALIBRATION REPEAT LOADS				
6118E	60	NORMAL FORCE	0.17 LB	0.043
	55	AXIAL FORCE	0.05 LB	0.10

These results are the same for both of the balances which, again, indicates that using the balance calibration residuals may be a consistent way of describing the repeatability of an internal strain gage balance.

The author used balance calibration residuals to characterize the repeatability of an internal strain gage balance and to estimate the drag coefficient repeatability at cruise conditions for a model tested in the Boeing Transonic Wind Tunnel. The NTF101B NASA-Langley Research Center balance was used for the test. The two sigma repeatabilities for normal and axial force based on calibration residuals (860) provided by NASA-Langley are 0.10 and 0.18 percent of full scale, respectively. The full scale values for normal and axial force are 6500 and 700 pounds, respectively. Hence, the two sigma repeatabilities for normal and axial force are 6.5 and 1.26 pounds, respectively. The two sigma repeatability used for the accelerometer which was used to measure angle of attack was 0.005 degrees (Reference 5). It was deemed that the 2 sigma repeatability for dynamic pressure would have a negligible effect on the drag coefficient repeatability. The cruise conditions were:

SREF = 6.5 square feet
M = 0.9
Dynamic pressure = 700 pounds per square feet
CL = 0.25
CD = 0.0210
Angle of attack = 2 degrees

The estimated drag coefficient two sigma repeatability was 0.0003 or 3 drag counts. In other words, for repeat testing of the model, we would expect 95 percent of the results to fall within a band of ± 3 drag counts. During the test, four runs at M = 0.9 were made within a Mach series, and the data near CL = 0.25 from these four runs fell within a band of ±2.5 drag counts compared to the estimate of ± 3 drag counts.

The author used balance calibration residuals to characterize the repeatability of an internal strain gage balance and to estimate the drag coefficient repeatability at takeoff conditions for an Energy Efficient Transport model tested in the NASA-Langley 14x22 Ft. Low Speed Wind Tunnel. The VST1 NASA-Langley Research Center balance was used for the test. The two sigma repeatabilities for normal and axial force based on calibration residuals (860) provided by NASA-Langley are 0.07 and 0.13 percent of full scale, respectively. The full scale values for normal and axial force are 2000 and 600 pounds, respectively. Hence, the two sigma repeatabilities for normal and axial force are 1.4 and 0.78 pounds, respectively. The two sigma repeatability used for the accelerometer which was used to measure angle of attack was estimated at 0.01 degrees. It was deemed that the 2 sigma repeatability for dynamic pressure would have a negligible effect on the drag coefficient repeatability. The takeoff conditions were:

SREF = 9.5 square feet
M = 0.2
Dynamic pressure = 60 pounds per square feet
CL = 1.63
CD = 0.158
Angle of attack = 7.9 degrees

The estimated drag coefficient two sigma repeatability was 0.0014 or 14 drag counts. In other words, for repeat testing of the model, we would expect 95 percent of the results to fall within a band of ± 14 drag

counts. During the test, 9 runs were made, and the data near CL = 1.63 from these nine runs fell within a band of ±13 drag counts compared to the estimate of ± 14 drag counts.

For these two cases, neither of which has extensive regions of separated flow, using the two sigma values of the balance calibration residuals to estimate the two sigma drag coefficient repeatability gives reasonably close agreement with the measured repeatability.

Comparison of Calibration Residuals Expressed in Percent of Balance Component Range

The generalized 2 sigma repeatability (precision) for internal balance normal force and axial force provided in Figure 1 is 0.10 percent of component range. What values of 2 sigma precision in percent of component range are produced by the calibration residuals? These values are tabulated and compared below for the balances discussed in this paper. For the Boeing blowing balances, a senior Boeing balance engineer stated several years ago that, in his experience, the blowing balance precision was about 1.4 times that of a non-blowing balance. So for this comparison, the author has divided the 2 sigma precisions obtained from the residual analysis for the blowing balances by 1.4 to make them comparable to the non-blowing balances.

All of these balances are essentially of one-piece construction. In the absence of any other information, the author would use 0.05 percent of range for normal force and 0.13 percent of range for axial force to characterize the 2 sigma precision of these kind of balances.

Calibration Load Range Versus Test Load Range

Normally, the balance calibration includes loading all six components to their maximum ranges, sometimes in combination. The balance calibration matrix is extracted from the results of these loadings and this process usually involves curve fits. In fact, the matrix represents a surface curve fit whose position in space (its location relative to the calibration points) is determined by all of the points and its location is significantly influenced by loads and combination loads at the maximum range conditions. Because repeat

BALANCE	OWNER	2 SIGMA NF % OF RANGE	2 SIGMA AF % OF RANGE	Generalized 2 Sigma % OF RANGE
635M	BOEING	0.022	0.125	0.10
6118D	BOEING	0.045	0.10	0.10
6118E	BOEING	0.043	0.10	0.10
AVERAGE		**0.037**	**0.108**	**0.10**
NTF101B	NASA-LANGLEY	0.10	0.18	0.10
VST1	NASA-LANGLEY	0.07	0.13	0.10
AVERAGE		**0.085**	**0.16**	**0.10**
6231A	BOEING	0.033	0.17	0.10
6231C	BOEING	0.034	0.12	0.10
6231D	BOEING	0.036	0.13	0.10
AVERAGE		**0.034**	**0.14**	**0.10**
AVERAGE Only Non-blowing Balances		**0.056**	**0.13**	**0.10**

loadings at these or other conditions are seldom done, the residuals (the difference between the applied load and the curve fit load) will be larger than those that would be obtained if these maximum loads were not used in extracting the balance calibration matrix (surface curve fit). It is instructive to compare the applied load coverage used for the balance calibration with the balance loads experienced during a wind tunnel test. Two of these comparisons are made in Figure 8, 9 and 10; one for a drag test for a subsonic commercial transport model using the Boeing 6244A internal strain gage balance; the other for a drag test of a High Speed Civil Transport (HSCT) type configuration using two different balances: the Boeing 6214A and 658Q internal strain gage balance. It is seen in Figure 8 that most of the axial force loads for the subsonic commercial transport model are positive while for the HSCT type configuration some of the axial force loads are negative (Figure 9). The situation illustrated by Figure 8 is an interesting one. The balance for this case was sized for testing in a transonic wind tunnel at a total pressure of about two and a half atmospheres. However, the loads shown in Figure 8 were obtained when the model was tested in the Boeing Transonic Wind Tunnel at a total pressure of one atmosphere. This illustrates another challenge facing the balance engineer, the desire of the customers to maintain a constant uncertainty in drag coefficient over a wide range of tunnel and test operating conditions.

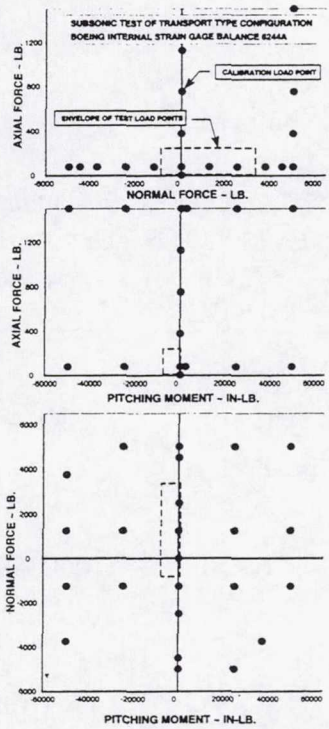

Figure 8. Comparison of Balance Calibration Loads With Test Loads BT2148, 6244A Balance.

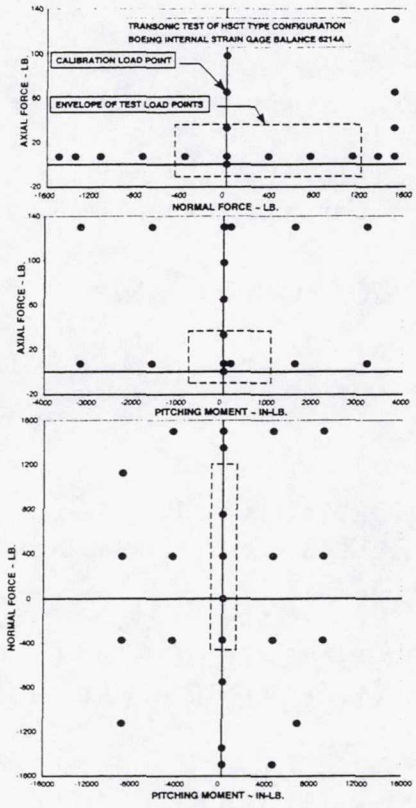

Figure 9. Comparison of Balance Calibration Loads With Test Loads BT2139, 6214A Balance.

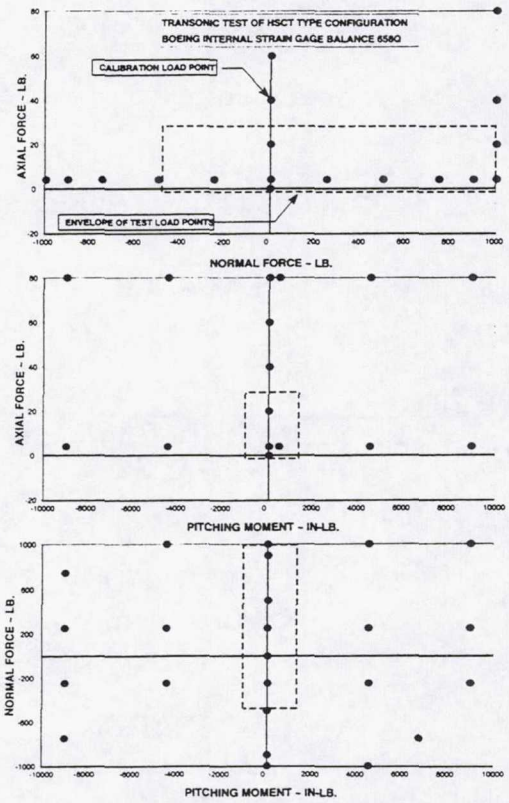

Figure 10. Comparison of Balance Calibration Loads With Test Loads BT2139, 658Q Balance.

These comparisons indicate that the load schedules used in normal internal strain gage balance calibrations do not produce the most applicable uncertainty for **drag** testing since the combination of balance component loads are much smaller during the test than the calibration loads. However, for **stability and control** testing, the load schedules normally used in the balance calibration are probably required because of the large load combinations in all six balance components encountered.

These comparisons indicate also that, if the residuals from all load combinations utilized in the balance calibration are used to estimate the two standard deviation repeatability of the balance normal and axial force components, the result produced will be conservative for drag testing. In drag testing, the only significant combined load components are normal force, axial force and pitching moment.

Balance Zero Shifts as a Measure of Repeatability

Wind-off balance end zero shifts for a Boeing 635 internal strain gage balance used during tests in the Boeing Transonic Wind Tunnel were statistically analyzed. The 368 zero shift values were taken from 8 tests over a time span of April 1992 to March 1996. The two standard deviation values for normal and axial force are 1.2 and 0.6 pounds, respectively. The two standard deviation values computed from all of the residuals from the 635 balance calibration are 0.7 and 0.4 pounds, respectively. This comparison indicates that using historical wind-off balance end zero shifts to estimate the repeatability of the normal and axial force of an internal strain gage balance during a test would be a conservative procedure, if conservatism is desired.

Summary of Repeatability Measurements for Boeing 635 Balance

Normal Force Range = ± 3200 lb., Axial Force Range = ± 240 lb.

2 STANDARD DEVIATIONS

*Estimated 2 sigma cruise drag coefficient repeatability based on normal and axial force

CASE	BALANCE	NO. OF LOADINGS	COMPONENT	2 STANDARD DEVIATIONS (LB OR IN-LB)	2 STANDARD DEVIATIONS (% OF RANGE)	2 Standard Deviations Cruise Drag Coefficient
1	BACK-T0-BACK LOADS					
	635	150	NORMAL FORCE	0.6 LB	0.019	0.000048*
		140	AXIAL FORCE	0.04 LB	0.017	
2	CALIBRATION REPEAT LOADS					
	635	50	NORMAL FORCE	0.6 LB	0.019	0.000059*
		45	AXIAL FORCE	0.10 LB	0.04	
3	CALIBRATION ALL LOADS					
	635	522	NORMAL FORCE	0.7 LB	0.022	0.00017*
		527	AXIAL FORCE	0.4 LB	0.125	
4	END ZEROS					
	635	368	NORMAL FORCE	1.2 LB	0.038	0.00025*
		368	AXIAL FORCE	0.6 LB	0.25	

repeatabilities on corresponding line in the table and a two sigma repeatability for angle of attack of 0.005 degrees. Cruise conditions of M = 0.8, C_L = 0.5 and C_D = 0.025.

Estimated cruise drag coefficient repeatability based on back-to-back loads or repeat calibration loads

are significantly less than those based on all calibration loads (3 times smaller) or on historical end zero shift data (4 times smaller).

Which of the repeatabilities in the above table should the balance engineer use for estimating purposes? The author suggests the following guidelines based on the classes of repeatability defined previously.

1. CASE 1. The repeatability of several back-to-back runs. A run involves changing only one test parameter during the run. Define this testing as short term repeatability.
2. CASE 2. The repeatability of runs separated by a change in wind tunnel test conditions, such as repeat runs within a Mach number series. Define this testing also as short term repeatability.
3. CASE 3. The repeatability of repeat builds of a given configuration within a test. Define this testing as near term repeatability.
4. CASE 4. The repeatability of repeat builds of a given configuration between tests. Define this testing as long term repeatability.

Acknowledgements

The author would like to thank Dr. R. S. Sawyer of Boeing for producing Appendix A, checking the author's mathematical derivations, and clarifying some of the author's thinking relative to uncertainty analysis and uncertainty budgets.

References

1. "Quality Assessment For Wind Tunnel Testing," AGARD Advisory Report No. 304, July 1994.

2. "Assessment of Wind Tunnel Data Uncertainty," AIAA Standard S-071-1995, May 1995.

3. Ewald, Prof. D. B., "Balance Accuracy And Repeatability As A Limiting Parameter In Aircraft Devel opment Force Measurements In Conventional And Cryogenic Wind Tunnels," AGARD-CP-429. Paper presented at the Symposium of the Fluid Dynamics Panel in Naples, Italy September 28 through October 1, 1987.

4. Coleman, H. W. and Steele, Jr., W. G., *Experimentation and Uncertainty Analysis for Engineers*, John Wiley & Sons, New York, New York, 1989.

5. Watzlavick, R. L., Crowder, J. P. and Wright, F. L., "Comparison of Model Attitude Systems: Active Target Photogrammetry, Precision Accelerometer, and Laser Interferometer," AIAA Paper No. 96-2252, 19th AIAA Advanced Measurement and Ground Testing Technology Conference, June 17-20, 1996, New Orleans, Louisiana.

6. Montgomery, D. C. and Peck, E. A., *Introduction to Linear Regression Analysis*, John Wiley & Sons, New York, New York, 1982.

7. Brown, K. K. and Coleman, H. W., "A Methodology for Determining Experimental Uncertainties in Regressions," Paper to be presented at the International Mechanical Engineering Congress and Exposition, November 17-22, 1996, Atlanta, Georgia.

8. Brown, K. K., Coleman, H. W., Steele, W. G. and Taylor, R. P., "Evaluation of Correlated Bias Approximations in Experimental Uncertainty Analysis," AIAA Journal, Volume 34, No. 5, May, 1996.

9. Natrella, M. G., *Experimental Statistics*, National Bureau of Standards Handbook 91, October 1966, U.S. Government Printing Office, Washington, D. C.

10. Hudgins, M. S., "NWTC Internal and External Balance Issues," Document No. NWTC-01-A-9921-02, NAS3-27330 Phase 2A Document, National Wind Tunnel Complex, Brook Park, Ohio, January 29, 1996.

11. Ewald, B. and Krenz, G., "The Accuracy Problem of Airplane Development Force Testing in Cryogenic Wind Tunnels," AIAA Paper No. 86-0776.

12. Steinle, F. and Stanewsky, E., "Wind Tunnel Flow Quality and Data Accuracy Requirements," AGARD Advisory Report No. 184, November 1982.

Appendix A - Estimation of Required Axial and Normal Force Repeatability

Consider a simplified 2-D force measurement in a wind tunnel using an internal balance, illustrated in the figure below. Lift and Drag are normal to and aligned with the freestream velocity vector, which is roughly aligned with the centerline of the tunnel. The Normal and Axial force components from the balance are normal to and aligned with the axis of the model. Consider the simple case where that orientation is separated from the freestream velocity vector by the angle of attack, α.

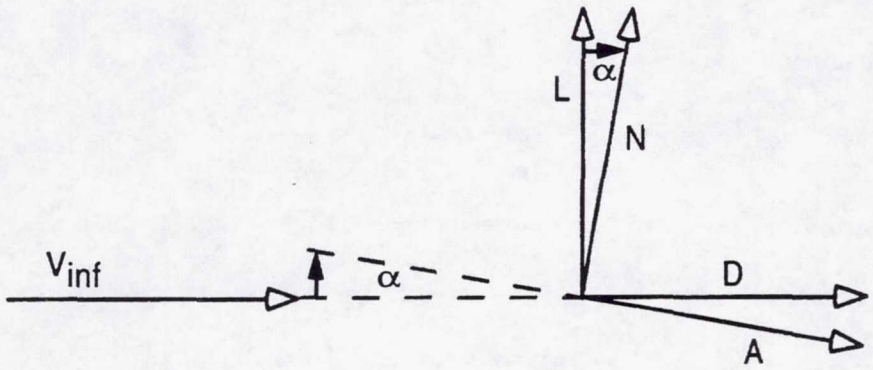

The Drag and Lift are calculated from measurements of the Axial and Normal force components, and the measurement of α. Thus:

$D, L = f(N, A, \alpha)$ Given by the relations:

$$D = N\sin\alpha + A\cos\alpha$$

$$L = N\cos\alpha - A\sin\alpha$$

It is desired to use these equations, the standard method for evaluating the repeatability of derived quantities and some algebra to estimate what Axial and Normal force repeatabilities are required to achieve a desired repeatability in Drag and Lift calculations.

The repeatability in Drag and Lift can be estimated in the normal fashion. (See reference 1.) Evaluate the partial derivatives:

$$\partial D/\partial N = \sin\alpha$$

$$\partial D/\partial A = \cos\alpha$$

$$\partial D/\partial \alpha = N\cos\alpha - A\sin\alpha$$

$$\partial L/\partial N = \cos\alpha$$

$\partial L/\partial A = -\sin\alpha$

$\partial L/\partial\alpha = -N\sin\alpha - A\cos\alpha$

Combine these as the root sum square of the influence coefficients times the repeatabilities of the measured quantities:

$$2\sigma_D = [[\sin\alpha\ 2\sigma_N]^2 + [\cos\alpha\ 2\sigma_A]^2 + [(N\cos\alpha - A\sin\alpha)\ 2\sigma\alpha]^2\ ]^{1/2}$$

$$2\sigma_L = [[\cos\alpha\ 2\sigma_N]^2 + [-\sin\alpha\ 2\sigma_A]^2 + [(-N\sin\alpha - A\cos\alpha)\ 2\sigma\alpha]^2\ ]^{1/2}$$

Squaring both sides, and rearranging:

$$(2\sigma_D)^2 - [(N\cos\alpha - A\sin\alpha)\ 2\sigma_\alpha]^2 = \sin^2\alpha\ (2\sigma_N)^2 + \cos^2\alpha\ (2\sigma_A)^2$$

$$(2\sigma_L)^2 - [(-N\sin\alpha - A\cos\alpha)\ 2\sigma_\alpha]^2 = \cos^2\alpha\ (2\sigma_N)^2 + \sin^2\alpha\ (2\sigma_A)^2$$

This can be cast in matrix form:

$$\begin{Bmatrix} (2\sigma_D)^2 - [(N\cos\alpha - A\sin\alpha)2\sigma_\alpha]^2 \\ (2\sigma_L)^2 - [(-N\sin\alpha - A\cos\alpha)2\sigma_\alpha]^2 \end{Bmatrix} = \begin{bmatrix} \sin^2\alpha & \cos^2\alpha \\ \cos^2\alpha & \sin^2\alpha \end{bmatrix} \begin{Bmatrix} (2\sigma_N)^2 \\ (2\sigma_A)^2 \end{Bmatrix}$$

Which is of the following form, and can be inverted:

$$\{J\} = [M]\ \{B\}$$

$$[M]^{-1}\ \{J\} = [M]^{-1}[M]\ \{B\} \Rightarrow [M]^{-1}\ \{J\} = [I]\ \{B\}$$

Therefore:

$$M^{-1} = \frac{1}{\sin^4\alpha - \cos^4\alpha} \begin{bmatrix} \sin^2\alpha & -\cos^2\alpha \\ -\cos^2\alpha & \sin^2\alpha \end{bmatrix}$$

Which yields:

$$\frac{1}{\sin^4\alpha - \cos^4\alpha} \begin{bmatrix} \sin^2\alpha & -\cos^2\alpha \\ -\cos^2\alpha & \sin^2\alpha \end{bmatrix} \begin{Bmatrix} (2\sigma_D)^2 - [(N\cos\alpha - A\sin\alpha)2\sigma_\alpha]^2 \\ (2\sigma_L)^2 - [(-N\sin\alpha - A\cos\alpha)2\sigma_\alpha]^2 \end{Bmatrix} = \begin{Bmatrix} (2\sigma_N)^2 \\ (2\sigma_A)^2 \end{Bmatrix}$$

Or:

$$\frac{1}{\sin^4\alpha - \cos^4\alpha}\left\{ \sin^2\alpha\,[(2\sigma_D)^2 - [(N\cos\alpha - A\sin\alpha)\,2\sigma_\alpha\,]^2] - \cos^2\alpha\,[(2\sigma_L)^2 - [(N\sin\alpha + A\cos\alpha)\,2\sigma_\alpha\,]^2]\right\} = (2\sigma_N)^2$$

And:

$$\frac{1}{\sin^4\alpha - \cos^4\alpha}\left\{ -\cos^2\alpha\,[(2\sigma_D)^2 - [(N\cos\alpha - A\sin\alpha)\,2\sigma_\alpha\,]^2] + \sin^2\alpha\,[(2\sigma_L)^2 - [(N\sin\alpha + A\cos\alpha)\,2\sigma_\alpha\,]^2]\right\} = (2\sigma_A)^2$$

Reducing the equation for repeatability in Normal force component:

$$(2\sigma_N)^2 = \frac{1}{\sin^2\alpha - \cos^2\alpha}\left\{ \sin^2\alpha\,[(2\sigma_D)^2 - (N^2\cos^2\alpha + A^2\sin^2\alpha - 2AN\cos\alpha\sin\alpha)(2\sigma_\alpha)^2] - \cos^2\alpha\,[(2\sigma_L)^2 - (N^2\sin^2\alpha + A^2\cos^2\alpha + 2AN\cos\alpha\sin\alpha)(2\sigma_\alpha)^2]\right\}$$

$$(2\sigma_N)^2 = \frac{1}{\sin^2\alpha - \cos^2\alpha}\left\{ \sin^2\alpha\,(2\sigma_D)^2 - \cos^2\alpha(2\sigma_L)^2 + (2\sigma_\alpha)^2(-N^2\sin^2\alpha\cos^2\alpha - A^2\sin^4\alpha + A^2\cos^4\alpha + 2AN\cos\alpha\sin^3\alpha + 2AN\cos^3\alpha\sin\alpha)\right\}$$

$$(2\sigma_N)^2 = \frac{1}{\sin^2\alpha - \cos^2\alpha}\left\{ \sin^2\alpha\,(2\sigma_D)^2 - \cos^2\alpha(2\sigma_L)^2 + (2\sigma_\alpha)^2[A^2(\cos^4\alpha - \sin^4\alpha) + 2AN(\cos\alpha\sin^3\alpha + \cos\alpha(1 - \sin^2\alpha)\sin\alpha)]\right\}$$

$$(2\sigma_N)^2 = \frac{1}{\sin^2\alpha - \cos^2\alpha}\left\{ \sin^2\alpha\,(2\sigma_D)^2 - \cos^2\alpha(2\sigma_L)^2 + (2\sigma_\alpha)^2[A^2(\cos^2\alpha - \sin^2\alpha) + 2AN(\cos\alpha\sin^3\alpha + \cos\alpha\sin\alpha - \cos\alpha\sin^3\alpha)]\right\}$$

$$(2\sigma_N)^2 = \frac{1}{\sin^2\alpha - \cos^2\alpha}\left\{ \sin^2\alpha\,(2\sigma_D)^2 - \cos^2\alpha(2\sigma_L)^2 + (2\sigma_\alpha)^2\,[A^2(\cos^2\alpha - \sin^2\alpha) + 2AN\cos\alpha\sin\alpha]\right\}$$

Reducing the equation for repeatability in Axial force component:

$$(2\sigma_A)^2 = \frac{1}{\sin^2\alpha - \cos^2\alpha} \left\{ -\cos^2\alpha \left[(2\sigma_D)^2 - (N^2\cos^2\alpha + A^2\sin^2\alpha - 2AN\cos\alpha\sin\alpha)(2\sigma_\alpha)^2\right] + \sin^2\alpha \left[(2\sigma_L)^2 - (N^2\sin^2\alpha + A^2\cos^2\alpha + 2AN\cos\alpha\sin\alpha)(2\sigma_\alpha)^2\right] \right\}$$

$$(2\sigma_A)^2 = \frac{1}{\sin^2\alpha - \cos^2\alpha} \left\{ \sin^2\alpha\,(2\sigma_L)^2 - \cos^2\alpha(2\sigma_D)^2 + (2\sigma_\alpha)^2\,(N^2\cos^4\alpha - N^2\sin^4\alpha + A^2\sin^2\alpha\cos^2\alpha - A^2\sin^2\alpha\cos^2\alpha - 2AN\cos^3\alpha\sin\alpha - 2AN\cos\alpha\sin^3\alpha) \right\}$$

$$(2\sigma_A)^2 = \frac{1}{\sin^2\alpha - \cos^2\alpha} \left\{ \sin^2\alpha\,(2\sigma_L)^2 - \cos^2\alpha(2\sigma_D)^2 + (2\sigma_\alpha)^2 \left[N^2(\cos^2\alpha - \sin^2\alpha) - 2AN(\cos\alpha(1 - \sin^2\alpha)\sin\alpha + \cos\alpha\sin^3\alpha)\right] \right\}$$

$$(2\sigma_A)^2 = \frac{1}{\sin^2\alpha - \cos^2\alpha} \left\{ \sin^2\alpha\,(2\sigma_L)^2 - \cos^2\alpha(2\sigma_D)^2 + (2\sigma_\alpha)^2 \left[N^2(\cos^2\alpha - \sin^2\alpha) - 2AN\cos\alpha\sin\alpha\right] \right\}$$

If it is further assumed that the repeatability in forces is related to the repeatability in coefficients, e. g.:

$$2\sigma_{C_D} = 2\sigma_D / (q * S)$$

Where q is the freestream dynamic pressure, and S is the reference planform area. The contributions to repeatability from q and S have been knowingly neglected. The summary equations can then be rewritten:

$$(2\sigma_{C_N})^2 = \frac{1}{\sin^2\alpha - \cos^2\alpha} \left\{ \sin^2\alpha\,(2\sigma_{C_D})^2 - \cos^2\alpha(2\sigma_{C_L})^2 + (2\sigma_\alpha)^2 \left[C_A{}^2(\cos^2\alpha - \sin^2\alpha) + 2\,C_A\,C_N\cos\alpha\sin\alpha\right] \right\}$$

And:

$$(2\sigma_{C_A})^2 = \frac{1}{\sin^2\alpha - \cos^2\alpha} \left\{ \sin^2\alpha\,(2\sigma_{C_L})^2 - \cos^2\alpha(2\sigma_{C_D})^2 + (2\sigma_\alpha)^2 \left[C_N{}^2(\cos^2\alpha - \sin^2\alpha) - 2\,C_A\,C_N\cos\alpha\sin\alpha\right] \right\}$$

If a small angle approximation is applied, where:

$\sin\alpha = \alpha$, α in radians

$\cos\alpha = 1$

Then the above equations reduce to:

$$(2\sigma_{C_N})^2 = \frac{1}{\alpha^2-1}\left\{ \alpha^2 (2\sigma_{C_D})^2 - (2\sigma_{C_L})^2 + (2\sigma_\alpha)^2 \left[C_A{}^2(1-\alpha^2) + 2\, C_A\, C_N\, \alpha\right] \right\}$$

And:

$$(2\sigma_{C_A})^2 = \frac{1}{\alpha^2-1}\left\{ \alpha^2 (2\sigma_{C_L})^2 - (2\sigma_{C_D})^2 + (2\sigma_\alpha)^2 \left[C_N{}^2(1-\alpha^2) - 2\, C_A\, C_N\, \alpha\right] \right\}$$

Page intentionally left blank

STRAIN GAUGE BALANCE UNCERTAINTY ANALYSIS AT NASA LANGLEY - A TECHNICAL REVIEW

John S. Tripp
NASA Langley Research Center
Hampton, Virginia 23681

Abstract

This paper describes a method to determine the uncertainties of measured forces and moments from multi-component force balances used in wind tunnel tests. A multivariate regression technique is first employed to estimate the uncertainties of the six balance sensitivities and 156 interaction coefficients derived from established balance calibration procedures. These uncertainties are then employed to calculate the uncertainties of force-moment values computed from observed balance output readings obtained during tests. Confidence and prediction intervals are obtained for each computed force and moment as functions of the actual measurands. Techniques are discussed for separate estimation of balance bias and precision uncertainties.

Background

The calibration of wind tunnel balances at NASA Langley Research Center (LaRC) is a lengthy labor-intensive process requiring fixture leveling, cable alignment, and dead weight application at each of 729 loading points. The first description of strain gage balance calibration methods at LaRC was reported by Hansen [1] in 1956. A refinement of these methods was reported by Guarino [2] in 1964. These two reports described the rationale for including all first and second order interaction coefficients for accurate balance characterization and devised a comprehensive calibration procedure to individually estimate each of the coefficients. This calibration procedure was also valuable in identifying error sources in balance design, strain gage installation, and inaccurate calibration load application. Reference [2] also presented a scalar iterative data reduction method, which was replaced in 1972 by a more efficient multivariable iterative matrix technique [3].

The proof-load concept wherein multiple loads are applied simultaneously was reported by Hansen as a means to verify balance accuracy. The overall accuracy of the balance was cited in reference [2] as the worst-case error among all components from the proof loadings. An alternative method was developed at NASA LaRC [4] which cites the accuracy of each of the six balance components. Each accuracy term is computed as twice the standard deviation of the predicted errors, expressed as a percentage of the full-scale load of the corresponding component. Efficient 63-point fractional factorial experimental designs have been studied by Dahiya [5] to reduce balance calibration effort and to minimize the covariances of the estimated coefficients. In 1994 Tripp and Tcheng developed a comprehensive technique for determination of measurement uncertainties of multiple-component wind tunnel balances [6].

Balance Input-Output Relationships

Mathematical Model

The six-component strain-gauge balance is modeled by a direct input/output relationship between the 6×1 applied force-moment vector **m** and the 6×1 output voltage vector **y**, represented by a second-degree multivariate polynomial. In particular, let **m** denote the six-component applied input vector:

$$\mathbf{m} = (N, A, P, R, Y, S)^{\mathrm{T}} \tag{1}$$

where

N = normal force
A = axial force
P = pitching moment
R = rolling moment
Y = yawing moment
S = side force.

Let the vector of second-order combinations of the elements of **m** be denoted by a 21×1 column vector **g(m)**,

$$\mathbf{g}(\mathbf{m}) = \begin{pmatrix} N^2, NA, NP, NR, NY, NS, A^2, AP, AR, AY, \\ AS, P^2, PR, PY, PS, R^2, RY, RS, Y^2, YS, S^2 \end{pmatrix}^{\mathrm{T}} \tag{2}$$

Let **y** denote the 6×1 column vector of measured strain gauge bridge output voltages, where

$$\mathbf{y} = (V_N, V_A, V_P, V_R, V_Y, V_S)^{\mathrm{T}} \tag{3}$$

Combine 1, **m**, and **g(m)** into a 28×1 extended input vector denoted by **z**, shown in partitioned form as follows:

$$\mathbf{z} = [1 \vdots \mathbf{m} \vdots \mathbf{g}(\mathbf{m})]^{\mathrm{T}} \tag{4}$$

where the unit element of **z** allows least-squares estimation of the output offset voltage at zero load. Let **C** denote the 6×28 coefficient matrix, partitioned into the form

$$\mathbf{C} = [\mathbf{c}_0 \vdots \mathbf{C}_1 \vdots \mathbf{C}_2] \tag{5}$$

where $\mathbf{c}_0$ is a 6×1 column vector of intercepts, $\mathbf{C}_1$ is the 6×6 matrix of linear sensitivities and first-order interactions, and $\mathbf{C}_2$ is the 6×21 matrix of quadratic sensitivities and cross interactions. The diagonal elements of $\mathbf{C}_1$ represent the balance sensitivities, and the off-diagonal elements of $\mathbf{C}_1$ represent the first-order balance interactions. The second order

multivariate polynomial representing the direct relationship between applied force-moment vector **m** and output voltage vector **y** is expressed in matrix notation as follows:

$$\mathbf{y} = \mathbf{Cz} = \mathbf{c}_0 + \mathbf{C}_1\mathbf{m} + \mathbf{C}_2\mathbf{g}(\mathbf{m}) \tag{6}$$

Some strain-gauge balance facilities employ a reversed mathematical model in which the applied force-moment vector **m** is represented as a polynomial function of the observed output voltage vector **y**.

Precision and Bias Uncertainties

Measurement uncertainty arises from two sources: random errors, termed precision errors, and systematic errors, termed bias errors [7]. Precision errors, although unpredictable, may be characterized statistically. The uncertainty due to precision errors can be reduced by replication. In this paper precision error is represented statistically as a zero-mean random variable described by a probability distribution. Strain-gauge balance precision errors arise from random strain gauge output voltage measurement errors due to noise, numerical round-off, thermal drift, etc. Additional precision uncertainty may arise during balance calibration due to random loading errors.

Consider a single six-component loading, **z**. The corresponding measurement of output vector **y** is corrupted by 6×1 precision error vector **e**, which is a zero-mean vector-valued random variable with 6×6 covariance matrix **S**. It is assumed that the probability distribution of **e** is stationary and that measurement error vectors $\mathbf{e}_j$ and $\mathbf{e}_k$, observed at the j^{th} and k^{th} measurements, are statistically independent. Hence, the 6×6 covariance matrix of $\mathbf{e}_j$ and $\mathbf{e}_k$ is zero for $j \neq k$. However, the elements of error vector $\mathbf{e}_k$ at the k^{th} observation may be correlated, in which case 6×6 covariance matrix **S** is non-diagonal. Inferences about confidence intervals developed subsequently require that precision error vector **e** be normally distributed.

Bias errors are systematic, although unknown, repeatable functions of input loadings. Strain-gauge balance bias uncertainty results from mathematical modeling errors due to neglected higher order interactions and inelastic effects such as hysteresis and creep, effects due to thermal gradients, and calibration errors. During calibration bias errors may arise due to calibration standard weight errors and cable misalignment. Following calibration, a fixed estimated value of coefficient matrix **C** is accepted, thereby introducing additional bias error during facility usage; this error is termed fossilized bias error resulting from both precision and bias uncertainties during calibration. It is to be noted that bias errors do not decrease with measurement replication. Let $\gamma(\mathbf{m})$ denote the 6×1 bias error vector, modeled as a deterministic vector-valued function of applied force/moment (input) vector **m**.

The actual relationship between the measured output voltage vector **y** and the applied loading vector **m**, including bias and precision errors, is expressed by the following equation:

$$\mathbf{y} = \mathbf{Cz} + \gamma(\mathbf{m}) + \varepsilon \tag{7}$$

Data Reduction

Given observed balance output voltage vector, **y**, the corresponding input force-moment vector is to be computed for data reduction. It can be shown [8] that a unique inverse of equation **(6)** exists provided that the Jacobian matrix of its right-hand side is nonsingular. The Jacobian matrix of the right hand side of **(6)**, evaluated analytically in Appendix equation **(34)**, is usually well-conditioned for six-component balances. Inversion of equation **(6)** by a Newton-Raphson iterative procedure, as employed in this paper, generally converges to the required precision in one or two iterations. Uncertainty of the inferred input loadings is estimated using techniques described below.

As outlined in references 1 and 2, the established LaRC calibration data reduction procedure estimates each element of matrices $\mathbf{C}_1$ and $\mathbf{C}_2$ independently from a selected subset of the calibration data. In the new method matrix **C**, including $\mathbf{c}_0$, is globally estimated in a single computation from the complete balance calibration data set using multivariate regression analysis.

Calibration Experimental Design

The balance is calibrated for estimation of coefficient matrix **C** based on an experimental design D containing K sets of applied loads, $\mathbf{z}_1,\ldots,\mathbf{z}_K$, where K typically equals 729 [4]. Experimental design D should be chosen to minimize the variance of the estimated balance output integrated over test envelope Ω. Let $\sigma_Y^2(\mathbf{m})$ denote the estimated balance output variance error due to precision uncertainty, to be derived below, and let V denote its average value over volume Ω.

$$v = \frac{1}{G}\int_{\Omega} \sigma_Y^2(\mathbf{m})\, d\mathbf{m} \tag{8}$$

where

$$G = \int_{\Omega} d\mathbf{m} \tag{9}$$

Similarly, let B denote the average estimated balance output variance due to bias uncertainty

$$B = \frac{1}{G}\int_{\Omega} \left\|\gamma(\mathbf{m})\right\|^2 d\mathbf{m} \tag{10}$$

Thus, experimental design D should be selected to minimize the sum:

$$J = V + B \tag{11}$$

It can be shown [9] that calibration points should generally be located at the boundaries of Ω to minimize the effects of random precision errors represented by V, whereas calibration points should be uniformly distributed over Ω to minimize the effects of mathematical modeling errors represented by B.

The NASA LaRC balance calibration experimental design contains N_K sets of nine loadings applied uniformly from zero to full scale load to zero [4], where N_K typically equals 81. Within the N_K loading sets are single and two-component combination loadings selected for estimation of sensitivities, first order interactions, and second order interactions.

Estimation of Sensitivities and Interaction Coefficients by Multivariate Regression

Coefficient matrix **C** is estimated from the calibration data set by multivariate multiple regression. Calibration design D contains K sets of applied loads, $\mathbf{z}_1,...,\mathbf{z}_K$. Arrange the load

$$\mathbf{Z} = \left[\mathbf{z}_1 \cdots \mathbf{z}_K\right] \tag{12}$$

vectors into $28 \times K$ design matrix **Z.**

Let $\mathbf{y}_1,...,\mathbf{y}_K$ denote the corresponding observed output voltage vectors, which are arranged into $6 \times K$ output matrix **Y** as

$$\mathbf{Y} = \left[\mathbf{y}_1 \cdots \mathbf{y}_K\right] \tag{13}$$

and let **E** denoted the $6 \times K$ matrix of calibration observation errors.

$$\mathbf{E} = \left[\varepsilon_1 \cdots \varepsilon_K\right] \tag{14}$$

As described above, the 6×6 covariance matrix between 6×1 vectors $\mathbf{e}_j$ and $\mathbf{e}_k$, denoted by, Σ_{jk} equals Σ for $j = k$, and zero for $j \ldots k$.

In the absence of bias uncertainty, output matrix **Y** as a function of design matrix **Z** and coefficient matrix **C** is obtained from equation **(7)** as

$$\mathbf{Y} = \mathbf{CZ} + \mathbf{E} \tag{15}$$

It is shown in reference [9] that the least-squares estimate of coefficient matrix **C**, denoted by $\hat{\mathbf{C}}$, is given by:

$$\hat{\mathbf{C}} = \mathbf{YZ}^{\mathrm{T}}\mathbf{Q}^{-1} \tag{16}$$

where $\mathbf{Q} = \mathbf{ZZ}^{\mathrm{T}}$. Matrix **Q** is nonsingular if design matrix **Z** has full rank (rank 28). It can be shown that the expected value of $\hat{\mathbf{C}}$ equals **C** and that the 28×28 covariance matrix between rows m and n of $\hat{\mathbf{C}}$, denoted by $\Sigma_{\mathbf{cmn}}$, is given by

$$\Sigma_{\mathbf{cmn}} = \mathbf{Cov}\left(\hat{\mathbf{e}}_m, \hat{\mathbf{e}}_n\right) = \sigma_{mn}\mathbf{Q}^{-1} \tag{17}$$

where σ_{mn} is the m,n element of Σ.

The $6 \times K$ residual matrix $\hat{\mathbf{E}}$, defined by

$$\hat{\mathbf{E}} = \mathbf{Y} - \hat{\mathbf{C}}\mathbf{Z} \tag{18}$$

consists of estimated calibration error vectors. It can be shown [10] that the expected value of $\hat{\mathbf{E}}$ equals $\mathbf{0}$. Let $1 \times K$ vector $\hat{\mathbf{e}}_n$ denote the n^{th} row of $\hat{\mathbf{E}}$. The $K \times K$ covariance matrix between $\hat{\mathbf{e}}_m$ and $\hat{\mathbf{e}}_n$ can be shown to be equal to

$$\Sigma_{\hat{\mathbf{e}}_{mn}} = \sigma_{mn}\left(\mathbf{I}_K - \mathbf{Z}\mathbf{Q}^{-1}\mathbf{Z}^T\right) \tag{19}$$

where $\mathbf{I}_K$ is the $K \times K$ identity matrix. It can be shown that an unbiased estimate of 6×6 calibration measurement covariance matrix Σ is given by

$$\hat{\mathbf{S}} = \frac{\hat{\mathbf{E}}\hat{\mathbf{E}}^T}{K - r - 1} \tag{20}$$

where $r = 28$.

Predicted Output Vector and Covariance Matrix

Test Facility Measurements

Consider a new measurement in a test facility after calibration. Let $\mathbf{m}_E$ denote the applied facility force-moment vector, and let $\mathbf{z}_E = [\mathbf{1} \vdots \mathbf{m}_E \vdots \mathbf{g}(\mathbf{m}_E)]^T$ denote the corresponding extended load vector as defined in equation **(4)**. Let $\mathbf{e}_V$ denote the precision error due to facility measurement noise, where $\mathbf{e}_V$ is zero-mean, has covariance matrix Σ_V, and is independent of calibration error matrix $\mathbf{E}$. If mathematical modeling error $\gamma(\mathbf{m})$ is zero, then actual output vector, $\mathbf{y}_E$, given by equation **(6)** is

$$\mathbf{y}_E = \mathbf{C}\mathbf{z}_E \tag{21}$$

However, the observed output vector, denoted by $\mathbf{y}_V$, corrupted by facility measurement noise is given by

$$\mathbf{y}_V = \mathbf{C}\mathbf{z}_E + \varepsilon_V \tag{22}$$

The output vector predicted by estimated coefficient matrix $\hat{\mathbf{C}}$, denoted by $\hat{\mathbf{y}}_E$, is given by

$$\hat{\mathbf{y}}_E = \hat{\mathbf{C}}\mathbf{z}_E \tag{23}$$

with expected value $\mathbf{C}\mathbf{z}_E$. The covariance matrix of predicted output vector, $\hat{\mathbf{y}}_E$, can be shown to

be given by

$$\Sigma(\hat{\mathbf{y}}_E) = E\left[\left(\hat{\mathbf{C}}\mathbf{z}_E - \mathbf{C}\mathbf{z}_E\right)\left(\hat{\mathbf{C}}\mathbf{z}_E - \mathbf{C}\mathbf{z}_E\right)^T\right] = \mathbf{z}_E^T\mathbf{Q}^{-1}\mathbf{z}_E\Sigma \tag{24}$$

where E denotes expected value. The diagonal of covariance matrix $\Sigma(\hat{\mathbf{y}}_E)$ represents bias uncertainty, i.e., the fossilized portion of the variance vector of estimated output vector $\hat{\mathbf{y}}_E$ due to calibration uncertainty.

The prediction error vector of the new measurement $\delta\hat{\mathbf{y}}_E$, defined as the difference between predicted output $\hat{\mathbf{y}}_E$ and observed output $\mathbf{y}_V$, is equal to

$$\delta\hat{\mathbf{y}}_E \equiv \hat{\mathbf{y}}_E - \mathbf{y}_V = \left(\hat{\mathbf{C}} - \mathbf{C}\right)\mathbf{z}_E - \varepsilon_V \tag{25}$$

The covariance matrix of prediction error vector, $\delta\hat{\mathbf{y}}_E$, is given by

$$\Sigma\left(\delta\hat{\mathbf{y}}_E\right) = E\left[\left(\hat{\mathbf{y}}_E - \mathbf{C}\mathbf{z}_E\right)\left(\hat{\mathbf{y}}_E - \mathbf{C}\mathbf{z}_E\right)^T\right] = \Sigma_V + \mathbf{z}_E\mathbf{Q}^{-1}\mathbf{z}_E^T\Sigma = \Sigma_V + \Sigma\left(\hat{\mathbf{y}}_E\right) \tag{26}$$

The diagonal of covariance matrix $\Sigma(\delta\hat{\mathbf{y}}_E)$ equals the total uncertainty of predicted output $\hat{\mathbf{y}}_E$. It is seen in equation **(26)** that matrix Σ_V represents the precision uncertainty due to facility measurement error vector $\mathbf{e}_v$, which is independent of calibration error matrix **E**. Matrix $\Sigma(\hat{\mathbf{y}}_E)$ represents the portion of the bias uncertainty of the new measurement due to fossilized calibration precision errors. If mathematical modeling error is nonzero, additional bias error must be included.

Confidence Interval and Prediction Interval

If the columns of calibration error matrix **E** are normally distributed, then $\hat{\mathbf{y}}_E$ is normally distributed. It can then be shown [9] that variable F, defined by the following quadratic form, is the F-distributed at confidence level 1-α with (p, K-r-p) degrees of freedom, where p=6 is the number of measured outputs and r=28 is the total number of input variables:

$$\left(\mathbf{y}_E - \hat{\mathbf{y}}_E\right)^T\hat{\mathbf{S}}^{-1}\left(\mathbf{y}_E - \hat{\mathbf{y}}_E\right) \le \frac{pK}{K-r-p}\mathbf{z}_E^T\mathbf{Q}^{-1}\mathbf{z}_E F_{p,K-r-p}(\alpha) \tag{27}$$

Equation **(27)** defines a calibration confidence ellipsoid in six-dimensional hyperspace which determines the boundaries of simultaneous confidence intervals for the predicted values $\hat{\mathbf{y}}_E$ of $\mathbf{y}_E$. The error bound of the nth measured output component is equal to the projection of the ellipsoid onto the y_n axis, which can be shown [9] to be equal in length to the corresponding diagonal element, $\hat{s}_{nn}$, of $\hat{\mathbf{S}}$ as defined in equation **(20)**. In particular, let $\hat{\mathbf{c}}_n^T$ denote the nth row of estimated coefficient matrix $\hat{\mathbf{C}}$ and let y_n denote the nth element of $\mathbf{y}_E$. Then, the predicted value, $(\hat{\mathbf{y}}_E)_n$, of the nth output component, y_n, is, with confidence level 1-α, in error by less than the following bound:

$$\left|y_n - \hat{\mathbf{c}}_n^{\mathrm{T}}\mathbf{z}_{\mathrm{E}}\right| < \left[\hat{s}_{nn}\frac{pK}{K-r-p}\mathbf{z}_{\mathrm{E}}^{\mathrm{T}}\mathbf{Q}^{-1}\mathbf{z}_{\mathrm{E}}F_{p,K-r-p}(\alpha)\right]^{1/2} \tag{28}$$

where $\hat{s}_{nn}$ is the nth diagonal element of $\hat{\mathbf{S}}$. Equation **(28)** defines the calibration confidence interval.

Similarly, using equation **(26)** the confidence interval of a new facility measurement prediction error, denoted the prediction interval, is given by

$$\hat{y}_n = \left|\hat{y}_n - \hat{\mathbf{c}}_n^{\mathrm{T}}\mathbf{z}_{\mathrm{E}}\right| < \left[\sigma_V^2 + \hat{s}_{nn}\frac{pK}{K-r-p}\mathbf{z}_{\mathrm{E}}^{\mathrm{T}}\mathbf{Q}^{-1}\mathbf{z}_{\mathrm{E}}F_{p,K-r-p}(\alpha)\right]^{1/2} \tag{29}$$

Computation of the Inferred Force-Moment Vector

Let $\mathbf{m}_{\mathrm{E}}$ denote an arbitrary applied facility load, and let $\mathbf{y}_{\mathrm{V}}$ denote the corresponding measured balance output vector, and let $\hat{\mathbf{m}}_{\mathrm{E}}$ denote the inverse solution to equation **(6)**. It is desired to estimate error, $\delta\hat{\mathbf{m}}_{\mathrm{E}} = \mathbf{m}_{\mathrm{E}} - \hat{\mathbf{m}}_{\mathrm{E}}$. This error arises from two sources: (1) observed balance voltage measurement error vector, $\mathbf{e}_{\mathrm{V}}$, and (2) error in the inverse solution of equation **(6)** due to the uncertainty, $\hat{\mathbf{C}} - \mathbf{C}$, of estimated coefficient matrix $\hat{\mathbf{C}}$. It is seen that the total error between the observed and predicted values is equal to error $\delta\hat{\mathbf{y}}_{\mathrm{E}}$ given in equation **(25)**, which can be rewritten as follows:

$$\delta\hat{\mathbf{y}}_{\mathrm{E}} = \left(\hat{\mathbf{C}} - \mathbf{C}\right)\mathbf{z}_{\mathrm{E}} - \varepsilon_{\mathrm{V}} = \delta\hat{\mathbf{y}}_{\mathrm{R}} - \varepsilon_{\mathrm{V}} \tag{30}$$

Error $\delta\hat{\mathbf{m}}_{\mathrm{E}}$ can be estimated by differentiating equation **(2)** to yield:

$$\delta\mathbf{g}(\mathbf{m}) = \frac{\partial\mathbf{g}(\mathbf{m})}{\partial\mathbf{m}} = \mathbf{W}\delta\mathbf{m} \tag{31}$$

where Jacobian matrix $\mathbf{W}$ is obtained in the appendix. Combining equations **(30)** and **(31)** equation yields the desired result

$$\delta\hat{\mathbf{m}}_{\mathrm{E}} = \left(\mathbf{C}_1 + \mathbf{C}_2\mathbf{W}\right)^{-1}\delta\mathbf{y}_{\mathrm{E}} = \mathbf{J}^{-1}\delta\hat{\mathbf{y}}_{\mathrm{E}} \tag{32}$$

where $\mathbf{J} = \mathbf{C}_1 + \mathbf{C}_2\mathbf{W}$ is the Jacobian matrix defined in Appendix equation **(33)**, and $\delta\hat{\mathbf{y}}_{\mathrm{E}}$ is set equal to the uncertainty obtained from equation **(26)**.

Detection of Systematic Errors

Systematic errors whose peak magnitude significantly exceeds that of random precision errors can be identified using residual plots. However, detection of bias errors whose order of magnitude is comparable to that of the precision errors is more difficult. A useful technique

exploits the fact that random measurement errors are likely to be normally distributed. Indeed, it is known by the Central Limit Theorem [11] that statistical variates, which are averages of arbitrarily distributed random samples, are asymptotically normal. If averaged balance calibration measurement errors are approximately normally distributed, then statistical tests for normality may disclose the presence of significant systematic errors. Let the residuals be plotted on a standard normal probability graph wherein normal samples lie on a straight line. The non-normally distributed residuals, which deviate from the line, may then be identified and plotted separately.

Having removed the normally-distributed precision error from total prediction error, the remaining systematic error can be examined for functional relations with the applied input. Such tests may identify regions in test space Ω where the mathematical model is inadequate. Extensions and enhancement of the mathematical model may then be developed to improve the fit. Note also that conservative selection of Ω based on planned facility tests may eliminate the need for calibration over unused regions of the input space and thereby avoid unnecessary model complexity.

Calibration Results

Coefficient matrices for a number of six-component LaRC balances have been obtained using global regression equation **(18)**. The following figures present error values and standard deviations in units of percent full-scale load (%FS) versus calibration point number.

Figures 1a and 1b illustrate calibration residuals for LaRC balance 748. The six calibration residual vectors, obtained from matrix $\hat{\mathbf{E}}$, were computed using equation **(19)** over the 729 calibration points. The residuals are the errors between the observed balance outputs and the predicted outputs, shown in Figure 1 as dot symbols at each loading point $\mathbf{z}_k$, for $1 \le k \le K$. The 95% calibration confidence interval obtained using equation **(28)** is shown by the inner pair of continuous curves as functions of the applied load. The corresponding 95% prediction interval, obtained using equation **(29)**, is shown by the outer pair of continuous curves. Standard errors are noted in each plot.

Input load vectors corresponding to the observed balance output voltages are inferred from the estimated coefficient matrix, $\hat{\mathbf{C}}$, using the iterative Newton-Raphson procedure given in the appendix, for the set of 729 calibration points.

Prediction errors for three proof-load data sets for the six components are shown in figures 2a and 2b. Proof-load data set 1 contains simultaneous loadings in normal, pitch, and roll at half scale and full scale loads. Proof- load data set 2 contains simultaneous loadings in side, yaw, and roll. Proof-load data set 3 contains simultaneous six-component loadings applied at half and full scale values. Estimated input loads corresponding to the observed balance output voltages were inferred using estimated coefficient matrix $\hat{\mathbf{C}}$; prediction errors are shown as dot symbols in figure 2. The 95% prediction intervals for the proof loads, computed as functions of the applied loadings, are shown by the solid curves. It can be seen that outlying points are most frequent in proof-load set 3 containing six-component loadings.

Experimental Detection of Systematic Errors

Figures 3a - 3c present histograms of the residuals scaled to units of standard deviation on the abscissa and fit to a normal distribution having the same mean and variance. Each of the six histograms indicates an excess of central points in comparison to the tails, suggesting the presence of systematic errors within the tails. Chi-square goodness-of-fit values are noted on each figure. The normal force residuals exceed the critical value at the 95% confidence level, indicating that the normal force residuals are not normally distributed. This also indicates that the outlying residuals may be due to systematic errors.

Figures 4a - 4c illustrate normal probability plots of residuals for each of the six components. Significant departure from the normal line can be seen for all components, although the effect is least pronounced for the axial component. Pitching moment residuals exhibit the most significant departure from normality for those values falling outside the middle 50th percentile.

Figures 5a - 5f illustrate, for each component, the departure of each residual from the normal probability line plotted versus test point number, where the loading points are partitioned into 81 sets of 9 loadings as shown by vertical dashed lines in the figures. The effect has been to remove the random residual errors leaving only systematic residual errors. The nature of the systematic errors is clearly visible. For example, note in figure 5a, normal force residuals, points 28 - 36, that the errors increase from zero, to a maximum, and back to zero, as the applied loading varies from zero, to full scale, to zero; this indicates a linear or cross-term coefficient error. On the other hand, note in figure 5a, points 289 - 297, that the errors increase from zero to a maximum over the nine-point loading. This indicates the presence of an inelastic shift under load, such as hysteresis of the material or strain gauge creep. It is seen in figure 5c that a preponderance of the systematic pitch residual errors do not return to zero, indicating predominantly inelastic error effects. In contrast, comparison of figure 5b with the others indicates that the axial component systematic errors have the lowest magnitude. Moreover, most of the axial systematic errors return to zero, indicating predominantly elastic error effects due to coefficient errors.

Concluding Remarks

The paper employs a global multivariate multiple regression technique for estimation of the balance coefficient matrix. The technique provides estimated calibration confidence intervals and prediction intervals of estimated balance outputs as functions of the applied loadings. From these values, calibration confidence intervals and prediction intervals for the inferred iniput loadings are obtained as functions of the applied loads. It is to be noted that although measurement precision uncertainties may be reduced by replication and averaging, systematic errors are not reduced by replication. Therefore, the portion of regression residuals due to mathematical modeling error should be removed prior to computation of the estimated standard measurement error. The standard bias error due to modeling error is computed separately, and later combined with standard precision error. Lumping bias and precision errors prior to computation of standard error may significantly underestimate overall balance uncertainty.

Proof load errors exceed the predicted error band limits for full six-component loadings. The

most likely cause may be offsets due to minute displacement or hysteresis in the mechanical attachments under bidirectional loads. The present mathematical model does not account for hysteresis effects. Another cause may be that the second-order model, presently estimated using primarily single and paired component loadings, may be inaccurate for three or more simultaneous loadings. The second order model has been shown to be adequate to an accuracy of 0.5 percent of full scale for most LaRC balances. However, a higher order model may be required for 0.1 percent accuracy with multiple loadings. A third cause may be slightly inaccurate six-component loadings. Calibration loads applied singly or in pairs can be controlled very accurately in magnitude and direction. However, cable realignment may not be possible to the required accuracy during full six-component loadings. Additional work is planned to investigate these possible error sources and to study the inclusion of higher order interactions in the balance model.

The use of normal probability plots indicates the presence of systematic errors among the calibration residuals, provided that precision errors are normally distributed. It is seen that plotting the departure of the residuals from the normal distribution line versus test point number provides an effective method of extracting systematic errors from the set of residuals. Examination of the systematic residuals discloses the presence of errors due to elastic effects such as coefficient errors, and other errors due to inelastic effects such as hysteresis and strain gauge creep.

References

1. Hansen, Raymond M.: *Evaluation and Calibration of Wire-Strain-Gage Wind-Tunnel Balances Under Load.* AGARD Report 13, February 1956.

2. Guarino, Joseph F.: *Calibration and Evaluation of Multicomponent Strain-Gage Balances.* NASA Interlaboratory Force Measurements Group Meeting, Jet Propulsion Laboratory, Pasadena, CA, April 1964.

3. Smith, David L.: *An Efficient Algorithm Using Matrix Methods to Solve Wind Tunnel Force-Balance Equations*. NASA TND-6860, 1972.

4. Ferris, Alice T.: *An Improved Method for Determining Force Balance Calibration Accuracy.* Proceedings of the 39th International Instrumentation Symposium, Instrument Society of America, Albuquerque, NM, May 1993, pp. 321-335.

5. Dahiya, Ram C.: *Statistical Design for an Efficient Calibration of a Six Component Strain Gage Balance.* Final Report Prepared for NASA LaRC, Task No. 30 under Master Contract NAS1-15648, Old Dominion University Research Foundation, Norfolk, VA, October 1980.

6. Tripp, J.; and Tcheng, P.: *Determination of Measurement Uncertainties of Multi-Component Wind Tunnel Balances*. AIAA-94-2589. 18th AIAA Aerospace Ground Testing Conference, Colorado Springs, CO, June 1994.

7. Coleman, H. W.; and Steele, W. G.: *Experimentation and Uncertainty Analysis for Engineers*. John Wiley & Sons, New York, NY, 1989.

8. Brand, Louis: *Advanced Calculus*. John Wiley & Sons, New York, NY, 1955.

9. Box, G. E. P.; and Draper, N. R. AA Basis for the Selection of a Response Surface Design.@ *American Statistical Association Journal*, September, 1959.

10. Johnson, Richard A.; and Wichern, Dean W.: *Applied Multivariate Statistical Analysis.* Prentice-Hall, Englewood Cliffs, NJ, 1982.

11. Wilks, Samuel S.: *Mathematical Statistics.* John Wiley & Sons, Inc., New York, NY, 1962.

Appendix

Iterative Solution of the Interaction Equations

Solution of equation **(6)** by Newton-Raphson iteration requires computation of the Jacobian matrix **J** of its right hand side as

$$\mathbf{J} = \frac{\partial \mathbf{y}}{\partial \mathbf{m}} = \mathbf{C}_1 + \mathbf{C}_2\mathbf{W} \tag{33}$$

where **W** is the Jacobian matrix of equation **(2)**. Jacobian matrix **W** is computed analytically as follows:

$$\mathbf{W} = \frac{\partial \mathbf{g}(\mathbf{m})}{\partial \mathbf{m}} \tag{34}$$

The Newton-Raphson iterative procedure to solve equation **(6)** is as follows: Let $\mathbf{y}_E$ denote the observed output vector, and let n denote the iteration number. The initial estimate of $\mathbf{m}_E$, denoted by $\mathbf{m}_1$, is computed by neglecting the second-order interactions in equation **(6)** as follows:

$$\mathbf{m}_1 = \mathbf{y}_E\mathbf{C}_1^{-1} \tag{35}$$

After the nth iteration the updated estimate of $\mathbf{m}_E$, denoted by $\mathbf{m}_{n+1}$, is computed by

$$\mathbf{m}_{n+1} = \mathbf{m}_n + (\mathbf{y}_E - \mathbf{C}\mathbf{z}_n)\mathbf{J}_n^{-1}$$

where $\mathbf{z}_n$ and $\mathbf{J}_n$ are computed at $\mathbf{m}_n$ using equations **(4)** and **(33)**. The computation iterates until the norm of $(\mathbf{m}_{n+1} - \mathbf{m}_n)$ becomes less than the required precision. For the balance data examined herein, the procedure was observed to converge in two iterations. Reference [3] reports that more than two iterations were required for convergence using a lower order iterative procedure.

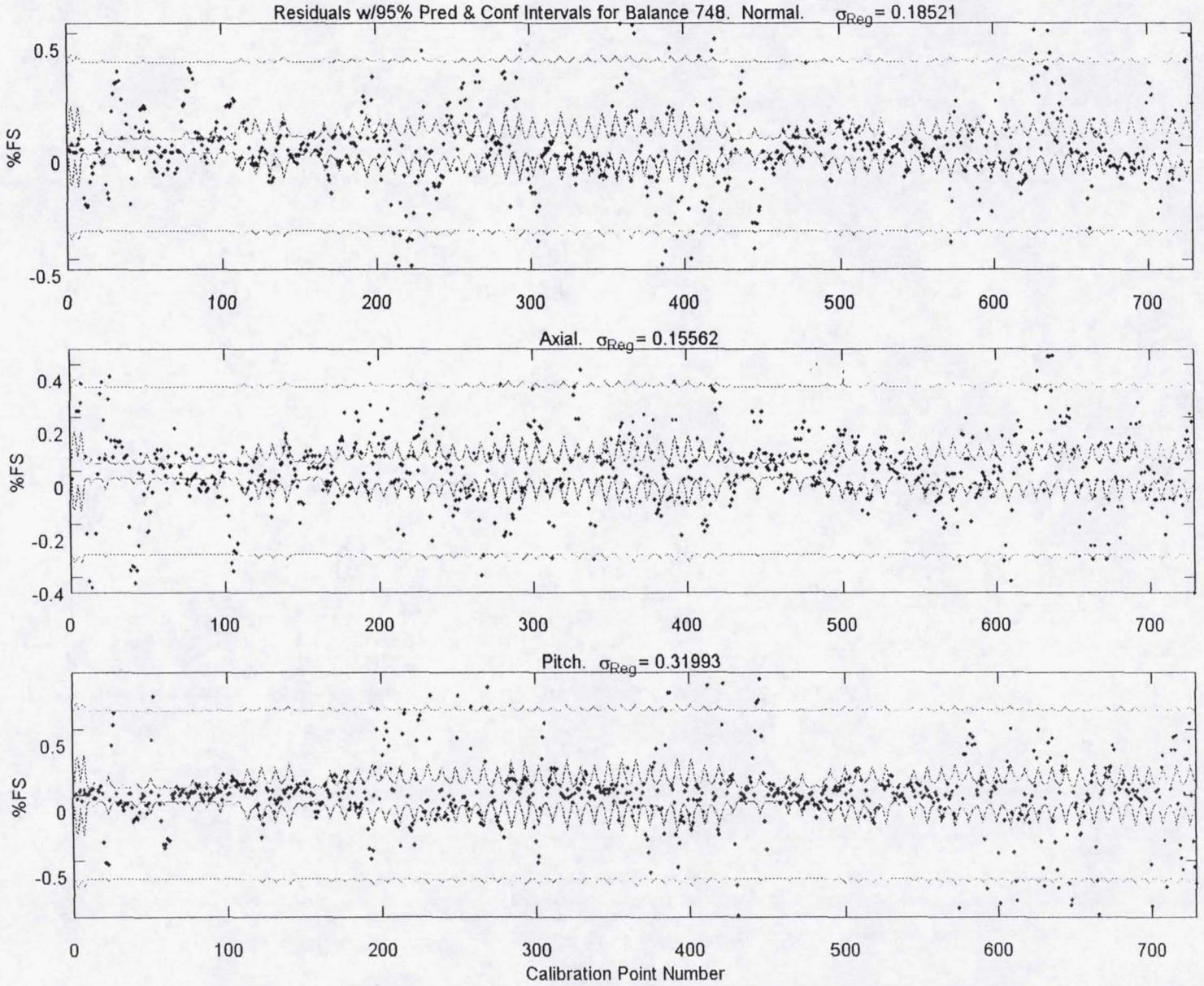

Figure 1a. Calibration Residuals with 95% Confidence and Prediction Intervals

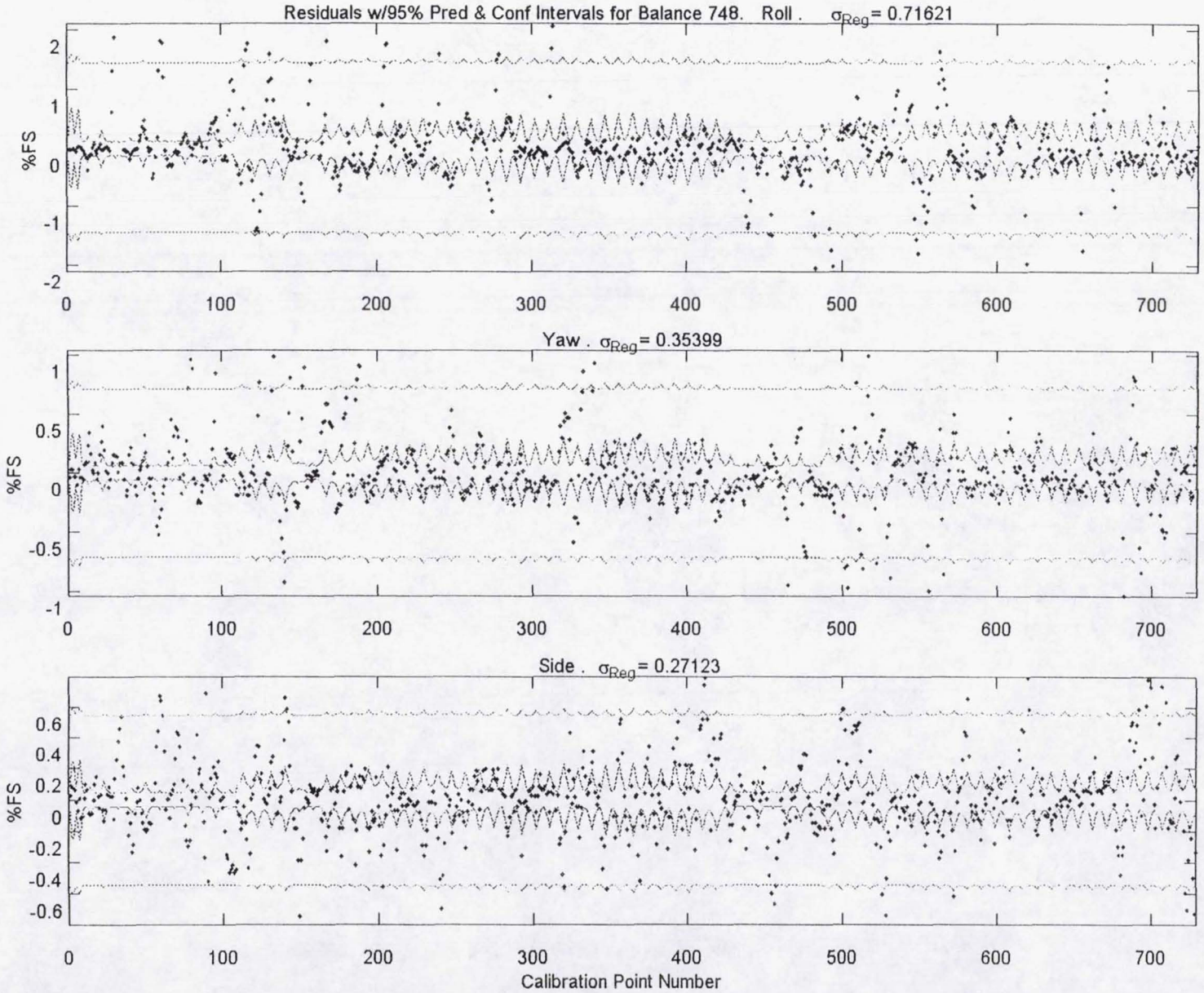

Figure 1b. Calibration Residuals with 95% Confidence and Prediction Intervals

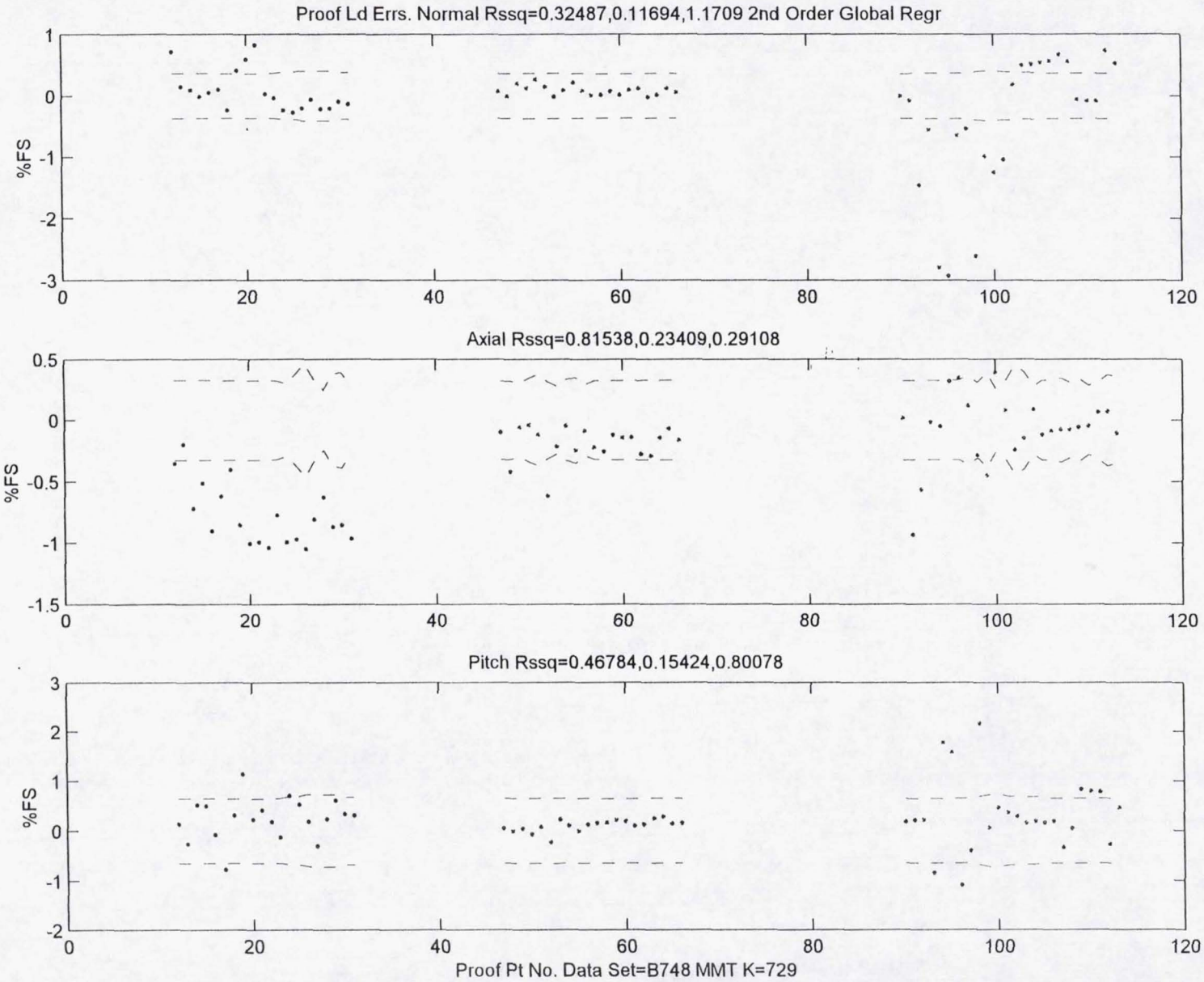

Figure 2a. Proof Load Residuals with 95% Prediction Intervals

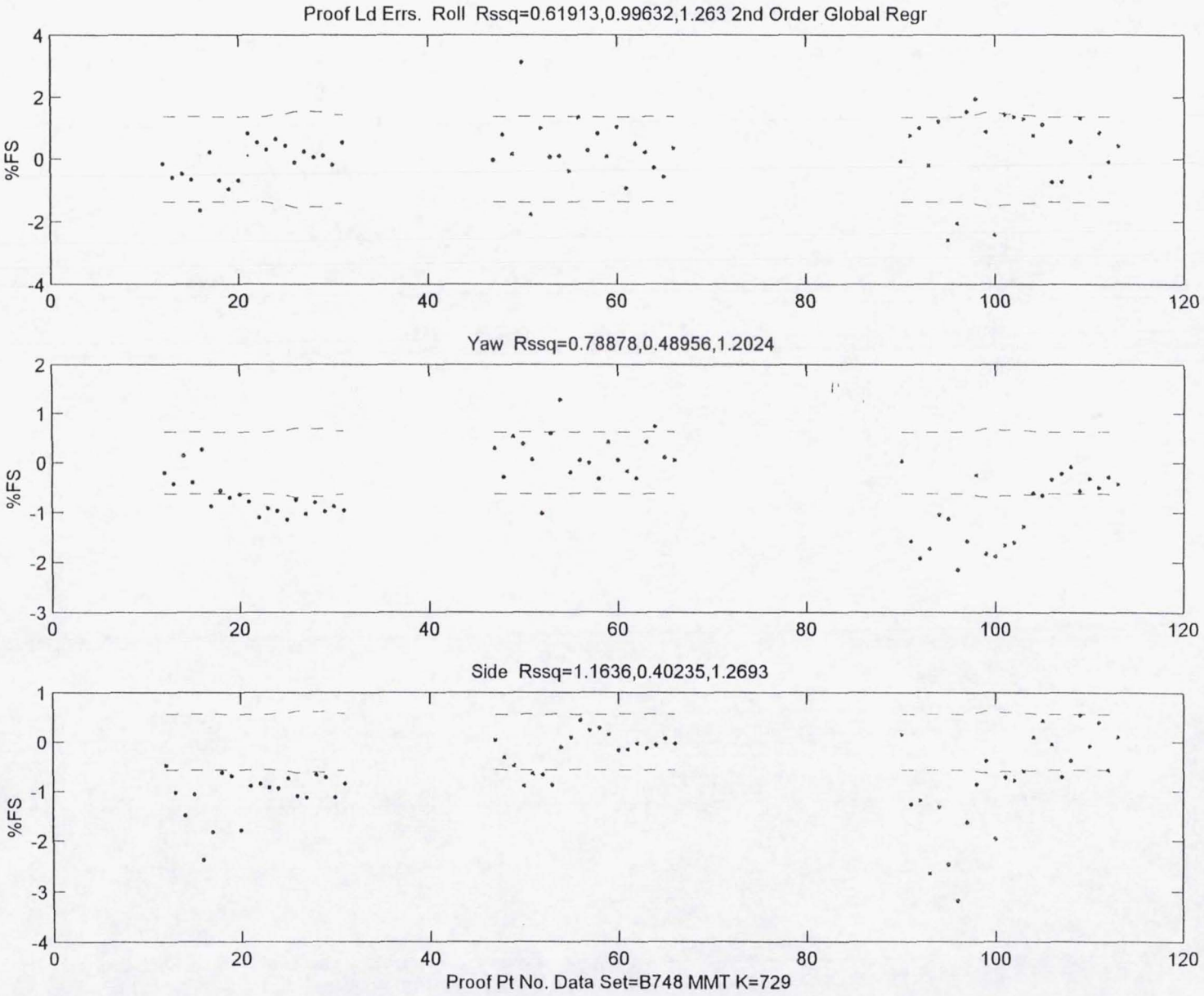

Figure 2b. Proof Load Residuals with 95% Prediction Intervals

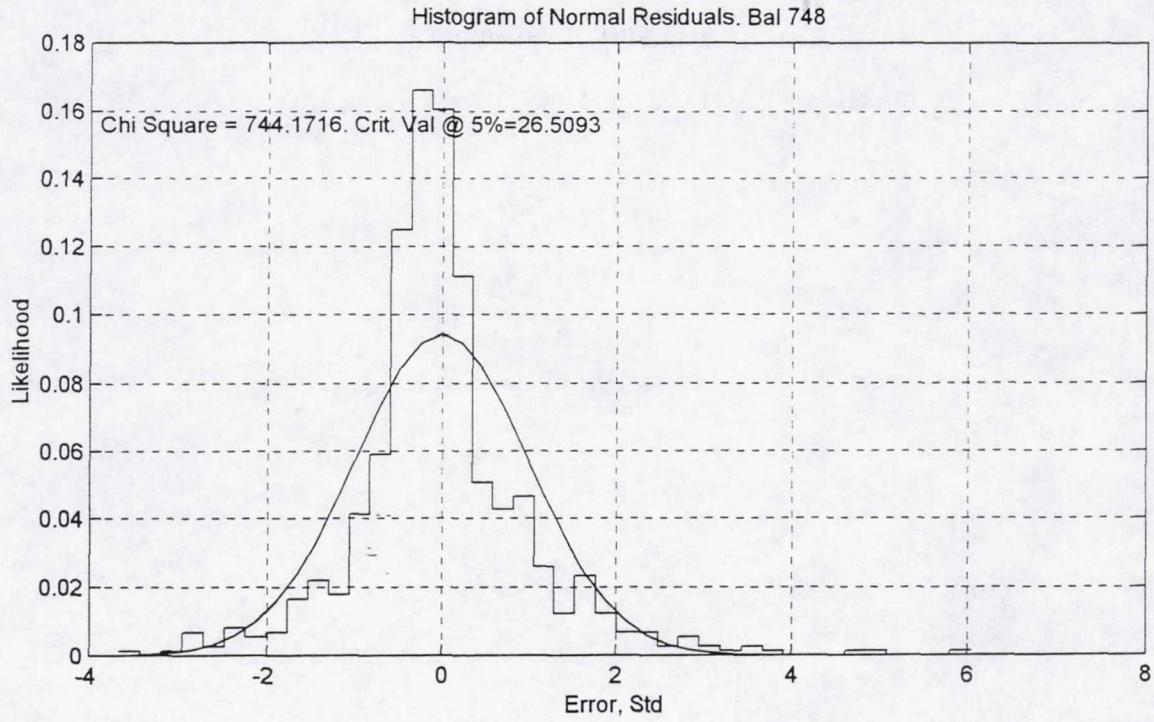

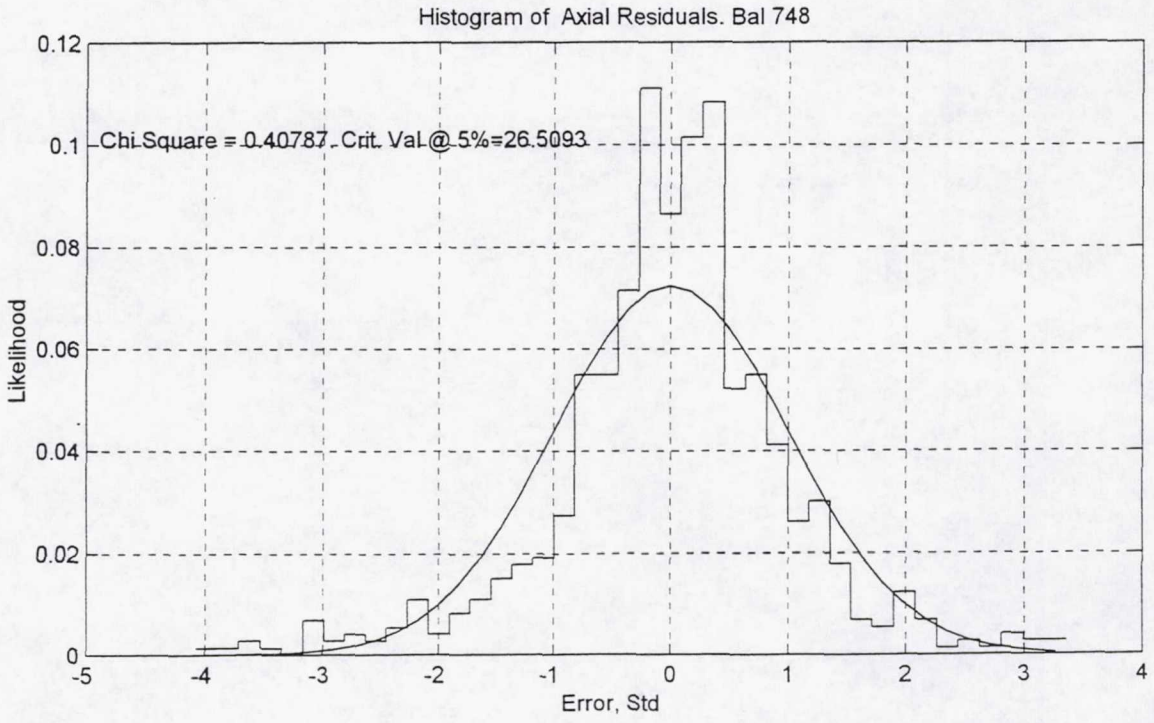

Figure 3a. Histograms of Calibration Residuals

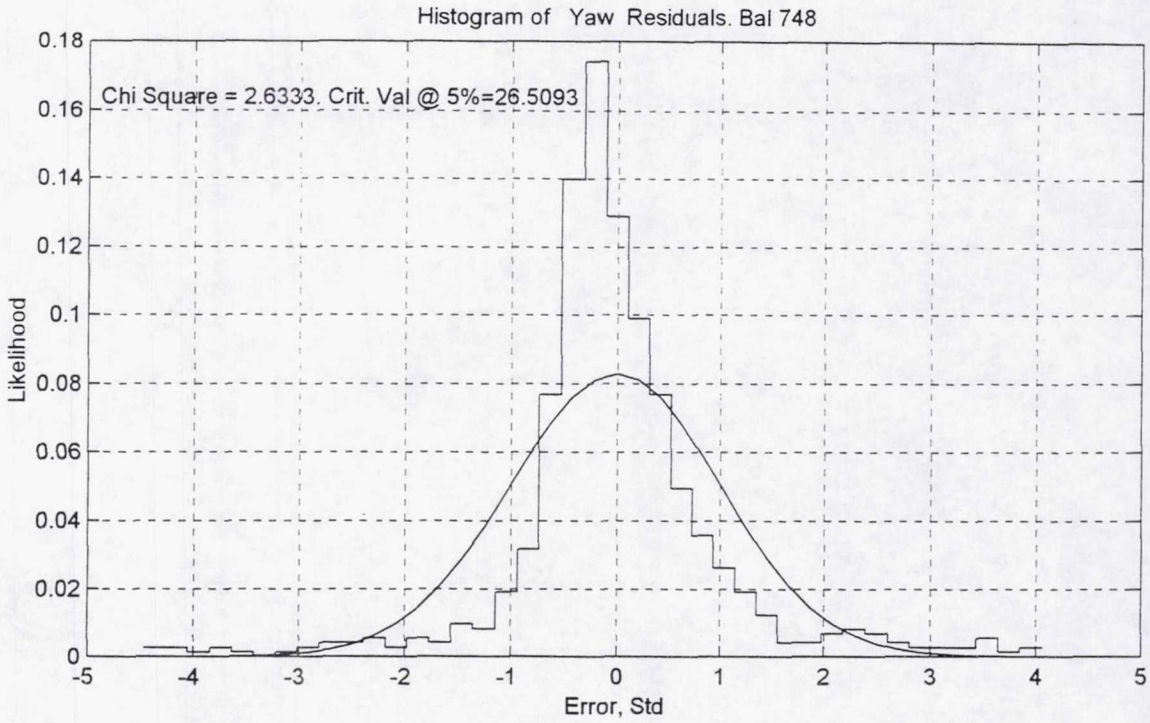

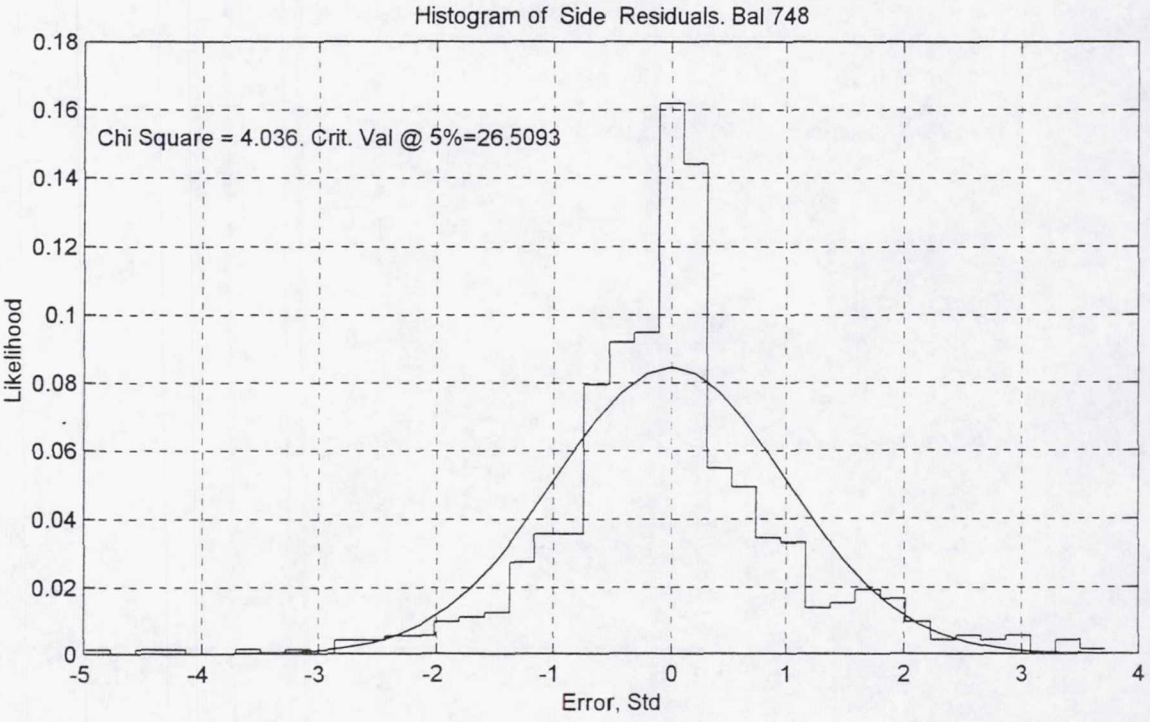

Figure 3b. Histograms of Calibration Residuals

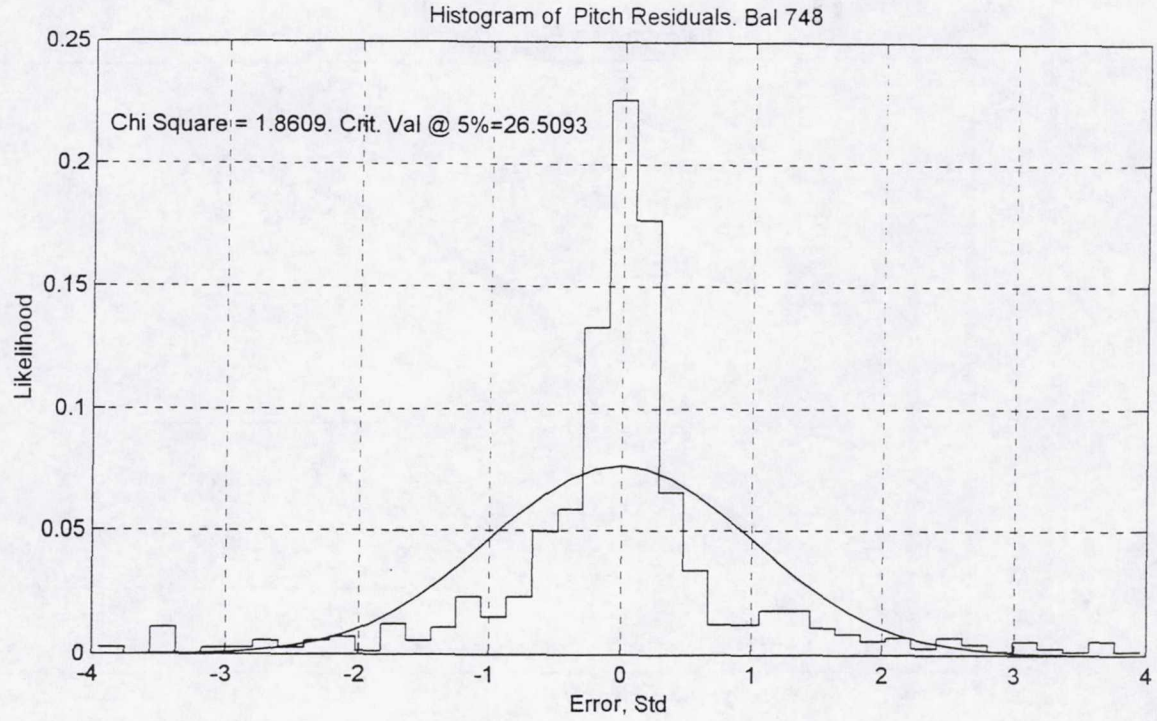

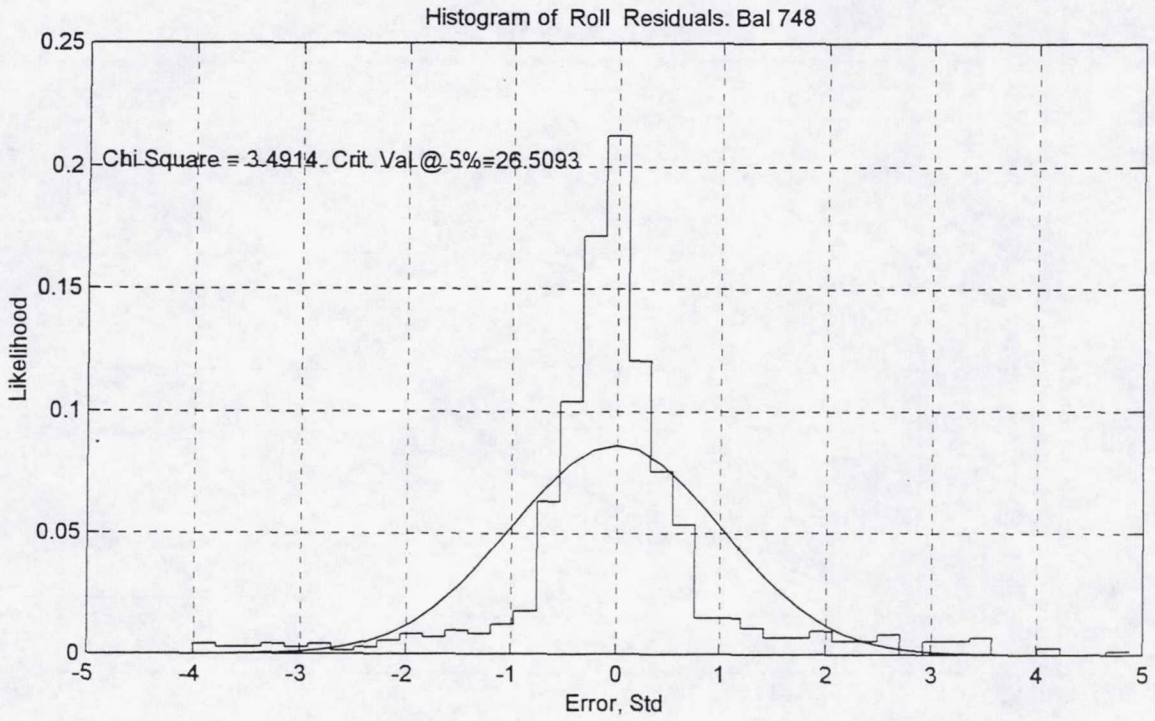

Figure 3c. Histograms of Calibration Residuals

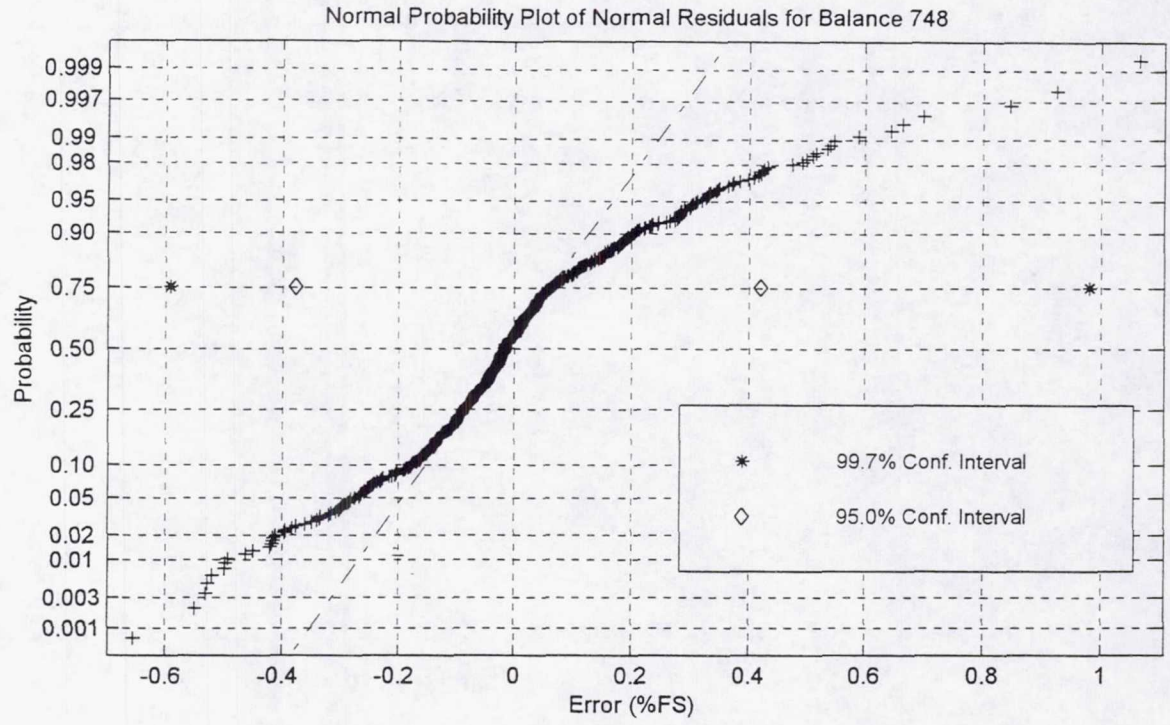

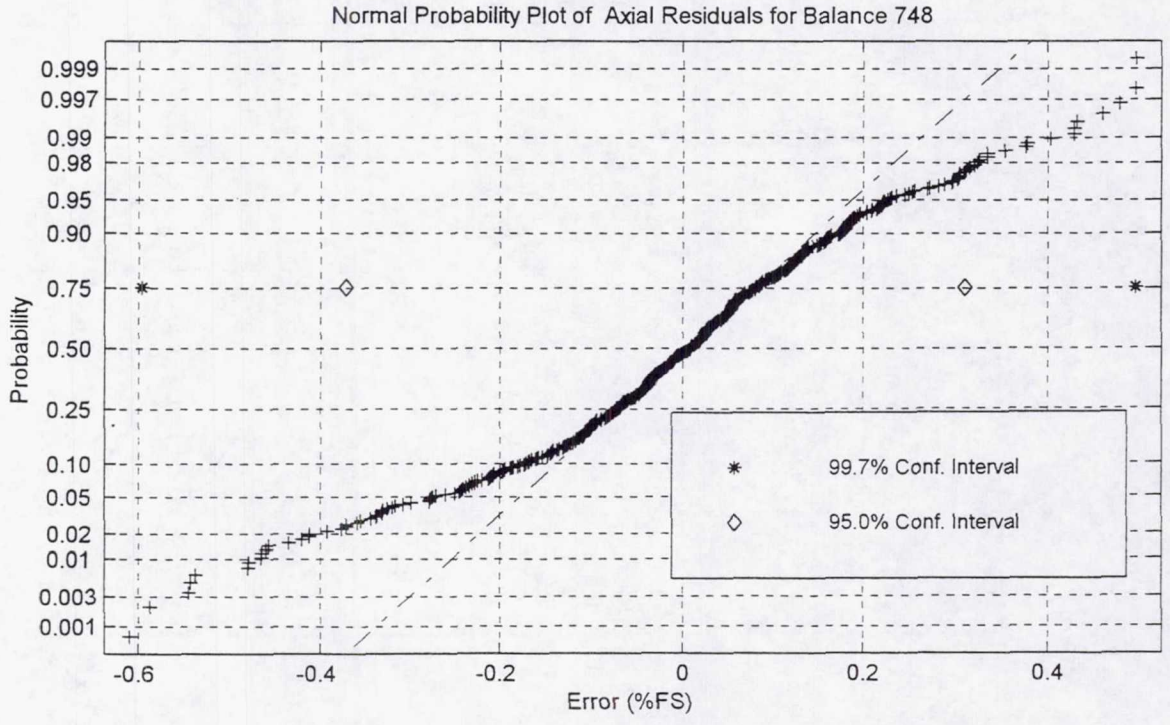

Figure 4a. Normal Probability Plots of Calibration Residuals

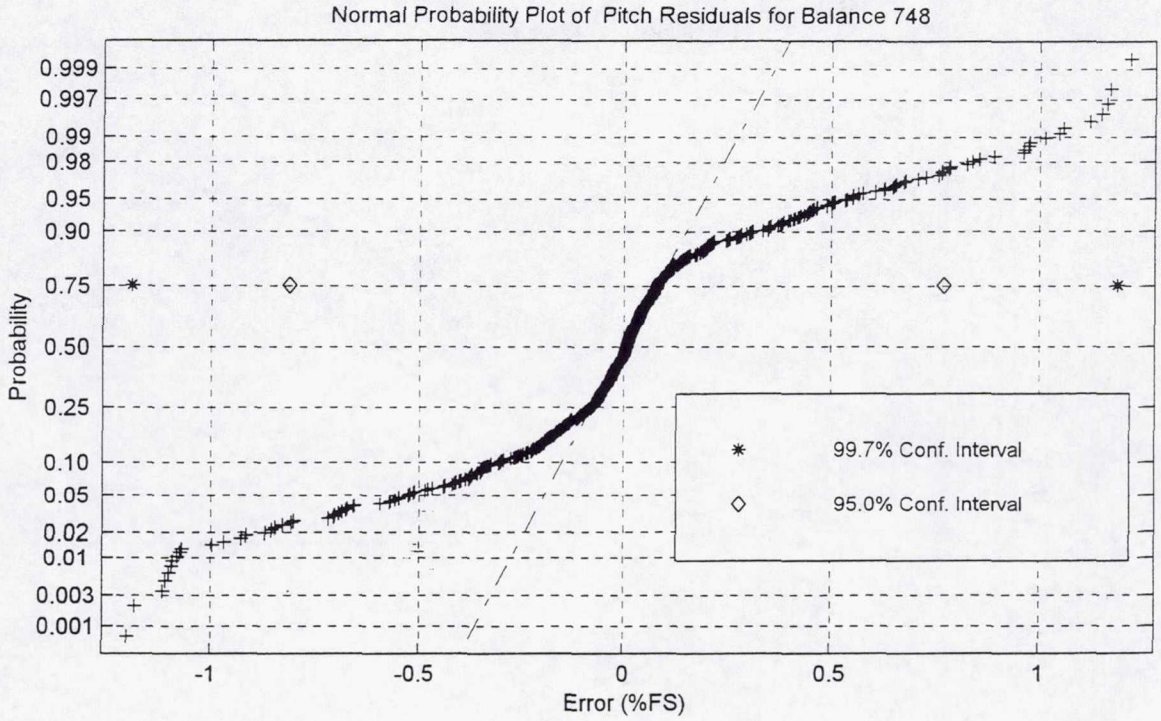

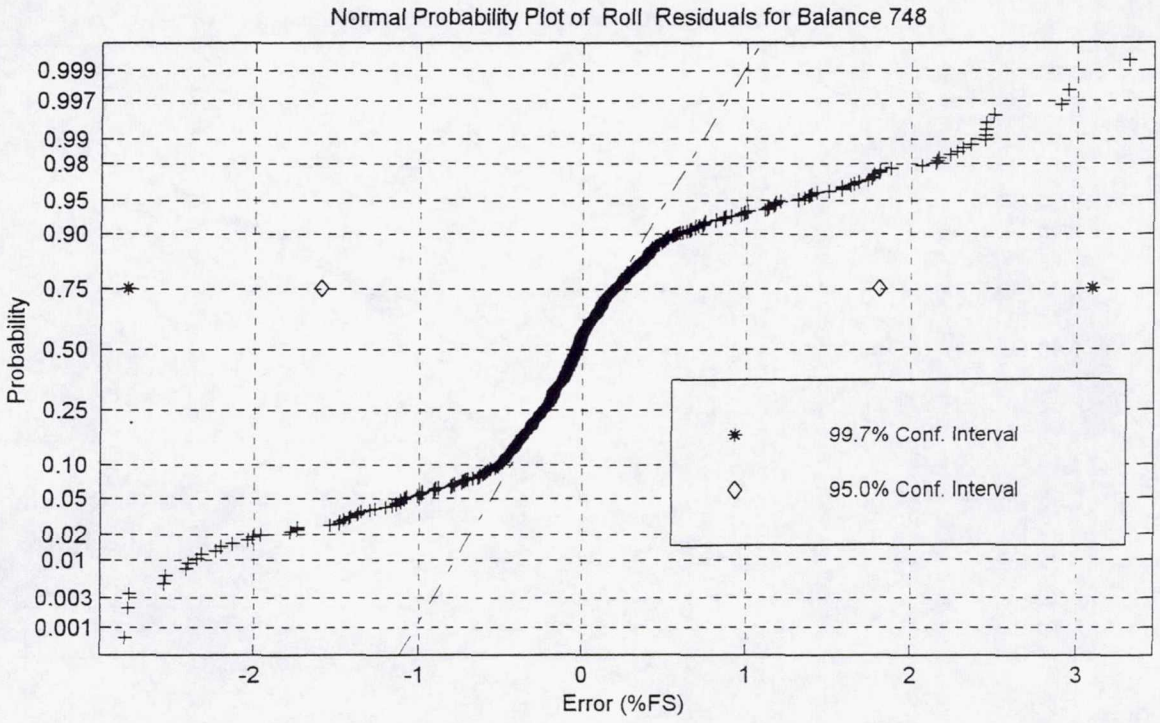

Figure 4b. Normal Probability Plots of Calibration Residuals

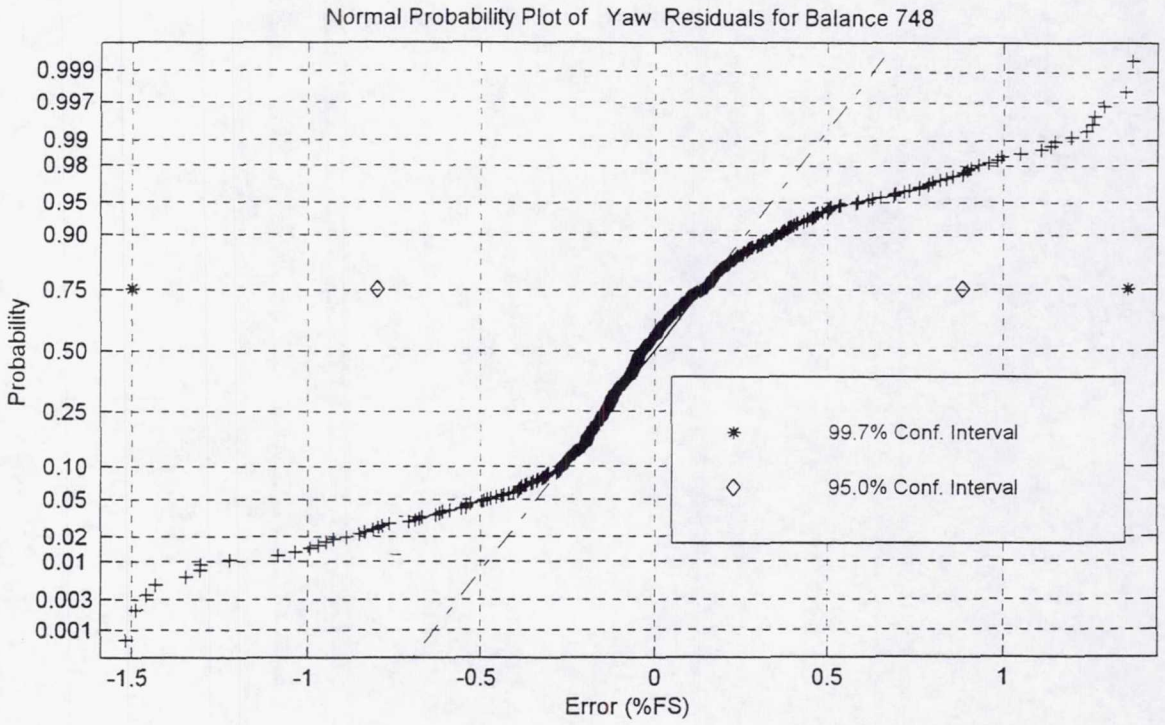

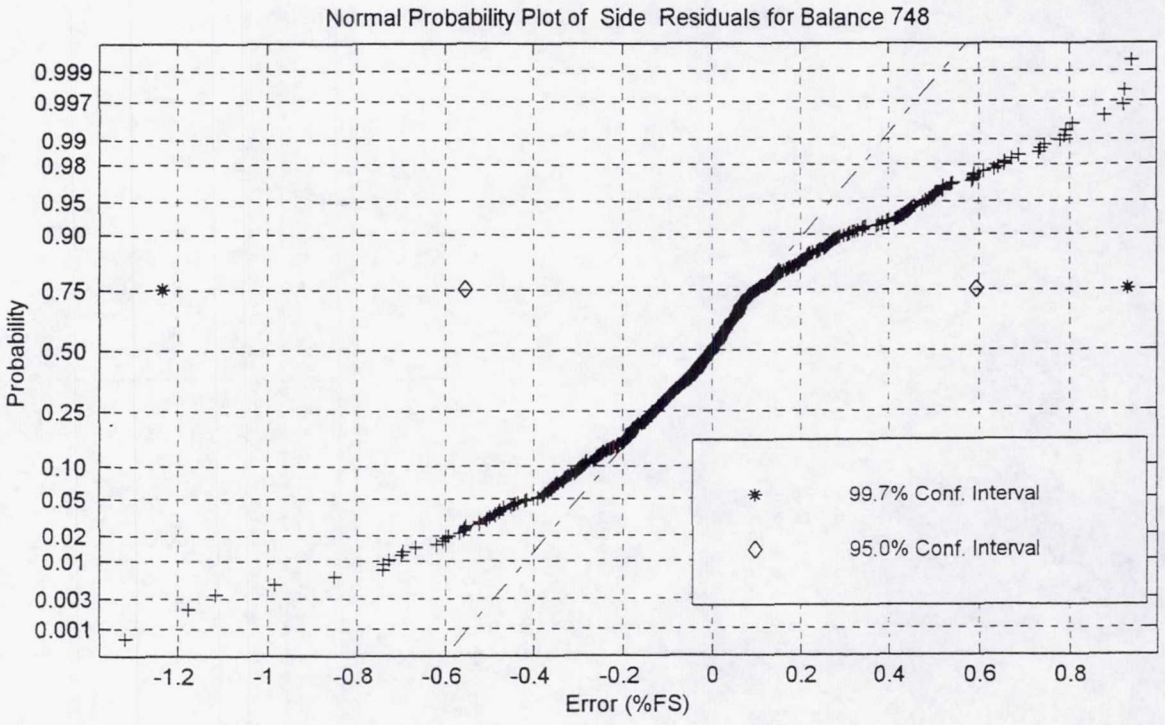

Figure 4c. Normal Probability Plots of Calibration Residuals

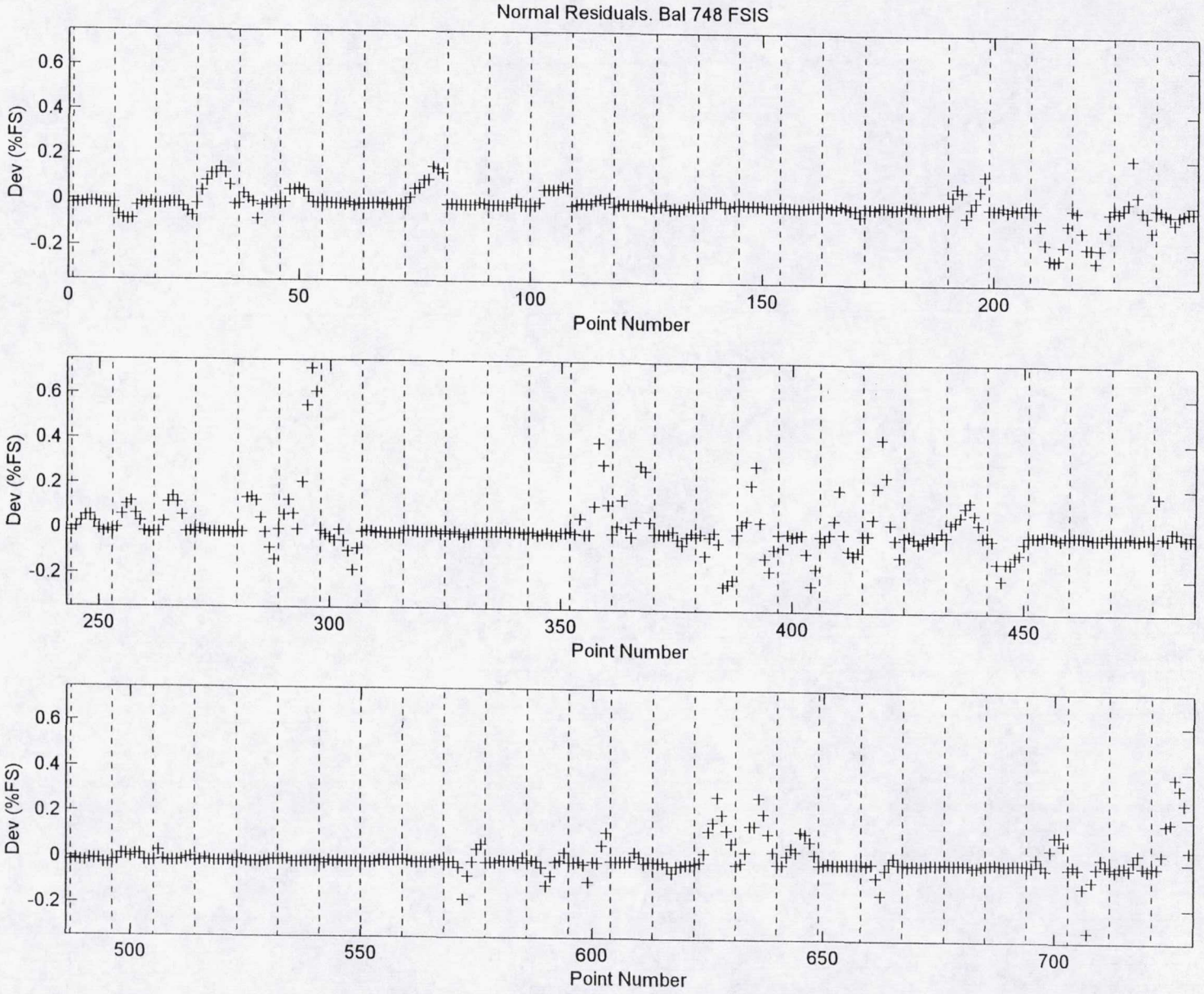

Figure 5a. Normal Force Systematic Calibration Errors

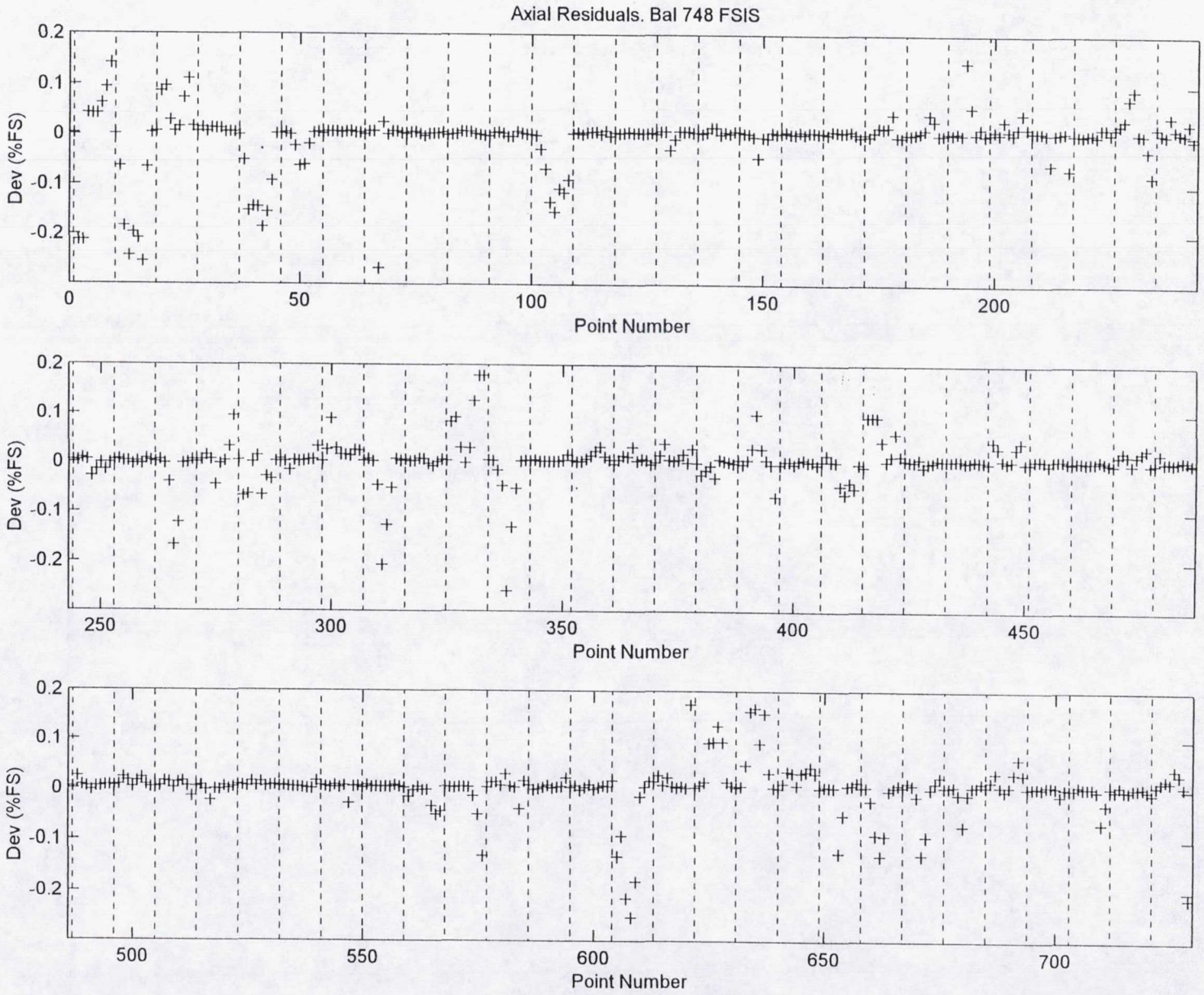

Figure 5b. Axial Force Systematic Calibration Errors

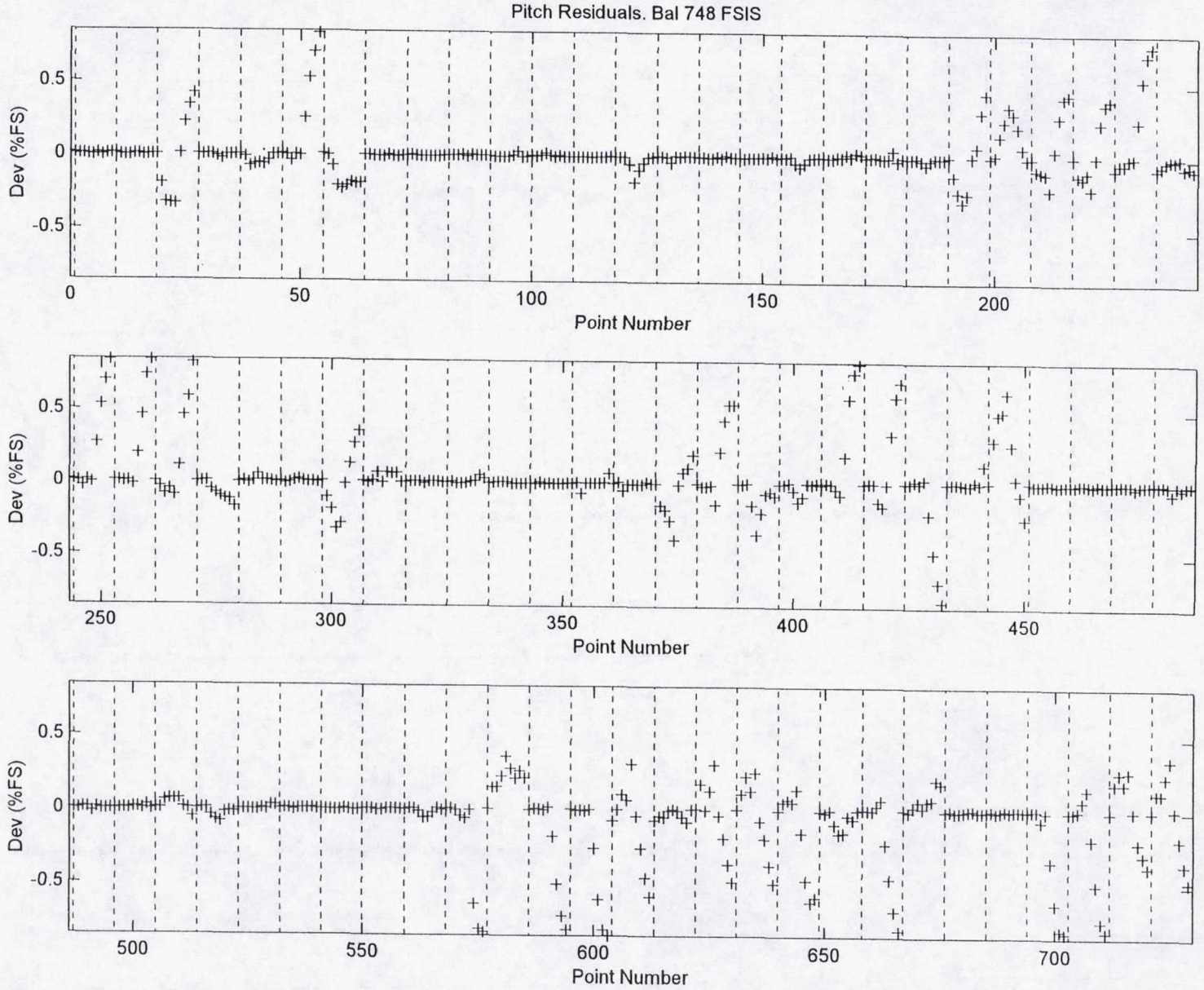

Figure 5c. Pitching Moment Systematic Calibration Errors

Figure 5d. Rolling Moment Systematic Calibration Errors

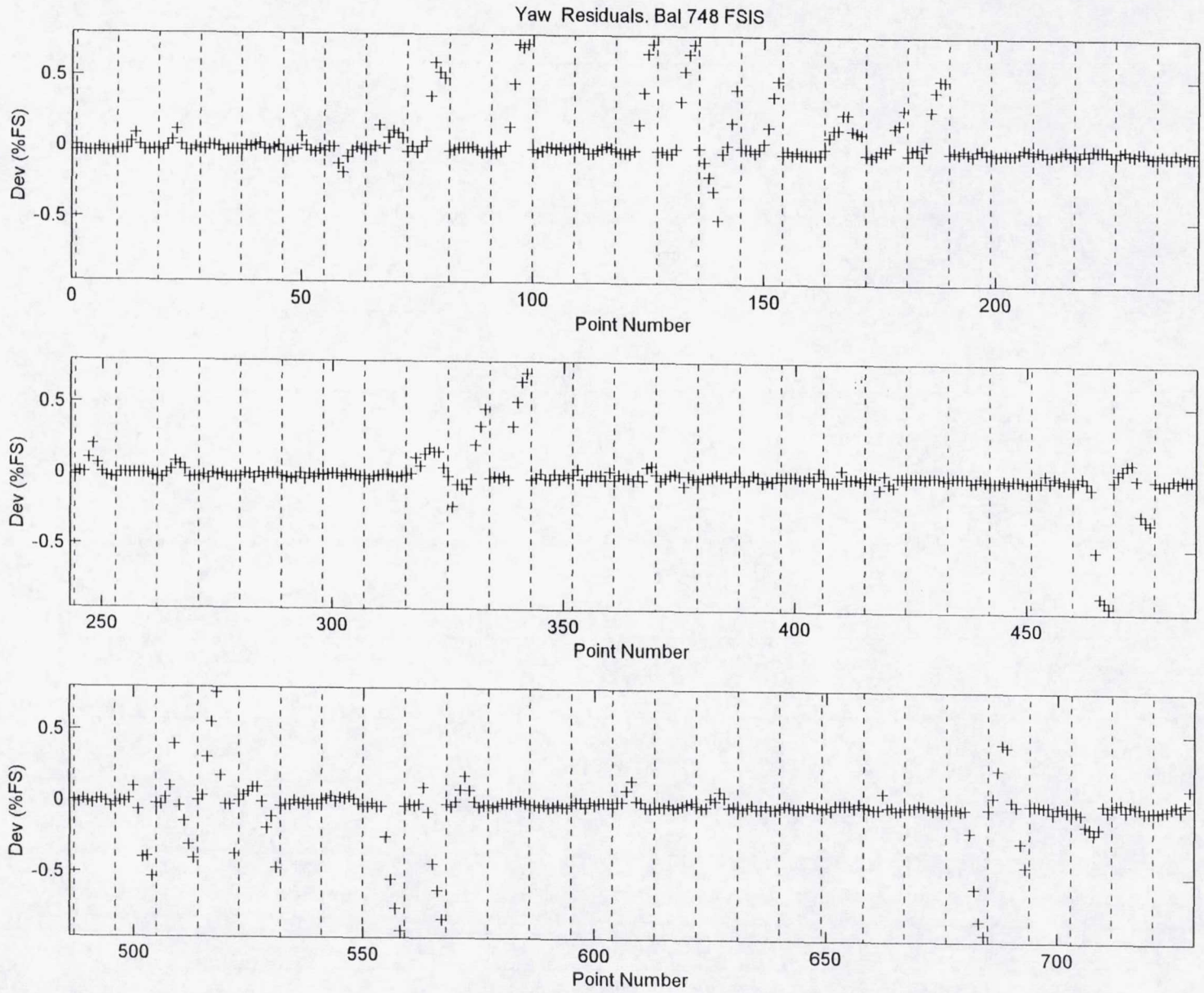

Figure 5e. Yawing Moment Systematic Calibration Errors

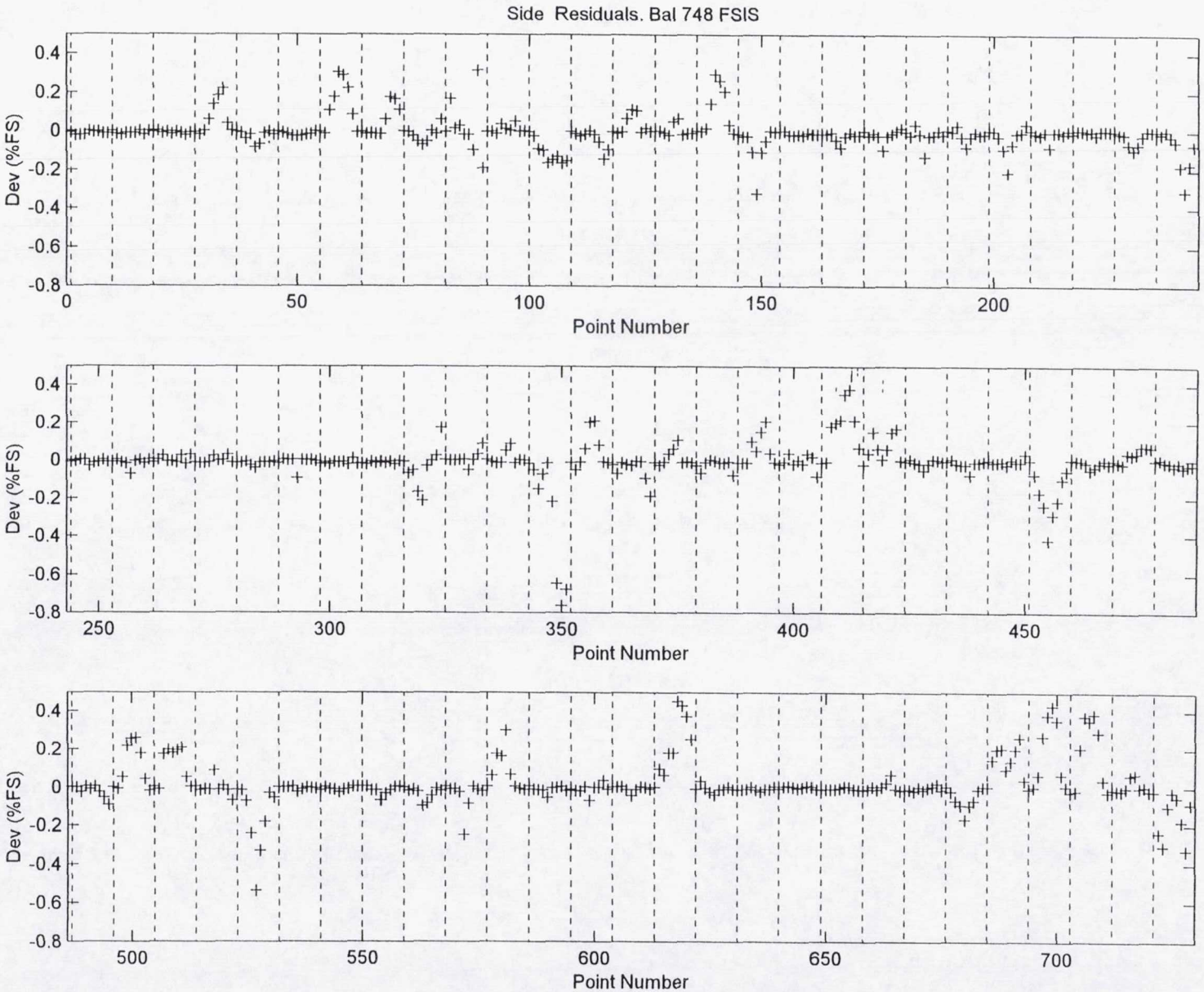

Figure 5f. Side Force Systematic Calibration Errors

DEVELOPMENT AND CONSTRUCTION OF FULLY AUTOMATIC CALIBRATION MACHINES FOR INTERNAL BALANCES

Prof. Dipl.Ing. Bernd Ewald, Technical University of Darmstadt, Germany
Dr.-Ing. Klaus Hufnagel, Technical University of Darmstadt, Germany
Dipl.Ing. Lubomir Polansky, Carl Schenck AG, Germany
Dipl.Ing. Eberhard Graewe, Daimler Benz Aerospace, Bremen, Germany
Dipl.Ing. Laurent Badet, European Transsonic Wind Tunnel, Cologne, Germany

Abstract

The requirements of aeroplane development for the accuracy of force testing in wind tunnels is extremely high. Besides of the design and construction of the strain gage balance the balance calibration technique is the most important contribution for the improvement of accuracy.

Balance calibration has been a more or less traditional procedure with more or less standard calibration rig designs. Recently balance calibration became a subject of research again. one motivation is the large amount of man power absorbed by the conventional balance calibration technique. The additional parameter temperature in the calibration of cryogenic balances multiplies the man power and resulted in the search for automatic calibration procedures. Another motivation for balance research is the finding, that calibration is an important key item to improve accuracy of balances.

Several automatic calibration rigs have been constructed in recent years. Some of them follow the idea of applying pure single loads or pairs of pure loads. These designs have complicated realignment mechanisms and were not fully successfully. Other machines were designed without realignment. In this case the misalignment must be measured. For the automatic balance calibration requirements of the European Transonic Wind Tunnel we developed the principle of the Inverse Calibration Machine. The loads are applied to the earth end of the balance. The loading condition is measured with a device called "External Balance" to which the balance is clamped.

In the case of the Inverse Calibration Machine the desired loads normally are also single loads or pairs of two single loads. The balance elasticity results in a misalignment of the loading system and so small loads in the other components occur. The loads are precisely known, since they are measured at the other end of the balance. Nevertheless the conventional evaluation methods can not handle such "Mixed Loading Cases". So a new algorithm was developed.

Following these principles an Automatic Calibration Machine was constructed for the European Transonic Tunnel (ETW) as a joint effort of the Carl Schenck Company, the Technical University of Darmstadt and the Deutsche Airbus GmbH at Bremen. The loads are generated by pneumatic push-pull actuators. The external balance follows the well known technology of the Carl Schenck AG External Wind Tunnel Balances. The machine is fully automatic and is controlled by a network of PC computers. A climate chamber allows the precise temperature conditioning of the examine, which is most important for a reliable calibration of cryogenic balances.

The successful operation of this machine encouraged the design of a second generation calibration machine. A prototype of this advanced machine is constructed at the Technical University of Darmstadt.

1. TABLE OF CONTENT

2. NOMENCLATURE

(For simplicity a nomenclature identical to [18] is used in this paper)

A, A_i, A_{ij}	Linear Matrix Coefficient
B, B_i, B_{ij}	Square Matrix Coefficient
C, C_i, C_{ij}	Cubic Matrix Coefficient
$Err_{i,m}$	Approximation Error of Component 'i' in loading case 'm'
F_i, F_j, F_k	Cal.Load of Component i,j,k
MIN	Minimum
$R0_i$	Zero Reading Component 'i'
$R_{i,m}$	Reading of Component'i' at Loading Case 'm'
S_i	Computed Signal of Component 'i'
$S_{i,m}$	Computed Signal of Component 'i' at Loading Case 'm'
SFQ_i	Sum of Squared Errors of Component 'i'

3. INTRODUCTION

Force testing is the most important wind tunnel measuring technique for aeroplane development and research work. So the force balance is the most important part of the tunnel instrumentation. In modern tunnels, especially in high speed tunnels, the balance normally is designed as an 'Internal Balance'. Figure 1 shows a typical example. This balance, designated W 618, was designed and fabricated for the ETW by Deutsche Airbus, Bremen and the Technical University of Darmstadt.

An Internal Balance needs a careful calibration. The calibration is achieved by loading the balance with calibrated forces. The signals of the balance are evaluated as a 'Calibration Matrix', which gives a set of equations 'Signals as function of Loads'. An inverse version of this set of equations 'Loads as functions of Signals' is used to evaluate the balance signals recorded during tests in the wind tunnel. Most calibration data evaluation methods used routinely today, have their origin in a time, when no or only very simple computers for the evaluation were available.

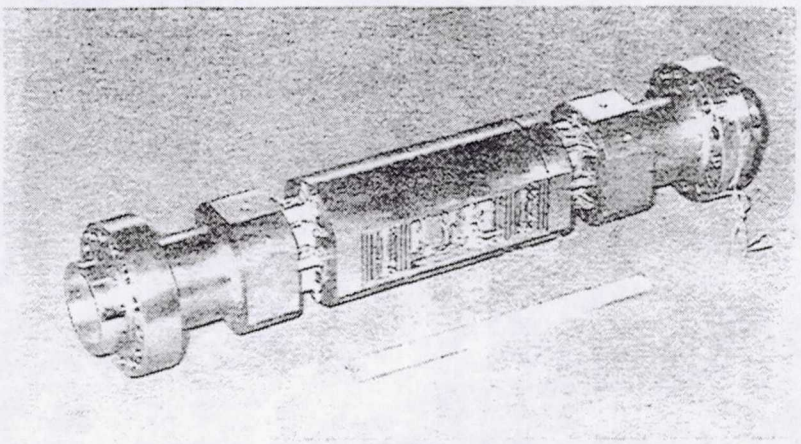

Figure 1. ETW-Balance W 618

Research on balance calibration was stimulated recently for two reasons. The man power used for the conventional calibration became more and more expensive. Experience at Deutsche Airbus demonstrated, that nearly one third of the total cost of a new balance is consumed by man power for calibration. On the other hand the introduction of the cryogenic tunnel brought the temperature as an additional parameter into the calibration, so calibration man power soared even more beyond price and the cryogenic tunnel with its much improved simulation capability asked for even more accurate balances. So automatic calibration was investigated and new calibration methods and calibration algorithms became necessary.

4. Conventional Calibration Rig Designs

The calibration of an internal Balance shall be valid for the body fixed axis system of the wind tunnel model. This is identical with good accuracy with the axis system of the model end connection of the balance. To calibrate the balance accordingly, in conventional rigs the balance is connected to the calibration rig with its sting end and a stiff "loading sleeve" is connected to the model end of the balance.

Loads are generated by hanging dead weights to precisely defined loading points on the sleeve. The use of pulleys or levers is avoided as far as possible for minimum hysteresis. Moments are also generated by hanging dead weights attached to the loading sleeve at an appropriate distance to the axis. Lateral loads (Side force, yawing moment) are generated after turning the balance through 90^{o} around its x-axis.

The balance is distorted by the calibration load. To realign the loading sleeve and the balance to the geodetic axis system, the conventional rig is equipped with an adjustment in pitch angle and roll angle. After each loading step the loading sleeve is realigned to the geodetic axis system either manually or by a servo drive. Figure 2 shows an example for such a conventional calibration rig.

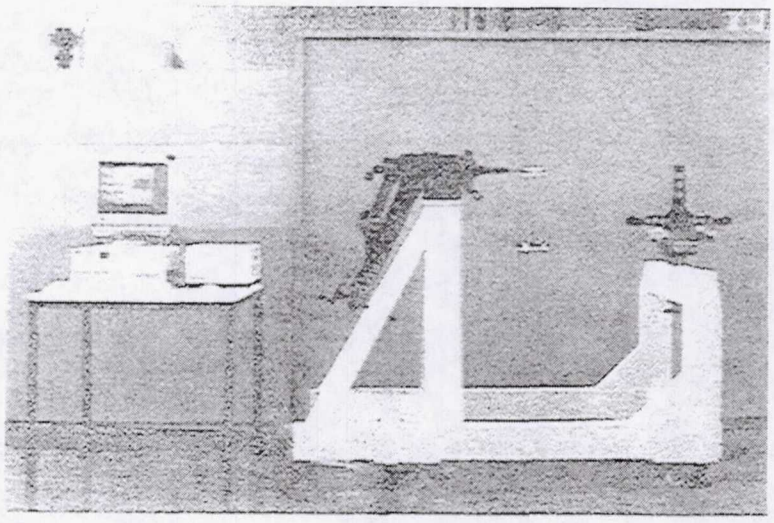

This principle allows complete freedom in the component loading only with the use of pulleys. Without pulleys the application of moments is possible only in combination with forces. On the other hand pulleys introduce disturbing hysteresis and should be avoided. The need for realignment after each loading step, which normally is done by hand, results in a lengthy calibration procedure.

Figure 2 Conventional Calibration Rig.

5. CONVENTIONAL CALIBRATION DATA EVALUATION

The simplest useful description of the balance behaviour is the linear calibration matrix. In this case the signal of the strain gage bridge for the component 'i' is characterised by the equation

$$S_i = R_{0,i} + \sum_{j=1}^{6} A_{ij} \cdot F_j \qquad (1)$$

For the use of the balance in the wind tunnel the system of equations is inverted to a set of equations :

'Loads' = Function of 'Signals'

by a simple inversion of the coefficient matrix. This method neglects any non-linear behaviour as well as effects generated by simultaneous action of two components.

The state of the art used by most wind tunnel operators is the so called 'Second Order Calibration'. In this case the signal of one strain gage bridge is described by the equation

$$S_i = R_{0.i} + \sum_{j=1}^{6} A_{ij} F_j + \sum_{j=1}^{6} \sum_{k=j}^{6} B_{ijk} F_j F_k \qquad (3)$$

This description covers non-linearities by the quadratic terms and it covers 'Product Interference's', which are caused by the simultaneous action of two components. Interference's of this type may occur with a considerable size, so the use of 'Second Order Calibration' is mandatory. Nevertheless this method causes problems.

The full 'second order' description of the balance according to equation (3) requires calibration loads with all six single loads and with all combinations of two loads (15 combinations). Some of these load cases can not be generated with the conventional calibration rig. A combination of two moment loads requires an additional load of one or two forces. So the evaluation of the matrix coefficients becomes very complicated.

The other problem is the matrix inversion for the use of the balance in the tunnel. In a mathematical sense inversion is possible only for a linear matrix. So less accurate approximate methods must be used for the 'inversion'.

The matrix coefficient evaluation methods used in most wind tunnel organisations are still influenced from the old time where no computers were available for the evaluation. The loads are applied in loading sequences for one pure component with all other components zero or at least constant. With least square error methods the coefficients of the matrix were evaluated and compiled step-by-step from such loading sequences.

6. The Need for Automatic Calibration

As stated already above, the man power consumed for calibration is a large part of the total cost of a balance. This problem is aggravated in the case of cryogenic balances. The temperature is an additional parameter, so the calibration effort is two to five times higher than in the case of a conventional balance. Also for higher accuracy the compilation of a larger data base for the evaluation of the calibration matrix is beneficial. So calibration efforts will increase even more.

The other reason for the search for automatic calibration methods is the sensitivity of the conventional calibration method against human errors. The utmost care and attention is necessary for the manual calibration. Especially with respect to the reference point accuracy errors occur easily since the balance is hidden in the loading sleeve, since the balance must be rotated during calibration and since the loading sleeve must be readjusted after rotation. A fully automatic machine avoids all these sources of human errors in the calibration.

So in several places of the world (ARA and DRA in Great Britain, FFA in Sweden, IAI in Israel) and in Germany the possibilities for automatic calibration were studied. A general target of these studies was to perform a complete six component calibration including all single loads and all pairs of two single loads in one working shift (8 hours).

7. Universal Mathematical Model of Balance Behaviour

Some concepts studied for the automatic calibration machine did not allow realignment. In this case the desired calibration loads are superimposed by small loads in the other components. With the conventional evaluation algorithms a calibration matrix can not be evaluated from such calibration data sets. So a new numerical method was developed.

First of all we introduced the 'Third Order Calibration'. The need for this was often questioned by balance experts. Nevertheless the third order approximation is a very logical step. Certainly there are physical reasons for a non-linear behaviour of the balance signals. Since a balance is a symmetrical piece of spring material, a curvature of the characteristic line in the positive quadrant should continue as a mirror inverted curvature in the negative quadrant as shown by the continuous line in Figure 3. There is certainly no reason for a continuous curvature like shown by the dotted line in Figure 3.

The continuous line in Fig. 3 can be approximated only by a third order polynom. Since a balance is used in the wind tunnel for both directions of the force, the choice of the third order calibration is the only logical one. Some experts argue, that the third order terms may be so small, that the third order evaluation is not worthwhile. Our experience showed, that this cubic interference term sometimes has a considerable size. Since the evaluation work is done by a computer and even a standard PC does this work in only some minutes, the higher complexity of the third order evaluation is no real argument against it. So our standard mathematical description of the balance behaviour is given by the set of equations :

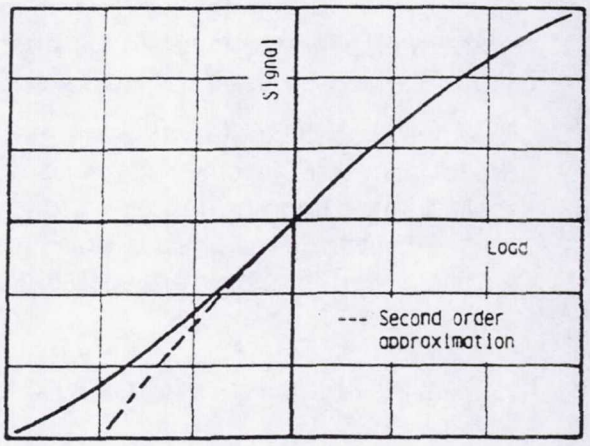

Figure 3 Non-linear Behaviour of Balance

$$S_i = R_{0,i} + \sum_{j=1}^{6} A_{ij} F_j + \sum_{j=1}^{6} \sum_{k=j}^{6} B_{ijk} F_j F_k + \sum_{j=1}^{6} C_{ij} F_j^3 \qquad (4)$$

8. THE NEW DATA EVALUATION ALGORITHM

As mentioned already above, certain types of automatic calibration machines create a calibration data base, where in each loading case the desired loads (normally one or two components) are superimposed by small loads in the other components. So a new algorithm had to be developed. This method was developed at the Technical University of Darmstadt [9] and was further improved and tested by the Experimental Aerodynamics Department of Deutsche Airbus, Bremen [18].

With this method the total coefficient matrix is computed in one mathematical step from the total calibration data set. This means, that each loading case contributes to all matrix coefficients. The criterion of the evaluation is again the least square error sum, but now it is the total sum of errors over the total set of loading cases. For a fixed order of approximation the result is the absolute best fit in a pure mathematical sense.

For any loading condition 'm' achieved during the calibration procedure the equation (4) gives the expected signal '$S_{i,m}$' from one strain gage bridge 'i'. This computed signal will differ from the real signal '$R_{i,m}$'. The difference is

$$F_{i,m} = R_{i,m} - S_{i,m} \qquad (5)$$

The final target of the evaluation process is to minimise the overall error sum SFQ_i for all components 'i':

$$SFQ_i = \sum_{m=1}^{M} F_{i,m}^2 = min \qquad (6)$$

This is achieved by application of the Gaussian Least Square Error Method. So the partial derivatives of SFQ_i for all coefficients of equation (3) must be set to zero. This gives a linear system of equations for the coefficients of equation (3) :

$$\frac{\partial SFQ_i}{\partial R_{0,i}} = 0$$

$$\frac{\partial SFQ_i}{\partial A_{i,j}} = 0$$

$$\frac{\partial SFQ_i}{\partial B_{i,j,k}} = 0 \qquad (7)$$

$$\frac{\partial SFQ_i}{\partial C_{i,j}} = 0$$

The new algorithm has some characteristics, which are very different from the conventional methods :

1. Sequence of Loading Conditions

The conventional methods depend on a stepwise evaluation of loading sequences, starting with sequences of pure loads of a single component. Load sequences of combinations of two single loads are evaluated for the product term coefficients. This evaluation is possible only with carefully organised sequences.

The new algorithm uses each loading condition with equal weight for the computation of the complete coefficient matrix. The sequence of the single component loadings has no significance at all. Nevertheless a quick look on line evaluation of the actual loading sequence is very useful to discover malfunctions in the calibration procedure, so the loading sequences certainly should not be generated by a random generator (but it would work !).

2. Load Combinations

With the conventional methods loadings cases with pure single components and combinations of two pure single components are required. This requirement calls for realignment of the load application system for each loading condition.

With the new methods for each loading case the complete vector of 6 components is used for evaluation. In principle each such loading case may consist of a combination of six loads. Nevertheless the observance of certain rules is advantageous for an optimum calibration.

Since the equation (4) describes only the influence of single components and the influence of products of two components, the main contribution of the loading cases should be one component or a pair of two components. The other components occurring in each loading case should be small compared to these loads. Another rule is to put more weight on the single load cases, since the linear coefficients describe approximately between 80 % and 99 % of the signal. So the single load sequences should contain more narrow steps than the sequences with two combined loads.

3. *Zero Reading of the Balance*

Most calibration methods do not give a well defined zero reading. The most popular definition of the zero reading is the mean value between a reading with the balance in an upside orientation and an upside down reading of the balance ('weightless balance model end').

If the balance is not rotated upside down during the calibration, which normally is not necessary in an automatic machine, the new method automatically gives the zero readings R_{0i} of the component 'i' for the unloaded balance in the orientation used during the calibration. These zero readings are evaluated precisely even if this condition was never achieved during the calibration procedure. This standard orientation of the balance in the calibration machine should be identical with the standard orientation of the model in the wind tunnel.

4. *'Calibration Matrix' and 'Tunnel Matrix'*

With all conventional methods a 'Calibration Matrix'

Signals = Function (Loads)

is evaluated during the calibration. For the use of the balance in the wind tunnel the inverted 'Tunnel Matrix'

Loads = Function (Signals)

is required. A mathematically exact inversion of the matrix is possible only in the case of a linear matrix, so normally more or less questionable approximation methods are used for the inversion. The new method in a mathematical sense makes no difference between 'signals' and 'loads' and so allows a direct evaluation of the matrix

Loads = Function (Signals)

without any loss of overall accuracy. The evaluation of the 'Calibration Matrix' is no longer necessary.

9. FULLY AUTOMATIC CALIBRATION MACHINE

As mentioned already above, the high man power consumption for calibration and the need for more accurate calibration motivated the search for automatic calibration techniques in several places. Compared to the conventional calibration rig (see Figure 4) these efforts in principle resulted in three different designs.

One design principle is realised in the DRA calibration machine. With this machine realignment is still used. The balance is connected to pneumatic load generators via a conventional loading sleeve and the load generators are supported against a very stiff cage. The total case is realigned by actuators to its correct position relative to the loading sleeve. The calibration forces are measured by pressure measurement in the pneumatic force generators.

Without realignment two principally different designs where realised. In one design the balance is clamped to earth at the sting end. The forces are generated by hydraulic or pneumatic generators acting on a loading sleeve connected to the model end of the balance. The force generators are supported to fixed earth points. The balance under load becomes misaligned.

This misalignment is measured care-fully and the actual calibration loads acting on the balance are computed from the measured generator forces and the measured misalignment.

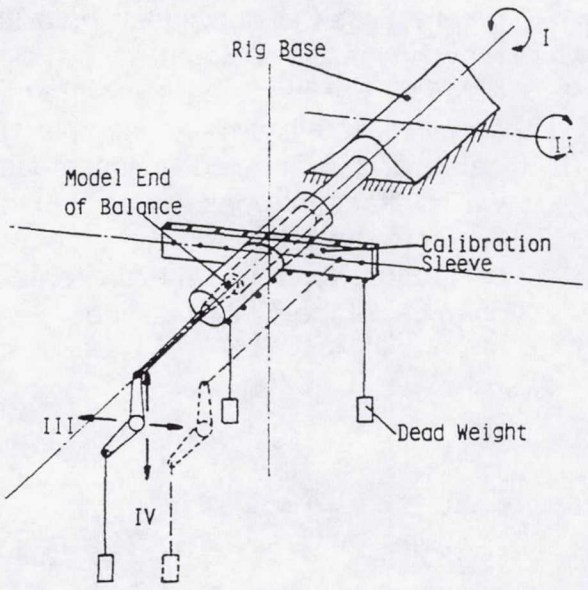

Figure 4 : Conventional Calibration Rig

The third design principle was invented by the author and realised by the Carl Schenck Company and Deutsche Airbus together with the Technical University of Darmstadt. With this machine the functions *'calibration load generation'* and *'calibration load measurement'* are totally separated. The Internal Balance is connected with its model end to a six component force measuring device similar to an external wind tunnel balance. This device (the 'measuring machine') measures the calibration loads applied to the balance precisely in the axis system of the model end of the balance. The 'Master Calibration Matrix' of this measuring machine allows for the small misalignment resulting from the elasticity of the connection between balance and measuring machine. Figure 5 demonstrates the design of the machine. The 'Measuring Machine' is accentuated by dots on the left side; the force generating system is located on the right side of the Internal Balance. The perfect separation of calibration load generation and measurement of the component loads contributes largely to the excellent accuracy of the machine.

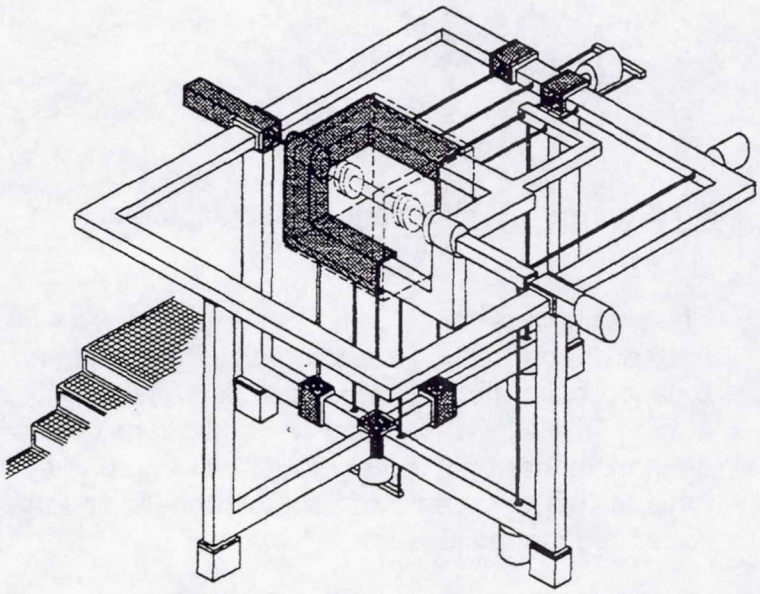

Figure 5. Design of Automatic Calibration Machine

The loads are generated by push-pull pneumatic load generators acting on a loading frame connected to the sting end of the balance. Since the loads are measured precisely at the model end, load generation can be done rather crude and fast.

The prototype of this machine was constructed for the ETW (European Transonic Wind Tunnel) and is successfully in operation at ETW. Figure 6 shows the ETW machine in the ETW Balance Calibration Lab. Figure 5 also demonstrates another big advantage of this machine. The internal

balance itself is not hidden by a loading sleeve or surrounded by loading levers. So balance may be easily enclosed by a climate chamber for perfect temperature conditioning of the balance. For the accuracy of cryogenic balance calibration a perfect temperature conditioning between 100 K and ambient temperature is a must. In the case of the ETW machine the balance is connected to the measuring machine and to the load generating system by thin walled titanium tubes, which transfer the forces and form a near perfect blockage for the heat flow into the chamber. So temperature gradients in the balance, which are disastrous for the calibration accuracy, are prevented. Figure 7 shows a balance installed in the open climate chamber of the ETW machine.

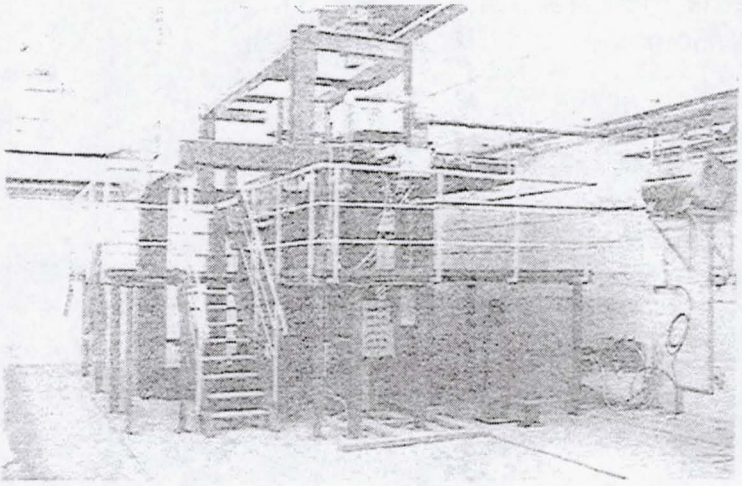

Figure 6. ETW Balance Calibration Machine

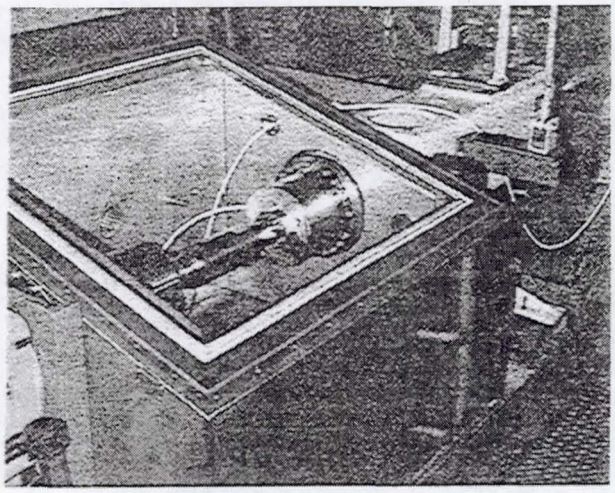

Figure 7. Climate Chamber of ETW Machine

The machine is fully computer controlled. The fast operation allows a complete six component third order calibration including all single loads and all pairs of two loads in one working shift. So balance calibration man power costs are largely reduced compared to the conventional procedures. This allows frequent re-calibrations, a provision which improves accuracy and reliability of wind tunnel testing very much. The improved reliability is especially important in expensive tunnels like cryogenic transonic tunnels or large transonic tunnels, where faulty test results cause big money losses.

10. Second Generation Automatic Calibration Machine

The success of the ETW Automatic Calibration Machine motivated for further development of this principle. A comprehensive analysis was done at the Technical University of Darmstadt on all lessons learnt with the ETW machine. The outcome was a machine with the same basic principles. The design was simplified and some minor imperfections of the first prototype were avoided. The main difference is, that the principle of a more or less dedicated force generator for each load component was abandoned. Three force generators are arranged in a triangle in vertical directions, which act on a very light loading beam. Equal forces commanded from these load generators generate an pure normal force. Differential forces from these load generators produce pure pitching and rolling moments. Two other force generators acting in Y-direction

generate side force and/or yawing moment; only the axial force is generated by a single and dedicated force generator.

The targets of this second generation design was a simplified design to save costs and an improved dynamic behaviour for increased speed.

The machine design demonstrated in Figure 8 is prepared for installation of a climate chamber to condition the balance to elevated or cryogenic temperature. Nevertheless for clarity the chamber is not shown in Figure 8.

A prototype of this machine is under construction at the Technical University of Darmstadt. Also this machine will be available on a commercial basis.

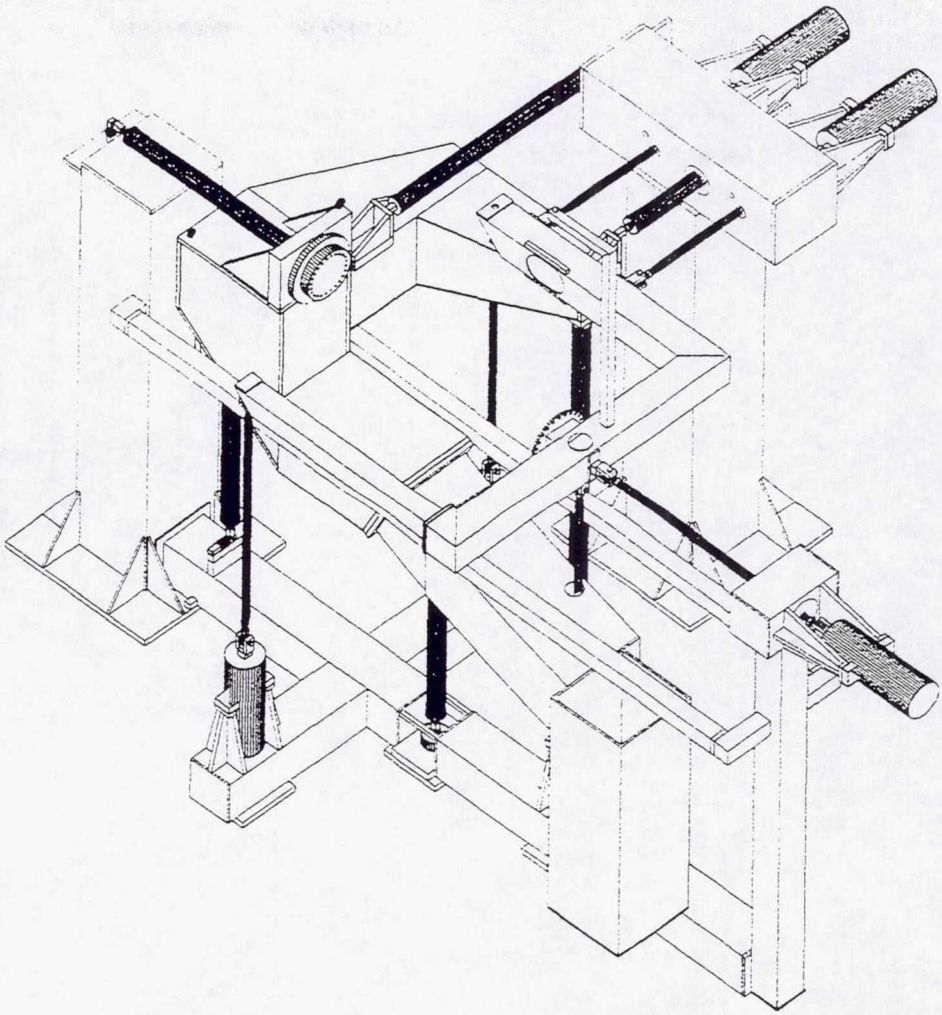

Figure 8 : Second Generation Calibration Machine Design

10. MASTER CALIBRATION

In the automatic calibration machine the calibration forces are measured by the 'measuring machine', which is very similar to an external wind tunnel balance. Obviously this machine needs an initial 'master calibration'.

Figure 9 shows the master calibration equipment, which is designed for the exclusive use of dead-weights. This design is based on the assumption, that the calibration room has a ceiling strong enough to withstand the vertical calibration loads. So for the vertical calibration loads the base for the levers can be mounted to the ceiling.

This design allows a perfect master calibration with a very high accuracy. All equipment parts can easily removed and stored (or used for master calibration of other machines!). So in operation the calibration machine is easily accessible.

Since this master calibration set-up is rather complicated and expensive, an alternative has been designed for the Darmstadt prototype. In this alternative for master calibration the simple push/pull rods from the force generators to the loading frame are exchanged with rod with a

high precision load cell and inclinometers. So the pneumatic force generators of the machine are used to generate the calibration forces. This system is in preparation.

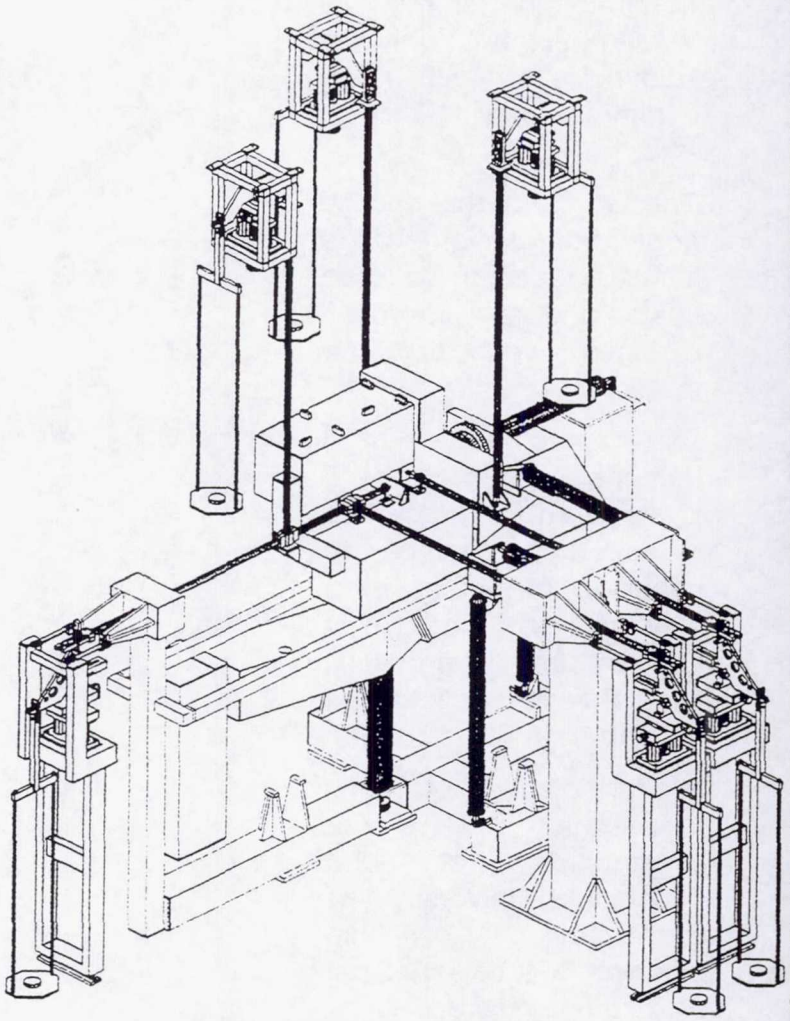

Figure 9 : Dead-weight Master Calibration Set-up

10. SUMMARY

Increased accuracy and reliability requirements for internal balance calibration and the high man power needed for this calibration initiated the search for automatic calibration procedures. The unique solution of the Carl Schenck AG Calibration Machine with the perfect separation of calibration load generation and measurement of actual calibration loads offers optimum accuracy and at the same time allows the design of a sophisticated climate chamber for perfect temperature conditioning of the internal balance.

Inevitably such a machine generates loading cases, where the desired loads (one or up to six components) are superimposed by small interference's in the other components. So the development of a new evaluation algorithm was necessary. This algorithm results in a closed least square error solution of the total calibration data base. Third order terms are taken into account.

The successful operation of the ETW Calibration Machine encouraged a study for a simplified and improved second generation machine. The design of this machine is finished and a prototype is under construction at the Technical University of Darmstadt.

11. REFERENCES

[1] B. Ewald, *"Development of Electron Beam Welded Strain-Gaged Windtunnel Balances"*, Journal of Aircraft Volume 16, May 1979

[2] Prof. B. Ewald, E. Graewe, *"Entwicklung einer 6-Komponenten-Waage für den Kryo-Bereich"* 3. BMFT-Status-Seminar, Hamburg, Mai 1983,

[3] E. Graewe, *"Development of a Six-Component Balance for Cryogenic Range"*. Forschungsbericht W 84-022, BMFT 1984

[4] Prof. B. Ewald, *"Grundsatzuntersuchung zum Temperatur-Verhalten von DMS- Axial-Kraftteilen"*, BMFT LVW 8420 10, Nr. 10/85, 1985

[5] Prof. B. Ewald, G. Krenz, *"The Accuracy Problem of Airplane Development Force Testing in Cryogenic Wind Tunnels"*, AIAA Paper 86-0776, Aerodynamic Testing Conference, März 1986

[6] Alice T. Ferris, *"Cryogenic Strain Gage Techniques used in Force Balance Design for the National Transonic Facility"*, NASA TM 87712, May 1986

[7] Prof. B. Ewald, E. Graewe, *"Development of Internal Balances for Cryogenic Wind Tunnels"*, 12th ICIASF, Williamsburg, VA, June 1987,

[8] Prof. B. Ewald , *"Balance Accuracy and Repeatability as a Limiting Parameter in Aircraft Development Force Measurements in Conventional and Cryogenic Wind Tunnels"*, AGARD FDP Symposion, Neapel, September 1987

[9] Friedrich Schnabel, *"Entwicklung eines numerischen Algorithmus und eines Rechnerprogramms zur Auswertung der Eichversuche an 6-Komponenten-DMS-Wagen"*, Technical University of Darmstadt, Diploma Thesis A-D-69/87

[10] Prof. B. Ewald, P. Giesecke, E. Graewe, T. Balden, *"Feasibility Study of the Balance Calibration Methods for the European Transonic Wind Tunnel"*, Report TH Darmstadt A 37/88, Januar 1988

[11] Prof. B. Ewald, Th. Balden, *"Balance Calibration and Evaluation Software"*, Proc. Second Cryogenic Wind Tunnel Technology Meeting, ETW, Cologne, 1988

[12] Prof. B. Ewald, T. Preusser, L. Polanski, P. Giesecke, *"Fully Automatic Calibration Machine for Internal Six Component Wind Tunnel Balances Including Cryogenic Balances"*, ISA 35th International Instrumentation Symposium, Orlando, Florida, May 1989

[13] Prof. B. Ewald, T. Preusser, L. Polanski, P. Giesecke, *"Fully Automatic Calibration Machine for Internal Six Component Wind Tunnel Balances Including Cryogenic Balances"*, ICIASF Congress, September 1989, Göttingen

[14] Prof. B. Ewald, L. Polanski, E. Graewe, *"The Cryogenic Balance Design and Balance Calibration Methods"*, AIAA "Ground Testing Conference", Juli 1992, Nashville,

[15] Prof. B. Ewald, K. Hufnagel, E. Graewe, *"Internal Strain Gage Balances for Cryogenic Windtunnels"*, Proceedings ICAS-Congress, Sept. 92, Peking, Bericht A 100/92

[16] Prof. B. Ewald, E. Graewe, *"The Development of a Range of Internal Wind Tunnel Balances for Conventional and Cryogenic Tunnels"*, European Forum on Wind Tunnels and Wind Tunnel Test Techniques,Sept. 92, Southhampton

[17] Prof. Dipl.Ing. Bernd Ewald, *"Advanced Force Testing Technology for Cryogenic and Conventional Tunnels"*, International Congress on Instrumentation in Aerospace Simulation Facilities (ICIASF). September 1993, Saint Louis, France.

[18] Dipl.Ing. T. Balden, *"Ein neues Konzept zur Kalibration von Kry-Windkanal-Waagen"*, Deutsche Airbus Bremen, DGLR Jahrestagung 1993, Göttingen

THE APPLICATION OF AN AUTOMATIC PRECISION BALANCE CALIBRATION MACHINE TO THE CALIBRATION OF WIND TUNNEL STRAIN-GAUGED BALANCES

R D Law
Defence Research Agency
Bedford, UK

SUMMARY

Tests are described in which a precision automatic balance calibration machine is used to calibrate a half model balance and assess the influence of a high pressure air-feed system passing through the balance to simulate aircraft engine loads. The recently developed calibration machine is described which is used both as a research tool and as a means of providing routine balance calibrations for wind tunnel model testing. The machine is installed at the 8ft x 8ft Wind Tunnel at DRA Bedford and uses computer controlled pneumatic force generators to apply precisely controlled loads to strain gauged balances. Theses loads are measured using a precision system of weighbeams. All six components can be represented in a light or heavy load range and normal force extends to a maximum of ±33kN. The specification of the machine is 0.02% on all ranges. All the loads can be applied sequentially in positive and negative directions or simultaneously as required, and represented without reorientating the balance. The procedure for calibrating both sting mounted and half model balances is described. The balance sensitivities and interactions are represented in a 6 x 27 matrix together with a graphical presentation of residuals.

INTRODUCTION

In large wind tunnels such as the 8ft x 8ft Wind Tunnel at DRA Bedford very large model forces are developed, particularly when testing half models. These forces are usually measured using strain gauged balances. These balances have to be calibrated periodically in order that they can accurately measure the aerodynamic loads. The accuracy requirements are high as the balances has to support the full magnitude of the loading condition while often measuring only small changes in load. Traditionally the balances would be calibrated in the six components of load using a mass and pulley system which is an unwieldy and time-consuming arrangement to operate, especially when the loads are large. The development of precision pneumatic force generators in the 1970s at DRA Bedford opened the possibility of automating a balance calibration system (Ref 1). The new availability of precision fused quartz pressure gauges and precision pneumatic controllers made it possible for force generators to be able to produce the accurate forces needed for balance calibration. To fulfil this function the force generators of course had to be calibrated themselves. Such a system was developed at DRA Bedford and deployed at the 5 Metre Wind Tunnel at DRA Farnborough in a precision balance calibration machine. Here, precise forces are produced by pneumatic force generators according to an accurately controlled pressure input without any recourse to measure the forces separately.

However at DRA Bedford a precision balance calibration machine has more recently been installed which uses a system of pneumatic force generators to produce the loads which are effectively then measured using a servo weighbeam balance. The servo weighbeam balance has of course in turn to be calibrated using dead loads, but its accuracy is superior to any strain gauged balance and its repeatable robustness make it an ideal transfer standard. The machine can accommodate both sting mounted strain gauged balances and half model balances. The machine can operate in a variety of configurations, some of which can be programmed to run automatically. The machine performance is discussed and a brief description is given on the normal calibration procedures and the method by which results are analysed.

A description is given of some recent special tests and calibrations. The first of these involves the application of the machine to the calibration of balances at a position away from their virtual centre. The requirement for this is particularly pertinent in the case of half model balances. A description of a static calibration of a dynamic balance is also included together with a method of using the machine in a novel way to assess the time related performance of the balance. Finally the special problems of assessing half model balance loads while the balance is being used to support a wing and engine configuration are discussed. The problems arise when a model jet engine has high pressure air passed through it to simulate the effect of the engine on the flow around the model during a wind tunnel test. For these tests a steel bellows is used to guide the air through the centre of the half model balance to the engine on the model. The effect of this bellows mounted within a half model balance has been investigated under calibration conditions while subject to pneumatic load.

DRA BEDFORD AUTOMATIC BALANCE CALIBRATION MACHINE

This is the main balance calibration facility at DRA Bedford (Fig 1) and comprises a precision fully automatic calibration machine capable of covering the ranges of most of the balances used at DRA Bedford (Fig 2). The machine is used in support of all three major Bedford wind tunnels as well as to meet the needs of external customers. The machine uses 22 pneumatic force generators to generate the loads (Fig 3), some of which act in parallel, and each comprise an enclosed piston fitted with a single rubber rolling diaphragm. The pneumatically generated forces are applied to the normal front end of the strain gauged balance by reaction through the rear of the balance. Measurement is made by the system of weighbeams responding to loads transmitted by levers floating in air bearings. The machine is operated by setting a series of jockey weight positions on the weighbeam lead screws, at positions appropriate to the desired loads, to cover the load range of the particular balance under consideration. At each setting, pneumatic pressures are applied automatically in sequence to the force generators to achieve equilibrium of the weighbeams. An error signal from each out-of-balance weighbeam is used to apply pressure to the appropriate force generator using a voltage to pressure converter. The pneumatic pressure required to null the error signal resulting from a set position of the machine weighbeam is supplied under computer control.

Positive and negative forces on the balance are applied using opposing force generators which act in tension for each component of load. The alternative directions of these loads can be represented without re-orientating the balance and if required all the loads can be applied simultaneously. Each generator responds to positive pressure with the diaphragm of the opposing

one having a small positive pressure applied to it to maintain the diaphragm in its correct convoluted form when being pushed backwards slightly as the balance deflects. To avoid an overload condition a predetermined maximum pressure can be set for each load component while the machine is programmed to go automatically through a loading sequence. To prevent accidental overload in the event of sudden failure of a generator diaphragm, a system of mechanical safety stops is deployed which closely follow the normal balance under load.

MACHINE PERFORMANCE

All six load components can be represented as three forces and three moments. The machine covers a range of ±7500lb (±33kN) of normal force to an accuracy of 0.02% of full scale, ie (1.5lb). The range in rolling moment is ±4500lbft (±6.1kNm) to an accuracy of 0.03% of full scale, ie (1.5lbft). A lighter loading range is available on all six channels, giving improved resolution and a better accuracy of reading, ie 0.5lb for normal force and 0.5lbft for rolling moment, to a similar full scale accuracy as for the higher range.

CALIBRATION METHOD

The calibration procedure normally adopted involves loading the primaries sequentially and following this with 15 cross products to suit analysis based on Cooke's method (Ref 2). Calibrations normally start with a preload followed by the application of positive loadings cycling to negative loadings and back to zero without any need to reorientate the balance. The cross product terms are normally applied at maximum and minimum values only but can be arranged differently to suit requirements. The strain gauged balance outputs are not tared and not affected by circuit loading so that an absolute calibration is produced. The calibration machine operates to produce a 6 x 27 calibration matrix covering second order terms. When programmed to run automatically this operation takes about 48 hours. The calibration matrix produced gives the balance sensitivities and the matrix is transposed, normalised and inverted to produce a user matrix. The balance outputs achieved during the calibration are applied to the user matrix to calculate the original loads and thereby produce a set of residuals to check the matrix integrity.

Any need for third order terms can be established by inspection of linearities in the calibration characteristics of the cross product pairs. However, procedures are being developed for producing a multi-point calibration which will enable alternative calibration procedures to be adopted (Ref 3). For this case different loads will be applied as a combination, to load all the channels simultaneously and a calibration matrix compiled from the resulting load data. The evaluation of third order terms will be more easily established by this procedure.

SPECIAL APPLICATIONS OF THE BALANCE CALIBRATION MACHINE

The Effect of Calibrating a Balance away from its Virtual Centre

Wind tunnel balances are usually calibrated about their virtual centre, as this is geometrically the most direct way of exercising the balance functionally. However, aerodynamic forces and moments usually act at a different location, often at an aerodynamic centre. This is particularly the case for half model balances. Methods currently in use for correcting for load centres being away from the calibrated centre have assumed a linear algebraic transposition of the measured quantities. Often only one ordinate is corrected and applied to the original balance calibration matrix. The DRA balance calibration machine lends itself particularly to checking the validity of this assumption. The balance can be moved positionally by a measured amount and the balance calibration programme re-run to exactly repeat the load settings with the balance at the new ordinate position.

A sting mounted cryogenic balance was calibrated at three different longitudinal positions giving a primary change in the pitching moment. The balance was calibrated about points one inch fore and one inch aft of the virtual centre and matrices produced to represent each position. Constraints on the lateral movement of the machine control arms prevented any larger positional changes being made without altering the length of the front and rear adaptors. Differences were observed as a change in the pitch ordinate by inspection of the raw sensitivities as represented in the leading diagonal of each matrix. These sensitivities which are proportional to the bridge excitation voltage, compare well with the setting ordinate in pitching moment to within 0.001 inch. However the effect of the interactions cannot be closely and directly related to the change in position on the ordinate. A matrix produced at the new position should never-the-less be correct. As a result of this observation it was appreciated that if it is not practical to calibrate a balance about its position of subsequent use then the correction by calculation should include more than just a single ordinate term. A revised input correction procedure was established to cover all six terms (Fig 4) (Appendix 1).

Static Calibration of a Dynamic Balance

There are situations in wind tunnel testing where the dynamic behaviour of a model needs to be represented. At DRA Bedford a dynamic half model balance is used to measure time dependent forces on wind tunnel models (Fig 5) (Ref 4). The range of this balance is up to 20kN and it functions in six components of load by using very stiff piezo-electric cells. The balance is normally mounted between the model and an underfloor weighbeam balance to enable both steady and unsteady aerodynamic forces to be measured on the model. It was felt that it would be useful to establish a static calibration of this special balance. Its dynamic performance would normally be aditional to the static response. The balance output response is produced by charge coupled amplifiers, and some checks were needed to see if the 'charge' could be held long enough to allow a static calibration to take place in the automatic balance calibration machine.

Static drift tests using dead loads showed that after the initial response the drift rate in normal force was about 0.3% of reading per hour. This rate varied slightly with time, but did not vary significantly with load and opened the way to applying a simple drift correction to the static calibration load data. A formal calibration of the dynamic balance was then undertaken in the automatic balance calibration machine without any recourse to a drift correction during the test (Fig 6). However, the innate stiffness of the balance helped the machine control conditions to be achieved quickly enough for the calibration to be assessed in the normal way. Balance sensitivities were obtained from the calibration matrix leading diagonal and these were similar to those observed in the dead load calibration and from inspection of the raw data, although high interactions were evident in the matrix. A plot of residuals showed that the errors were all within 1% of the loading range and although this puts the balance accuracy outside what would be acceptable for a conventional strain gauged balance, such an accuracy should be sufficient for dynamic work (Fig 7).

It would appear however that the use of charge coupled amplifiers in the dynamic balance measurement system reduce the effectiveness of a static calibration. Although a repeatable drift term was achievable for the static calibration it was important to check the short term time response to see if the static sensitivities could be related to the short term time responses. In order to investigate this problem some step load calibrations were performed where a single point loading was applied to one channel at a time and the load was suddenly relieved by venting the pneumatic force generators that had been applying the load. Although an oscilloscope trace could be used to indicate the peak response of the dynamic balance, the data logging system for the calibration machine was used to successively record the outputs from all the channels. The time cycle of the scanner (20 seconds) prevented an instant recording of the balance response but was a lot faster than the time taken to reach a control condition in the machine under automatic operation (typically 3 minutes). In practice however, because of the action of the safety stops impinging on the machine loading frame as it was suddenly freed, it could take as long as three scans to achieve an unadulterated reading. However, successive readings were recorded after step loadings from different loading levels in model side force. These step loadings gave a greater output in relation to the applied load when compared with static tests on the calibration machine (0.085mV/lb). An additional observation was that the output per unit load decreased with applied load tending towards the static case at the higher loads (Fig 8). This is likely to be a feature of the dynamic response of the balance and would require further investigation to fully explain this result.

Calibration of Half Model Balance with Bellows

Calibrations are presently being undertaken to examine the effect of a pressurised bellows mounted within a conventional half model balance. This is as a result of concerns about the integrity of wind tunnel test results when using half models in an engine blowing configuration. For these tests high pressure air (up to 350 psi) is fed through the balance via a steel bellows and out of a wing mounted engine into the tunnel flow (Fig 9). As the bellows effectively joins the earth side of the balance to the live side, its operation under pressure could impose a loading on the balance. Initially some direct dead load tests were carried out on the balance with the bellows mounted between the earth side of the balance and a frame attached to the front end of the balance. It was found that there was an increase in axial load for a given applied side force pressure from the bellows but this was small in magnitude (Fig 10). It was appreciated that it would not be possible to

reproduce in the calibration machine exactly the tunnel conditions experienced by the balance. However, it seemed appropriate to assess the performance of the balance under similar yet controlled conditions. Two end plates were manufactured to attach the bellows directly between the earth and live side of the balance, so that the complete assembly could be accommodated within the automatic balance calibration machine (Figs 11&12). The balance support cradle position was adjusted to make the virtual centre of the half model balance coincident with the virtual centre of the balance calibration machine. The arrangement was such that loads would be reacted through the rear of the balance with the model end of the balance connected to the measuring part of the machine as for a conventional balance calibration (Fig 13). In this configuration calibrations with the bellows fitted could be compared with those without (Fig 14).

The first calibration in the machine was carried out using a system of single point loadings in axial force at different bellows pressures which would load the ungauged side force channel. Here any change in interactive axial force as a result of bellows pressure could be compared with the primary axial loading. The axial force was applied using the calibration machine in side force mode between -1000lbs and +1000lbs at 250lb increments while at each load station the bellows pressure was set at zero, and applied at 75 psi and 150 psi. Error distributions were drawn of the calibrations at the three pressures, but the accuracy of the setting values of the machine at each loading condition precluded a clear indication of the exact interaction on axial force. The previous test using a dead load which remained constant enabled small incremental changes in interactive load to be more directly evident. However changes in slope between the error distributions obtained from the machine balance calibration at different bellows pressures were observed. These indicated a similar but higher error in interactive axial force as a result of pressurising the bellows than had been indicated in the dead load test, (equivalent to 0.3% of reading at 150 psi (Fig 15)). The raw calibration envelope produced by plotting these distributions is about 50% higher in terms of error compared to that obtained from the balance without a bellows being fitted, mainly due to apparent hysteresis. The accuracy envelope obtained from this type of balance would normally be within ±0.1% of full scale reading and the imposed loading observed by pressurising the bellows just measurable. From these first experiments in the current investigation of the problem it can be concluded that the effect of pneumatic bellows pressure is observable in incremental tests but is only slightly significant in terms of balance calibration accuracy. However, the addition of the bellows to the structure of the balance does reduce the accuracy of its performance.

CONCLUSION

The DRA balance calibration machine can be used as a research tool to investigate certain special problems associated with wind tunnel balances, as well as providing the accurate calibrations needed of conventional balances in support of a major wind tunnel. The automatic nature of the machine means that multi-position tests can be carried out quickly and easily at repeatable locations without having to alter the physical positioning of the test balance to achieve negative loadings. The dynamic balance responded well to a static calibration. The automatic machine could supply the loading conditions quickly enough for the static calibration not to need further corrections for zero drift. However, the very short term response of the dynamic balance should be investigated further if a worthwhile dynamic calibration is to be achieved. The balance calibration machine lends itself particularly to the calibration of half model balances which are especially unwieldy to calibrate

manually. The special tests carried out on the half model balance when fitted with a bellows for model blowing are still being carried out. Early indications are that the bellows pressure does have a small but measurable effect on the balance accuracy in terms of interactive load. However the bellows itself does appear to add some hysteresis to the primary calibration.

APPENDIX

Moment reference centre at 'A' (Fig 4)

X, Y, Z, L, M & N are apparent forces and moments
X^1, Y^1, Z^1, L^1, M^1, N^1 are real forces and moments

$$Z = a_{11}Z^1 + a_{12}M^1 + a_{13}Y^1 + a_{14}N^1 + a_{15}L^1 + a_{16}X^1$$

$$M = a_{21}Z^1 + a_{22}M^1 + a_{23}Y^1 + a_{24}N^1 + a_{25}L^1 + a_{26}X^1$$

$$Y = a_{31}Z^1 + a_{32}M^1 + a_{33}Y^1 + a_{34}N^1 + a_{35}L^1 + a_{36}X^1$$

$$N = a_{41}Z^1 + a_{42}M^1 + a_{43}Y^1 + a_{44}N^1 + a_{45}L^1 + a_{46}X^1$$

$$L = a_{51}Z^1 + a_{52}M^1 + a_{53}Y^1 + a_{54}N^1 + a_{55}L^1 + a_{56}X^1$$

$$X = a_{61}Z^1 + a_{62}M^1 + a_{63}Y^1 + a_{64}N^1 + a_{65}L^1 + a_{66}X^1$$

With the moment reference centre at 'B' (Fig 4) we have,

$$Z^1 = Z^1_1 \qquad Y^1 = Y^1_1 \qquad X^1 = X^1_1$$

$$M^1 = M^1_1 + lZ^1_1$$

$$N^1 = N^1_1 - lY^1_1$$

$$L^1 = L^1_1$$

Substituting for Z^1, Y^1, X^1, M^1 etc in terms of Z^1_1, Y^1_1 one can obtain

$$Z = a_{11}Z^1_1 + a_{12}(M^1_1 + lZ^1_1) + a_{13}Y^1_1 + a_{14}(N^1_1 - lY^1_1) + a_{15}L^1_1 + a_{16}X^1_1$$

$$M = a_{21}Z^1_1 + a_{22}(M^1_1 + lZ^1_1) + a_{23}Y^1_1 + a_{24}(N^1_1 - lY^1_1) + a_{25}L^1_1 + a_{26}X^1_1$$

$$Y = a_{31}Z^1_1 + a_{32}(M^1_1 + lZ^1_1) + a_{33}Y^1_1 + a_{34}(N^1_1 - lY^1_1) + a_{35}L^1_1 + a_{36}X^1_1$$

$$N = a_{41}Z^1_1 + a_{42}(M^1_1 + lZ^1_1) + a_{43}Y^1_1 + a_{44}(N^1_1 - lY^1_1) + a_{45}L^1_1 + a_{46}X^1_1$$

$$L = a_{51}Z^1_1 + a_{52}(M^1_1 + lZ^1_1) + a_{53}Y^1_1 + a_{54}(N^1_1 - lY^1_1) + a_{55}L^1_1 + a_{56}X^1_1$$

$$X = a_{61}Z^1_1 + a_{62}(M^1_1 + lZ^1_1) + a_{63}Y^1_1 + a_{64}(N^1_1 - lY^1_1) + a_{65}L^1_1 + a_{66}X^1_1$$

$$Z = (a_{11} + la_{12})\, Z^1_1 + a_{12}M^1_1 + (a_{13} - la_{14})\, Y^1_1 + a_{14}\, N^1_1 + a_{15}L^1_1 + a_{16}\, X^1_1$$

$$M = (a_{21} + la_{22})\, Z^1_1 + a_{22}M^1_1 + (a_{23} - la_{24})\, Y^1_1 + a_{24}\, N^1_1 + a_{25}L^1_1 + a_{26}\, X^1_1$$

$$Y = (a_{31} + la_{32})\, Z^1_1 + a_{32}M^1_1 + (a_{33} - la_{34})\, Y^1_1 + a_{34}\, N^1_1 + a_{35}L^1_1 + a_{36}\, X^1_1$$

$$N = (a_{41} + la_{42})\, Z^1_1 + a_{42}M^1_1 + (a_{43} - la_{44})\, Y^1_1 + a_{44}\, N^1_1 + a_{45}L^1_1 + a_{46}\, X^1_1$$

$$L = (a_{51} + la_{52})\, Z^1_1 + a_{52}M^1_1 + (a_{53} - la_{54})\, Y^1_1 + a_{54}\, N^1_1 + a_{55}L^1_1 + a_{56}\, X^1_1$$

$$X = (a_{61} + la_{62})\, Z^1_1 + a_{62}M^1_1 + (a_{63} - la_{64})\, Y^1_1 + a_{64}\, N^1_1 + a_{65}L^1_1 + a_{66}\, X^1_1$$

LIST OF SYMBOLS

Z	=	Normal force
M	=	Pitching moment
Y	=	Side force
N	=	Yawing moment
L	=	Rolling moment
X	=	Axial force
a_{11} to a_{66}		Are matrix co-ordinates
l	=	Distance between moment centres

REFERENCES

1. Law, R. D., *Tests on pneumatically powered precision force generators.* RAE TR79013 (Jan 1979).

2. Cook, T. A., *A note on the calibration of strain gauge balances for wind tunnel models.* RAE Technical Note Aero 2631 (Dec 1959).

3. Holmes, J. W., *The calibration of wind tunnel balances to the third order.* DRA Working Paper AP4(92)WP13 (1992).

4. Welsh, B. L., Pyne, C. R., *A dynamic balance for the measurement of time-dependent aerodynamic forces on wind tunnel models.* RAE Technical Memorandum TM2182, (April 1990).

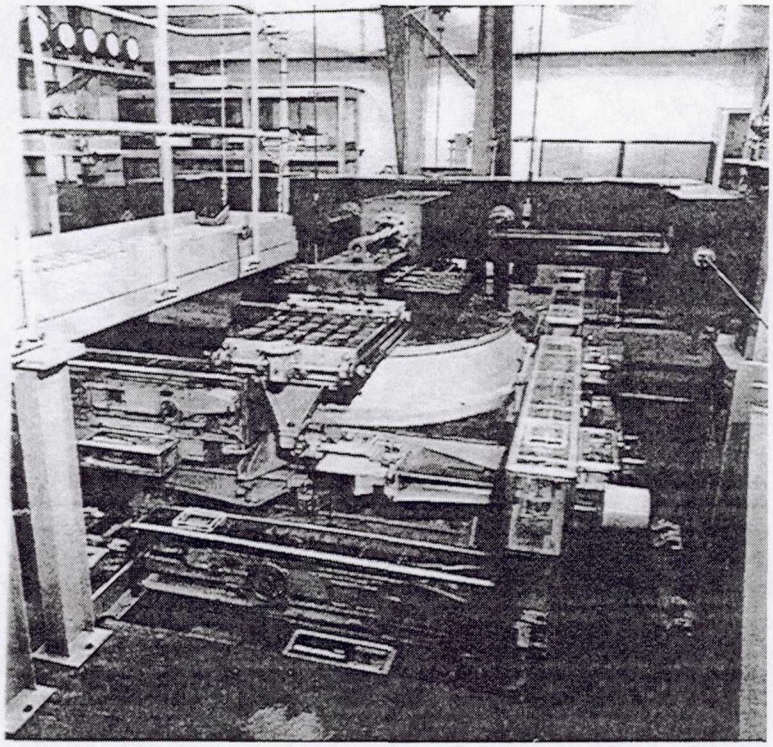

Figure 1. DRA Bedford precision automatic balance calibration machine

Balance Load Channel	Machine Max Load Range lbs or lbsft	Full Load Range 8' x 8' Wind Tunnel (3" diam)	Balances (2¼" diam)	lbs or lbsft (large half model balances)		Machine channel excited by half model balance loading
				Type E	Type F	
Lift	7500	4000	1200	10000	6000	Lift
Pitching Moment	5000	1670	600	4200	1670	Rolling Moment
Side Force	3000	940	1200	N/A	N/A	Axial Force
Yawing Moment	2500	535	600	5200	1250	Yawing Moment
Rolling Moment	4500	535	100	40000	18700	Pitching Moment
Drag	1900	500	120	1000	350	Side Force

Figure 2. Balance loading ranges compared to machine ranges

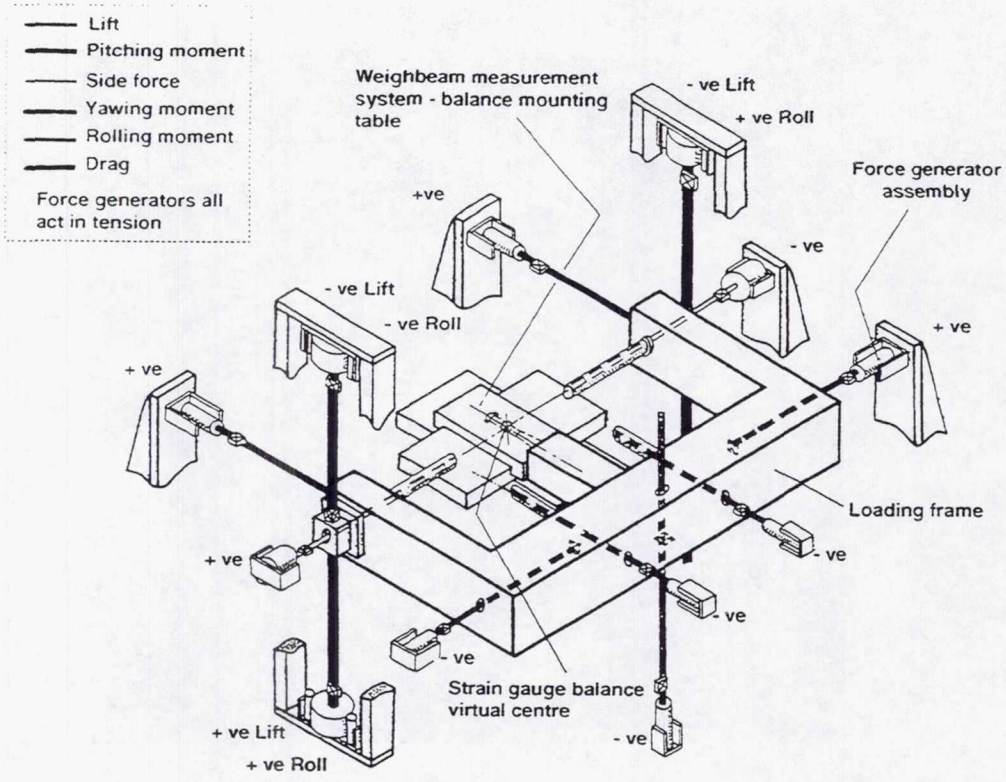

Figure 3. Balance calibration machine arrangement of force generators

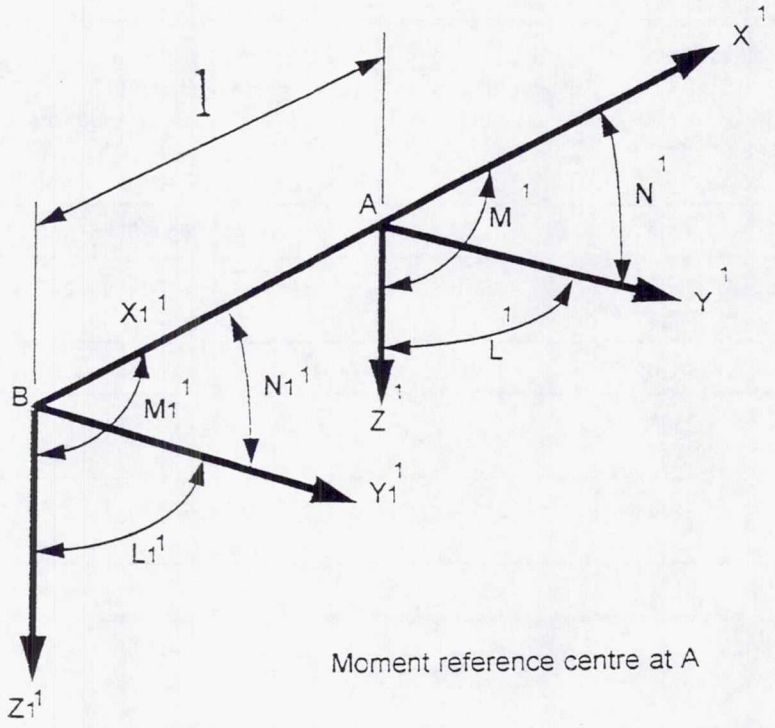

Figure 4. Change in moment reference point

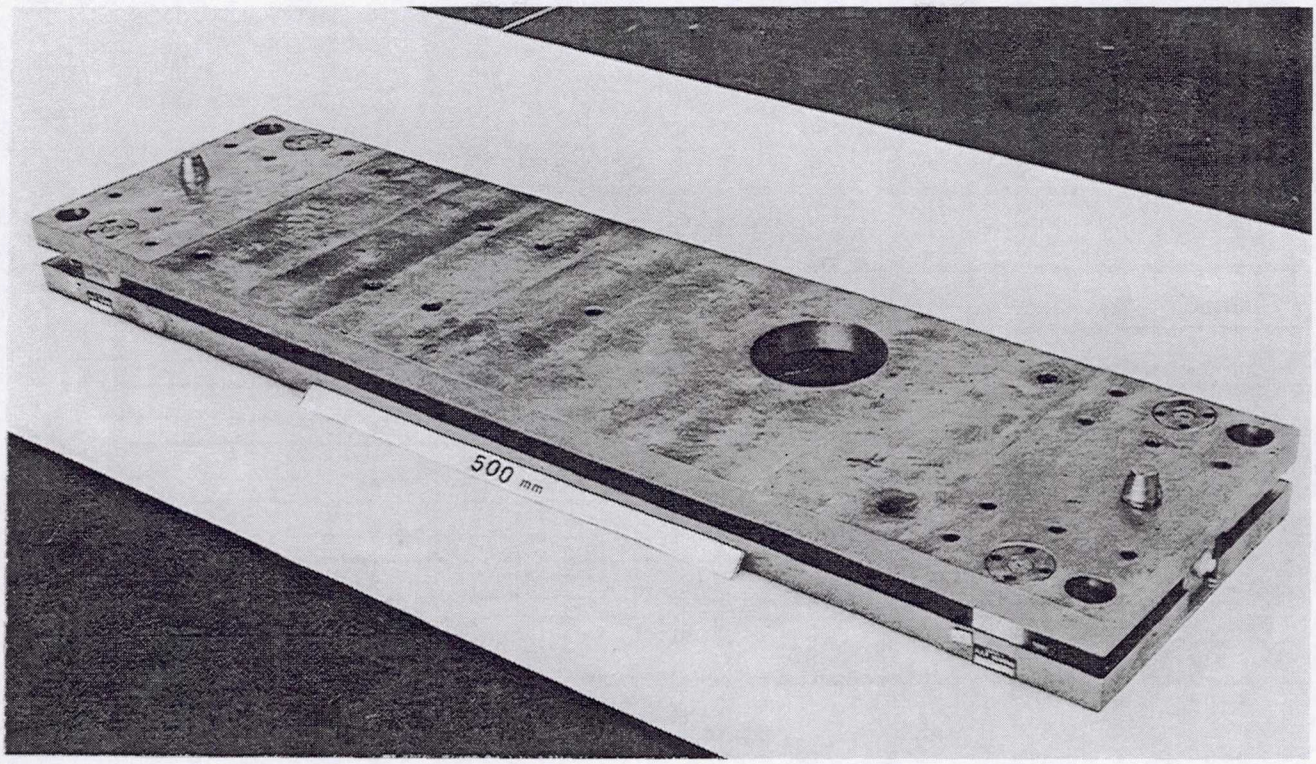

Figure 5. DRA dynamic balance

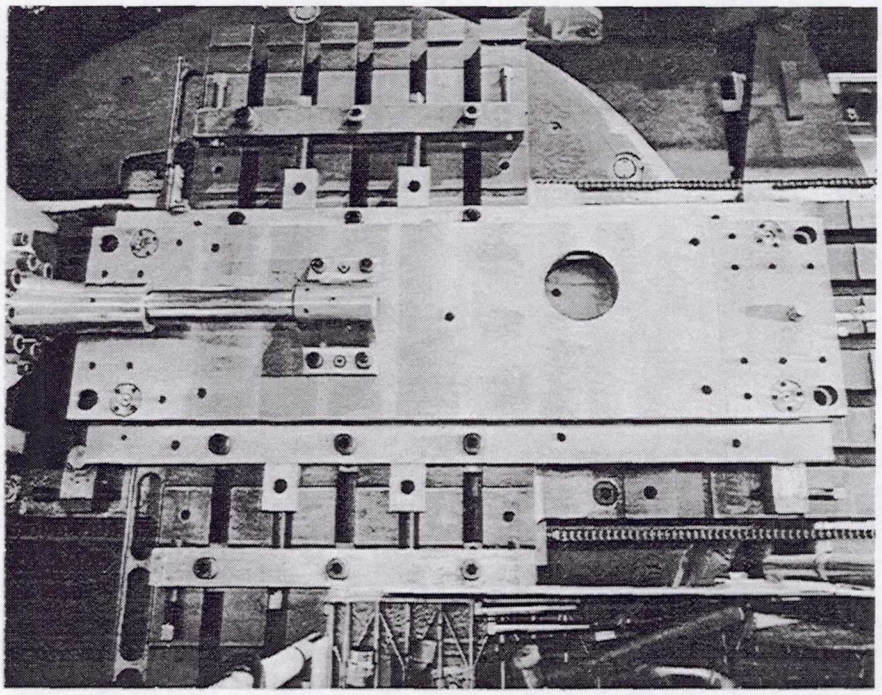

Figure 6. Dynamic balance mounted in the balance calibration machine

Channel	Loading range	Error
Z	500 lbs	±1.8 lbs
m	600 lbs ft	±1.5 lbs ft
Y	1600 lbs	±6.5 lbs
n	600 lbs ft	±4 lbs ft
l	160 lbs ft	±1 lbs ft
X	800 lbs	±8 lbs

Figure 7. Dynamic balance static calibration residuals

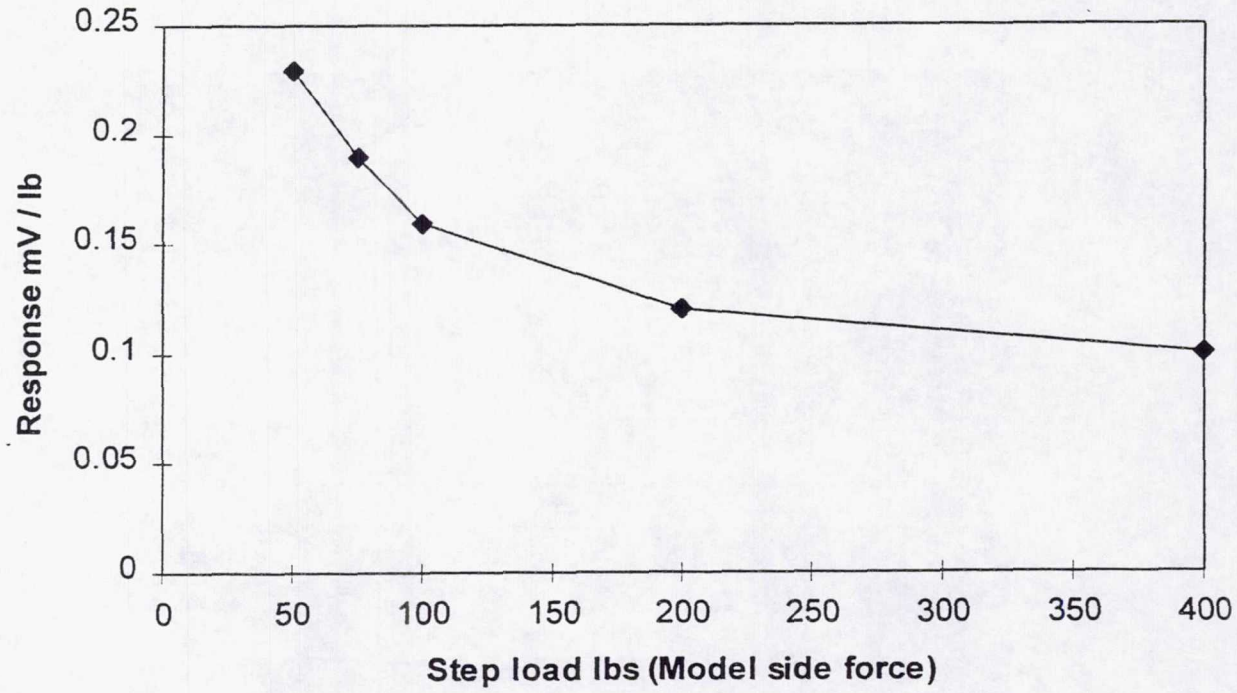

Figure 8. Dynamic balance response to steploads

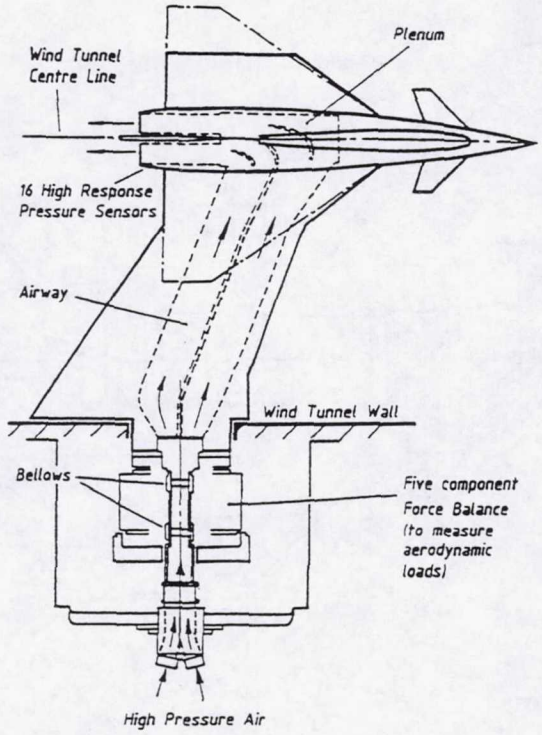

Figure 9. Model undergoing blowing test in Wind Tunnel

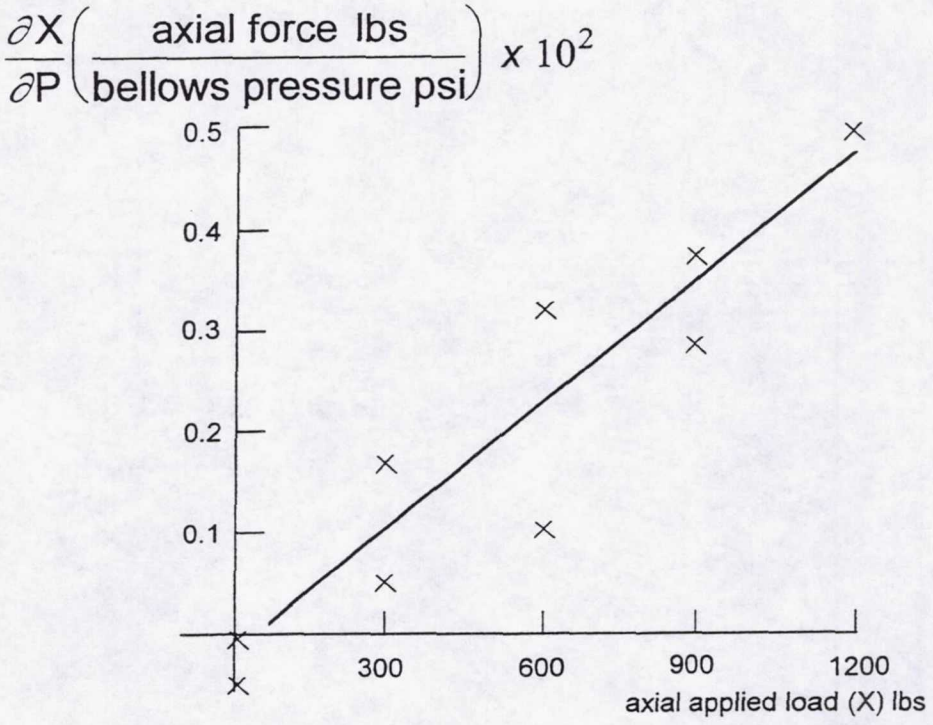

Figure 10. Effects of bellows pressure on loaded half model balance

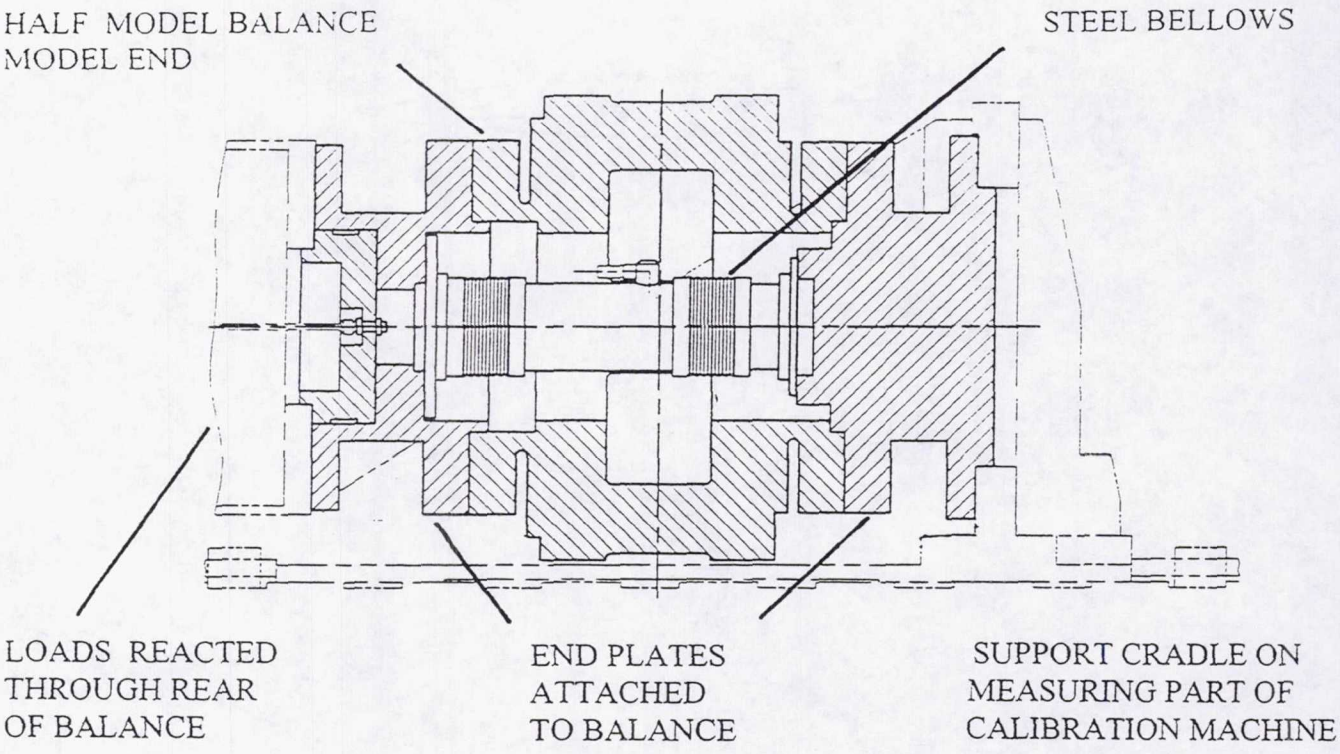

Figure 11. Bellows mounted within half model balance

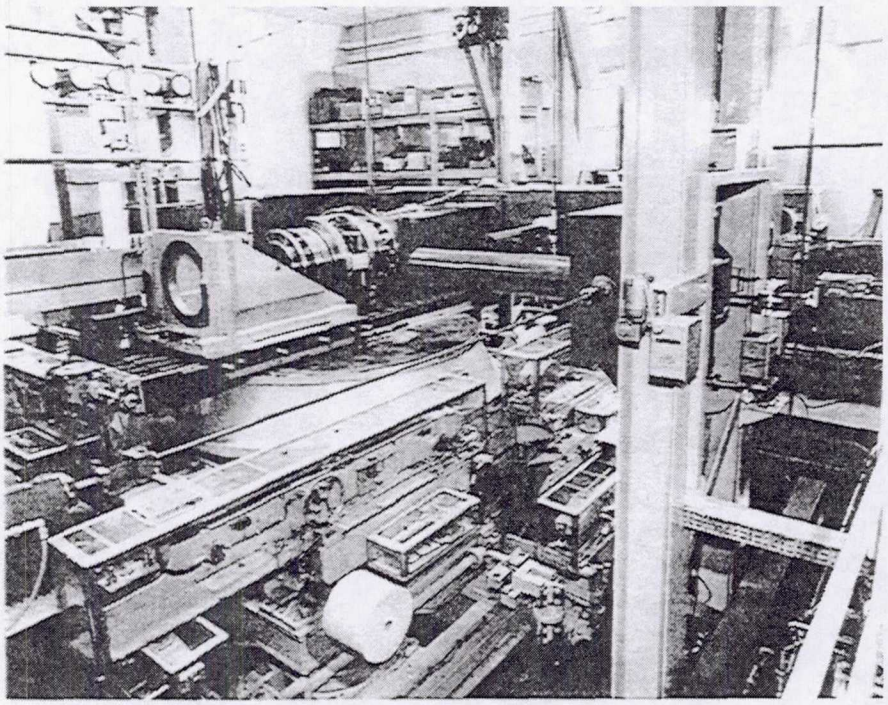

Figure 12. Half model balance being connected to cradle on balance calibration machine

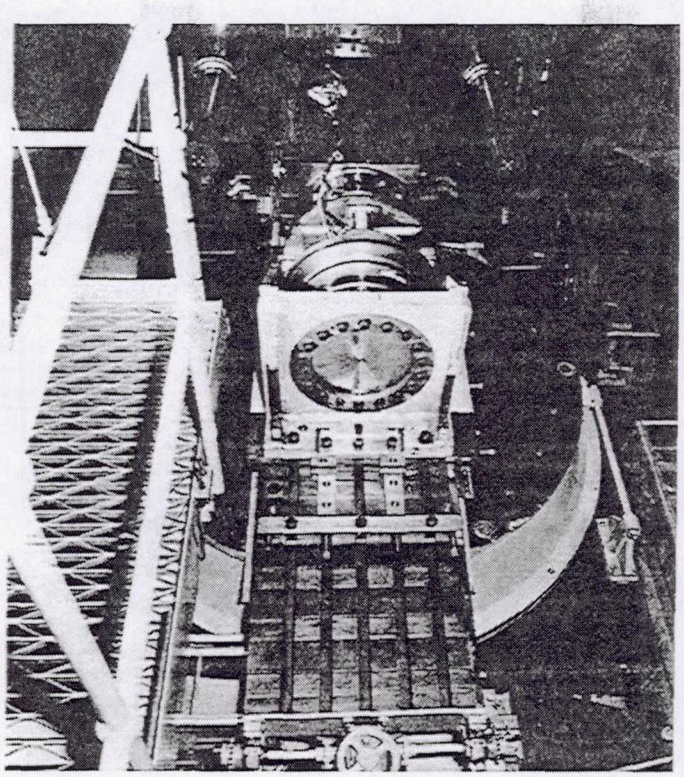

Figure 13. Half model balance mounted in balance calibration machine

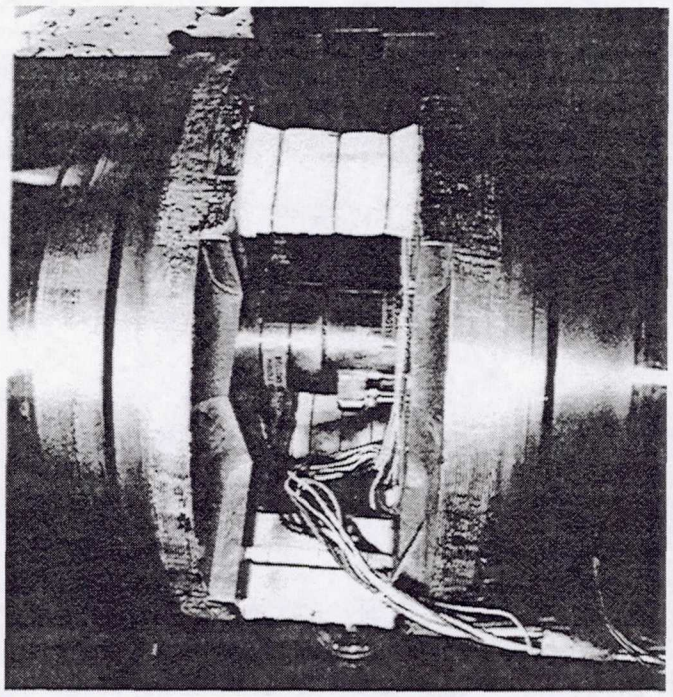

Figure 14. Half model balance fitted with removable bellows

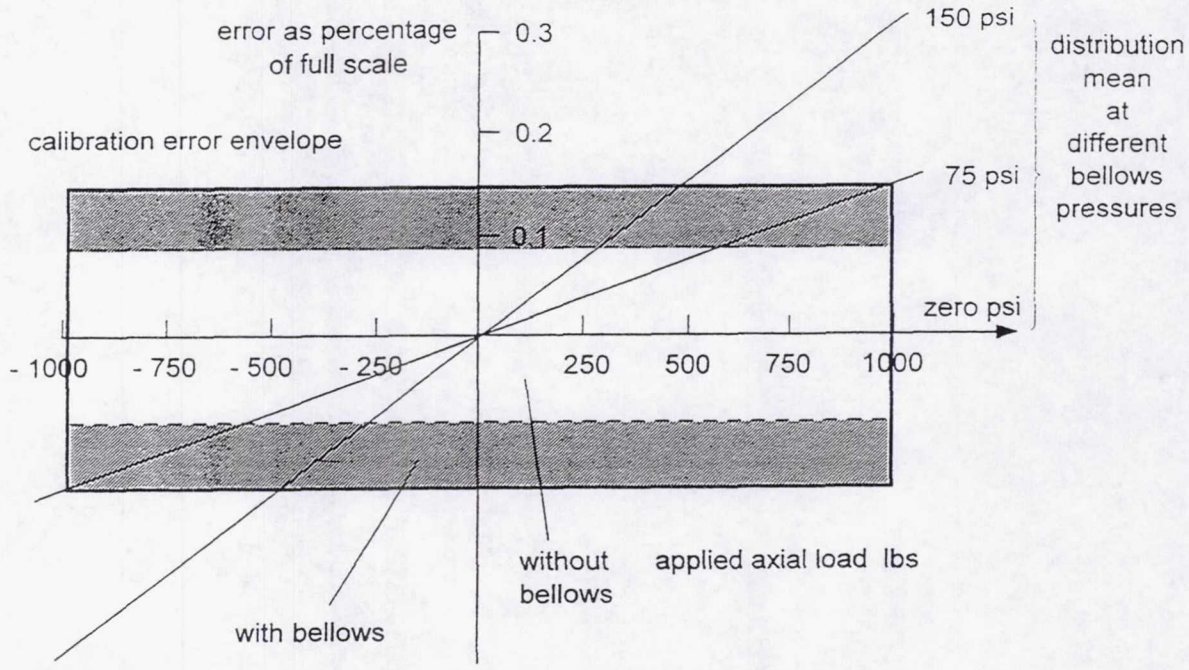

Figure 15. Error distributions for different bellows pressures

A FULLY AUTOMATIC CALIBRATION SYSTEM FOR SIX COMPONENT INTERNAL STRAIN GAUGE BALANCES FOR HIGH SPEED WIND TUNNELS

Zhang Yingpei, Yan Junren

China Aerodynamics Research and Development Center
Mianyang,Sichuan ,P.Rof China

ABSTRACT

The paper outlines the design principles, structure, technical speci fications, precision and accuracy tracebility and quality guarantee system, as well as application advantages of the fully automatic calibration system developed and manufactured by CARDC,for conventional six component internal strain gauge balances for high speed wind tunnels.

INTRODUCTION

The High Speed Aerodynamics Institute(HSAI) of CARDC has been equipped with balances and fully automatic balance calibration systems ranging from 0.01 N to 30,000 N, in connection with its wind tunnels.As is well known, a lot of wind tunnel testing time is allocated in measuring the static aerodynamic forces and moments acting on a variety of vehicle models under testing, and the balance used constitutes an important factor affecting uncertainty of the wind tunnel force testing. The uncertainty of a designed and manufactured balance is mainly related to the uncertainty of the balance calibration system and the calibration method used. The body axis calibration is the most ideal method which can obviously improve the calibration precision and accuracy.

The paper mainly describes the design principles, structure, technical specifications and quality guarantee system of the fully automatic body axis calibration system for balances of 30,000 N normal force.

DESIGN PRINCIPLES

Balance calibration must duplicate as nearly as possible the real working condition of the balance under vehicle model testing in wind tunnels . Thus the calibration system must be designed according to the body axis calibration principle of repositioning-ype.

Development of the calibration system must center on the three essential factors of a force from beginning to end, and the precision and accuracy uncertainty of the whole system must strictly be traced.

Arrangement of the force system must guarantee the realization of pure single-component loading, cross-roduct loading and arbitrarily combined loading.

In the maximum range of the calibration system, balances of different ranges can be calibrated according to the corresponding full-range precision and accuracy requirement desired.

Half model balances of correspondent ranges can also be calibrated.

STRUCTURE

The system consists of the following nine subsystems(Fig.1 and 2).

Force-Exerting and Positioning Subsystem

A three dimensional force-exerting and positioning system is adopted. The system is under unloading condition during the whole loading process. It is made of the material after long duration strain processing and automatically exerts forces to the application points on the adapter through the force transfer link. Original position of the adapter is both the installation datum during the general as sembling and the repositioning datum during the loading process. Standard dynamometers are connected in series in the force transfer link. Thus, a 3-D force-exerting and positioning system is formed. The precise positioning of the application orientation and point is guaranteed by precise processing, accurate metering and precise assembling, and the precise application point and orientation during loading process is guaranteed by measuring the micro displacement changes of the adapter after its precise repositioning. Magnitudes of the exerted forces are determined by the standard dynamometers.(Fig.3)The force-exerting and positioning subsystem and the six-degree-of-freedom repositioning manipulator which will be described below are put on a base platform having a loading capability of more than 10 tons. The former is tightly fixed on the platform, and the latter can

be accurately translated and positioned along X and Z on the platform.

Loading Subsystem

It is a 3-D rigid and strong enongh system consisting of 6 force generators and being accurately positioned by the force-exerting and positioning subsystem.

A force generator consists of driving motor, precision turbo-regulator, positive and inverse force-transfer link, multi-range extender and force-transfer mechanism.

The subsystem automatically exerts pure single-component loading, cross-product loading and arbitrarily combined loading to the six component balances. Resolution of the exerted force is better than 0.001%.

The subsystem is independently fixed on the correspondent installation foundations which are isolated from the grand platform on which the force-exerting and positioning subsystem is installed.

Adapter and Its Equilibrium Subsystem

The adapter is a force-transfer mechanism for exerting forces to the balance. Its structure is different from that of a conventional calibration rig.

The origin of the body-axis coordinates is taken at the balance reference center. The X-axis coincides with the body axis, forward being positive, for Y-axis up ward being positive, and for Z-axis rightward being positive. The six force-appplication points on the adapter are accurately fixed by precise machining. The intersection point of the three force-exertion axes of normal force Fyt, side force Fzt and axial force Fxt is the origin of the coordinates. Before au
tomatically loading to the balance, the balance reference center is automatically adjusted by the six-degree-of-freedom manipulator to coincide with the coordinates' origin, then the balance is tightly attached to the adapter.

The adapner is a positioning datum of the force-application point and the force-exertion orientation. The planeness and the perpendicularity of its six planes are made very precisely and accurately, being 2 μ. The adapter is accurately positioned and still during the unloading process, its spatial position at this time is taken as its original zero position.

In order to meet the needs for calibrating balances of different ranges, the weight of the adapter itself is balanced through the equilibrium system, and the equilibrium accuracy is higher than the force-exertion precision requirement for the balances of minimum ranges.

Six-Degree-of-Freedom Manipulator for Adapter Repositioning

The manipulator is used to achieve the six degrees of freedom fine adjustments in the linear displacements along three force-exertion axes X,Y and Z, as well as in the angular displacements of three angles α, β and γ, thus assuring repositioning the adapter precisely.

The manipulator has been elaborately designed based on the principles on manupulators and dynamics in the whole development process. The loading subsystem is elastically coupled with the manipulator during the loading process. Automatic calibration of elastic angle of the sting was also taken into account. Therefore, the balance must be calibrated together with the sting supporting model in the wind tunnel. This makes the repositioning manipulator bear a very large dynamic load. On the other hand, the adjustment sensibility of the manipulator must be very high, the resolution in the linear displacement adjustment being 0.0003mm/ a pulse, in the angular adjustment being 0.1"/ a pulse.

Six degrees of freedom motion of the manipulator are all driven by motors. It can travel 1500mm along the X axis, thus making it very convenient to calibrate balances with different ranges, as well as balances with stings so as to measure elastic angles of stings.

The Subsystem for Automatically Detecting the Adapter Repoitoning Condition

As mentioned above, the force-exerting and positioning subsystem accurately positions the force-exerting orientation and point. The adapter is automatically repositioned during the loading process. The repositioned condition of the adapter reflects the small changes in the force-exertion orientation and point. Therefore, a group of non-contact micro probes of high accuracy and reliability and by which small changes in the force-exertion point and orientation are detected, are adopted to form the subsystem for automatically detecting the adapter repositioning condition. The subsystem can detect not only the linear displacements of the adapter along X, Y and Z, but also the small changes in the force-exertion orientations of normal force Fyt, side force Fzt, axial force Fxt, and all the exerted forces forming pitching moment Fmzt, yawing moment Fmyt and rolling moment Fmxt. The subsystem is under unloading condition.

Automatic Clibration Subsystem of the Elastic Angle

The elastic body under special loading is taken as a rigid body in this system.Based on the theory on rigid body's rotation, the six degree-of-freedom mechanism comprises a mechanical part and measuring instruments for automatic calibration of the elastic angles, thus making the calibraton very convenient and with higher accuracy.

Force-Generating Control Subsystem

Each of the six force generators comprising the loading subsystem is automatically controlled by one of the STD multi-master CPUs separately. The standard dynamometers connected in series in the force-exertion link provide the feedback signals for loading. The automatic step loading is thus exerted in conjuction with the repositioning control of the six degree-of-freedom mechanism.

Control Subsystem of the Six Degree-of-Freedom Mechanism

Each of the six degrees of freedom of the six DOF manipulator is automatically controlled by one of another STD multi-master CPUs separately. The probes detecting the micro linear and angular displacements in X,Y,Z and α , β , γ in the adapter repositioning detecting system provide micro-variant feedback signals for controlling each of the six degrees of freedom of the manipulator. Values of the exerted forces of the loading subsystem are the corresponding loading values under the condition that the adapter is repositioned by tracking and controlling of the six DOF manipulator during the loading process.

The control mathematical model for the automatic calibration in the system is as follows.

$$LCE(X(t),Y(t),Z(t),\alpha(t),\beta(t),\gamma(t),fx(t),fy(t),fz(t),fmz(t),fmy(t),fmx(t))$$
$$=C(X_0,Y_0,Z_0,\alpha_0,\ \beta_0,\ \gamma_0,\ \Delta fx,\Delta fy,\ \Delta fz,\Delta fmz,\Delta fmy,\Delta fmx) \qquad (1)$$

So long as the corresponding condition of formula (1) is changed , the single-component, cross-product and arbitrarily combined loading can be realized. And it is not difficult to find out that the solution to equation (1) is divided into two parts. One is the step loadings of the loading system,the other is the zero condition of the repositioned adapter:

$$R_D\ (\ X(t),Y(t),Z(t),\alpha(t),\beta(t),\gamma(t))=R_{D0}\ (\ X_0,Y_0,Z_0,\alpha_0,\ \beta_0,\ \gamma_0)$$
$$fx(\Delta t)=\Delta fx$$
$$fy(\Delta t)=\Delta fy$$

$$fz(\Delta t)=\Delta fz$$
$$fmx(\Delta t)=\Delta fmx$$
$$fmy(\Delta t)=\Delta fmy$$
$$fmz(\Delta t)=\Delta fmz$$

Data Acquisition and Processing Subsystem for the Loaded Force Values and the Balance being Calibrated

In the process of loading and calibrating a balance in the load range of the automatic calibration system according to equation (1) the loaded force value and the output of the corresponding balance component are sampled separately by the data acquisition subsystem of 0.005% high accuracy. The output of each component is represented by a third order polynomial in the form (2):

$$F_i = a_I \cdot \Delta u_i + \sum_{\substack{J=1 \\ J \neq i}}^{6} (b_{IJ} \cdot P_j) + \sum_{j=1}^{6} \sum_{k=J}^{6} (C_{ijk} \cdot P_j \cdot P_k) + \sum_{j=1}^{6} (d_{iii} \cdot P_j^3) \qquad (2)$$

Behaviour of the balance being calibrated is thus fully described by these six similar formulas. Conventional practice to calibrate a six component internal balance has shown that term of the third and higher order Can be enghected. SO all second coefficients in the formulas can be defined by iteratively or regressively processing the 6×27 matrix. Then, the operation formulas of the six component balance are found out respectively.

For half model or external balance calibration, the operation formulas are obtained by processing according to their own regularities.

Owing to the fact that arbitrarily combined loading can be conveniently realized in this calibration system, balances can be calibrated in a new loading manner and calibration method so as to fully duplicate the working conditions of the balances under wind tunnel testing. And balances can also be calibrated more accurately by taking into consideration of the third and higher order terms if desired.

PERFORMANCE AND TECHNICAL SPECIFICATIONS

Four range groups: normal forces of 2,000 Newtons, 8,000 Newtons, 16,000 Newtons and 30,000 Newtons. The standard dynamometers in the force-exertion link can conveniently be changed so as to achieve the best calibration precision for balances of different load ranges.

Force-exertion precision and accuracy for each component is better than 0.02%.

Positioning accuracy of the force-application point for each component is less than 0.02mm.

Positioning accuracy of the force-application orientation for each component is less than 15", with the accuracy relative to X being less than 2".

Resolution of the force-exertion is better than 0.001%.

Time needed to calibrate a balance is four to six hours.

Main tasks performed during 4 to 6 hours include:

- Pure single-component loading;
- Cross-product loading;
- Arbitrarily combined loading;
- Calibration of balance accuracy and precision;
- Iteration processing of the 6 × 27 matrix to find out the balance operation formulas. The combined calibration uncertainty of the balance is not larger than 0.1%.
- Automatic calibration of the elastic angle of the balance sting, the calibration accuracy being less than 15".

Fully automatic calibration of half model balances of corresponding load ranges.

QUALITY GUARANTEE SYSTEM

The fully antomatic balance calibration system is a multi-component, multi-range, multi-degree-of-freedom force-transfer and metering system of higher grade of accuracy. The technology involved is very complicated. Therefore, the whole system has been designed by very experienced specialists based on a quantity of testing and research. And it was precisely manufactured by local machinery of higher grade of precision according to ISO 9000 family.

It is very important to measure accurately and precisely the forec-application point, the force-exertion orientation and the micro linear and angular displacements. Uncertainties of the TESA inductance instrunent and MINIL EVEL electronic level (made in Swiss),PMM 18106 and UMC 850-C large three-coordinate measuring machine (made in LEITZ, ZEISS Company of ermany),laser collimator, and the force-generation standard of the order of 10^{-5} uncertainty, which were practically used in measuring during the manufacturing process, were traced through the relevant national and international measurement standards. That is to say, in the manufacturing process, the value tracebility relation has been established between all the precision measuring instruments and the appropriate national standards of China,thus forming a unbroken comparative chain. Therefore, there

is a fully trustworthy quality quarantee system with the whole calibration system.

ADVANTAGES

There are four functions with the fully automatic balance calibration system:1. force generation, loading, and accurate measurement of the loaded force; 2. automatic repositioning control of the adapter in the loading process and accurate measurement of the micro geometric variants in the repositioning process; 3. calibration of elastic angle of the sting; 4. acquisition and processing of the loaded force and the output of each balance component, and automatic control of various variants, in the loading process. Reference center of the balance is automatically and precisely aligned with the origin of the coordinates after the balance is attached to the calibration system. The desired loading table is set and put into the computer system. The fully automatic operation of the balance calibration system is then started automatically according to the pre-set program. The force application point and orientation are precisely positioned by way of precision machining and assembling so as to avoid unnecessary human interferences. Being of very high repositioning accuracy, the adapter guarantees the precise force application point and orientation.

Pure single-component loading, cross-product loading and arbitrarily combined loading can be implemented conveniently.

Automatic calibration of elastic angle of the sting can also be performed.

Calibration uncertainty for single component can be up to the order of 0.02%, the combined calibration uncertainty up to and better than 0.1%.

Higher accuracy and precision can be provided for calibrating balances of large lift to drag ratioes.

Time needed to calibrate a balance can be greatly reduced.

CONCLUDING REMARKS

Under excitation of the competition in commercial aircraft markets, aircraft manufacturers have payed great attention to the development of the commercial aircraft of large lift to drag ratioes, thus putting forward much higher requirements-both in developing balances of high sensibility drag elements and in developing correspondent fully automatic balance calibration systems.

A quantity of research has shown that the body-axis calibration can duplicate the working

conditions of the balances under wind tunnel testing more really than the earth-axis calibration. And there are more advantages with the body-axis fully automatic calibration device of the type of adapter repositioning than other types of calibration rigs: the accuracy and precision of the exerted forces being higher, and being capable of automatic calibration of sting elastic angles.

This calibration system is developed according to the principle of body-axis and adapter repositioning type. Adjustment and application have shown that the development is successful: the accuracy and precision being high, being easier to be operated, reliable, efficient and maintainable.

In developing the force generators of the automatic loading system, different drive sources must be chosen based on dif ferent load ranges. According to our experience, calibration with deadweights to exert forces and without pulleys to transter forces gives the best accuracy for balances of small load ranges. It is more rational for force generators to be driven by pneumatic pressure in the calibration systrm for balances of small load ranges below 2,000 N, by electric motors for balances of load ranges from 5,000 N to 300,000 N, and also by hydraulic pressure for balances of load ranges up to 300,000 N.

It brings much convenience for the repositioning manipulator to be designed according to the principle of six degrees of freedom. Not only automatic loading to and calibration of the six components, but also automatic calibration of the sting elastic angles can be realized with it. This is undoubtedly like " killing two birds with one stone " for calibration of balances with large loads.

REFERENCES

1. He Dexin etc., The balance for wind Tunnl CARDC June.1996

2. Robert A. Kilgore, Internal Strain-Gage Balances: An Inter national Survey. CES-Hampton, Hampton, Virginia USA, September 1995.

3. R.D.Galway . , A Comparison of Methods for Calibration and Use of Multi-Component Strain Gauge Wind Tunnel Balances. March 1980

4. E.C.Brown . A Heavy Duty Balance Calibration Machine For The RAE 5m Low Speed Wind Tunnel. November 1979.

5. John E. Holmes., Static Mltiple-Load Measurement Technique As Utilized In The Naval Surface Weapons Center's Wind Tunnels 30 April.1976

6. David L.Smith., An Effecint Algorithm Using MatrixMethods To Solve Wind-Tunnel Force-Balance Equations. August 1972.

7. B.Ewald , P.Gieseckl,L.Polanski , C.Schenck,and E.Grecwe.AIAA90-1396. Automatic Calibration Machine for Cyrogenic and Conventional Internal Strain Gage Balance. June 18-20 1990/Seattle, WA.

8. G.I.Johnson., A New Type of Calibration Rig For Wind Tunnel Balances 1989.

9. Han Buzhang NAI . China , Zhao Lei , SARI China and Johnson. G.I.FFA. " An Investigation of Methods on Strain Gage Wind Tunnel Balance Calibration for a Rig without Repositioning " FFA TN 1988-06 and FFA TN 1988-14, 1988.

10. Wang Ming Ying, Lars Danielsson, Sigvard Widmak , Calibration of Coupled Balances FFA TN 1992-32

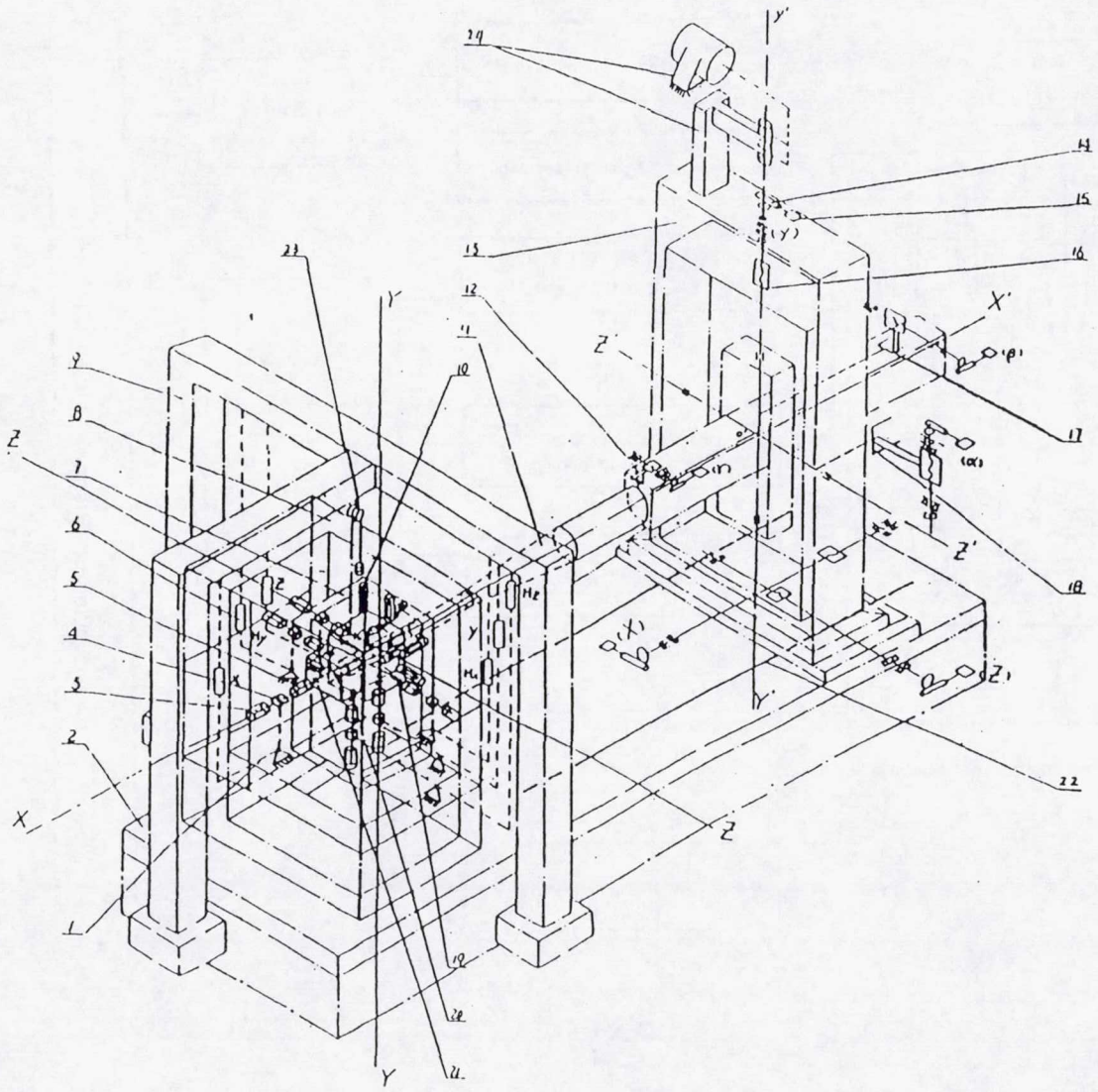

Note:

1. The lever for exerting force.
2. Base.
3. Rear support for transferring force.
4. Head of the lever for exerting force.
5. Dynamometer.
6. Force generator.
7. Base frane for the measurement of the orientation and point of force—application.
8. Position frame for exerting force.
9. Support frame of loading system.
10. Probe.
11. Balance with the sting.
12. Y machine.
13. Six degree—of—feedon manipulator.
14. Decelerator.
15. Motor.
16. Guide screw.
17. β machine .
18. α machine.
19. Hinge.
20. Force—application on point.
21. Adapter.
22. Track.
23. The equitibrium of the adapter.
24. The equitibium of y orientation dead wight of the manipulator.

Fig. 1 The comstruction principle figure of fully automatic calibration system for six component sting balance.

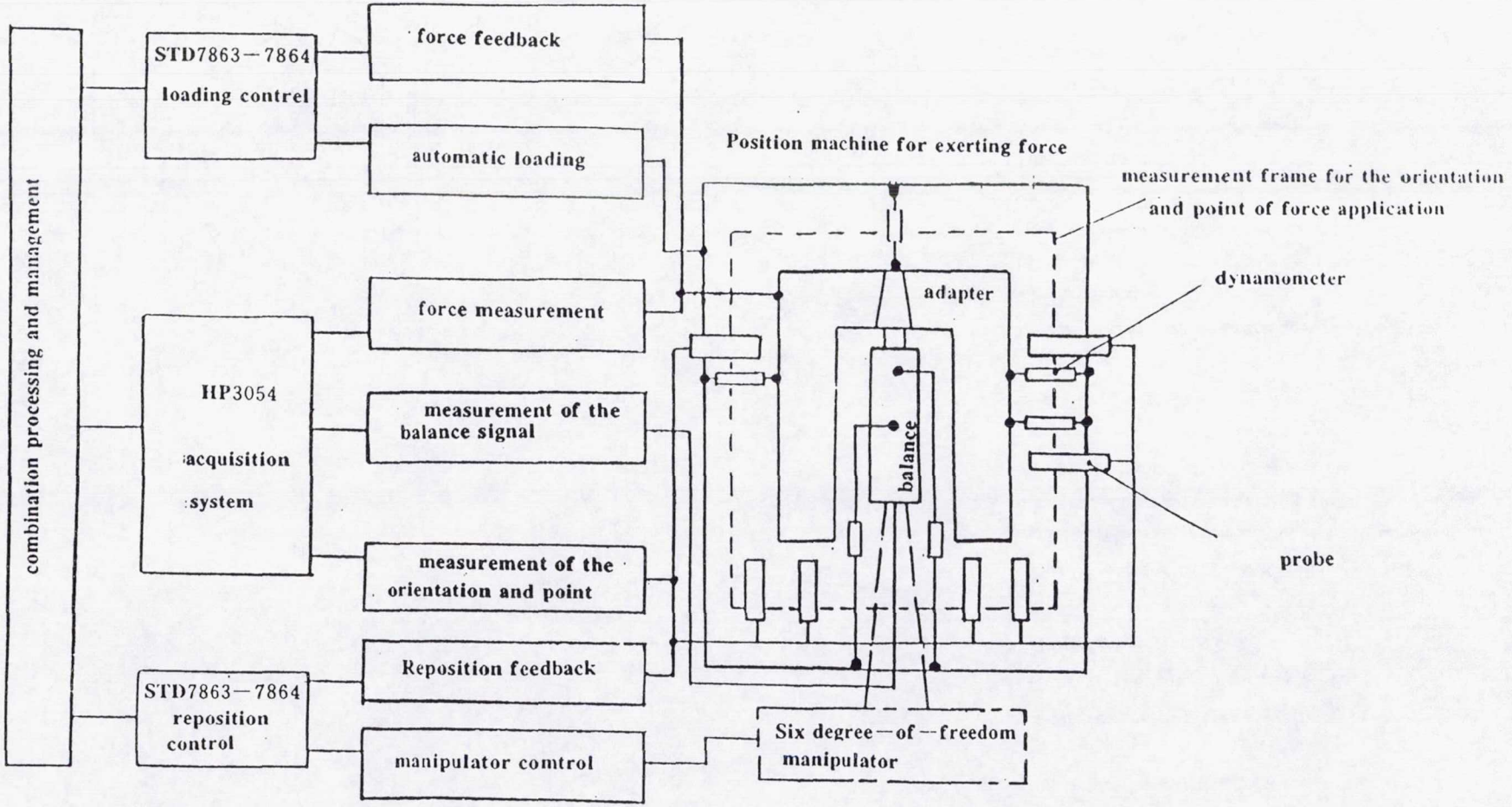

Fig. 2 Schematic diagram of the fully automatic calibration system.

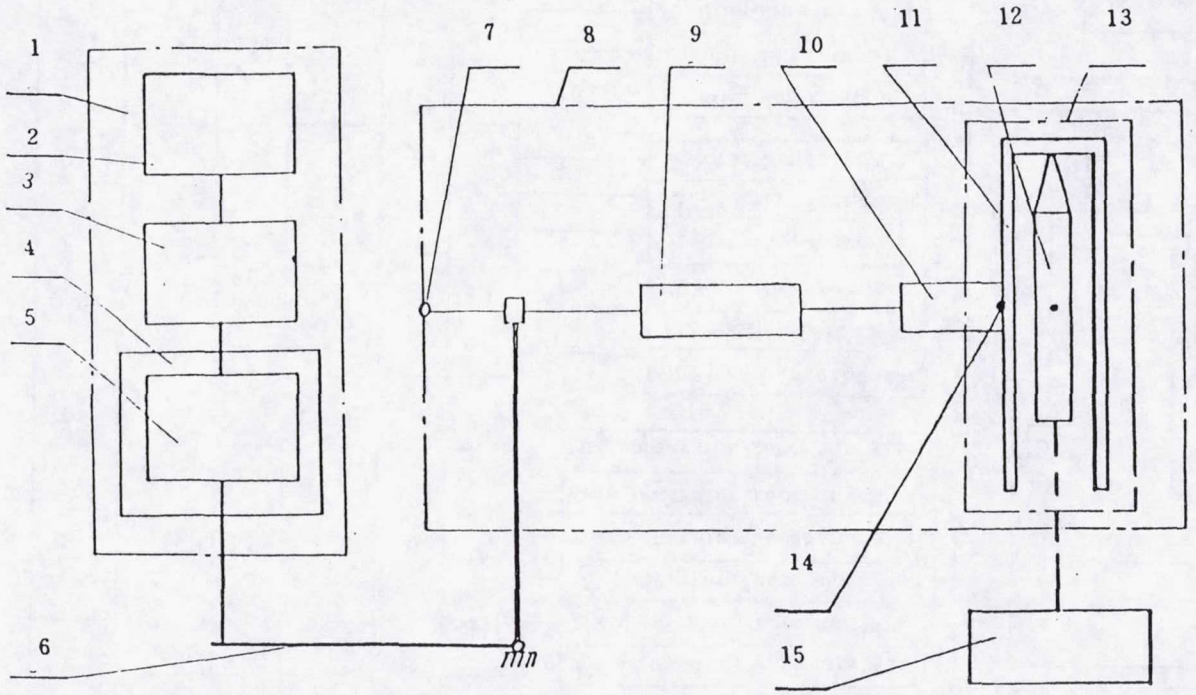

Note:

1. Force generator.
2. Motor.
3. Deceterator
4. Positive and inverse transferring force chain.
5. Extender
6. Lever.
7. Orientation machine.
8. Position frame.
9. Dynamometer
10. Hinge.
11. Adapter.
12. Batance
13. Reposition measurement.
14. Force—application point.
15. sixdegree—of—freedom maniputator.

Fig. 3 Schematic diagram of the force generator and exerting force for the fully automatic calibration system

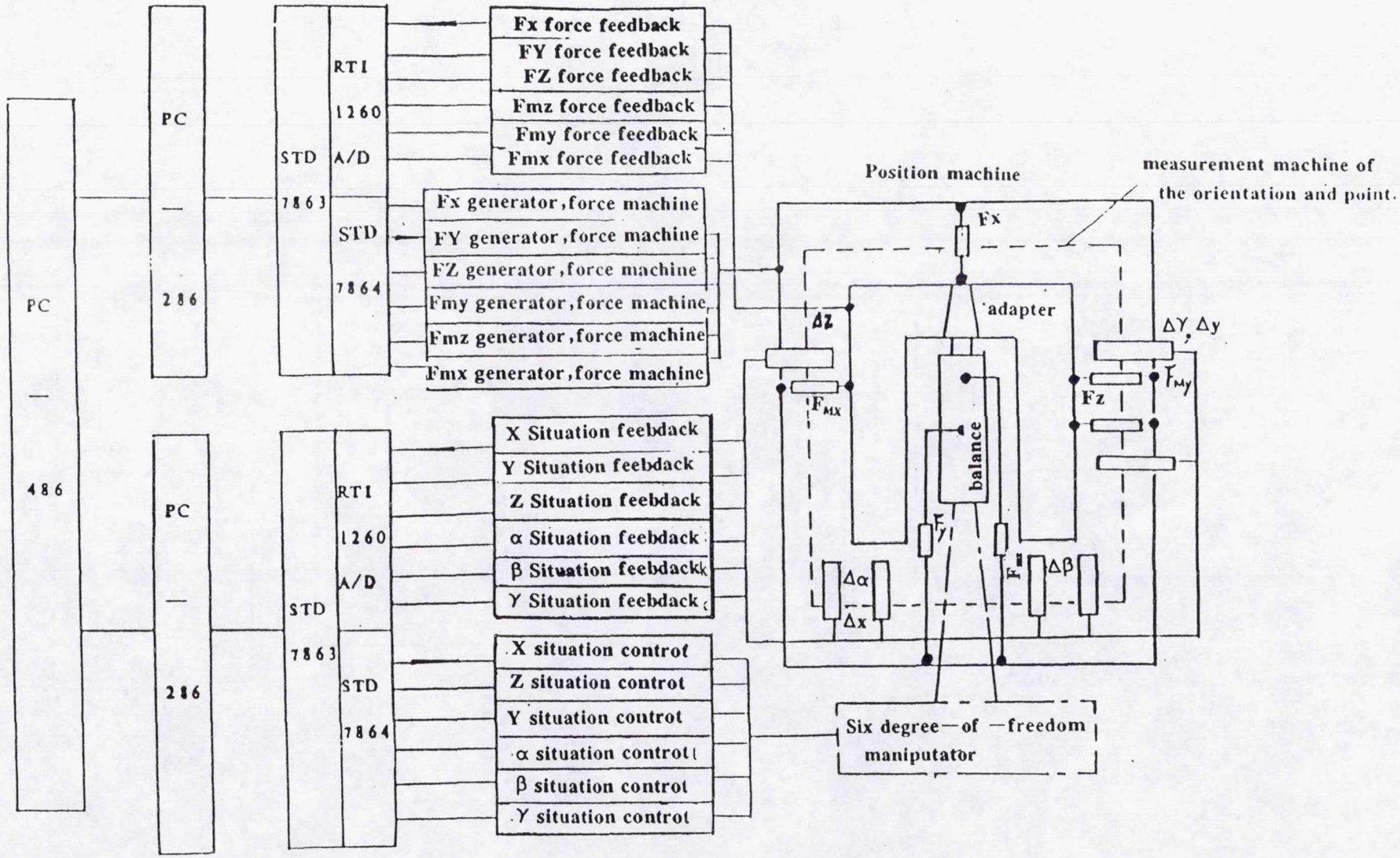

Fig. 4 The control schematic diagram of the fullt automatic calibratjon system.

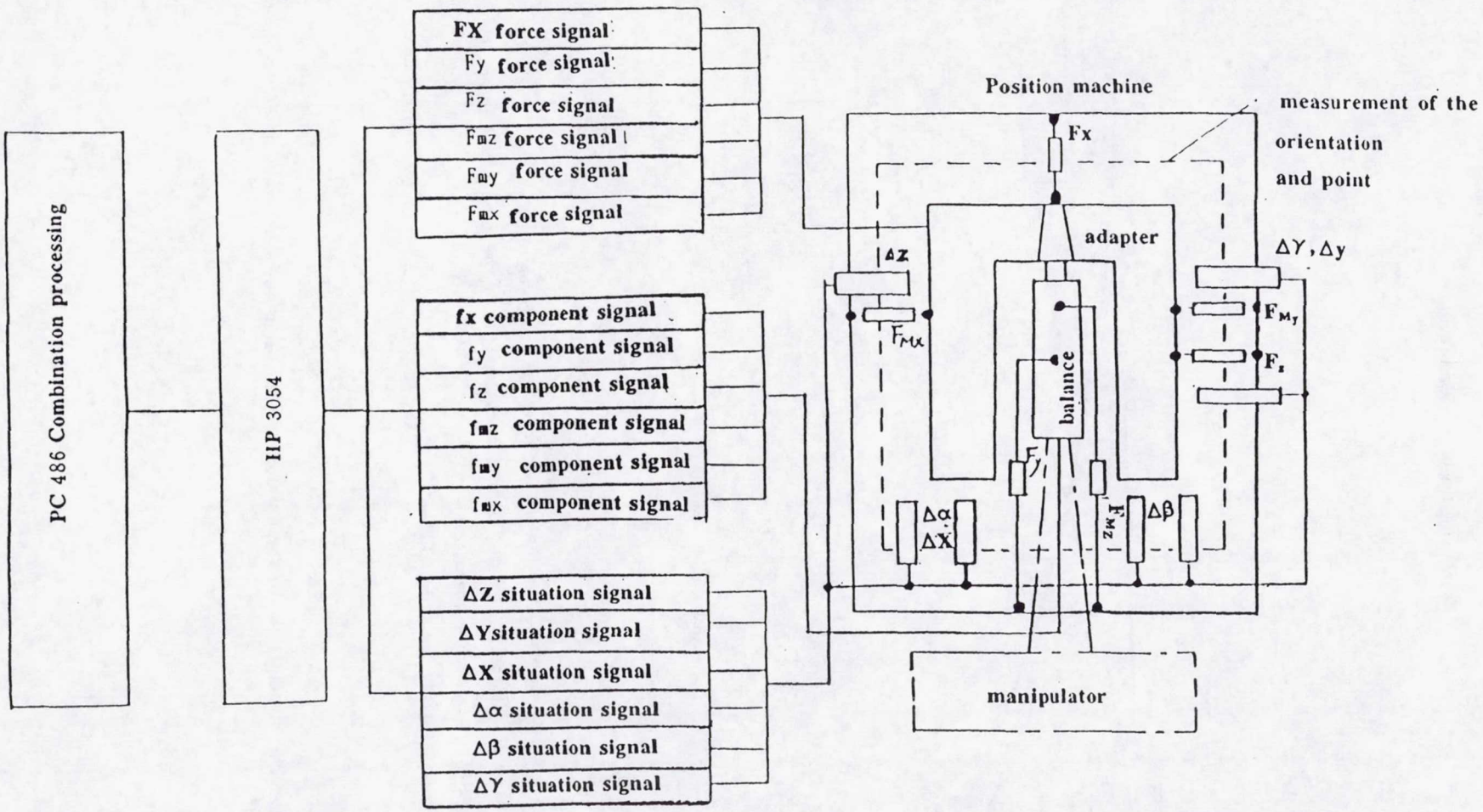

Fig. 5 Schematic diagram for the measurement and processing subsystem of the fully automatic calibration system.

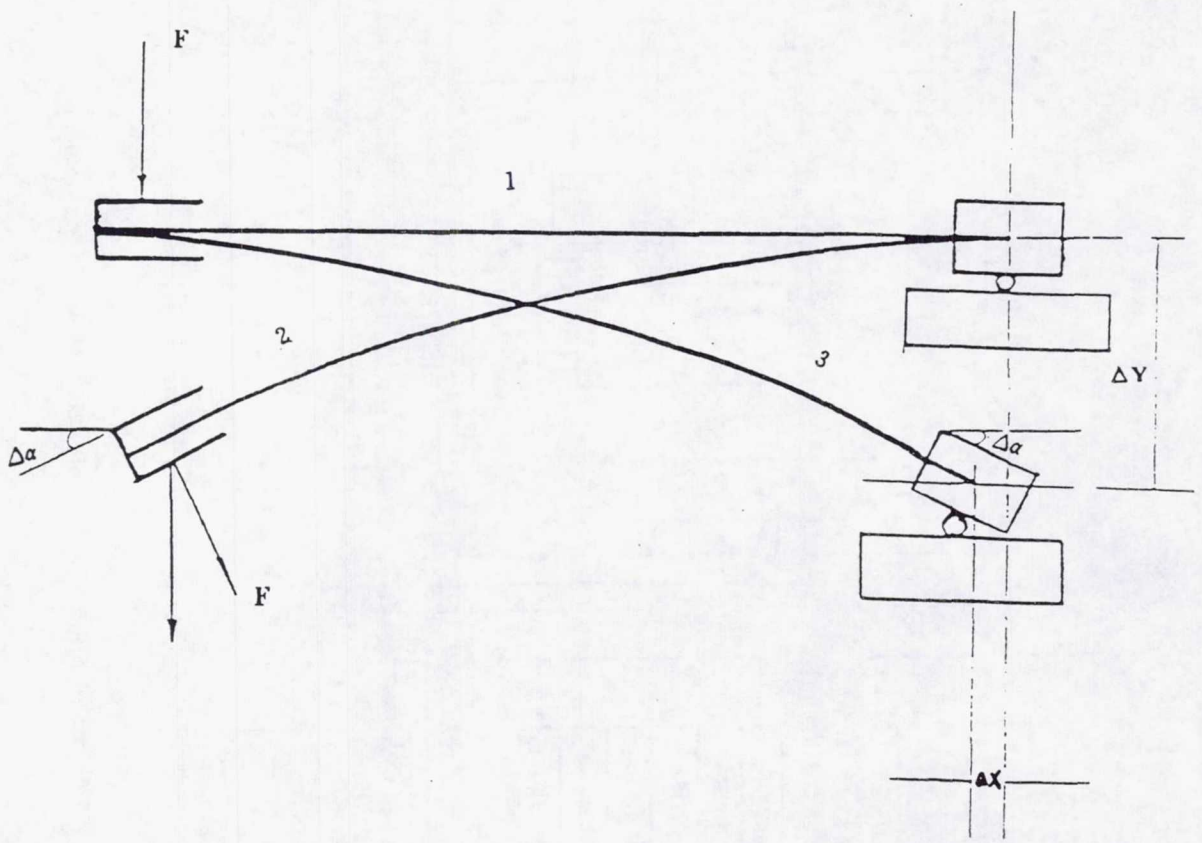

Note:

1. No exerting force situation (no counting the dead weight)
2. The principte for catibration and measurement of the model elastic angle with comventional manner.
3. The principle for automatic calibration and measurement of the modet elastic angle.

Fig. 6 The principte figure for automatic calibration and measurement of the model elastic angle.

Preliminary Statistical Analysis of the 1995 Evaluation by NASA LaRC of the IAI Automatic Balance Calibration Machine

Ping Tcheng and John S. Tripp

NASA Langley Research Center
Hampton, VA 23681

Introduction

The NASA Langley Research Center (LaRC) participated in a national cooperative evaluation of the Israel Aircraft Industries (IAI) automatic balance calibration machine at Microcraft, San Diego in September 1995. A LaRC-designed six-component strain gauge balance was selected for test and calibration during LaRC's scheduled evaluation period. Eight calibrations were conducted using three selected experimental designs. Raw data were exported to LaRC facilities for reduction and statistical analysis using the techniques outlined in reference 1. This report presents preliminary assessments of the results, and compares IAI calibration results with manual calibration results obtained at the Modern Machine and Tool Co., Inc. (MM & T), Newport News, VA. A more comprehensive report is forthcoming.

Objectives

The comparisons described herein of the automatic balance calibration machine with the traditional manual loading apparatus, with its knife edges, cables, pulleys, weight pans, and deadweights, and its associated loading schedules, had the following objectives:

1. To compare machine calibration estimated parameters with traditional manually loaded calibration parameters
2. To ascertain the overall accuracy of the device, and if possible, to establish the calibration uncertainties and the prediction uncertainties of the balance being calibrated by the machine.
3. To assess preparational requirements and the operational efficiency of the automatic balance calibration machine.
4. To validate machine calibrations with checkloads, a validation process LaRC has employed for over 35 years.
5. To ascertain the repeatability of the automatic balance calibration machine.
6. To assess enhanced high-order loading schedules with multiple or replicated loadings which are not feasible with manual calibrations.

Test Apparatus, Test Techniques, and Computational Procedures

Balance Specifications:

LaRC Balance # UT63B
Construction: One-piece, maraging 300 stainless steel
Diameter: 1.435"
Length: 10.945"
Attachment: 0.9375" tapered fit

Table 1. Full-Scale Load Values of Balance UT63B

Axial	Side	Normal	Roll	Pitch	Yaw
85 lb	± 300 lb	± 800 lb	± 400 in lb	±2000 in lb	± 800 in lb

Mathematical Model

The mathematical model used for characterizing the balance performance is the standard LaRC second-order multivariate polynomial forward model with 27 linear and second order coefficients for each of 6 components. These coefficients are ordered into a 6 × 27 matrix.

Calibration Experimental Design Specifications

1. LaRC Deadweight Loading Schedule.

   The standard proven loading schedule used at LaRC since the early 1960's is described in reference 2. The normal schedule, which contains 729 loadings, is used to estimate the 6 × 27 coefficient matrix by means of single and partial two-component loadings. Additional multi-component check loads are obtained in pitch, side, and six-component loadings to facilitate validation of the estimated coefficients after calibration.

2. IAI Machine Loading Schedule.

   The IAI automatic calibration machine can be programmed to employ any desired loading schedule. IAI normally employs a full second-order multivariate polynomial model enhanced with additional single-component cubic terms. The IAI experimental design is a complete second-order design containing 1323 loadings, i.e., all first-degree and second-degree cross-load combinations. Check load data is not obtained in the IAI schedule.

3. LaRC Reduced Schedule.

   A recently developed "reduced" loading schedule containing 649 points designed to include all first-degree, second-degree, and cubic loading combinations is described in reference 3.

Data Reduction

The global multiple multivariate regression technique described in reference 1 is employed to estimate calibration regression coefficients, and to provide calibration confidence intervals and

prediction intervals (of new measurements) as functions of the applied loading, at a 95% confidence level.

Discussion of Experimental Calibration Results

Description of Test Procedure

Eight automatic calibrations of the LaRC UT63B strain gauge balance, numbered 631-638 were conducted over a 5-day period at Microcraft, San Diego. Seven of the eight calibrations were observed by LaRC personnel on site; calibration number 635 was aborted and rerun later. Two different machine operators conducted the tests. The balance was initially installed and calibrated for runs 631-635; it was then removed and re-installed for runs 636-638. It was necessary to reduce some of the peak LaRC schedule loading values in magnitude in order to not overload the calibration machine's load cells. Three experimental designs were employed: the LaRC 729-point calibration schedule plus check loadings; the 1323-point IAI calibration loading schedule, and a "reduced" 649-point tetrahedral experimental design. The actual calibration loading time required for the LaRC schedule was approximated 1½ hours, excluding machine setup time. Similarly, the actual calibration loading time for the IAI schedule was approximately 2½ hours. Raw uncorrected calibration data were recorded on computer diskettes and were carried back to NASA LaRC for post-test analyses.

Discussion of Calibration Results

1. Loading Schedules.

   Figures 1 - 3 graphically illustrate the LaRC, IAI, and Reduced calibration loading schedules, respectively, for each of the six components. Note in figure 1 that the LaRC schedule is a partial design, without positive axial loadings and certain cross loadings. The illustration includes check loads in additional to calibration loads. It can be seen in figure 2 that the IAI loading schedule includes all cross-loading combinations necessary for estimation of first and second order polynomial coefficients. Figure 3 illustrates the tetrahedral design described in reference 3.

2. MM & T Calibration.

   Figure 4 illustrates the residuals, 95% calibration confidence intervals (inner envelope), and 95% prediction intervals (outer envelope) as functions of the applied loads for a MM & T manual calibration. Note the significant variation of the calibration confidence interval as a function of the applied loading. As discussed in reference 4 these calibration uncertainties become fossilized bias uncertainties after calibration for facility usage of the balance. It is to be noted that the standard error of the regression for each component appears in Table 2.

   Figure 5 illustrates check load error plots superimposed with 95% prediction intervals as functions of the corresponding applied load. Note that not all errors lie within the 95%

prediction intervals. It is believed that a major cause of outlying points is the difficulty of precisely applying multi-component loads, especially with respect to proper cable alignment in the presence of deflections. Never-the-less the worst-case root-mean-square (RMS) error over each check load segment is found to be no greater than 0.25% FS.

3. IAI Automatic Strain Gauge Balance Calibration Machine Calibration

A total of eight calibration runs, using five LaRC, two IAI and one LaRC reduced schedules. were conducted on IAI automatic calibration machine.

The results of the eight calibrations are summarized in Table 2. In particular, the standard errors of the regression for all six components are separately tabulated for each calibration. The column labeled "RMS" is the root-mean-square of the six standard errors for each calibration run. It is included only for comparison among calibrations including proofs or among calibrations excluding proof loads; inter-comparisons between runs including proofs and runs excluding proofs are not meaningful.

Among the eight runs using the IAI Automatic Strain Gauge Balance Calibration Machine, note that run 632 may be abnormal due to something or other, and will be excluded from further discussion. It will be seen below that the results of runs 631-634 (except 632) cluster together (cluster 1) and that runs 636-638 cluster together (cluster 2) as groups.

For cluster 1 we exhibit a representative LaRC schedule run, namely run 631 in figures 6 and 7, and a representative IAI schedule run, namely run 634 in figure 8. Figures 6 and 8 illustrate the residuals, 95% calibration confidence intervals (inner envelope), and 95% prediction intervals (outer envelope) as functions of the applied loads for runs 631 and 634, respectively. Note that the errors are not all random. Figure 7 illustrates check load error plots superimposed with 95% prediction intervals as functions of the corresponding applied load for run 631. The RMS value of the checkload errors is shown explicitly above each checkload error subplot, i.e., normal loads, side loads, and six-component loads. These values are compared below. Note that not all errors lie within the 95% prediction intervals.

The RMS checkload errors for each component are displayed in a set of comparison matrix plots. These plots enable both intra-cluster and inter-cluster comparisons of checkload uncertainties as functions of the estimated strain gauge balance coefficient set and the checkload data set. All comparative matrices compare RMS checkload errors for regression coefficients estimated from run A, denoted by the first run number in the heading of each subplot, using checkloads obtained from run B, denoted by the second run number in the heading of each subplot. The symbols "o, +, ×" denote normal, side, and six-component check loadings, respectively. Abcissa symbols "A, S, N, R, P, Y" denote axial force, side force, normal force, rolling moment, pitching moment, and yawing moment, respectively. RMS checkload error magnitudes are shown on the ordinate axis in units of percent full scale load of the corresponding component.

Figures 9 and 10 depict comparative matrix plots for clusters 1 and 2, respectively. To wit, the cluster 1 subplots in figure 9 show RMS errors obtained during *checkload* runs 631 and 633, computed with regression coefficients estimated from *calibration* runs 631, 633 and 634. It is to be noted that calibration runs 631 and 633 follow the LaRC loading schedule, whereas calibration run 634 follows the IAI loading schedule. The largest cluster 1 RMS checkload error observed in figure 9 is ±0.40% FS.

Similarly, the cluster 2 subplots in figure 10 illustrate RMS errors obtained during *checkload* runs 637 and 638, computed with regression coefficients estimated from *calibration* runs 636-638. It is to be noted that calibration run 636 follows the IAI loading schedule, whereas calibration runs 637 and 638 follow the LaRC loading schedule. The largest cluster 2 RMS checkload error observed in figure 10 is ±0.30% FS.

One of the objectives of the San Diego tests was to ascertain the repeatability of the automatic balance calibration machine. To wit, how well are replicated calibrations validated using checkload data? LaRC has employed this validation strategy for over 35 years. It is to be noted that, within themselves, cluster 1 calibrations and cluster 2 calibrations show reasonable repeatability with tolerable RMS checkload errors, namely, less than 0.5% FS per component. However, the repeatability between clusters 1 and 2 is less than satisfactory, as is now demonstrated.

Four comparative inter-cluster matrix plots comparing cluster 1 and 2 test data appear in figure 11. Matrix subplots (1,1) and (2,2) illustrate RMS errors using *checkload* runs 631 and 637 computed with regression coefficients estimated from the **corresponding** *calibration* runs, i.e., runs 631 and 637, respectively. On the other hand, subplots (1,2) and (2,1) illustrate RMS errors using *checkload* runs 631 and 637 computed with regression coefficients estimated from the **opposing** *calibration* runs, i.e., runs 637 and 631, respectively.

The following observations can be drawn from comparison of cluster 1 and cluster 2. Figure 11 clearly demonstrates the lack of repeatability between cluster 1 calibration runs and cluster 2 calibration runs. Although within themselves, cluster 1 and cluster 2 results appear to be adequate, the repeatability of cluster 1 coefficients using cluster 2 check loads, and vice versa, is inadequate. For example, the RMS roll error for 631 checkloads using 637 estimated coefficients is 1.13% FS, and the RMS roll error for 637 checkloads using 631 estimated coefficients is 0.83% FS. In contrast, the RMS roll error for 631 checkloads using 631 estimated coefficients is 0.16% FS, and the RMS roll error for 637 checkloads using 637 estimated coefficients is 0.14% FS.

4. Summary of Results.

The results of the eight calibrations are now summarized and tabulated in Tables 2 and 3. In particular, Table 2 lists a "standard error" columnwise for each balance component for Runs 631 through 638. In addition the column labeled "RMS" contains the root-mean-square of

the six component standard errors, providing an overall indication of the total balance performance. Note that data set 637 appears twice in the table. The RMS standard error of the first row labeled 637, which includes checkloads, equals 0.06252 %FS whereas that of the lower row labeled 637, which does not include checkloads, equals 0.05108 %FS, an 18% reduction.

It is of interest to observe that the larger IAI loading schedule which provides the complete set of cross component loadings, and the reduced loading schedule based on a tetrahedral experimental design, offer no improvement over the traditional LaRC loading schedule for this particular balance. Indeed, after comparing the RMS column values without checkload residuals, it is seen that IAI run 636 and 634 RMS values are 0.08669 %FS and 0.06859 %FS, respectively. Reduced schedule run 635 has an RMS value of 0.06565 %FS. Finally LaRC runs 637 and 631 have RMS values of 0.05108 %FS and 0.06275 %FS, respectively, both of which are less than all of the IAI and reduced schedule RMS errors.

Table 2. Standard Error (%FS) of Each Component for Calibration Runs 631-638

Run No	Axial	Side	Normal	Roll	Pitch	Yaw	RMS	Schedule	Remarks
631	0.06682	0.07999	0.03974	0.06713	0.04511	0.06814	0.06275	LaRC	
632	0.59160	0.12230	0.04668	1.32200	0.61660	0.09430	0.64600	LaRC	* #
633	0.07740	0.09737	0.04194	0.05998	0.04510	0.06734	0.06757	LaRC	
634	0.05200	0.09943	0.04429	0.06628	0.04033	0.08752	0.06859	IAI	
635	0.05807	0.07732	0.04668	0.06523	0.06314	0.07804	0.06565	Reduced	
636	0.06608	0.13590	0.05594	0.07005	0.07534	0.09243	0.08669	IAI	
637	0.05990	0.07276	0.04319	0.06365	0.04887	0.07916	0.06252	LaRC	*
637	0.05038	0.05675	0.03424	0.04064	0.04559	0.07068	0.05108	LaRC	
638	0.05039	0.05683	0.03432	0.04056	0.04571	0.07076	0.05113	LaRC	
MM&T	0.06058	0.03679	0.02394	0.04330	0.02736	0.04277	0.04093	LaRC	
* Indicates Check Loads Included									
# Indicates a Possible Bad Run									
RMS = Root-Mean-Square of the 6 Component Residuals									

Note further that the RMS standard errors for runs 631-638 are all greater than the RMS standard error corresponding to the manual loading performed at MM&T. This is now illustrated in detail in Table 3, which provides a comparison between IAI automatic balance calibration machine calibration run 637 using the LaRC schedule and a manual calibration conducted at MM&T prior to the San Diego event. The standard errors of the regression residuals are tabulated for each of the six components, for both calibrations along with the checkload RMS standard errors. In addition, for comparison purposes each machine calibration standard error is shown as a percentage of the corresponding manual calibration standard error. Note that a majority of the manual calibration standard errors are significantly less than their machine calibrated counterparts. Note, however, that all of the machine calibrated axial values are less than their manually calibrated counterparts except for the six-component check load which is *drastically* larger (1385% of the manual calibration value).

Table 3. Comparison of Hand Loaded Calibration with Automatic Machine Calibration. Values Expressed as %FS

	MM & T Hand Calibration					IAI Automatic Calibration			
Component	Residuals	Proof Loads			Component	Residuals	Proof Loads		
		Normal	Side	Six			Normal	Side	Six
Normal	0.02394	0.03870	0.03400	0.04820	Normal	0.03424	0.10300	0.05010	0.10100
					%MM&T	143%	266%	147%	210%
Axial	0.06058	0.12800	0.07190	0.09170	Axial	0.05038	0.06710	0.02760	0.12700
					%MM&T	83%	52%	38%	138%
Pitch	0.02736	0.09630	0.02640	0.08880	Pitch	0.04559	0.07240	0.02310	0.09630
					%MM&T	167%	75%	88%	108%
Roll	0.04330	0.11000	0.03260	0.10600	Roll	0.04064	0.14000	0.07090	0.08850
					%MM&T	94%	127%	217%	83%
Yaw	0.04277	0.21200	0.05040	0.24400	Yaw	0.07068	0.13600	0.11500	0.28500
					%MM&T	165%	64%	228%	117%
Side	0.03679	0.08180	0.03890	0.11400	Side	0.05675	0.08530	0.10600	0.17200
					%MM&T	154%	104%	272%	151%

Concluding Remarks

1. The machine operates rapidly and smoothly. The machine calibration process is obviously more efficient than manual calibration, especially for multiple-component loadings. It offers the potential for rapid calibration turnaround on the order of one day compared to two to four weeks required for manual calibration. Likewise, it can reduce typical calibration manpower requirements by a factor of 20 or more.

2. The machine seems to be capable of meeting a 0.5% accuracy requirement most of the time. However, manual calibration still provides the best calibration precision and accuracy at present.

3. Calibration results seem to be operator dependent; more experienced operators obtain superior results. Moreover, the complexity of the machine requires a full-time, highly-skilled, senior technician for operation.

4. The automatic calibration machine is especially suitable for high density loading schedules or new innovative loading schedules with multiple component loadings and replications.

5. The operating software is versatile and user-friendly.

6. Overall accuracy of the machine, including load cell accuracies and spatial positioning accuracies, needs to be specified at a 95% confidence level. Other factors such as temperature sensitivity, long term stability, and steady-state stability need to be addressed.

7. Additional effort is needed for the machine to mature to production-level repeatability.

Acknowledgments

The authors would like to graciously thank Mr. Michael Leftkovitch of IAI and the Microcraft, San Diego staff for their cooperation and assistance during the tests. Mr. Paul W. Roberts of NASA LaRC is also to be commended for his participation as an observer of the calibration evaluation activities.

References

1. Tripp, J. S., and Tcheng, P.: *Determination of Measurement Uncertainties of Multi-Component Wind Tunnel Balances.* AIAA paper AIAA-94-2589, 18th AIAA Aerospace Ground Testing Conference, Colorado Springs, CO, 1994.

2. *Force Balance Practice at Langley Research Center.* Prepared by Model Instrumentation Team, Experimental Testing and Technology Division, NASA, Langley Research Center, Hampton, VA for AIAA - GTTC Internal Balance Calibration Technology Working Group Meeting, January 1995, Reno, NV.

3. Bursal, Faruk H.: *Analysis of Uncertainty in Force Balance Calibration.* Final Report, NASA/ASEE Summer Faculty Fellowship Program, NASA Langley Research Center, Hampton, VA, 1995.

4. Coleman, H. W., and Steele, W. G.: *Experimentation and Uncertainty Analysis for Engineers.* John Wiley & Sons, N. Y., NY, 1989.

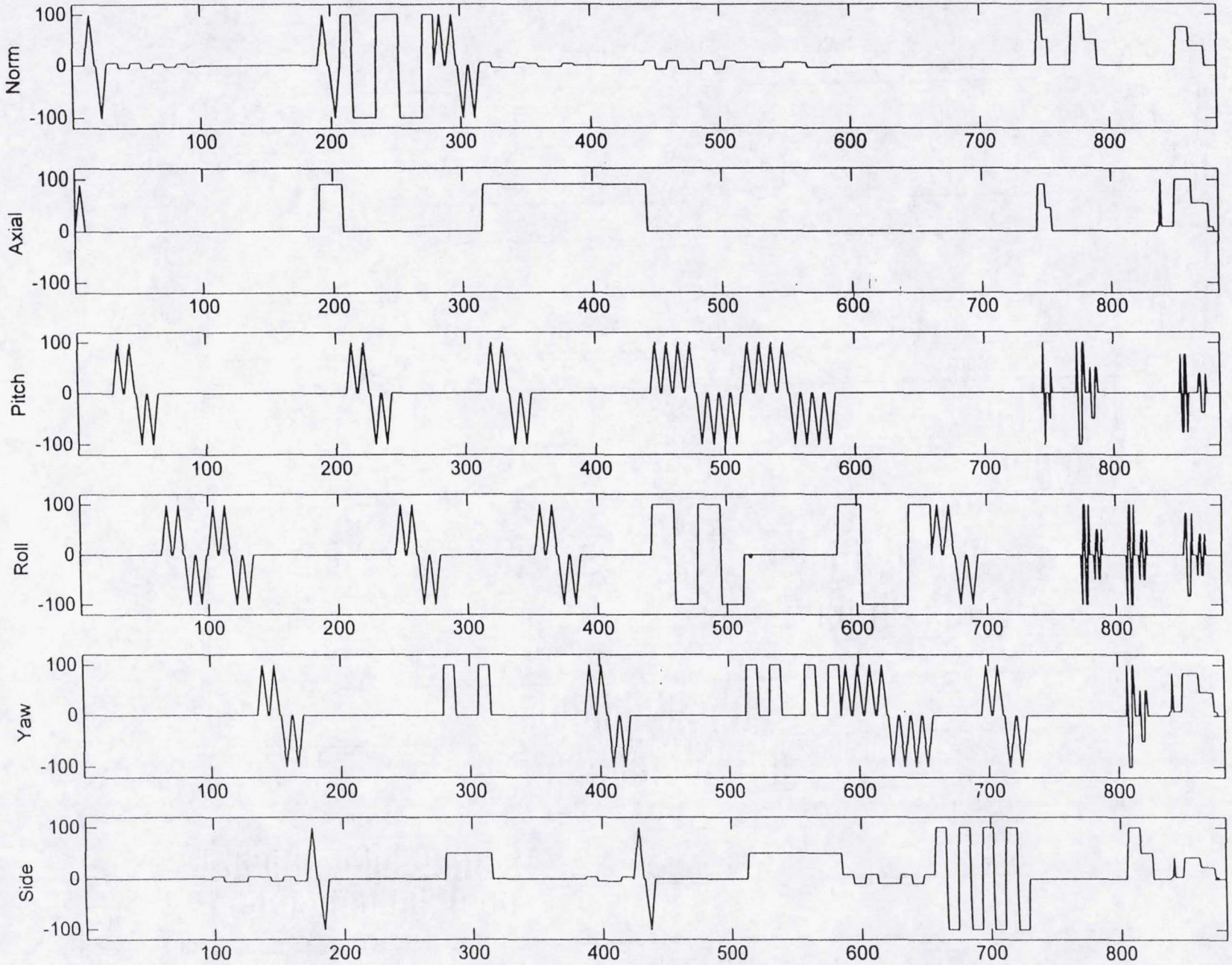

Figure 1. Langley Manual Calibration Loading Schedule (729-Point Calibration Loading and Check Loadings)

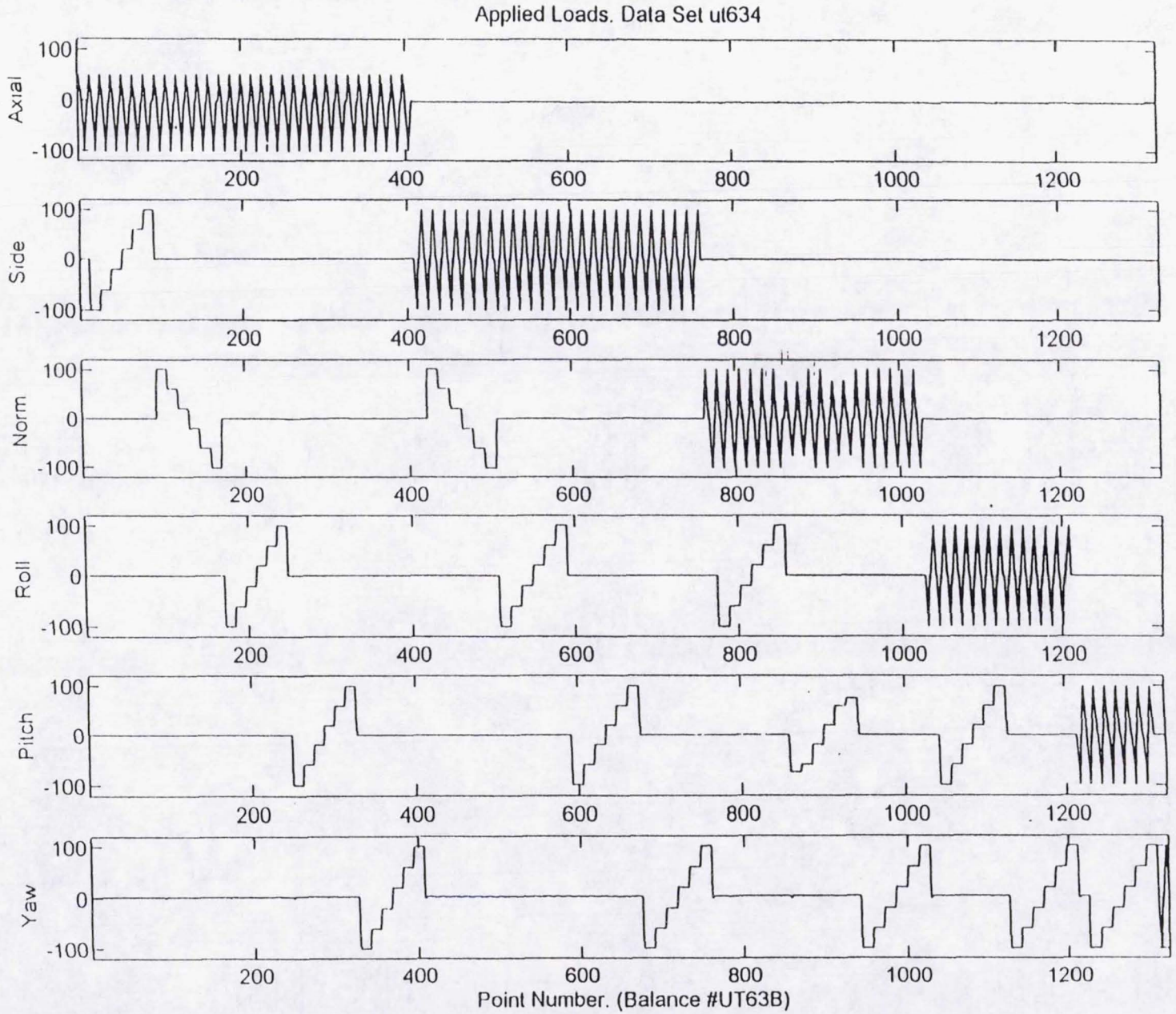

Figure 2. 1323-Point IAI Automatic Calibration Machine Loading Schedule

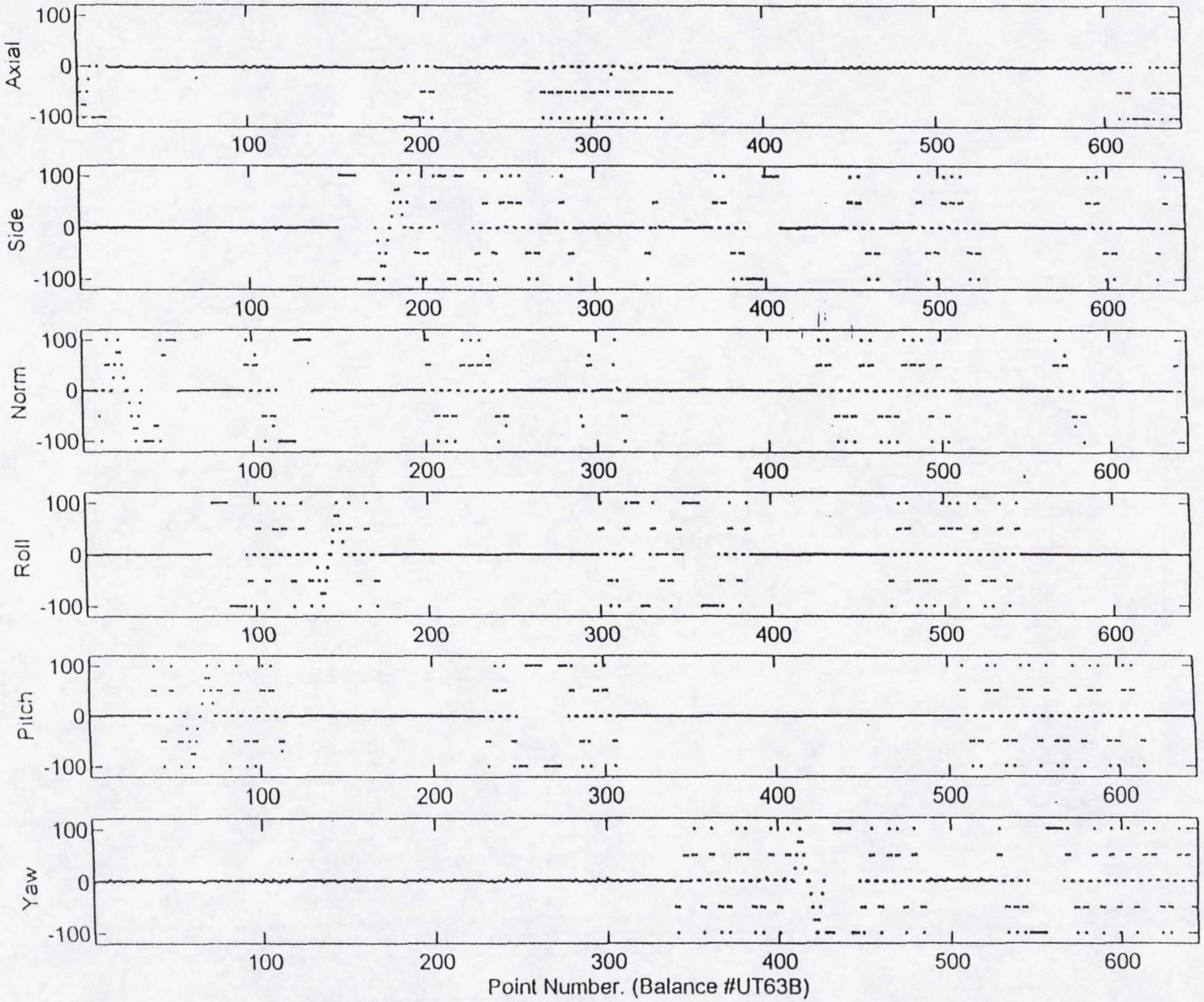

Figure 3. 649-Point Reduced Tetrahedral Balance Calibration Loading Schedule

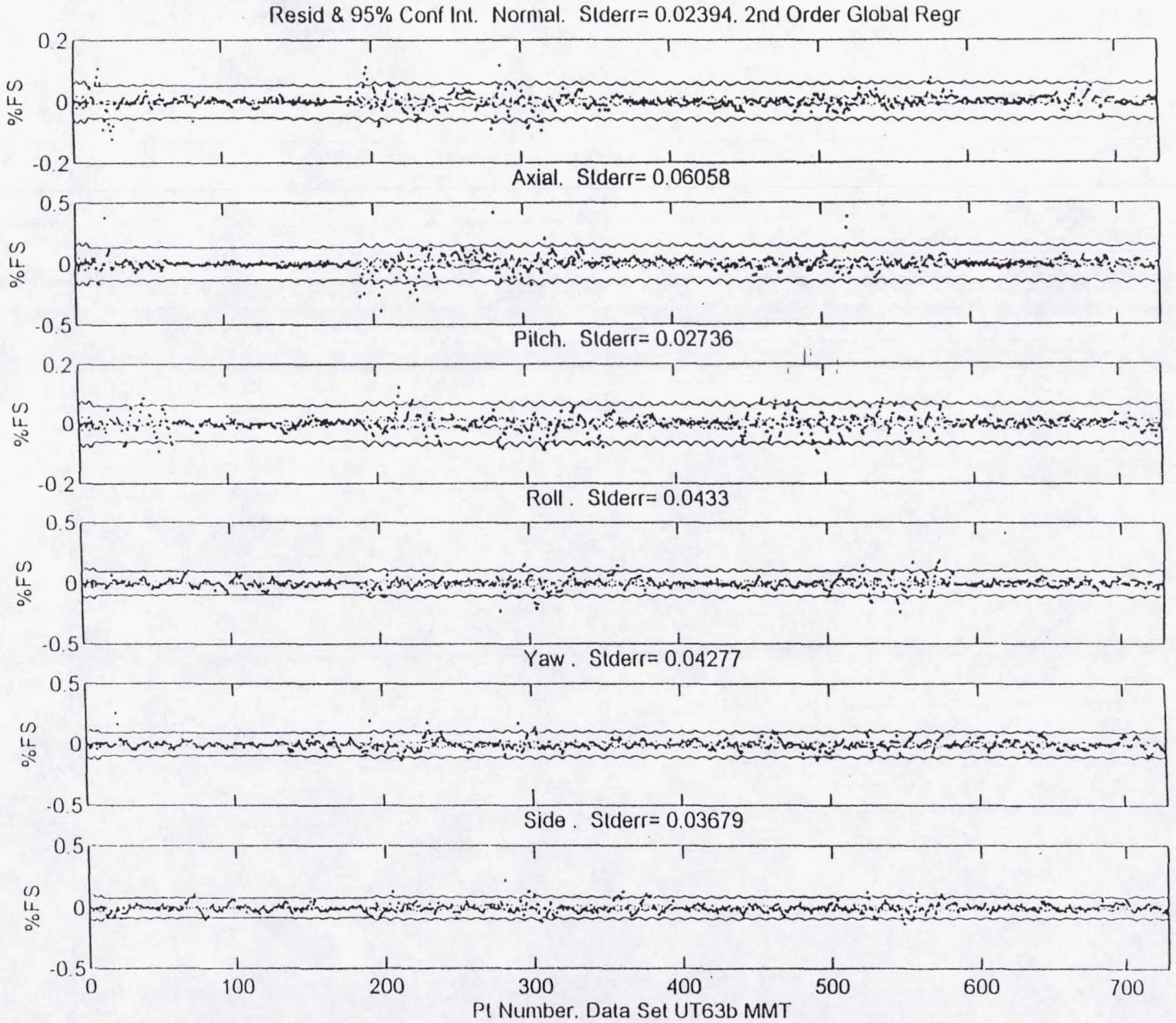

Figure 4. Residuals, 95% Confidence Intervals, & 95% Prediction Intervals for MM & T Manual Calibration with LaRC Loading Schedule

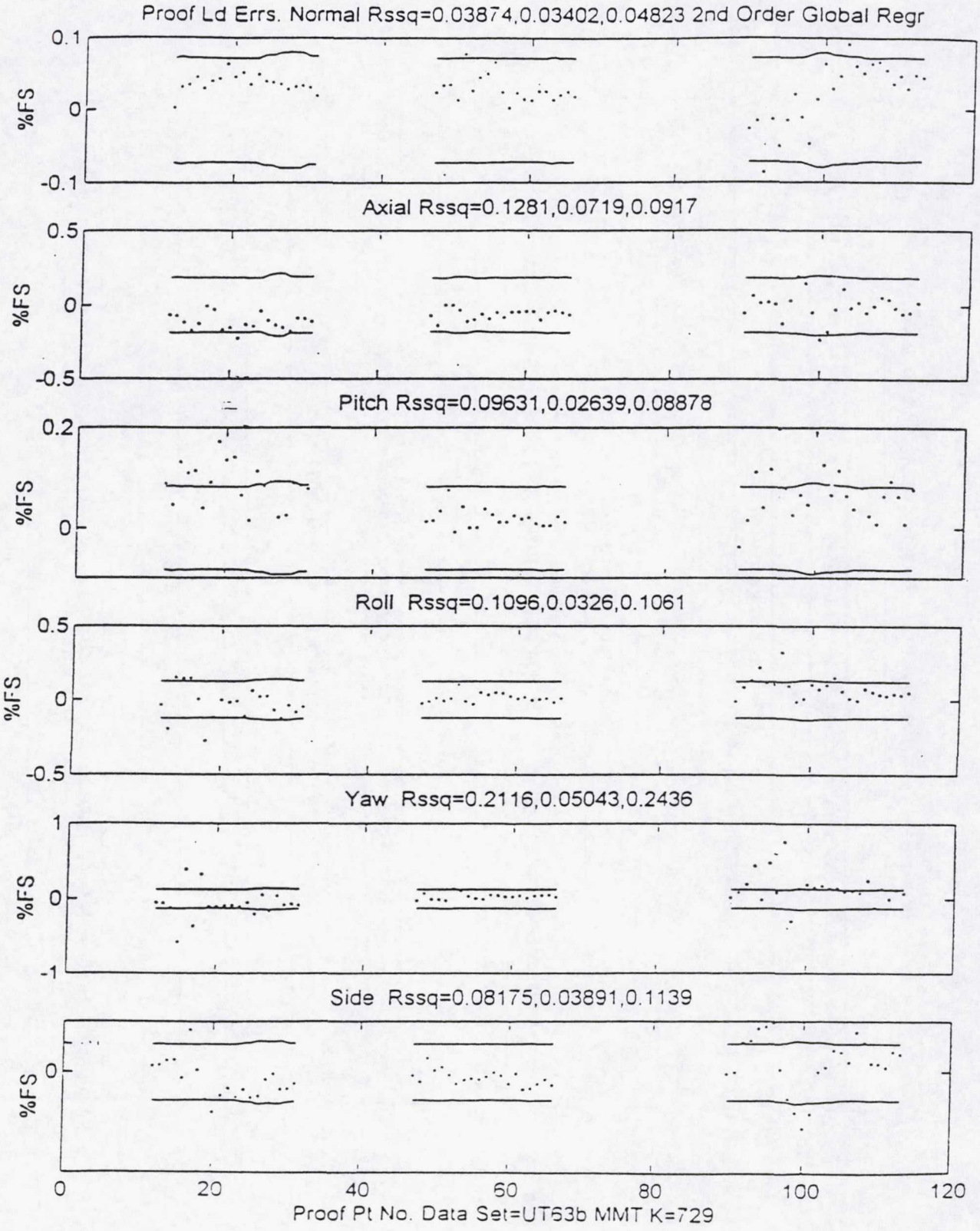

Figure 5. Checkload Errors with 95% Prediction Intervals for MM & T Manual Calibration with LaRC Loading Schedule

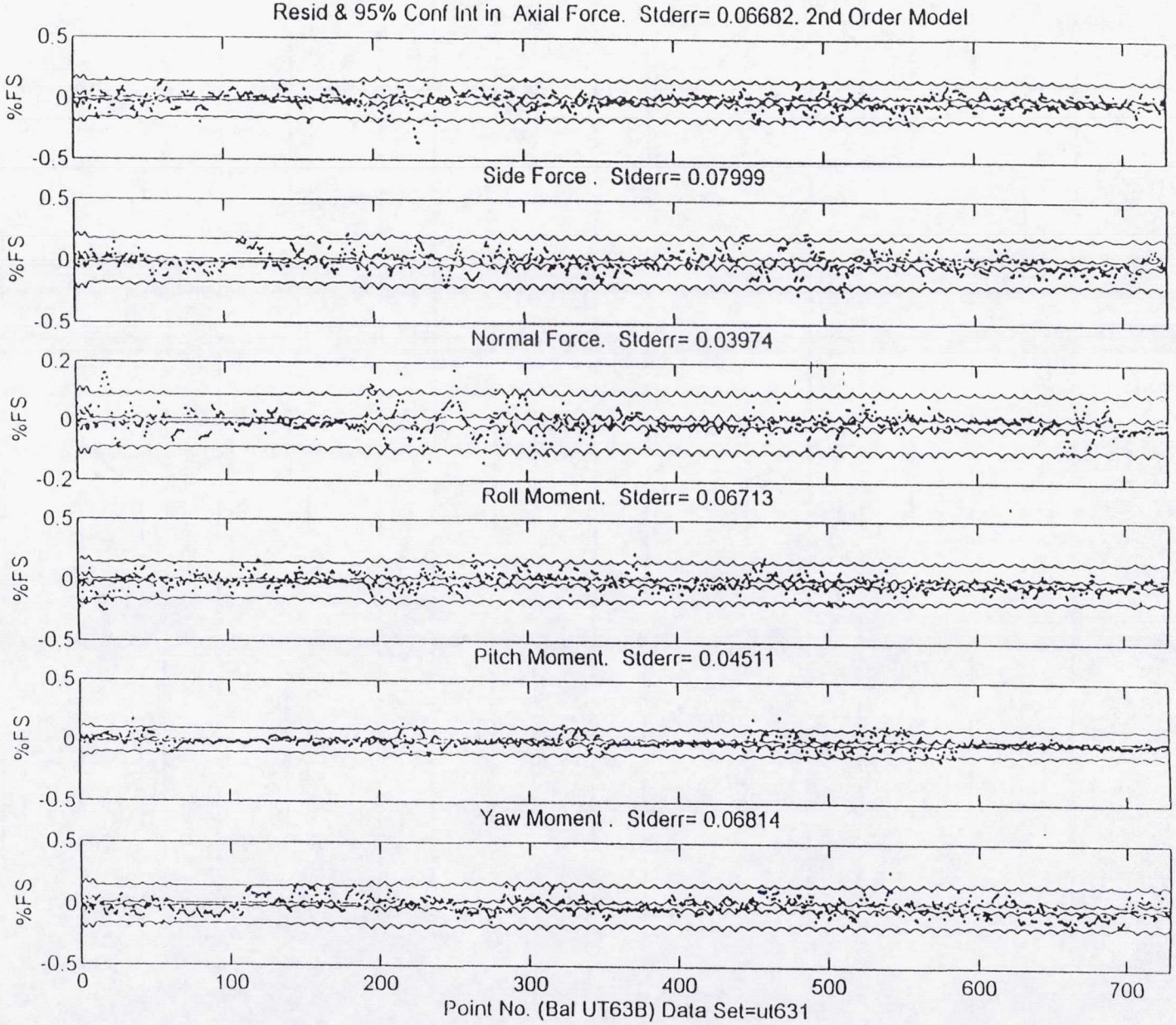

Figure 6. Residuals, 95% Confidence Intervals, & 95% Prediction Intervals for Machine Calibration with LaRC Loading Schedule (Run 631)

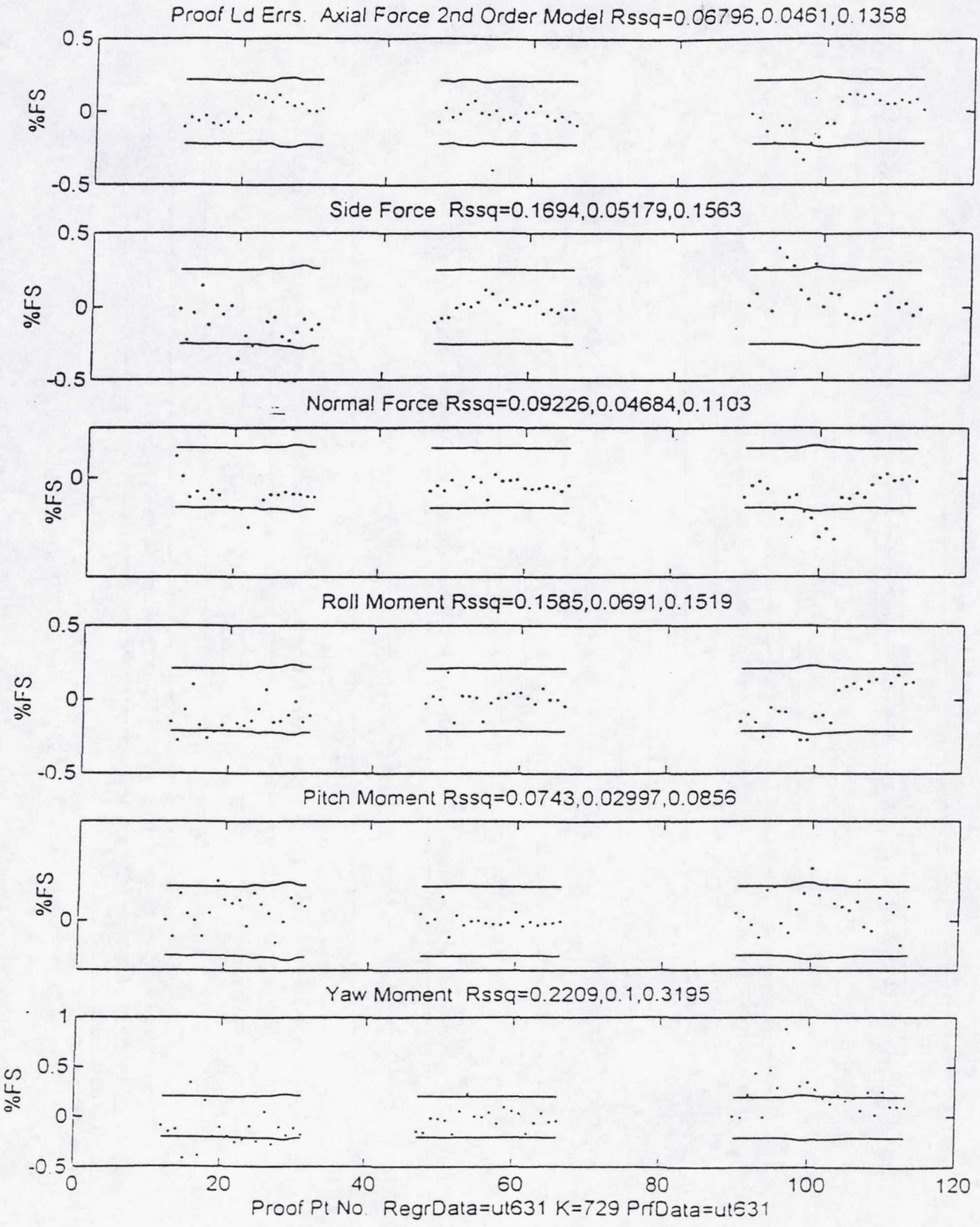

Figure 7. Checkload Errors with 95% Prediction Intervals for Machine Calibration with LaRC Loading Schedule (Run 631)

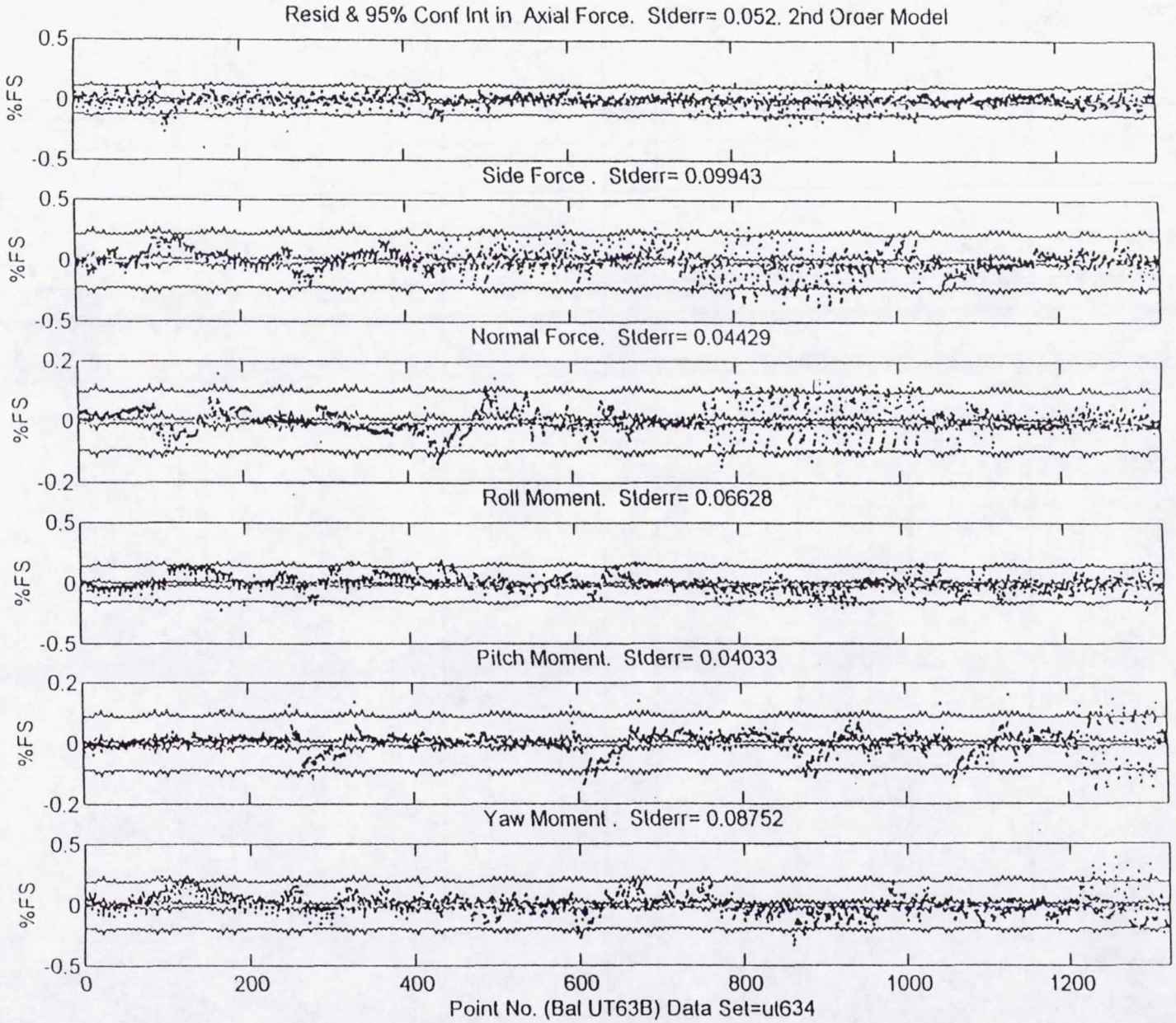

Figure 8. Residuals, 95% Confidence Intervals, & 95% Prediction Intervals for Machine Calibration with IAI Loading Schedule (Run 634)

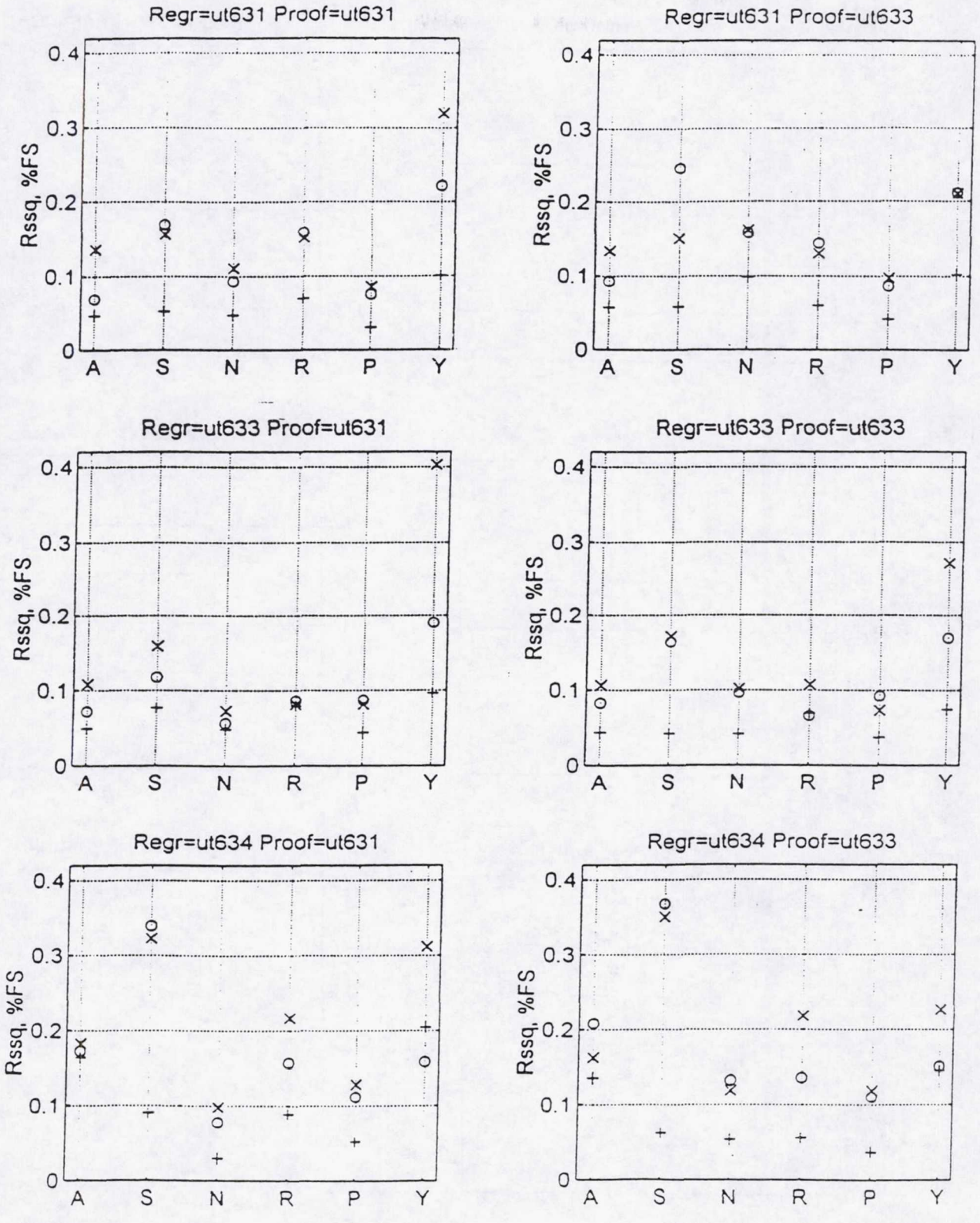

Figure 9 Cluster 1 Comparative Matrix Plots of RMS Checkload Errors

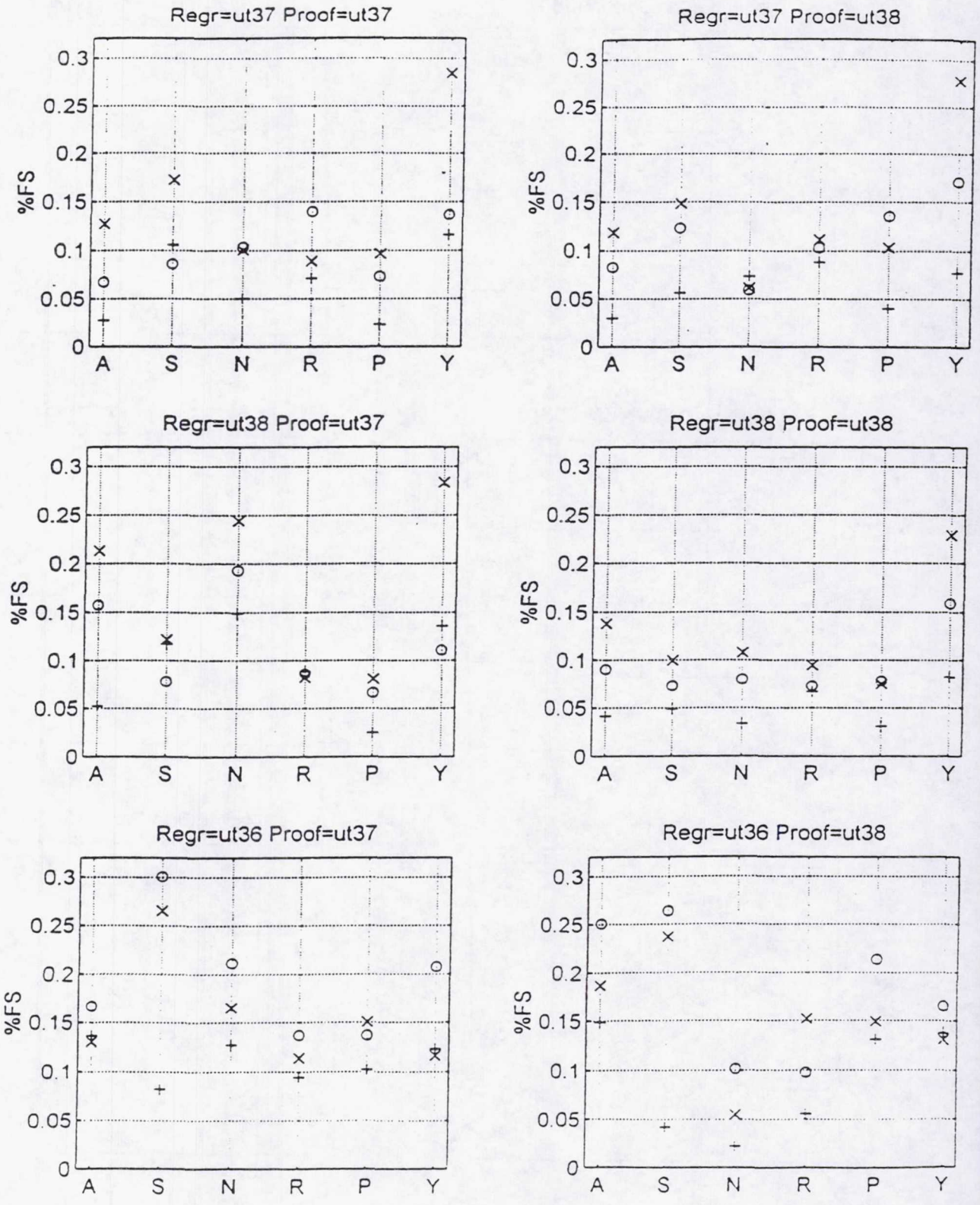

Figure 10. Cluster 2 Comparative Matrix Plots of RMS Checkload Errors

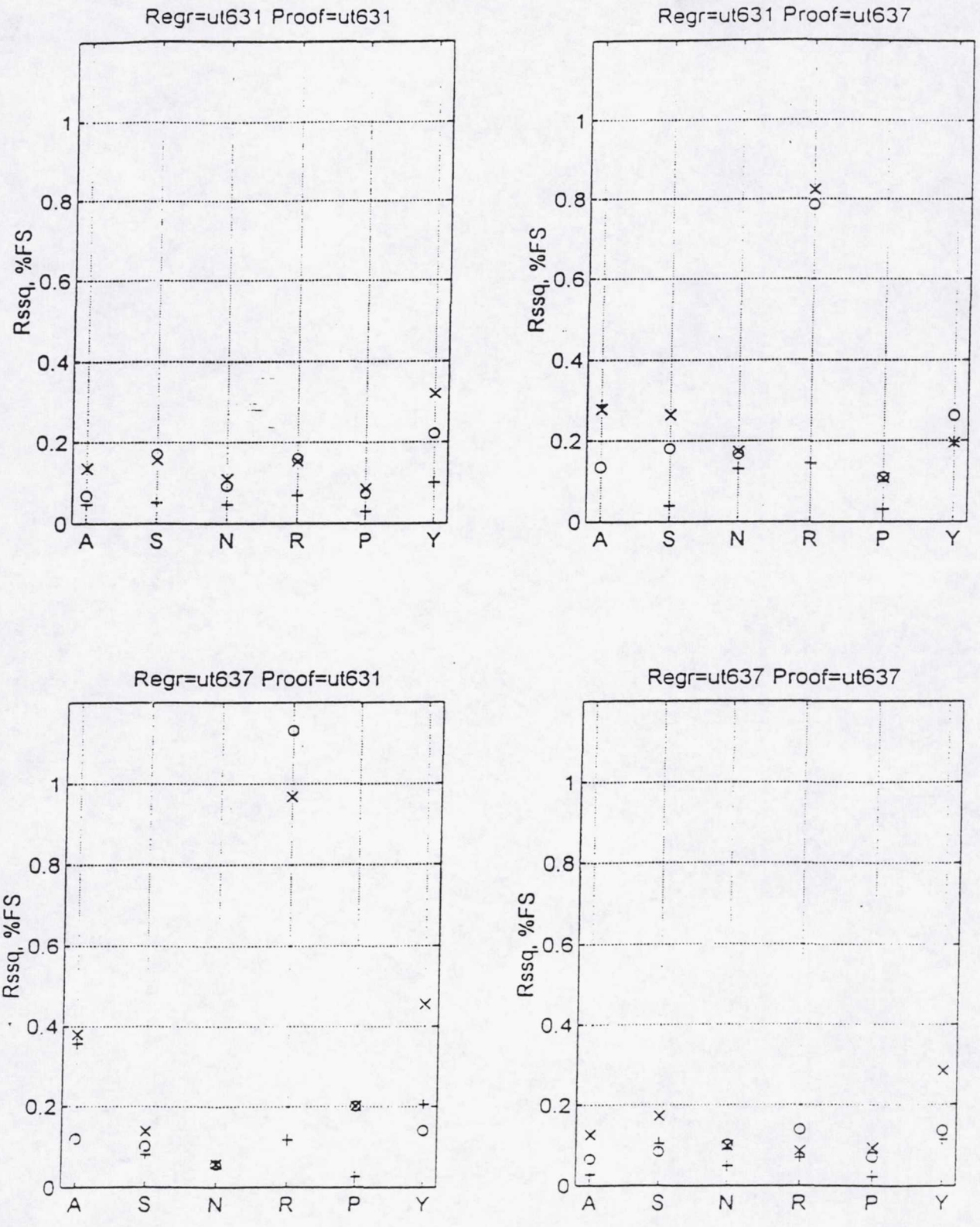

Figure 11. Inter-Cluster Comparative Matrix Plots of RMS Checkload Errors

Page intentionally left blank

DEVELOPMENT OF A SIX COMPONENT UNITIZED FLEXURED FORCE BALANCE

Dennis Booth
Force Measurement Systems
Micro Craft Technology

Introduction

Present day aircraft configurations and flight envelope requirements demand higher loads per unit diameter from wind tunnel balances. The constant drive to improve aircraft and to operate at very high angles of attack and potentially high sideslip angles. Additionally, these aircraft have exterior lines which limit the ability to provide large diameter balances or balances with higher deflections to meet these high load requirements. To test at these conditions, a wind tunnel balance must be capable of providing accurate model loads data under high combined loading conditions while allowing the model to maintain it's aerodynamic shape.

The following paper describes the development of a patented wind tunnel balance designed to meet the higher load requirements of these advancing testing needs. Based on the floating frame or two-shell concept, the Unitized Flexured Force Balance (UFFB) incorporates a separate axial element thus allowing for higher load per unit diameter, reduced primary load interaction, and greater flexibility in load range selection. Described is the design process, fabrication steps, gaging and calibration results of the UFFB. Supporting data and accuracies are provided for the prototype as well as for one of the flexured balances recently finished. The repair and refurbishing process on this balance type as well as design changes for upgrades of this balance concept will also be discussed.

Balance Description and Theory of Operation

The Flexured Balance is a force measuring device (i.e. directly measures two forces in both the normal and side force planes as well as roll and axial). Moments are resolved from the forces and distances to the Balance moment center. Shown pictorially in Figure 1, the balance consists of an outer shell, inner rod (i.e. inner shell), four axial adapters, and separate axial element. The outer shell measuring elements consist of eight integral sections of one or more webs completely machined prior to assembly with the inner rod. The inner rod is oven brazed to the outer shell over the journals at each end, using nickel braze AMS 4777 alloy. This brazing process thus permanently joins these two pieces into a single unitized piece, the only

way to separate the two pieces is to machine them apart. The flexured axial element is installed in the centerline bore of the inner rod. The axial element is pinned at each end (non-metric) to the inner rod (non-metric) and the center section (metric) attaches to the outer shell (metric) using the axial adapters and press fit pins. The wind tunnel model bore is fit to the journals on the outside of the outer shell and attaches to the balance using two pins. These pins are located one on top and the other on the bottom of the balance in the center between the forward and aft measuring elements. The tunnel support system attaches to the balance aft taper using two push-in set screws 180 ° apart and two roll pins also 180 ° apart.

The central section of the outer shell is floating on the web sections and restrained by the axial element. Two webs of each of the eight integral sections are strain gaged. The web sections are designed so that a force applied in either the normal or side direction will produce tension in one section of the webs and compression in the web section 180 ° opposite. The strain gages are applied to the center area of the webs. The combination of gages on the tension webs with gages on the compression webs (180° apart) into four arm active bridges measures the forces applied at each end of the balance in two planes. Using these force measurements and the distance to the balance moment center of each section the total normal force, pitching moment, side force and yawing moment are resolved.

The rolling moment is measured by gages placed near the center line of these same webs. The application of rolling moment to the outer shell will produce tension (or compression alternately) in the web sections around the circumference of the outer shell on either end. Selection of the rolling moment gages is accomplished using a technique we call 'Single Gage'. This process selects the bridge producing the highest output with minimum interaction. The rolling moment bridge consists of two four arm active bridges wired in parallel. One of these bridges is wired from selected gages located on the forward web sections. The other bridge is wired from gages located on the aft web sections. The propose of parallel bridges is to improve the overall characteristics of the final bridge, In some of the balances the roll bridges are wired to only use either the forward or the aft section of gages.

The axial force is measured using gages located on the webbed section of the separate axial element. The majority of the axial loads applied to the outer shell (from the model journal) are passed to the axial element since it is more rigid than the long slender webs attaching the outer shell directly to the inner rod. The separate axial element actually contains two measuring sections. Half of the axial force is applied to the forward axial element measuring section (pinned to the forward part of the inner rod) creating a tension load on this half of the element. The other half of the axial force is applied to the aft axial element measuring section (pinned to the aft part of the inner rod) creating a compression load on this half of the element. The load applied to both measuring sections forces the oval sections on either end to bend. This results in tension or compression stress on the center of the two long legs of the

oval section. Two strain gages are placed on the centerlines of each long leg and are wired into four arm active bridges on both the forward and aft axial oval sections. The purpose of this parallel bridge hook-up is to cancel the effects of differences in the outer shell, inner rod and axial element expansion due to temperature on the balance.

Design

The design rational for the Flexured Balance may be summarized as follows:

a) There are presently load limitations (per unit diameter) with standard force balance designs used over the last thirty years. These limitations occurred as a result of all applied loads acting on each element. The Flexured Balance reduces the magnitude of the loads in all directions except the primary load direction. The position of the gages on the flexured balance webs allows higher loads with lower gage stress than the force balance.
b) The Flexured balance allows for higher accuracy and closer matched output for all components, since the outer shell webs are gaged for only two components instead of three components (as on the standard force balance). This allows for less compromise of the outputs during design. The gages are placed on the much lower stressed center- line of the flexured web instead of the higher stressed ends (on the force balance).
c) Stiffness and dynamic frequency equal to the standard force balance.
d) Lower interactions since the axial element is flexured and separate from the higher stressed ends of the normal force and side force webs.
e) Lower zero shifts since the flexured action reduces the redundant stress of the webs on the standard force balance.
f) The flexures result in temperature effects that are lower and more repeatable.

The Flexured Balance concept required several major changes in the standard force balance design. The use of higher number of longer more slender normal force and side force webs (Figure 2) results in the high flexibility of the webs in the axial direction and allows 82% of the axial force load to be applied to the axial element. However, use of the long slender webs results in larger ear (the section that the webs attach to) stresses due to the required reduction in the ear size to accommodate the increase in web length. Therefore, the ear design was changed (Figure 2). The new design starts the ear at the edge of the group of normal force webs and increases in size across the balance freeing cuts. This redesign reduces the ear stress significantly and provides for a stiffer ear section allowing the design of longer length webs. The separate internal axial element (Figure 3) allowed the removal of the axial gages from the ends of the outer shell webs. This allowed the reduction of the design axial stress which increased the balance's overall maximum loads. This reduction of web size (and resulting

increase in flexibility in the axial direction), reduces the stress due to the bending of the inner rod significantly.

Fabrication

The fabrication process for this balance is very complex. Each step is carefully planned and parts inspected regularly to ensure conformance to design. The entire fabrication process requires approximately 3 to 4 months and is more involved than a standard force balance. Some of this is attributed to the learning curve involved with building a new balance, and some were attributed to the following design differences between the standard force and the flexured force balances:

- Increased web fabrication effort, since more webs are used.
- Fabrication of the separate axial element.
- Installation of the axial element in the balance with the installation of all press fit pins.
- Fabrication and installation of the four axial adapters.

The following represents the major steps completed during the fabrication of the prototype type Flexured Balance:

a) Machining of the outer shell (Figure 4) with webs completed to final size.
b) Machining of the inner rod (Figure 5) is completed.
c) Machining of the axial element (figure 6) is completed.
d) Assembly of the outer shell to the inner rod. Match drill and fit the eight pin holes through the braze joint of both the outer shell and inner rod.
e) Inspect the outer shell, inner rod, axial element and finished webs for dimensional accuracy prior to the braze operation.
f) Prepare balance for braze. Complete the braze and heat-treat operation. After the braze operation an ultrasonic inspection of the braze joints is performed.
g) Complete final machining of the outer shell and inner rod assembly.
h) Complete the final machining of the balance assembly including the attachments of the axial adapters and the axial element. Remove the axial element and complete the machining process on all components.
i) The final assembly (Figure 7) is completed after gaging and checkout of the axial element. The completed axial element is then installed in the balance. The axial element outputs are monitored during each step of the installation. This provides a history of the final preload of the axial element.

Strain Gaging

The axial element was gaged with two full bridges on each axial section (Figure 8). Each forward section bridge was wired in parallel with a bridge from the aft section. The parallel hookup cancels the output of the axial element due to differences in temperature expansion of the outer shell, inner rod and the axial element. The axial element was then tension loaded independently to insure accuracy of the axial bridges prior to installation in the balance. The repeatability of the bridges for full load was 0.033% full scale. The forward and aft section bridges indicated deviations from a straight line of +/-0.155 %. These deviations were equal and opposite and canceled when they where wired in parallel for the balance assembly. The deviation is caused by changes in the moment arm as the oval element is loaded. The axial element was then installed in the balance prior to outer shell web gaging. This procedure was followed in order to determine the axial element performance. Additional temporary gages were installed on the ends of the outer shell webs and balance ears to measure the stress in these areas. The balance was loaded with maximum calibration or design loads. The axial element performance, as well as the web stress and ear stress from the gages on the outer shell are shown in Table 1.

Table 1 - Initial Axial Element Loading Performance with Outer Shell Web and Ear Stresses.

WEB STRESS	EAR STRESS
(Max. PSI)	(Max. PSI)
43,580	21,190

INITIAL AXIAL ELEMENT LOADING
% FULL SCALE

Characteristic	(Individual bridges)	(Parallel bridge)
Hysteresis	0.17%	0.07%
Zero Shift	0.06%	0.02%
Non-Linearity	0.44%	0.28%
Interaction	3.30%	3.33%

The outer shell webs were then gaged (Figure 9) with three gages on each outside web of each set (48 gages in total). The individual gages on the centerline of the webs were wired into four arm active bridges to measure forward normal (N1), aft normal (N2), forward side force (Y1), and aft side force (Y2) depending on the location of the web. The remaining two gages on each outside web were preliminarily wired as single gages. Each component of the balance was loaded to maximum load and the N1, N2, Y1, Y2, Axial paralleled, and single gages were recorded and reduced. All full bridges performed very well and were ready for temperature

compensation. The single gages, which are used in the rolling moment bridges, were reduced using a special single gage computer program designed to determine the highest output and least interaction bridge configuration. The best bridges were wired on the forward and aft web section. These bridges were paralleled to cancel differential expansion in the same manner as the axial element bridges. Since all the data recorded during the loading indicated that all bridges and single gages operated with low interactions and good zero returns, the balance was prepared for temperature compensation. Six thermistors (Omega 44034) were installed in the balance. These thermistors were positioned as follows: one top forward on the inner rod, one top forward on the outer shell, one top aft on the inner rod, one top aft on the outer shell, one forward on the axial element flange and one aft on the axial element flange.

Temperature compensation was performed over a temperature range of 77° to 154 °F. The zero shift over this range was compensated within 0.10% of full scale.
The final gaging operation was to protect all the bridges and wiring with waterproofing. All bridges (except the axial element bridges which were done previously) were covered with Micro-Measurement, M- coat-A, air drying polyurethane coating. The axial element bridges were covered with both the Micro-Measurement, M- coat-A and M-coat-C, silicone rubber, both coatings were air dried.

Sensitivity Checks

The sensitivity or modulus compensation was evaluated by performing elevated temperature loadings on the balance by inclosing the balance and calibration equipment in a temperature controlled box and applying heat. The sensitivity effects being matched between the room temperature and the elevated temperature loadings within .10% of Full Scale. In the event that the modulus of the gages does not match that of the balance then either modulus compensation is installed or a correction constant is applied.

Calibration

The balance was set-up in the balance calibration rig. The balance was calibrated with the loading as follows in table 2.

Table 2 - Flexured Balance Load schedule

	Component	Load
a	Axial force	+/- 800 lbs.
b	Rolling moment (transferring weights)	+/- 4000 in-lbs
c	Normal force at stations inside the bridges	+/- 5000 lbs
	Normal force at the N1 and N2 bridges	+/- 2250 lbs
d	Side force at stations inside the bridges	+/- 2000 lbs
	Side Force at the Y1 and Y2 bridges	+/- 1000 lbs
e	Combination loads in combinations of two and	each at Max
	three components being loaded simultaneously	
f	Combination loads in combinations of all six	all at Max
	components being loaded simultaneously	

All loadings a), b), c) and d) were loaded from zero to full load at a minimum of five incremental load levels and repeat of all increments back down from maximum. Loadings e) and f) were completed with applying Normal, Side and Axial forces Pitch, Yaw and Rolling moment in combinations. The combination loads were applied in combinations of two and three components for loading e). These loadings group each component with the other components, (AF with RM, NF & PM, SF & YM), RM with NF & PM, SF & YM),(NF & PM with SF & YM) the NF & PM, SF & YM are applied at various locations to separate the NF from PM and the SF from YM. The f) loadings were with all six components loaded simultaneously in different combinations and at different percentages of full load. This data is used to perform a check of the matrix verses data that would be representative of wind tunnel conditions.

A summary of the basic data characteristics of the completed balance are in table 3.

Table 3 - Flexured Balance Characteristics

COMPONENT	N1	N2	Y1	Y2	R1	X1
Millivolt Output	9.50	9.38	8.68	8.89	6.30	8.65
Excitation Volts	6.00	6.00	6.00	6.00	6.00	6.00

Max Signal Conditioning Error +/-.02%
Axial Loadings
Data in % of Full Scale (% FS)

COMPONENT	N1	N2	Y1	Y2	R1	X1
Interaction	.50	.44	.11	.16	.44	----
Hysteresis	.01	.01	.01	.01	.01	.02
Zero Shift	.01	.00	.01	.02	.01	.01

Roll Loadings

COMPONENT	N1	N2	Y1	Y2	R1	X1
Interaction	.44	.72	.70	.38	----	2.76
Hysteresis	.03	.01	.01	.01	.04	.01
Zero Shift	.01	.01	.01	.01	.03	.01

Normal Force and Pitching Moment

COMPONENT	N1	N2	Y1	Y2	R1	X1
Interaction	----	----	2.26	2.42	1.87	.49
Hysteresis	.03	.03	.02	.02	.02	.02
Zero Shift	.04	.04	.01	.01	.01	.01

Side Force and Yawing Moment

COMPONENT	N1	N2	Y1	Y2	R1	X1
Interaction	-.44	.58	----	----	1.73	.29
Hysteresis	.01	.01	.05	.05	.03	.03
Zero Shift	.01	.01	.02	.04	.04	.01

The deflection of this type of balance are very low (compared with conventional single piece balances) and somewhat less than typical deflections of force type balances. Deflection data is shown in Table 4.

Table 4 - Flexured Balance Deflection Data

Maximum Loads	Normal Force	Pitching Moment	Side Force	Yawing Moment	Rolling Moment	Axial Force
Flexured Force	5,000 Lbs	15,000 In-Lbs	2,000 Lbs	7,500 In-Lbs	4,000 In-Lbs	800 Lbs
Deflection Degrees	.84	.47	.35	.34	.21	.001"
Single Piece	1200 Lbs	3600 In-Lbs	1200 Lbs	3600 In-Lbs	400 In-Lbs	400 Lbs
Deflection Degrees	.52	.94	.36	1.28	.24	.005"

The calibration data was used to determine the balance force and moment constants required for wind tunnel testing. In order to determine the balance accuracy, all of the original loading data was back calculated to loads and moments using the computed constants. The balances accuracy, in particular the first standard deviation error are summarized in Table 5.

Table 5 - Flexured Balance Calibration Performance Summary.
(Data in % of FS)

	Normal Force	Pitching Moment	Side Force	Yawing Moment	Rolling Moment	Axial Force
Maximum Loads	5,000 Lbs	22,500 In-Lbs	2,000 Lbs	7,500 In-Lbs	4,000 In-Lbs	800 Lbs
Primary Loadings	.025	.017	.030	.038	.123	.028
Combined Loadings	.040	.025	.048	.069	.208	.051

Several other special tests were completed on the balance. These tests included a creep test. Here each component was loaded to maximum load for two hours. Data was recorded every ten minutes. The results are shown in Table 6.

Table 6 - Creep Test Results
(in % of FS per Hour)

COMP	LOAD	N1	N2	Y1	Y2	R1	X1
AF	800 Ibs	*.00*	*.00*	*.00*	*.00*	*.00*	*.02*
RM	4000 in-lbs	*.00*	*.00*	*.00*	*.00*	*.01*	*.00*
NF	5000 Ibs	*.00*	*.02*	*.00*	*.00*	*.00*	*.00*
SF	2000 Ibs	*.00*	*.00*	*.02*	*.03*	*.00*	*.00*

To insure a proper glue bond area (no air bubbles), the installation of the balance in a vacuum chamber at 9.0 PSI absolute for 30 minutes. The data in percent of full scale is shown in Table 7.

Table 7 - Vacuum Chamber Test Results

Pressure	Comp.	N1	N2	Y1	Y2	R1	X1
9.7	% change	*.01*	*.03*	*.03*	*.00*	*.01*	*.02*

Repair and Refurbishment

The Flexured balance design allows for easy access to the strain gages for any check-out or repairs that might be needed during the life of the balance. The outer shell is readily accessible and the axial element is removable for any needed repairs.

The recent need for the replacement of the axial element on the prototype balance was necessitated by a severe overloading condition to the axial component. The damaged axial

element and the associated hardware were removed from the balance. The manufacturing, strain gaging and installation of a new axial element was performed on this balance. With the replacement element installed the balance was recalibrated with the data compared to the original calibration, the overall performance and characteristics of the balance did not change significantly. The balance has since performed without incident on numerous test with satisfactory results in all areas. The data from wind tunnel tests conducted prior to the replacement of the axial element were compared to data from tests conducted after the balance was repaired, this data from these two tests plotted on top of each other.

The repair and replacement of the balance's cable is accessible at the aft web section of the outer shell. The need to regage the outer shell's gages doesn't require the removal of the axial element thus saving time and reducing the effort required for rework on the balance.

SUMMARY

The following is a summary of the key elements effecting the design, fabrication, gaging and calibration of the Flexured Balance. While we were extremely pleased with the performance of this unit, a number of issues have been addressed and improved upon in the design and development of subsequent balances.

a) It took a great effort to optimize the computer stress program, this was required because of the large increase in maximum design loads. All program changes were checked by installation of strain gages on the critical areas in order to check the computer stress calculations by application of loads. The stress programs are now more automated to improve efficiency and maximize balance design criteria.
b) The fabrication process is more involved for several reasons.. We have made significant progress in the optimization of the fabrication process, thus insuring a high quality balance while controlling the fabrication costs and schedules.
c) The use of the flexured force design in the air flow balance design concept will be more complicated because the axial flexure element. This element is installed in the centerline bore which is used for air supply tubes on the air flow balance. We are considering axial element designs that can solve this problem.

The flexured balance design produced many improvements. These improvements were anticipated when originally considering the development of this balance.

a) The web stress was much lower on the flexured balance than the standard force balance with the maximum load three times as large. The standard force balance maximum load, for this diameter could not be increased because of the high inner deflection stress

imposed on the webs. This flexured balance design will allow us in the future to obtain even greater loads. The 2.00 diameter balance maximum load could be increased to the 3500 lbs to 6000 lbs range with the use of high strength steel and one of several improved web designs, as well a new generation of flexured force balance design.

b) The gaging was simplified, since a lower number of strain gages were used than the standard force balance
c) Temperature effects were reduced and more repeatable. The axial element was temperature compensated before installation and didn't change after assembly.
d) The interactions were significantly lower and more linear than the standard force balance or those from a single piece moment beam type balance.
e) The zero shifts and drift were especially low on all components.

This balance is very stiff for a high load 2.5 inch diameter size.

Future Improvements

The planned improvements for the near future include the following

a) Further increased load capacity per unit diameter.
b) Further flexuring of additional elements for increased accuracy.
c) Improved shielding of gaged sections, for additional protection of gaged sections.
d) Increased loading schedule for calibrations, to offer larger data set which will better define the balance's matrix for various testing conditions. The increased loadings will be possible with use of the Automatic Balance Calibration System.

Page intentionally left blank

TYPICAL BALANCE TEST TASKS FOR AEROGASDYNAMIC FACILITIES OF TSNIIMASH.

Vladimir I. Lapygin,
Vyacheslav I. Lagutin
(TSNIIMASH, Russia)

SUMMARY

General survey of balance tests which provided on the facilities of TSNIIMASH's Centre of Aerogasdynamics is given. Among the tasks solved by balance tests the following are considered: investigation of complex systems (e.g. launch vehicle with strap-on blocks); study of loading of flight vehicle elements (stabilizers and control surfaces, nozzles, etñ.); investigation of models with simulation of power or control engines jets; investigation of models with parañhute; study of launch pad elements loading; study of model loading during heat protection cover erosion in arc-heater tunnel; measuring of forces during models free oscillation; measuring of short-time loading (e.g. in piston gasdynamic units, in shock tubes, in shock waves rigs, in vacuum chambers).

To illustrate peculiarities of provided tests technique and applied measuring means several examples are given.

INTRODUCTION

Center of Aerogasdynamics (CAGD) which history started in 1947 is a significant part of Central Research Institute of Machine Building (TSNIIMASH) - leading Russian institute in rocket and aerospace technology. The Center works in theoretical and experimental aerogasdynamics of rocket - space objects. The widely known results of the work concern aerogasdynamic aspects of Soviet and Russian launch vehicles Vostok, Zyklon, Kosmos, Proton, Zenit, Energia; various missiles; space vehicles Vostok, Soyus, Zond, Buran; landing modules Luna, Mars, Venera; orbital stations Salut, Mir and others.

To realize experimental investigations there is a complex of aerogasdynamic facilities which includes a wide variety of various scales conventional and unconventional (e.g. piston gasdynamic unit - PGU) wind tunnels with Mach number range from subsonic to hypersonic; shock tubes; vacuum chambers and rigs for special items studying (launch vehicle take off, stage separation, space modules docking - undocking, landing, etc.). General performances of the CAGD's principal facilities are given in Table.

Wind tunnels			
	Mach number range	Size of nozzle exit [m]	Reynolds number range [per m] $\times 10^{-6}$
U - 3	0.25 ... 1.75	0.6 x 0.6	6 ... 20
U - 3M	0.2 ... 3	0.6 x 0.6	0.9 ... 90
U - 21	0.2 ... 1.8	1.4 x 1.4	0.04 ... 100
U - 1	2 ... 4	0.4 x 0.4	30 ... 85
U - 4M	2 ... 6	0.6 x 0.6	0.8 ... 200
U - 6	6 ... 10	∅0.27; ∅0.35	7 ... 70
U - 306 - 3	2 ... 10	∅1.2	0.5 ... 200
PGU U - 7	6 ... 20	∅0.4; ∅0.8	0.1 ... 300
U - 11	6 ... 15	∅0.4; ∅0.8	0.1 ... 300
Shock tubes			
U - 8M	12 ... 18	∅1.5	up to 1
U - 12	0.5 ... 10	∅1.5	1 ... 20
Vacuum chambers			
U - 22M	vol. - 170 m^3, diam. 5 m		
U - 22	vol. - 1000 m^3, diam. 8 m		

The provided tests mostly include balance measurements and many conventional and specialized balances are used in dependence on peculiarities of applied facilities, test task and tested model shape and size. Now CAGD has a set of strain-gage balances (more than two hundred actual units) various type and size for loading range from grams to tons and various combination of measuring loading components values.

Let us consider some typical balance test tasks.

A number tasks concern balance tests of various reentry vehicles (e.g. ref. 1). In the most cases we deal with two groups of reentry vehicle configuration. The first is large drag and small aspect ratio bodies, i.e. blunted cones with large vertex angle, segmental and segmental - conical bodies (e.g. "Mars", "Soyuz" reentry vehicles). The second group includes small-drag cones with small vertex angle and bodies with wings (large-lift) such as aerospace vehicle "Buran". In many cases the tests are provided in wide range of M, Re numbers and angle of attack. For example in cases similar to determination of aerodynamic characteristics (ADC) for objects "Soyuz" type it is necessary to provide tests in ranges of Mach number 0.6...15, angle of attack $0...180^0$ and Reynolds number $10^5...10^7$.

Launch vehicle ADC determination is another large group of balance test tasks (e.g. ref. 2). Nowaday launch vehicles have complicated configurations (e.g. "Energia - Buran" system with several strap-on blocks) and during tests several balances (2...4 units) can be used simultaneously both in cases of complete model test and strap-ons separation test.

ADC determination of models with parachute systems is a task from time to time met in our practice. Two varieties of the task are possible. The first is ADC determination for parachute system in presence of model body. The second is "body + parachute" system ADC determination. As an example it was a task when various reusable "Energia" boosters were researched. On Figure 1 such a model mounted (through a balance) on wind tunnel injection - incidence changing gear is shown. It can be seen a parachute fixing mechanism which provides stretching the parachute during model injection into the wind tunnel test section (to avoid the parachute and balance overloading) and their releasing after the model injection.

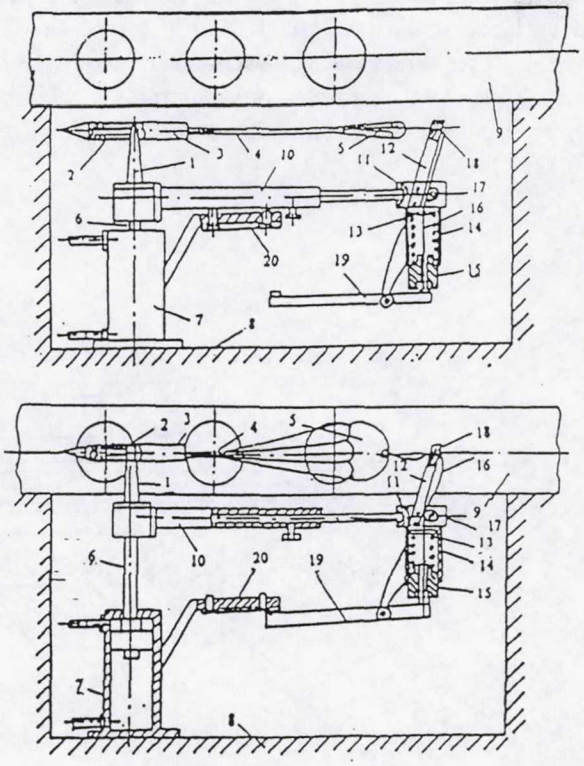

Figure 1. Scheme of "model + parachute" system balance test

1 - main model support; 2 - balance; 3 - model; 4 - parachute links; 5 - parachute; 6, 7 - rod and pneumatic cylinder (respectively) of model injection mechanism; 8, 9 - wind tunnel working section and test channel; 10 - additional support; 11 - fork; 12 - upright; 13 ... 18 - parachute fixing mechanism (spring, case, piston, link, role and slide, respectively); 19, 20 - driver of the fixing mechanism (lever and rest)

One of the important task is measuring of forces - moments acted on flight vehicle elements (e.g. stabilizers and control surfaces, nozzles, etc.). Thereat the measurements can be provided either with a separate element or with the element in composition with the model of tested flight vehicle. As an illustration of such kind test a scheme of deflected nozzle hinge moment studying is presented on Figure 2. Peculiarity of the scheme consists in usage of so - called "false nozzle" mounted on tubular type balance. The false nozzle is a thin shell with outer shape similar to tested nozzle and separated from it by small gap. During the test the balance provides measuring of 4...6 components aerodynamic loading of the nozzle in presence of jet through the nozzle.

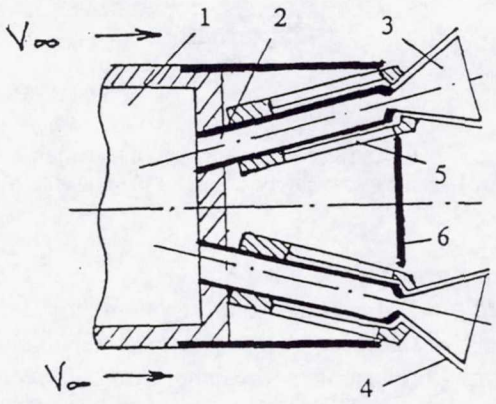

Figure 2. Scheme of deflected nozzle hinge moment measuring.

1 - pressure chamber; 2 - air supply pipe; 3 - nozzle; 4 - "false nozzle"; 5 - multicomponent balance; 6 - base case.

Investigation of flight vehicle models with jets simulation is a task very often met in CAGD's practice. There are several variants of the task: ADC determination in cases of power or reactive control system (RCS) engine jet with jet thrust or without it. In dependence on the case various balances and test technique have to be used. Two examples are illustrated on Figure 3. and Figure 4. A scheme of balance test of a model of "Soyuz" space vehicle emergency escape system is shown on Figure 3.

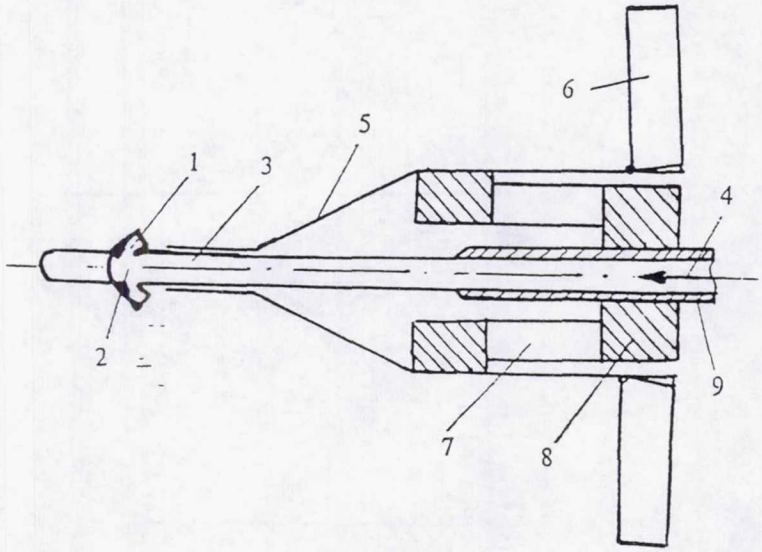

Figure 3. Scheme of balance test of emergency escape system model with jet simulation
1 - nozzle; 2 - pressure chamber; 3 - pipe of air supply; 4 - compressed air; 5 - model case; 6 - stabilizer; 7 - six component balance; 8 - balance base; 9 - sting.

There is a case of balance measuring in presence of power engines jets (i.e. measuring without jets' thrust). During the test aerodynamic loading the escape system (without nosepart) is determined at the beginning without jets and then with jets. Loading of the nosepart is found separately by using an additional balance. A scheme of ADC determination of cone model with RCS jets is given on Figure 4.

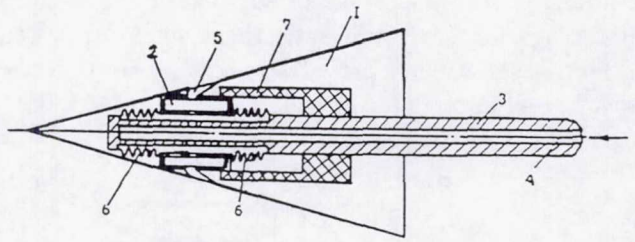

Figure 4. Scheme of balance test of models with RCS
1 - model body; 2 - pressure chamber; 3 - sting; 4 - gas supply channel; 5 - nozzle of RCS; 6 - metal bellow; 7 - multicomponent balance.

Peculiarity of the scheme (in compare with Figure 3) consists in loading determination together with jets' thrust. It can be used two variants gas supply systems for jets generation: external (with model and gas supply pipe connection by a flexible element - e.g. metal bellow - ref. 3) and internal (e.g. solid propellant gas generator). During the test at the beginning model loading is determined in vacuum condition without external flow (i.e. only jets thrust to be measured) then model's ADC are obtained into acted flow without jets and then - together with jets.

Among aerogasdynamics problems of launch vehicle taking off some balance test tasks are also existed. It may be experimental investigation of aerogasdynamic loading (which is a result of launch vehicle engines jets action) of launching containers, cable masts, launching silo or pad elements, etc. The only principal peculiarity of such kind tests is launch vehicle model nozzle (or nozzles) jet as a flow generator. The jets may be cold or hot (in cases of gas heaters or propellant grains usage). As measuring units conventional or special balances can be used.

One of the new balance test task is study of models loading during heat protection cover erosion in arc - heater tunnels (it is a cooperative work of CAGD and Heat Exchange Research Center of TSNIIMASH). In our practice we have two variants of the tests. The first variant has no sufficient difference (from balance tests point of view) from the tests in conventional wind tunnels excepting high temperature flow (1500 ... 4500^{0}C) problem. Solution of the problem is found either by limitation of test duration or by usage of balance cooling systems. It must be noted that model's heat protection cover is enough good mean not only for the model (or flight vehicle) frame, but for the balance too and as a rule test duration of 10 ... 15 s is enough in order to make negligible the most problems of the balance heating. During the test variations of model surface and loading are observed. The second variant presents the model testing inside the tunnel's nozzle (ref. 4). The conical model is mounted with a gap respect to nozzle wall (see Figure 5) by means of a special in-model balance and an automatic model feed mechanism.

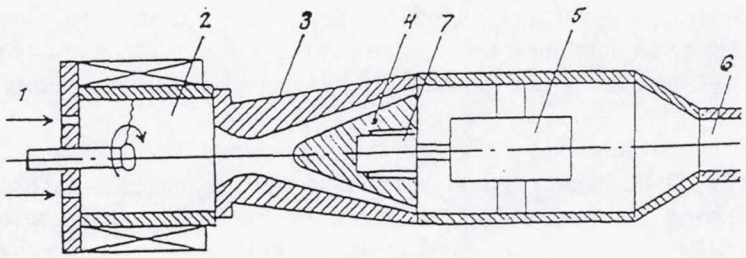

Figure 5. Arc-heater wind tunnel balance test

1 - gas supply; 2 - high pressure chamber with arc-heater; 3 - nozzle; 4 - model; 5 - model feed mechanism; 6 - exhaust channel; 7 - internal strain-gage balance.

A peculiarity of the test is very strong conditions on the model surface (e. g. heat flux 300 ... 2000 kcal/m^{2}s at surface temperature ~ 3000^{0}C and tension of friction 800 ... 3000 N/m^2) required for intensive erosion of model's heat protection cover and closed to natural flight ones. Another peculiarity is necessity (as a rule) to sense during the test rather small changing of the model loading when the average level of loading is very high (e.g. for a model with diameter ~ 150 ... 180 mm axial force value may be about 25 ... 30 kN while role moment changing is about 10 ... 20 Ncm). It must be noted that the considered tests can be complemented by tests in conventional wind tunnel (i.e. balance tests of the eroded models).

A large group of balance tests concerns tasks of short duration loading measurements. We met the tasks in cases of PGU (test duration 0,1 ... 1 s), shock tubes (0,03 ... 0,15 s), vacuum chambers (0,03 ... 0,5 s) and specialized rigs (0,03 ... 0,5 s) tests. But the cases are sufficiently different by loading level. The mostly hard strain - gage balance tests provided in vacuum chambers concern problems of high altitude docking-undocking. In these cases level of loading is tens or hundreds grams (for typical model diameter 50 ... 150 mm). As an example it was a task of determination of solar battery panels gasdynamic loading due to RCS engines jets action when docking-undocking problems for "Apollo"-"Soyuz" and "Space shuttle"-"Mir" programs were investigated. Other cases sometimes are rather difficult too. As an example it is rocket structure elements (e. g. nozzle) shock waves loading measurement (provided in a

specialized rig) during engine ignition. The task is included in aerogasdynamics problems of launch vehicle taking off or stage separation.

An example of the similar task is investigation for cone-cylinder model of aerodasdynamic interaction of plasma jet and supersonic flow (ref. 5). Scheme of testing model is shown on Figure 6. Test duration (plasma generator work duration) is 0.05 ... 0.1 s.

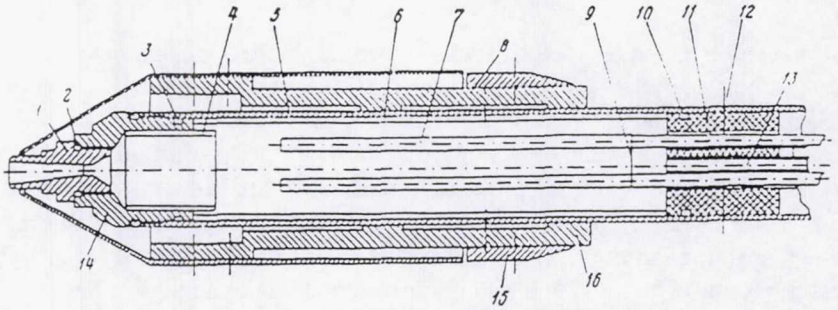

Figure 6. Scheme of balance test of model with plasma generator.

1 - nozzle; 2, 3, 10 - rubber rings; 4, 6 - electrical insulators; 5 - model body; 8, 12 - fixing screws; 9 - thin copper wire; 11 - teflon insulator; 13 - pipe for pressure measuring; 14 - adapter; 15 - base shield; 16 - strain-gage balance.

In the most cases short duration loading measurements can be realized and acceptable accuracy can be reached only by careful choice of "model - strain - gage balance - sting" system elements characteristics (it means that mass and moment of inertia of the model must be provided minimal with sufficient rigidity, rigidity of the balance and the sting must be provided maximal with the balance sufficient sensitivity).

One of the unconventional balance test technique is aerodynamic load measuring during free oscillation of model hinged in wind tunnel flow. Two variants of applied balance are possible: balance combined with base sting (i. e. immovable balance and oscillated model), balance combined with adapter for the model mounting (i. e. oscillated model and balance). In dependence on the hinge design (number of degrees of freedom) the balance may be with various number of measured components. In addition to force measuring elements the balance is also supplied by transducers of model angle attitude and angle acceleration. One of the typical balance design is shown on Figure 7.

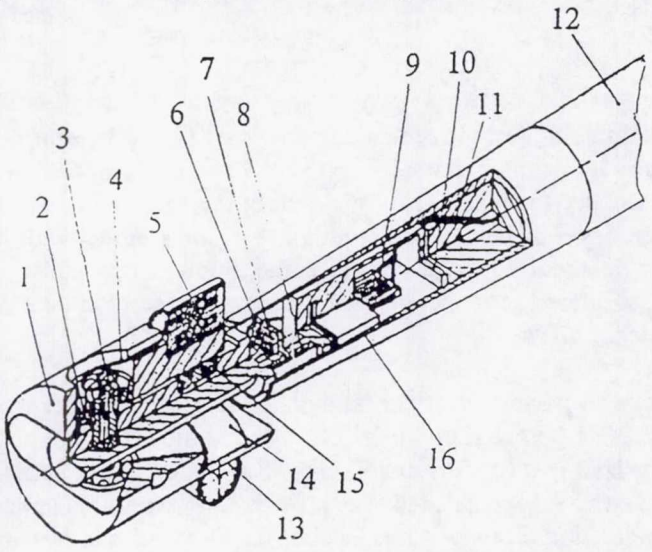

Figure 7. Strain-gage balance combined with free oscillation device.

1 - adapter for testing model mounting; 2 - ball bearing; 3 - rod (axis of oscillation); 4, 11 - wires; 5, 13 - inductive type transducers of angle rate and acceleration, respectively; 6 - sensitive element of Y-force dynamometer; 7, 9 - strain gages;8, 10 - flexible elements of Y, X - force dynamometers; 12 - sting; 14, 15 - armature and inductive type sensitive element of angle attitude transducer; 16 - shield.

During the test instantaneous values of aerodynamic X, Y force components, angle attitude, angle rate and acceleration are measured. Aerodynamic moment component is obtained by calculation through angle acceleration. In addition to usual for balance test set of ADC the free oscillation technique allows to obtain some unsteady aerodynamic characteristics (e. g. pitching moment static derivative and pitch damping derivative). It must be also noticed that the technique in cases of model configurations with large base size (e. g. conical or segmental bodies) provides ADC study in wide range of angle of attack (sometimes up to $\pm$ 30 ... 40^0 respect to trim angle of attack if coincide flight vehicle center of gravity and position of balance hinge). Besides in cases of Strouhal number simulation (together with M and Re numbers) it appears a possibility of ADC studying under condition more close to natural flight than usual ones. It is a very important circumstance when model flow - around structure (transition and separated zones) rearrangement lag takes place.

Free oscillation balance test technique may be also used in combination with other techniques: surface pressure distribution measuring, engines jets simulation, flow visualization, etc. For example Figure 8 presents a shadowgraph of a free oscillated conical model with jet of brake engine when surface pressure distribution and aerodynamic forces were measured (with usage of sting-balance, pressure transducers of inductive type and in - model solid propellant gas generator).

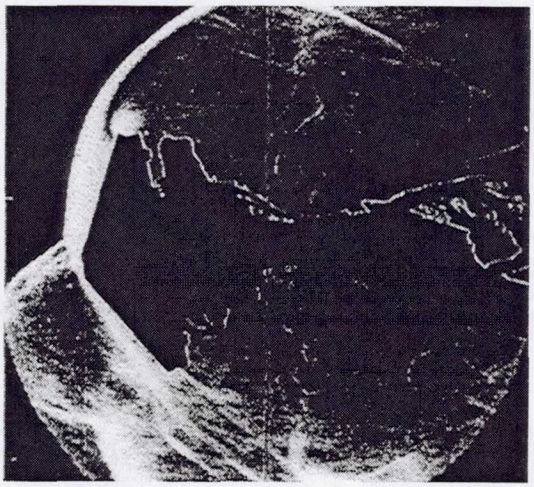

Figure 8. Free oscillation balance test with pressure distribution measuring and jet simulation ($M_\infty = 6$).

CONCLUSION

Considered tasks are not comprehensive but only typical ones for CAGD practice. New aerogasdynamics problems and new balance test tasks arise time by time following development of cosmonautic and rocket technique.

REFERENCES

1. Kazakov, M.N.: Selection of Wingless Descent Vehicle with Increased Lift-to-Drag Ratio, *J. Cosmonautic and Rocket Engineering*, no. 3, TSNIIMASH, Kaliningrad, Moscow reg., 1995, p. 101.

2. Kazakov, M.N.; Kudryavtsev, V.V.; and Lapygin, V.I.: Strap-on Boosters and Stabilizer Mounting Error Influence on Cluster Configuration Rocket Launcher Aerodynamic Characteristics, *J. Cosmonautic and Rocket Engineering*, no. 3, TSNIIMASH, Kaliningrad, Moscow reg., 1995, p. 95.

3. Ganiev, Yu.Kh.; Golubin, N.V.; and Shmanenkov, V.N.: Techniques for Experimental and Theoretical Investigations of Aerodynamic Characteristics of a Flight Vehicle Fitted with Gas Jet Control, *J. Cosmonautic and Rocket Engineering*, no. 3, TSNIIMASH, Kaliningrad, Moscow reg., 1995, p. 113.

4. Zolotarev, S.L.; Lagutin, V.I.; Lapygin, V.I.; and Murzinov, I.N.: Methodology of Pilot Research on the Influence of Hypersonic Space Vehicle Surface State Change on their Aerodynamic Characteristics. *Theses and Abstracts of Reports of International Conference on Scientific - Technical Problems of Cosmonautics and Rocket Engineering*, TSNIIMASH, Kaliningrad, Moscow reg., Apr. 1996, p. 164.

5. Gordeyev V.P.; Krasilnikov A.V.; Lagutin V.I.; and Otmennikov V.N.: An experimental investigation of possibilities of aerodynamic drag decreasing at supersonic speeds with plasma technique usage, *Academy of Sciences News, "Liquid and Gas Mechanics"*, no. 2, Moscow, 1996, p. 177.

ACCURATE AXIAL FORCE MEASUREMENT WITH SMALL DIAMETER BALANCES UNDER HIGH NORMAL

D. Levin and M.Ringel
Department of Aerospace Engineering, Technion I.I.T.,
Haifa, Israel.

SUMMARY

Accurate measurement of the aerodynamic drag by internal balances in wind tunnel testing is a difficult task to accomplish. The adverse relation between the balance sensitivity and stiffness leads to designs with high nonlinear interactions. The problems become even more acute when the balances are of small diameter (less than 3/4 inch), and when the loading in the pitch and yaw direction acting simultaneously are much higher than the axial load in the order of several hundreds kgxcm. There is no one solution that can be prescribed to overcome the problems. This paper presents several technical improvements that have yielded enhanced accuracy in the axial force measurement in the Technions wind tunnel laboratory. The first improvement was obtained by a modification of the drag measuring element design. Additional improvement was obtained by a new calibration rig, and a more comprehensive data reduction process. A different approach is based on disengaging the drag element from the other five components, thus evading the nonlinear interactions.

INTRODUCTION

The design of small-diameter accurate six component internal balance for wind tunnel force measurements, has been a long uphill struggle for wind tunnel laboratories. The reasons for this difficulty are the inherently conflicting demands made on the balance design. The demand for high sensitivity requires flexible metric elements, a demand on low level of interaction between the measuring elements prescribes that the measuring element be very tiff in all directions except the one direction being measured, and that the flexures between the metric elements be elastic to transfer only the force being measured. High overall rigidity is also important to ensure small deflections and avoid nonlinear elastic phenomena and lesser uncertainty in the spatial positioning of the model.

Two major approaches were taken to meet those requirements. A composite balance approach that allows mechanical motion between metric elements, and an integral balance approach. The composite balance approach meets most of the requirements mentioned above, however it suffers from friction induced uncertainties and hysteresis, Gorlin and Slezinger (ref. 1) . An integral balance design eliminates the friction induced inaccuracies, but tends to amplify the interaction between the metric elements due to the structural distortion and the non linear elastic phenomena. The reduction of these interactions by means of

complicated designs, expensive manufacturing and comprehensive calibration and data reduction processes, still leaves the measurement of the axial force lacking in accuracy.

The axial direction in the sting balance is highest in rigidity, yet, it has to measure the typically smallest component of the aerodynamic load. Thus the metric element is to be made very sensitive. Such a typical design shown in Fig. 1, results in sensitivity not only to axial load, but to the structural distortion generated by the other load components. This distortion is non linear, and amplified when the element is simultaneously being loaded with axial load and bending moments resulting from loads perpendicular to the balance axis, such as normal and side force, and pitching and yawing moments.

In general there are two sources that cause interaction output. The first source is related to strain gage techniques, and the second one to the structural mechanism of the axial force element. Strain gage techniques and methods for electrical, thermal and mechanical compensations were presented by White (ref. 2), and Seginer et al (ref. 3). Improvement can be achieved by using new type of Self-Temperature-Compensated (STC) strain gages as will be discussed later. The second group of interaction is related to the structural mechanism of the balance and the combined nature of the aerodynamic loading. The main constituents of this group are : 1) Machining inaccuracies

2) Reorientation of the loads due to balance deflections

3) Deflection of the main strut of the axial force measuring element

4) Additional deflection of the drag flexures due to combined loading

While machining inaccuracies can be reduced by careful design and new manufacturing technique, it has been shown by Richard (ref. 4) that a non linear interaction of an orthogonal force is inherent. Shown in Fig. 2 is a sketch of a balance under a normal load N. A false axial force reading i_D is recorded due to this deflection, and is proportional to N^2/I. This interaction can be reduced only by increasing the stiffness (moment of inertia) or the diameter. A second false axial force reading is recorded when the flexure beams of the axial force element are deflected under combined normal and axial force loads, as shown in Fig. 3. To the axial load deflection δ_D, a false reading δ_N is added due to the normal load effect. This interaction is linear, it can be reduced by increasing the strut stiffness at the expanse of reduced sensitivity. Calibration and data processing permit making allowance for interactions, as long as the non linearity is substantially low.

IMPROVEMENT OF THE AXIAL FORCE MEASUREMENT ACCURACY

Higher accuracy of the axial force measurement is being obtained by improvements in all the parameters that contribute to those inaccuracies. Modern machining techniques such as Electrical Discharge Machining (EDM) or Electron Beam Welding (EBW), yield reduced machining inaccuracies, and allow for higher level of design features. New strain gages technology offers Self Temperature Compensated (STC), such as the FTKB2-S10075000 manufacture by Micro Measurement group Inc. This gages have a 5KΩ resistance and can support higher input voltage (18-36 V) in the Whetstone bridges, thus obtaining higher sensitivity without increasing hysteresis effects or overheating, and without decreasing the stiffness. However the main

effort is invested in new designs of the drag measuring element, and more cumbersome calibration and data reduction procedures.

Design of a New Drag Element

In a conventional drag element as shown in Fig. 1 the metric beam of the drag element is one of the beams carrying the loads. This beam is deflected under combined axial and normal loads in the fashion presented in Fig. 3. A new design of the axial force element is shown schematically in Fig. 4. In this design the metric flexure is not carrying the main loads. It is connected to the main strut, and follows the deflections of the main strut in a fashion that cancels the asymmetric output due to the torque generated by a pitching moment, the effects of the pure axial and normal forces on the metric flexure output is presented in Fig. 5. The deflection of the drag element under combined loads is presented in Fig. 6. A comparison test was conducted between two similar balances differing only by the drag element design. The parasitic drag output as a function of the normal force and pitching moment is presented in Fig. 7 and Fig. 8 respectively. The nonlinear part of the interaction is expressed by the standard deviation (S_tD_v) of the linear curve. It is evident that the improvement in this term is large, by an order of magnitude for the normal force output where the curve is practically linear, and 60% improvement for the pitching moment interaction output.

Calibration and Data Reduction

Even with the new drag measuring element design, the inherent interaction in the balance output prevails, and needs to be resolved by appropriate calibration and data reduction processes. Since the output of the axial force measuring element is a nonlinear one in essence, second order calibration and data reduction procedures are required. An analysis of the second order calibration technique was carried out by Smith (ref. 5), resulting in a 6x6 first order interaction coefficient matrix, and a 6x21 second order interaction coefficient matrix. The equation is being solved iteratively. It is essential to conduct a careful calibration in order to resolve and identify each of the coefficients accurately. For this target, a calibration rig described by Ringel, Levin and Seginer (ref. 6) was designed. The main features of the calibration rig are: Dead weight loading. Moment loading with force smaller than 10% of the force full scale, after the recommendations of Dubois (ref. 7). Pulleys used only for the axial force loading, with extreme care to minimize friction by applying bearings and V notches. Use of counterweights to simulate a "weightless" sleeve, so a "zero shift" of the loads is not required.

The force loading is applied at the balance moment center (BMC), and a second order best fit is performed to define the linear and quadratic terms of the single forces. The moment loading is performed using a constant load and varying the moment arm. The load is first applied at the BMC and its weight is zeroed out by a counter weight. It is than translated along the long arm to apply the moment about the BMC. Although the moment thus produced is nominally pure, this procedure raised an additional problem. A significant scatter (Fig. 9 a) was observed when a single curve was fitted to all the moment data that were obtained with both positive and negative loads. It became obvious that two curves should be used to better fit the results (Fig. 9 b and c). One for the case where M/L ratio is positive and the other , when the ratio is negative. Apparently, the method of applying the moment generated a secondary effect caused by the positioning of the load, either forward or aft of the BMC. This effect was especially pronounced in the output of the axial force sensing bridge. Similar results were obtained for the yaw moment and side force.

Consequently, sixteen matrices were formed to contain all the combinations of normal and side forces and pitch and yaw moment signs. An additional step was added to the iterative procedure suggested by Smith. This iteration loop selects the appropriate matrix according to the signs of the forces and moments obtained in the previous iteration.

The sixteen matrices procedure is compared with a nonlinear procedure with one matrix, and a linear calibration with axial load corrections, in reconstructing accurately known load combinations, that are applied to the balance on the calibration rig. The results are presented in Fig. 10, as a function of the eccentricity of the loads, or, the distance of the load application point from the Electrical Center (EC) of the balance. An improvement of more than 50% in the accuracy of the axial force measurement was obtained, compared with the nonlinear procedure involving one matrix. taking into consideration that these results were obtained small diameter balances performing under high strain with deflections in the order of 8-10 degrees, a 0.1% error in the reconstruction of the axial load for a wide range of loads and load eccentricity is a significant improvement in the measuring ability.

Design of a New External axial Force Sensing Element

Non-integral Axial force element for wind tunnel balances were studied before, Gorlin and Slezinger (ref. 1), but failed to reach the required accuracy criteria for wind tunnel work. The reasons for the failure were that these external elements, usually large load cells, too large to fit in the model, were located further downstream at an area where large bending moment exist. These moments distorted the load cell and its output. Moreover, these bending moment were also exerted on the bearings that were used to permit relative axial motion between the axial load cell and the other metric component.

The non-integral axial force element configuration presented in the following paragraph was designed to avoid the above mentioned problems, Ringel and Levin (ref. 8). The external element was positioned near the center of the model to reduce the bending moment, and friction induced errors were reduced also as a result of recent advances in technology of bearings. This technology ensures almost pure axial motion with minimal friction between the main five component balance and the model, and is complemented by a single valued mechanical link between the main balance and the separate axial force unit. Fig. 11 describes the new design. The axial force unit (no. 1 in Fig. 11) is composed of a metric plate (Fig. 12) to measure the axial force, a flange that connects the metric plate rigidly to the model and a Morse taper that connects it to the main five component balance (no. 2 in Fig. 11). The connection to the balance is via a Thomson shaft (no. 3 in Fig .11), that is separated from the model (no. 5 in Fig. 11), by two linear ball bushings (no. 4 in Fig. 11). This arrangement permits an almost pure axial displacement of the model relative to the axial force element while the Thomson shaft prevents the transmission to the metric plate of vibrations that are perpendicular to its axis. The static friction coefficient of the linear ball bushing is 0.0018. With a normal force to axial force ratio of 20 : 1, the uncertainty of in the axial force would be in the order of 3.6% which is an order of magnitude higher than being achieved by an integral sting balance. However in the noisy wind tunnel environment, the much lower dynamic friction is dominant and the uncertainty in the axial force measurement is lower by an order of magnitude.

the external axial force element was calibrated with a calibration sleeve replacing the model. The axial load varied from zero to 2.0 kgf, and with normal force loads of zero, 20 and 40 kgf. The results are presented in Fig. 13. The output in all three cases was practically linear, the linear coefficient varied slightly from 2228

μV/kg with pure actual loading to 2221 μV/kg when 40 kgf normal force (20 : 1 ratio) is applied simultaneously. The standard deviation of 3.6 constitutes a 0.008% axial force uncertainty of full scale for pure loading , and grows to 0.37% uncertainty when the 40 kgf normal force is applied. These results are obtained directly from the external element output, and could be improved using a linear calibration for the interactions. The calibration results of the external axial force element are compared with similar results of two integral balances with a conventional drag element and a new drag element as was presented previously. The comparison is shown in Fig. 14. For pure axial loading all output data are linear, the external element can obtain higher sensitivity (Fig. 14 a), however the output due to a normal load shows the advantage of the external element. The conventional drag element has high non linearity, the new drag element output is linear but considerably higher than the external drag element. A further advantage of the external drag element is that even with high normal loads, the large deflections occurring with conventional integral balances, mainly due to the reduced stiffness at the drag measuring element, is prevented.

The external axial force element is designed to fit a series of standard five component main balances, making it a more veritable tool. the overall expanse of manufacturing a five component main balance and an external force element are less than 50% of the expanse of manufacturing a ix component balance.

CONCLUSIONS

Three methods t improve the accuracy of the axial force measurement of small balances have been presented. The improvements were obtained by a new design of the axial force element, by modified calibration and data reduction procedures, and by applying a new bearing technology and a new approach to the veteran idea of implementing an eternal force measuring element. The results obtained are quite satisfactory, considering the high loads and large deflection small balances undergo during wind tunnel testing. As further improvements are expected to be required to accommodate for constantly growing demands on the measurements accuracy, all possible avenues should be explored. New materials, designs, calibration techniques, strain gage technology, and new approaches should be considered.

REFERENCES

1. Gorlin, S. M.; Slezinger, I.: Wind Tunnels and Their Instrumentation (translated from Russian). *Israel Program for Scientific Translations,* Jerusalem, 1966, pp. 379-425.
2. White, G.: Temperature Compensation of Bridge Type Transducers. *Statham Instruments Notes,* No. 5, Oct.-Nov. 1948. Revised Aug. 1951.
3. Seginer, A., Brosh, A., and Richard, R. D.: A Parametric Investigation of an Elastic Parallelogram for the Measurement of Aerodynamic Drag. Technion-Israel Institute of Technology, Haifa, Israel, TAE Rept. 419, July 1980.
4. Richard, R. D.: Calibration of Wind Tunnel Strain gage Balances. . Technion-Israel Institute of Technology, Haifa, Israel, Research Center Report No. 0-197, July 1980.
5. Smith, D. L.; An Efficient Algorithm Using Matrix Methods to Solve Wind-Tunnel Force-Balance Equations. *NASA TN D-6860*, Aug. 1972.

6. Ringel, M., Levin, D., and Seginer, A.: Nonlinear calibration of Integral Wind Tunnel Balances. *ICIASF 10th Conference Proceedings.* Stanford University, CA, USA, 1985.

7. Dubois, M.: Calibration of Six-Component Dynamometric Balance. *Onera t.P No. 1976-79,* 1976.

8. Ringel, M., Levin, D.: A Non-Integral, Axial-Force Measuring Element. *Experiments in Fluids* 7, 56-60, 1989.

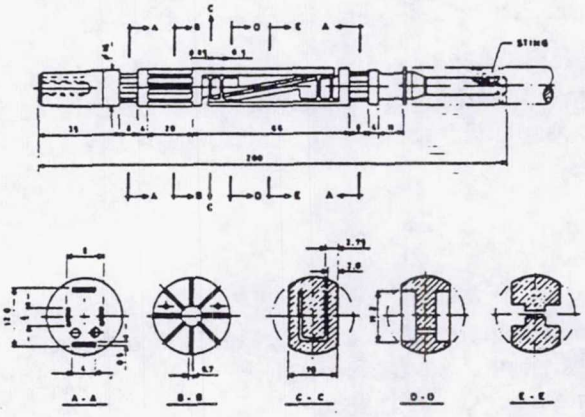

Figure 1. Conventional 6-component balance.

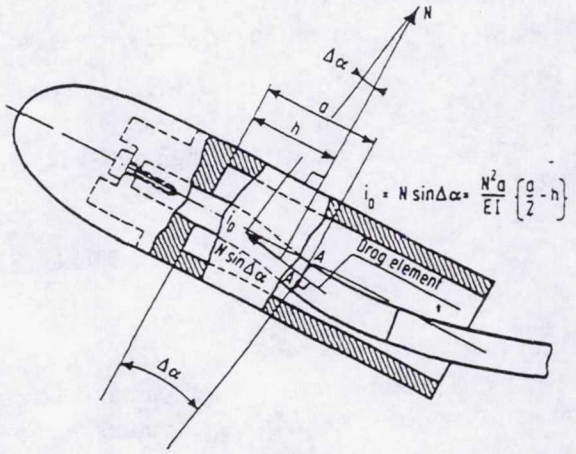

Figure 2. Interaction due to angular deflection of the model relative to the axial-force element.

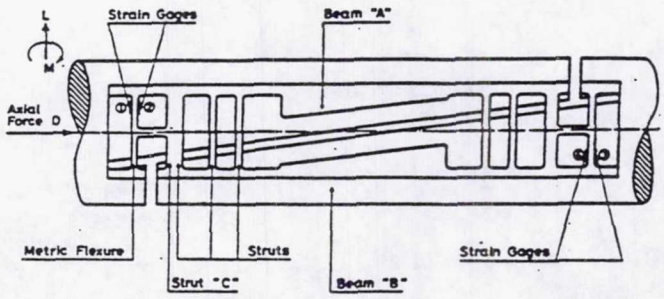

Figure 4. Schematic of new design.

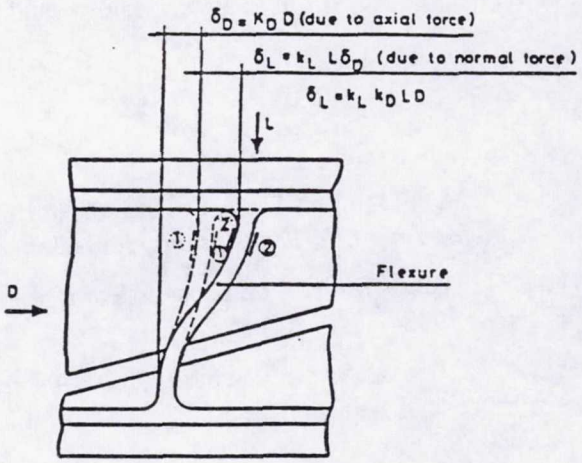

Figure 3. Interaction due to axial deformation of the drag element under a force normal to its axis.

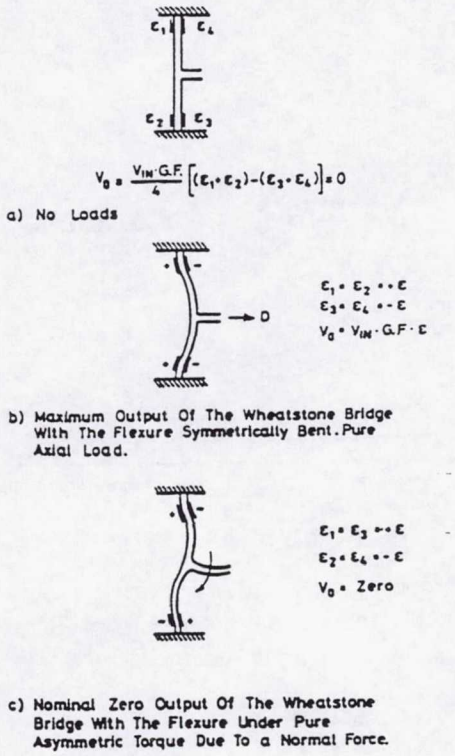

Figure 5. Nominal output of the drag bridge under pure axial and normal loads.

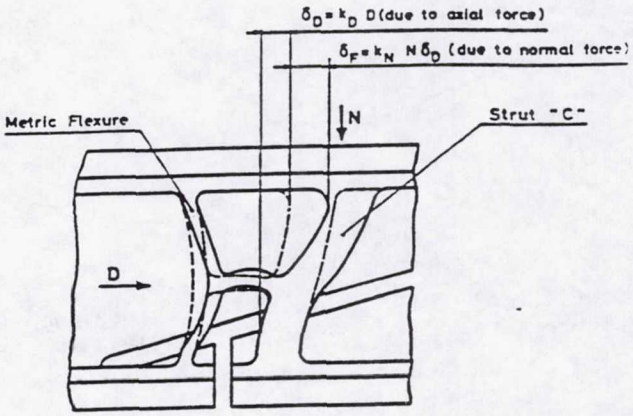

Figure 6. Schematic of new element deflection under combined load.

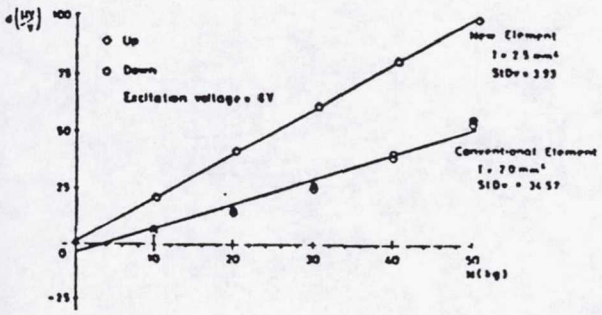

Figure 7. Parasitic drag output under normal force.

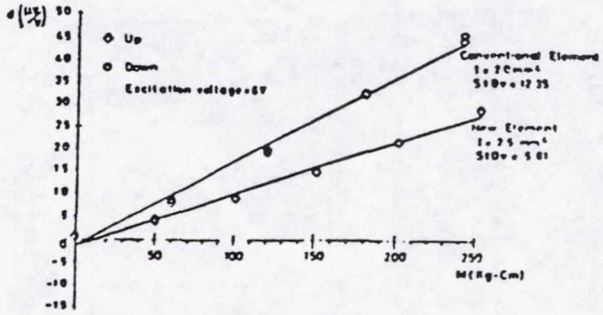

Figure 8. Parasitic drag output under pitching moment.

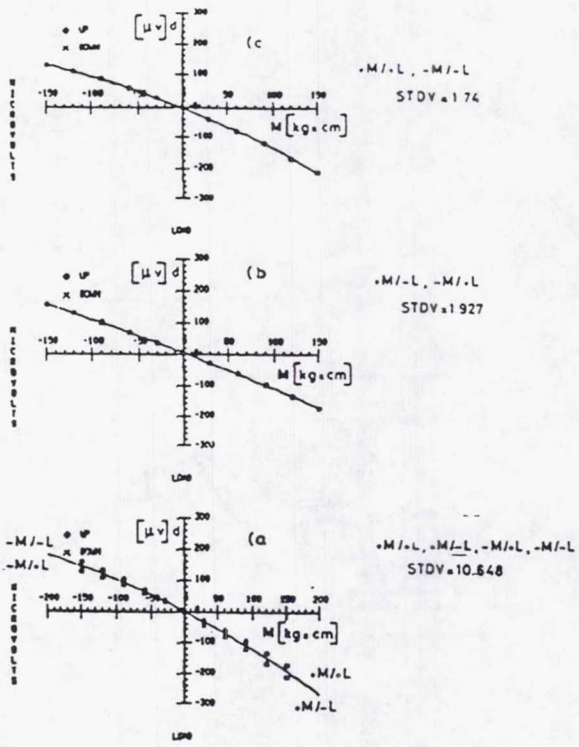

Figure 9. effect of M/L ratio on pitching moment interaction on drag.

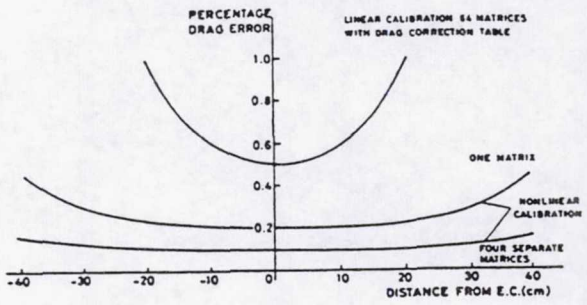

Figure 10. percentage drag error Vs. application distance from EC of force in pitch plane.

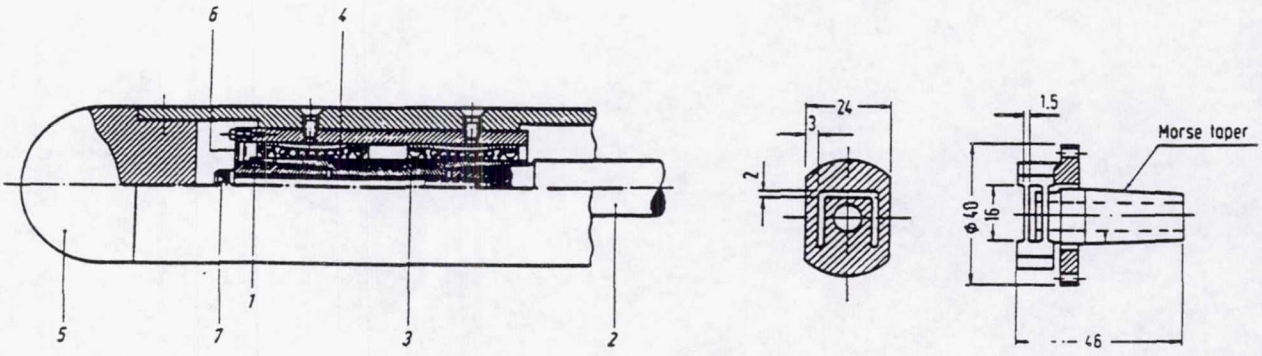

Figure 11. Non-integral axial-force element: *1* load cell, *2* balance, *3* Thomson shaft, *4* ball bushing, *5* model, *6* flexure plate and strain gages, *7* clamping screw.

Figure 12. Metric plate configuration in the axial force unit.

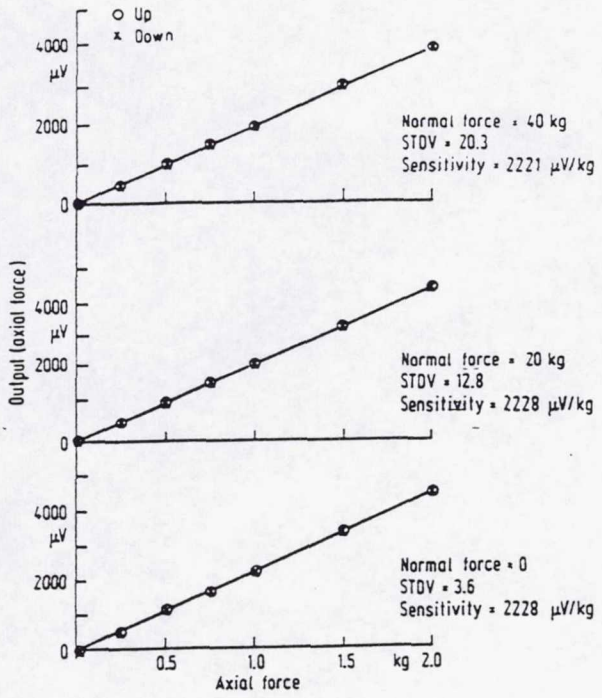

Figure 13. Axial-force element output vs. axial load under simultaneous acting normal force.

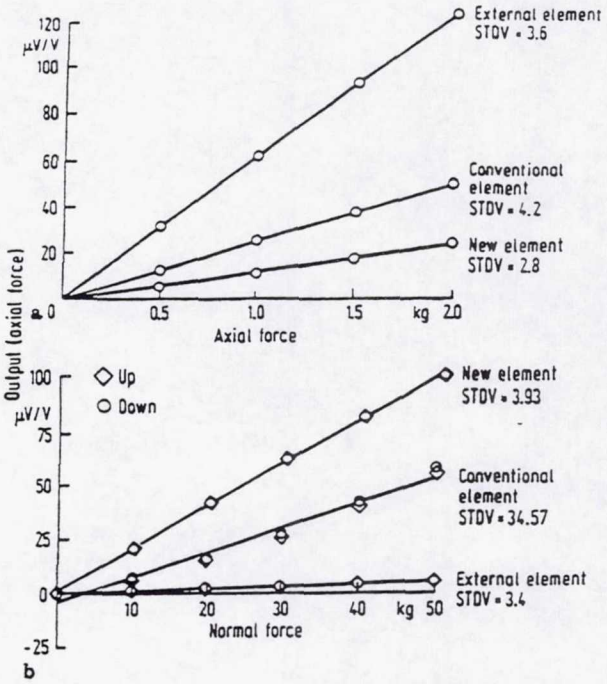

Figure 14. Comparative output of various axial-force elements.

Page intentionally left blank

SOME PECULIARITIES OF BALANCE TESTS IN THE TRANSONIC TsAGI T-128 WIND TUNNEL

A.R. Gorbushin
Central Aerohydrodynamics Institute,
Zhukovsky, Russia

SUMMARY

The procedure of special balance tests in the T-128 wind tunnel is given and some test data for internal and external balance are considered. The method of taking account for zero balance reading variations is suggested. The repeatability test results obtained in the T-128 wind tunnel for Tu-144 and reference models are presented to demonstrate the capabilities of the method of taking account for zero balance reading shift before and after the run.

INTRODUCTION

The current development of aerodynamics imposes increased requirements for the wind tunnel test accuracy. Especially it concerns passenger aircraft model tests carried out on strain-gage balances. The aerodynamic characteristics of models, first of all, the data on drag must be reliable and exact. The influence of temperature on the strain-gage balance measurement accuracy is a basic factor hampering the solution of this problem. Below are considered some methodical points regarding the balances used in the T-128 wind tunnel.

The main T-128 wind tunnel parameters are as follows:

test section size	2.75m·2.75m
Mach number range	0.15 to 1.7
maximum dynamic pressure	80kPa
total pressure range	20 to 400kPa

Maximum dynamic pressure and total pressure values attained in the T-128 wind tunnel, rather high for transonic wind tunnels, imply more severe temperature operation conditions for models and strain-gage balances installed in the test section. A set of strain-gage balances with different load ranges are available in the T-128 wind tunnel which enable tests of various models in a wide range of flow parameters. The strain-gage balances used in the T-128 wind tunnel can be divided into two groups: internal and external ones. The internal balances installed in the test section are attached on a sting mounted in a crescent-shaped rigid strut (Fig.1). As for the external balances applied in the T-128 wind tunnel, they can conditionally be divided into three groups. The first group involves plenum chamber-installed 5-component balances for half-models (Fig.2). The second group includes 6-component balances installed in the plenum chamber in a form of a frame suspended by two supports to be connected to the test section via strain dynamometers. The model is attached to an enclosing frame using three thin metal strips. This type of balance is intended for testing at high angles of attack. The third group comprises the 6-component strain-gage balances placed behind the model to serve simultaneously as a sting (Fig.3). As compared with the internal balances, these balances feature great overall dimensions and mass, as well as a rather complex fairing design. Its advantages are a simpler design of models having a free space inside the body to place additional instrumentation, as well as a small time required to replace models. The balances used in the T-128 wind tunnel are basically manufactured at TsAGI. As for the strain-gage balances aimed at

determining the model characteristics at cruise flight regimes, their preparation to wind tunnel tests must be especially careful. The first stage of the balance preparation in the T-128 wind tunnel implies the control of the strain-gage and temperature gage bonding for the presence of air bubbles in the bonding layer. To do this, the internal balance is placed in a small high- and low-pressure chamber, while the external balance is installed in the plenum chamber for the test time period. The readings of all balance channels (loads and temperature) are recorded at a small rate of pressure variations. If pressure variations do not result in deviations in the balance readings, the balance is accepted for further tests. Due regard must be had to the fact that high rates of pressure variations can lead to appreciable temperature variations inside the chamber. The TsAGI division that deals with the balance designing and manufacturing is also charged with the minimization of the temperature influence on the balance readings. As a rule, this process suggests the choice of an optimal balance design and the bonding of thermo-compensating gages to compensate for the influence of uniform balance heating. To accomplish this, the heat chamber test results are applied.

SPECIAL BALANCE TESTS

Special tests are undertaken in the T-128 wind tunnel to take account of the residual temperature influence. In this case, the balance is installed as usual in the test section. The balance is covered by an axisymmetric fairing attached to the sting in the case of the internal balance or to the external balance fairing. The fairing, having several orifices in its rear portion, is intended to prevent the force flow action on the balance components. In similar tests of the balance destined for half-models, the body is attached to the test section wall and its position remains the same as in balance tests. The internal and external balances are installed at zero angles of attack and sideslip angles to provide constant angles during a run. Then the tests are conducted according to the program corresponding to characteristic balance tests with the registration of flow parameters and balance temperature gage readings, as well as balance channels (zero balance readings). In order to reduce the run time period, the cooler water mass flow rate is decreased. Similar experimental studies are carried out, as a rule, at increased pressures because the heat conditions for the balance prove to be more severe. The balance and fairing configuration of this kind does not ensure a complete model-balance system simulation but, nevertheless, it enables a sufficient information to be obtained.

External balance tests

As an example, Figs. 4.a-4.c and 5.a-5.c present the results of such tests for two balances. Figs. 4.a-4.c show the test results for the external balance installed in the strut. The load range for this balance is as follows:

AF	NF	SF	RM	YM	PM
3500N	20000N	3000N	1000Nm	1500Nm	3000Nm

This balance is rather old and the thermocompensation for strain gages is not provided in it. Fig. 4.a gives variations of the test section Mach number and total pressures Pt related to atmospheric pressure with the run time, while Fig. 4.b presents the time variations of readings of one of balance temperature (Tb) and stagnation temperature (Tt) gages, the temperature scale being in °C . During the run, the stagnation temperature rises almost linearly in time to be about 20°C . The balance temperature rise behavior is the same and the temperature variation is substantially less than 3°C, although a closer examination reveals two linear portions with different slopes: the first portion lasts from the 3rd minute to the 6th minute, and the second one from the 6th minute to 10th minute. Most likely, this resulted from the interaction of two heat fluxes acting on the balance: the first heat flux

flows through the fairing base orifices, and the second one flows from the heated fairing nose. In the first time section, the heat is supplied by the first heat flux, while in the second time section the second heat flux is added. In spite of the decreased temperature in the test section, the balance temperature continues to rise on completion of the run, though not at a high rate. This is caused by the fact that the balance is rather bulk (250kg) which requires much time for its temperature stabilization. Fig. 4.c illustrates characteristic plots of zero readings for the drag component (AF) in N and the pitching moment component (PM) in Nm during the run. It can be seen that the zero balance readings correlate rather well with the balance temperature. The zero reading variation is 1% of the range for the drag component, 0.4% for the pitching moment component and not in excess of 0.4% for the remaining balance components during the test time.

Internal balance tests

Figs. 5.a-5.c present the data on similar tests of the internal balance featuring the same load range. This balance is provided with the strain gage thermocompensation. The Mach number and total pressure vary almost in the same way during the run (Fig.5.a). In this run, the cooler water mass flow rate is slightly greater than in the case of the external balance, therefore, the total temperature variation shows an increase to be 10°C. (Fig. 5.b). The balance temperature variation behavior remains the same, only the temperature variation value decreases (ΔT_b=1.5°C). Fig.5.c shows zero reading variations for the drag component (AF) and the normal force (NF) in N during the run. A small influence of static pressure variations in the test section at the wind tunnel start and stopping moments on the readings of the NF component is caused by the fact that the balance was placed immediately inside the fairing. The zero variation is 0.3% of the range for the drag component and 0.07% for the NF component, while not in excess of 0.1% for the other components. Note that in comparison with the external balance the component readings for the internal balance become stable rather rapidly after the experiment (the balance mass is almost 16kg).

Half model balance tests

Similar tests of the balance of 60kg destined for half-models and installed in the plenum chamber have not revealed a significant influence of the flow both on the balance temperature and on the readings of measured components.

BALANCE ZEROS DRIFT CORRECTION METHOD

Reasoning from the similar data obtained in the T-128 wind tunnel, a method of taking account of the influence of the temperature on the balance zero readings was suggested. A very simple technique was chosen based on the linear dependence of zero readings on time, i.e., zeros were calculated for each test point. It is based on the following assumptions. First, the forward balance cone is always connected with the model and the main heat flux flows to the balance from the model. Second, a series of tests is carried out, as a rule, in similar conditions during one run which ensures almost the same heat flux towards the model. Third, the tests have shown that variations in the balance zero readings during the run time do not in excess of 1% of the range and, accordingly, the neglected error of this technique becomes a next-order value. A number of other methods of taking account of the temperature influence based on readings of temperature gages installed in the balance may also be proposed.

REPEATABILITY TESTS

A possible way of verifying the approach under consideration is repeated model tests on the balance. Figs.6.a-6.c show the results of testing a supersonic passenger aircraft Tu-144 model in the T-128 wind tunnel at M=1.0 on the external balance mentioned in Figs. 4.a-4.c. The lift coefficient CL is plotted on the abscissa axis and the profile drag coefficient CDV which is the model drag coefficient minus the principal term of the induced drag is plotted on the ordinate axis. For the scale to be up, the quadratic dependence of the drag on the lift coefficient is subtracted from the drag coefficient. Fig. 6.a shows the test data processed using the balance zeros obtained before the test, while in Fig. 6.b presents the same polars but processed using the balance zeroes obtained after the test. Finally, Fig. 6.c gives the data acquired by applying the above-outlined technique of taking account of zero variations during the run. It is easy to see that a maximum difference between the drag coefficients of two repeated polars decreases from 0.0005 in the case of the test data processed using the balance zeroes before and after the test (Figs.6.a, 6.b) down to 0.0003 when the suggested technique is applied (Fig.6.c). The characteristic model profile drag coefficient value at moderate lift values is 0.02. For positive lift coefficient values, respective difference values are 0.00023 (or 1.2% of the drag value) and 0.00008 (0.4%). Similar data for the reference aircraft model tested on the internal balance at M=0.8 are given in Figs. 7.a - 7.c. A maximum difference between the profile drag coefficients, obtained in two repeated tests using the balance zeroes before the test for the data processing, equal to 0.0004 (or 2% of the drag value) at small values of CL (Fig.7.b) decreases to down 0.0001 (0.5%). A maximum scatter in the drag coefficient processed using the balance zeroes before and after the test is 10% for the first model (Figs.6.a, 6.b) and 3% for the second model (Figs. 7.a, 7.b). Higher errors of the model tests on the balance are caused by the fact that in contrast to the lift covering the total balance range, the model drag is essentially zero in the balance coordinate system.

The above considered examples demonstrate clearly the validity of the suggested technique. In the balance coordinate system, the errors are slightly smaller because the angle-of-attack gage error is added when scaling from the balance coordinate system to the stability coordinate system.

The author is indebted to the working team of the T-128 wind tunnel and its Chief, V.M. Neyland for assistance in preparing the report.

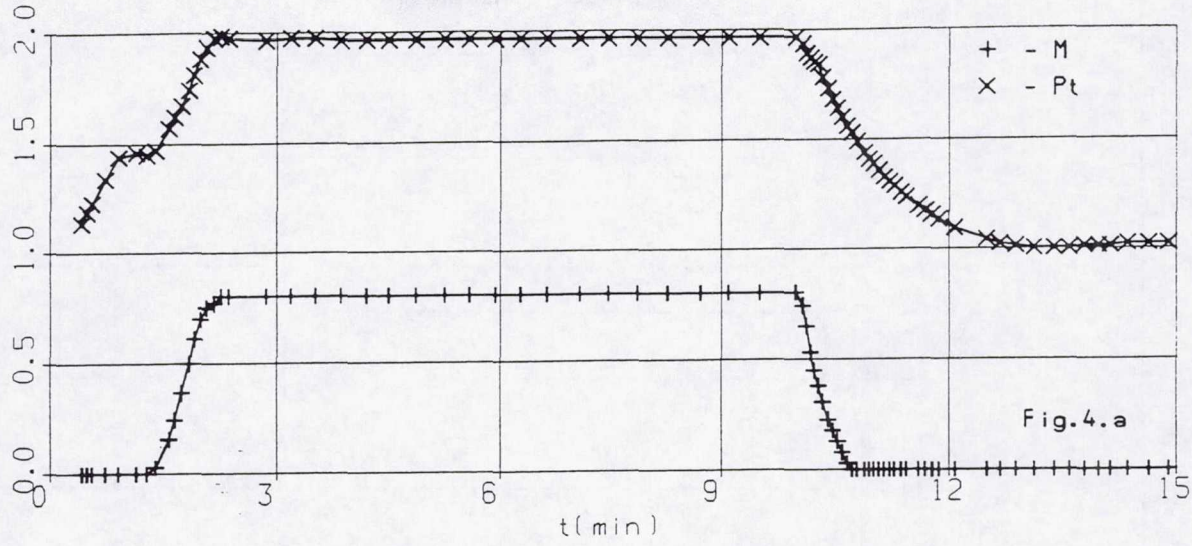

Fig.4.a

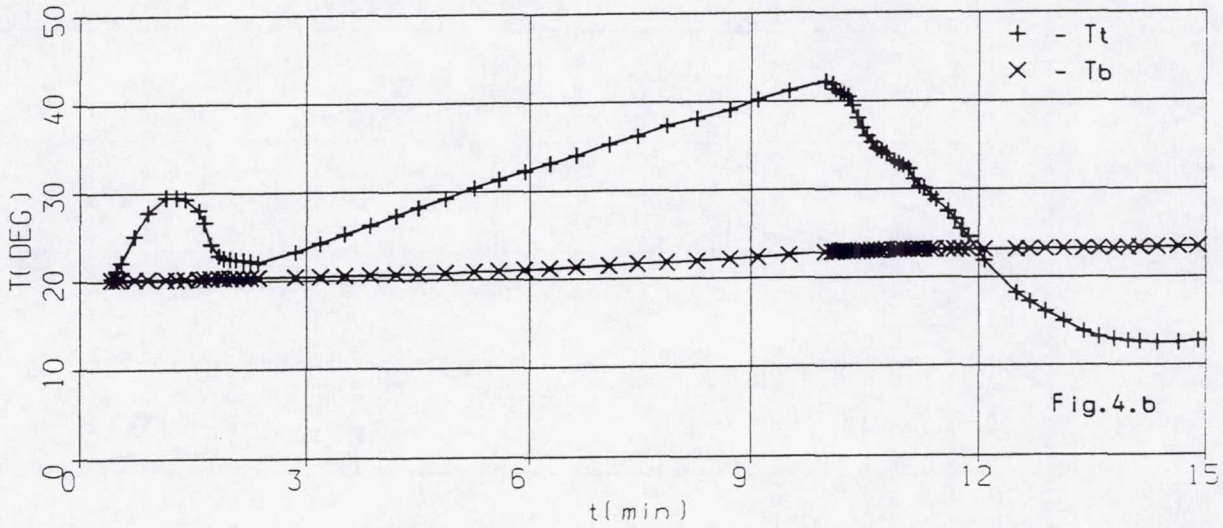

Fig.4.b

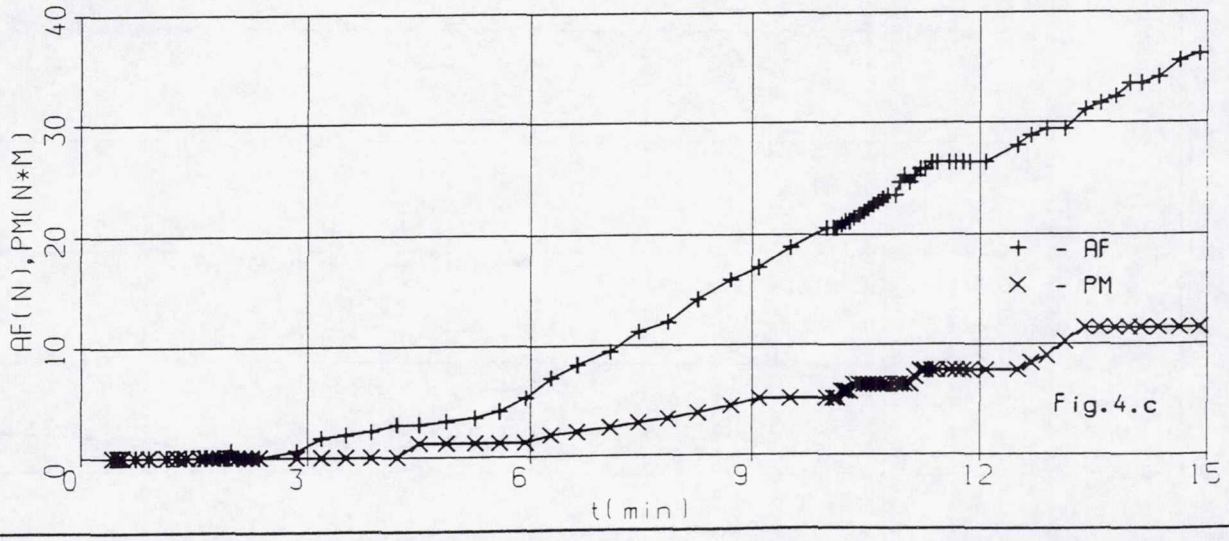

Fig.4.c

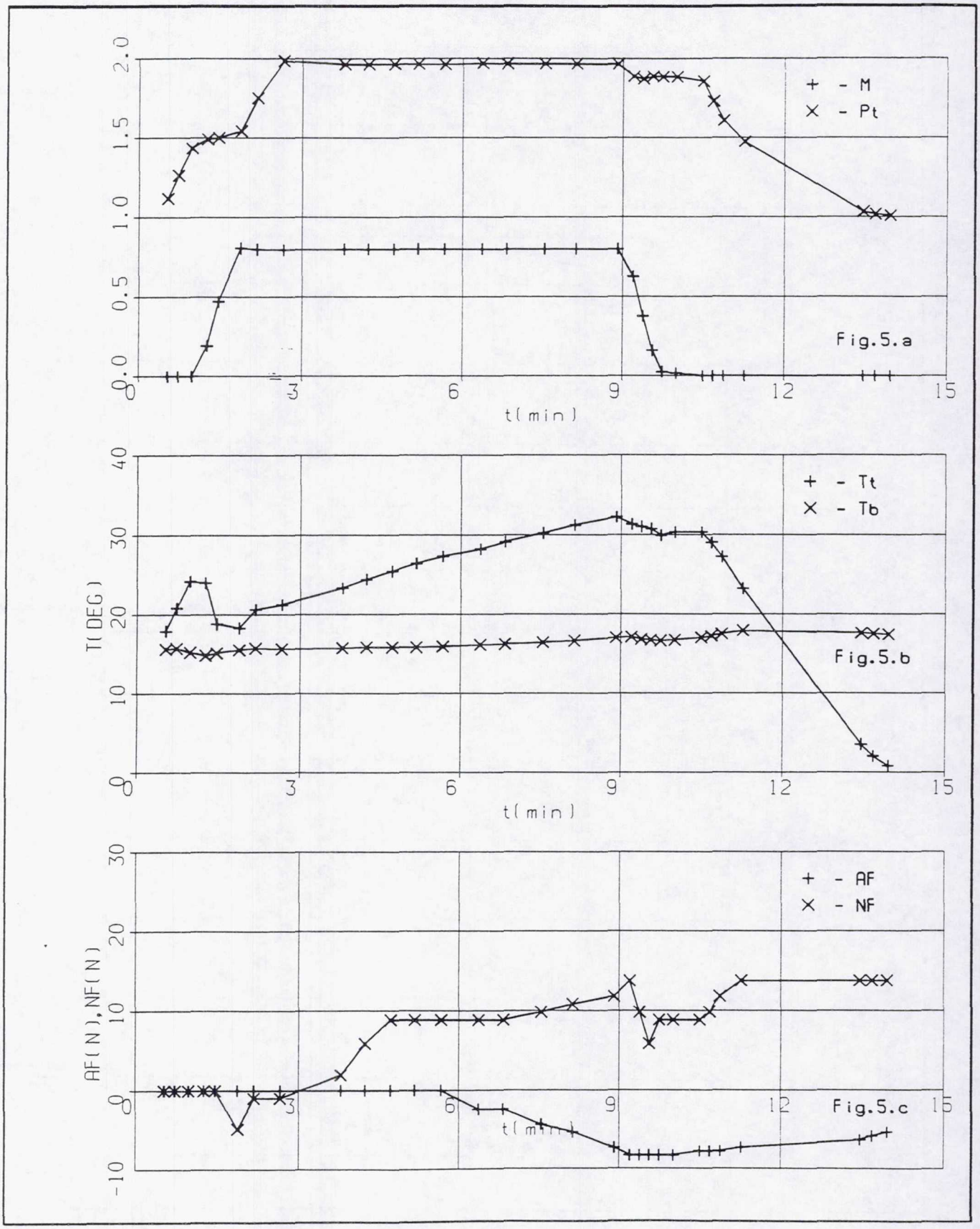
2.0
1.5
1.0
0.5
0.0
0
3
6
9
12
15
t(min)
+ - M
× - Pt
Fig.5.a
T(DEG)
40
30
20
10
0
+ - Tt
× - Tb
Fig.5.b
AF(N),NF(N)
30
20
10
0
-10
+ - AF
× - NF
Fig.5.c

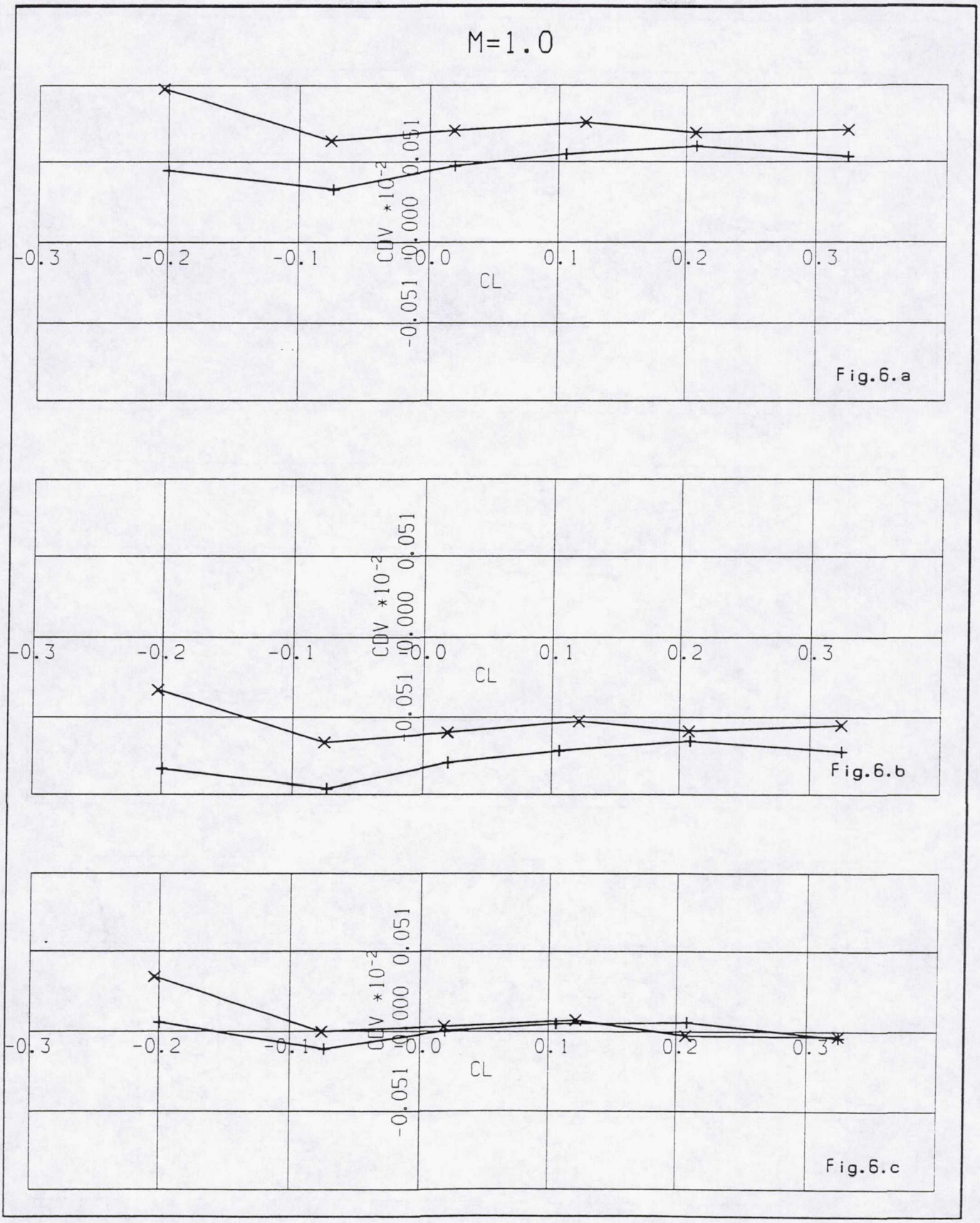
M=1.0
COV *10-2
0.051
0.000
-0.051
-0.3
-0.2
-0.1
0.0
0.1
0.2
0.3
CL
Fig.6.a
COV *10-2
0.051
0.000
-0.051
-0.3
-0.2
-0.1
0.0
0.1
0.2
0.3
CL
Fig.6.b
COV *10-2
0.051
0.000
-0.051
-0.3
-0.2
-0.1
0.0
0.1
0.2
0.3
CL
Fig.6.c

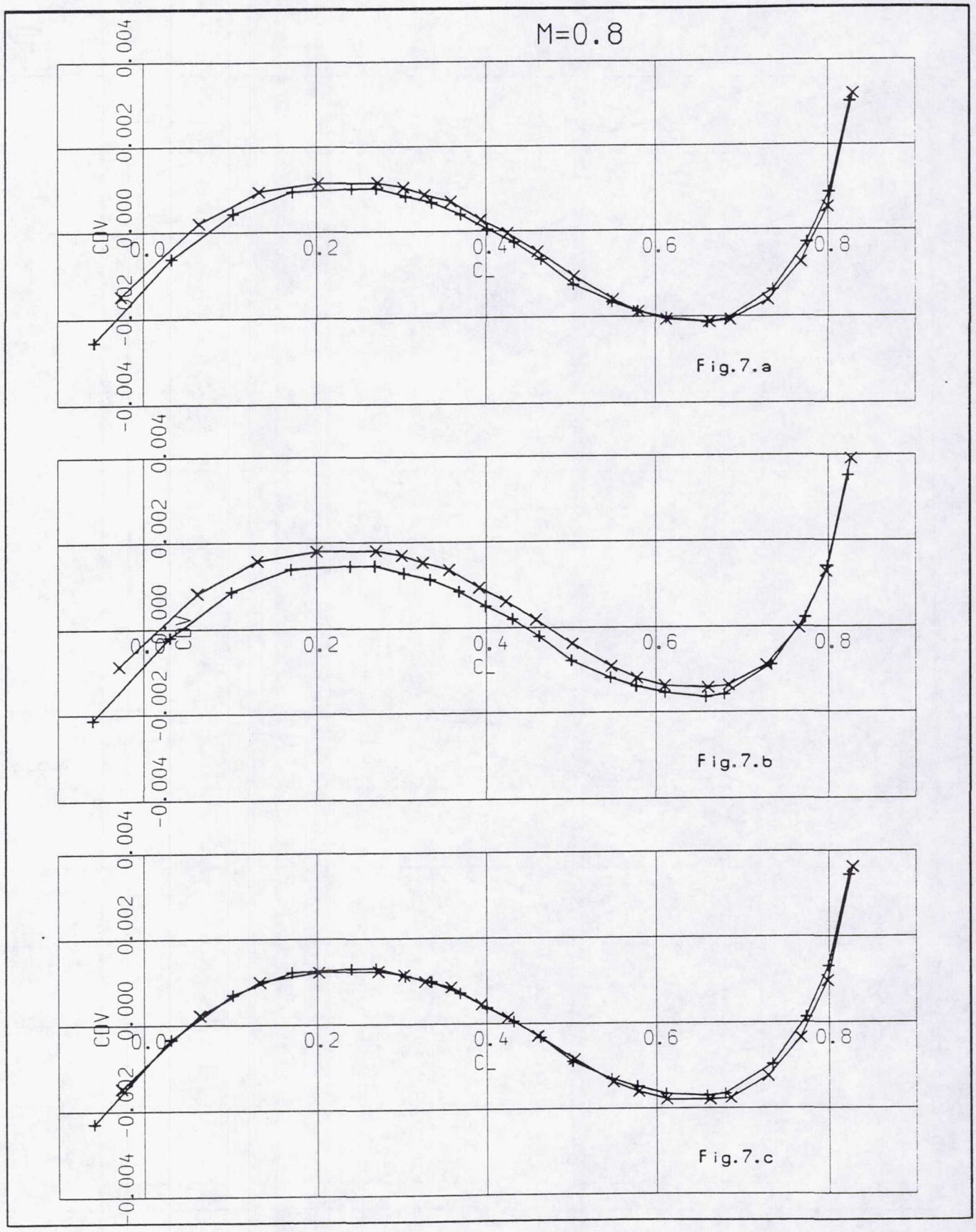

Fig.7.a

Fig.7.b

Fig.7.c

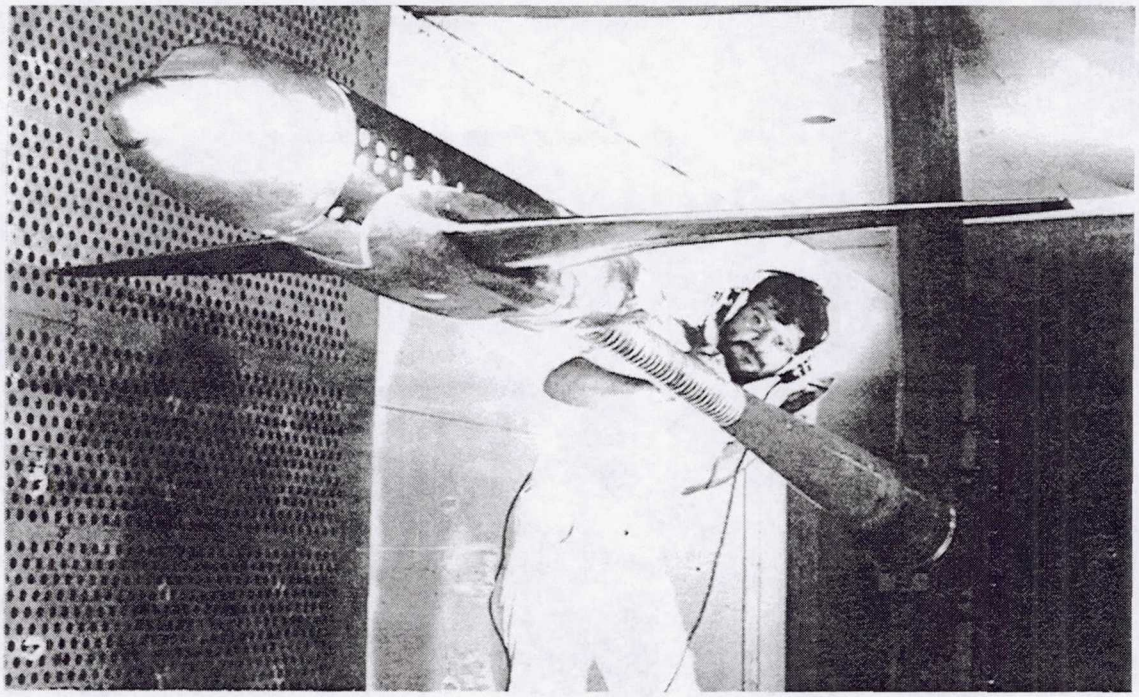

Figure 1 Reference model on internal balance in test section 1

Figure 2 Large scale half model in test section 2.

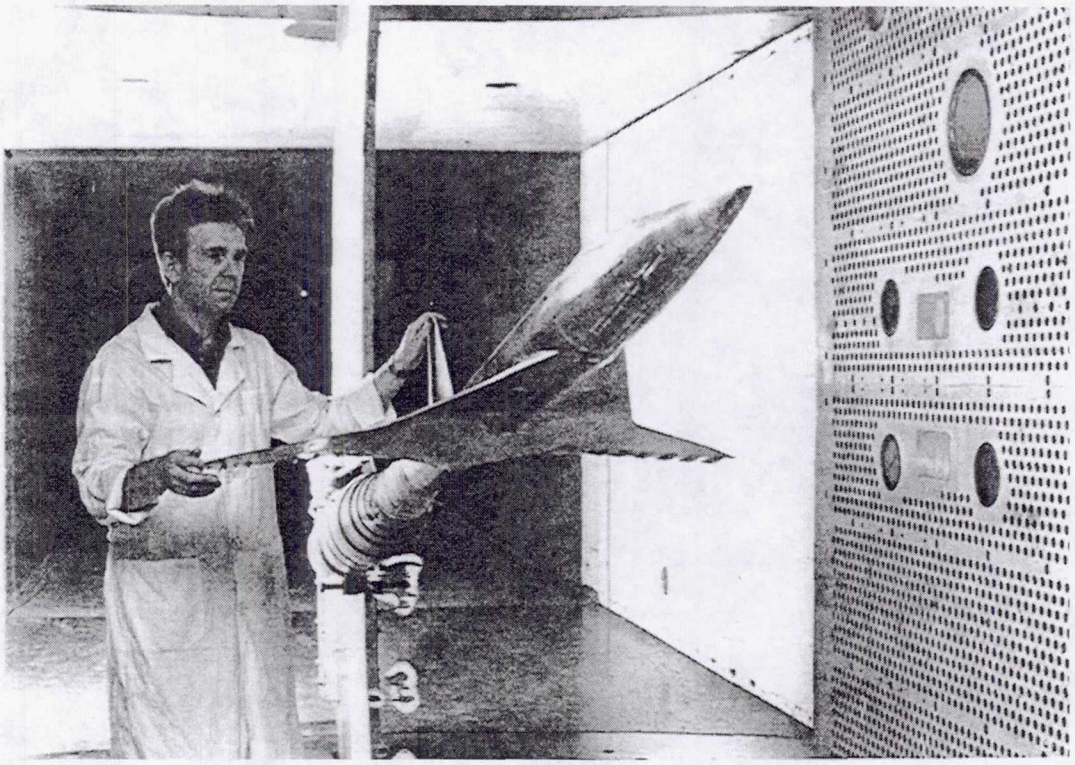

Figure 3 TU-144 model on external balance in test section 1.

STRAIN GAGES IN USE AT NASA LANGLEY - A TECHNICAL REVIEW

Thomas C. Moore, Sr.
NASA Langley Research Center
Hampton, VA

INTRODUCTION

Surface mounted strain gages and strain gage application techniques are as varied as they are versatile. There is an abundance of technical literature, available throughout the strain gage community, offering techniques for installing strain gages and methods of obtaining useful information from them. This paper, while providing more of the same, will focus its discussions on recent Langley developments for using strain gages reliably and accurately in very harsh environments. With Langley's extensive use of wind tunnel balances, its ongoing effort in materials development, and its currently focused activities in structural testing, the use of strain gages in unusual and demanding environments has led to several innovative improvements in the "how to gage it" department. Several of these innovations will be addressed that hopefully will provide some practical information for the strain gage user who is finding the test environment and (or) the materials to be tested too demanding for previously utilized strain gage application technology. Specifically, this paper will include discussions in the following three areas:

(1) technical considerations when gaging cryogenic wind tunnel balances, including areas for improving accuracy and reliability;
(2) addressing technical difficulties associated with gaging composite test articles and certain alloys for testing at temperatures approaching -450°F, or elevated temperatures up to 350°F, or both temperatures inclusive during the same test scenario;
(3) gaging innovations for testing metal/matrix and carbon/carbon composites at temperatures above 700°F.

GAGING OF WIND TUNNEL BALANCES FOR CRYOGENIC SERVICE

This portion of the paper will review sources of inaccuracies associated with strain gages installed on cryogenic wind tunnel force balances and the techniques developed for correcting those inaccuracies. Reliability issues for balances used in this environment and methods for improving dependability are also discussed.

Sources of Inaccuracies

There are a number of potential sources for the inaccuracies in strain gage data generated with force balances operating within a temperature range of -185°C (-300°F) to 65°C (150°F). Included are four basic sources of potential data inaccuracy that are a function of the *strain gages themselves* when utilized for this temperature range. This discussion will focus on the uncertainty of the spurious signals generated by the *gage* itself and methods for reducing the magnitude of these signals in such a way that corrections will be very small or unnecessary when processing the actual test data. Three of the four basic inaccuracies are a function of the apparent strain characteristics of the strain gages. These correctable strain gage traits are stated here as, ***loop data, nonlinearity, and apparent strain curves of the bridge***. The fourth strain gage generated inaccuracy is the ***shift in gage sensitivity*** (gage factor) as a function of temperature change. Each of these inaccuracies is explained and a correcting technique is offered.

Loop data are stated here as a difference in the thermally induced output of a strain gage bridge, at a temperature, during a decreasing temperature excursion and the thermally induced output at the same temperature during an increase in the temperature excursion. This discussion will differentiate between 'small loop' data and 'large loop' data and attempt to explain how each may be generated. The 'small loop' data as shown in Figure 1 is caused by, either, one or more arms of the bridge sensing the changing temperature in advance of the other gages, or it is generated as a function of the differences in the apparent strain curves of the individual gages comprising the bridge. When the latter is the cause, a "matching" of the gages (to be discussed later under Matching Apparent Strain Curves of Strain Gages) prior to installation eliminates this unwanted signal. When "matched" gages are used any remaining thermally induced output, or 'small loop' data, is correctable with current balance design. Because this loop data appears to be, primarily, the result of changing thermal gradients through the measuring beams during the temperature excursion and because the cryogenic balances are designed as moment balances, a logical solution for eliminating this data is to utilize Poisson's ratio gaging configuration. This configuration pairs tension and compression gages in one area of the measuring beam allowing for each half-bridge pair of gages to see the same temperature during temperature excursions. This, in turn, helps to null any apparent

strain in the bridge that might othwise be present when gages do not change temperature at the same rate.

The 'large loop' data, typically seen with the Axial component on cryogenic balances, is primarily the result of thermal gradients along the length of the axial section. These gradients cause thermally induced stresses in the axial measuring beams with a resulting axial component thermal hysteresis signal as large as 5 percent of full scale under transient conditions. A method for reducing this unwanted signal incorporates the use of temperature sensitive resistors physically placed on the body of the balance near the outer portions of the Axial section (see Figure 3)where the largest gradients typically occur. Electrically, they are placed in two arms of the bridge circuit. Details for using this method in reducing the large loop data is presented in a technical memorandum authored by Judy Ferris (NASA Technical Memorandum 87712, May 1986), titled, "Cryogenic Strain Gage Techniques Used In Force Balance Design For The National Transonic Facility".

Nonlinearity is defined for the thermal output of strain gage bridges as the maximum deviation of the thermal output occurring above or below a line drawn between the room temperature thermal output and the thermal output at the maximum temperature encountered during that particular temperature excursion. For cryogenic force balances this is typically between 25°C and -195°C. This nonlinearity, as shown in Figure 2, can be significantly reduced with "matched gages" and though not normally needed, virtual elimination of any remaining nonlinearity can be achieved by inserting an appropriate amount of Manganin wire (an alloy of copper, manganese, and nickel) internally in one arm of the bridge. Manganin wire is chosen because its resistance change is nonlinear from room temperature to -195°C, thus, when a predetermined amount is placed in the proper arm of the bridge it offsets the original nonlinearity. This technique, while correcting nonlinearity, changes the room temperature electrical zero of the bridge a considerable amount due to the wire's high resistivity. Additionally, the original apparent strain of the bridge is slightly altered due to the Manganin wires' thermal coefficient of resistance. This new thermal output may then be corrected with silver-clad copper wire also placed internally in one or two arms of the bridge.

The apparent strain curve of the bridge circuit is primarily the result of the differences in the apparent strain curves of the individual gages comprising that particular bridge. Also, the differences in the resistance changes of the interbridge wiring used to connect the arms of the bridge can be a contributing factor. For this paper 'apparent strain' refers to gage output as a function of changing temperature. With moment type balances, equal resistance of interbridge wiring is usually achievable and the resistance of each wire is very small, hence, the 'apparent strain' they generate is minimal. The apparent strain of the strain gage bridges on Langley's cryogenic balances are compensated by inserting temperature sensitive wire(s) in one or two arms of the bridge. This is typically done with silver-clad copper wire. **note:** Nickel is normally used with

conventional balances but for the cryogenic balances copper is preferred because its coefficient of resistance is essentially linear throughout the balance's operating temperature range. While this method of reducing the apparent strain of a strain gage bridge is quite conventional, it has shortcomings when large temperature excursions are encountered, especially in the cryogenic region. The scatter in apparent strain from gage to gage is greater going cold than when going hot. Consequently, the apparent strain of the bridge is often much greater when going cold. This, in turn, requires a larger amount of compensating wire. With wind tunnel balances, providing space for the correcting wire (or in some instances, foil-type resistors) is an issue, as is the ability to subject the compensator(s) to the same rate of temperature change as the gages.

Given these three difficulties, i.e., apparent strain, loop data, and nonlinearity, it would be advantageous to provide gages, prior to installation, whose apparent strains were matched such that there would be virtually only one apparent strain curve signature generated by the four gages that would comprise any strain gage bridge for cryogenic balances. The next paragraph describes this "matching of strain gages".

Matching Apparent Strain Curves of Strain Gages

There are inherent differences in the apparent strain curves of all resistance type strain gages and since these differences are magnified at cryogenic temperatures, a resultant apparent strain output is obtained when four gages are arbitrarily chosen to form a four active-arm bridge circuit. Therefore, it would be beneficial to have strain gages whose apparent strain curves are accurately predetermined and 'matched' with respect to each other. The previously stated, undesirable, strain gage generated signals, i.e., loop data, nonlinearity, and apparent strain curve of the bridge, are significantly reduced when matched gages are used.

This matching of apparent strain curves has been accomplished by means of a "temporary bonding technique" and through computerized data comparison of each gage. The gages, after computer matching, are disbonded and made ready for permanent installation on the balance.

The gages Langley selects for its cryogenic balances are a modified Karma series gage which is heat-treated by the manufacturer to Langley specifications. This particular heat-treatment provides the least apparent strain at -195°C and, at the same time, provides modulus compensation for reducing the degree of sensitivity shift as a function of temperature change. The optimum number of gages to be matched at one time currently is 16. These gages are positioned on a test block and bonded with a methyl-2 cyanoacrylate adhesive using standard bonding procedures. Typical three-wire single gage hookup is used with 16 bridge completion networks. The bridge completion networks are outside the test chamber with outputs fed directly to a custom data acquisition system programmed for this effort.

This computer system samples the outputs of the 16 gages at selected temperature intervals from 25°C to -195°C and back to 25°C. Groups of four-gage outputs are then computed and matched by mathematically adding and subtracting the individual outputs to simulate the resultant output as if the four gages were comprising a standard 4-arm bridge. The gages that mathematically "match" are grouped into fours that fall within predetermined tolerances for allowable amount of loop, nonlinearity, and apparent strain. The outputs of the more promising matched groups are then plotted so final selections can be made by comparing the plots of the "matched" groups of gages over the entire temperature range.

Following the computer matching of the temporarily bonded gages, they are disbonded by simply subjecting the gages to an elevated cure cycle. The disbonded gages are next unsoldered and following a gage preparation procedure are then ready for installation on the balance.

Shift in gage sensitivity with temperature is the fourth inaccuracy generated as a trait of the gage itself. Gage sensitivity, or gage factor, changes as a function of temperature. An additional factor affecting the sensitivity of the strain gage signal is the changing of the modulus of elasticity of the balance material with temperature. One means of minimizing this shift in gage sensitivity (also referred to as span variation with temperature) would be to have a gage with a gage factor that would change with temperature, an appropriate amount to offset the changing modulus of the balance itself. At Langley, several types of gages and several lots of gages within a type were tested under load at room temperature and at cryogenic temperatures in an attempt to locate a gage type and lot that changed gage factor an amount that would compensate for the change in modulus in the balance material when subjected to cryogenic temperatures. An encapsulated, modified Karma, 350 ohm gage was found to produce the least sensitivity shift of all gages tested. With four of these gages in a typical bridge circuit, mounted to measure strain in the principal stress direction, the change in sensitivity was -0.7 to -1.0 percent over the entire temperature range of the cryogenic balance. An unexpected benefit was realized by using bridges that have two of the four gages mounted transverse to the principal stress direction, i.e., Poisson's ratio. Because of Poisson's ratio of the balance material and the change in transverse sensitivity of the strain gages with temperature, the sensitivity shift was reduced to 0 to -0.3 percent.

IMPROVEMENTS IN STRAIN GAGING AND WIRING METHODS INCORPORATED IN LANGLEY CRYOGENIC BALANCES

In addition to identifying and correcting inaccuracies associated with strain gages used on balances in a cryogenic environment, other, strain gage related, measures have been incorporated which enhance the accuracy and reliability of Langley's cryogenic balances. Explanations for most of these innovations are somewhat lengthy and are discussed in other papers.

Therefore, rather than attempting to detail these measures, this paper will simply list several of them. Strain gage related improvements for Langley's cryogenic balances which enhance the accuracy and reliability of these balances (see Figures 3,4, and 5) include the following:

- Strain gages manufactured specifically for cryogenic balances which minimize the change in sensitivity (signal vs. load) with a change in temperature
- Strain gages which are "matched" for reducing initial apparent strain and non-linear thermal output such that corrections to data are minimal or unnecessary
- Redundant strain gage bridges for all components which provide two totally independant sets of load constants for the balance
- Platinum resistance thermometers (PRT's) replace thermocouples which eliminates concerns with accuracy and reliability of thermocouples and their leadwires
- Connectors are now an integral part of the balance instead of being attached at the end of a leadwire system
- A protective cover(s) is installed over the cage areas and the Axial section providing mechanical protection, more effective purging, and a reduction in the thermal gradients for the gages
- Machining modification in the end of the balance sting provides for a more reliable gaseous nitrogen purging of the balance
- Laboratory testing is now conducted for verification of performance characteristics of moisture-barrier(s) prior to implementation on balances

Other innovations and improvements for these balances that are not strain gage related have been incorporated, but, it is not the intent of this paper to address non-strain gage related topics.

STRAIN GAGING APPROACHES FOR ALLOYS AND COMPOSITES IN CRYOGENIC AND ELEVATED TEMPERATURE ENVIRONMENTS

Langley uses between 8000 and 10,000 strain gages per year on laboratory test panels/coupons and structural test articles. For the majority of the tasks, the installations are routine requiring standard gaging practices and materials. However, with some of the newer aerospace alloys and composites being examined in harsh test environments, changes in the gaging approaches have become necessary. This portion of the paper will describe gaging difficulties that were encountered when very demanding tests were to be conducted for these structural test articles. Also presented are solutions that have been successfully employed for gaging the following test items for these severe testing conditions:

- Aluminum/Lithium Bi-Axial Test Panels for testing at -320°F and at room temperature with high strain levels anticipated
- Graphite/Epoxy Test Panels for testing at -450°F to 350°F
- Large Aluminum/Lithium and Composite Structural Test Panels for testing at -350°F to 250°F

Aluminum-Lithium Bi-Axial Test Panels

Certain aluminum-lithium alloys are being considered for several future aerospace applications including the external tank for the next generation NASA space shuttle. Strain gages are being used extensively for determining the mechanical properties of this material at room temperature, cryogenically, and at elevated temperatures. An example of the testing of this type of material is shown in Figure 6 where cruciform panels were strain gaged for biaxial testing. These particular specimens were used to determine the yield locus for metals. This is considered especially important with alloys whose mechanical properties are anisotropic. A series of panels (similar to that shown in the figure) were to be tested at rather high strain levels. Herein lies the problem with strain gaging this material.

The most widely used room temperature curing adhesive for strain gages is a cyanoacrylate based material. Though this adhesive has been used with strain gages to read strains in excess of 30,000$\mu\epsilon$ on aluminum, this adhesive's bond-line failed under strain at approximately 3000$\mu\epsilon$ on the aluminum-lithium alloys. The requirement for this series of testing was to read strains up to 10,000$\mu\epsilon$. Various techniques were employed in the laboratory to improve the performance of the cyanoacrylate adhesive but to no avail. The reason for the poor bond-line between the gage and the substrate using this type of adhesive is not yet fully understood. Finally, through lab testing, it was learned that several of the solvent-thinned epoxy adhesive systems that are typically used for transducer gaging worked well on this alloy. Unfortunately, these adhesives all require elevated cure cycles and no elevated curing was allowed on the aluminum-lithium panels due to possible aging effects. Now, the difficulty shifted to finding an adhesive system that would cure at room temperature and survive at strain levels four times higher than was currently being achieved with the standard room temperature strain gage adhesive. Through simple "test and see" efforts in the laboratory, two adhesive systems were found that provided the bond-line integrity necessary for testing these panels. The adhesives were able to maintain a bond between the gage and the aluminum-lithium surface sufficient to record strains up to 15,000$\mu\epsilon$. Both adhesives are two-component 100% solids epoxy systems. These are not new to the gaging community and have been used fairly extensively at Langley for a number of years. There are two reasons that kept these adhesives from initial consideration. One, they required some type of clamping arrangement during curing, and two, the time element for the curing was considerable compared to that of a cyanoacrylate adhesive. One of these epoxy systems is now routinely used in the successful testing of the aluminum-lithium bi-axial panels.

Another series of aluminum-lithium specimens to be tested in a harsh environment required strain gaging of lab-type coupons for tensile tests at various temperatures from room temperature down to -320°F. Again, through lab testing, it was found that the same two-component adhesives discussed above worked well for this temperature range. The one area of concern for the adhesive system is that it

does not tolerate high humidity during the application process. The humidity must be kept below 50% in order to assure a completely cured adhesive bond.

Graphite/Epoxy Test Panels

Several series of graphite/epoxy panels were to be instrumented with strain gages and thermocouples for testing in a number of harsh environments. One series of panels would be subjected to testing in a liquid nitrogen/liquid helium environment followed by testing at elevated temperatures up to 350°F. A second series of panels would be subjected to a severe thermal gradient environment in which one side of the panel would see cryogenic temperatures while the other side would be heated to 350°F. A third series of panels would be tested at elevated temperatures following a long duration "wet soak" in water. The difficulties in gaging the three series of panels and the solutions for those difficulties are briefly discussed here.

The primary difficulty Langley had in strain gaging the first and second series of panels as described above was the fact that the surface was too coarse for strain gaging. A solution for this would be to apply a basecoat to the original coarse surface that could then be conditioned to accept the strain gages. This basecoat would be required to possess the following features; (1) it must have an operating temperature range from -450°F to 350°F, (2) it must be capable of providing a tenacious, creep-free bond-line between the gage and the substrate throughout the temperature range and strain range for the gages, (3) it must not generate micro or macro-cracking at cryogenic temperatures, (4) it must be sandable, and, (5) it must be compatible with the strain gaging adhesive. With these attributes, the basecoat could be applied, cured, sanded down to where the peaks of the composite surface are reached, then, micro-sandblasted so that the strain gage could be installed using a conventional strain gage adhesive system for this type of application. Through laboratory efforts, a two-part, resin type structural adhesive was found to contain all of the above characteristics. This adhesive was subsequently used on the graphite/epoxy specimens in conjunction with a two-component, solvent-thinned, epoxy-phenolic adhesive for installing the gages. Because cryogenic as well as elevated temperature testing were involved, nickel-chromium alloyed strain gages, teflon insulated wiring, and a eutectic solder containing Antimony were used.

The third series of graphite/epoxy panels did not have the very coarse surface. Therefore, the basecoat of structural adhesive with its necessary sanding was not required. However, it was observed that this particular series of panels was somewhat porous. Thus, when the gage was installed using conventional gaging practice, the bond-line was "starved". The solution for this was also the use of a basecoat. A technique was developed, using the gaging adhesive described above, such that the basecoat would not require any sanding prior to installing the gage once the basecoat was cured.

Large Aluminum-Lithium and Composite Structural Test Panels

A series of rather large (approximately 35 square feet of surface area per side) aluminum-lithium alloy and graphite/epoxy composite structural test panels are being instrumented at NASA Langley. These panels are complex in construction with curved surfaces and reinforcing stiffeners. Instrumentation includes strain gages, thermocouples, temperature diodes, and displacement sensors, for testing in harsh environments that include liquid helium, elevated temperatures as high as 300°F, and pressure during loading sequences. These panels are being tested as part of NASA's Reusable Launch Vehicle program.

With the lessons learned through gaging the test panels and laboratory coupons as described previously, application techniques for these structural panels were in place. The one obstacle with respect to the actual strain gaging task was in finding a means of applying pressure and heat to the installed gages during adhesive curing operations. Details of the construction of these panels cannot be presented for this paper, but, it can be stated that due to certain design features, there was a requirement that any pressure applied to a gage area must have an equal pressure on the opposing corresponding surface. With 90 areas to be strain gaged on each of these panels and with each panel having its own design features, a simple set of clamping bars would not suffice. Additionally, with the gage installation process requiring elevated temperature curing while pressure was being applied to the gages, a means of uniformly heating the panel was needed. A custom thermal/mechanical strain gage application fixture was designed which would provide the means for installing, clamping, and curing, at elevated temperatures, a large number of gages at a time. The fixture included a uniform support for the entire curved panel, adjustable clamping bars for all panel surfaces (including adjustment capability for the various designs among the panels), spring-loaded pressure pads/rods for each gage location, and a means of applying equal pressure on both sides of the panel at a given location. For each strain gage installation curing cycle the entire fixture and panel were enclosed in a heating chamber which featured a closed-loop convection heating system. With this system, it was found that controllable heating rates with uniform heating of all panel surfaces were achieved.

GAGING CARBON/CARBON AND TITANIUM/MATRIX COMPOSITES FOR TESTING ABOVE 700 DEGREES F

The difficulties in obtaining useful strain data at temperatures above 700°F have been well documented over the years. Recently, solutions for overcoming several of these difficulties have emerged. This portion of the paper will address several sources of high-temperature strain gage failures with corresponding solutions for each. One important development appears in the area of apparent strain reduction. A strain gage developed at NASA Langley dramatically reduces the precipitous slope and nonrepeatability of

apparent strains historically encountered with high-temperature gages. The operational theory for this gage and its performance in service are summarized.

Difficulty 1 - Debonding of high-temperature gages have shown to be a major problem when gaging carbon/carbon and titanium/matrix composites. Carbon/carbon in use for many aerospace applications actually contains a silicon carbide surface. This material with its low energy surface, low coefficient of thermal expansion, and its high modulus of elasticity presents a formidable task for any bonding scheme. Titanium matrix composites with their rapid oxidation rate and their oxidation resistant surface coatings also present bonding problems for high-temperature gages.

Solution 1 - With silicon carbide (SiC) coated surfaces on carbon/carbon there are two basic deterrents to obtaining and maintaining a good bond with ceramic cement or flame sprayed aluminum oxide (Al2O3), either of which may be used to attach high-temperature strain gages. The first deterrent is the very hard SiC surface finish. The simplest and least costly solution for providing a bondable surface for this material was to texture the surface with a very coarse silicon carbide abrasive powder. The second deterrent to bonding gages on this surface is the micro-cracking of the surface itself that occurs during processing of the carbon/carbon composite. When heated, these micro-cracks re-generate and cause localized stresses in the strain gage basecoat that, at times, are sufficient to shear strain gage convolutes and in some instances cause basecoat debonding. One solution for this shearing is to use a ceramic basecoat followed by a flame sprayed Al2O3 over that basecoat prior to installing the gages. However, the optimum bonding for high-temperature strain gages on SiC surfaces, thus far, has included the use of plasma-arc flame spraying of Al2O3 as the primary basecoat prior to installing the gage.

Difficulty 2 - Detachment of high-temperature strain gage exit leads (or trunk leads) from the gage has caused "gage failures" in high-temperature gages. The technique used in attaching the exit leads to the strain gage leads has not been consistent and has failed in some instances during elevated temperature testing.

Solution 2 - Figure 7 illustrates an incorrect technique for mating the strain gage lead to the exit lead. As shown, the strain gage lead encompasses the exit lead in a full 360 degree spiral and both of the spotwelder probes are spanning only the strain gage lead. A correct technique would have the strain gage lead wrapped only half way around the exit lead such that the spotwelder probes contact each of the two conductors. These failures are often reported as "gage failures" when actually it is an electrical connection problem.

Difficulty 3 - The most widely used high-temperature strain gage for aerospace test programs, to date, has been a foil type gage which has not shown an affinity for surviving numerous thermal cycles on carbon/carbon or titanium matrix composites. Additionally, its

apparent strain characteristics are such that data accuracy is compromised when mechanical strain data are recorded during temperature excursions.

Solution 3 - Temperature compensation for the apparent strains generated by high-temperature strain gages is a reasonable approach for dramatically reducing the large magnitude of these unwanted outputs riding on the mechanical and thermally generated strain signals of the gages. The remainder of this paper will address the theory of operation and use of a NASA Langley designed temperature compensated gage that is now in use in several countries.

Active/Compensating (Half-bridge) Gaging Concept

The concept to be described for reducing the apparent strains associated with high-temperature strain gages is a relatively straightforward half-bridge approach. In a Wheatstone bridge circuit, when the resistance of adjacent arms remains equal to each other, the output remains nulled. Therefore, if two strain gages having identical thermal coefficients of resistance were wired to form a half-bridge and one of the gages could be placed on a surface to be tested in a strain-free manner while the other was bonded to the surface to respond to mechanical strains, the only apparent strain would be due to the mismatch in the thermal coefficient of expansion of the bonded strain gage and the substrate. Coincidentally, this number can be quite large, but it is easily correctable with a temperature sensitive wire such as platinum. The Langley gage, installed and ready for leadwire hook-up, is shown in Figure 8. The ability to have one of the gages (compensating gage) non-responsive to mechanical strains while encountering the same temperature change as the bonded gage (active gage) is achieved via the procedure for installing both gages. This gaging procedure requires many detailed steps and, therefore, is not described in this paper. Advantages of this gaging concept include the ability to obtain static strain data during the first temperature excursion. This is due to the gages' half-bridge configuration which provides a large degree of cancellation of the non-linearity, non-repeatability, and zero shift seen with a single active gage. The approach also offers the capability of minimizing the apparent strain output throughout the temperature excursion as opposed to nulling at one temperature only, which, again is a limitation with a single element high-temperature strain gage. Finally, with the precipitous slope and the non-repeatability of the apparent strain curves of high-temperature gages reduced by an order of magnitude, data accuracy has been improved dramatically. Figure 9 is a plot comparing the magnitude of the apparent strain curves of a popular high-temperature gage and the Langley developed gage as generated on a titanium matrix test panel.

Two Beta 21S titanium/matrix panels were instrumented with 23 of these gages at Langley for testing at temperatures up to 1200°F. Test results with the panels indicated that all 23 gages produced reliable data through a series of thermal cycles with applied loads to design load limits up to the 1200°F temperature limit. The gages

measured strains at 1200°F that generally agreed with linear analysis predictions. This agreement may be seen on the load plot in Figure 10 where some measured strains were within 1 percent of the predicted strain.

SUMMARY

The NASA Langley Research Center uses an average of 14,000 strain gages a year. A large portion of these gages are in service in harsh environments, including balances in use in cryogenic wind tunnels, test articles seeing cryogenic and elevated temperature excursions during a single test scenario, and testing of aerospace materials at temperatures up to 1500°F. This paper has described several of the difficulties encountered when strain gages are required to perform accurately and reliably in these harsh environments and solutions for overcoming these difficulties. Improvements in strain gage performance, especially in extreme environments, have been achieved through fundamental, continuous, and dedicated laboratory research and development effort.

ACKNOWLEDGEMENT

The author wishes to express his appreciation to Modern Machine & Tool Company and their strain gage applications specialists whose insight and innovative wisdom provide the basis for the successful use of strain gages in very demanding environments at Langley.

REFERENCES

1. A.T. Ferris, T.C. Moore, Sr.: FORCE INSTRUMENTATION FOR CRYOGENIC WIND TUNNELS USING ONE-PIECE STRAIN-GAGE BALANCES. ISA 27th International Instrumentation Symposium, April 1981

2. A.T. Ferris: CRYOGENIC STRAIN GAGE TECHNIQUES USED IN FORCE BALANCE DESIGN FOR THE NATIONAL TRANSONIC FACILITY. NASA Technical Memorandum 87712

3. T.C. Moore: PRACTICAL APPROACHES FOR APPLICATION OF STRAIN GAGES ON EXTREME TEMPERATURE NASP CANDIDATE MATERIALS. NASA Technical Memorandum 1134

4. H.K. Holmes, T.C. Moore: HIGH TEMPERATURE STRAIN GAGE APPARENT STRAIN COMPENSATION. Langley Measurement Technology Conference, April 1992

5. D. Seidensticker, T.M. Wilson, T.W. Hesterman, G.P. Clifft: TESTING OF TMC STRUCTURAL COMPONENTS. 1993 NASP Technology Review

6. T.C. Moore: DEVELOPMENT OF A TEMPERATURE COMPENSATED HIGH-TEMPERATURE STRAIN GAGE. Society for Experimental Mechanics, Fall Conference, November, 1993

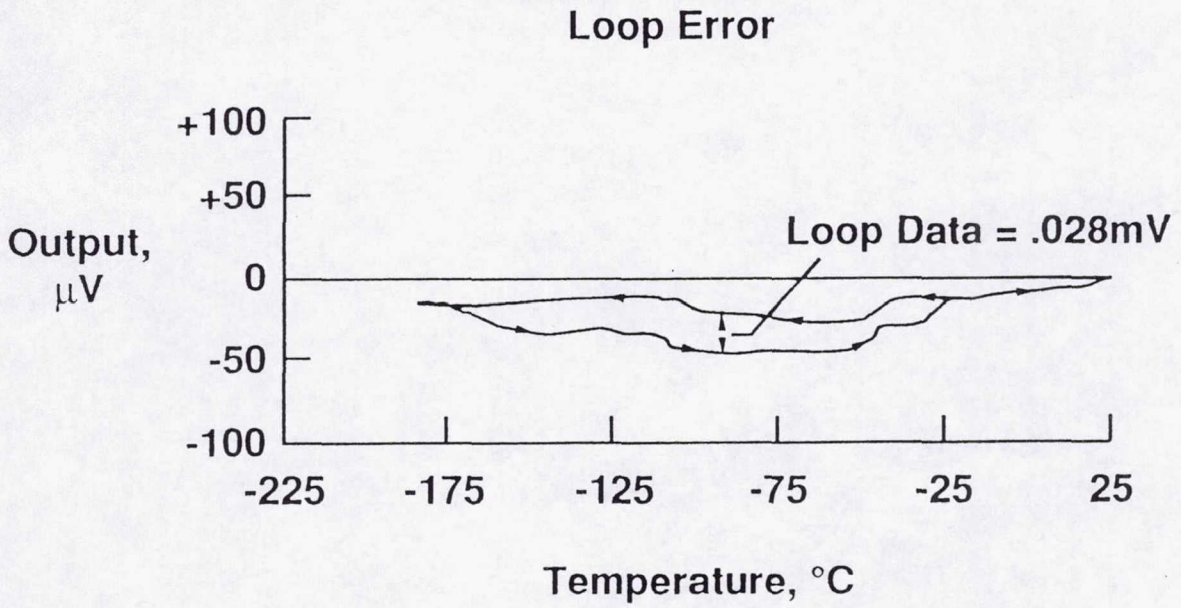

Figure 1 "Loop" Error Associated with Transient Temperatures

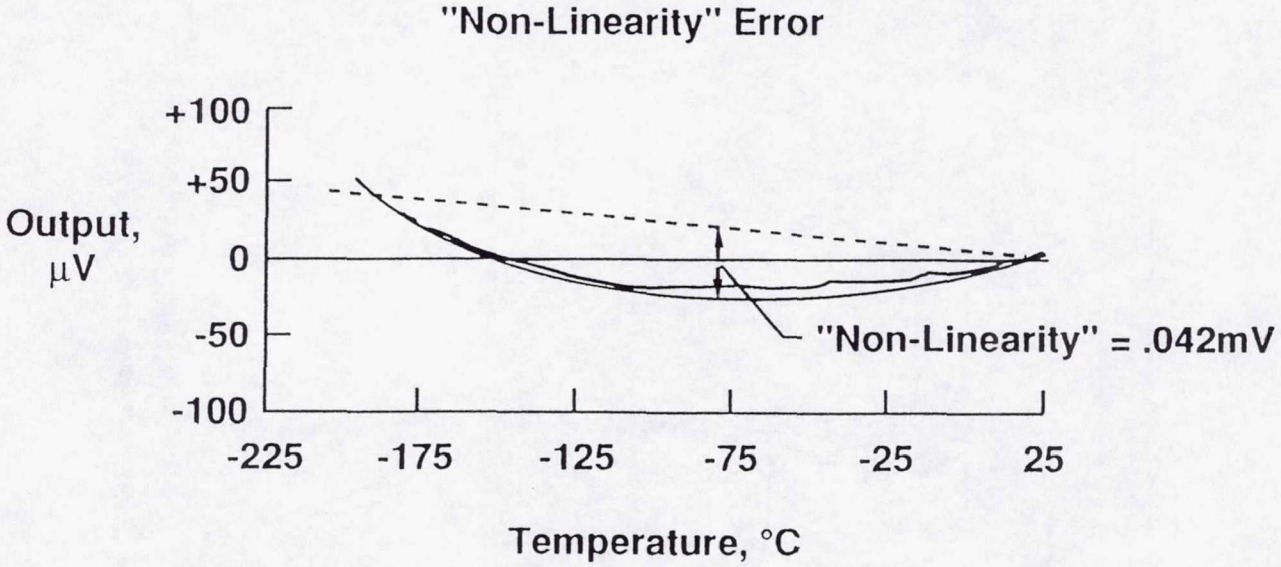

Figure 2 "Non-Linearity" Error Associated with Transient Temperatures

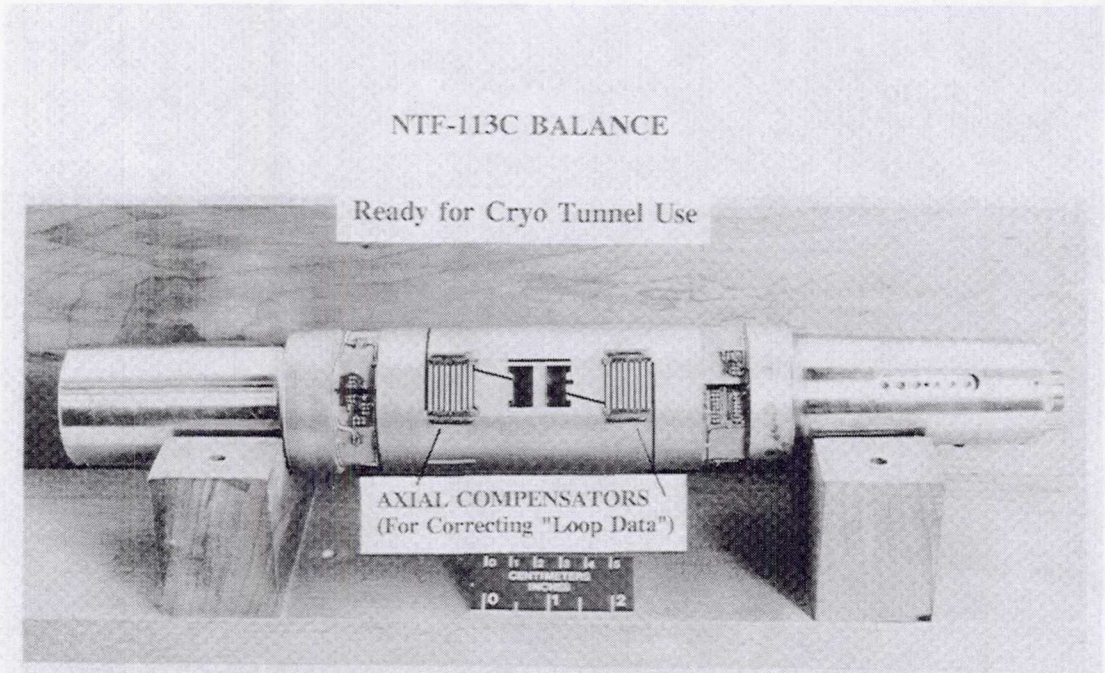

Figure 3

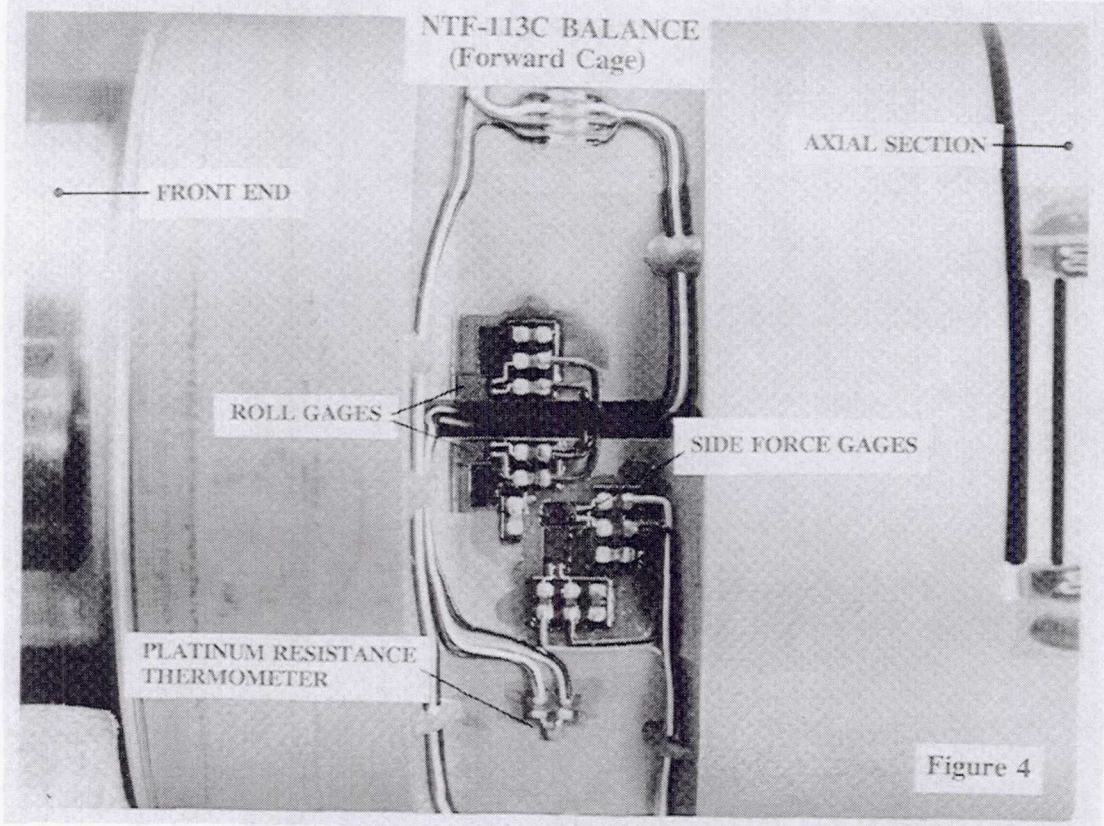

Figure 4

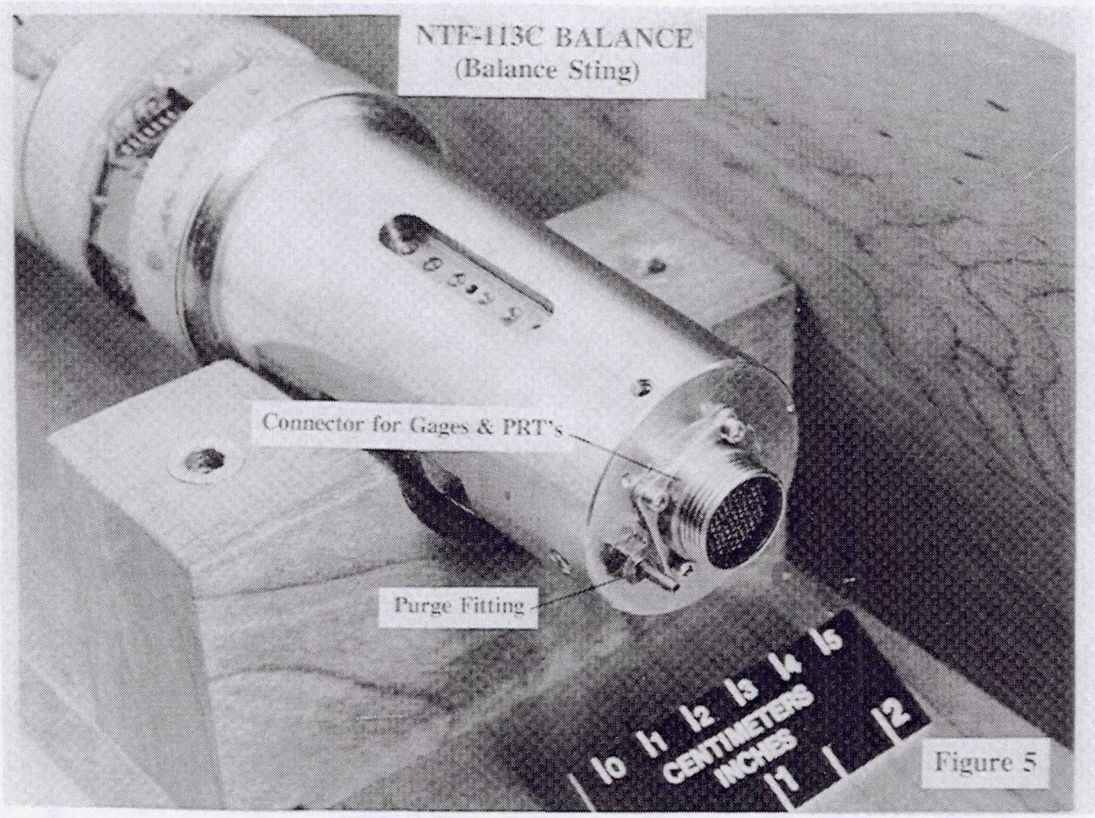

Figure 5

NASA

Aluminum-Lithium Cruciform Panel

Close-up of Single Element & Rosette Gages

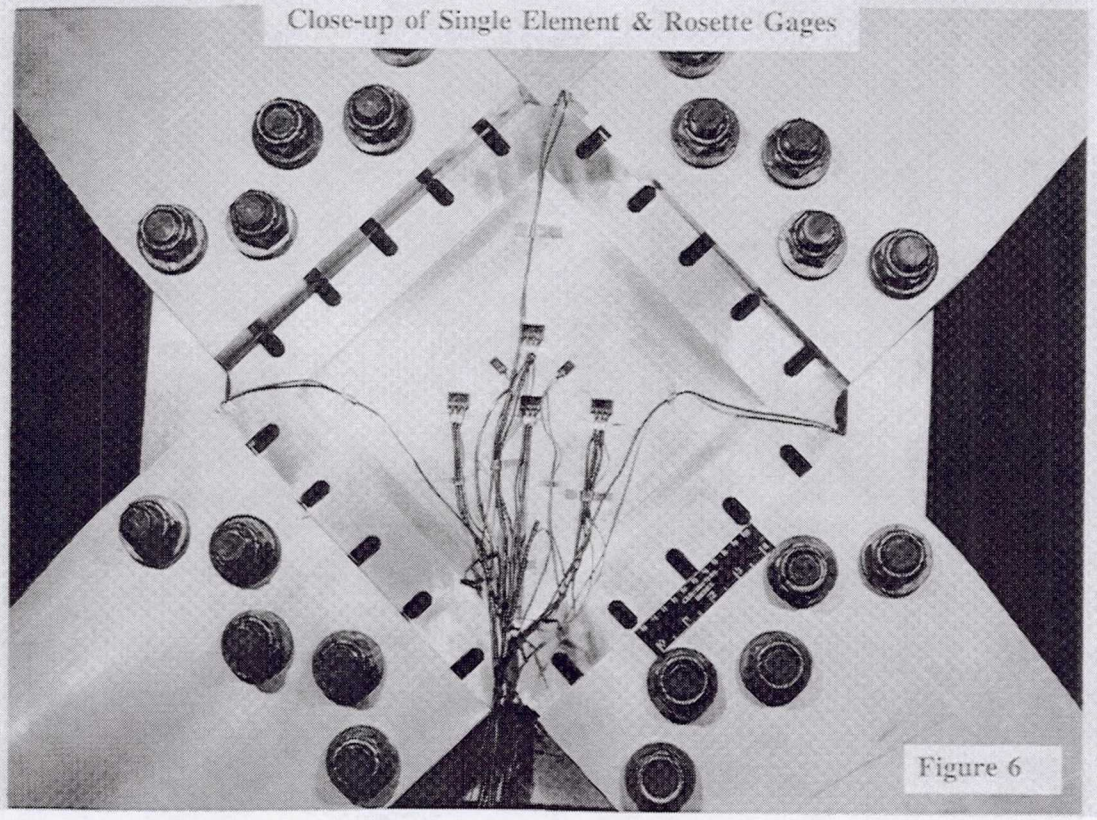

Figure 6

HI-TEMP. LEADWIRE ATTACHMENT TO A HI-TEMP. STRAIN GAGE

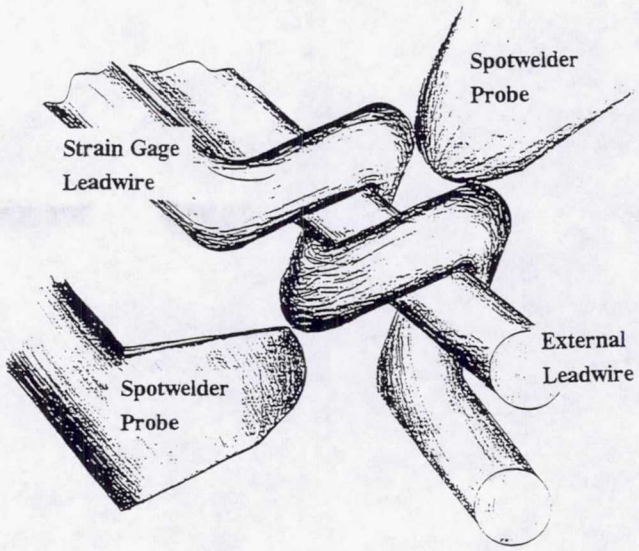

NOTE THAT SPOTWELDER PROBES CAN
ONLY CONTACT ONE WIRE CONDUCTOR

Figure 7

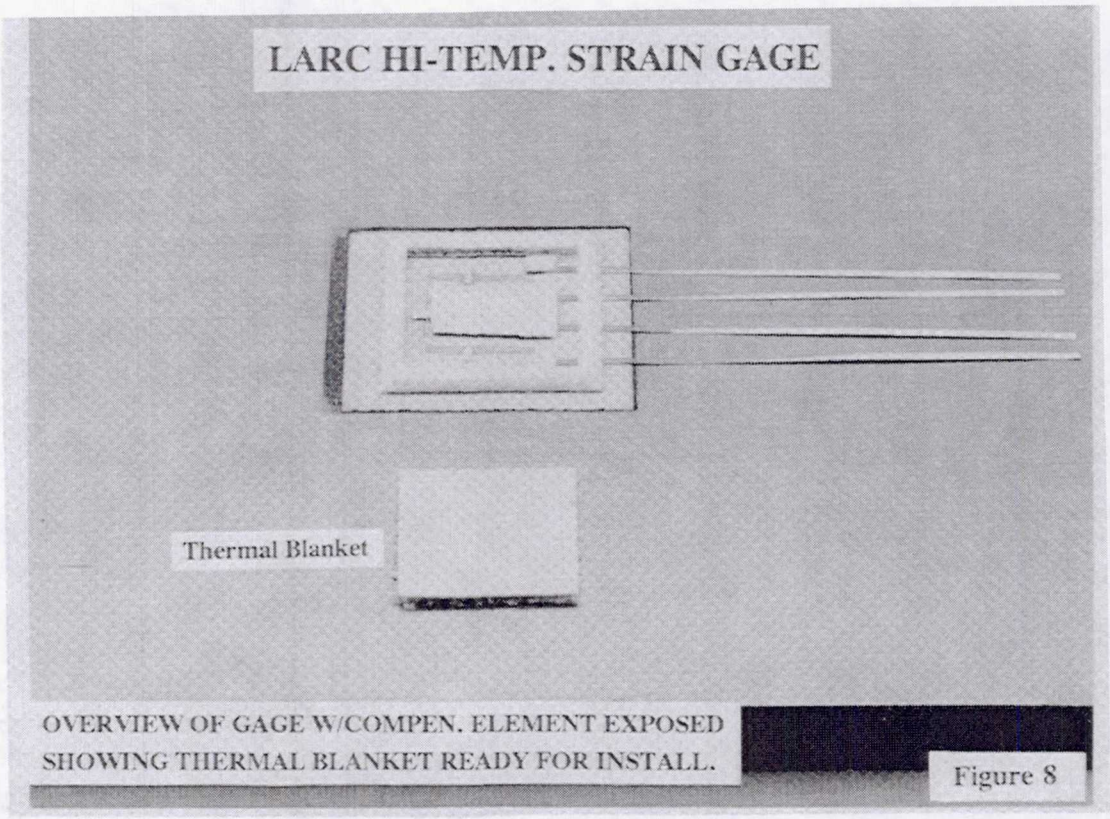

OVERVIEW OF GAGE W/COMPEN. ELEMENT EXPOSED
SHOWING THERMAL BLANKET READY FOR INSTALL.

Figure 8

LaRC COMPENSATED GAGE AND NZ UNCOMPENSATED GAGE

Apparent Strain Comparisons

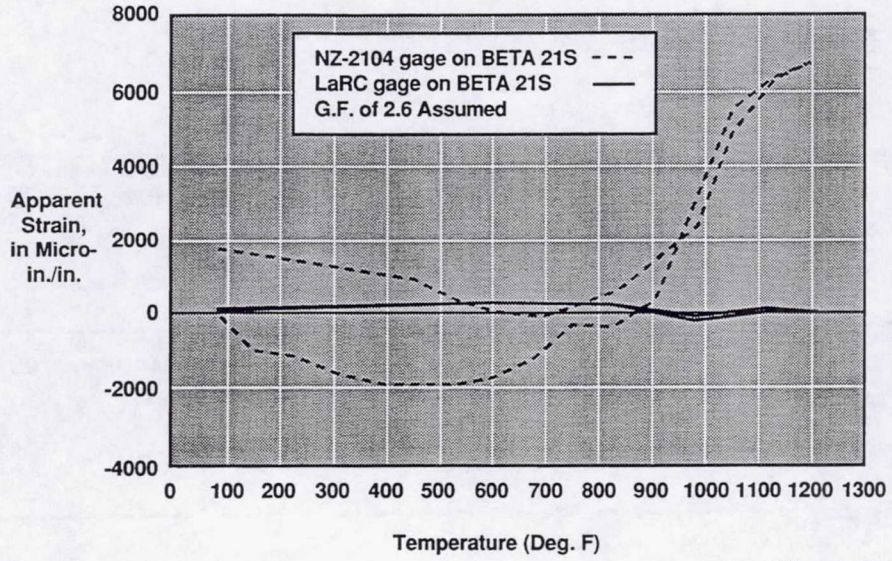

Figure 9

NET MECHANICAL STRAIN TO 100 % DLL AT 1200° F-STRAIN GAGE NUMBER TEN (EXPERIMENTAL)

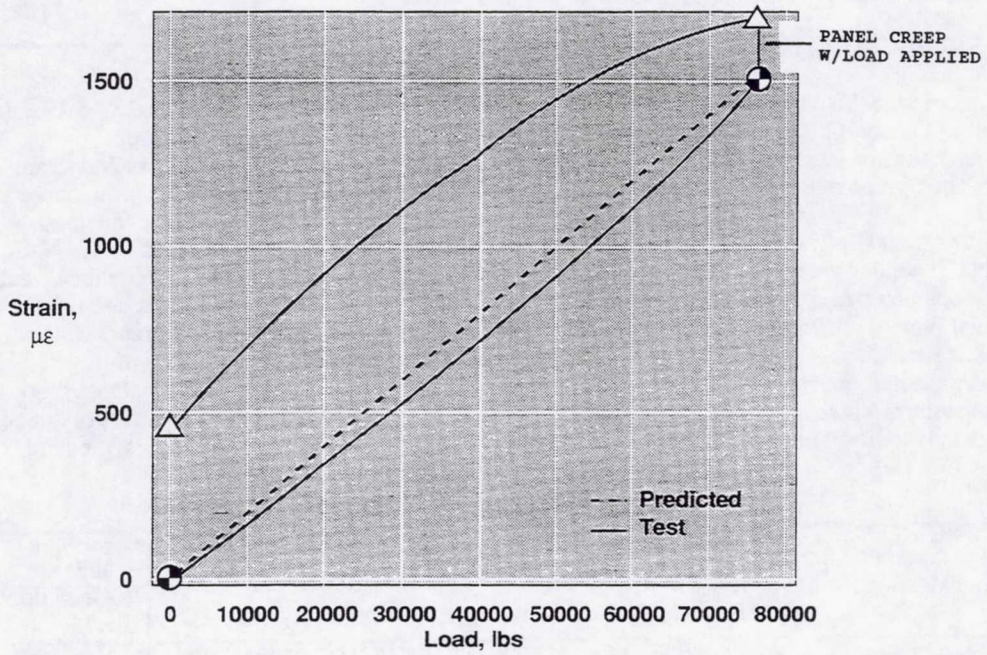

Figure 10

REPORT DOCUMENTATION PAGE

Form Approved
OMB No. 07704-0188

1. AGENCY USE ONLY *(Leave blank)*	2. REPORT DATE	3. REPORT TYPE AND DATES COVERED
	March 1999	Conference Publication

4. TITLE AND SUBTITLE
First International Symposium on Strain Gauge Balances

5. FUNDING NUMBERS
992-35-12-18

6. AUTHOR(S)
John S. Tripp and Ping Tcheng, Editors

7. PERFORMING ORGANIZATION NAME(S) AND ADDRESS(ES)
NASA Langley Research Center
Hampton, VA 23681-2199

8. PERFORMING ORGANIZATION REPORT NUMBER
L-17809A

9. SPONSORING/MONITORING AGENCY NAME(S) AND ADDRESS(ES)
National Aeronautics and Space Administration
Washington, DC 20546-0001

10. SPONSORING/MONITORING AGENCY REPORT NUMBER
NASA/CP-1999-209101/PT 1

11. SUPPLEMENTARY NOTES

12a. DISTRIBUTION/AVAILABILITY STATEMENT
Unclassified–Unlimited
Subject Category 35 Distribution: Standard
Availability: NASA CASI (301) 621-0390

12b. DISTRIBUTION CODE

13. ABSTRACT ***(Maximum 200 words)***

The first International Symposium on Strain Gauge Balances was sponsored and held at NASA Langley Research Center during October 22-25, 1996. The symposium provided an open international forum for presentation, discussion, and exchange of technical information among wind tunnel test technique specialists and strain gauge balance designers. The Symposium also served to initiate organized professional activities among the participating and relevant international technical communities. Over 130 delegates from 15 countries were in attendance. The program opened with a panel discussion, followed by technical paper sessions, and guided tours of the National Transonic Facility (NTF) wind tunnel, a local commercial balance fabrication facility, and the LaRC balance calibration laboratory. The opening panel discussion addressed "Future Trends in Balance Development and Applications." Forty-six technical papers were presented in 11 technical sessions covering the following areas: calibration, automatic calibration, data reduction, facility reports, design, accuracy and uncertainty analysis, strain gauges, instrumentation, balance design, thermal effects, finite element analysis, applications, and special balances. At the conclusion of the Symposium, a steering committee representing most of the nations and several U.S. organizations attending the Symposium was established to initiate planning for a second international balance symposium, to be held in 1999 in the UK.

14. SUBJECT TERMS	15. NUMBER OF PAGES
Proceedings; Symposium; Strain gauge balance; Wind tunnel instrumentation; Aerodynamic testing	443
	16. PRICE CODE A19

17. SECURITY CLASSIFICATION OF REPORT	18. SECURITY CLASSIFICATION OF THIS PAGE	19. SECURITY CLASSIFICATION OF ABSTRACT	20. LIMITATION OF ABSTRACT
Unclassified	Unclassified	Unclassified	UL